

University of Cape Town

a dissertation submitted in fulfilment of the degree of

Doctor of Philosophy

in the Department of Geological Sciences

High-temperature metamorphism in the western Namaqua–Natal Metamorphic Province (South Africa): implications for low–pressure granulite terranes

University of Cape Town

Author
Simon Schorn

Supervisor
Dr Johann Diener

Cape Town

June 11, 2019

The copyright of this thesis vests in the author. No quotation from it or information derived from it is to be published without full acknowledgement of the source. The thesis is to be used for private study or non-commercial research purposes only.

Published by the University of Cape Town (UCT) in terms of the non-exclusive license granted to UCT by the author.

University of Cape Town

Plagiarism Declaration

I know the meaning of plagiarism and declare that all of the work in the dissertation, save for that which is properly acknowledged, is my own.

Signed by candidate

Declaration of free licence

I hereby:

1. grant the University free license to reproduce the above thesis in whole or in part, for the purpose of research;
2. declare that:
   (a) the above thesis is my own unaided work, both in conception and execution, and that apart from the normal guidance from my supervisor, I have received no assistance except as stated below;
   (b) neither the substance nor any part of the thesis has been submitted in the past, or is being, or is to be submitted for a degree at this University or at any other University, except as stated below.

I am now presenting the thesis for examination for the Degree of PhD.

Do. Or do not. There is no try.
–Yoda

Abstract

The interpretation of pressure (P)–temperature (T)–time (t) data is key to reconstruct the geologic evolution of ancient exhumed orogens. Of these, temperature is regarded as proxy for the heat energy available during orogenic metamorphism. Heat – the ultimate driving force of metamorphism – is consumed by a number of processes occurring during orogeny. Metamorphic rocks evolve through chemical reactions that consume energy in order to advance. As long as strongly energy-intensive processes advance in the crust, the temperature that is effectively attained is controlled by the interplay between the rate of heat energy supplied to the site of reaction and the rate of heat consumed by the process(es). Melting reactions in particular are strongly endothermic and consume a substantial proportion of the orogenic heat budget. Fertile metapelites are volumetrically minor but petrologically significant, as P–T–t–deformation constraints and burial-exhumation paths are preferentially derived from this lithology, whereas refractory granites *sensu lato* compose the bulk of orogenic crust. Metapelites are affected by a number of heat-consuming reactions that cause a near-isothermal state as long as they advance, however granites intersect few endothermic melt-producing reactions during orogenic metamorphism. Granitoids therefore may effectively reach a higher temperature compared to metapelites exposed to the same heat input. Temperature determined from metapelites may therefore not represent the true thermal maximum experienced by a portion of metamorphic crust – especially in granulite terranes where partial melting is widespread. Because temperature is an effect rather than the cause of heat energy transferred into the crust, it may not represent the most geodynamically relevant parameter to describe metamorphism.

In this study a suite of supracrustal litholgies from the Bushmanland Subprovince (BSP) of the Namaqua–Natal Metamorphic Province (NNMP) of southern Africa are investigated via thermodynamic modelling and zircon–monazite U–Pb in-situ geochonology. Regional P–T–t distribution reveals a complex polyphasic evolution with two major tectonometamorphic episodes at ∼1.2–1.1 and 1.04–1.0 Ga, respectively. The older event is temporally linked to the emplacement of the felsic pre- to syn-tectonic Little Namaqualand Suite that caused widespread greenschist- to amphibolite facies contact metamorphism. This is recorded in garnet–cordierite–sillimanite gneisses exposed at the northernmost locality investigated here and as cm-sized porphyroblasts (e.g. andalusite) hosted in rare Mg–Al-rich gneisses. The younger event is characterised by granulite facies metamorphism peaking at 1040–1000 Ma in the entire BSP, with pelitic granulites recording variable apparent temperatures of between ∼760 and <900 °C at 5–6 kbar.

Coarse-grained porphyroblasts of andalusite in an example of Mg–Al-rich gneiss were replaced by symplectites of high-grade phases during heating at the granulite event. At upper-greenschist facies conditions the immobility of Al caused the formation of monomineralic coronae at the expense of andalusite, effectively isolating the porphyroblasts from the matrix. Diffusion of Fe + Mg along respective gradients of μFe and μMg with simultaneous immobility of Al + Si led to the breakdown of andalusite to symplectites of cordierite + spinel during near-isobaric heating to peak conditions. Monomineralic coronae of sapphirine developed during near-isobaric cooling at the expense of previously-formed symplectites.

Detailed investigation of a conformable sequence of sedimentary and mafic granulites from the locality Hytkoras in central Bushmanland reveal a disparity of some 60–70 °C in estimated peak metamorphic temperature. Aluminous metapelites equilibrated at ∼770–790 °C whereas two-pyroxene granulite and garnet–orthopyroxene–biotite gneiss record distinctly higher conditions of ∼830–850 °C. Semipelite and Mg–Al-rich gneisses yield poorly-constrained estimates that span the range derived from other lithologies. All samples record peak pressure of ∼5–6 kbar, and followed a roughly isobaric heating path from andalusite-greenschist / lower-amphibolite facies conditions through a tight clockwise loop at near-peak conditions, followed by near-isobaric cooling. The disparity in peak temperatures appears to be robust, as the low-variance assemblages in all samples reflect well-known melting reactions that only occur over narrow temperature intervals. The stable coexistence of both products and reactants of these melting reactions indicates that they did not go to completion before metamorphism waned.

Calculated pressure–enthalpy diagrams show that the melting reactions are strongly endothermic and therefore buffer temperature while heat is consumed by melting. Because the respective reactions occur at distinct P–T conditions and have different reactant assemblages, individual lithologies are thermally buffered at different temperatures and to different degrees, depending on the occurrence and abundance of reactant minerals. If little to no thermal communication is assumed, this implies that lithology exerts a first-order control over the heating path and the peak temperature that can be attained for a specific heat budget. Calculations show that all lithologies received essentially the same suprasolidus heat budget of 19 $\pm$ 1 kJ.mol^{-1}, which led to manifestation of lower peak temperatures in the more fertile and strongly buffered aluminous metapelites compared to more refractory rock types.

The heat source responsible for near-isochronous high-grade metamorphism at a regional scale most likely was a mixture of mafic mantle underplating combined with radiogenic heating in a slowly buried juvenile crust. Heat transfer to higher levels of the crust was aided by advective heating via the syn-metamorphic emplacement of the post-tectonic Spektakel Suite that locally led to near-ultrahigh temperature (UHT) conditions recorded by proximal pelitic granulites. The overall characteristics of the BSP, namely (i) heating from shallow low-grade conditions to granulite facies temperatures at a maximum depth of $\sim$20 km along a roughly isobaric heating path with minor concomitant burial, (ii) seemingly coeval peak metamorphism recorded at a regional scale that was accompanied/preceded by voluminous felsic magmatism (iii) that was followed by (iv) slow, largely isobaric cooling to an ambient geotherm with no significant attending exhumation, are consistent with a long-lived evolution in a continental back-arc mobile belt setting.

Contents

1 Introduction **1**
1.1 Heat and temperature – two sides of the same coin? . . . 1
1.2 Aims of the thesis . . . 3

2 The concept of thermal buffering **5**
2.1 Phase diagram modelling . . . 7
2.2 Thermal model . . . 7
2.3 Results . . . 9
2.3.1 Magnitude of thermal retardation . . . 9
2.3.2 Critical length and time scales . . . 13
2.3.3 Melt loss versus retention . . . 13
2.3.4 Convergence of orogenic temperatures . . . 16
2.3.5 Implications for the thermal and rheological structures of orogens . . . 16

3 The Namaqua–Natal Metamorphic Province (NNMP) **17**
3.1 Tectono-metamorphic architecture of the Namaqua Sector . . . 17
3.1.1 Bushmanland Subprovince . . . 17
3.1.2 Richtersveld Subprovince . . . 20
3.1.3 Kakamas Domain . . . 21
3.1.4 Aus Domain . . . 22
3.1.5 Areachap Domain . . . 22
3.1.6 Kaaien Domain . . . 23
3.2 Structural evolution of the Namaqua Sector . . . 23
3.3 Geodynamic setting of the Namaqua Sector . . . 24
3.4 Regional-scale sampling . . . 26
3.4.1 Field occurrence of aluminous metapelites . . . 26
3.5 Detailed sampling – Hytkoras . . . 31

4 Petrography and mineral chemistry **40**
4.1 Regional sampling – aluminous metapelites . . . 40
4.1.1 Lepel se Kop . . . 40
4.1.2 Paulshoek . . . 42
4.1.3 Nababeep . . . 45
4.1.4 Ratelpoort . . . 46
4.1.5 Geselskapbank . . . 48
4.2 Hytkoras . . . 52
4.2.1 Aluminous metapelites . . . 52

4.2.2 Magnesian metapelite . . . 55
4.2.3 Semi-metapelite . . . 56
4.2.4 Metagreywacke . . . 58
4.2.5 Mafic granulites . . . 59
4.2.6 Magnesian gneisses . . . 61
4.2.7 Other magnesian gneisses . . . 62
4.3 Inferred equilibrium assemblages . . . 67
4.3.1 Regional sampling – aluminous metapelites . . . 67
4.3.2 Detailed sampling – Hytkoras . . . 70

5 Phase equilibrium modelling **73**
5.1 Considerations for modelling . . . 73
5.1.1 Residuum compositions . . . 73
5.1.2 Protolith compositions . . . 75
5.1.3 Selected magnesian gneisses . . . 75
5.2 Modelling results . . . 76
5.2.1 Residuum compositions – aluminous metapelites . . . 76
5.2.2 Residuum compositions – Hytkoras . . . 81
5.2.3 Protolith compositions – Hytkoras . . . 85
5.2.4 Simplified magnesian gneiss compositions . . . 89

6 Zircon and Monazite geochronology and geochemistry **92**
6.1 Zircon and monazite morphology and petrography . . . 92
6.2 U–Pb geochronology – results . . . 97
6.2.1 Lepel se Kop . . . 97
6.2.2 Paulshoek . . . 98
6.2.3 Hytkoras . . . 100
6.2.4 Nababeep . . . 103
6.2.5 Ratelpoort . . . 103
6.2.6 Geselskapbank . . . 106

7 P–T–t distribution and metamorphic evolution of the Namaqua Sector **110**
7.1 Regional P–T evolution . . . 110
7.2 Hytkoras . . . 115
7.2.1 Pseudomorph-formation in magnesian gneisses . . . 118
7.3 Timescales of sedimentation and metamorphism . . . 127
7.3.1 Detrital age spectra and origin of detritus . . . 127
7.3.2 Timing of regional high-T–low-P metamorphism . . . 130

8 Concluding remarks **134**
8.1 Tectonometamorphic characteristics of the Namaqua Sector . . . 134
8.1.1 Temporal relationship between sedimentation and metamorphism . . . 136
8.1.2 Correlation of plutonism and metamorphism . . . 138
8.2 Thermal buffering at the outcrop scale . . . 141
8.2.1 Contrasting peak temperatures in coexisting rocks? . . . 141
8.2.2 Calculated pressure–enthalpy relations . . . 143
8.2.3 A common enthalpy budget to account for disparate temperatures . . . 146
8.2.4 Could the same apparent disparity be achieved by melt retention? . . . 146

8.2.5 Length scale of thermal buffering 148
8.2.6 Implications for thermobarometry 149
8.3 Thermal buffering at the regional scale 149
8.3.1 Implications of apparent peak temperature on potential heat sources . 149
8.3.2 Relationship of P–T path and apparent peak temperature 153
8.3.3 Preconditioning and polymetamorphism 154

References **157**

A Enthalpy calculations in THERMOCALC **178**

B Methods **180**
B.1 Mineral chemistry determination 180
B.2 Bulk rock composition determination 180
B.3 Phase diagram modelling 181
B.4 Zircon and Monazite geochronology and geochemistry 181
B.4.1 Sample preparation 181
B.4.2 Laser ablation split stream inductively coupled plasma mass spectrometry (LASS ICP-MS) 182

C Mineral chemical data **185**

D U–Pb isotopic and geochemical data **203**

E Evolution of a_{H_2O} during granulite metamorphism **226**

F Acknowledgements **229**

Chapter 1

Introduction

1.1 Heat and temperature – two sides of the same coin?

Metamorphic rocks record a most complex history defined by changes of pressure (P), temperature (T) and deformation in time (t). These are key in understanding the evolution of the crust and the active processes that shaped the Earth as we see it today. Progressive metamorphism is the continuous re-organisation of elements in minerals with changing ambient conditions in the Earth. These conditions are controlled by the geodynamic environment in which the rocks have formed, with specific crustal processes involving a specific pressure and temperature transformation path, which will, in turn, translate into diagnostic compositional and textural attributes. Using samples of exhumed ancient orogens, metamorphic petrologists attempt to retrace the evolution of the orogenic crust through time, as the birthplace of the studied rocks is effectively inaccessible. Historically, pressure and temperature conditions have been estimated through what is considered 'conventional thermobarometry', based on inter-mineral exchange of major elements (e.g. Fe–Mg, Na–Ca, Si–Al, etc.). These thermobarometers are commonly based on natural observations and/or calibrated against experimental results in simplified chemical systems, and often ignore the effect of minor, but crucial components (e.g. ferric vs. ferrous iron). Additionally, calibrations based on major element exchange have a rather low closure temperature that might be inferior to the maximum temperature attained during metamorphism, making them inaccurate in retracing the true metamorphic evolution of natural samples (e.g. Fitzsimons and Harley, 1994; Frost and Chako, 1989). Solvus-based thermometers are affected by similar caveats (Bohlen and Essene, 1979).

To bypass these shortcomings, thermometers based on slowly-diffusing trace elements in accessory minerals (e.g. Zr-in-rutile, Ti-in-zircon, Zr-in-titanite; Zack *et al.*, 2004; Watson *et al.*, 2006; Hayden *et al.*, 2008) have recently been developed. Although they are found to better constrain orogenic parameters, even for extreme metamorphism, they only offer a limited view – a 'snapshot' – of a much more complex evolution through P–T space. In contrast to this classic inverse modelling discussed so far, forward pseudosection-modelling

based on bulk rock composition allows for a more complete investigation of metamorphic rocks and reaction textures in particular. This approach allows to predict the potential mineral assemblages a specific rock would ideally host in function of pressure and temperature. This method not only bypasses retrograde compositional re-equilibration of assemblages, but allows to interpret a large range of petrological information (e.g. mineral compositional zoning, pseudomorphs after low-grade phases, mineral inclusions in porphyroblasts, etc.) in terms of P–T evolution (Powell and Holland, 1994, 2008).

Conventionally, the pressure values calculated from natural specimens are taken as direct proxy for the depth of rock formation. However, several recent contributions have stressed the fact that the pressure calculated from mineral compositions may actually not directly translate to depth, due to what is known as tectonic overpressure (i.e. pressure larger than lithostatic pressure; e.g. Moulas *et al.*, 2013; Yamato and Brun, 2017; Reuber *et al.*, 2016, and references therein). Moreover, heterogeneous pressure distribution at the grain-scale is suggested to control the formation and preservation of 'disequilibrium' textures such as symplectites, coronae and chemical zoning patterns (e.g. Vrijmoed and Podladchikov, 2015; Tajčmanová *et al.*, 2015) which may lead to erroneous pressure estimates. Similarly, temperature is a mere manifestation of the thermal properties of rocks and the locally available heat, and the thermal properties of the material affected by heat flow might have a more far-reaching effect on the attainable temperature than perhaps previously assumed. So what do the determined pressure and temperature actually mean?

These thermodynamic parameters are routinely constrained from metamorphic rocks preserved in ancient orogens, and metapelites are traditionally favoured for this task because of the large number of P–T-sensitive mineral assemblages that occur in these lithologies (e.g. Harley, 1998; Brown, 2007; Brown and Johnson, 2018, and references therein). In contrast to their petrological significance, metapelites are volumetrically negligible in comparison to (meta-)granitoids that constitute the bulk of the continental crust; nevertheless metamorphic conditions deduced from metapelites are conventionally extrapolated and assumed for large areas where other lithologies might dominate.

Unlike the volumetrically dominant rock types, metapelites encounter a number of sub- and suprasolidus reactions that are strongly endothermic (e.g. Thompson and Connolly, 1995; Lyubetskaya and Ague, 2009). Melting reactions are known to be particularly endothermic (e.g. Vielzeuf *et al.*, 1990; Stüwe, 1995; Thompson and Connolly, 1995; Bea, 2012), and metapelites are preferentially affected by these under granulite facies conditions (e.g. Clemens and Vielzeuf, 1987; White *et al.*, 2001; Diener *et al.*, 2014b; Yakymchuk and Brown, 2014). Seeing how melting requires substantial amounts of energy, it seems likely that strongly endothermic reactions might influence the temperature recorded in fertile lithologies and metapelites may ultimately reach lower temperatures compared to coexisting, more refractory lithologies such as metagranitoids (Schorn *et al.*, 2018). Therefore, metapelites might not provide the most appropriate record of orogenic conditions, particularly in high-grade granulite terranes where partial melting is widespread (Schorn *et al.*, 2018).

Similarly, this has been observed for ultrahigh-temperature (UHT) rocks, for which conditions are typically inferred from rare diagnostic mineral assemblages found in unusual and volumetrically minor Mg–Al-rich rocks (e.g. Kelsey and Hand, 2015; Kelsey, 2008). The refractory nature of these bulk compositions implies limited melting and associated thermal retardation (Vielzeuf *et al.*, 1990; Harley, 1998; Kelsey and Hand, 2015), potentially allowing them to record a higher apparent metamorphic temperature compared to relatively fertile host rocks (Schorn *et al.*, 2018), such as ordinary gneisses (e.g. Tsunogae and Santosh, 2003; Mouri *et al.*, 2003; Santosh *et al.*, 2004; Nishimiya *et al.*, 2010; Nakano *et al.*, 2011) or metapelites (e.g. Santosh *et al.*, 2007; Rao *et al.*, 2012).

This has been previously alluded to by Rao *et al.* (2012) where discrete lenses of Mg–Al-rich sapphirine–quartz granulites are found in ordinary metapelites (khondalites). Equilibration conditions of 620–880 °C and 4–11 kbar are constrained for the metapelite hostrock, whereas UHT conditions of >1000 °C at 10 kbar are estimated from the Mg–Al-gneisses. Rao *et al.* (2012) extrapolate the inferred UHT conditions to the entire region, ascribing the apparent discrepancy of more than 100 °C to retrogression of the metapelites due to residual melt crystallization. Nevertheless, it could alternatively be argued that the spread in apparent temperature is, at least in part, due to thermal buffering of the metapelites through partial melting, such that the metapelites never recorded UHT conditions even when the Mg–Al lithology did (cf. Kelsey and Hand, 2015; Schorn *et al.*, 2018).

1.2 Aims of the thesis

The main objective of this study is the investigation of the thermal consequences of major melting reactions in a classic low-P–high-T terrane, through a combined multi-scale approach using conventional thermodynamic modelling and U–Pb geochronology. For this purpose, I investigated a series of P–T–t estimates for a variety of lithologies preserved in the high-grade Namaqua Sector of the Namaqua–Natal Metamorphic Province (NNMP) in South Africa. The NNMP is a Grenvillian-aged, Mesoproterozoic (∼1.1 Ga) metamorphic mobile belt related to the assembly of the supercontinent Rodinia (e.g. Li *et al.*, 2008) that correlates with similar terranes in east Antarctica (Jacobs *et al.*, 1993, 2008; Thomas *et al.*, 1994). The NNMP is classified as so-called 'hot orogen', with high geothermal gradients (dP/dT) of up to 1500 °C.GPa^{-1} (e.g. Brown, 2001, 2006, 2007; Brown and Johnson, 2018, and references therein). The rock record suggests that geothermal gradients were particularly elevated in Precambrian times, with a maximum in the mid-Mesoproterozoic. This was probably due to thermal insulation of the mantle beneath the supercontinent of Columbia, prior to the assembly of Columbia into Rodinia (Brown and Johnson, 2018). The NNMP therefore is, as many granulite terranes characterising hot orogens, temporally linked to supercontinent assembly (Li *et al.*, 2008; Clark *et al.*, 2015; Sizova *et al.*, 2014). Hot orogens typically experience high-temperature–low-pressure metamorphism that involves roughly isobaric heating and cooling along hairpin clockwise or anticlockwise paths (e.g. Waters, 1989; Cagnard *et al.*,

2007; Chardon *et al.*, 2009). Metamorphic conditions are commonly laterally homogeneous and recorded over a vast areal extent (Waters, 1989; Nironen, 1997; Cagnard *et al.*, 2007). Long-lived (>80 Ma) and/or repeated juvenile magmatism and high-grade metamorphism is typically coeval with crustal shortening (e.g. Cagnard *et al.*, 2007; Collins and Vernon, 1991; Dumond *et al.*, 2007; Chardon *et al.*, 2009, and references therein). Deformation is distributed rather than localised and accommodated by three-dimensional flow of a viscous lower crust (Chardon *et al.*, 2009), forming generally regional anastomosed transpressive shear zones exposed at the present-day surface (Gapais *et al.*, 2005, 2008; Chardon *et al.*, 2009, and references therein). Both heating- and cooling path commonly overlap geotherms, with generally limited topography-building followed by exhumation of the high-grade units via distributed erosion, rather than orogenic collapse (e.g. Gapais *et al.*, 2009).

The Namaqua Sector is a typical granulite terrane, which experienced long-lived high grade metamorphism characterised by roughly isobaric heating and cooling (e.g. Waters, 1986b, 1989; Raith and Harley, 1998; Diener *et al.*, 2013). The relatively simple P–T history, combined with a well-preserved stratigraphic sequence containing diverse lithologies makes the Namaqua Sector an ideal case study to explore the potential influence of partial melting in determining metamorphic temperature.

An introduction into the geological background of the NNMP, including a macroscopic description of the sampled rock types is given in chapter 3, followed by a more detailed petrographic description (chapter 4) of the samples used for P–T determination via conventional thermodynamic modelling (chapter 5). A temporal framework of the crustal processes including sedimentation and metamorphism in the Namaqua Sector was constrained through zircon and monazite U–Pb geochronology (chapter 6) followed by a discussion of the time-integrated metamorphic evolution at the regional scale with particular focus on a key locality (chapter 7). Subsequently the thermal effect of melting reactions on recorded peak temperatures with consequences for thermobarometry are discussed in terms of local metamorphic heat budget including an extrapolation to the regional scale with implications on possible heat sources (chapter 8).

Chapter 2

The concept of thermal buffering

Temperature attained during metamorphism is a function of the thermal properties of the rocks combined with locally-available heat, e.g. via regional heat flow. Heat is consumed through (i) the diffusion of elements, (ii) the nucleation and growth of new phases and, in high-grade environments, (iii) partial melting. Only after these processes are accounted for can heat be translated into temperature. At equilibrium, rocks cannot exceed the temperature of a reaction before it has gone to completion. Similarly, for a constant regional heat flow, the heat consumed by a reaction retards the rate at which temperature increases (Fyfe *et al.*, 1978; Ridley, 1986; Vielzeuf *et al.*, 1990; Stüwe, 1995). Partial melting is by far the most energy intensive process that occurs in the orogenic crust, because the latent heat of fusion ($\sim$400 kJ.kg^{-1}; Bea, 2012, and references therein) must be overcome to generate melt. Consequently, considerable energy is required to produce even small amounts of granitic melt ($\sim$1.08x10^{15} kJ.km^{-3}; Bea, 2012). Granite production in, and its appearance above, high-grade metamorphic terranes is linked to the partial melting of fertile lithologies such as metasedimentary rocks (Vielzeuf *et al.*, 1990; Brown, 2010). Melt production in these lithologies is continuous but episodic, with most melting occurring at reactions involving the breakdown of specific hydrous minerals (e.g. Vielzeuf and Holloway, 1988; Yakymchuk and Brown, 2014).

Although the general effect of reaction heat on the large-scale thermal evolution of metamorphic terranes has long been known (Ridley, 1986; Zen, 1988; De Yoreo *et al.*, 1989; Thompson and Connolly, 1995; Lyubetskaya and Ague, 2009), the overall conclusion of those studies is that heat of reaction is generally subordinate in the total heat budget of an evolving portion of orogenic crust unless partial melting occurs (Stüwe, 1995). However, the thermal effect of specific endothermic reactions occurring in rock types that constitute orogenic crust has not been quantified. This becomes highly relevant when one considers that the very same rocks that are used to derive the geodynamic parameters of orogens (i.e. metapelites) are affected by a number of strongly endothermic reactions (e.g. Thompson and Connolly, 1995) relative to the rocks that are volumetrically dominant, such as granitoids.

In this chapter this issue is addressed by using modern thermodynamics data sets to

quantify the thermal consequences of partial melting in fertile metapelites. The results are then compared to the thermal evolution of more refractory granitoids undergoing the same metamorphism.

Metamorphic rocks are routinely used to quantify the pressure–temperature (P–T) evolution of orogens. However, whereas temperature is the physical expression of heat flow into a portion of crust, heat flow is the geodynamically-relevant parameter to quantify the effect of endothermic reactions. Consequently, the relationship between heat of reaction and temperature are explored for two compositional end-members involved in orogenic metamorphism.

The average amphibolite facies metapelite composition of Ague (1991) is chosen to represent a sedimentary sequence involved in anatectic metamorphism, and the average A-type granite composition of Whalen *et al.* (1987) is taken to represent H_2O-undersaturated felsic crust. First, pressure–temperature phase diagrams are presented (Fig. 2.1). Calculations span temperatures from 600 to 1000 °C, to roughly cover the window of orogenic conditions for granulite terranes (Vielzeuf *et al.*, 1990; Stüwe, 1995; Brown, 2010; Clark *et al.*, 2011).

Calculated pressure–enthalpy relations presented in Figure 2.2. The diagrams consider an enthalpy interval of 35 kJ.mol^{-1}, roughly overlapping with the temperature range of the diagrams in Figure 2.1. Whereas temperature is an intensive thermodynamic variable that is independent of the amount of material, enthalpy is extensive and therefore dependent on bulk composition (cf. Powell *et al.*, 2005). Hence the absolute enthalpy values for the diagrams in Figure 2.2 are not the same for the different samples, but relative changes can be quantitatively compared. An arbitrary temperature of 600 °C has been chosen as common reference point.

The subsolidus part for diagrams of the metapelite (Fig. 2.1b and 2.2d–f) has been calculated assuming fluid-saturated conditions; the extensive property of enthalpy implies that the slope of the isotherms is slightly different to the suprasolidus part. It should be noted that the relative spacing between the isotherms remains unvaried compared to the suprasolidus conditions. This indicates that in both the sub- and suprasolidus parts of the diagrams the same increase in enthalpy generally produces the same increment in temperature. Figure 2.2a and d show the calculated pressure–enthalpy diagrams contoured for temperature for the refractory granite (Fig. 2.2a) and the fertile metapelite (Fig. 2.2b).

For each composition an isobaric heating path beginning at 600 °C and encompassing an enthalpy interval of 35 kJ.mol^{-1} is calculated to illustrate the energetic evolution (Fig. 2.2b and e). The diagrams are calculated at 6 kbar (∼22 km depth for an average crustal density of 2750 kg.m^{-3}), representative of mid-crustal conditions where peak metamorphism is attained along roughly isobaric solidus-to-peak temperature paths (Waters, 1989; Harley, 1998; Raith and Harley, 1998; Brown, 2007; Diener *et al.*, 2013).

2.1 Phase diagram modelling

Phase diagrams are constructed in the eleven-component MnNCKFMASHTO (MnO–Na_2O–CaO–K_2O–FeO–MgO–Al_2O_3–SiO_2–H_2O–TiO_2–O) model system. For both bulk compositions a reduction of CaO in proportion to P_2O_5 assumed to be sequestered in apatite was applied. For the metapelite the fluid content is chosen to stabilize the fluid-saturated solidus at 10 kbar whereas for the granite, the fluid content was chosen in order to resemble that of dry, refractory continental crust. Unedited XRF-bulk compositions are listed in Table 2.1, model compositions employed for thermodynamic modelling are presented in Table 2.2. Full description of modelling parameters is given in appendix B. Theoretical background for enthalpy calculation is given in appendix A. Mineral abbreviations are those used by THERMOCALC and are as follows: andalusite (and), apatite (ap), aqueous fluid (H_2O), augite (aug), biotite (bi), cordierite (cd), corundum (cor), garnet (g), gedrite (ged), granitic melt (liq), hornblende (hb), ilmenite (ilm), K-feldspar (ksp), kyanite (ky), tonalitic melt (L), magnetite (mt), monazite (mnz), muscovite (mu), orthopyroxene (opx), sum of rutile, ilmenite, magnetite and spinel (ox), plagioclase (pl), quartz (q), rutile (ru), sillimanite (sill), spinel (sp), zircon (zrc).

Table 2.1: Bulk-rock compositions (wt.% oxides).

Lithology	SiO_2	TiO_2	Al_2O_3	Fe_2O_3	FeO	MnO	MgO	CaO	Na_2O	K_2O	P_2O_5	F^{3+}/Fe^{2+}
avg. A-type granite*	73.81	0.26	12.40	1.24	1.58	0.06	0.20	0.75	4.07	4.65	0.04	0.41
avg. amphibolite facies metapelite†	56.25	1.05	20.18	9.31	-	0.18	3.23	1.54	1.80	4.02	0.19	0.33

*Whalen *et al.* (1987); †Ague (1991).

Table 2.2: Bulk-rock compositions used in phase equilibria modeling (mol.%).

Lithology	H_2O	SiO_2	Al_2O_3	CaO*	MgO	FeO	K_2O	Na_2O	TiO_2	MnO	O
avg. A-type granite**	0.10	80.35	7.96	0.81	0.32	2.21	3.23	4.30	0.21	0.06	0.45
avg. amphibolite facies metapelite†	6.15	60.16	12.72	1.48	5.15	7.49	2.74	1.87	0.84	0.16	1.24

*corrected in proportion to the P_2O_5-content to account for CaO accommodated in apatite. **Whalen *et al.* (1987); †Ague (1991).

2.2 Thermal model

To estimate the critical length- and time scales of thermal buffering in the fertile metapelite, a simple thermal model for a number of orogenic heat budgets, parametrised in terms of variable heat production at constant regional heat flow, is calculated.

The model is based on the formulation that describes the rate of temperature change due to heat input

$$\frac{dT}{dt} = \frac{S}{\rho C_P} \tag{2.1}$$

(Stüwe, 2007, eq. 3.21, p. 65) where S is the volumetric rate of heat production ($W.m^{-3}$). ρ is the density ($kg.m^{-3}$) and C_P is the heat capacity at constant pressure. Prograde meta-

morphic reactions consume energy in order to advance (i.e. endothermic). Therefore, it is discriminated between heat that is added (S) from heat that is consumed by the advancing reactions. S is the heat production for which a range of values between 2–10 μW.m^{-3} (Andreoli *et al.*, 2006, p.) are assumed. The values for ρ are calculated along an isobaric heating path at 6 kbar assuming a closed system with full melt retention. In this simplest of cases the effect of thermal buffering is likely underestimated as melt retention neglects advective cooling via melt extraction occurring in natural systems. The values for the heat capacity C_P are calculated via

$$C_P = \frac{\Delta H}{\Delta T} \tag{2.2}$$

for a given enthalpy (ΔH) and temperature interval (ΔT), as calculated by THERMOCALC. The modelling yields the enthalpy of reaction at any point in P–T space for the given bulk composition. Contrary to the latent heat of fusion (∼400 kJ.kg^{-1} of granite; Bea, 2012) the enthalpy of reaction also considers energy released by the crystallisation of peritectic phases (e.g. feldspars and aluminosilicates for the muscovite-breakdown) and represents a more realistic estimate for the energetics involved in the investigated reactions. The values for C_P are normalised to the molar weight of the bulk composition of Ague (1991), calculated as 0.0646 kg.mol^{-1}. From Eq. 2.1 the time parameter dt of thermal buffering is calculated for a given temperature interval via

$$Delta\ t = \frac{\Delta T \rho C_P}{S} \tag{2.3}$$

From the characteristic time scale of thermal equilibration, given by the relationship

$$t_{eq} \sim \frac{L^2}{\kappa} \tag{2.4}$$

(e.g. Stüwe, 2007, eq. 3.18, p. 63) the critical length scale of thermal equilibration L is estimated using Delta t calculated from Eq. 2.3 and taken as the time scale of thermal equilibration (t_{eq}). Eq. 2.4 is reformulated to

$$L \sim \sqrt{\kappa} t_{eq} \tag{2.5}$$

where κ is the thermal diffusivity (m^2.s^{-1}) calculated from

$$\kappa = \frac{k}{\rho C_P} \tag{2.6}$$

assuming a constant thermal conductivity k of 2.5 J.s^{-1}mK^{-1}. Values for typical crystalline rocks range between 2.0–3.0 J.s^{-1}mK^{-1} (e.g. Stüwe, 2007); this range of values affects the results by ± 25%, therefore less than an order of magnitude. Homogeneous thermal conductivity is assumed for this schematic model.

The calculated values for the critical length scale (Eq. 2.5) for a variable heat production

are plotted against temperature (Fig. 2.4). Figure 2.5 illustrates the calculated critical length scale (Eq. 2.5, Fig. 2.5a) and buffering time (Eq. 2.4, Fig. 2.5b) for the investigated reactions as a function of heat production. Figure 2.6 shows the relationship of temperature and rate of temperature increment for the investigated reactions, calculated from Eq. 2.1.

2.3 Results

The granite is dominated by K-feldspar and quartz over the entire temperature-range considered. Minor augite coexists with garnet and biotite below the solidus and with orthopyroxene at suprasolidus conditions before the latter is exhausted at high-T–low-P conditions (Fig. 2.1a, 2.2a and c). Melting commences only at 750–800 °C due to low bulk H_2O contents (Fig. 2.1a, 2.2a–c). The heating path (Fig. 2.2b) describes a largely linear increase of temperature with enthalpy to a maximum temperature of ∼1000 °C at the end of the chosen 35 kJ.mol^{-1} enthalpy interval. The fluid-saturated metapelite commences melting at ∼700 °C (Fig. 2.1b, 2.2d–f). The associated heating path (Fig. 2.2e) shows two substantial changes in slope corresponding to the major melt-producing reactions:

$$\text{muscovite} + \text{quartz} = \text{garnet} + \text{sillimanite} + \text{biotite} + \text{K feldspar} + \text{melt} \tag{2.7}$$

and:

$$\text{biotite} + \text{sillimanite} + \text{quartz} = \text{garnet} + \text{cordierite} + \text{K feldspar} + \text{melt} \tag{2.8}$$

(cf. White *et al.*, 2014a). Reactions 2.7 and 2.8 are accompanied by extensive phase rearrangement as reactants are consumed to generate solids and significant amounts of melt (Fig. 2.2f). The reactions 2.7 and 2.8 have a major impact on the enthalpy–temperature profile which remains near-isothermal as they proceed (Fig. 2.2e): reaction 2.7 is calculated to consume ∼1 kJ.mol^{-1} whereas 2.8 requires almost 3 kJ.mol^{-1} to be completed (Fig. 2.2e). The evolution of the metapelite terminates at a maximum temperature of ∼900 °C by which point it has produced almost 60 vol.% melt (Fig. 2.2f). For the same heat budget, the granite reaches a temperature of ∼1000 °C but produces only small volumes of melt (<10 vol. %; Fig. 2.2b and c). The term 'buffer' is applied to assemblages that resist to changes in specific parameters during metamorphism (Rice and Ferry, 1982). Here, the resistance of assemblages to temperature change when subjected to heat input is referred to as 'thermal buffering' (Vielzeuf *et al.*, 1990; Stüwe, 1995). Melting reactions 2.7 and 2.8 are examples of such buffers, characterised by the mineral assemblages indicated by the coloured boxes in Figure 2.2e and f.

2.3.1 Magnitude of thermal retardation

Assuming constant regional heat flow and no thermal communication between the individual modelled lithological units, an end-member scenario for the enthalpy–temperature evolution of high-grade orogenic crust is presented (Fig. 2.3). The enthalpy changes are calculated

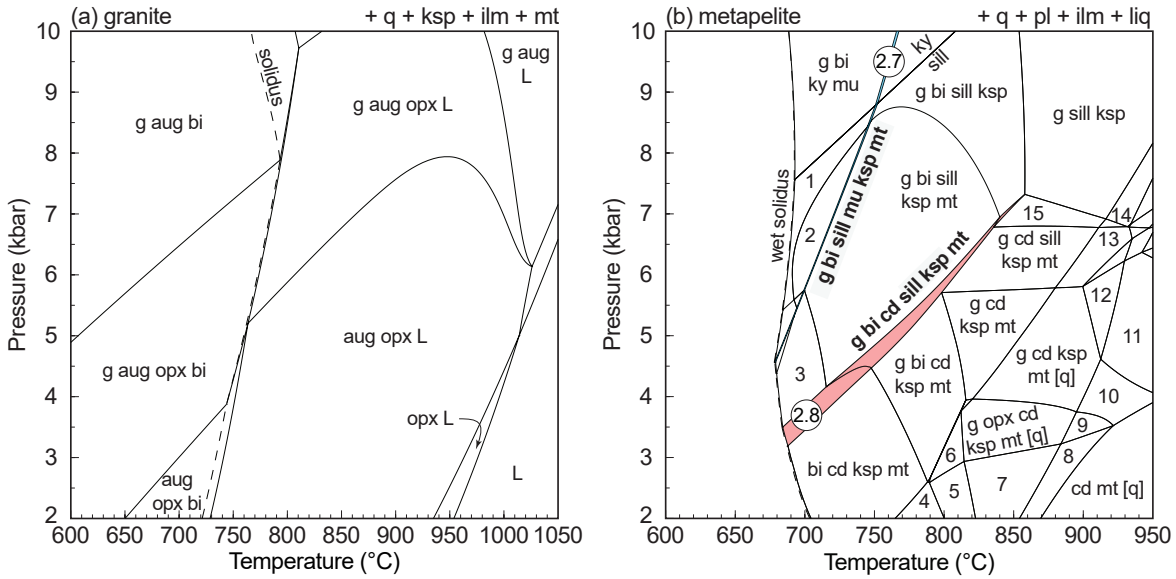


Figure 2.1: Results of model calculations. Pressure–temperature phase diagrams for average granite (a) and average metapelite (b). Highlighted fields in (b) correspond to the melting reactions 2.7 and 2.8 (see text). Numbers refer to assemblage fields (with q, pl, ilm and liq in excess). 1 g–bi–sill–mu; 2 g–bi–sill–mu–mt; 3 bi–sill–ksp–mt; 4 bi–cd–ksp–mt–[q]; 6 g–bi–opx–cd–ksp–mt [q]; 7 opx–cd–ksp–mt [q]; 8 opx–cd–mt [q]; 9 g–opx–cd–mt [q]; 10 g–cd–mt [q]; 11 g–cd–sp–mt [q]; 12 g–cd–sp–ksp–mt [q]; 13 g–cd–sill–ksp–mt [q]; 14 g–sill–ksp [q];15 g–cd–sill–ksp

relative to the enthalpy content at 600 °C for both lithologies. Figure 2.3 highlights that each composition reaches different temperatures despite the same heat input. In the enthalpy interval of reaction 2.8 the granite would manifest temperatures of ∼880 °C whereas the metapelite would achieve maximum temperatures as much as 80 °C lower. Also, the enthalpy–temperature path of the granite remains roughly linear whereas the metapelite experiences two near-isothermal episodes, occupying as much as a fifth of its modelled suprasolidus evolution. Because thermal buffering during melting consumes significant amounts of energy, it can prevent fertile rocks from heating to UHT conditions (Vielzeuf *et al.*, 1990; Stüwe, 1995; Kelsey and Hand, 2015). In fact, most rocks indicating UHT conditions are refractory lithologies, such as Mg–Al rich metapelites, that have experienced few major melting reactions and thus were less thermally retarded (e.g. Harley, 1998; Kelsey and Hand, 2015). Classic regional UHT terranes typically host these assemblages in gneissic rather than migmatitic rocks (Sandiford, 1985; Ouzegane *et al.*, 2003), suggesting that these terranes were melt-depleted and thus 'preconditioned' prior to the UHT event (Vielzeuf and Holloway, 1988; Vielzeuf *et al.*, 1990; Clark *et al.*, 2011; Caddick, 2013). Conversely, granulite terranes with similarly high geothermal gradients but without 'preconditioning' consist of strongly migmatitic rocks that lack UHT mineral assemblages (e.g. White *et al.*, 2004; Diener *et al.*, 2013).

The calculations presented above represent only one possible end-member for the thermal

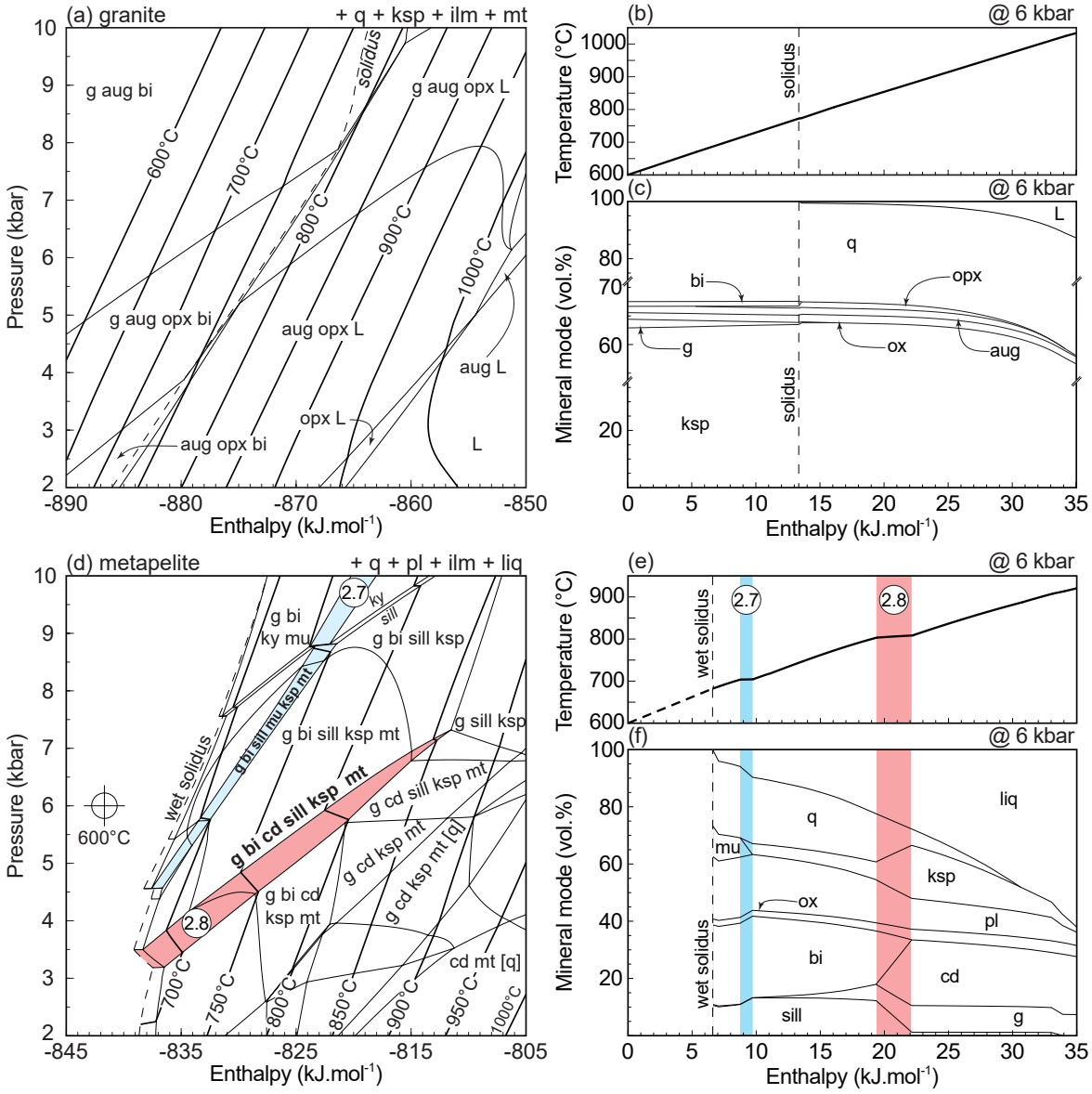


Figure 2.2: Results of model calculations. a–c: Average granite. d–f: Average metapelite. Shown are: pressure–enthalpy phase equilibrium diagrams (a, d); isobaric heating paths at 6 kbar represented by temperature versus relative enthalpy-input using 600 °C as arbitrary reference point (b, e); and isobaric modebox plots showing the modal evolution versus enthalpy-input calculated at 6 kbar (c, f). Highlighted fields in d–f correspond to the melting reactions 2.7 and 2.8 (see text). Note breaks in scale on y-axis in panel c.

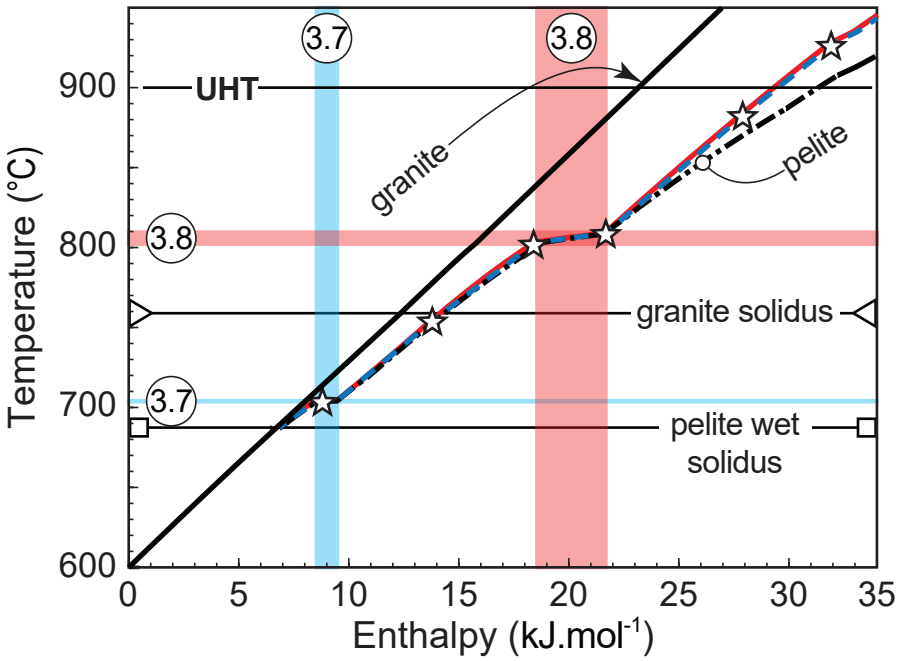


Figure 2.3: Schematic temperature–heat path for modelled granite and metapelite at 6 kbar. The coloured areas correspond to thermal buffering due to major melting reactions (see text). For the metapelite, open system melting is modelled for comparison to a closed system scenario (dot–dash line). Episodic melt extraction is modelled by extracting 5 vol.% melt as soon as a threshold of 7 vol.% is reached (e.g. Yakymchuk and Brown, 2014) (red line). Each melt extraction event corresponds to a star. Continuous melt extraction is simulated by removing all melt in excess of a 2 vol.% threshold as soon as it is produced (blue dashed line). UHT–ultrahigh temperature.

evolution of the orogenic crust. Where different rock types are interlayered on a meter- to decameter scale, partial to complete thermal communication and equilibration during metamorphism is likely. In this case the temperature attained depends on the average thermal properties of that part of the metamorphic terrane, as well as the length- and time scales involved.

2.3.2 Critical length and time scales

If the thickness of alternating lithological layers exceeds a critical length scale over which conductive thermal equilibration is slower than the rate of temperature increase due to enthalpy production, the individual layers would record different thermal histories. This length scale is estimated by comparing the rate of enthalpy production with the rate of external heat input, for example through radiogenic heat production or regional heat flow. Within a typical range of radiogenic heat production (S) for high-grade terranes (2–10 μW.m^{-3}; e.g. Andreoli *et al.*, 2006) the critical length scale is estimated to decrease by an order of magnitude, from between 10,000 and 5,000 m in the unbuffered case to 1,000–500 m when reaction 2.7 advances, or to 4,000–1,500 m for reaction 2.8 (Fig. 2.4 and 2.5a). This simplified thermal model does not account for geometric factors or advective cooling via melt extraction and thus likely overestimates the critical length scale. It is therefore suggested that the effect could potentially be manifested in exhumed terranes on a large outcrop scale. This might be the case for coexisting fertile metapelites and refractory, more magnesian rock types from central Namaqualand (South Africa) where granulite formation occurred due to distinct melting reactions (Waters, 1988) with different loci in P–T space.

In this model, the buffering time of each reaction is highly dependent on the rate of external heat production and varies between ∼1.5–0.2 m.y. and ∼4–0.6 m.y. for reaction 2.7 and 2.8, respectively, over the range of heat production considered (Fig. 2.5b). Similarly, the rate of temperature increment decreases by an order of magnitude as long as buffering is effective (Fig. 2.6).

2.3.3 Melt loss versus retention

Rocks become more refractory when hydrous melt is extracted (e.g. Vielzeuf *et al.*, 1990), thereby allowing them to heat more efficiently and reach higher temperatures (Stüwe *et al.*, 1993; Brown, 2010; Kelsey and Hand, 2015). In order to explore this process, the cumulative enthalpy–temperature evolution for both episodic and continuous melt extraction from the metapelite is calculated, by modelling the removal of melt and thereby changing the chosen bulk composition accordingly during the prograde heating path (Fig. 2.3). Independently of the style of melt removal, the thermal development is identical to that of the closed-system example until reaction 2.8 has gone to completion, indicating that the buffering capacity is not diminished by melt extraction (cf. De Yoreo *et al.*, 1989). Beyond this point the evolution diverges from that of the closed-system case because the more refractory rock is

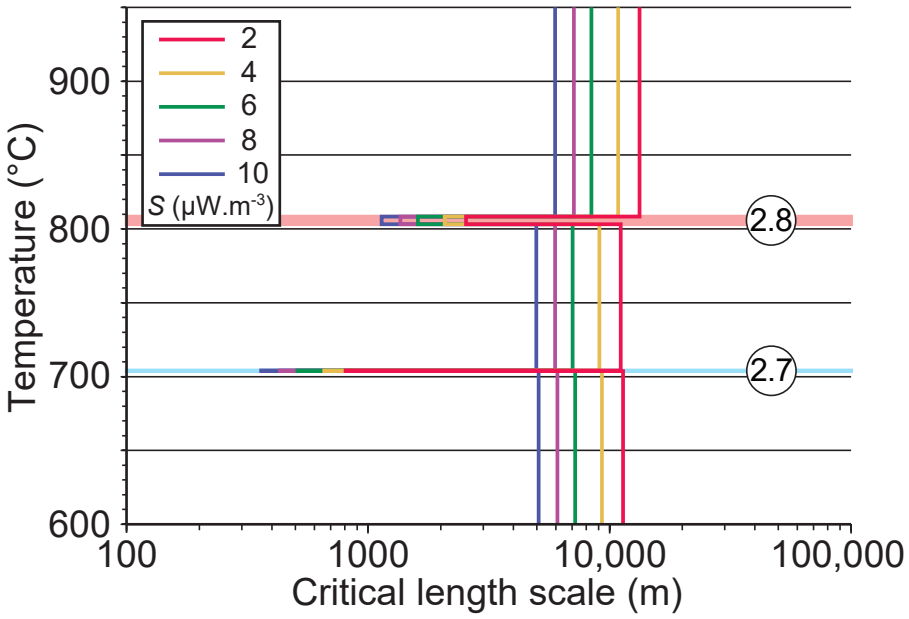


Figure 2.4: Relationship between temperature and critical length scale of thermal buffering in function of external heat production *(S)*. The coloured shading indicates the temperature of reaction 2.7 and 2.8, respectively.

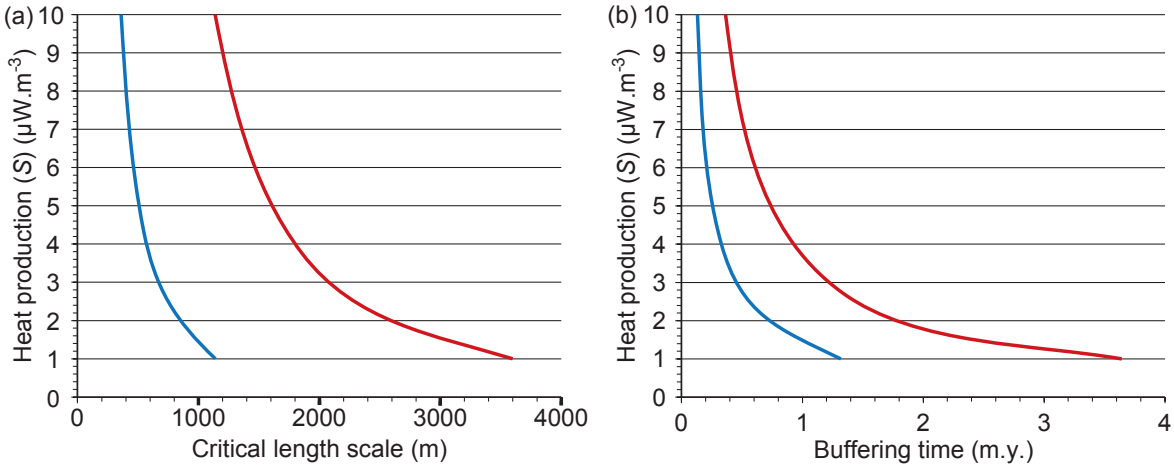


Figure 2.5: Effect of variable heat production *(S)* on critical length scale (a) and buffering time (b) for reaction 2.7 (blue) and 2.8 (red).

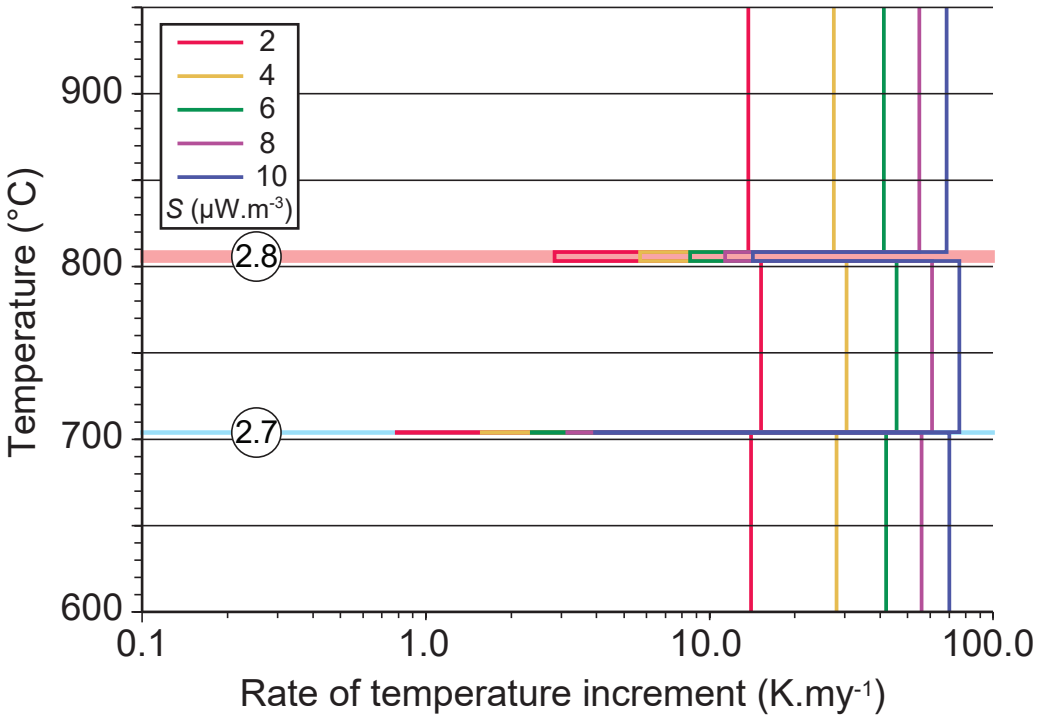


Figure 2.6: Relationship between temperature and heating rate during thermal buffering in function of external heat production *(S)*. The coloured shading indicates the location of reaction 2.7 and 2.8, respectively.

able to transform heat to temperature more efficiently. Notably, the style of melt extraction does not influence the later thermal evolution (Fig. 2.3).

Melt extraction is not always efficient and some fraction of melt may be present as the rocks commence cooling. Crystallization of trapped melt would exert an opposite, exothermic effect and partially reverse energy-intensive reactions. Melt crystallization would partially restore the buffering assemblage, with the apparent coexistence of reactants and products, even though one of the reactants had been exhausted during the prograde evolution (e.g. Kriegsman and Hensen, 1998).

2.3.4 Convergence of orogenic temperatures

It has been shown that different lithologies will encounter specific melting reactions at different stages during their prograde evolution and are thermally buffered at those conditions to different extent and duration. This implies that specific lithologies may attain and record different apparent temperatures despite an identical heat input. Similarly, rocks with comparable bulk composition may express the same equilibrium mineral assemblage and metamorphic temperature for a range of heat budgets. Approximately 15% of the heat budget spanning from the solidus to UHT conditions would result in a typical metapelite experiencing reaction 2.8 at a temperature of ∼800 °C (Fig. 2.3). This may lead to the preferential preservation of the reaction 2.8 assemblage and could explain its common occurrence in low–P high–T terranes worldwide, despite having rather restricted P–T stability (e.g. White *et al.*, 2004; Diener *et al.*, 2013, Fig. 2.1D and 2.3). This result also highlights that the temperatures derived from metapelites may not be the best representation of the true geodynamic thermal structure of orogens.

2.3.5 Implications for the thermal and rheological structures of orogens

The results presented here indicate that temperature is buffered and homogenized along a depth profile in the anatectic crust when a metapelite experiences a melting reaction (cf. Hodges *et al.*, 1988; Stüwe, 1995; Depine *et al.*, 2008). Melting reactions in other rock types such as sub-aluminous metapelites and metagreywackes (Vielzeuf and Holloway, 1988; White *et al.*, 2014a; Yakymchuk and Brown, 2014) and mafic granulites can be expected to exert a similar thermal response. In addition to the buffering effect of strongly endothermic reactions, the advective distribution of heat via melt extraction and ascent can further homogenize the temperature well above the anatectic zone (Depine *et al.*, 2008) and amplify the process of thermal homogenization and stratification. A layer affected by a melting reaction would not only sustain an isothermal temperature but would also remain melt-bearing during buffering. Such layer(s) of low viscosity in the mid- to lower crust have been suggested to control topography, crustal thickness and style of deformation of active orogens such as the Himalayas (Clark and Royden, 2000; Beaumont *et al.*, 2001).

Chapter 3

The Namaqua–Natal Metamorphic Province (NNMP)

The NNMP forms a ∼1800 km long, up to 400 km wide mobile belt wrapping around the southern margin of the Kalahari Craton (inset map in Fig. 3.1; Nicolaysen and Burger, 1965; Eglington and Armstrong, 2004; Hartnady *et al.*, 1985; Thomas *et al.*, 1994b; Cornell *et al.*, 2006; Miller, 2008, 2012, and references therein). It stretches from the west coast of Namibia to the south-eastern coast of South Africa and consists of the eastern Natal Sector and the western Namaqua Sector, with the intervening region covered by younger Phanerozoic sediments (e.g. Cornell *et al.*, 2006). Here the focus lies on the amphibolite- to granulite facies Namaqua Sector, consisting of polydeformed and polymetamorphosed orthogneisses and minor metasedimentary and metamafic lithologies that formed during two main tectonometamorphic cycles in the Paleoproterozoic (∼2050–1800 Ma) and the Mesoproterozoic (1300–1080 Ma; Clifford *et al.*, 2004; Eglington, 2006; Cornell *et al.*, 2006; Cornell and Pettersson, 2007a; Cornell *et al.*, 2009; Thomas *et al.*, 2016; Macey *et al.*, 2017).

3.1 Tectono-metamorphic architecture of the Namaqua Sector

The Namaqua Sector is interpreted as a stack of thin, but laterally extensive fault-bounded thrust sheets that constitute several tectonostratigraphic domains (e.g. Macey *et al.*, 2018). Structurally, from bottom to top (geographically west to east), these are (Fig. 3.1):

3.1.1 Bushmanland Subprovince

The Bushmanland Subprovince (BSP) is the structurally lowermost and geographically the most southerly domain of the Namaqua Sector (Fig. 3.1). It is dominated by voluminous pre- and post-tectonic felsic gneisses of the Little Namaqualand Suite and the Spektakel Suite, respectively (see figure 2 in Macey *et al.* (2018) for geographic distribution). The Little Namaqualand Suite consists of penetratively deformed orthogneisses hosting strongly

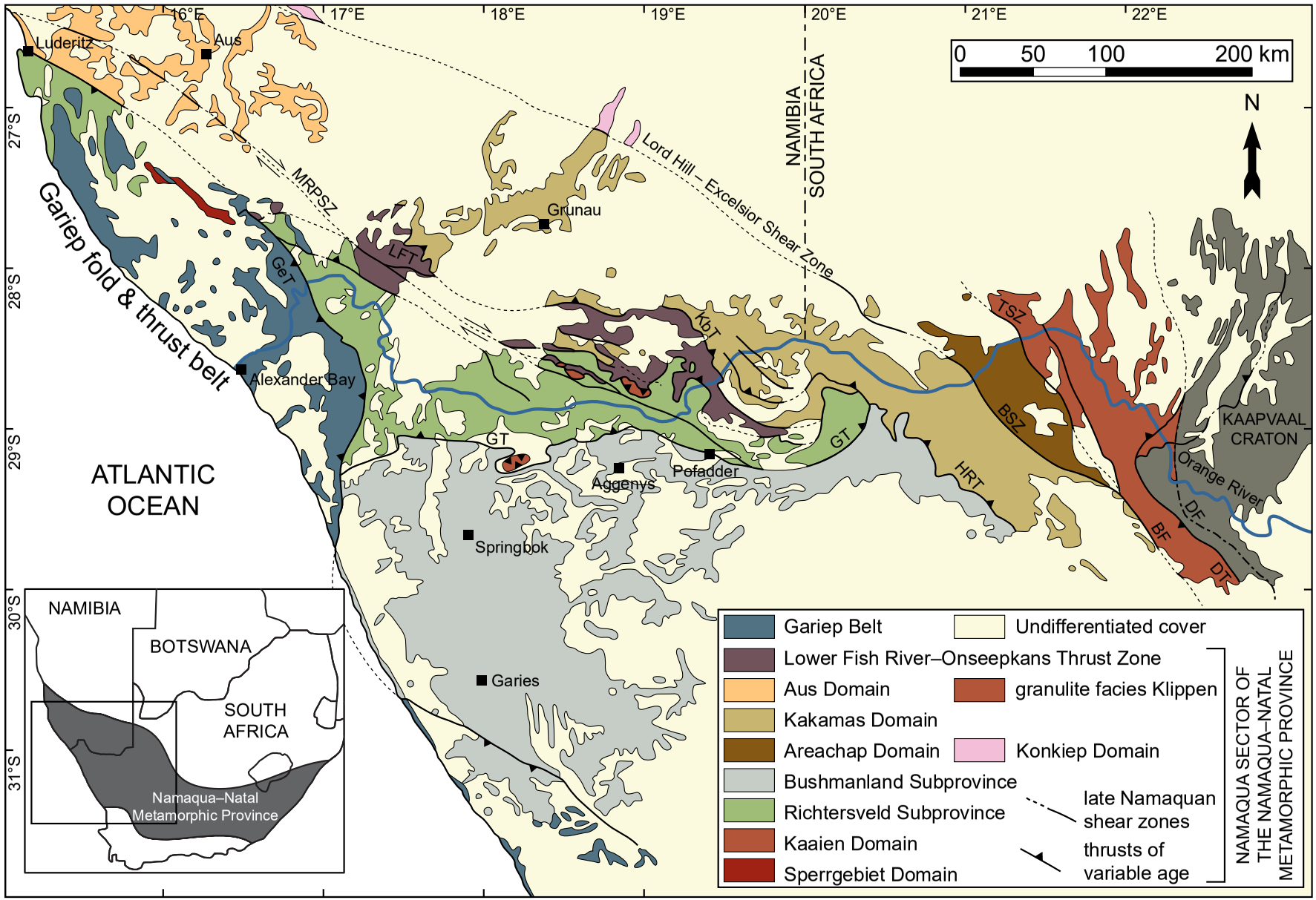


Figure 3.1: Simplified tectonostratigraphic map of the Namqua Sector of the NNMP (modified after Macey *et al.*, 2018). Namaqua-age shear zones and thrusts: Kêrelbad Thrust (KbT), Hartebees River Thrust (HRT), Lower Fish River Thrust (LFT), Groothoek Thrust (GT), Marshall Rocks–Pofadder Shear Zone (MRPSZ), Boven Rugzeer Shear Zone (BSZ), Trooilapspan Shear Zone (TSZ), Brakbosh Fault (BF), Doornberg Fault (DF), Dabep Thrust (DB). Pan African thrusts: Gemsbokvlei Thrust (GeT). Insert shows the approximate areal extent of the Namaqua–Natal Metamorphic Province.

recrystallised K-feldspar augen immersed in a biotite-rich matrix. Orthogneisses of the Little Namaqualand Suite display crystallisation ages of between 1212 and 1191 Ma (Robb *et al.*, 1999; Clifford *et al.*, 2004; Macey *et al.*, 2011; Cornell and Pettersson, 2007b). The gneisses host inherited zircon xenocrysts of Paleoproterozoic age (∼2.0–1.7 Ga; Clifford *et al.*, 2004), consistent with published Sm–Nd ages of *c.* 2.0 Ga (T_{CHUR}) and 1.7 Ga (T_{DM}) for the same unit (Clifford *et al.*, 1995). Overgrowths on magmatic zircons yield $^{207}Pb/^{206}Pb$ ages of 1032 ± 18 Ma (Robb *et al.*, 1999), 1040–1020 Ma (Clifford *et al.*, 2004), 1022 ± 5 Ma and 1027 ± 25 Ma (Raith *et al.*, 2003) as well as 1038–1030 Ma (Cornell and Pettersson, 2007b), interpreted as age of high-grade metamorphism overprinting the Little Namaqualand Suite. The penetrative fabric in the Little Namaqualand Suite resulted from regional deformation during the main Namaqua Orogeny (D_2, see below).

The post-tectonic Spektakel Suite hosts largely undeformed, coarse-grained, megacrystic granites and charnockites (Macey *et al.*, 2018). The Spektakel Suite intruded the BSP during the late to post-tectonic phase of the main Namaqua Orogeny over a period of >60 Ma between 1098 and 1033 Ma (Macey *et al.*, 2018). The geochemical signature of the Spektakel Suite indicates a variety of source regions including a significant mantle input (Macey *et al.*, 2018). Published T_{DM} model ages between 1.54 and 1.75 Ga and inherited zircon xenocryst ages of ∼1.75 Ga have been interpreted as important contribution of older crust in magma generation (Macey *et al.*, 2018; Yuhara *et al.*, 2001; Pettersson *et al.*, 2009), such as Paleoproterozoic crust equivalent to the adjacent Sperrgebiet Domain and the Richtersveld Subprovince (Macey *et al.*, 2018). Mafic magmatism is subordinate in the BSP, represented by pre-tectonic amphibolites and precursors to mafic granulites (low–K tholeiites; Reid *et al.*, 1987) and minor Cu-bearing norite intrusions of the Koperberg Suite (∼1030 Ma crystallisation age; Kent, 1980; Albat, 1984; Clifford *et al.*, 1995; Robb *et al.*, 1999; Clifford *et al.*, 2004).

Supracrustal units in the BSP are currently grouped into the Bushmanland and Kamiesberg Groups, however multiple detrital ages and age groups are present in detritus from the Namaqua Sector, showing no systematic variation with geography or lithology (McClung, 2006; Raith *et al.*, 2003; Cornell *et al.*, 2009; Agenbacht, 2007; De Beer, 2010; Macey *et al.*, 2011). Therefore more data are required to resolve the litho- and chronostratigraphy of the Namaqua Sector. Peak metamorphism ranges from amphibolite- to granulite facies conditions and occurred around 1040–1030 Ma (e.g. Robb *et al.*, 1999; Bailie *et al.*, 2007; Cornell *et al.*, 2009). The thermal maximum is interpreted to post-date the termination of the main D_2 event by some 35–80 Ma (e.g. Macey *et al.*, 2018), as confirmed by microtextural evidence such as L_2-parallel needles of sillimanite preserved exclusively as inclusions in garnet, whereas later, coarse-grained matrix sillimanite is randomly oriented (Waters, 1989). Similarly, peak granulite assemblages including leucosomes are seen to have obliterated younger D_2 fabrics (Waters, 1989). Waters (1986b, 1989) documented a symmetrical zonation pattern of peak metamorphic conditions in the BSP, outlined by roughly E–W-trending isograds that delimit southern and northern amphibolite facies zones separated by a wide granulite facies zone at

the centre. Peak conditions in the granulite core vary between ∼750 and 870 °C and 4.5 to 6 kbar (Waters and Whales, 1984; Waters, 1986a,b, 1989; Raith and Harley, 1998; Clifford *et al.*, 2004). Potentially ultrahigh-temperature (UHT) assemblages hosting hercynite + quartz (Waters, 1986b), osumilite (Nowicki *et al.*, 1995) and corundum + quartz (Mouri *et al.*, 2003, 2004) have been documented in the central BSP. The northern amphibolite facies zone around Aggeneys (Fig. 3.1) reached subsolidus conditions of 650 °C at 5 kbar (Diener, 2014). *P–T* paths proposed for the BSP are anticlockwise, involving concomitant heating and minor burial from conditions of andalusite stability to peak *P–T*, followed by slow isobaric cooling during retrogression (Waters, 1986b, 1989; Raith and Harley, 1998; Robb *et al.*, 1999; Diener, 2014). Late pegmatite swarms mark the waning stage of high-grade metamorphism at 1000–950 Ma (Hugo *et al.*, 1986; Lambert, 2013). Cooling below $^{40}Ar/^{39}Ar$ closing temperature in hornblende (∼500 °C; Harrison, 1981) occurred between *c.* 1026–995 Ma (Pettersson, 2008; Büttner *et al.*, 2013) whereas the closure temperature of the same radiogenic system in biotite and muscovite was reached between 985 and 962 Ma in large parts of the Namaqua Sector, including the BSP (Pettersson, 2008).

Waters (1986b) suggested that the increased heat flow required to produce extensive high-grade metamorphism in the BSP was due to convective heat transfer by the ascent of hot and dry granitic melts that originated in the lower crust. The spatial and temporal relationship of intrusions of the Little Namaqualand Suite (∼1212–1191 Ma, Robb *et al.*, 1999) and the Spektakel Suite (∼1109–1097 Ma, Macey *et al.*, 2018) with supracrustals recording peak granulite metamorphism between ∼ 1050–1020 Ma (peaking at around 1030 Ma, e.g. Macey *et al.*, 2018) is consistent with this model. However, heat transfer due to the prolonged granitic intrusions was likely insufficient to drive the long-lived metamorphism in the area and therefore does not represent the primary heat source. Waters (1986b, 1989, 1990) proposed the ultimate driving force was heating due to mafic underplating of the lower crust, potentially accompanied by radiogenic heating (Andreoli *et al.*, 2006). In support of this scenario, Macey *et al.* (2018) interpret the Spektakel Suite and related granitic intrusives to be generated due to heat transferred in the lower crust from an underplating mantle. The presence of temporally associated but volumetrically minor mafic rocks intruding the BSP (Robb *et al.*, 1999; Clifford *et al.*, 2004; Macey *et al.*, 2015) may be tentatively interpreted as representatives of the envisaged underplating melts (Macey *et al.*, 2018).

3.1.2 Richtersveld Subprovince

The ∼1.9 Ga low to medium-grade Richtersveld Subprovince structurally overlays the BSP, with the Groothoek Thrust forming the tectonic boundary between the two blocks (Fig. 3.1). The Richtersveld Subprovince hosts the oldest material in the Namaqua Sector and is dominated by a calc-alkaline volcanic-plutonic succession (the Vioolsdrif Suite) intruded in its volcanic edifice of equivalent age (the Orange River Group; Macey *et al.*, 2017, and references therein). The geochemical signature of the Richtersveld Arc is characteristic for an island-arc setting, with magmatism taking place between 1910 and 1865 Ma (Macey *et al.*,

2017). Archean-aged detrital zircons from migmatitic slivers are interpreted as possible indication for amalgamation of fragments of the Archean Kaapvaal Craton basement into the Richtersveld Subprovince prior to ∼1885 Ma (Macey *et al.*, 2017). The newly described Sperrgebiet Domain (Thomas *et al.*, 2016) forms a ∼2020 Ma calc-alkaline tectonic inlier within the Neproterozpoic Gariep Belt (Fig. 3.1), interpreted as upfaulted block within the belt. ∼1885 Ma alkali granite and microgranodiorite intruding part of the Sperrgebiet Domain are seen as equivalents of the Vioolsdrif Suite of the Richtersveld Subprovince. Macey *et al.* (2017) consequently suggested a two-arc model with the early Sperrgebiet Arc evolving at ∼2020 Ma subsequently cannibalised by the Richtersveld Arc at around 1885 Ma. Limited Namaqua-aged metamorphism is recorded in amphibolites in the eastern Pella Domain of the Richtersveld Subprovince, reaching conditions of ∼600 °C and 5–6 kbar between ∼1.2 and 1.0 Ga (Macey *et al.*, 2017). Metamorphism in the eastern Vioolsdrif Domain did not exceed greenschist facies conditions (Macey *et al.*, 2017).

3.1.3 Kakamas Domain

The Kakamas Domain tectonically overlies the Richtersveld Subprovince to the north-east (Fig. 3.1) and consists of granulite facies metasediments (∼1220–1200 Ma) and voluminous granite intrusions (the Keimoes Suite) of 1.21–1.08 Ga in age (e.g. Pettersson *et al.*, 2007; Bial *et al.*, 2015,b, 2016; Macey *et al.*, 2015; Bailie *et al.*, 2017). Recent work suggests that the rocks may be subdivided into an older group of penetratively deformed syn-tectonic gneisses (1175–1146 Ma) and weakly-deformed to undeformed late- to post-tectonic bodies (1110–1078 Ma; Bailie *et al.*, 2017). The older orthogneiss derived from fractionated, metaluminous to peraluminous leucogranites with Meso- to Paleoproterozoic Nd model ages of 1.57–1.91 Ga (Bailie *et al.*, 2017). The group of younger granitoids include unfoliated megacrystic granodiorites, monzogranites and charnockites of strongly metaluminous character and I-type signature with arc-type affinities (Bailie *et al.*, 2017). The granitoids are comparable to the deformed orthogneisses in terms of geochemistry and similar T_{DM} model ages (1.38–1.99 Ga), but they are suggested to derive from relatively depleted sources with a variable enriched/crustal component (Bailie *et al.*, 2017).

Thermobarometric and geochronological investigation of aluminous metapelites documents highest-grade metamorphism with peak conditions of 800–900 °C at ∼5 kbar and 640–680 °C at 4.0–4.5 kbar in shallower units (Bial *et al.*, 2015). Rare pseudomorphs after osumilite are interpreted as indicator that UHT conditions were locally attained. Inclusions of staurolite in garnet and pseudomorphs after kyanite constrain inferred medium–pressure amphibolite facies conditions for early prograde metamorphism (Bial *et al.*, 2015). Post-peak cooling is interpreted as largely isobaric. Bial *et al.* (2015) recognise two generations of zircon, recording anatexis in metapelites at 1351–1299 Ma, and a younger generation documenting partial melting at around 1200 Ma. (Bial *et al.*, 2015b) interpret mesocratic granitoids in their field area as the product of magmatic differentiation of mantle-derived, hot parental magmas, whereas the authors recognise leucocratic granitoids as crystallised melts derived

from fluid-present melting of metapelites. Zircon U–Pb dating suggest lower-crustal plutonism between 1220–1180 Ma, spanning over an interval of 30–40 Ma, coinciding with the thermal peak in the region (Bial *et al.*, 2015b). The authors recognise a second heat pulse at ∼1100 Ma from zircon overgrowths in older plutons and the emplacement of a younger suite of granite. Cooling to sub-amphibolite facies conditions is thought to have occurred over an extended period of time, as much as ∼100 Ma (Bial *et al.*, 2015b).

The long-lasting (∼1350 and <1100 Ma) high–temperature history accompanied by slow, largely isobaric, heating and cooling (e.g. Bial *et al.*, 2015,b) is comparable to the evolution of the BSP, and, similar to felsic magmatism in the BSP, the ∼1.18–1.14 Ga syn-tectonic magmatic episode in the Kakamas Domain points towards long-lived high-heat flow accompanying magmatism and metamorphism at this time (Bailie *et al.*, 2017).

The Kakamas Domain is separated from the BSP and Richtersveld Subprovince by a wide thrust-related mélange known as the Lower Fish River–Onseepkans Thrust Zone (LFROTZ, Fig. 3.1; Macey *et al.*, 2017). The LFROTZ is an amphibolite facies mixture of exotic slivers and thrust slices including granulite facies klippen (Fig. 3.1) and portions of Richtersveld Subprovince material (Macey *et al.*, 2017).

3.1.4 Aus Domain

The granulite facies Aus Domain (Fig. 3.1) is dominated by pre- to syn-tectonic granitoids known respectively as Tsirub Gneiss and Kubub Gneiss (Jackson, 1976). Volumetrically minor aluminous metasediments, metagreywacke, mafic granulite, quartzite, iron stone, marble and calc-silicate form the Garub sequence, are metamorphosed to amphibolite to granulite facies conditions (Jackson, 1976). Diener *et al.* (2013) estimated metamorphic peak conditions of ∼825 °C at 5.5 kbar from aluminous metapelites reached along a roughly isobaric, hairpin-type clockwise path. Early prograde conditions of ∼550–600 °C and <4 kbar are determined from inferred pseudomorphs after andalusite (Diener *et al.*, 2013). Isobaric cooling is deduced from beards of retrograde sillimanite replacing peak cordierite. Pre-tectonic granitic plutonism occurred at ∼ 1120–1085 Ma; metamorphism is constrained to have taken place at around 1065–1045 Ma from overgrowths on magmatic zircons (Diener *et al.*, 2013). Cooling below the solidus is inferred from a late granitic dyke intruding the terrane at 1004 ± 6 Ma. Similar to the Bushmanland Subprovince and Kakamas Domain, a long-lasting (>50–70 Ma), large-scale heat source is invoked to justify the observed thermal anomaly. Both timing and type of long-lived high-grade metamorphism suggests an evolution comparable to other terranes of the Namaqua Sector (Diener *et al.*, 2013).

3.1.5 Areachap Domain

The 1.30–1.22 Ga old Areachap Domain is bounded to the east by the Kaaien Domain and to the west by the Kakamas Domain (Fig. 3.1). It is dominated by juvenile arc-related mafic to intermediate metavolcanics and their redeposited equivalents (Cornell and Pettersson, 2007a).

The amphibolite facies supracrustal material is intruded by ∼1.20 to 1.10 Ga granitoids (Geringer *et al.*, 1986, 1994; Cornell *et al.*, 1990, 2015; Pettersson *et al.*, 2007; Cornell and Pettersson, 2007a; Bailie *et al.*, 2010, 2011, 2017). Age of high-grade metamorphism in both the Kakamas Domain and Areachap Domain of between ∼1.20 and 1.18 Ga is estimated from zircon rims and crystallisation ages of leucogranites (e.g. Cornell and Pettersson, 2007a; Moen and Toogood, 2007; Bial *et al.*, 2015b). Penetrative deformation is constrained to wane at around 1110 Ma (Bailie *et al.*, 2017). Cornell and Pettersson (2007a) proposed a tectonic model that envisages the older Kakamas Domain and younger Areachap Domain as minor crustal fragments within a major oceanic basin delimited by the BSP and the Kaapvaal block. The closure of this basin is thought to have led to terrane assembly by collision at ∼1.2 Ga (Cornell and Pettersson, 2007a).

3.1.6 Kaaien Domain

The Kaaien Domain corresponds to a zone of tectonic transition between the Namaqua Sector and the western margin if the Archean Kaapvaal Craton (Fig. 3.1). It is consists of ∼1.77 Ga metaquartzites (van Niekerk, 2006) and the ∼1.17–1.10 Ga Koras Group, a bimodal volcanosedimentary suite of basaltic andesites and rhyolites sandwiched between metasediments (Bailie *et al.*, 2012). The mafic succession is tholeiitic, calcic to calc-alkalic in character and was extruded in a continental rift setting. Rhyolites are peraluminous and alkalic; their A-type geochemical signature suggests emplacement in an intra-plate setting (Bailie *et al.*, 2012). Both successions have a distinct subduction-related signature (Bailie *et al.*, 2012). In terms of age, major- and trace element composition the Koras Suite is interpreted as kin to the granitoids of the Koras Suite of the Kakamas Domain (Bailie *et al.*, 2012). Variable T_{DM} model ages of >1.5 Ga are interpreted as fingerprint of melting of subduction-related subcontinental lithospheric mantle following slab detachment beneath previously thickened crust, with melt emplacement on the western edge of the Kaapvaal Craton in a trans-tensional regime (Bailie *et al.*, 2012).

3.2 Structural evolution of the Namaqua Sector

A simplified four-phase tectonic model for the BSP is suggested by Joubert (1971, 1986a). The oldest (Paleoproterozoic) D_1 deformational event is preserved exclusively in the Vioolsdrif Domain of the Richtersveld Subprovince and in the Gladkop Suite of the northern BSP (Van Aswegen, 1983; Macey *et al.*, 2017). In the Richtersveld Subprovince, D_1 deformation is associated with the so-called Orange River Orogeny, which is characterised by large-scale, open to isococlinal, upright to recumbent folding (F_1) of original sedimentary beds (S_0). Axial planar S_1 foliation and L_1 is associated to the folds. Greenschist facies conditions were not exceeded during this D_1 event (Macey *et al.*, 2017).

In the BSP, the main (Mesoproterozoic) Namaqua Orogeny is subdivided into three broad phases associated with ductile deformation and metamorphism between ∼1.2 and 1.0 Ga.

These are:

- D_2: Large-scale thrusting and isoclinal folding producing a regionally penetrative, roughly E–W striking, moderate to shallow dipping foliation throughout the terrane. Related shallow to moderately plunging L_2 stretching lineations trend roughly NW in the southern BSP and are seen to rotate to tend north around the centre of the BSP (around Garies, Fig. 3.1) to finally tend to the NE in the north of the terrane (e.g. Macey *et al.*, 2018). Recently reported emplacement ages of the late- to post-tectonic Spektakel Suite constrain the termination of D_2 deformation to between 1109 and 1097 Ma (Macey *et al.*, 2018). Furthermore, Macey *et al.* (2018) interpret published geochronological data as implication for the main D_2 event to have consisted of not one, but two major orogenic episodes at ∼1.2 and 1.1 Ga, respectively. The two phases are thought to have been separated by a time of 'uplift, erosion, extension and sedimentation' (Macey *et al.*, 2018). Similar to Little Namaqualand Suite and Spektakel Suite in the BSP, the timing of emplacement of the post-tectonic granitoids of the Keimoes Suite constrains peak D_2 deformation in the Kakamas Domain at ∼1.13–1.10 Ga, with peak D_2 between ∼1.18–1.13 Ga (Bailie *et al.*, 2017).

- D_3: Reorientation of D_2 fabrics and thrust planes by mega-scale folding (F_3) into open dome-and-basin structures with a wavelength of km- to 10 km (Macey *et al.*, 2018). Locally, the subhorizontal D_2 gneissosity is transposed into narrow, discontinuous, E-trending monoclinal subvertical features ('steep structures', Kisters *et al.*, 1996). The axial-planar orientation of steep structures with respect to large-scale D_3 folds led to their interpretation as localised high-strain shear zones that accommodated part of the N–S directed bulk inhomogeneous shortening accompanying the D_3 event (Kisters *et al.*, 1996). Small bodies of the cupriferous Koperberg Suite preferentially intruded into these structures in a short temporal interval (<10 Ma) at around 1030 Ma (Gibson *et al.*, 1996; Clifford *et al.*, 2004).

- D_4: Development of large-scale, sub-vertical, transcurrent NW-trending D_4 shear zones that cross-cut and rework fabrics in the entire Namaqua Sector. The Marshall Rocks–Pofadder Shear Zone (MRPSZ, Fig. 3.1) represents the largest of these structures. The emplacement of coeval pegmatites and deformation of granites intruded into the shear zones constrains D_4 deformation to between 1005 and 958 Ma (Macey *et al.*, 2015; Melcher *et al.*, 2008; Lambert, 2013).

3.3 Geodynamic setting of the Namaqua Sector

Most published *P–T–t* paths for the Namaqua Sector involve minor to moderate compression and are dominated by slow, near-isobaric heating to amphibolite- to granulite facies conditions at the metamorphic peak. The evolution follows clockwise (Diener *et al.*, 2013)

or anticlockwise paths (Waters, 1986b, 1989; Raith and Harley, 1998; Robb *et al.*, 1999; Diener, 2014), commonly not exceeding crustal depths of ∼18–22 km (5–6 kbar and an average crustal density of 2750 kg.m^{-3}). The post-peak evolution is typically dominated by slow near-isobaric cooling (IBC) to an ambient geotherm, with limited concomitant exhumation (e.g. Diener *et al.*, 2013; Waters, 1986b; Raith and Harley, 1998; Robb *et al.*, 1999). However, Cornell *et al.* (1992) document an evolution involving significant vertical crustal movement for a small region located at the eastern border of the Namaqua Sector with the Kaapvaal Craton (Prieska Copper Mine, Kaaien Domain; Fig. 3.1). The authors propose a steep beta-shaped P–T path reaching a maximum pressure of 7 kbar (∼26 km depth assuming a density of 2750 kg.m^{-3}) followed by near-isothermal decompression (ITD) to ∼4.5 kbar and 600 °C. Near-isobaric heating to 700–800 °C and cooling to a stable continental geotherm concludes the proposed metamorphic evolution (figure 16 in Cornell *et al.*, 1992). The data are interpreted in terms of a Wilson Cycle spanning between 1300–900 Ma, dominated by burial to the pressure peak during the collision of Namaqualand with the western border of the Kaapvaal Craton. Isobaric heating and cooling following decompression is interpreted as short-lived contact metamorphism related to local magmatism (Cornell *et al.*, 1992). A similar view was shared by several contributions, favouring a similar Wilson-Cycle-type geodynamic scenario (e.g. Blignault *et al.*, 1983; Joubert, 1986a; Stowe, 1986; Jacobs *et al.*, 1993) suggesting terrane breakup, subduction, amalgamation and collision of geologically unrelated units (Miller, 2012). High-grade terranes forming in such a setting are commonly affected by a period of ITD because tectonic thickening is in most cases followed by exhumation via erosion or tectonic denudation (e.g. England and Thompson, 1984; Harley, 1989).

However, to date no concrete evidence for collisional/subduction related tectonism (i.e.high-P–low-T assemblages, ophiolites, signs of large-scale post-orogenic collapse of thickened lithosphere and related ITD, contrasting geochronological- and geochemical signatures suggesting the assembly of large allochtonous terranes) has been identified. Therefore, the Namqua Sector would rather fall within the group of granulite terranes following an evolution dominated by IBC. These are classically related to "areas of large magmatic accretion" (Harley, 1998), in particular those characterised by anticlockwise paths. This is supported by Bial *et al.* (2015) referring to the overall similarity in the geochronological inheritance across the Namaqua Sector, thereby ruling out a Wilson Cycle scenario. The authors interpret the long-lasting, roughly isobaric high temperature conditions recorded over vast areal extents to be consistent with a continental back-arc mobile belt setting. Such a geodynamic environment "with an up to 1000 km wide region of thin hot lithosphere behind an active continental margin" that "...might exist over hundreds of million years" is regarded as favourable for the formation of high-T–low-P conditions as documented throughout the Namaqua Sector (Bial *et al.*, 2015). The authors suggest the Damara front in central Namibia (Miller, 2008) – active at 1260–1200 Ma (Cornell *et al.*, 2015) – as related arc, causing the elevated geotherms necessary to produced extensive high-grade metamorphism. Macey *et al.* (2018) support the Bial *et al.* (2015) back-arc model and interpret the post-tectonic Spektakel Suite a product of heat flux through

mantle underplating. Furthermore, abundant inherited ∼2.0–1.7 Ga zircon xenocrysts in the Little Namaqualand Suite (Clifford *et al.*, 2004) and ∼1.75 Ga inheritance in the Spektakel Suite (Macey *et al.*, 2018) may be interpreted as fingerprint of crustal recycling dominating over a juvenile source of both felsic suites.

3.4 Regional-scale sampling

Sampling for this thesis occurred at roughly two scales, beginning with regional-scale sampling of various localities of the BSP (Fig. 3.2). Samples of aluminous metapelites occurring at each locality were collected, with the aim of large-scale P–T–t determination. In order to facilitate the description of the different sampling sites, they are informally divided into a number of geographic areas, typically named after a nearby settlement or farm (Fig. 3.2). From south to north these are: Lepel se Kop, Paulshoek, Hytkoras, Nababeep, Ratelpoort and Geselskapbank (Figure 3.2). Detailed sampling was carried out at the locality of Hytkoras in the central BSP, where the large variety of lithologies was collected in order to investigate the effect of a common heat budget on a variety of bulk rock compositions. Sample coordinates and key information is summarised in Table 3.1.

Table 3.1: Sample localities and main mineralogy.

sample	locality	lithology	main assemblage	latitude	longitude	Figure
NMC47	Lepel se Kop	aluminous metapelite	g–bi–cd–sill–q–feldspars	30°40'59.7" S	18°41'02.1" E	3.3a
NMC102	Lepel se Kop	aluminous metapelite	g–bi–cd–sill–q–feldspars	30°40'50.5" S	18°40'56.9" E	3.3a
NMC46	Paulshoek	aluminous metapelite	g–(bi–)cd–sill–sp–q–feldspars	30°21'57.3" S	18°18'20.1" E	3.3b
NMC101	Paulshoek	aluminous metapelite	g–(bi–)cd–sill–sp–q–feldspars	30°23'48.8" S	18°11'02.6" E	3.3c
NMC89	Hytkoras	aluminous metapelite	g–bi–cd–sill–q–feldspars	29°54'36.2" S	18°13'14.6" E	3.6a
NMC71	Hytkoras	aluminous metapelite	g–bi–cd–sill–q–feldspars	29°55'15.1" S	18°09'01.2" E	3.6b
NMC65	Hytkoras	aluminous metapelite	g–bi–cd–sill–q–feldspars	29°56'36.1" S	18°09'16.9" E	3.6c
NMC37	Hytkoras	magnesian metapelite	g–bi–cd–opx–q–feldspars	29°56'44.8" S	18°09'06.4" E	3.7
NMC67	Hytkoras	semi-metapelite	g–cd–sill–q–feldspars	29°56'36.1" S	18°09'16.9" E	-
NMC68	Hytkoras	metagreywacke	g–bi–q–feldspars	29°56'36.1" S	18°09'16.9" E	3.8
NMC69	Hytkoras	mafic granulite	hb–two-pyroxenes–q	29°56'36.1" S	18°09'16.9" E	3.10a
NMC27	Hytkoras	mafic granulite	(hb–)two-pyroxenes–q	29°56'21.0" S	18°09'21.7" E	3.10d
NMC44	Hytkoras	magnesian gneiss	opx–bi–cd–q	29°56'42.8" S	18°09'02.6" E	3.11a
NMC88	Hytkoras	nodular magnesian gneiss	sa–sp–bi–cd	29°54'36.4" S	18°13'14.6" E	3.11b
NMC90	Hytkoras	nodular magnesian gneiss	sp–cor–bi–cd	29°54'36.4" S	18°13'17.0" E	3.11c
NMC91	Hytkoras	nodular magnesian gneiss	ged–opx–sp–cd	29°54'36.8" S	18°13'13.0" E	3.11d
NMC24	Nababeep	aluminous metapelite	g–bi–cd–sill–q–feldspars	29°34'08.9" S	17°46'52.0" E	3.3d
NMC21	Ratelpoort	aluminous metapelite	g–cd–(sill)–q–feldspars	29°26'12.0" S	17°57'07.4" E	3.3f
NMC05	Geselskapbank	aluminous metapelite	g–bi–cd–sill–q	29°12'10.7" S	18°04'14.7" E	3.3g
NMC11	Geselskapbank	aluminous metapelite	g–bi–cd–sill–q	29°12'10.7" S	18°04'14.7" E	3.3g
NMC15	Geselskapbank	aluminous metapelite	bi–cd–sill–q–feldspars	29°12'16.6" S	18°04'27.3" E	3.3h
NMC16	Geselskapbank	aluminous metapelite	bi–cd–sill–q–feldspars	29°12'12.4" S	18°04'43.3" E	3.3h

3.4.1 Field occurrence of aluminous metapelites

Pelitic granulites of the BSP are predominantly medium- to fine grained, commonly showing distinct metamorphic layering of leucosomes rich in peritectic garnet and feldspars and melanosomes hosting biotite and sillimanite (Fig. 3.3a–d). Stromatic migmatites commonly show structures related to melt migration and extraction, such as collapsed foliation (Fig. 3.3e)

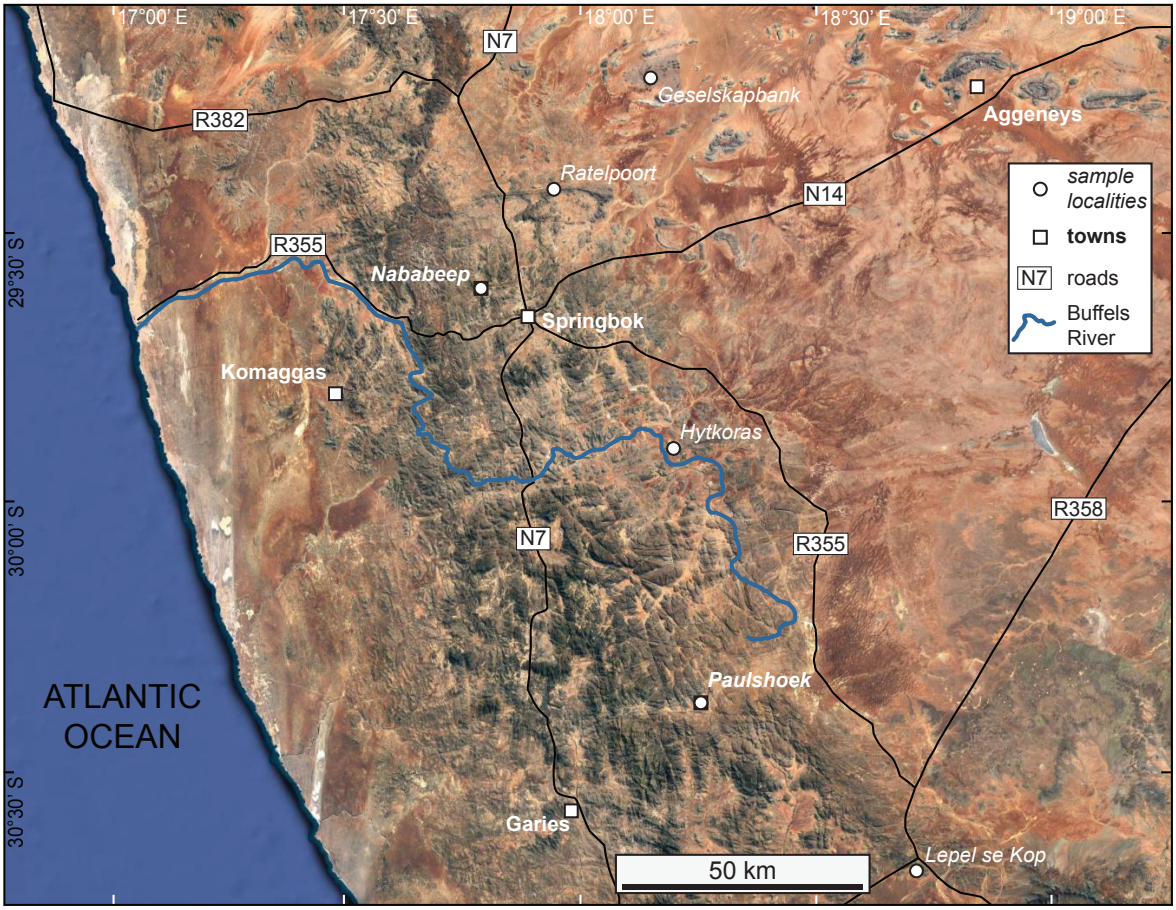


Figure 3.2: Locality map of the Bushmanland Subprovince showing the position of sample sites. Background map from Google Earth®.

and/or pucker structures (Fig. 3.3h). Rocks occurring in the northern part of the Namaqua Sector display coarse-grained prisms of sillimanite, interpreted as paramorphs after early andalusite (Fig. 3.3f, g). More residual pelitic granulites exhibit smaller portions of leucosome and have an overall massive, granofelsic texture (Fig. 3.3f). At Geselskapbank (Fig. 3.2) aluminous metapelites occur as massive, fine-grained granoblastic varieties and as sheared L-tectonites displaying a strong mineral lineation delineated by large prisms of sillimanite (possible paramorphs after andalusite, Fig. 3.3g). Garnet, biotite, sillimanite and cordierite are recognised in hand-specimen of both varieties, however indications of partial melting are absent. A ∼350 m wide thrust zone separates these rocks in the footwall from isolated pods of dark, garnet-absent, stromatic biotite–cordierite–sillimanite–K-feldspar migmatites in the hangingwall (Fig. 3.3h; cf. Grütter, 1986). Field relations suggest that the leucosome-absent rocks form part of the amphibolite facies part of the BSP (cf. Waters, 1986b, 1989) with characteristics similar to rocks from the Aggeneys terrane ∼70 km east of Geselskapbank (Diener, 2014). Therefore, the migmatites are interpreted as allochtonous granulite facies klippen of the LFROTZ that were thrusted onto the BSP along the Groothoek Thrust during assembly of the BSP (Fig. 3.1; cf. Macey *et al.*, 2017).

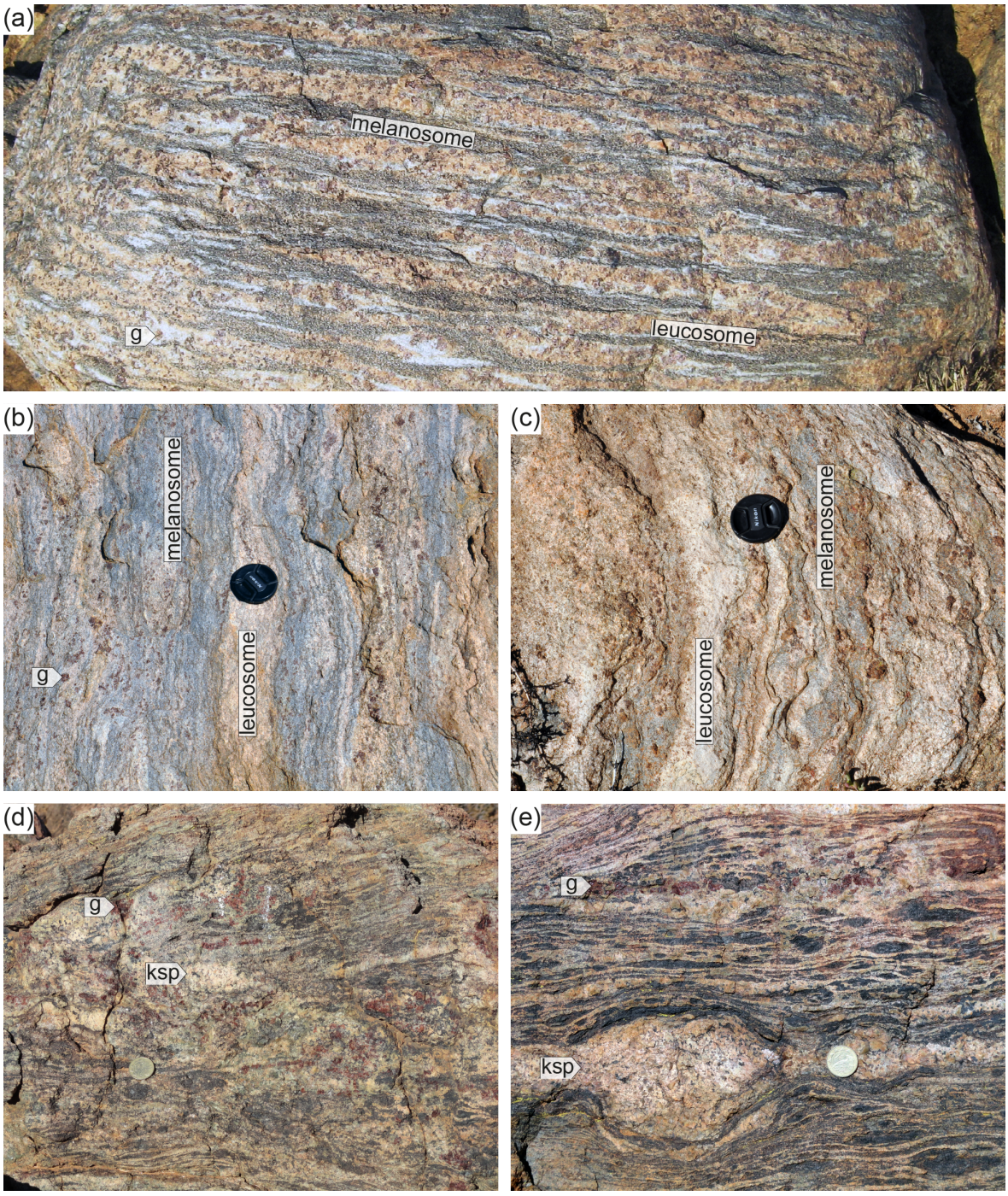

(a)
melanosome
g
leucosome
(b)
melanosome
g
leucosome
(c)
melanosome
leucosome
(d)
g
ksp
(e)
g
ksp

Figure 3.3

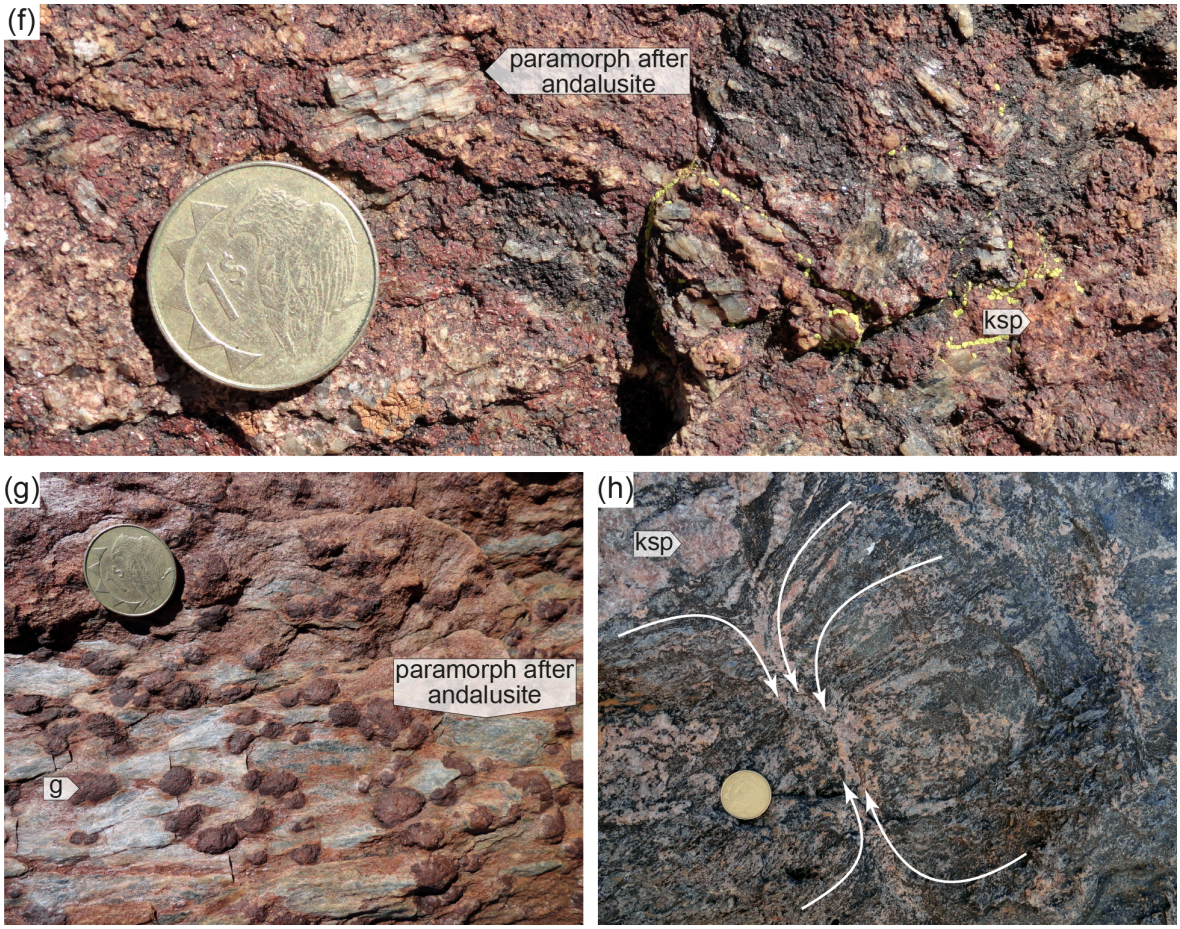


Figure 3.3: (continued) Field occurrences of aluminous metapelites of the Namaqua Sector. (a) Coarse-grained sillimanite-rich migmatite with stromatic leucosome hosting peritectic garnet and feldspars. Sample NMC102, Lepel se Kop. (b, c) Fine-grained layered rocks showing stromatic leucosome hosting poikilitic garnet overgrowing the fabric. Sample NMC99 (b) and NMC101 (c), Paulshoek. (d, e) Coarse-grained variety hosting thin stromatic leucosomes locally disrupting the pre-migmatisation foliation, forming feldspar-rich segregations. Centimetre-thick leucosomes locally display boudinage and necking (e), likely due to fabric-collapse accompanying melt extraction. Sample NMC23 (d) and NMC24 (e), Nababeep. (f) Massive, granoblastic aluminous metapelite rich in feldspars hosting large (up to ∼2 mm) prisms of sillimanite replacing andalusite. Sample NMC21, Ratelpoort. (g, h) Samples collected at Geselskapbank. (g) Massive, fine-grained leucosome-absent variety dominated by garnet and paramorphs of sillimanite after andalusite. Note the well developed mineral stretching lineation. Sample NMC05. (h) Dark, leucosome-rich variety displaying coarse-grained segregations rich in feldspar and pucker structures, indicating pathways of melt-migration (white arrows indicating interpreted direction of melt extraction). Camera lens cap and coin have a respective diameter of 6.7 cm and ∼2 cm.

3.5 Detailed sampling – Hytkoras

The main study area is located on the farm Hytkoras, about 35 km south-east of the town of Springbok and within the granulite facies core of the BSP (Fig. 3.4). The area was first described as part of the so-called Buffels River Shear Zone in the regional tectonic interpretation of Joubert (1971) before it was subjected to detailed petrological investigations by Moore and Waters (1990); Waters (1986a,b, 1988); McStay (1991). Much of this early work focused on the occurrence of unusual mineral assemblages in preserved in Mg–Al-rich gneisses (Moore and Waters, 1990; Waters, 1986a). Peak metamorphic conditions of ∼750–800 °C at 5 kbar were estimated from these lithologies at Hytkoras, and are similar to estimates from other parts of the central BSP (Waters and Whales, 1984; Waters, 1986b, 1989; Raith and Harley, 1998; Clifford *et al.*, 2004).

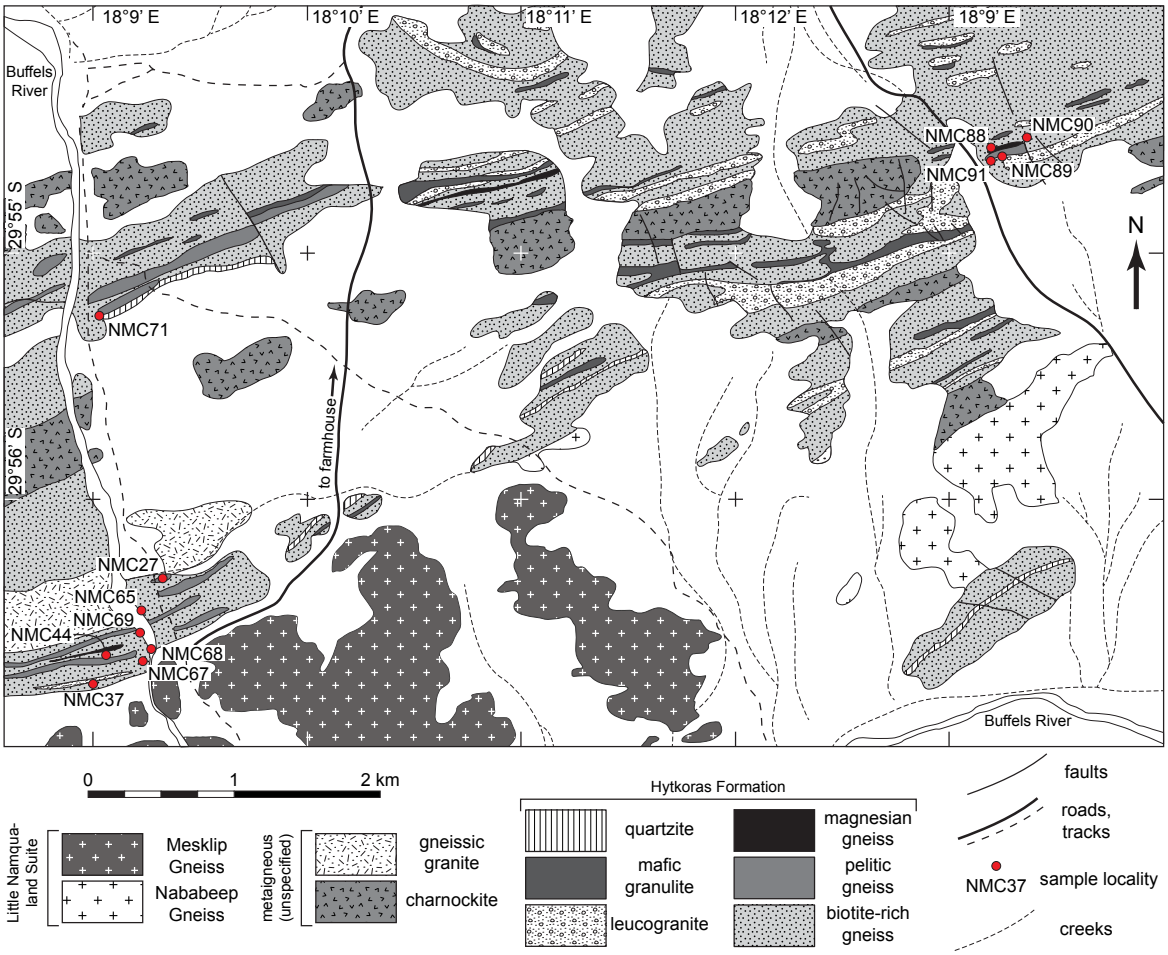


Figure 3.4: Simplified geological map of Hytkoras (modified after McStay, 1991).

The area is dominated by felsic gneisses of the Little Namaqualand Suite, namely the Mesklip Gneiss and the Nababeep Gneiss that form large tabular bodies and crop out as smooth domes (Fig. 3.5a). The gneisses consist of variably deformed plagioclase, quartz and K-feldspar augen with minor garnet. Locally, incipient charnockitisation can be recognised

as greenish patches, containing coarse-grained K-feldspar, plagioclase, quartz and brown hornblende (Fig. 3.5b). Pseudomorphs of dark green biotite, chlorite and Fe-oxides are locally present. Garnet is associated with clots of biotite and surrounded by feldspar-rich haloes, indicating that garnet grew at the expense of igneous biotite, possibly in the presence of minor melt fractions (Fig. 3.5b). Largely anhydrous garnet-leucogranites (Fig. 3.5d) form sheets of variable thickness of up to $\sim$ 2 m dominated by K-feldspar, plagioclase, quartz and garnet are interpreted as crystallised melt accumulations extracted from adjacent migmatites (cf. Waters, 1988). Outcrops of the post-tectonic Spektakel Suite are notable absent.

Outcrops of supracrustal lithologies of the Hytkoras Formation of the Kamiesberg Group occur as more or less continuous, E–W striking and steeply southward-dipping belts and lenses. The largest of these is some 100 m wide and extends for about 2 km along strike. The Hytkoras Formation consists of high-grade metasedimentary and metavolcanic rocks, including aluminous metapelite, magnesian metapelite, semi-pelite, metagreywacke, biotite-rich gneisses, quartzites, two-pyroxene mafic granulite, calc-silicate and Mg–Al-rich gneisses (Fig. 3.4; McStay, 1991). The sequence is intruded by thin sheets of garnet leucogranite that are interpreted as segregations and accumulations of melt generated from adjacent migmatites (cf. Waters, 1988).

Primary sedimentary bedding (S_0) has been partly transposed into well-developed compositional metamorphic layering (regionally referred to as S_2; Joubert, 1971, 1986b,a) during main D_2 deformation (Fig. 3.6a, b and 3.7a, b). Transposition of S_0 into S_2 is recognised by isoclinal folds (F_2) showing round to sharp hinge zones and limbs lying in the plane of the gneissic foliation, striking roughly E–W and dipping steeply (40–80°) to the south. In metapelites, sillimanite, biotite and garnet define the L_2 mineral lineation, plunging roughly parallel to the axes of minor F_2 folds in an overall southerly direction. The S_2 fabric may be locally disrupted by melt segregations (Fig. 3.6c). The granitic gneisses show overfolding and thrusting, but have a shallower-dipping S_2 fabric than the supracrustals. Augen in the gneisses are aligned parallel to L_2 (Joubert, 1971). Strain partitioning in the supracrustal sequence resulted in boudinage of competent lithologies such as Mg–Al-rich gneisses and mafic granulites. These lithologies typically have a massive granoblastic texture and are only weakly foliated or undeformed (Fig. 3.10c, d and 3.11a–c). Leucosome-rich metapelites and other less competent lithologies have a well-developed migmatitic or gneissic layering (Fig. 3.6).

Aluminous metapelites display stromatic (Fig. 3.6a, b) or nebulitic leucosomes (Fig. 3.6c) that host variably-sized peritectic garnet (5–50 mm), cordierite, K-feldspar, plagioclase and quartz whereas melanosomes consists of a well-foliated matrix of biotite and sillimanite. Large garnets are wrapped in a feldspar-rich matrix and are strongly poikiloblastic, hosting abundant inclusions of biotite and sillimanite (Fig. 3.6d).

Magnesian metapelites host leucosomes with black, cm-sized polygonal orthopyroxene (Fig. 3.7a), poikilitic red garnet of similar size and coarse-grained feldspars (Fig. 3.7). The rocks may be more or less massive (Fig. 3.7c), or show patchy (Fig. 3.7a, d) to stromatic leucosomes (Fig. 3.7b), in which case they display well-developed metamorphic layering.

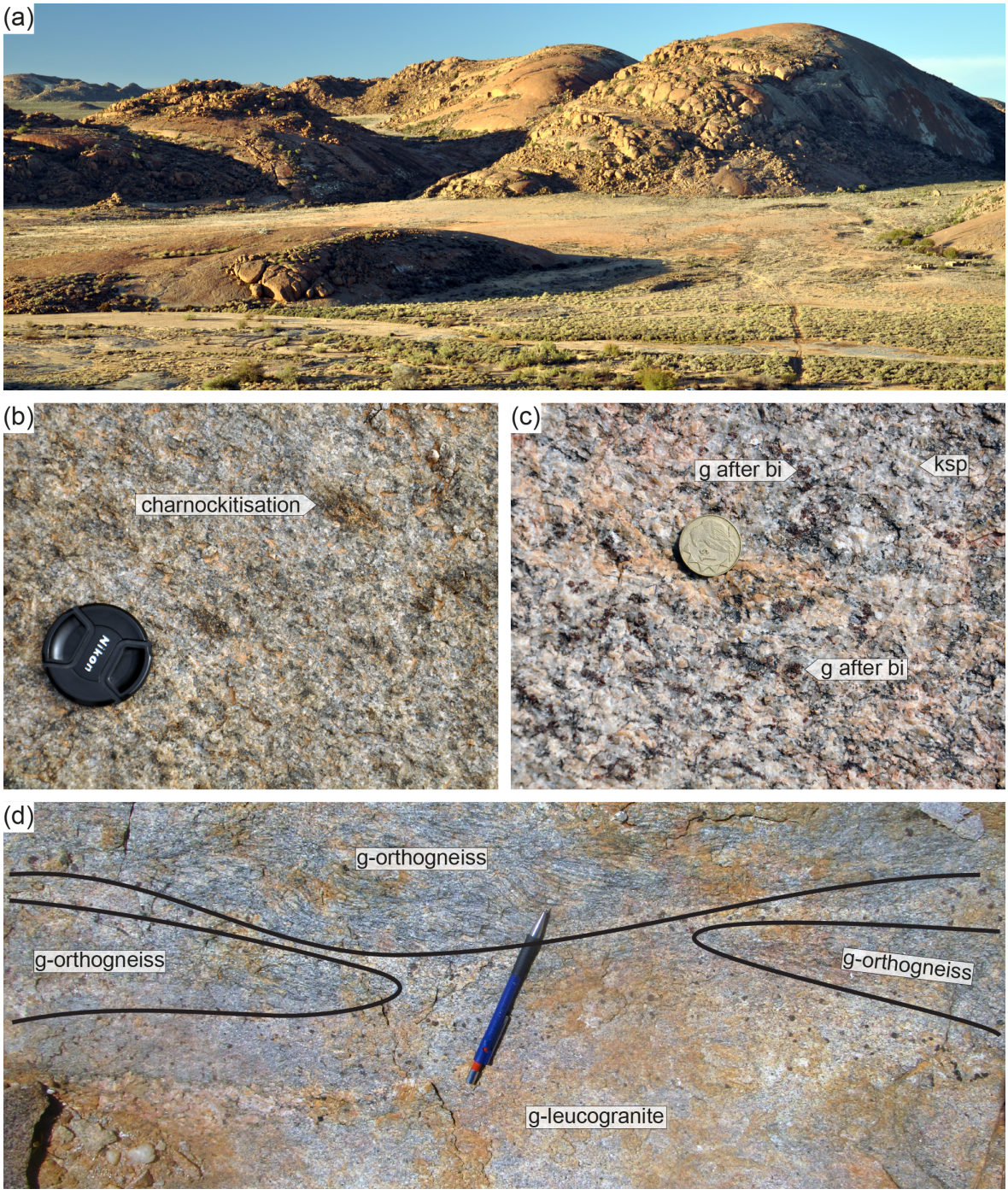


Figure 3.5: Field photographs of orthogneiss occurrences at Hytkoras. (a) Panoramic view on domes of the Little Namaqualand Suite cropping out in field area. (b) Charnockitised Mesklip Gneiss, greenish patches consist of clots of hornblende ± chlorite, possibly replacing former pyroxenes. (c) Augen gneiss displaying garnet (g) overgrowing igneous biotite (bi) and surrounded by thin haloes of feldspars (ksp). (d) Foliated garnet-bearing orthogneiss intruded by garnet-leucogranite, possibly representing segregations from nearby melting supracrustals. Camera lens cap and coin measure 6.7 cm and ∼2 cm, respectively. Pencil measures ∼14 cm.

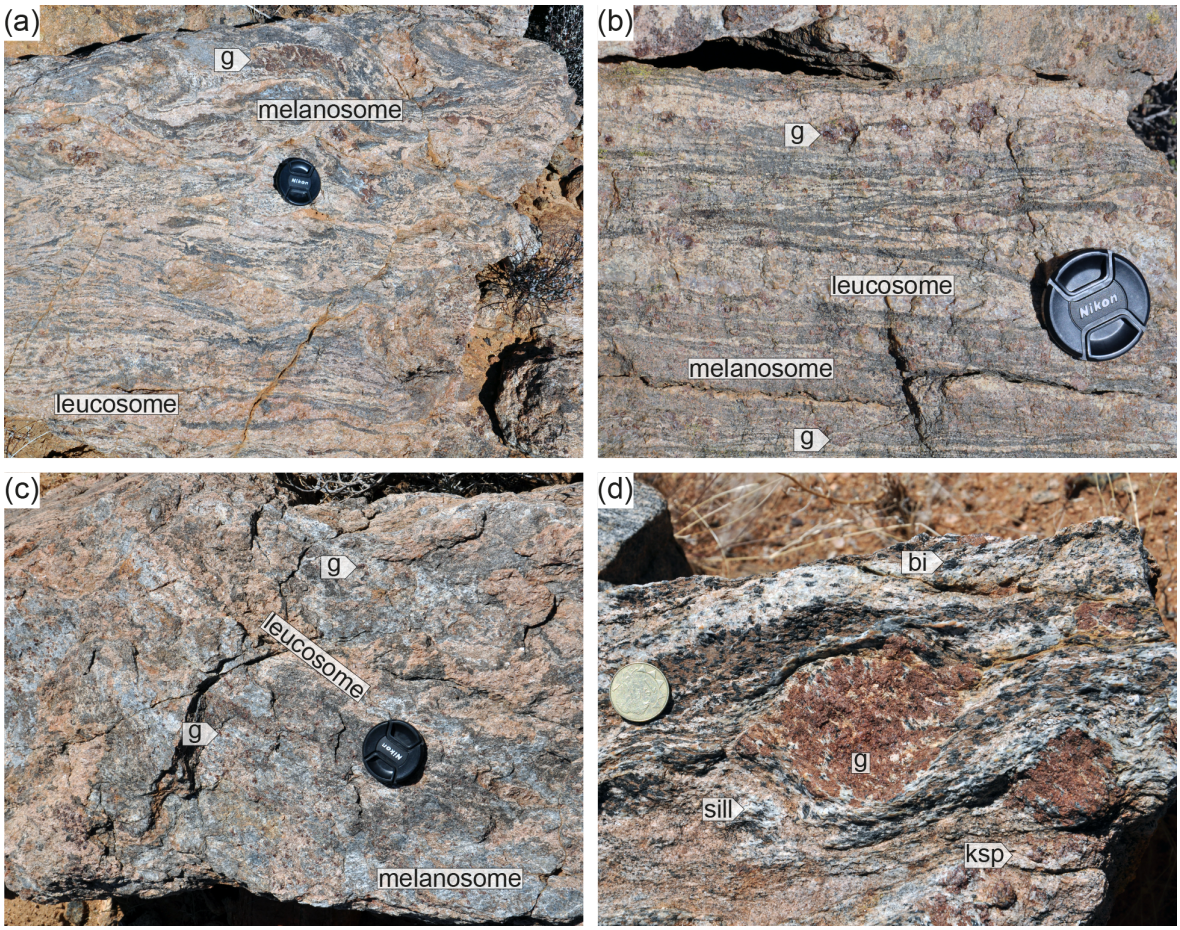


Figure 3.6: Field photographs of aluminous metapelites. (a, b) Stromatic migmatites displaying clear metamorphic layering in leucosome and melanosome. (c) Fine-grained variety displaying nebulitic feldspar-rich leucosomes. (d) Close-up of large peritectic garnet (g) poikiloblast rich in inclusions of biotite (bi) and sillimanite (sill), embedded in biotite–sillimanite–K-feldspar (ksp) matrix. Camera lens cap and coin have a respective diameter of 6.7 cm and ∼2 cm.

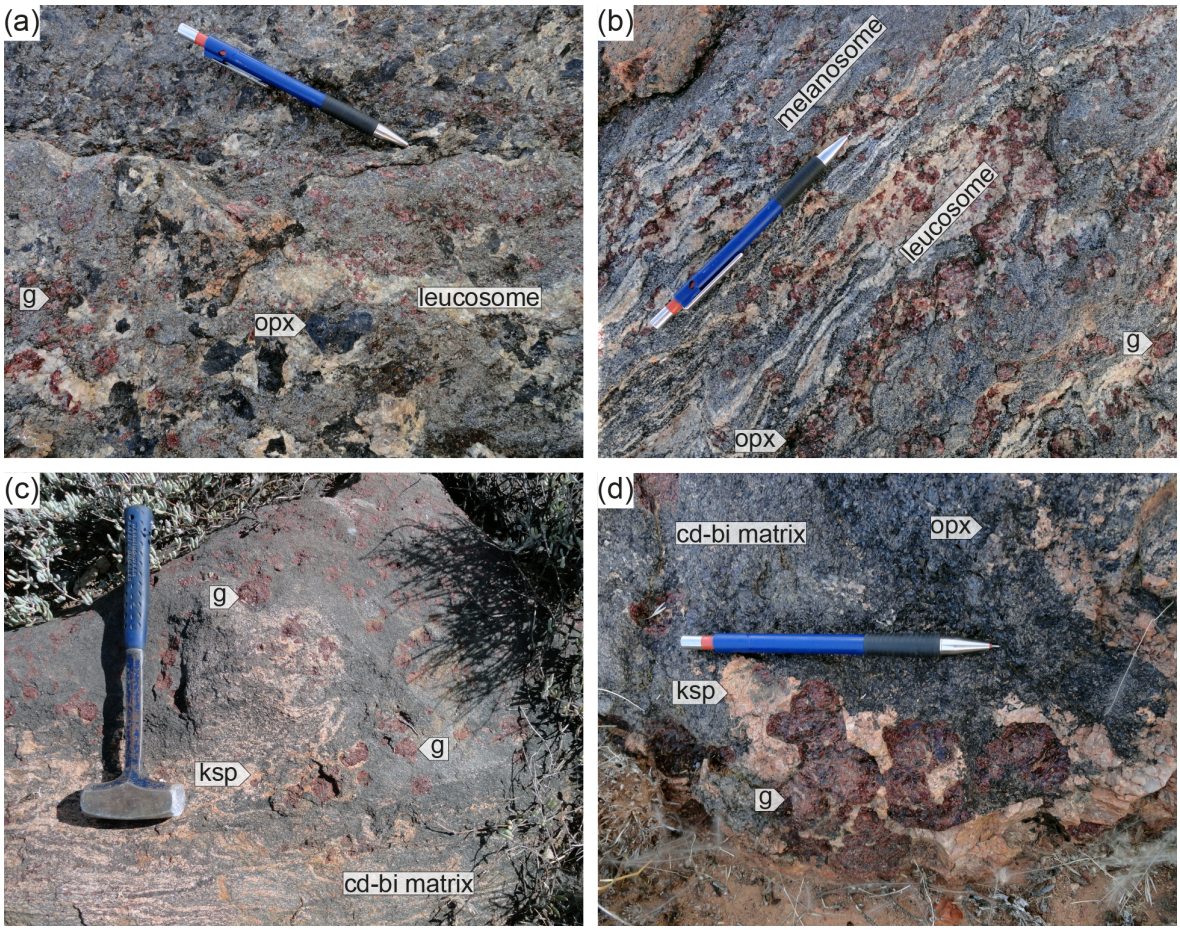


Figure 3.7: Field photographs of magnesian metapelites. (a, b) Strongly migmatised variety hosting large black orthopyroxene (opx) and red poikilitic garnet, surrounded by light-coloured leucosome dominated by feldspars defining weak gneissic layering (b). (c) Massive variety hosting large peritectic garnet porphyroblasts and feldspar-rich segregations embedded in granoblastic matrix of cordierite and biotite. (d) Close-up of large garnet porphyroblasts surrounded by pink, K-feldspar-rich segregation. Hammer and pencil is ∼40 cm and ∼14 cm long, respectively.

Fine-grained granoblastic cordierite and biotite dominate the melanosome in this rock type (Fig. 3.7). In exceptional cases garnets reach up to 50 mm in size and are embedded in pegmatitic feldspar-rich segregations (Fig. 3.7d).

Metagreywackes are volumetrically subordinate. They occur as leucocratic, meter-sized layers and lenses in close association with other metasedimentary rocks, suggesting a co-depositional relationship. The rocks are dominated by a fine-grained, granoblastic, quartzofeldspathic matrix with minor biotite. A weak metamorphic layering is discernible in the form of cm-sized biotite-poor but quartz–feldspar-rich leucosomes hosting small (generally <5 mm) garnet porphyroblasts, suggesting minor partial melting (Fig. 3.8).

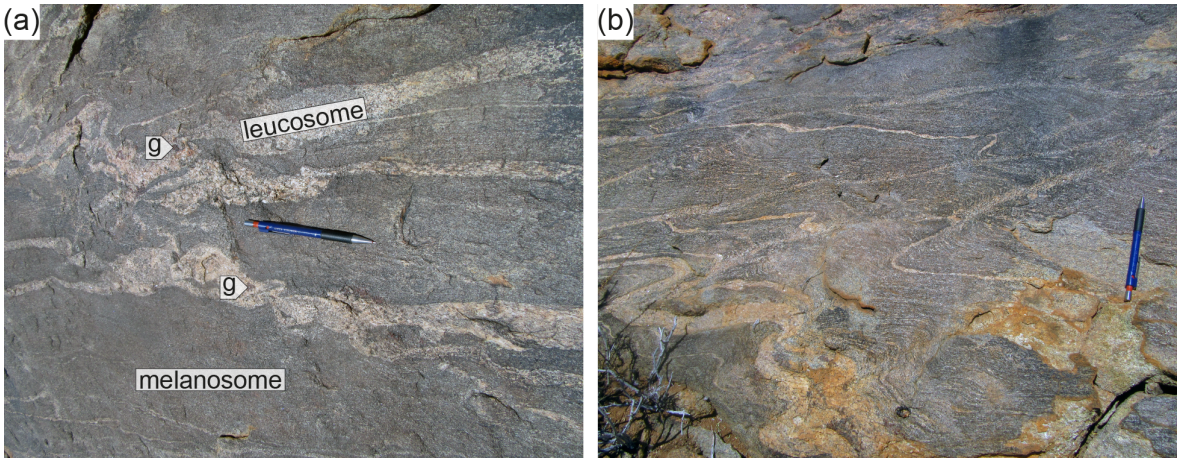


Figure 3.8: Field photographs of metagreywacke. (a) In-situ melting forming discrete garnet-bearing quartzofeldspathic leucosomes. (b) Leucosomes locally disrupting an earlier metamorphic fabric. Pencil ∼14 cm long.

Amphibole-bearing rock types range from intermediate (Fig. 3.9) to more mafic end-members (Fig. 3.10) and bracket coarse-grained leucosome-absent rocks (Fig. 3.10d) and varieties that display incipient melting and metamorphic layering (Fig. 3.9a and 3.10a, c). Leucosomes may be well-developed and interconnected in a stromatic network (Fig. 3.9b) including features indicative of melt transfer, such as pucker-structures (Fig. 3.9b and 3.10b, e.g. Diener *et al.*, 2014b). Common to all mafic granulites is the presence of orthopyroxene, which is strongly poikilitic when occurring in feldspar-rich segregations (Fig. 3.9a, b and 3.10a, c). Dark-green, coarse-grained peritectic hornblende may also be part of segregations (Fig. 3.10b). Waters (1988) describes discrete (1–5 cm thick) symmetric anhydrous margins of pyroxene granulite on narrow (10 cm–3 m) layers of hornblende-granulite at Hytkoras. Figure 3.10c shows an example of hornblende-granulite hosting cm-sized leucosomes of porphyroblastic orthopyroxene and plagioclase as well as narrow dehydrated margins of pyroxene-granulite lacking evidence for partial melting. Leucosome-absent dehydrated margins are plagioclase-poor and dominated by granoblastic, interlocked poiklitic pyroxenes hosting numerous inclusions of hornblende (Fig. 3.10c). Similarly, massive, leucosome-absent mafic granulites consist of interstitial plagioclase and strongly poikilitic to skeletal clino- and orthopyroxene rich in

inclusions of hornblende (Fig. 3.10d).

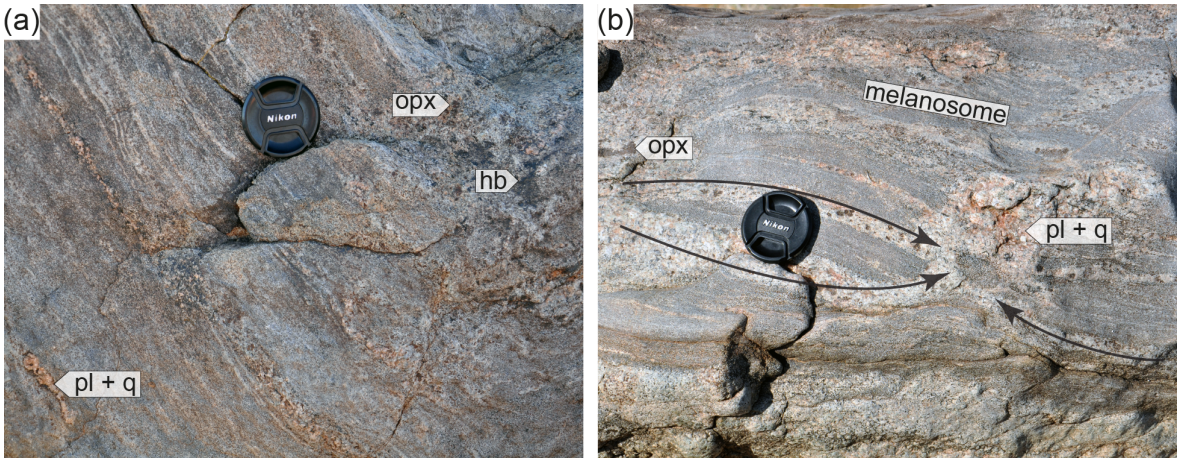


Figure 3.9: Field photographs of intermediate gneisses. (a) Orthopyroxene-bearing variety displaying metamorphic layering of hornblende–biotite–quartz-rich melanosome and plagioclase (pl)–quartz-rich leucosome, locally accumulating in pegmatitic segregations. (b) Migmatised variety displaying a stromatic network of coarse-grained leucosome of peritectic feldspars and orthopyroxene, locally ponding in pucker-structures. Locally collapsed foliation indicates melt transfer (indicated by black arrows). Camera lens cap has a diameter of 6.7 cm.

Moore and Waters (1990) described a suite of massive, leucosome-absent Mg–Al rich gneisses that occur as metre-sized lenses and layers commonly sandwiched between metabasite and metapelite. Mixtures of chlorite-rich altered and redeposited volcano-sedimentary material including evaporitic and clay sedimentary elements are suggested as potential protoliths for magnesian gneisses (Moore and Waters, 1990). These rocks typically lack any internal fabric and are dominated by granoblastic cordierite and phlogopite-rich biotite (Fig. 3.11), most commonly in association with orthopyroxene (Fig. 3.11a). A variety of unusual minerals may be present, occasionally in rock-forming abundances. These include sapphirine, spinel, gedrite, garnet, feldspars and minor sillimanite, corundum, tourmaline and rare kornerupine (Waters, 1986a). Quartz may be present, but is never in association with sapphirine or spinel. Cm-sized porphyroblasts after various low-grade metamorphic phases are common. A spectacular example hosts cm-sized, oval to hypidiomorphic orthopyroxene surrounded by a cm-wide reaction halo (insert on Fig. 3.11a) which are suggested to have formed after gedrite (Waters, 1986a). Up to 10 cm long prismatic porphyroblasts with square cross-sections (Fig. 3.11b) have been interpreted as pseudomorphs after andalusite (Waters, 1986a). Blue–green prismatic textures are inferred to have pseudomorphed staurolite and possibly Al-silicate (Fig. 3.11c; Waters, 1986a). Rare varieties are dominated by gedrite, coexisting with coarse-grained spinel and poikilitic orthopyroxene, displaying a weak planar fabric (Fig. 3.11d).

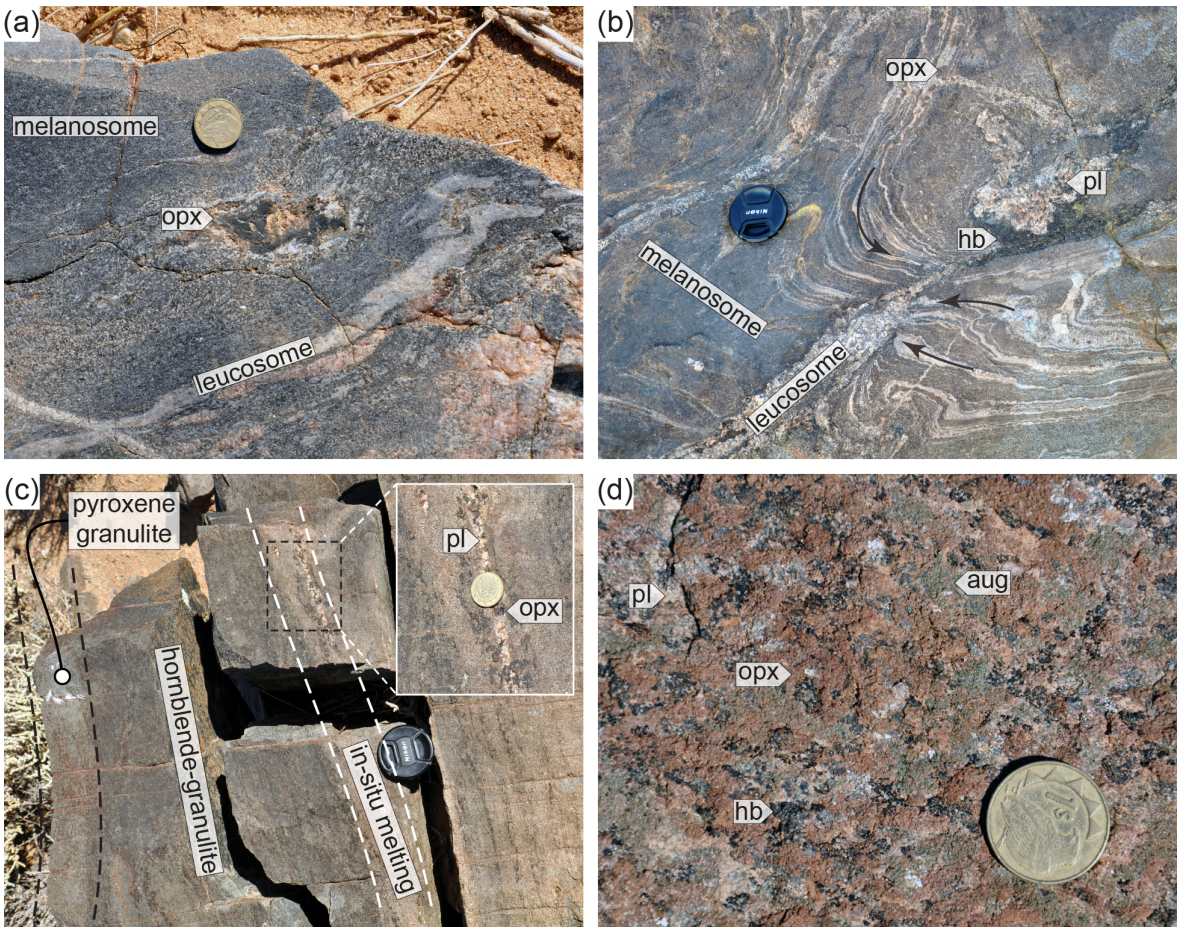


Figure 3.10: Field photographs of mafic granulites. (a, b) Migmatitic mafic granulite with fine-grained massive melanosome disrupted by plagioclase-rich leucosome. (a) Large peritectic orthopyroxene surrounded by a halo of plagioclase (sample NMC69). (b) Pervasively migmatised mafic granulite displaying stromatic leucosome locally ponding in inferred melt-extraction channel. Arrows indicate inferred direction of melt movement and extraction. Note coarse-grained accumulations of dark-green hornblende (hb) and light-coloured plagioclase. (c) Dark hornblende-granulite showing small-scale in-situ melting with the formation of coarse-grained segregations of peritectic orthopyroxene and plagioclase (see blow-up) and dehydrated margins of pyroxene granulite. (d) Close-up of coarse-grained pyroxene-granulite with minor hornblende included in pyroxene-poikiloblasts (sample NMC27). Camera lens cap and coin have a respective diameter of 6.7 cm and ∼2 cm.

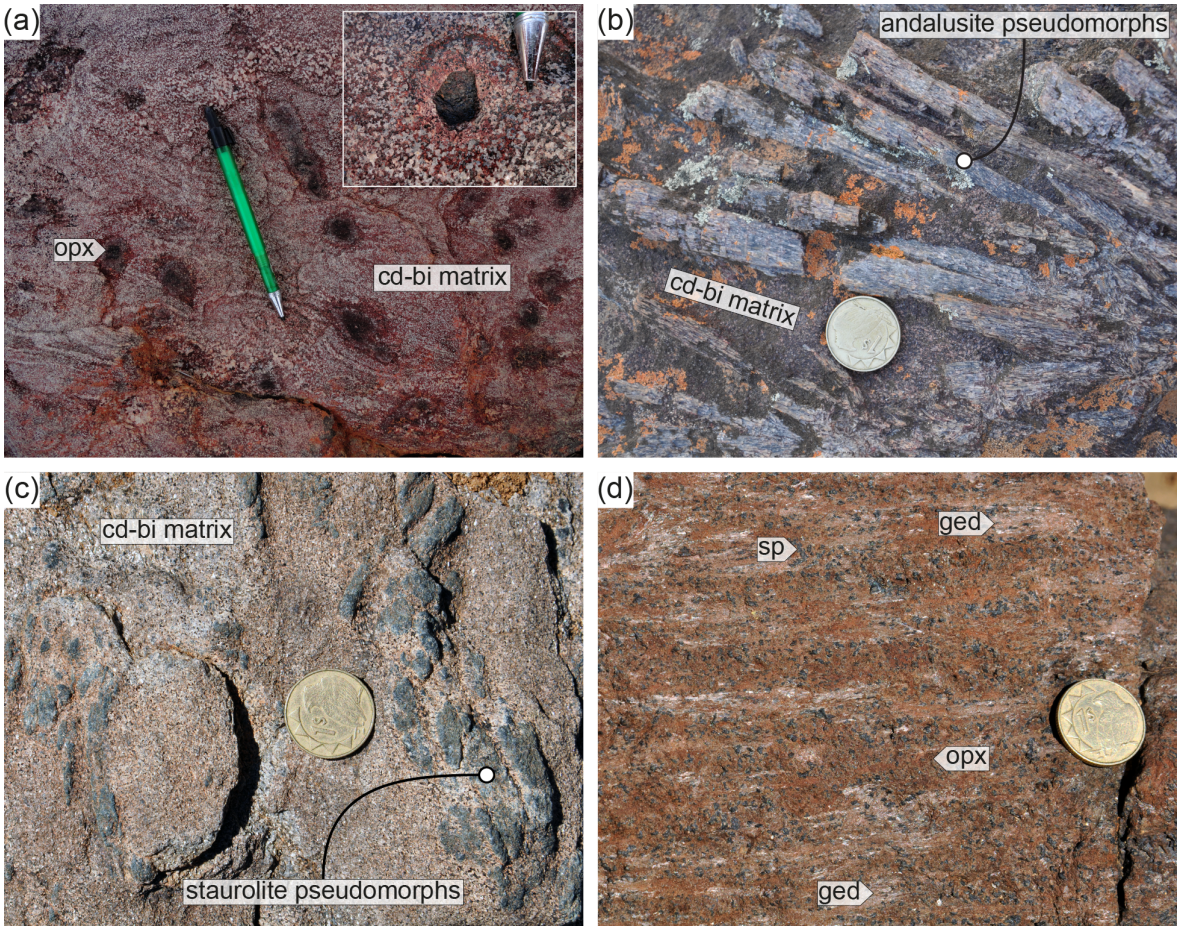


Figure 3.11: Field photographs of magnesian gneisses. (a) Massive, leucosome-absent rock hosting cm-sized dark brown orthopyroxene porphyroblasts in granoblastic matrix of cordierite (cd) and phlogopite-rich biotite. Insert shows subhedral orthopyroxene surrounded by weathered, cordierite-rich halo (sample NMC44). (b) Large prismatic pseudomorphs after andalusite in fine-grained matrix of cordierite and phlogopite-rich biotite (sample NMC88). (c) Pseudomorphs of spinel–magnetite ± corundum after staurolite in matrix of granoblastic cordierite and phlogopite-rich biotite (sample NMC90). (d) Foliated gedrite–orthopyroxene–spinel magnesian gneiss (sample NMC91). Coin is 6.7 cm in diameter, pencil is ∼14 cm long.

Chapter 4

Petrography and mineral chemistry

This chapter summarises the main petrographic and mineral compositional observations of the investigated samples. Representative electron-microprobe analyses are reported in appendix .

4.1 Regional sampling – aluminous metapelites

Regional sampling targeted aluminous metapelites occurring in the Namaqua Sector. The rocks are typically characterised by the assemblage garnet–sillimanite–cordierite–plagioclase–ilmenite ± biotite ± K-feldspar ± magnetite ± spinel in variable modal ratios. Common accessories are apatite, zircon and monazite. Petrographic descriptions for aluminous metapelites from each sample locality is followed by a detailed investigation of various rock types found at Hytkoras (see below).

4.1.1 Lepel se Kop

Pelitic granulites of this locality are characterised by the coexistence of garnet (∼5–10 vol. %), cordierite (∼10–15 vol. %), biotite (∼5 vol. %), sillimanite (∼5–10 vol. %), plagioclase (∼10 vol. %), K-feldspar (∼20–30 vol. %), quartz (∼30 vol. %), ilmenite and magnetite (∼1 vol. %). The investigated samples NMC47 and NMC102 are highly residual and dominated by feldspars and quartz, with garnet and cordierite forming large porphyroblasts hosting abundant inclusions.

Garnet forms skeletal to rounded poikiloblasts (∼2–5 mm) with inclusions of randomly oriented fibrolitic sillimanite, ilmenite, magnetite, quartz and rare blue–green spinel. Inclusions predominantly occur at the core surrounded by an inclusion-free, commonly serrated rim (Fig. 4.1a, c). Grains display quartz-rich haloes (Fig. 4.1a). Garnet is compositionally Fe-rich ($X_{\mathrm{Fe}} = \frac{\mathrm{Fe}^{2+}}{\mathrm{Fe}^{2+}+\mathrm{Mg}} = 0.69$–$0.76$) and roughly homogeneous, with cores slightly impoverished in almandine and enriched in pyrope ($X_{\mathrm{alm}} = 0.66$–0.68; $X_{\mathrm{py}} = 0.27$–0.29) compared to rims ($X_{\mathrm{alm}} = 0.70$–0.72; $X_{\mathrm{py}} = 0.23$–0.25). Grossular- and spessartine-component are constant from core to rim ($X_{\mathrm{grs}} = 0.02$–0.04, $X_{\mathrm{sps}} = 0.01$–0.02, respectively).

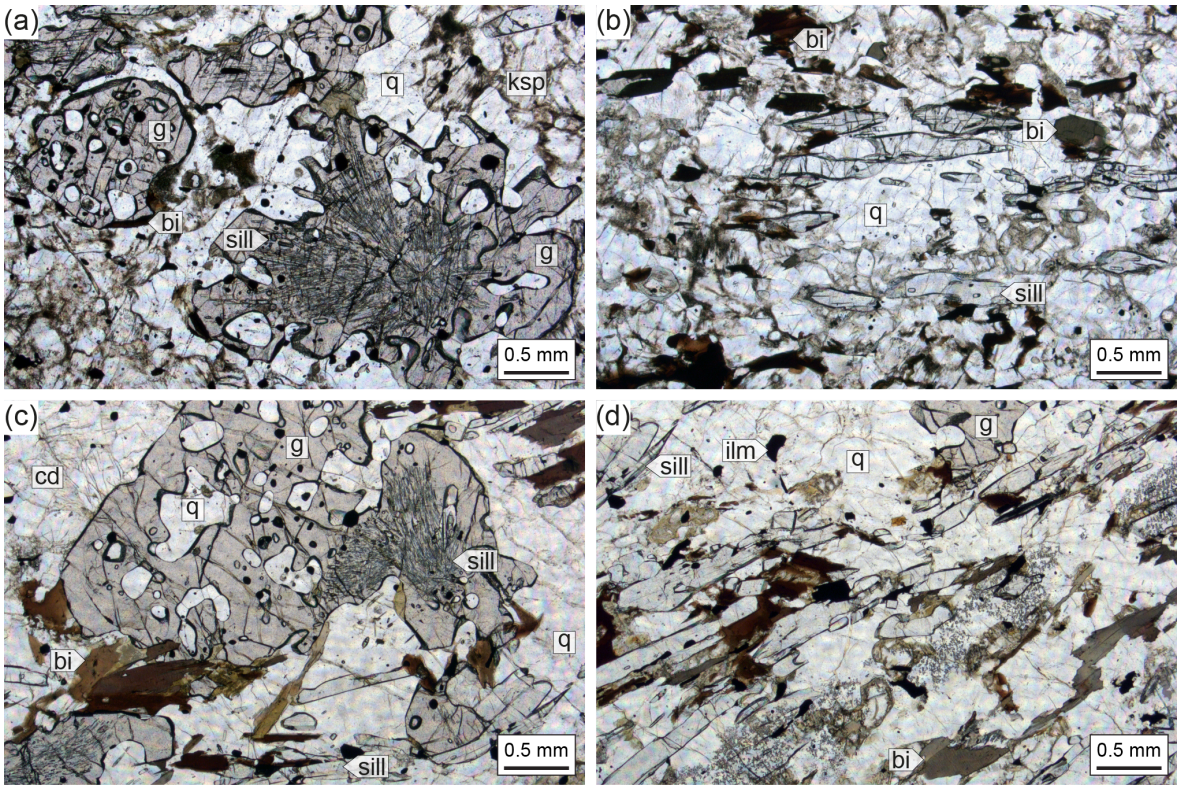


Figure 4.1: Thin section microphotographs in plain polarised light for aluminous metapelites from Lepel se Kop. (a, b) Sample NMC102. (c, d) Sample NMC47. (a, c) Large garnet poikiloblasts including radial to randomly oriented sprays of fibrolite and rounded grains of quartz and opaques at the core. Note clear, serrated rims surrounded by quartz-rich halo. (b, d) Coarse-grained blades of isoriented sillimanite and flakes of biotite defining a planar fabric in a groundmass of feldspars, cordierite and quartz.

Biotite is, together with sillimanite, a main fabric-forming constituent of the samples. It occurs as single flakes (∼0.5–1.5 mm) or roughly isoriented clots consisting of several, intergrown grains (Fig. 4.1b–d). Biotite is generally Fe-rich ($X_{\mathrm{Fe}} = 0.30$–0.45) with somewhat variable composition. Ti varies between 0.19–0.29 atoms per formula unit (a.p.f.u., based on 11 O), F-contents are 0.25–0.37 a.p.f.u. Cl is negligible. $\mathrm{Al^{VI}}$ varies between 0.17–0.29.

Cordierite occurs as rounded, anhedral grains that are largely pinitised. Compositionally cordierite is homogeneous and Mg-rich, with X_{Fe} of 0.28–0.30.

Sillimanite is found in two textural varieties, with a fibrolitic variety exclusive to garnet cores (Fig. 4.1a, c) and large needles (∼0.3–1.0 mm) defining a distinct mineral lineation in the rock matrix that is roughly parallel to felsic leucsomes (Fig. 4.1b, d). In the groundmass sillimanite is commonly intergrown with biotite, to which it displays sharp grain boundaries (Fig. 4.1d).

Feldspars are found in leucocratic and melanocratic portions of thin sections. K-feldspar forms anhedral grains (∼1–3 mm) decorated by perthitic exsolutions and variably altered at the rims to a fine-grained mesh of white mica. K-feldspar displays undulose extinction. Compositionally K-feldspar contains variable albite component ($X_{\mathrm{ab}} = \frac{\mathrm{Na}}{\mathrm{Na+Ca+K}}$) of 0.10–0.20 and low anorthite component ($X_{\mathrm{an}} = \frac{\mathrm{Ca}}{\mathrm{Na+Ca+K}}$) of ∼0.01. Exsolution-lamellae are albite-rich with $X_{\mathrm{ab}} = 0.71$ and negligible anorthite-content. Oligoclasic plagioclase occurs as small (< 1 mm) interstitial grains in the rock matrix, with 0.25–0.28 anorthite-content and limited orthoclase component ($X_{\mathrm{or}} = \frac{\mathrm{K}}{\mathrm{Na+Ca+K}}$) of 0.01. Opaques occur both as inclusions in garnet and the matrix as rounded droplets of magnetite and ilmenite that are commonly intergrown.

4.1.2 Paulshoek

Samples from this locality display the ubiquitous presence of poikilitic garnet (∼5–15 vol. %), cordierite (∼15–20 vol. %), plagioclase (∼10 vol. %), K-feldspar (∼10–30 vol. %), ilmenite and magnetite (∼1 vol. %), hercynitic spinel (∼5–10 vol. %) and quartz in variable proportions as well as inconstant modal amounts of biotite and sillimanite. Accessory phases are apatite, zircon and monazite. Sample NMC46 and NMC101 are described in detailed.

Poikiloblastic garnet occurs as skeletal to hypidioblastic, rounded grains of variable size (∼0.1–5.0 mm) hosting inclusions of biotite, randomly oriented fibrolite (Fig. 4.2a), rounded cordierite (Fig. 4.2e), ilmenite, magnetite and rounded quartz. Inclusions are concentrated at garnet cores, whereas rims are predominantly clear. Garnet forms monomineralic coronae around nearby grains of spinel (Fig. 4.2a and insert therein), whereas occasionally the transition from garnet porphyroblast to coronae on spinel is gradational (Fig. 4.2b). Locally garnet coronae develop idioblastic crystal faces towards the groundmass, hosting vermicular inclusions of quartz. Garnet is rich in Fe, with roughly constant X_{Fe} of 0.63–0.67 for cores and rims. Coronae on spinel are slightly enriched, with X_{Fe} of 0.69–0.72. X_{alm} of 0.62–0.63 and X_{py} of 0.31–0.32 is measured for garnet porphyroblasts, whereas coronae show X_{alm} of 0.66–0.67 and X_{py} of 0.27–0.29. Grossular and spessartine are virtually constant, with X_{grs}

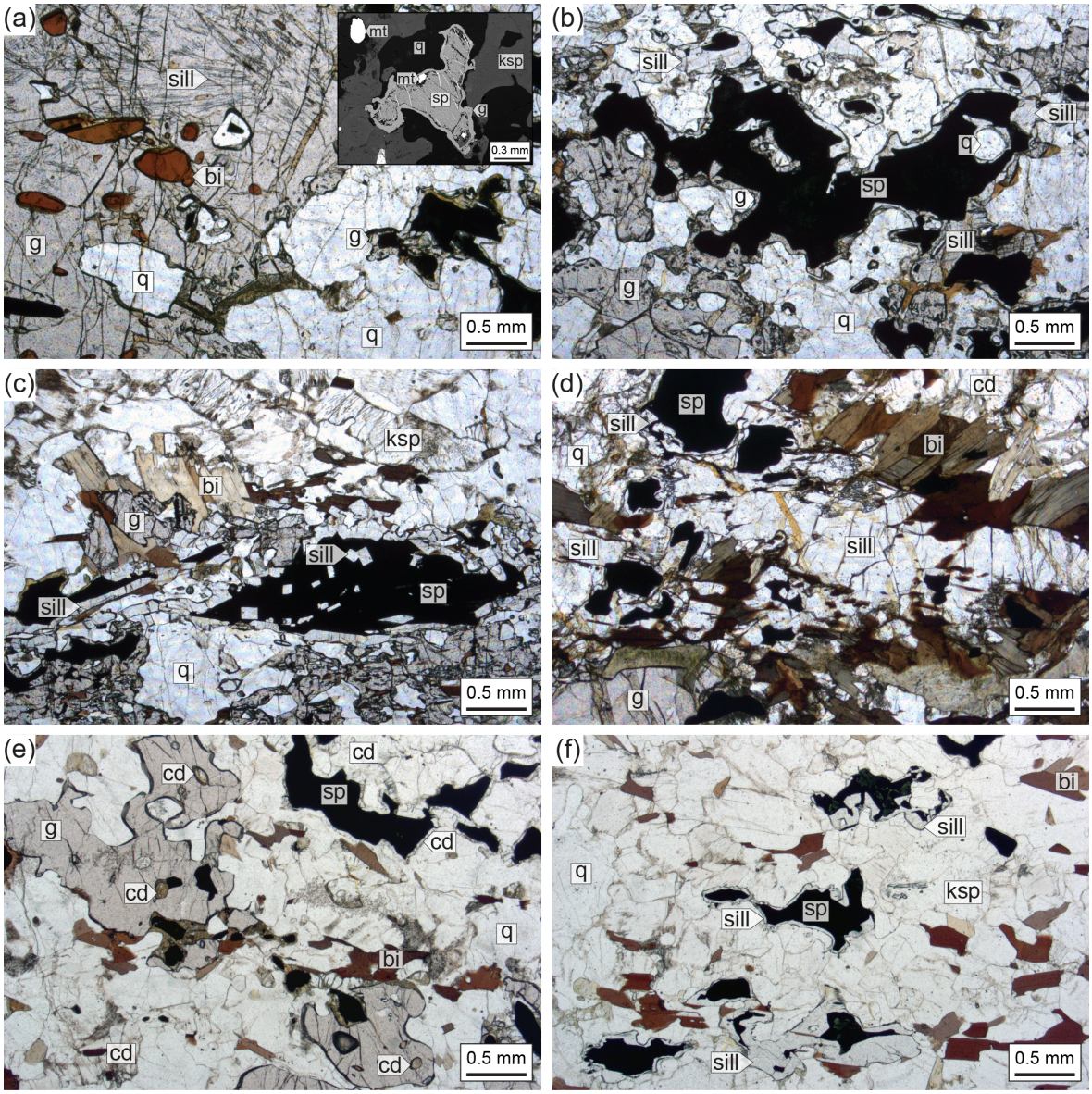


Figure 4.2: Thin section microphotographs in plain polarised light and BSE-image for aluminous metapelites from Paulshoek. (a–d) Sample NMC101. (e, f) Sample NMC46. Note various textural occurrences of hercynitic spinel (sp), armoured by garnet (a, b), cordierite (e) and sillimanite (b–d, f). (a, e) Large garnet poikiloblasts hosting randomly oriented fibrolite, biotite and rounded quartz (a) and rounded cordierite (e). (b) Large xenoblastic spinel shielded from quartz by garnet (left hemisphere) and sillimanite (right hemisphere). (c) Intergrowths of biotite and sillimanite in textural equilibrium with garnet and K-feldspar next to spinel armoured by sillimanite. (d) Stringer of biotite–sillimanite next to spinel rimmed by sillimanite. (f) Flakes of biotite scattered in matrix of cordierite, K-feldspar and quartz. Spinel is shielded by coronae of sillimanite.

$= X_{\mathrm{sps}} = 0.02$–$0.03$.

F–Ti-rich, dark brown biotite occurs as isolated inclusions in garnet (Fig. 4.2a) and as single flakes or clots in the rock matrix (Fig. 4.2f). Biotite mode is highly variable, roughly between < 0.05 and ~ 0.20 for different thin sections. Biotite preferentially occurs near / in contact with sillimanite, to which it shows sharp grain boundaries (Fig. 4.2c, d). Individual stringers of biotite–sillimanite next to minor spinel are locally dominant at the thin section scale (Fig. 4.2d). Inclusions in garnet are slightly more magnesian in comparison to matrix biotite ($X_{\mathrm{Fe}} = 0.24$ and 0.35–0.38, respectively). F amounts to $\sim$0.38–0.46 a.p.f.u. for inclusions and 0.35–0.39 a.p.f.u. for matrix mineral, whereas Ti is 0.25–0.27 and 0.23 a.p.f.u., respectively. Cl is negligible. $\mathrm{Al}^{\mathrm{VI}}$ is homogeneous with 0.04–0.06.

Cordierite is present as xenoblastic, elongated to rounded or interstitial grains in the matrix with highly variable size ($\sim$0.2–2.0 mm) and as spherical inclusions in garnet. Cordierite also forms thin, monomineralic coronae on nearby spinel. Matrix cordierite contains fine inclusions fibrolite, biotite and rounded quartz. X_{Fe} is roughly constant at 0.27–0.30. Alteration to pinite is commonly restricted to thin veinlets.

Sillimanite occurs as inclusions and matrix phase. Fine-grained fibrolitic sillimanite is randomly oriented in porphyroblastic garnet (Fig. 4.2a) and, less frequently, cordierite. Matrix sillimanite forms needles and prisms up to $\sim$1.0 mm in length, commonly intergrown with biotite (Fig. 4.2c, d). Thin coronae of sillimanite engulf nearby grains of spinel, commonly branching out from a larger prism of sillimanite, in a similar manner as garnet and cordierite (Fig. 4.2c, d and f). The mode of sillimanite is highly variable. In sample NMC101 sillimanite is abundant ($\sim$10–20 vol. %), whereas in sample NMC46 it is largely confined to coronae around spinel and rare, individual prisms scattered in the rock matrix, commonly in contact with biotite. In this sample sillimanite amounts to < 5 vol. %.

K-feldspar is a main constituent in the studied samples, forming large ($\sim$0.5 mm) xenoblastic to rounded grains in the rock matrix (Fig. 4.2c, f). Grains may include fine-grained fibrolite and are decorated by numerous fine-grained perthitic exsolutions. Interfaces with matrix quartz are commonly serrated. Compositionally variable, K-feldspar has X_{ab} of 0.10–0.33 and X_{an} of 0.00–0.02. Plagioclase forms smaller grains (< 0.5 mm) that occur in the interstices between matrix phases or as distinct, xenoblastic grains. Occasionally plagioclase forms, similar to garnet, cordierite and sillimanite, thin coronae that branch out from a larger grain to a nearby blast of spinel. Oligoclase has X_{an} of 0.33–0.37 and negligible X_{or} of 0.01.

Dark-green to black spinel forms elongated to xenoblastic grains of variable size ($\sim$0.5–3.0 mm) that are always surrounded by thin, uniform monomineralic coronae of garnet, cordierite, sillimanite or plagioclase depending on the adjacent phase (Fig. 4.2). Individual grains may display different coronae, defining one hemisphere rimmed by garnet and one by sillimanite. In both cases the corona-forming phase branches out from a nearby porphyroblast of garnet and sillimanite, respectively (Fig. 4.2b). Spinel is therefore never in direct contact with quartz, biotite or K-feldspar, because coronae are invariably present at the interface, even when rounded quartz is included in spinel. Fine-grained, mesh-like exsolutions of magnetite

decorate spinel porphyroblast (insert on Fig. 4.2a). Magnetite and ilmenite also form distinct, drop-shaped grains included in spinel. Compositions were determined using a defocussed electron beam to homogenise the exsolutions. Spinel is rich in hercynite, with X_{Fe} of 0.65–0.72 and low gahnite component ($X_{\mathrm{Zn}} = \frac{\mathrm{Zn}}{\mathrm{Zn+Fe^{2+}+Fe^{3+}+Mg+Mn+Cr}}$) of 0.01.

The investigated samples are rich in quartz, forming large (∼0.5–1.0 mm) rounded to xenoblastic grains showing lobate grain boundaries and undulose extinction. Magnetite and ilmenite are present as droplets included in garnet and spinel, and as distinct grains in the rock matrix.

4.1.3 Nababeep

The sample from this locality (NMC24) displays a distinct planar fabric defined by isoriented sillimanite (∼5–10 vol. %) and biotite (∼15–20 vol. %), wrapping garnet poikiloblasts (∼5 vol. %). Pinitised cordierite (∼5 vol. %), plagioclase (∼10–15 vol. %), K-feldspar (∼15–20 vol. %), magnetite and ilmenite (∼1 vol. %) and quartz (∼30 vol. %) complete the assemblage observed in the rock. Common accessories include apatite, monazite and zircon.

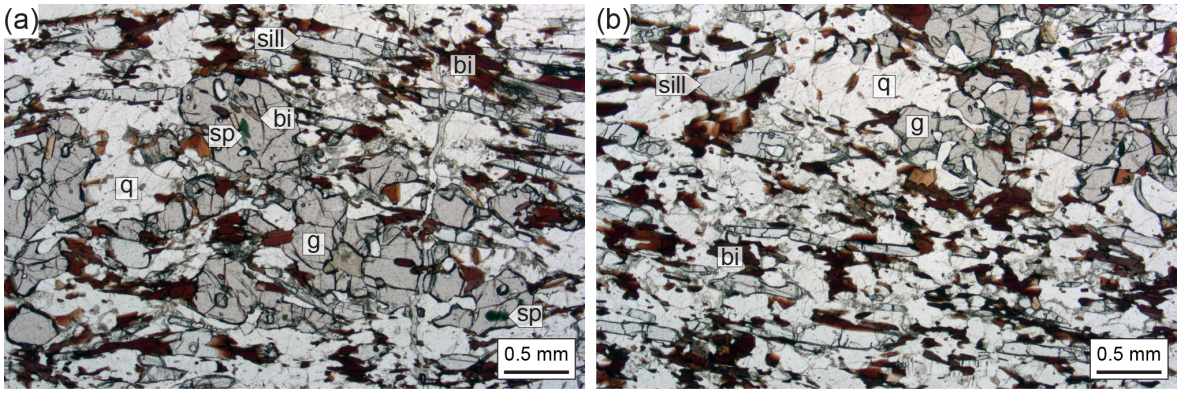


Figure 4.3: Thin section microphotographs in plain polarised light for aluminous metapelite sampled at Nababeep, sample NMC24. Note textural equilibrium between garnet, biotite and sillimanite in quartzofeldspathic matrix. Needles of sillimanite and biotite flakes define a distinct planar fabric.

Garnet occurs as skeletal to rounded poikiloblasts and in clusters of variable size, with individual grains ranging from ∼0.2–3.0 mm in diameter (Fig. 4.3). Garnet hosts abundant inclusions of rounded quartz, biotite and opaques as well as rare blue–green spinel. Almandine-rich garnet is compositionally homogeneous with X_{Fe} of 0.71–0.73, X_{alm} of 0.67–0.69, X_{py} of 0.27 and $X_{\mathrm{grs}} = X_{\mathrm{sps}} = 0.02$–0.03. No clear compositional variation is observed for cores and rims.

Red-brown pleochroic biotite is a dominant matrix constituent (Fig. 4.3), where it occurs as foliation-defining flakes and aggregates oriented roughly parallel to coexisting sillimanite and quartzofeldspathic segregations. Rounded individual flakes are embedded in garnet whereas thick clots are dominant in pressure shadows of large garnet porphyroblasts. Compositionally inclusion-biotite is distinctively more magnesian compared to the matrix mineral,

with X_{Fe} of 0.27–0.29 versus 0.34–0.36, respectively. F-contents are appreciable, amounting to 0.31–0.38 a.p.f.u. for inclusions and 0.28–0.33 a.p.f.u. in the matrix. Similarly, Ti is slightly higher in inclusions (0.26–0.30 a.p.f.u.) compared to matrix-biotite (0.21–0.28 a.p.f.u.). Al^{VI} is roughly homogeneous at 0.16–0.20.

Cordierite is heavily pinitised, forming xenoblastic aggregates of fine-grained white mica. Microprobe analyses did not yield satisfactory results due to extensive alteration.

Sillimanite is a main fabric-defining phase, occurring as large ∼0.5–1.0 mm) needles and prisms. Feldspars occur in the melanosome but are dominant in the leucosome, where they form xenoblastic grains of highly variable size (∼0.05–0.8 mm) displaying serrated interfaces to quartz. K-feldspar, plagioclase and quartz form anhydrous segregations alternated to melanocratic portions at thin section scale.

K-feldspar is characterised by X_{ab} of 0.12–0.23 and X_{an} of 0.01, whereas andesine plagioclase has X_{an} of 0.36–0.38 and X_{or} of 0.01. Magnetite and ilmenite are present as drop-shaped grains included in garnet and as distinct grains in the rock matrix.

4.1.4 Ratelpoort

Sample NMC21 from this locality is dominated by a largely anhydrous assemblage of garnet (∼5–10 vol. %)t, cordierite (∼20 vol. %), plagioclase (∼10–15 vol. %), K-feldspar (∼30 vol. %), ilmenite and magnetite (∼2 vol. %) and quartz (∼25 vol. %). Biotite and sillimanite are confined to rare, large intergrowths armoured by cordierite. Accessories in the sample are apatite, zircon and monazite.

Garnet is present as elongated to rounded porphyroblasts of variable size (∼1.0–20 mm) hosting inclusions of biotite, rounded cordierite, opaques and quartz (Fig. 4.4a). Rims are occasionally serrated (Fig. 4.4a). Compositionally garnet is homogeneous and Fe-rich with X_{Fe} of 0.68–0.71, X_{alm} of 0.65–0.70, X_{py} of 0.0.27–0.29 and $X_{grs} = X_{sps} = 0.03$ for cores and rims.

Ti-rich biotite is a minor phase and restricted to intergrowths with sillimanite (Fig. 4.4b–d). Small, individual flakes may be present as inclusions in garnet, cordierite or K-feldspar. X_{Fe} is 0.41–0.48, F-content is negligible whereas Cl-contents amount to 0.02–0.08 a.p.f.u. Notably, Ti amounts to between 0.14–0.30 a.p.f.u., with the highest values measured for individual grains in the matrix and those adjacent to ilmenite. Al^{VI} is 0.22–0.28.

Cordierite is a main phase in the investigated sample, forming xenoblastic to rounded grains of variable size (∼0.5–3.0 mm, Fig. 4.4b–d) and rounded inclusions in garnet (Fig. 4.4a). Cordierite is ubiquitous in the matrix and preferentially associated with sillimanite, which it includes or armours from other matrix phases. Compositionally matrix-cordierite is unzoned, displaying X_{Fe} of 0.28–0.30. Inclusions in garnet are distinctly more magnesian, with a homogeneous X_{Fe} of 0.23.

Sillimanite is volumetrically minor (< 5 vol. %) and found in two textural settings. Coarse-grained prisms and laths occurring in large (up to 2 cm, Fig. 3.3f) prismatic aggregates intergrown with cordierite and bleb-shaped ilmenite and magnetite are interpreted as paramorphs

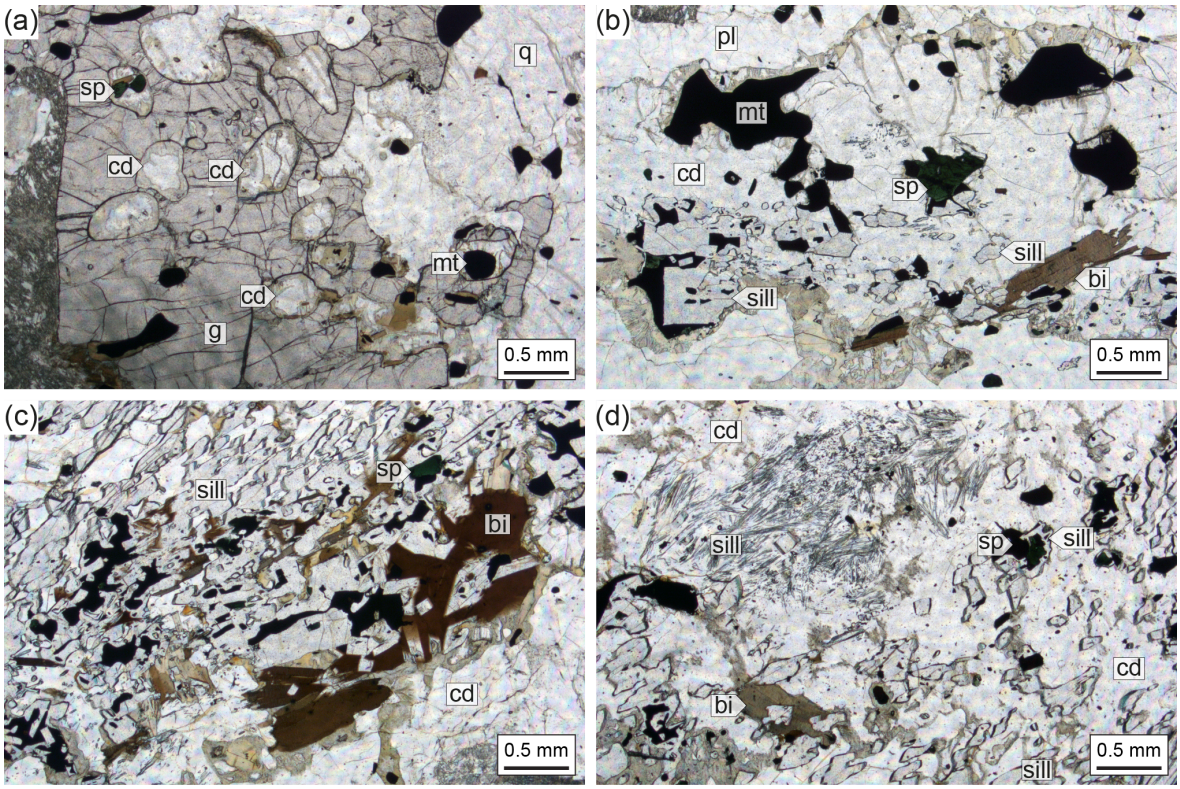


Figure 4.4: Thin section microphotographs in plain polarised light for aluminous metapelite collected at Ratelpoort, sample NMC21. (a) Large garnet porphyroblast including spherical cordierite and opaques, embedded in quartzofeldspathic matrix. (b) Prismatic sillimanite intergrown with biotite and including magnetite and spinel. partly pinitised cordierite armours the intergrowths. (c, d) Textural varieties of sillimanite. (c) Aggregate of prismatic sillimanite intergrown with cordierite, biotite and opaques. Note armouring by cordierite at right bottom corner. (d) Fibrolitic sillimanite engulfed in cordierite-porphyroblast and separated by cordierite from neighbouring sillimanite-aggregate.

after early-metamorphic andalusite (Fig. 4.4c). A randomly oriented, fine-grained fibrolitic variety is embedded in large porphyroblasts of cordierite (Fig. 4.4d). Sillimanite also forms large (∼0.5 mm) prisms intergrown with magnetite/ilmenite and spinel (Fig. 4.4b). In all cases sillimanite and sillimanite–biotite is armoured by cordierite and not found in contact with garnet, feldspars or quartz (Fig. 4.4b–d).

Feldspars form prismatic to rounded grains, commonly associated with cordierite and lobate quartz. K-feldspar is somewhat compositionally variable, with X_{ab} of 0.14–0.37 and X_{an} of 0.01–0.02 whereas plagioclase is homogeneous oligoclase–andesite with X_{an} of 0.28–0.30 and X_{or} of 0.02.

Abundant ilmenite and magnetite are scattered in the matrix (Fig. 4.4b), found as inclusions in garnet (Fig. 4.4a) and associated with paramorphs after andalusite (Fig. 4.4c, d), commonly displaying a drop-like to angular shape. Rare blue-green spinel is included in garnet and prisms of sillimanite or spatially associated with magnetite.

4.1.5 Geselskapbank

At Geselskapbank, leucosome-absent amphibolite facies pelites host the assemblage garnet (∼10 vol. %), biotite (∼2–5 vol. %), sillimanite (∼15–20 vol. %), cordierite (∼25 vol. %), plagioclase (∼5 vol. %), magnetite and ilmenite (∼3 vol. %) and quartz (∼0-30 vol. %). Modes may however vary, in particular for quartz. K-feldspar is not present. These rocks either as undeformed, granoblastic lenses or as highly deformed L-tectonites. Nearby pods of migmatites display the high-grade assemblage of biotite (∼10–15 vol. %), cordierite (∼5–10 vol. %), sillimanite (∼20 vol. %), plagioclase (∼5 vol. %), K-feldspar (∼30 vol. %), ilmenite and magnetite (∼5 vol. %) and quartz (∼20–25 vol. %; see subsection 3.4.1). Zircon, apatite and monazite are accessories in both units.

Amphibolite facies metapelites – garnet–cordierite–sillimanite gneisses

Undeformed specimens (sample NMC05) are highly domainal, with domains hosting hypidioblastic, poikilitic garnet (∼0.1–0.5 mm) overgrowing randomly oriented sillimanite in a largely anhydrous matrix of quartz, ilmenite/magnetite and minor cordierite and plagioclase. This 'garnet-domain' is virtually devoid of biotite, except for a few individual flakes (Fig. 4.5a). Garnet is Fe-rich and compositionally unzoned, with X_{Fe} of 0.79–0.81. X_{alm} is 0.77–0.79, X_{py} is 0.20–0.21, X_{grs} is 0.02 and X_{sps} equals to 0.01 for cores and rims. Cordierite forms minute (< 0.1 mm) xenoblastic grains spatially associated to garnet. Compositionally relatively Fe-rich, cordierite has X_{Fe} of 0.33. Opposed to this is a garnet-absent 'biotite-domain', dominated by fine-grained, randomly oriented intergrowths of biotite, sillimanite, quartz, minor opaques and plagioclase (Fig. 4.5b). Red-brown pleochroic biotite is rich in iron, with X_{Fe} of 0.50–0.56. Biotite contains minor Ti, measured at 0.17–0.23 a.p.f.u. F- and Cl-contents are negligible. $\mathrm{Al}^{\mathrm{VI}}$ is roughly constant at 0.40–0.44. Plagioclase forms small interstitial grains present in both domains and displays some compositional variation across

domains. X_{an} of 0.20–0.35 defines plagioclase as oligoclase and andesine, respectively. X_{or} is negligible.

Deformed samples (NMC11 and NMC08) display the same assemblage, but are characterised by distinctively lower amounts of biotite (< 5 vol. %) and a strong fabric defined by isoriented sillimanite and polygonal but elongated cordierite and quartz occurring in variable amounts. Garnet (∼5–10 vol. %) forms rounded skeletal poikiloblasts (∼0.5–3 mm) and aggregates of hypidioblastic grains hosting randomly oriented fibrolite ('sill I' on Fig. 4.5c, d) and drop-shaped magnetite and ilmenite (Fig. 4.5c, d). Garnet porphyroblasts displace matrix sillimanite ('sill II' on Fig. 4.5c–e) but appear overall unrotated (Fig. 4.5c). Compositionally garnet is almandine-rich with X_{Fe} of 0.84–0.86. X_{alm} is 0.78–0.80, X_{py} is 0.14–0.16, X_{grs} is 0.05 and X_{sps} equals to 0.02 for both cores and rims.

Biotite forms few individual flakes (< 0.5 mm) scattered in the rock matrix and preferentially occurring in pressure shadows of large garnets (Fig. 4.5c). Biotite is iron rich and displays X_{Fe} of 0.54–0.57, F-contents are null and Cl amounts to 0.08–0.10 a.p.f.u. Al^{VI} is 0.38–0.47. Cordierite is present as polygonal, elongated grains in the rock matrix (∼0.3–0.6 mm) and rare large (∼2.0 mm) rounded porphyroblasts hosting randomly oriented fibrolite and droplets of opaques (Fig. 4.5d). Matrix cordierite is commonly decorated by texturally-late fibrolite at grain boundaries ('sill III' on Fig. 4.5e) and partly replaced by texturally late rosettes of faint-green chlorite (Fig. 4.5f). X_{Fe} in cordierite is 0.35–0.38.

Sillimanite is found in three textural varieties: 'sill I' is randomly oriented fibrolite present exclusively in porphyroblastic garnet (Fig. 4.5c, d) and cordierite (Fig. 4.5d). 'sill II' is the main fabric-forming phase, forming strongly isoriented stringers of thin needles wrapping around garnet (Fig. 4.5c, d) and large cordierite (Fig. 4.5d) as well as individual needles scattered in the groundmass (Fig. 4.5e, f). 'sill III' is texturally-late fibrolite forming minute, static beards on grain boundaries of cordierite (Fig. 4.5e). Plagioclase is compositionally comparable to undeformed sample NMC05. Oxides are ubiquitous in the form of fine-grained, rounded droplets of ilmenite and magnetite (Fig. 4.5c–f).

Sample NMC11 hosts abundant quartz in the matrix and as inclusions; in sample NMC08 quartz is confined to small rounded inclusions in matrix-cordierite and modally minor.

Migmatites – K-feldspar–cordierite–sillimanite gneisses

Migmatites differ from amphibolite facies gneisses due to the absence of garnet and the presence of abundant K-feldspar concentrated in leucosomes. Texturally the rocks are generally fine-grained and weakly deformed, with early, coarse-grained sillimanite being randomly oriented and late fibrolite defining a weak planar fabric (Fig. 4.6).

Biotite in the investigated samples (NMC15 and NMC16) forms minute (∼0.10 mm) olive–green to brown flakes that from a weak planar fabric together with fibrolitic sillimanite ('sill II' on Fig. 4.6). Biotite is relatively magnesian, with X_{Fe} of 0.30–0.32 and negligible F- and Cl-content. Al^{VI} is 0.43–0.50. Cordierite occurs as small (∼0.1 mm) xenoblastic to rounded grains that are compositionally homogeneous and iron-poor ($X_{Fe} = 0.16$). Sillimanite

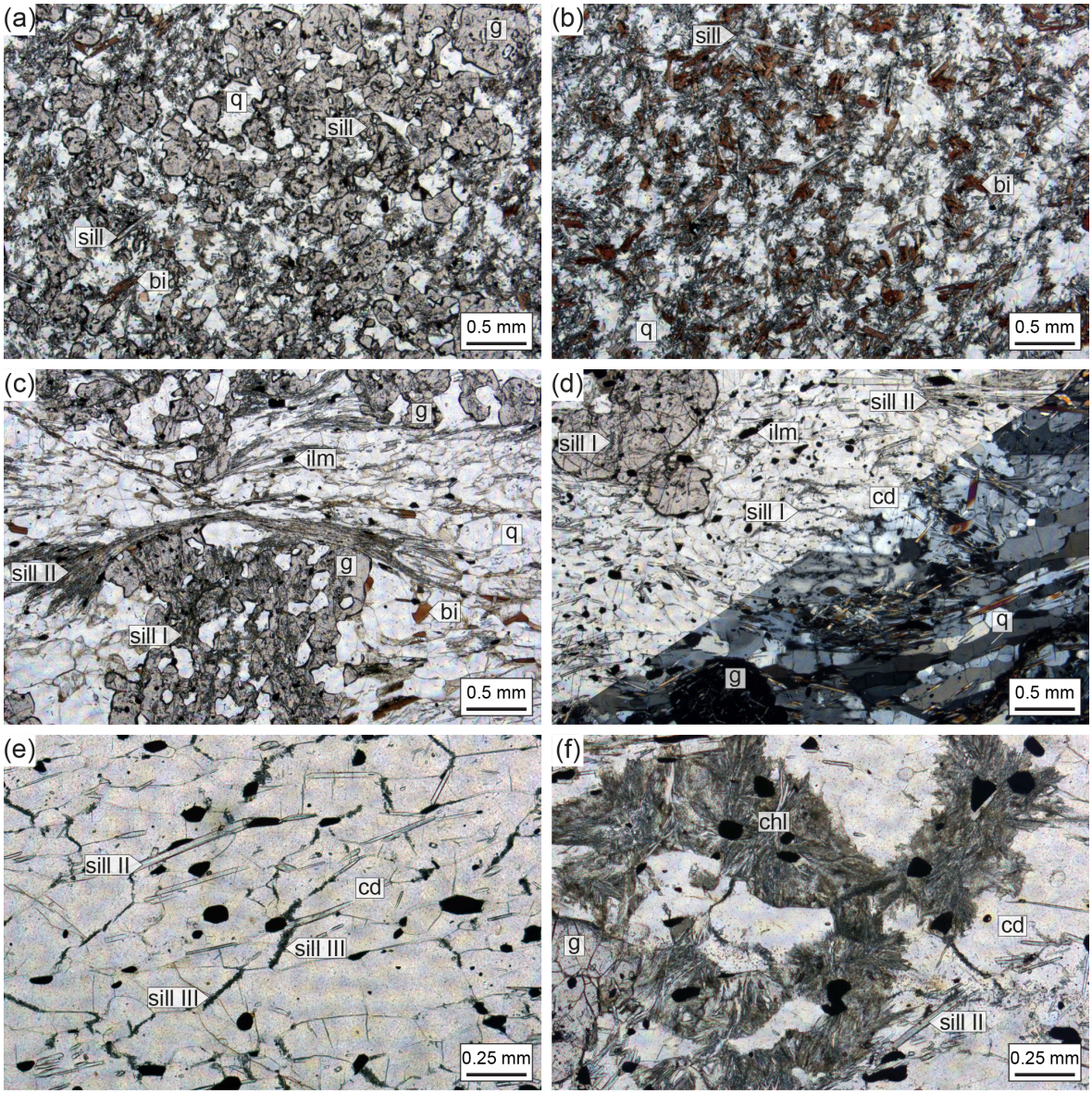


Figure 4.5: Thin section microphotographs in plain- and cross polarised light for garnet–cordierite–sillimanite gneisses collected at Geselskapbank. (a, b) Domainal, undeformed sample NMC05. (c–f) Sheared varieties, sample NMC11 (c, d) and NMC08 (e, f). (a) 'Garnet-domain' dominated by garnet statically overgrowing randomly oriented sillimanite in quartz-rich matrix. (b) 'Biotite-domain' of unoriented clots of biotite–sillimanite–quartz. (c) Large skeletal garnet poikiloblasts hosting fibrolite (sill I) and wrapped by stringers of sillimanite (sill II). (d) Large, rounded cordierite porphyroblasts hosting fibrolite (sill I) and wrapped by sill II. (e) Beards of texturally-late fibrolite (sill III) statically replacing peak cordierite at the rims. (f) Cordierite replaced by texturally late stellar chlorite.

appears in two textural varieties. Coarse-grained, randomly oriented sillimanite ('sill I' on Fig. 4.6) forms large (up to ∼5.0 mm) poikilitic laths and prisms hosting numerous fine-grained inclusions of round quartz and xenoblastic magnetite (Fig. 4.6). 'sill I' is partly to completely replaced by fine-grained fibrolite ('sill II' on Fig. 4.6) that defines a weak planar fabric. Exsolution-free K-feldspar is a main constituent that forms rounded grains of homogeneous size (∼0.3–0.5 mm) and composition, with X_{ab} of 0.13–0.24 and negligible anorthite-content. Plagioclase is andesine with X_{an} of 0.27–0.32. X_{or} is negligible. Magnetite is abundant, present as ubiquitous fine-grained round droplets and xenoblastic inclusions in sillimanite (Fig. 4.6). Ilmenite is spatially associated with magnetite but volumetrically minor.

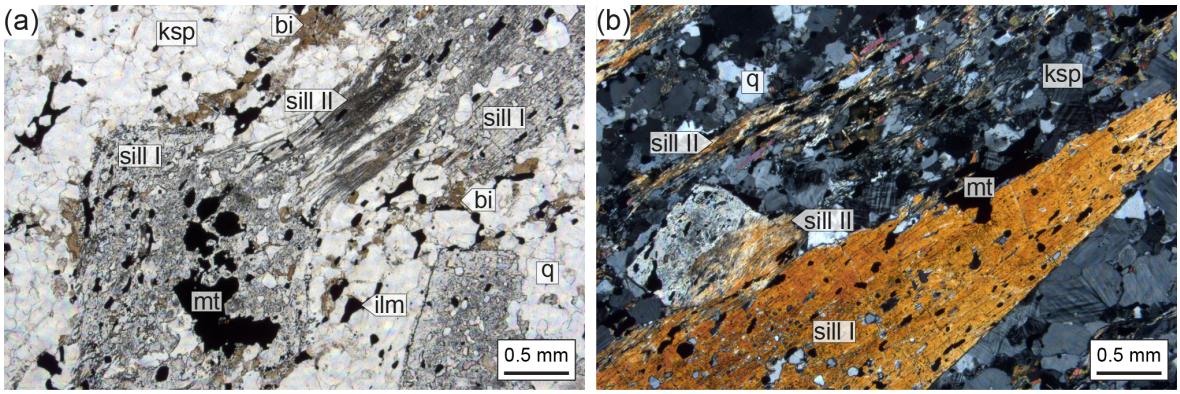


Figure 4.6: Thin section microphotographs in plain- and cross polarised light for migmatites sampled at Geselskapbank. (a) sample NMC15 and (b) sample NMC16. Shown are large, unoriented, poikilitic laths of coarse-grained sillimanite (sill I) including abundant fine-grained quartz and magnetite partly replaced by isoriented fibrolite (sill II) imprinting a weak fabric. Groundmass is weakly aligned, fine-grained biotite and fibrolite (sill II) is alternated to leucocratic accumulations of rounded K-feldspar and quartz.

4.2 Hytkoras

Specimens collected during detailed sampling at Hytkoras are grouped in terms of lithology. Three samples of aluminous metapelite and one sample each of magnesian metapelite, semi-pelite, metagreywacke, mafic granulite and magnesian gneiss were selected from a large sample suite for detailed petrographical analysis and thermodynamic modelling.

4.2.1 Aluminous metapelites

Aluminous metapelites show the coexistence of variable amounts of garnet, cordierite, biotite, sillimanite, plagioclase, K-feldspar, quartz and ilmenite, commonly associated with magnetite and rarely with spinel. Accessory minerals include apatite, monazite and zircon. Aluminous metapelites display some textural variety with changing modal amounts of phases and grain size. The investigated samples are NMC89, NMC71 and NMC65.

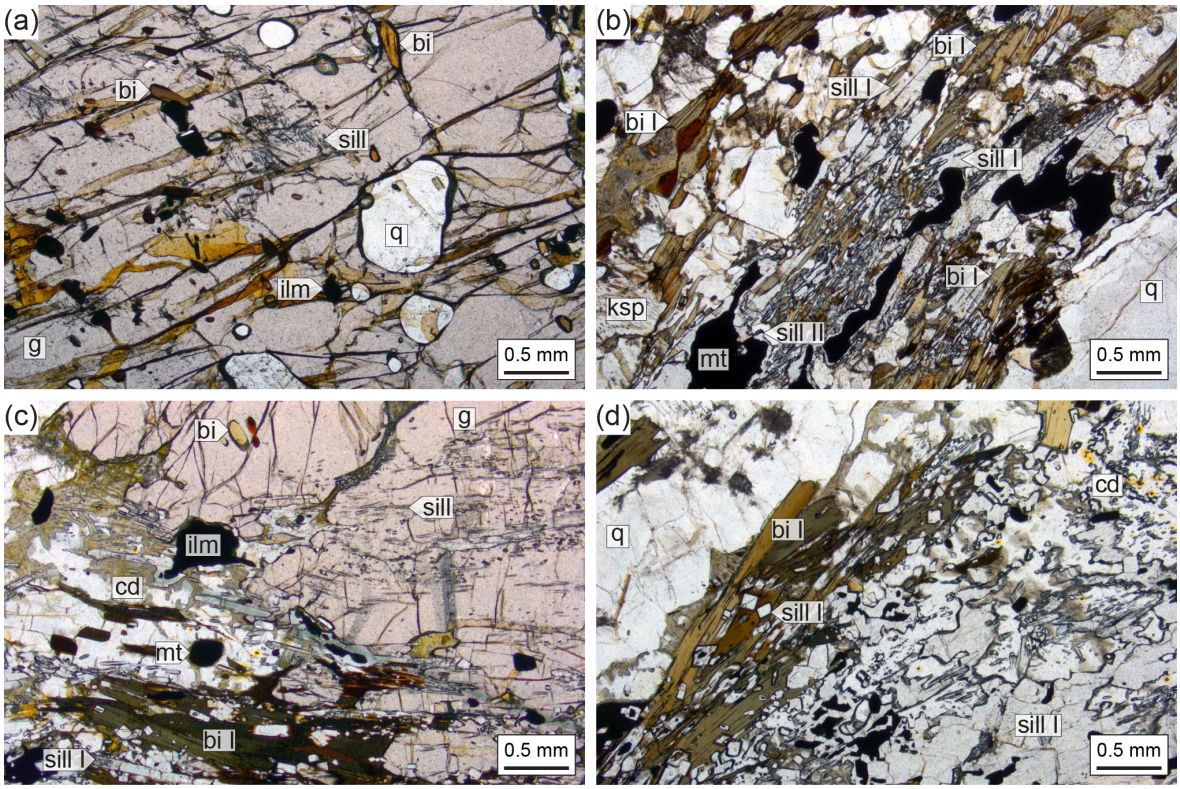


Figure 4.7: Thin section microphotographs in plain polarised light for aluminous metapelites. (a–f) aluminous metapelites dominated by garnet, biotite, sillimanite and cordierite. (a) sample NMC89, large garnet poikiloblast hosting abundant inclusions of biotite, quartz, oxides and randomly oriented fibrolite. (b) coexisting biotite and sillimanite with oxides in sample NMC89. Texturally-late sillimanite forming thin rims on magnetite and ilmenite. (c) sample NMC71, poikilitic garnet hosting biotite and aligned fibrolite in matrix of sillimanite, biotite and cordierite. (d) Blocky sillimanite coexisting with biotite and cordierite, sample NMC71.

Garnet forms rounded to elongated subidiomorphic to anhedral porphyroblasts, rang-

ing from ∼5 to 30 mm size. Large grains commonly host abundant rounded inclusions of quartz, biotite, ilmenite, magnetite and sillimanite that are distributed throughout the grain (Fig. 4.7a, c and 4.8a). Garnet in the leucosome is typically smaller (max. ∼5 mm), rounded to elongated, and contains few inclusions of rounded quartz. Garnet is generally weakly zoned and Fe-rich (X_{Fe} = 0.63–0.73), with the cores of large grains having somewhat lower almandine and higher pyrope content (X_{alm} = 0.57–0.69; X_{py} = 0.31–0.34) relative to garnet rims or smaller grains (X_{alm} = 0.64–0.71; X_{py} = 0.25–0.28. Both the grossular and spessartine contents are low and fairly constant from core to rim (X_{grs} = 0.02–0.04, X_{sps} = 0.02–0.07).

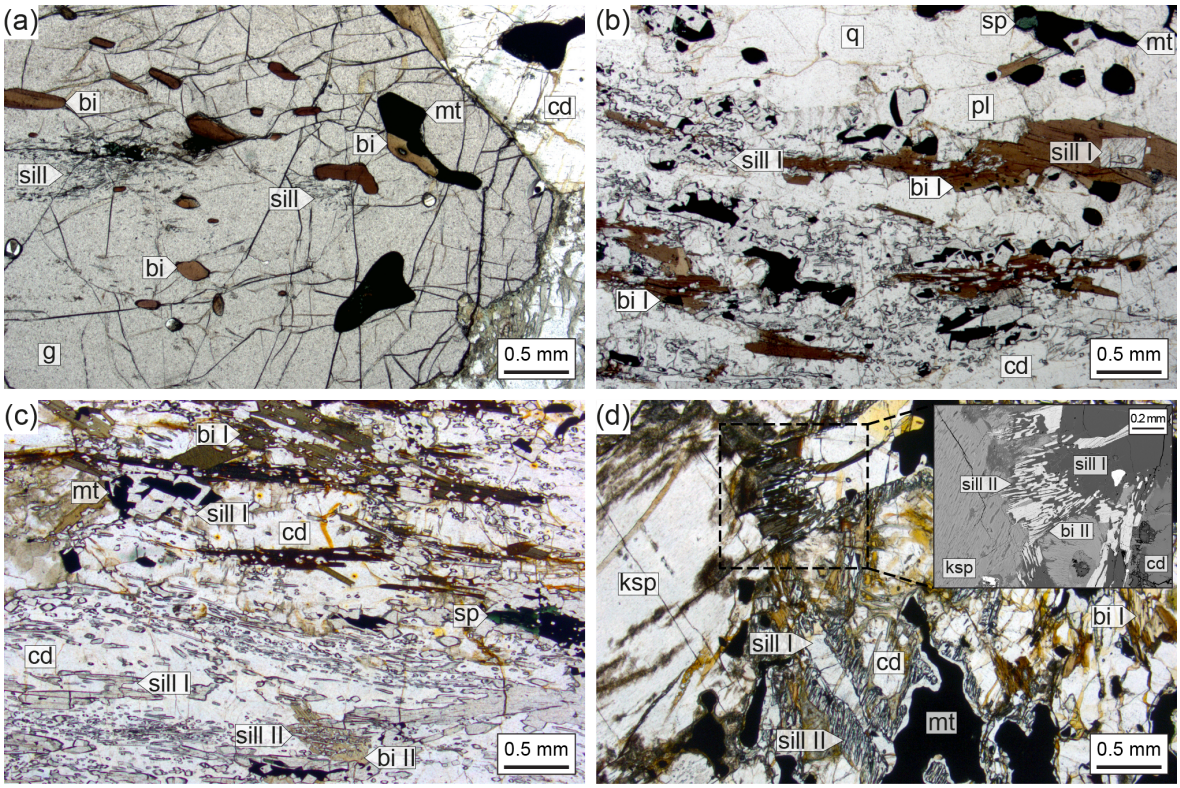


Figure 4.8: Thin section microphotographs in plain polarised light and BSE-images for aluminous metapelites. (a) sample NMC65, large garnet porphyroblast including biotite, weakly isoriented fibrolite and opaques. (b) matrix of sample NMC65, dominated by cordierite, plagioclase and blocky sillimanite coexisting with biotite and forming rims on magnetite and ilmenite. (c, d) Textural occurrences of sillimanite–biotite in aluminous metapelites. (c) Sillimanite-rich layer showing relationship of sillimanite, biotite, oxides and cordierite in sample NMC71. Texturally-late sillimanite and biotite forming symplectic intergrowths. (d) Early retrograde reaction textures indicating partial reaction reversal, sample NMC89. Beards of symplectic sillimanite replacing blocky aluminosilicate, intergrowing with late biotite and rimming oxides. Zoom-in: BSE-image showing textural relationships of replacement texture.

Biotite is found as rounded inclusions in garnet (Fig. 4.7a, c and 4.8a) cordierite, K-feldspar or quartz, and as idioblastic flakes (up to ∼1.5 mm in length) forming aligned aggregates in the rock matrix. Biotite occurs in two texturally distinct habits. In the rock

matrix, large (∼0.5–1.5 mm) flakes ('bi I' in Fig. 4.7–4.11) are intimately associated with large (∼0.5–1 mm) prismatic sillimanite (Fig. 4.7b–d and 4.8b, c) whereas fine-grained (< 0.1 mm) biotite locally forms symplectic intergrowths ('bi II' in Fig. 4.7–4.11) with similarly sized and shaped sillimanite (Fig. 4.8c, d). Biotite inclusions in garnet are more magnesian than matrix biotite ($X_{\mathrm{Fe}} = 0.20$–0.30 vs. 0.33–0.39, respectively). Biotite contains appreciable Ti (0.20–0.33 atoms per formula unit; a.p.f.u., based on 11 O for inclusions and 0.23–0.27 a.p.f.u. for matrix grains) and F (0.35–0.46 a.p.f.u. for inclusions and 0.27–0.35 a.p.f.u. for matrix flakes). $\mathrm{Al^{VI}}$ varies between 0.13–0.31 a.p.f.u. for inclusions and matrix biotite. Symplectic biotite intergrown with sillimanite has a comparable composition to the matrix mineral.

Cordierite forms elongated, generally anhedral grains of variable size (∼0.1–2 mm), frequently hosting abundant aligned inclusions of sillimanite needles and rarely biotite (Fig. 4.7d, 4.8b, c). Polygonal cordierite occasionally forms a moat around garnet and large sill1 grains (e.g. Fig. 4.8b). Late pinitisation affects cordierite to different extents, from alteration confined to small veinlets to complete obliteration of the original grain. Cordierite is chemically unzoned with a constant X_{Fe} of 0.26–0.28.

Sillimanite is present in two distinct textural habits. It occurs as prismatic, randomly oriented needles or blocky grains (¡0.1 mm in thickness, up to ∼1 mm long; 'sill I' in Fig. 4.7–4.11) closely associated with biotite (Fig. 4.7b–d, 4.8b, c), or as fine aligned needles when included in garnet (interpreted as relic S_2; Waters, 1989, Fig. 4.7a, c and 4.8a). Sillimanite also forms texturally late fibrolitic to symplectic intergrowths ('sill II' in Fig. 4.7–4.11) with biotite in the proximity of cordierite (Fig. 4.8c), symplectites overgrowing prismatic sillimanite in contact with cordierite (Fig. 4.8d) and thin rims shielding oxides from the rock matrix (Fig. 4.7b, 4.8b, c).

K-feldspar forms large (up to ∼3 mm) rounded to elongated grains in the leucosome and smaller grains (up to ∼1 mm sized) in the melanosome, hosting abundant perthitic exsolution (Fig. 4.8d). Compositionally K-feldspar contains variable albite component of 0.07–0.25 and low anorthite component of ∼0.01. Andesine plagioclase occurs as small (max. ∼0.5 mm) anhedral grains, mostly in the melanosome. It contains 0.26–0.35 anorthite component and up to 0.02 orthoclase component.

Aluminous metapelites contain moderate proportions of ilmenite (∼5 vol. %) and minor magnetite (∼1 vol. %), both occurring as rounded blebs or elongated grains. Ilmenite shows lamellar exsolutions and thin rims of magnetite. Ilmenite and magnetite are commonly associated with sillimanite, occurring either as coarse intergrowths with blocky sillimanite (Fig. 4.7d, 4.8b and c) or with thin rims of texturally late sillimanite (Fig. 4.7b, 4.7d, 4.8b and d). Rare, blue-green spinel occurs as exsolutions from magnetite or as distinct blocky grains associated with magnetite. Spinel is always rimmed by either cordierite or sillimanite and is never in contact with quartz (Fig. 4.8b). Spinel is iron rich ($X_{\mathrm{Fe}} \approx 0.67$) and has a gahnite component ($X_{\mathrm{Zn}} = \frac{\mathrm{Zn}}{\mathrm{Zn+Fe^{2+}+Fe^{3+}+Mg+Mn+Cr}} = 0.06$).

4.2.2 Magnesian metapelite

This lithology is characterized by the assemblage of garnet (∼10 vol. %), orthopyroxene (∼5–10 vol. %), biotite (∼5–10 vol. %), cordierite (∼30 vol. %), plagioclase (∼3 vol. %), K-feldspar(∼15–20 vol. %), quartz (∼20–25 vol. %) and minor oxides (∼1 vol. %). Accessories include apatite, monazite and zircon. In thin section no clear fabric can be discerned with garnet and orthopyroxene embedded in a matrix of granoblastic cordierite and randomly oriented biotite flakes. The investigated sample is NMC37.

Garnet forms large (∼5–15 mm) irregularly-shaped poikiloblasts with numerous rounded inclusions of biotite, cordierite and quartz (Fig. 4.9a, c). Garnet rims show sharp boundaries when in contact with matrix cordierite (Fig. 4.9a) and forms symplectic intergrowths with biotite and quartz (Fig. 4.9c, d). Garnet poikiloblasts are compositionally homogeneous and almandine-rich (X_{alm} = 0.57–0.64) with X_{py} = 0.28–0.38, $X_{\mathrm{grs}} \approx 0.04$ and $X_{\mathrm{sps}} \approx 0.03$. Cores are slightly more magnesian ($X_{\mathrm{Fe}} = 0.60$) compared to rims ($X_{\mathrm{Fe}} = 0.71$). Symplectic rims (Fig. 4.9c, d) display slightly higher almandine-contents (X_{alm} = 0.67–0.68) compared to unaltered grains.

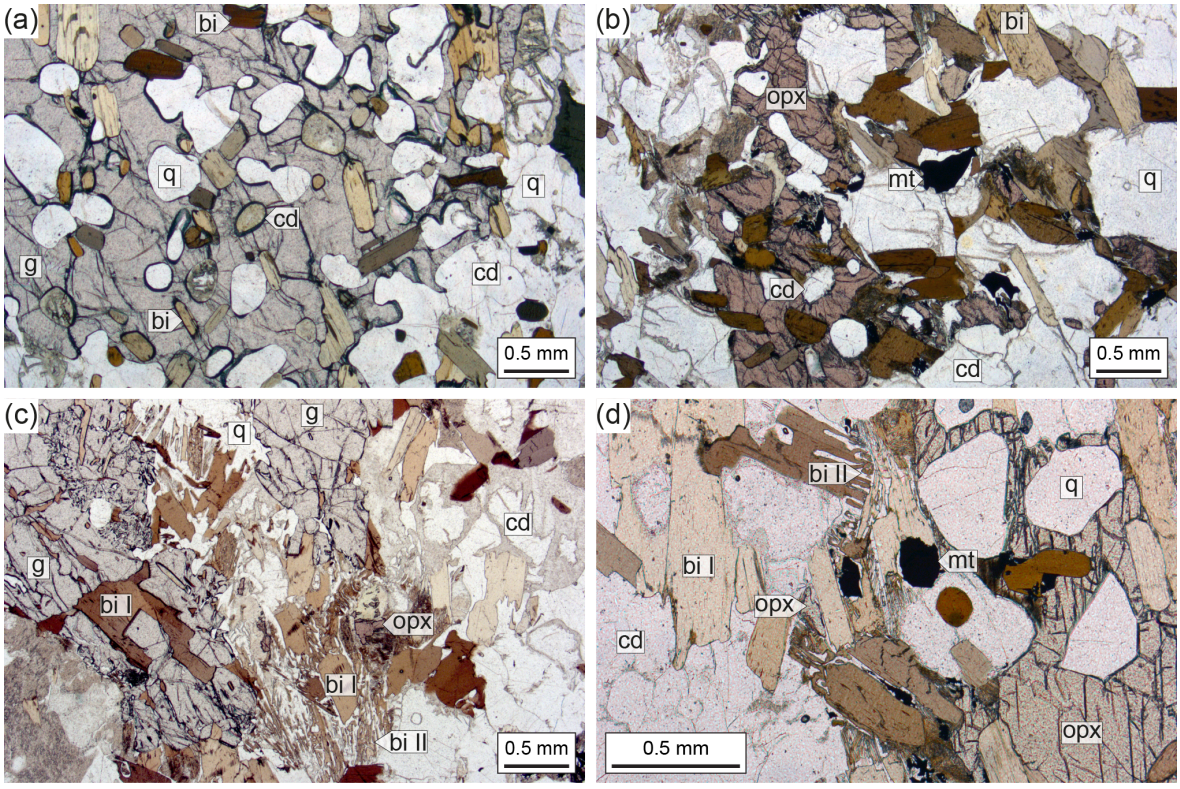


Figure 4.9: Thin section microphotographs in plain polarised light for magnesian metapelite (sample NMC37). (a) large garnet poikiloblast hosting numerous rounded inclusions of biotite, cordierite and quartz. (b) skeletal poikiloblast of reddish orthopyroxene in association with biotite, cordierite and magnetite. (c) Garnet porphyroblast hosting inclusions of biotite, partly replaced by symplectites of texturally-late biotite and quartz. (d) Symplectites of biotite and cordierite ± magnetite replacing orthopyroxene.

Biotite is included in garnet and orthopyroxene as rounded flakes (∼0.1–0.5 mm). In the matrix biotite occurs as single flakes (∼0.5–1 mm) or weakly-aligned aggregates (Fig. 4.9b). Additionally, biotite forms fine-grained symplectites with garnet and quartz (Fig. 4.9c) and with cordierite, ilmenite and magnetite where in contact with orthopyroxene (Fig. 4.9d). Biotite inclusions are more magnesian compared to matrix biotite ($X_{\mathrm{Fe}} = 0.28$–0.33 vs. 0.36–0.40, respectively), but have slightly lower Ti contents (∼0.25–0.29 a.p.f.u, based on 11 O) than the matrix mineral (0.28–0.30). F content is negligible. $\mathrm{Al^{VI}}$ varies between 0.10–0.21 a.p.f.u for inclusions and 0.15–21 a.p.f.u for matrix biotite.

Orthopyroxene forms large (∼0.1–3 mm) interstitial to skeletal poikiloblasts hosting abundant inclusions of spherical biotite and cordierite (Fig. 4.9b, d). Orthopyroxene displays sharp boundaries against cordierite and occasionally biotite; however, grain boundaries with biotite are typically symplectic and intergrown with cordierite and magnetite (Fig. 4.9d). X_{Fe} is largely homogeneous with values of 0.40–0.42, whereas Al-in-orthopyroxene ($y_{\mathrm{opx}} = \frac{\mathrm{Al^{tot}} - \mathrm{Fe^{3+}}}{2}$) is 0.15–0.18 a.p.f.u. (based on 6 O).

Cordierite occurs as round inclusions in both garnet (Fig. 4.9a) and orthopyroxene (Fig. 4.9b) (∼0.1–0.5 mm) and rounded to granoblastic polygonal grains and aggregates in the rock matrix. By contrast to aluminous metapelites, no sillimanite inclusions are present in cordierite or garnet from magnesian metapelites. Cordierite inclusions in garnet and orthopyroxene are typically more magnesian ($X_{\mathrm{Fe}} \approx 0.16$) than matrix grains ($X_{\mathrm{Fe}} = 0.20$–$0.25$). Grains show limited pinitization, mostly confined to grain boundaries and thin veinlets.

K-feldspar and plagioclase occur as small (∼0.1–0.5 mm) irregularly-shaped grains showing variable alteration. K-feldspar grains contain variable albite component of 0.14–0.21 and anorthite component of 0.01–0.03 whereas plagioclase is oligoclase with 0.24–0.26 anorthite component and ∼0.01 orthoclase component.

Ilmenite occurs as irregular bleb-shaped grains that are partly surrounded by thin rims of magnetite. Rare small grains (∼0.1 mm) of light blue-green spinel occur within larger ilmenite grains. Ilmenite and magnetite are separated from orthopyroxene by thin rims of cordierite and/or plagioclase. A second variety of magnetite forms fine-grained symplectites with cordierite and/or biotite at the edges of orthopyroxene.

4.2.3 Semi-metapelite

Semi-metapelite is distinguished from aluminous metapelite by the scarcity or absence of biotite, which, if present, is always armoured by K-feldspar, cordierite or quartz and never in contact with sillimanite (e.g. Fig. 4.10a). The investigated sample is NMC67. It consists of garnet (∼5 vol. %), cordierite (∼10–15 vol. %), sillimanite (∼5 vol. %), plagioclase (∼10 vol. %), K-feldspar (∼40–45 vol. %), quartz (∼20 vol. %) and ilmenite and magnetite (∼4 vol. %).

Garnet forms rounded to elongate inclusion-poor porphyroblasts of up to 10 mm in size. Composite inclusions of plagioclase and quartz, quartz, rare elongated biotite, ilmenite and magnetite are distributed over entire grains, but aligned fibrolite occurs preferentially towards

the rims (interpreted as relic S_2; Waters, 1989, Fig. 4.10a). Most garnets display irregular to serrated grain boundaries when in contact with cordierite (Fig. 4.10b, c). Garnet is iron-rich (X_{Fe} = 0.63–0.65) and compositionally homogeneous with almandine contents of X_{alm} = 0.56–0.58, pyrope contents of X_{py} = 0.32–0.34, grossular contents of $X_{grs} \approx 0.03$ and spessartine contents of $X_{sps} \approx 0.07$.

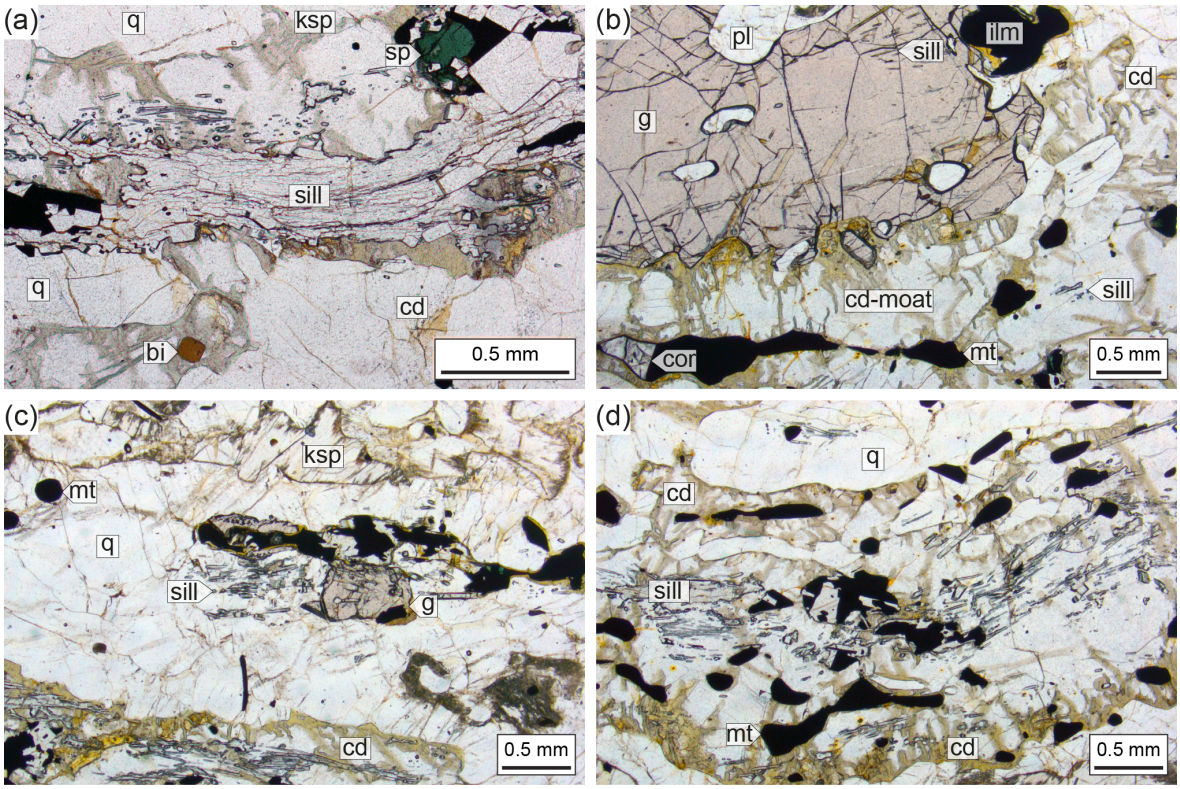


Figure 4.10: Thin section microphotographs in plain polarised light of semi-metapelite (sample NMC67). (a) stringer of fine-grained sillimanite in cordierite–feldspar–quartz matrix and blocky sillimanite associated with opaques and spinel. Biotite is armoured by K-feldspar and never in contact with sillimanite. (b) large garnet porphyroblast hosting composite inclusions of plagioclase–quartz, quartz and aligned fibrolite partially consumed by a moat of cordierite. Corundum is in contact with magnetite and surrounded by a thin rim of pinitised cordierite. (c) Isoriented needles of sillimanite embedded in quartz–feldspar and blocky sillimanite intergrown with magnetite next to garnet. (d) Stringer of sillimanite embedded in peritectic cordierite; blocky sillimanite intergrown with magnetite and ilmenite.

Biotite occurs exclusively as small (∼0.1–0.5 mm in length), single flakes included predominantly in K-feldspar (Fig. 4.10a), but also to a lesser extent in garnet, cordierite or quartz (Fig. 4.10b). X_{Fe} of biotite included in garnet is lower compared to biotite hosted in K-feldspar or cordierite (∼0.28 vs. 0.35–0.47, respectively) with Ti contents of ∼0.22 a.p.f.u for inclusions in garnet and ∼0.18–0.30 a.p.f.u. for biotite hosted in K-feldspar or cordierite (based on 11 O). F-contents are negligible. Biotite hosted in garnet shows Al^{VI} ∼0.20 a.p.f.u whereas inclusions in feldspar and cordierite has Al^{VI} between 0.20–41 a.p.f.u (based on 11 O).

Cordierite forms elongated, anhedral to granoblastic polygonal grains of variable size (∼0.1–2 mm), frequently bordering or including aggregates of aligned fibrolitic or blocky sillimanite (Fig. 4.10a, c and d). Polygonal cordierite forms a moat around garnet (Fig. 4.10b). Cordierite is compositionally homogeneous with $X_{\mathrm{Fe}} = 0.20$–0.23.

Sillimanite occurs in two textural varieties. Fine-grained fibrolitic aggregates occur as inclusions in garnet (Fig. 4.10b), quartz–feldspars (Fig. 4.10c) or cordierite (Fig. 4.10d), whereas coarse-grained blocky or prismatic sillimanite is associated with spinel (Fig. 4.10a) and ilmenite or magnetite (Fig. 4.10).

K-feldspar occurs as granoblastic to elongated grains, ranging from ∼0.1 to 0.5 mm in size (Fig. 4.10a, c). Larger grains are typically irregularly-shaped and host rounded inclusions of quartz. K-feldspar contains 0.08–0.19 albite component and low (∼0.01) anorthite component. All grains are decorated by ubiquitous perthitic exsolutions and show limited to extensive alteration. Plagioclase occurs as small (∼0.5 mm) anhedral to granoblastic grains usually in contact with sillimanite. Plagioclase is oligoclase with 0.21–0.30 anorthite component and up to 0.02 orthoclase component.

Abundant ilmenite occurs as bleb-shaped grains exhibiting complex exsolution and intergrowth textures with magnetite and blue-green and dark-brown spinel (Fig. 4.10a). Isolated ilmenite grains commonly have thin rims of magnetite and cordierite that separates them from most other minerals. Coarse-grained ilmenite is frequently associated with sillimanite (Fig. 4.10) or embedded in cordierite or K-feldspar, whereas spinel and rare corundum are always associated with magnetite and/or ilmenite and are never in contact with quartz (Fig. 4.10a). Spinel is iron-rich with $X_{\mathrm{Fe}} \approx 0.70$ and has a gahnite component ($X_{\mathrm{Zn}} = 0.03$).

4.2.4 Metagreywacke

Metagreywacke is dominated by a granoblastic quartzofeldspathic matrix and is generally fine-grained (< 0.5 mm), with except of few porphyroblasts of garnet occuring in quartz-rich leucosome. Internal organisation is generally lacking with only single flakes of biotite defining a weak planar fabric. Accessory phases are ilmenite, magnetite, apatite, zircon and monazite. The investigated sample is NMC68.

Garnet is a minor constituent in this rock type and forms small hypidioblastic to rounded porphyroblasts, seldom exceeding ∼0.5 mm in diameter (Fig. 4.11a). Some larger grains are decorated by elliptic inclusions of quartz and single flakes of biotite (Fig. 4.11a). Quartz forms a distinct halo around garnet (Fig. 4.11a), suggesting a genetic relationship of the two phases. Compositionally garnet is homogeneous and iron-rich ($X_{\mathrm{Fe}} = 0.65$–0.67). Almandine-contents vary between 0.58 and 0.61, pyrope is 0.29–0.31, whereas grossular- and spessartine-component are nearly constant at 0.04 and 0.07, respectively. Biotite forms small (max. ∼0.5 mm), isolated flakes displaying weak isorientation (Fig. 4.11). It shows near-constant X_{Fe} of 0.46, Ti of 0.30 a.p.f.u and minor F-contents 0.09 a.p.f.u. $\mathrm{Al}^{\mathrm{VI}}$ is 0.15 to 0.18. Plagioclase and K-feldspar dominate the rock matrix together with quartz. They form small rounded to interlocked grains of similar size (≤0.4 mm). Both feldspars are compositionally homogeneous.

K-feldspar contains 0.05–0.09 albite component and negligible anorthite-content. Andesine plagioclase is similarly homogeneous, with near-constant anorthite-component of 0.36–0.38 and low orthoclase content (0.03). The rock is generally poor in opaques, represented by minute (< 0.1 mm) drop-shaped grains of ilmenite and magnetite.

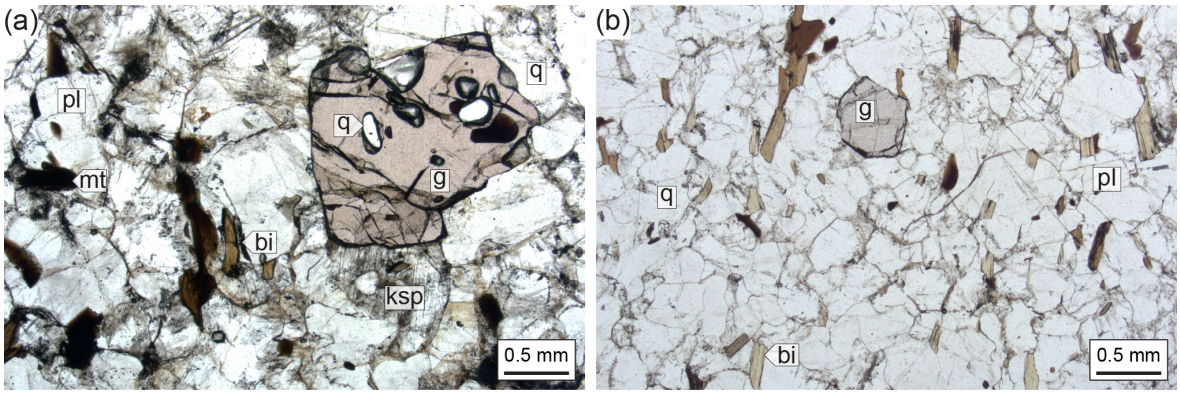


Figure 4.11: Thin section microphotographs in plain polarised light of metagreywacke (sample NMC68). (a, b) Hypidiomorphic garnet showing elliptic inclusions of quartz and biotite (a), surrounded by quartz-rich halo, coexisting with biotite and ilmenite–magnetite in quartzofeldspathic matrix.

4.2.5 Mafic granulites

Mafic granulites host the assemblage augite–orthopyroxene–plagioclase–quartz–ilmenite ± hornblende ± magnetite in grossly variable proportions. Texturally the spectrum ranges from massive, granoblastic, leucosome-absent rocks to well-foliated, stromatic mafic migmatites (see section 3.5).

Leucosome-bearing mafic granulite

This type of mafic granulite is rich in rounded, interlocked plagioclase; pyroxenes occur as elongated skeletal grains of pinkish, pleochroic orthopyroxene and greenish augite. Minor constituents are hornblende, biotite and quartz (Fig. 4.10c). Interstitial ilmenite and minor magnetite occur as rounded to elongated grains. A weak planar fabric is recognized in the investigated sample NMC69.

Orthopyroxene (∼15–20 vol. %) is Mg-rich with homogeneous X_{Fe} of 0.30–0.34 and negligible y_{opx} of 0.01. Augitic clinopyroxene (∼5–10 vol. %) is diopside-rich with X_{Fe} of 0.19–25 and low X_{jd} ($= \frac{\mathrm{Na}}{\mathrm{Na+Ca}}$) of 0.03. Plagioclase (∼50 vol. %) is bytownite with 0.74–0.82 anorthite component and low orthoclase component of 0.01. Brown-green pleochroic hornblende (∼5 vol. %) occurs as small (∼0.1 mm) rounded grains included in pyroxenes, plagioclase and rarely in biotite (Fig. 4.12a, b). Amphibole classifies as magnesiohornblende–pargasite according to Leake *et al.* (1997) with X_{Fe} of 0.26–0.38, A-site Na of 0.29–0.36, A-site K of 0.22–0.31, 0.15–0.22 $\mathrm{Al^{VI}}$ and negligible M4-site Na (based on 23 O). Biotite (∼5 vol. %)

forms flakes of up to ∼1 mm or occurs as fine-grained (∼0.1–0.5 mm) inclusions in pyroxenes. It displays homogeneous X_{Fe} of 0.29–0.32 and Ti contents of 0.22–0.28 a.p.f.u. with appreciable F of 0.09–0.13 a.p.f.u. Al^{VI} is constant at ∼0.05.

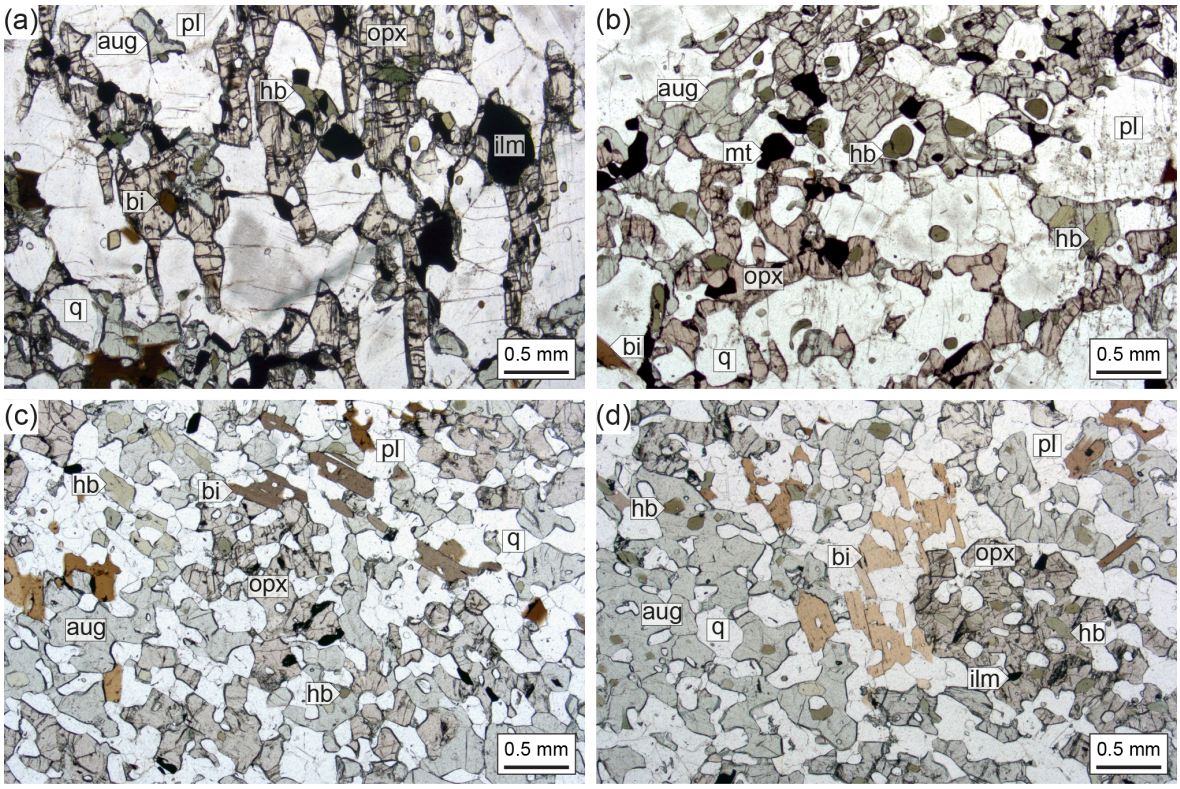


Figure 4.12: Thin section microphotographs in plain polarised light of leucosome-bearing (a) and leucosome-absent (b) mafic granulites. (a) Sample NMC69. Skeletal grains of pinkish orthopyroxene and greenish augite including olive-green rounded hornblende and biotite in a matrix of granoblastic plagioclase. (a, b) Sample NMC27. Coarse-grained poikiloblastic pyroxenes hosting abundant inclusions of rounded hornblende and oxides in matrix of fine-grained granoblastic plagioclase and quartz. Biotite forms large flakes showing optical continuity.

Leucosome-absent mafic granulite

This variety is dominated by large (up to ∼5 mm) poikiloblasts of pale-green augite (∼25 vol. %) and pinkish orthopyroxene (∼20 vol. %), both decorated by abundant inclusions of lozenge-shaped or rounded olive-green hornblende (∼10 vol. %; Fig. 4.12c, d). Plagioclase (∼20–30 vol. %) forms small (< 0.2 mm) polygonal to interlocked grains. Biotite (∼5 vol. %) forms few, large flakes (up to ∼1 mm in size) and occurs as sporadic inclusions in other phases. Minor ilmenite and magnetite complete the mineral assemblage of the investigated sample (NMC27). Mg-rich orthopyroxene displays near-constant X_{Fe} of 0.34 and moderate y_{opx} of 0.03. Augite is rich in diopside-component with X_{Fe} of 0.25 and low X_{jd} of 0.03. Bytownitic plagioclase is rich anorthite (0.84–0.87) and has negligible orthoclase-content. Dark-green

amphibole is defined as edenite–pargasite following the classification of Leake *et al.* (1997). Hornblende has X_{Fe} of 0.30–0.33, A-site Na of 0.33–0.37, A-site K of 0.24–0.27, 0.12–0.16 Al^{VI} and null M4-site Na (based on 23 O). Biotite form flakes of several mm in size, displaying optical continuity (Fig. 4.12c, d). Values of 0.30–0.34 for X_{Fe} of biotite as well as 0.24–0.28 a.p.f.u Ti, 0.08 a.p.f.u F and Al^{VI} of 0.05 are reported.

4.2.6 Magnesian gneisses

Mg–Al-rich rocks are commonly dominated by biotite and cordierite; the most frequent addition to this assemblage is orthopyroxene ± quartz. Here, end-members of a wide spectrum are described in detail (for further information see Waters, 1986a; Moore and Waters, 1990).

Orthopyroxene–magnesian gneiss

The selected sample (NMC44) is a finer-grained variety of magnesian gneiss consisting of granoblastic cordierite (∼30–35 vol. %), biotite (∼20–30 vol. %), orthopyroxene (∼25–30 vol. %), quartz (∼15–25 vol. %) and minor oxides (< 1 vol. %). Accessories are zircon and apatite. Feldspars have not been found in thin section.

Cordierite occurs as large (up to ∼0.5 mm) rounded to granoblastic grains that contain abundant flakes of biotite and rounded quartz (Fig. 4.13a). Cordierite also occurs as small (¡0.1 mm) spherical inclusions in large orthopyroxene (Fig. 4.13b). The mineral is mostly compositionally homogeneous, with X_{Fe} = 0.19–0.22, regardless of textural location. Cordierite contains 0.11–0.17 wt.% Na_2O and trace amounts of CaO (∼0.02 wt.%). The mineral is commonly extensively altered, with pinitisation occurring as a network of veinlets (Fig. 4.13a).

Dark-brown biotite forms aggregates of weakly aligned, interlocked grains (Fig. 4.13a) and occurs as single flakes included both within cordierite and orthopyroxene (Fig. 4.13b). There is no clear compositional distinction in terms of X_{Fe} (0.28–0.31) and Ti-content (0.17–0.21 a.p.f.u.) between grains in different textural settings. However, F-contents are slightly higher for the matrix variety (0.03–0.07 a.p.f.u.) compared to inclusions (0.03–0.05 a.p.f.u.). Biotite also forms symplectic intergrowths with quartz, particularly when in contact with orthopyroxene (Fig. 4.13a and inset therein). This variety of biotite is compositionally comparable to the matrix phase. Al^{VI} is ∼0.17, independent of textural setting. Biotite contains appreciable amounts of Na_2O measured at 0.24–0.33 wt.%.

Pleochroic orthopyroxene is present as large (up to 3 cm in exceptional cases, Fig. 3.11a) oval to hypidiomorphic poikiloblasts containing numerous inclusions of biotite and spherical cordierite, which may include biotite or quartz (Fig. 4.13a). Orthopyroxene is chemically homogeneous with virtually constant X_{Fe} of 0.37 and y_{opx} of 0.15. Late chlorite is present as alteration on orthopyroxene rims. Waters (1986a) suggested gedrite as amphibolite facies precursor phase to cm-sized orthopyroxene. Quartz occurs as rounded grains in the matrix (Fig. 4.13a) and as anhedral blebs interstitial to ferromagnesian phases (Fig. 4.13b). In the

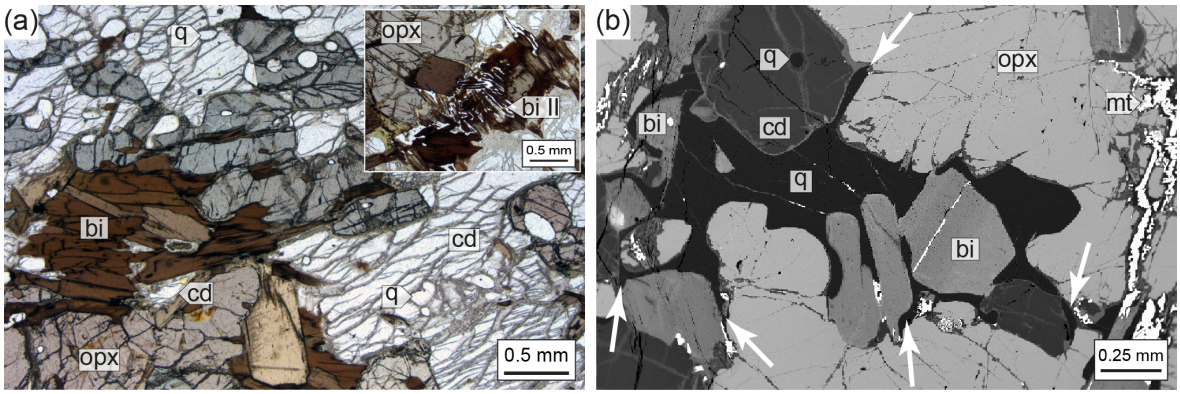


Figure 4.13: Thin section microphotographs in plain polarised light and BSE-images of orthopyroxene–magnesian gneiss (sample NMC44). (a) Anhedral orthopyroxene showing green–red pleochroism in matrix of dark brown biotite, pinitised cordierite and rounded quartz. Insert shows texturally-late biotite forming symplectites with quartz at the contact with orthopyroxene. (b) BSE-image of lobate-cuspate shaped quartz, interpreted as pseudomorph after melt-filled pore with white arrows indicating low dihedral angles.

latter case quartz forms a cuspate-lobate shape with low dihedral angles towards orthopyroxene, cordierite and biotite (highlighted by white arrows on Fig. 4.11b). Similar textures have been interpreted as pseudomorphs of melt-filled pores, indicative for the former presence of melt (e.g. Holness and Sawyer, 2008; Ferrero *et al.*, 2012). Fine-grained opaque oxides are present as elongated aggregates, found in association with texturally-late biotite (Fig. 4.13b).

4.2.7 Other magnesian gneisses

The following samples commonly display distinct large nodular textures that have been interpreted as pseudomorphed lower-grade minerals such as andalusite, gedrite or staurolite (Waters, 1986a). The described rocks all are texturally massive and granoblastic. Notably, both quartz and feldspars are absent.

Nodular sapphirine–spinel–magnesian gneiss (sample NMC88)

This sample is characterised by large (up to ∼2 cm in cross section), prismatic textures consisting of graphic to symplectic intergrowths of sapphirine–spinel/magnetite–cordierite ± corundum in a granoblastic matrix of biotite and cordierite (Fig. 4.14 and 4.15a). Early-metamorphic andalusite is suggested as precursor to the replacement textures (Waters, 1986a). Rare skeletal grains of orthopyroxene are present in the matrix (Fig. 4.14 and 4.15b). Accessories are ilmenite, magnetite, zircon and monazite.

Cordierite occurs in three textural varieties. In the matrix it forms rounded to polygonal, interlocked grains that are notably larger (> 0.5 mm, Fig. 4.14) when compared to cordierite found within the texture (< 0.5 mm, Fig. 4.15a). In the latter case the grains are polygonal to xenoblastic. The third variety forms a monomineralic corona of homogeneous thickness (∼1 mm) that separates the textures from the rock matrix (Fig. 4.14). The corona

consists of individual, rounded large (∼0.5–0.8 mm) grains. Compositionally cordierite is homogeneous and Mg-rich, with X_{Fe} of 0.23–0.25, without notable differences in function of textural location. Cordierite is affected by more or less extensive pinitisation, occurring as thin veinlets.

Biotite forms large (∼0.5–1 mm) flakes organised in aggregates with no preferential orientation in the rock matrix (Fig. 4.14). Texturally late biotite ('bi II' on Fig. 4.14) randomly overgrows texture-forming minerals. Biotite displays homogeneous composition, with X_{Fe} = 0.26–0.28, Ti of 0.14–0.21 a.p.f.u and F-contents of 0.13–0.19 a.p.f.u. $\mathrm{Al^{VI}}$ is ∼0.16–0.20.

Pleochroic, skeletal orthopyroxene forms a minor constituent of the rock matrix (Fig. 4.14 and 4.15b). The grains are elongated to anhedral and partly to almost completely consumed by chlorite. Grain boundaries are straight when shared with cordierite, however a thin rind of pinitisation commonly separates the two phases. When bordered by biotite grain boundaries are either sharp or, more commonly, diffuse or serrated. In these instances a narrow rim of fine-grained opaques is present between orthopyroxene and biotite. The mineral is Mg-rich with X_{Fe} = 0.29–0.31 and has y_{opx} of 0.08–0.10.

Sapphirine exclusively occurs within the andalusite-pseudomorphs as xenoblastic grains or displays graphic intergrowth with spinel at the core (Fig. 4.14 and 4.15a). The mineral is strongly pleochroic, ranging from bright blue–green to faint blue–grey. Sapphirine is rich in Mg, with X_{Fe} of 0.26.

Dark-green spinel forms intimate intergrowths with sapphirine and is rimmed by the latter in most cases, suggesting that the introduction of sapphirine postdates that of spinel. However, spinel also occurs as distinct, xenoblastic grains within the texture but is not present in the rock matrix (Fig. 4.14 and 4.15a). Spinel is clear or decorated by fine lamellar exsolutions of magnetite. The latter also occurs as distinct grains at the rims of spinel and rare corundum (Fig. 4.15a). Spinel is rich in hercynite-solid solution with X_{Fe} of 0.54–0.57 and negligible Zn-content.

Rare grains of dark-brown rutile are scattered in the texture, commonly neighboured by or included in sapphirine. Texturally late biotite displays sharp grain boundaries towards texture-forming phases (Fig. 4.15a).

Nodular spinel–corundum–magnesian gneiss (sample NMC90)

The rock consists of porphyroblastic spinel including rare corundum and surrounded by a clear halo of cordierite, found in a matrix of cordierite and biotite. Waters (1986b) speculates that prograde dehydration of staurolite and possibly aluminosilicate gave rise to the described textures. Accessories of this specimen are minor ilmenite and magnetite as well as rare zircon and monazite.

Cordierite forms medium-sized (∼0.5 mm) rounded or elongated grains in the matrix and large (> 0.5 mm) polygonal grains arranged in a monomineralic corona around spinel-textures (Fig. 4.16a, b). Grains are commonly pinitised along the grain boundaries and intra-grain veinlets. Faint brown–green biotite occurs as large (∼0.5–1 mm) flakes clustering

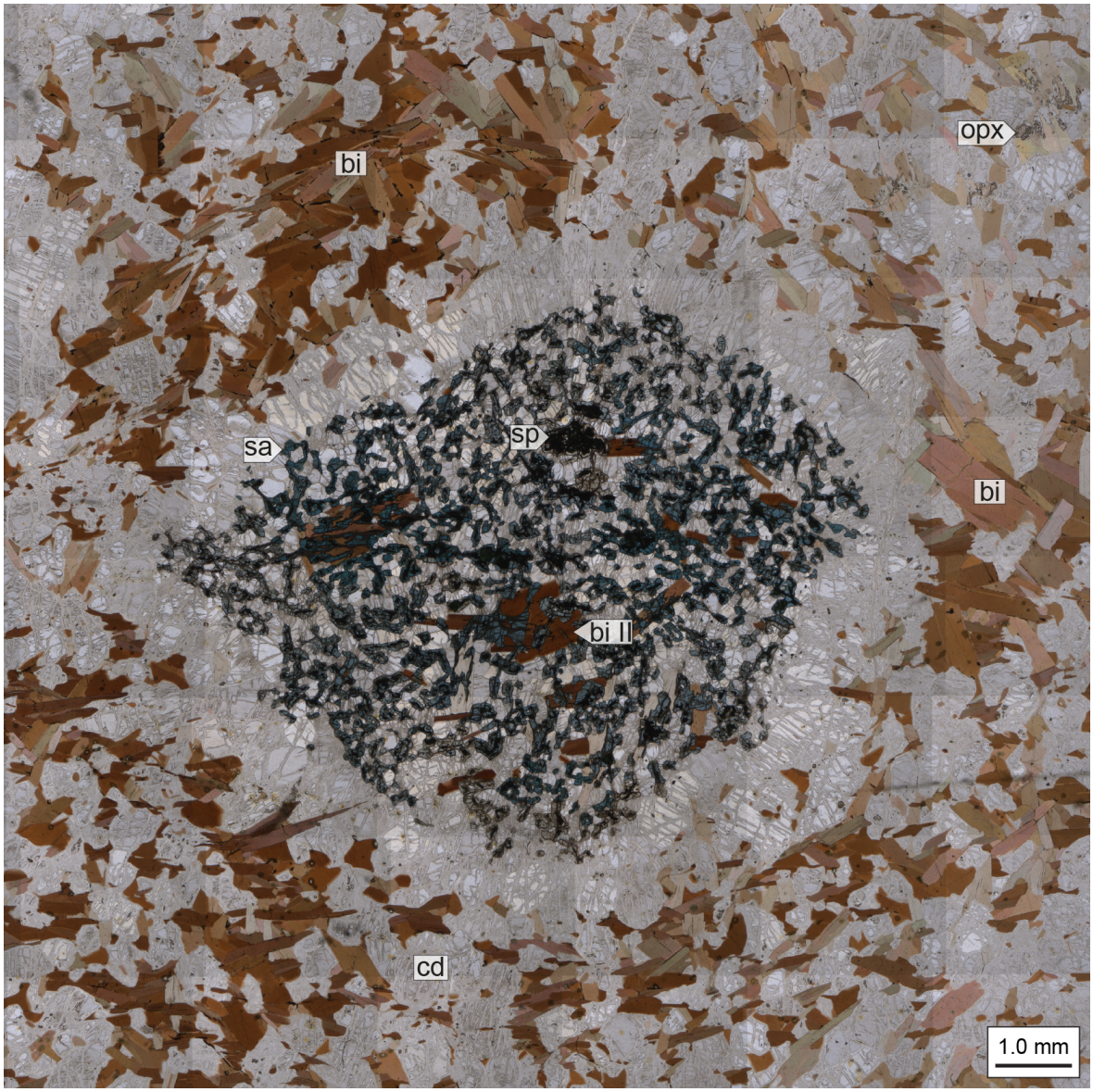


Figure 4.14: Thin section microphotograph in plain polarised light of pseudomorph after andalusite (sample NMC88). Texture of symplectic sapphirine–spinel/magnetite–cordierite partly overgrown by texturally late biotite ('bi II'). Note cordierite-halo surrounding the texture. Matrix of granoblastic cordierite, biotite and rare, relic orthopyroxene.

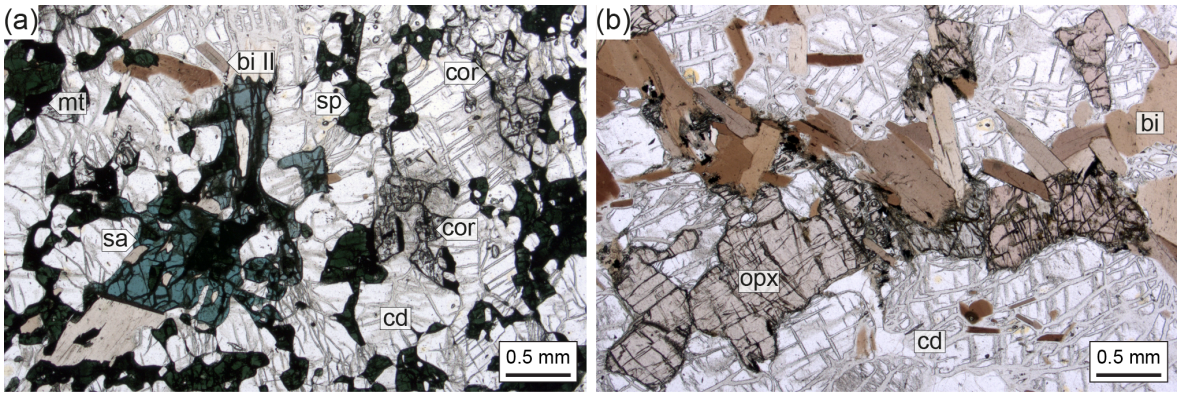


Figure 4.15: (a) Detail of Figure 4.14 showing textural relationships of sapphirine–spinel–corundum forming the reaction textures. (b) Elongated orthopyroxene as part of the rock matrix dominated by cordierite and biotite (sample NMC88). Note fine-grained opaques at the interfaces of biotite and orthopyroxene. Plain polarised light.

in aggregates and stringers ranging several mm in size. Both biotite and cordierite are decorated by abundant pleochroic haloes formed around radioactive accessories, such as zircon and monazite. Dark green, almost opaque, spinel forms oval to lozenge-shaped porphyroblasts, inferred to be pseudomorphing early-metamorphic staurolite (Fig. 4.16a, b; cf. Waters, 1986a). The textures are variable in size, ranging from ∼0.5–5 mm in thin section (Fig. 4.16a, b) and up to several cm in hand specimen (Fig. 3.11c). Spinel making up the bulk of the textures is rich in exsolutions of magnetite and forms aggregates of anhedral grains. The rims of the pseudomorphs are serrated, with spinel branching out between individual grains of cordierite (Fig. 4.16a, b). Rare corundum is present in the interstices of spinel. Single grains of anhedral spinel–magnetite intergrowths are also present in the rock matrix.

Gedrite–orthopyroxene–spinel–magnesian gneiss (sample NMC91)

This specimen is dominated by intergrowths of orthoamphibole and orthopyroxene, coexisting with minor amounts of cordierite, biotite, spinel and sapphirine (Fig. 4.16c, d). Accessories include minor ilmenite, magnetite, zircon and apatite.

Orthoamphibole occurs as interlocked sprays, plates and lozenges that define a weak planar fabric in this rock type (Fig. 3.11d and 4.16c, d). Single prisms of gedrite range between ∼0.5 up to 5 mm in length. Orthoamphibole is pleochroic, ranging from faint yellow–green to faint pink. Compositionally it defines as sodicgedrite (Leake *et al.*, 1997). The mineral is Mg-rich but chemically homogeneous, with X_{Fe} of 0.26, A-site Na of 0.59–0.65, negligible A-site K, 0.31–0.64 $\mathrm{Al^{VI}}$, low M4-site Ca of max. 0.04 and null M4-site Na (based on 23 O). Orthopyroxene forms large (up to ∼2 mm) elongated poikiloblasts overgrowing orthoamphibole, suggesting a prograde replacement of amphibole by pyroxene.

Orthopyroxene is pleochroic, ranging from faint green to pinkish in colour. No significant chemical variation is observed. Orthopyroxene is Mg-rich, with low X_{Fe} of 0.21–0.23 and y_{opx} = 0.10–0.13.

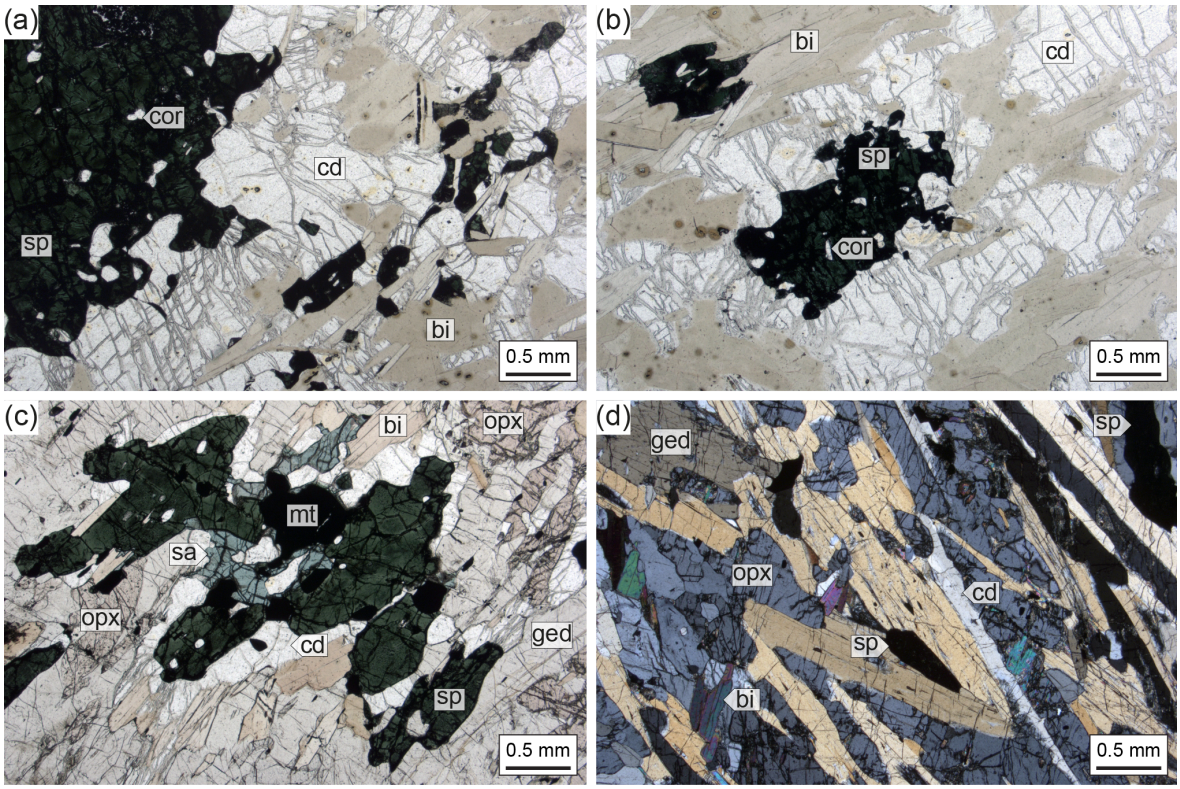


Figure 4.16: Thin section microphotographs in plain polarised light (a–c) and cross-polarised light of spinel–magnesian gneiss (a, b) and gedrite–magnesian gneiss (c, d). (a, b) Rounded spinel–corundum porphyroblast pseudomorphing staurolite surrounded by halo of variably pinitised cordierite, embedded in cordierite and biotite, sample NMC90 (c) Intergrowth of spinel–sapphirine–magnetite in gedrite–orthopyroxene matrix. (d) Matrix of sample NMC91. Sprays of gedrite (yellow interference colours) intergrown with orthopyroxene (grey interference colours) and biotite.

Rare, orange–brown biotite occurs as disseminated flakes between fabric-forming amphibole and orthopyroxene. The grains are small (∼0.5 mm) compared to the chain silicates, but similarly rich in Mg, with X_{Fe} of 0.16. Ti is measured with 0.10–0.15 a.p.f.u and F is 0.12–0.15 a.p.f.u.

Cordierite is minor in this rock type, occurring as thin (∼0.2 mm) monomineralic coronae around grains of spinel and spinel–sapphirine–magnetite textures (Fig. 4.16c), displaying a comparable textural setting to cordierite in other nodular magnesian gneisses. It also occurs as dispersed elongated grains interstitial to laths of gedrite and orthopyroxene (Fig. 4.16d). Cordierite is magnesian with $X_{\mathrm{Fe}} = 0.08$–0.10. Pinitsation is limited to thin veinlets.

Dark-green spinel is commonly surrounded by a thin halo of cordierite, similar to the other samples. It also occurs in association with anhedral sapphirine and rounded magnetite (Fig. 4.16c) or as single rounded to drop-shaped to anhedral grains disseminated in the rock matrix (Fig. 4.16d). Spinel is rich in hercynite with X_{Fe} of 0.40–0.42 and negligible Zn-content. Blue–green to blue–grey pleochroic sapphirine exclusively occurs in association with spinel and magnetite, forming thin rinds on spinel or anhedral grains around magnetite (Fig. 4.16c). The mineral is magnesian with X_{Fe} of 0.20.

4.3 Inferred equilibrium assemblages

For the following thermodynamic modelling representative samples of each locality have been selected. The inferred peak equilibrium assemblages and key petrographic information is summarised in Table 4.1.

4.3.1 Regional sampling – aluminous metapelites

Aluminous metapelites from all localities, with exception for amphibolite facies gneisses from Geselskapbank, display compelling macroscopic evidence for partial melting (see subsection 3.4.1). Moreover, the investigated samples contain well annealed assemblages in apparent textural equilibrium, consistent with having developed at high-grade conditions in the presence of silicic melt at or near the thermal peak.

Lepel se Kop and Nababeep

Pelitic granulites from the localities Lepel se Kop (sample NMC102 and NMC47) and Nababeep (sample NMC24) show the intimate intergrowth of biotite and sillimanite displaying sharp boundaries when in contact. Both phases also occur in mutual contact with both garnet and cordierite. This is interpreted as evidence for the stable coexistence of all four minerals at peak conditions. Biotite and sillimanite also occur as fine-grained inclusions in large garnet poikiloblasts, suggesting their coexistence prior to peak metamorphic garnet growth. The inferred peak metamorphic assemblage is therefore garnet–biotite–cordierite–sillimanite–plagioclase–K-feldspar–quartz–ilmenite–magnetite–granitic melt for samples of both localities. Textures

indicative of post-peak retrogression (e.g. coronae or symplectites) are not observed in these samples.

Paulshoek

At this locality (samples NMC101 and NMC46), hercynitic spinel is present in rock-forming amounts and coexists with garnet, cordierite, sillimanite, plagioclase, magnetite and ilmenite, is however always shielded from biotite, K-feldspar or quartz by monomineralic coronae. Disequilibrium textures such as coronae and symplectites in high-grade rocks are interpreted to have formed in response to the development of domains of local bulk equilibrium due to the removal of melt during cooling, shortly postponing the thermal maximum (e.g. White and Powell, 2011). In the rocks from Paulshoek the type of corona around spinel appears to be controlled by the dominant phase nearby, and single grains of spinel may be engulfed by two different monomineralic layers (e.g. garnet and sillimanite). The high degree of spatial organisation of coronae suggests their formation was controlled by local gradients in chemical potential with at least one immobile component (Baldwin *et al.*, 2015; Schorn and Diener, 2017; Štípská *et al.*, 2010; White and Powell, 2011; White *et al.*, 2008) that does not imply large degrees of cooling or decompression along convoluted P–T paths following the thermal peak (cf. Doukkari *et al.*, 2018). Because coronae separating spinel from matrix phases, in particular from quartz, are inferred to have formed during minor cooling, spinel is interpreted to have coexisted in equilibrium with other rock-forming phases at the thermal maximum (also see Waters, 1991). Locally-abundant stringers of sillimanite intimately intergrown with F–Ti-rich biotite suggests that biotite persisted throughout the high-grade evolution. However, some biotite might also have been re-introduced during minor post-peak melt crystallisation (e.g. Ashworth, 1976; Waters, 1988; White and Powell, 2011). The absolute amount of biotite present at the thermal maximum is therefore difficult to estimate with certainty. However, in light of the modal abundance, textural appearance and significant fluorine-contents that are known to critically expand biotite stability (e.g. Munoz and Luddington, 1977; Peterson *et al.*, 1991; Icenhower and London, 1997), biotite is inferred as stable rock-forming mineral at the thermal maximum experienced at Paulshoek. Therefore, the inferred peak metamorphic assemblage is garnet–biotite–cordierite–sillimanite–spinel–plagioclase–K-feldspar–quartz–ilmenite–magnetite–granitic melt for sample NMC101 where sillimanite is modally abundant. Sample NMC46 is poor in aluminosilicate, which is largely confined to coronae on spinel. Sillimanite is therefore excluded from the inferred peak assemblage of this sample, consisting of garnet–biotite–cordierite–spinel–plagioclase–K-feldspar–quartz–ilmenite–magnetite–granitic melt. Inclusions of spherical cordierite and other phases in garnet porphyroblasts suggests that garnet was of relatively late paragenesis, postponing the stabilisation of cordierite during high-grade metamorphism.

Ratelpoort

At Ratelpoort (sample NMC21) garnet, cordierite, plagioclase, K-feldspar, ilmenite, magnetite and quartz occur in textural equilibrium, biotite and sillimanite however are confined to rare coarse-grained aggregates interpreted as paramorphs after early andalusite that are invariably armoured by coarse-grained cordierite. This textural relationship suggests that both biotite and sillimanite have been isolated from the rock matrix due to the extensive crystallisation of peak metamorphic cordierite during the thermal maximum. In conclusion the phases are excluded from the inferred peak assemblage of garnet–cordierite–plagioclase–K-feldspar–quartz–ilmenite–magnetite–granitic melt. Similar to samples from Paulshoek, spherical cordierite is included in garnet, indicating that coridierite-growth preceded the introduction of garnet. Clear indications for retrogression are largely missing in the investigated samples, however, some biotite/and or sillimanite may have been re-introduced during minor melt crystallisation shortly after the thermal peak (White and Powell, 2011).

Geselskapbank

At the northernmost locality of Geselskapbank, leucosome-absent gneisses and leucosome-bearing migmatites have been sampled. Amphibolite facies gneisses host garnet–biotite–cordierite–sillimanite–plagioclase–ilmenite–magnetite ± quartz that coexist in textural equilibrium only in sheared varieties. Undeformed, granoblastic specimens (sample NMC05) are highly domainal, with garnet and biotite being mutually exclusive in domains of local bulk composition, rendering the 'effective bulk composition' (Stüwe, 1997) at the moment of domain-development unknown. Therefore, only deformed and equilibrated samples have been considered for thermodynamic modelling (sample NMC11 and NMC08). Large prisms of sillimanite are inferred to have paramorphed early metamorphic andalusite (see subsection 3.4.1). Whereas sample NMC11 is oversaturated in silica, in sample NMC08 quartz is limited to rare inclusions in cordierite and therefore excluded from the inferred peak assemblage of garnet–biotite–cordierite–sillimanite–plagioclase–K-feldspar–ilmenite–magnetite. Fluid saturation is assumed for amphibolite facies pelites due to the presence of minor biotite and the absence of K-feldspar as well as indications for partial melting. The main fabric-forming deformational event is inferred to have occurred close to or at the thermal peak, or at least to have postponed garnet growth, as interpreted from randomly oriented fibrolite in garnet as opposed to fabric-defining sillimanite present in the matrix. Texturally late beards of unoriented fibrolite on cordierite are interpreted as a static replacement postponing the thermal maximum experienced by these samples. Migmatites at Geselskapbank (sample NMC15 and NMC16) are characterised by the inferred equilibrium assemblage of biotite–cordierite–sillimanite–plagioclase–K-feldspar–quartz–ilmenite–magnetite–granitic melt. Modally-abundant magnetite present as inclusions in coarse-grained sillimanite and in the rock matrix, together with the absence of garnet and a low X_{Fe} of ferromagnesian phases suggests a high degree of oxidation. The formation of texturally-late sillimanite, extensive pinitisation of peak cordierite in both the

amphibolite facies gneisses and migmatites, as well as the formation of chlorite, is interpreted as late fluid assisted reworking that overprints earlier, peak metamorphic fabrics.

4.3.2 Detailed sampling – Hytkoras

The investigated samples mostly contain well annealed assemblages in apparent textural equilibrium, consistent with having developed at high-grade conditions in the presence of silicic melt at or near the thermal peak. Fine-grained, typically symplectic intergrowths are found to partly replace coarse-grained peak metamorphic phases, indicating partial reversal of reactions that have produced the peak assemblages (e.g. Waters, 1988). Partial retrogression likely occurred in the presence of small vestiges of melt, thus, the symplectic textures are interpreted to have formed shortly after the thermal maximum, where trapped vestiges of melt could crystallise and drive minor high-T retrogression (Ashworth, 1976; Ashworth and McLellan, 1985; Waters, 1988; Kriegsman and Hensen, 1998; White and Powell, 2011).

Aluminous metapelite

The aluminous metapelite (sample NMC89, NMC71 and NMC65) shows the intimate intergrowth of coarse-grained biotite and sillimanite displaying sharp boundaries when in contact. Both phases also occur in mutual contact with both garnet and cordierite. This is interpreted as evidence for the stable coexistence of all four minerals at peak conditions. Biotite and sillimanite also occur as fine-grained inclusions in large garnet poikiloblasts, suggesting their coexistence prior to peak metamorphic garnet growth. Spinel occurs exclusively in association with opaque oxides and is never in contact with other matrix minerals, particularly quartz. Spinel is regarded as variably recrystallized exsolution product from opaque oxides such as magnetite. Corundum occurs exclusively in association with opaques and is separated from the matrix by other phases. Therefore both spinel and corundum are excluded from the inferred peak metamorphic assemblage of garnet–biotite–cordierite–sillimanite–plagioclase–K-feldspar–quartz–ilmenite–magnetite–granitic melt. Sillimanite and biotite form fine-grained symplectites where in contact with cordierite. Sillimanite also forms symplectic beards on prisms of large sillimanite and thin rims on oxide minerals. Symplectites of biotite and sillimanite are inferred to be reintroduced at the expense of peak metamorphic cordierite reacting with final vestiges of melt.

Magnesian metapelite

In the magnesian metapelite (sample NMC37) cordierite occurs as inclusions in poikiloblasts and in the matrix, suggesting the presence of cordierite prior to and during peak metamorphic conditions. It displays sharp boundaries to both garnet and orthopyroxene, suggesting a stable coexistence of these phases at the thermal maximum, including feldspars, quartz and silicic melt. Magnetite forms thin rims on ilmenite or is intergrown with fine-grained biotite. It is therefore unclear whether magnetite was part of the stable peak assemblage, in-

ferred to consist of garnet–biotite–orthopyroxene–cordierite–plagioclase–K-feldspar–quartz–ilmenite–granitic melt ± magnetite. Biotite additionally occurs in intimate symplectic intergrowths with quartz next to garnet and with cordierite and magnetite next to orthopyroxene. The biotite and quartz symplectites are interpreted to be retrograde and formed at the expense of peak metamorphic garnet whereas the biotite and cordierite symplectites grew at the cost of orthopyroxene, both reacting with minor droplets of melt.

Semi-pelite

In the semi-pelite (sample NMC67) biotite is never found in direct contact with sillimanite but is armoured by minerals such as K-feldspar. This suggests that biotite was present prior to peak metamorphic conditions but effectively removed from the equilibration volume during prograde metamorphism and melting where abundant peritectic phases are expected to crystallise. In analogy to the metapelites, spinel is interpreted to not form part of the equilibrium assemblage assumed to consist of garnet–cordierite–sillimanite–plagioclase–K-feldspar–quartz–ilmenite–magnetite–granitic melt. Cordierite additionally occurs as monomineralic coronae around garnet, suggesting that this cordierite reflects a small increase of cordierite-mode at the expense of garnet.

Mafic granulite

The leucosome-bearing mafic granulite (sample NMC69) is characterised by poikilitic pyroxenes including abundant rounded inclusions of hornblende and minor biotite. Both are also present in the matrix interlocked with plagioclase forming a granoblastic texture. Straight, sharp boundaries between pyroxenes, pyroxenes and hornblende–biotite and plagioclase with all phases indicate textural equilibrium achieved at or near the metamorphic peak. The presence of inclusions in poikiloblasts additionally suggests the stability of both hornblende and biotite prior to thermal maximum. The inferred equilibrium assemblage for the mafic granulite is hornblende–biotite–augite–orthopyroxene–plagioclase–quartz–ilmenite–magnetite–tonalitic melt. The investigated samples of mafic granulite show no clear retrogression textures, likely due to efficient and near-complete melt loss.

Orthopyroxene–magnesian gneiss

The magnesian gneiss (sample NMC44) is dominated by cordierite and biotite, with minor quartz. These phases are also present as abundant inclusions in orthopyroxene, indicating their stability prior to and during the thermal maximum. Unlike the other samples investigated here, the magnesian gneiss lacks compelling macroscopic evidence for partial melting, such as leucosomes. However, microtextures indicative of pseudomorphs after melt (Holness and Sawyer, 2008) are interpreted to reflect small degrees of partial melting. Magnetite is considered to be part of the equilibrium assemblage; it is, however, not clear if ilmenite is also part of the stable peak assemblage or exclusively a retrograde phase. The inferred peak

assemblage for this sample is therefore taken to be biotite–cordierite–orthopyroxene–quartz–magnetite–granitic melt ± ilmenite. Similar to the magnesian metapelite, late biotite forms symplectites with quartz in the proximity of orthopyroxene.

Table 4.1: Summary of key petrographic observations.

sample	locality	lithology	inferred peak assemblage	inclusions in porphyroblasts	accessories
NMC47	Lepel se Kop	aluminous metapelite	g–bi–cd–sill–pl–ksp–q–ilm–mt–liq	bi, sp, sill, q, mt, ilm	zrc, mnz, ap
NMC102	Lepel se Kop	aluminous metapelite	g–bi–cd–sill–pl–ksp–q–ilm–mt–liq	bi, sp, sill, q, mt, ilm	zrc, mnz, ap
NMC101	Paulshoek	aluminous metapelite	g–bi–cd–sill–sp–pl–ksp–q–ilm–mt–liq	bi, cd, sill, q, mt, ilm	zrc, mnz, ap
NMC46	Paulshoek	aluminous metapelite	g–bi–cd–sp–pl–ksp–q–ilm–mt–liq	bi, cd, sill, q, mt, ilm	zrc, mnz, ap
NMC89	Hytkoras	aluminous metapelite	g–bi–cd–sill–pl–ksp–q–ilm–mt–liq	bi, sill, q, mt, ilm	zrc, mnz, ap, cor, sp
NMC71	Hytkoras	aluminous metapelite	g–bi–cd–sill–pl–ksp–q–ilm–mt–liq	bi, sill, q, mt, ilm	zrc, mnz, ap, cor, sp
NMC65	Hytkoras	aluminous metapelite	g–bi–cd–sill–pl–ksp–q–ilm–mt–liq	bi, sill, q, mt, ilm	zrc, mnz, ap, cor, sp
NMC37	Hytkoras	magnesian metapelite	g–bi–opx–cd–pl–ksp–q–ilm–liq ± mt	bi, cd, q, mt, ilm	zrc, ap, sp
NMC67	Hytkoras	semi-metapelite	g–cd–sill–pl–ksp–q–ilm–mt–liq	bi, sill, pl, q, mt, ilm	zrc, mnz, ap
NMC69	Hytkoras	mafic granulite	hb–bi–aug–opx–pl–q–ilm–mt–L	hb, bi, mt, ilm	ap
NMC27	Hytkoras	mafic granulite	hb–bi–aug–opx–pl–q–ilm–mt–L	hb, bi, mt, ilm	ap
NMC44	Hytkoras	magnesian gneiss	bi–cd–opx–q–liq ± ilm ± mt	bi, cd, q, mt, ilm	zrc, ap
NMC24	Nababeep	aluminous metapelite	g–bi–cd–sill–pl–ksp–q–ilm–mt–liq	bi, sp, sill, pl, q, mt, ilm	zrc, mnz, ap
NMC21	Ratelpoort	aluminous metapelite	g–cd–sp–pl–ksp–q–ilm–mt–liq	bi, cd, sill, q, mt, ilm	zrc, mnz, ap
NMC11	Geselskapbank	aluminous metapelite	g–bi–cd–sill–pl–q–ilm–mt–H_2O	bi, sill, q, mt, ilm	zrc, ap
NMC08	Geselskapbank	aluminous metapelite	g–bi–cd–sill–pl–ilm–mt–H_2O	bi, sill, mt, ilm	zrc, ap
NMC15	Geselskapbank	oxidised metapelite	bi–cd–sill–pl–ksp–q–ilm–mt–liq	q, mt, ilm	zrc, ap
NMC16	Geselskapbank	oxidised metapelite	bi–cd–sill–pl–ksp–q–ilm–mt–liq	q, mt, ilm	zrc, ap

Chapter 5

Phase equilibrium modelling

Selected analyses were converted to the MnO–Na_2O–CaO–K_2O–FeO–MgO–Al_2O_3–SiO_2–H_2O–TiO_2–O_2 (MnNCKFMASHTO) model system by converting appropriate amounts of total Fe to Fe^{3+} in order to reproduce the measured X_{Fe} of the silicate mineral assemblage for each sample (see chapter 4).

For the orthopyroxene-magnesian gneiss from Hytkoras (sample NMC44) the total amount of CaO was reduced by ∼0.22 wt. %, based on the amount of P_2O_5 that would sequester Ca in apatite and taking into account the minor Ca stored in cordierite. Additionally, the Na_2O content of this sample was reduced by ∼0.20 wt. % to allow for the amounts held in rock-forming biotite. This was done in order to reduce the calculated mode of feldspar to approximate the observed absence of feldspars in the thin section assemblage as the current biotite a–X models do not include Na_2O. The apatite correction was not performed for the rest of the samples because of the presence of abundant accessory monazite, which is interpreted as the main P_2O_5 reservoir in these rocks.

MnO was excluded from the model composition for metamafic rocks since Mn is not yet included in the latest activity–composition formulations for amphibole or clinopyroxene of Green *et al.* (2016). Whole rock analyses are presented in Table 5.1; model compositions employed in phase diagram calculations are reported in Table 5.2. Full description of methodology is given in appendix B.

5.1 Considerations for modelling

5.1.1 Residuum compositions

The presence of macroscopic leucosomes and microscopic pseudomorphs after melt-filled pores indicate more or less extensive melt production for the investigated granulites. The high degree of preservation of the high-grade assemblages and general lack of retrogression around leucosomes indicates efficient removal of melt prior to cooling (White and Powell, 2002; Diener *et al.*, 2013). The removal of melt implies that the analysed bulk compositions are that of melt-depleted residua, and different from the original protolith. In the case of the

Table 5.1: XRF whole-rock analyses of investigated samples (wt. %).

sample	locality	lithology	SiO_2	Al_2O_3	CaO	MgO	Fe_2O_3	K_2O	Na_2O	TiO_2	MnO	P_2O_5	L.O.I	total
NMC102	Lepel Se Kop	aluminous metapelite	67.34	16.23	0.81	1.63	5.54	4.29	1.80	0.85	0.07	0.11	0.53	99.20
NMC47	Lepel Se Kop	aluminous metapelite	64.81	17.91	0.85	1.97	7.33	3.24	0.99	0.90	0.09	0.05	0.48	98.62
NMC101	Paulshoek	aluminous metapelite	63.84	18.73	0.64	1.85	7.05	3.97	1.30	0.98	0.08	0.05	0.83	99.33
NMC46	Paulshoek	aluminous metapelite	66.65	14.67	0.90	2.25	8.04	3.55	1.48	1.06	0.13	0.10	0.36	99.19
NMC89	Hytkoras	aluminous metapelite	49.88	24.59	0.62	2.24	12.04	5.14	1.99	1.48	0.26	0.07	1.03	99.34
NMC71	Hytkoras	aluminous metapelite	54.95	22.32	2.04	3.51	10.52	1.93	2.00	0.97	0.29	0.05	0.98	99.56
NMC65	Hytkoras	aluminous metapelite	52.94	21.94	1.47	4.00	13.91	1.05	2.17	0.63	0.27	0.03	0.93	99.34
NMC37	Hytkoras	magnesian metapelite	58.16	17.32	0.45	6.53	8.85	3.28	0.74	0.93	0.16	0.04	2.17	98.63
NMC67	Hytkoras	semi-metapelite	62.26	17.87	0.73	1.49	6.86	5.31	2.23	0.80	0.13	0.05	1.25	98.98
NMC69	Hytkoras	mafic granulite	53.42	18.01	9.27	5.40	9.95	0.63	1.26	0.89	0.18	0.28	0.20	99.49
NMC44	Hytkoras	opx-magnesian gneiss	52.37	14.73	0.25	12.18	12.88	2.66	0.26	0.61	0.18	0.16	2.51	98.79
NMC88	Hytkoras	sa–sp-magnesian gneiss	42.73	27.37	0.11	12.36	7.36	2.90	0.69	0.99	0.10	0.04	4.58	99.23
NMC90	Hytkoras	sp–cor-magnesian gneiss	38.40	26.59	0.13	14.50	10.44	4.87	0.56	0.51	0.09	0.06	2.81	98.96
NMC24	Nababeep	aluminous metapelite	63.88	17.11	0.95	3.05	7.51	4.16	1.22	0.72	0.16	0.04	0.38	99.18
NMC21	Ratelpoort	aluminous metapelite	62.93	17.22	0.95	2.36	7.29	3.79	1.86	0.95	0.08	0.04	1.32	98.79
NMC11	Geselskapbank	aluminous metapelite	61.03	21.47	0.91	2.77	10.03	0.43	0.35	1.13	0.11	0.01	0.79	99.02
NMC08	Geselskapbank	aluminous metapelite	41.90	29.66	3.20	5.20	13.31	0.37	0.92	1.70	0.24	0.01	2.85	99.17
NMC15	Geselskapbank	oxidised metapelite	55.48	22.69	0.28	2.05	9.98	4.52	1.07	0.85	0.23	0.12	1.70	98.97
NMC16	Geselskapbank	oxidised metapelite	56.00	22.76	0.16	1.99	9.90	4.65	0.89	0.86	0.20	0.10	1.14	98.64

Table 5.2: Bulk compositions used in thermodynamic calculations (mol. %).

sample	locality	lithology	comment	H_2O	SiO_2	Al_2O_3	CaO	MgO	FeO	K_2O	Na_2O	TiO_2	MnO	O	XFe^{3+}	Figure
NMC102	Lepel se Kop	aluminous metapelite	residuum	1.10	73.86	10.49	0.95	2.66	4.57	3.00	1.91	0.70	0.07	0.69	0.30	5.1a
NMC47	Lepel se Kop	aluminous metapelite	residuum	1.40	71.65	11.67	1.01	3.24	6.09	2.29	1.06	0.75	0.09	0.76	0.25	5.1b
NMC101	Paulshoek	aluminous metapelite	residuum	1.00	71.10	12.30	0.76	3.07	5.91	2.82	1.40	0.82	0.07	0.74	0.25	5.1c
NMC46	Paulshoek	aluminous metapelite	residuum	1.50	71.99	9.34	1.04	3.63	6.54	2.45	1.55	0.86	0.12	0.98	0.30	5.1d
NMC89	Hytkoras	aluminous metapelite	residuum	1.60	57.07	16.58	0.76	3.82	10.36	3.75	2.21	1.28	0.25	2.33	0.45	5.2a
NMC71	Hytkoras	aluminous metapelite	residuum	2.20	60.41	14.46	2.40	5.75	8.70	1.35	2.13	0.80	0.27	1.52	0.20	5.2b
NMC65	Hytkoras	aluminous metapelite	residuum	2.50	57.71	14.09	1.72	6.49	11.41	0.73	2.30	0.52	0.25	2.28	0.40	5.2c
NMC37	Hytkoras	magnesian metapelite	residuum	2.50	63.44	11.13	0.53	10.62	7.26	2.28	0.78	0.76	0.15	0.54	0.15	5.2d
NMC67	Hytkoras	semi-pelite	residuum	0.80	69.88	11.82	0.88	2.50	5.80	3.80	2.42	0.67	0.12	1.30	0.45	5.2a
NMC69	Hytkoras	mafic granulite	residuum	0.80	57.15	11.36	10.62	8.61	8.01	0.43	1.30	0.72	-	1.00	0.25	5.2b
NMC44	Hytkoras	opx-magnesian gneiss	residuum	4.30	54.47	9.03	0.04	18.88	10.08	1.76	0.05	0.48	0.15	0.75	0.15	5.2c, d
NMC89	Hytkoras	aluminous metapelite	protolith	7.08	59.37	13.84	0.62	2.82	7.65	3.45	2.34	0.94	0.18	1.71	0.44	5.3a, b; 7.1b; 8.4a
NMC37	Hytkoras	magnesian metapelite	protolith	5.06	64.28	10.46	0.57	8.77	6.09	2.52	1.12	0.62	0.12	0.44	0.14	5.3c, d; 7.1c; 8.4c
NMC67	Hytkoras	semi-pelite	protolith	5.26	68.44	10.91	0.77	2.04	4.73	3.64	2.51	0.54	0.10	1.06	0.45	5.3e, f; 7.1d; 8.4b
NMC69	Hytkoras	mafic granulite	protolith	3.45	61.10	10.53	8.71	6.33	6.08	1.44	1.11	0.52	-	0.72	0.24	5.3g, h; 8.4d
NMC44	Hytkoras	opx-magnesian gneiss	protolith	5.34	53.87	8.93	0.04	18.68	9.97	1.75	0.04	0.47	0.15	0.75	0.15	5.3a, b; 8.4e
NMC44	Hytkoras	opx-magnesian gneiss	KFMASH	sat	57.81	9.58	-	20.04	10.70	1.87	-	-	-	-	-	5.4a
NMC88	Hytkoras	sa–sp-magnesian gneiss	KFMASH	sat	50.47	19.05	-	21.75	6.55	2.18	-	-	-	-	-	5.4b
NMC90	Hytkoras	sp–cor-magnesian gneiss	KFMASH	sat	44.33	18.09	-	24.94	9.06	3.58	-	-	-	-	-	5.4c
NMC24	Nababeep	aluminous metapelite	residuum	2.70	68.98	10.89	1.10	4.91	6.10	2.86	1.27	0.58	0.15	0.46	0.15	5.1e
NMC21	Ratelpoort	aluminous metapelite	residuum	1.10	70.08	11.33	1.40	3.95	6.04	2.58	2.08	0.78	0.06	0.60	0.20	5.1f
NMC11	Geselskapbank	aluminous metapelite	protolith	sat	68.86	14.27	1.10	4.65	8.51	0.31	0.38	0.96	0.10	0.85	0.20	5.1g
NMC08	Geselskapbank	aluminous metapelite	protolith	sat	49.94	20.83	4.08	8.92	11.94	0.28	1.06	1.52	0.24	1.19	0.20	5.1h
NMC15	Geselskapbank	oxidised metapelite	residuum	1.80	62.55	15.08	0.34	3.45	8.47	3.25	1.17	0.72	0.22	2.96	0.70	5.1i
NMC16	Geselskapbank	oxidised metapelite	residuum	1.90	63.24	15.15	0.19	3.35	8.41	3.35	0.97	0.73	0.19	2.52	0.60	5.1j

orthopyroxene-magnesian gneiss from Hytkoras (sample NMC44), melt production was likely limited, such that melt likely adhered to the grain boundaries without forming an interconnected network. Hence, melt probably did not escape the rock and did not affect the bulk rock composition, which can be approximated as that of the unaltered protolith. In modelling the residuum compositions it is assumed that the peak assemblages were in equilibrium with minor amounts of melt, reproducing the conditions after the last melt extraction event (cf. White *et al.*, 2004; Diener *et al.*, 2008a, 2013). The H_2O content of the investigated samples is therefore chosen to first stabilise the inferred peak assemblage at the residuum solidus, before being fine-tuned to reproduce the relative proportions of hydrous and anhydrous phases, such as the ratio of biotite to garnet and K-feldspar. Similarly, the O content is chosen to not only reproduce the oxide assemblage but also fit the measured X_{Fe} of the silicates. Due to this individual 'tailoring' for each sample, the predicted modal amounts and X_{Fe} of main phases of the respective inferred peak assemblage correspond reasonably well to petrographic observations.

Sample NMC11 and NMC08 from Geselskapbank hosts an amphibolite facies assemblages that most likely were not subjected to partial melting. Therefore the measured bulk composition is assumed to correspond to that of the original protolith. Fluid saturation is assumed for modelling the prograde evolution of this sample. Calculated P–T pseudosections for residuum compositions of regionally sampled metapelites are presented in Figure 5.1, diagrams for Hytkoras are shown on Figure 5.2.

5.1.2 Protolith compositions

Residuum compositions are not appropriate to investigate the prograde evolution prior to melt loss, or to reproduce and compare the melt production history of different lithologies (White *et al.*, 2004; Diener *et al.*, 2008a; Korhonen *et al.*, 2010). Consequently, model protolith compositions for samples from Hytkoras are estimated via the multi-step melt-reintegration approach outlined by White *et al.* (2004) and Diener *et al.* (2008a, 2013). This involves incrementally adding melt of equilibrium composition along the inverse of the inferred prograde path until a hydrous, amphibolite facies assemblage coexists with aqueous fluid at the wet solidus. This approach is found to confidently reproduce the pre-melt loss bulk composition involved in the prograde metamorphic evolution (White *et al.*, 2004; Korhonen *et al.*, 2013a; Alessio *et al.*, 2017; Bartoli, 2017).

Whereas stepwise melt reintegration is deemed necessary to estimate the most realistic subsolidus protolith compositions and derive a detailed melt production history, we did not consider progressive melt loss along the prograde path. The style and timing of melt loss has important implications for the mineralogical evolution and strength of the residuum, and can also influence the composition of later melt batches, but these aspects are beyond the scope of this thesis (Handy *et al.*, 2001; Rosenberg and Handy, 2005; Yakymchuk and Brown, 2014; Diener and Fagereng, 2014; Palin *et al.*, 2016a; Stuck and Diener, 2017). Crucially, Schorn *et al.* (2018) demonstrated that the buffering capacity of a lithology is not diminished or affected by melt loss until all focused melting reactions have gone to completion, as is the case here (see below). It is therefore not deemed necessary to consider stepwise of continuous prograde melt loss in the calculations.

Melt was reintegrated along an isobaric prograde path at 5.5 kbar, reflecting the average pressure corresponding to the prograde to thermal maximum at Hytkoras (see below). Sample NMC89 was chosen to represent the aluminous metapelites.

5.1.3 Selected magnesian gneisses

For the orthopyroxene-magnesian gneiss (sample NMC44) no melt-reintegration was deemed necessary since only low degrees of melting, without melt extraction, are assumed. The prograde evolution of this specimen is simulated using the 'residuum' composition and adding appropriate amounts of H_2O to saturate the solidus at 5.5 kbar.

In the other selected samples of magnesian gneiss (samples NMC88 and NMC90) no

indications for melting (i.e. macroscopic leucosomes or microscopic pseudomorphs after melt-filled pores) have been identified. Hence, melt-reintegration was omitted and a fluid-saturated subsolidus evolution is assumed. These samples display petrographic evidence for arrested equilibration (e.g. coronae-formation and symplectic intergrowths), and by definition the 'effective bulk composition' (Stüwe, 1997) at the moment of texture formation is not known. An approach based on equilibrium is therefore unsuitable to investigate the process(es) that led to pseudomorphic replacement. However, whole-rock compositions can be used to estimate the stability range of potential precursor phases before the textures developed into separate domains of local bulk composition. This information can be used to deduce the metamorphic evolution that the samples must have experienced before the precursor phases were obliterated by the process.

For this purpose the chemical system was further simplified to the six-component K_2O–FeO–MgO–Al_2O_3–SiO_2–H_2O (KFMASH)-model system by omitting MnO, Na_2O, CaO, TiO_2 and P_2O_5. In the case of the selected Mg–Al-rich gneisses the whole-rock composition naturally approximates the reduced system, because feldspars are absent and the rocks are poor in titanium-bearing oxides. Conversely, non-KFMASH components do not exceed ∼2 wt. % in these samples (Table 5.1). It is therefore argued that the stability fields of major rock-forming minerals and precursors to pseudomorphs can be satisfactorily reproduced.

The employed model compositions and resulting protolith compositions are listed in Table 5.2, and the calculated pseudosections, contoured for melt production, as well as isobaric modebox plots illustrating phase abundances along the prograde path are presented in Figure 5.3. Diagrams for selected magnesian gneisses are shown in Figure 5.4.

5.2 Modelling results

First, diagrams tailored for residuum compositions of regionally sampled aluminous metapelites are described. Secondly, pseudosections for residuum compositions of granulites collected at Hytkoras are discussed, followed by diagrams calculated for melt-reintegrated protolith compositions from this locality.

5.2.1 Residuum compositions – aluminous metapelites

Lepel se Kop and Nababeep

Diagrams for rocks from localities Lepel se Kop (sample NMC102 and NMC47; Fig. 5.1a, b) and Nababeep (sample NMC24; Fig. 5.1e) display a similar topology, with the residuum solidus at ∼750–800 °C. Garnet is present at pressures in excess of ∼4 kbar and coexists with cordierite at intermediate pressure and with sillimanite at intermediate to high pressure (Fig. 5.1a, b, e). Biotite is predicted at the low-temperature–high-pressure side of the diagrams (Fig. 5.1e). Samples from Lepel se Kop are modelled to bear spinel ± sillimanite at intermediate to low pressure and highest temperature considered (Fig. 5.1a, b),

whereas in the rock from Nababeep orthopyroxene is predicted to replace garnet and sillimanite at high-temperature–low-pressure conditions. Ilmenite is ubiquitous, whereas magnetite stability is confined to intermediate- to low pressure. The rocks are modelled to host two feldspars and quartz over the entire P–T range investigated. The inferred peak assemblage of garnet–biotite–cordierite–sillimanite–plagioclase–K-feldspar–quartz–ilmenite–magnetite–melt occupies a narrow field in P–T space, stable between 760–820 °C and 4.5–6.5 kbar. It is delineated by the residuum solidus at low temperature, the demise of biotite and cordierite towards lower and higher pressure and the exhaustion of magnetite towards higher temperature (Fig. 5.1a, b, e).

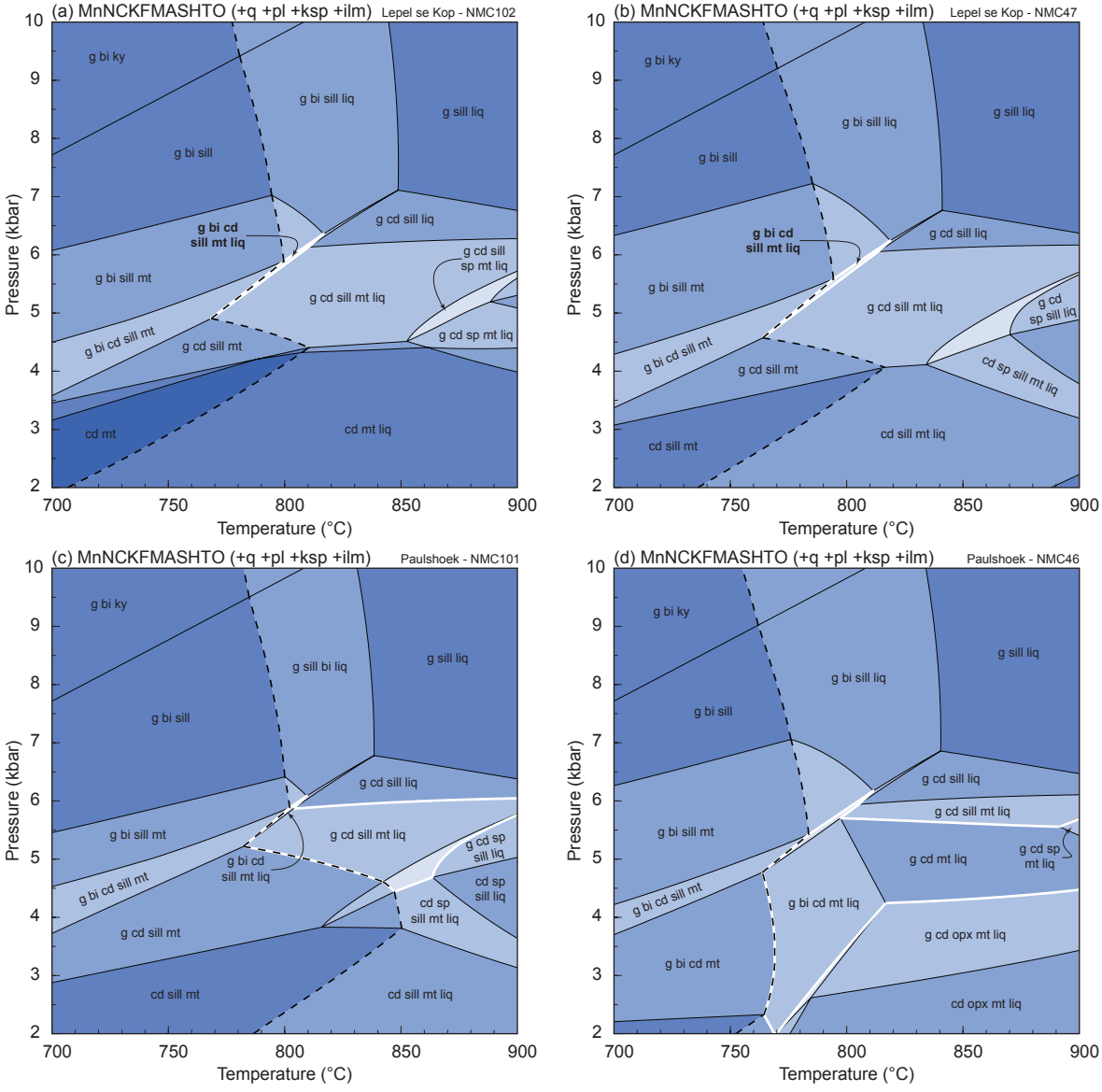


Figure 5.1

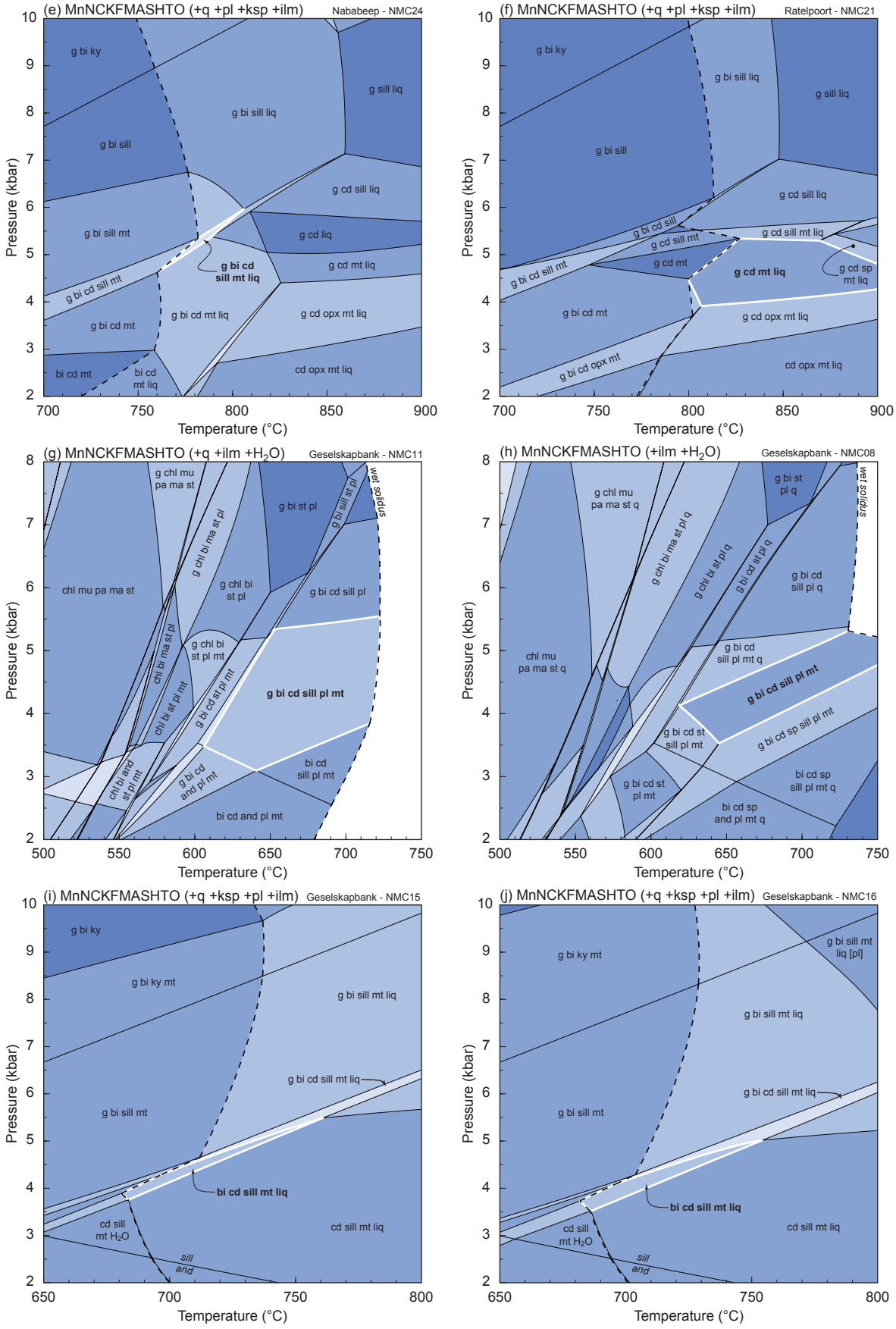


Figure 5.1: (continued)

Figure 5.1: Calculated pseudosections for residuum compositions of regionally sampled aluminous metapelites. Solidus is highlighted by bold dashed line. Inferred peak assemblage are in bold, respective fields are highlighted with bold white border.

Paulshoek

Phase equilibria diagrams for spinel-bearing specimens from this locality (sample NMC101 and NMC46; Fig. 5.1c, d) are comparable in topology, with an elevated residuum solidus calculated at ∼800–850 °C (sample NMC101; Fig. 5.1c) and ∼750–800 °C (sample NMC46; Fig. 5.1d). Garnet is predicted as ubiquitous phase, except for the lowest pressure investigated. It coexists with cordierite and sillimanite at intermediate pressure; cordierite is confined to pressure inferior to ∼6 kbar. Biotite is stable at the lower temperature side of the diagrams (Fig. 5.1d, e). Spinel is predicted to join the assemblage at intermediate pressure and highest temperature; it coexists with cordierite and sillimanite in sample NMC101 (Fig. 5.1c) and with cordierite and garnet in sample NMC46 (Fig. 5.1d). Importantly, biotite and spinel are mutually exclusive and are not predicted to coexist in the diagrams (Fig. 5.1c, d). In both samples ilmenite, two feldspars and quartz are calculated as ubiquitous phases over the full P–T range considered; magnetite is restricted to intermediate-to low pressure. The inferred peak assemblage of garnet–biotite–cordierite–spinel–plagioclase–K-feldspar–quartz–ilmenite–magnetite–melt (sample NMC46) and additional sillimanite (sample NMC101) is therefore not reproduced by the modelling (Fig. 5.1c, d). For sample NMC101, the assemblage of garnet–cordierite–sillimanite–plagioclase–K-feldspar–quartz–ilmenite–magnetite–melt spans from ∼800 °C to > 880 °C between ∼4.5–6 kbar, encompassing the stability of biotite and spinel at low- and high-T, respectively. The residuum solidus delimits the stability field towards low temperature and pressure whereas the loss of magnetite constrains the equilibration conditions towards high temperature and pressure (Fig. 5.1d). In sillimanite-absent sample NMC46, the area spanning from biotite- to spinel stability occupies a large field in P–T space ranging from ∼750 to > 900 °C and 2–6 kbar.

Ratelpoort

The phase diagram for sample NMC21 (Fig. 5.1f) displays the residuum solidus intersected at around 800 °C. Garnet is a main ferromagnesian phase stable at pressure exceeding ∼2–4 kbar, depending on temperature. Garnet is joined by cordierite at intermediate- to low pressure and by sillimanite at higher pressure, with all three coexisting over a narrow pressure range at intermediate conditions (Fig. 5.1f). Biotite is ubiquitous at lower temperature and higher pressure. Garnet coexists with spinel in a narrow field at highest temperature and medium pressure and is replaced by orthopyroxene and cordierite towards high–T-low–P. Ilmenite, two feldspars and quartz are ubiquitous whereas magnetite is present at intermediate- to low pressure. The inferred peak assemblage of garnet–cordierite–plagioclase–K-feldspar–quartz–

ilmenite–magnetite–melt is confined by the residuum solidus and the appearance of biotite at low temperature, whereas the respective introduction of sillimanite and orthopyroxene delimits the assemblage field towards higher and lower pressure. Spinel joins the assemblage at highest temperature considered. The preferred assemblage field tightly constraints pressure to 4–5.5 kbar, but allows only for a poor temperature constraint of ∼800 °C to > 900 °C (Fig. 5.1f).

Geselskapbank

Amphibolite facies gneisses are modelled to commence fluid-present melting at around 700 °C independently of pressure (sample NMC11; Fig. 5.1g) and at pressure exceeding ∼5 kbar (sample NMC08; Fig. 5.1h). Whereas sample NMC11 is modelled as silica-oversaturated (Fig. 5.1g), sample NMC08 is expected to become quartz-absent towards higher temperature and lower pressure (Fig. 5.1h). Garnet is modelled as ubiquitous phase at amphibolite facies conditions, but disappears at greenschist facies temperatures and at high-T–low-P conditions. Cordierite is expected at intermediate- to low pressure and temperature exceeding ∼550 °C. Aluminosilicate dominates at high-T–low-P, but is replaced by staurolite towards lower temperature. White micas are modelled at greenschist facies conditions, where muscovite takes the place of biotite and plagioclase is replaced by paragonite and margarite (Fig. 5.1g, h). Ilmenite is always present; magnetite stability is restricted to intermediate- to low pressure. The inferred peak assemblage of garnet–biotite–cordierite–sillimanite–plagioclase–ilmenite–magnetite ± quartz is confined by the wet solidus towards higher temperature and pressure and the introduction of staurolite towards low temperature in both samples (Fig. 5.1g, h). In sample NMC11 the demise of magnetite and garnet restricts the assemblage field towards higher and lower pressure, respectively, as well as the polymorphic transition of sillimanite to andalusite towards low-T–low-P. The field is stable over a rather large P–T range, spanning from ∼600–720 °C and 3–5.5 kbar (Fig. 5.1g). For sample NMC08, the respective appearance of quartz and spinel confine the field towards higher and lower pressure, stable between ∼620–750 °C and approximately 3.5–5 kbar. Diagrams for oxidised migmatites at Geselskapbank are characterised by few large high-variance assemblage fields separated by narrow low-variance fields (Fig. 5.1i, j). The residuum solidus is calculated at ∼680–730 °C, depending on pressure. Garnet is absent at conditions inferior to 3–6 kbar in function of temperature. Garnet coexists with cordierite over a narrow area at intermediate pressure and with biotite at intermediate to high pressure towards lower temperature. Aluminosilicate, two feldspars, ilmenite and quartz are modelled as stable throughout the P–T range investigated (Fig. 5.1i, j). The inferred peak assemblage biotite–cordierite–sillimanite–plagioclase–K-feldspar–quartz–ilmenite–magnetite–melt is delimited towards lower temperature by the residuum solidus and by the introduction of garnet and the demise of biotite towards higher and lower pressure, respectively. In both samples the narrow wedge-shaped peak assemblage fields are modelled as stable between ∼680–750 °C and 3.5–5.5 kbar (Fig. 5.1i, j).

5.2.2 Residuum compositions – Hytkoras

Aluminous metapelite

The topology of the diagrams for samples NMC89, NMC71 and NMC65 are fairly similar (Fig. 5.2a–c), with the residuum solidus occurring between ∼750–800 °C for samples NMC89 and NMC71 (Fig. 5.2a, b). The residuum solidus for sample NMC65 varies from < 700 °C in the absence of K-feldspar at higher pressure to about 780 °C at low pressure (Fig. 5.2c). Garnet is stable over the entire *P–T* range considered, except for low pressure conditions. Garnet always coexists with aluminosilicate, and with biotite at lower temperature and higher pressure. Spinel is predicted only at high temperature and low pressure for sample NMC89 (Fig. 5.2a). Orthopyroxene is modelled to be present exclusively at very low pressure and high temperature for sample NMC71 and NMC65 (Fig. 5.2b, c). Magnetite is ubiquitous but disappears at high pressure. Gedrite is predicted at low temperature and high pressure for sample NMC65 (Fig. 5.2c). The inferred peak mineral assemblage of garnet–biotite–cordierite–sillimanite–plagioclase–K-feldspar–quartz–ilmenite–magnetite–melt falls in a narrow *P–T* field between 750–850 °C and 5–7 kbar for aluminous metapelites (Fig. 5.2a–c). It is delimited towards lower temperature by the residuum solidus, and by the demise of biotite towards higher temperature and lower pressure. Cordierite and/or K-feldspar is removed towards higher pressure and lower temperature.

Magnesian metapelite

The pseudosection for sample NMC37 has the residuum solidus at more than 800 °C (Fig. 5.21d). Garnet coexists with aluminosilicate at high pressure and with cordierite at intermediate pressure before disappearing towards lower pressure. Biotite is ubiquitous except for very high temperature conditions. The coexistence of garnet, sillimanite, cordierite and biotite defines a narrow, roughly isobaric assemblage field spanning over the entire temperature range considered. Orthopyroxene is modelled to appear at low- to intermediate pressure. The stability of magnetite is confined to low pressure. The inferred peak assemblage of garnet–biotite–cordierite–orthopyroxene–K-feldspar–plagioclase–quartz–ilmenite–melt ± magnetite is calculated to occur at ∼830–880 °C and 4.5–6.5 kbar (Fig. 5.2d). The field is delimited by the residuum solidus and the introduction of magnetite towards lower temperature, whereas the demise of biotite bounds the field towards higher temperature. The removal of garnet and orthopyroxene respectively bounds the assemblage to lower and higher pressure. Modelled Al-in-orthopyroxene approximately overlaps with measured values (see section 4).

Semi-metapelite

The diagram for sample NMC67 is similar to the diagrams for the aluminous metapelites, but with the residuum solidus shifted towards slightly higher temperature (Fig. 5.2e). The inferred peak assemblage of garnet–cordierite–sillimanite–plagioclase–K-feldspar–quartz–ilmenite–magnetite–melt occupies a large field, from ∼800 to > 900 °C and 4–7 kbar. It is confined

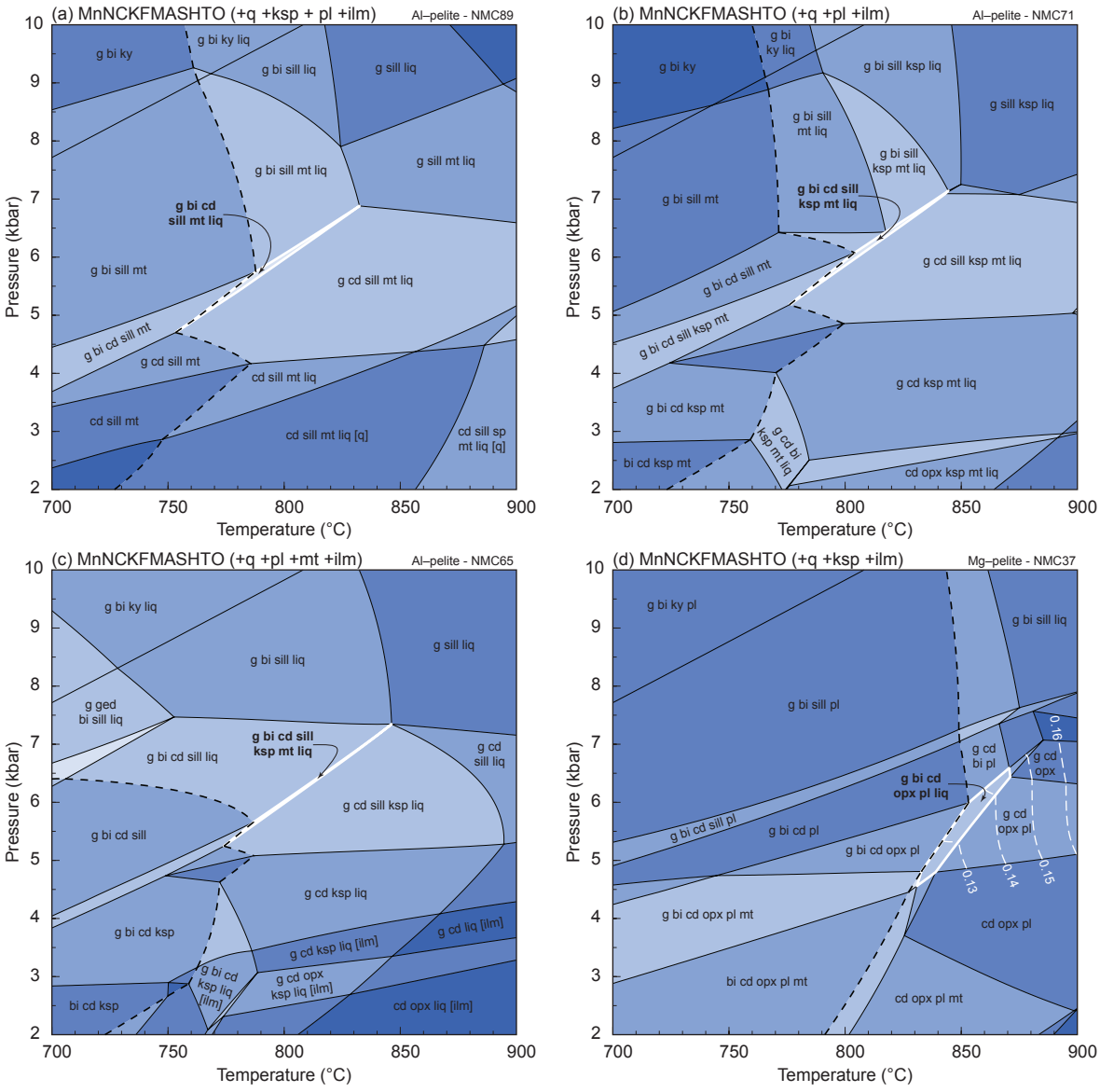

(a) MnNCKFMASHTO (+q +ksp + pl +ilm)
Al–pelite - NMC89
g bi ky
g bi ky liq
g bi sill liq
g sill liq
g bi sill mt liq
g sill mt liq
g bi cd sill mt liq
g bi sill mt
g cd sill mt liq
g bi cd sill mt
g cd sill mt
cd sill mt liq
cd sill mt
cd sill mt liq [q]
cd sill sp mt liq [q]
(b) MnNCKFMASHTO (+q +pl +ilm)
Al–pelite - NMC71
g bi ky
g bi ky liq
g bi sill ksp liq
g sill ksp liq
g bi sill mt liq
g bi sill ksp mt liq
g bi sill mt
g bi cd sill ksp mt liq
g cd sill ksp mt liq
g bi cd sill mt
g bi cd sill ksp mt
g cd ksp mt liq
g bi cd ksp mt
g cd bi ksp mt liq
bi cd ksp mt
cd opx ksp mt liq
(c) MnNCKFMASHTO (+q +pl +mt +ilm)
Al–pelite - NMC65
g bi ky liq
g bi sill liq
g sill liq
g ged bi sill liq
g bi cd sill liq
g bi cd sill ksp mt liq
g cd sill liq
g cd sill ksp liq
g bi cd sill
g cd ksp liq
g bi cd ksp
g cd ksp liq [ilm]
g cd liq [ilm]
g bi cd ksp liq [ilm]
g cd opx ksp liq [ilm]
bi cd ksp
cd opx liq [ilm]
(d) MnNCKFMASHTO (+q +ksp +ilm)
Mg–pelite - NMC37
g bi ky pl
g bi sill liq
g bi sill pl
g cd bi pl
g cd opx
g bi cd opx pl liq
g bi cd sill pl
g bi cd pl
g cd opx pl
g bi cd opx pl
g bi cd opx pl mt
cd opx pl
bi cd opx pl mt
cd opx pl mt
0.13
0.14
0.15
0.16
Pressure (kbar)
Temperature (°C)
2
3
4
5
6
7
8
9
10
700
750
800
850
900

Figure 5.2

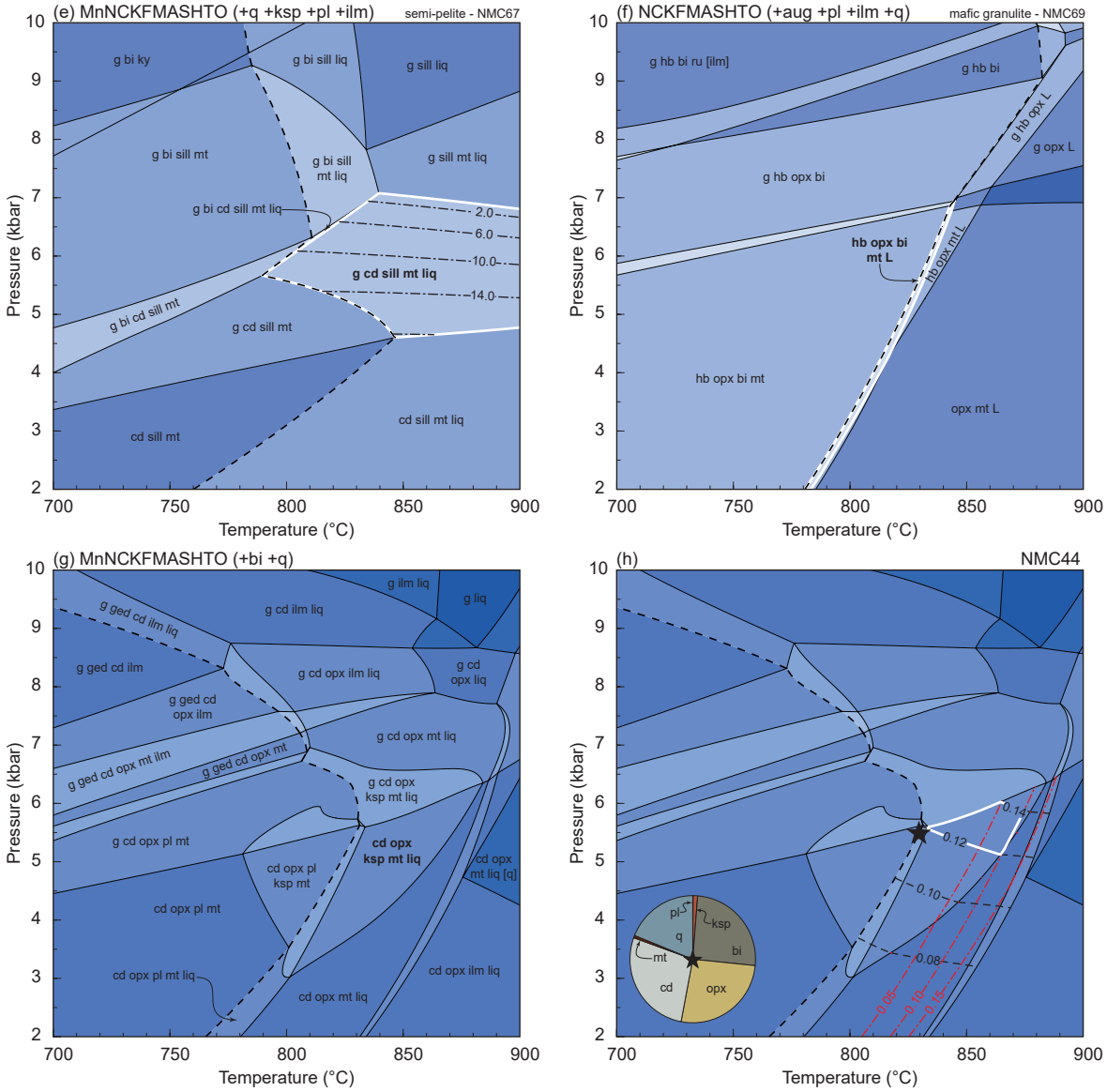


Figure 5.2: (continued) Calculated pressure–temperature phase equilibrium diagrams for residuum compositions. Solidus is highlighted by bold dashed line. Inferred peak assemblage are in bold, respective fields are highlighted with bold white border. (a–c) aluminous metapelites. (d) magnesian metapelite. White dashed lines are contours for Al-in-orthopyroxene (y_{opx}). (e) Semi-pelite. (f) Mafic granulite. (g, h) Magnesian gneiss. Red dot-dash lines on (h) are contours for melt mode (vol. %), black dashed lines are contours for Al-in-orthopyroxene (y_{opx}). Pie chart in (h) displays phase modes (vol. %) calculated at the residuum solidus and 5.5 kbar (black star): biotite ∼25 – cordierite ∼28 – orthopyroxene ∼27 – plagioclase ∼0.001 – K-feldspar ∼1 – quartz ∼19 – magnetite ∼0.005.

by the residuum solidus or introduction of biotite towards lower temperature, the demise of garnet towards lower pressure and removal of cordierite to higher pressure (Fig. 5.2e).

Mafic granulite

The pseudosection for sample NMC69 shows the residuum solidus between ∼800 and 870 °C, depending on pressure (Fig. 5.2f). Garnet is introduced at intermediate pressure and replaces orthopyroxene towards higher pressure. Hornblende and biotite are stable at subsolidus conditions and coexist with tonalitic melt over a narrow temperature range. Rutile replaces ilmenite at the highest pressure considered. Magnetite is confined to intermediate and low pressure (Fig. 5.2f). The inferred peak assemblage of hornblende–biotite–augite–orthopyroxene–plagioclase–quartz–ilmenite–magnetite–melt occurs in a narrow field between 780 and 840 °C below 7 kbar (Fig. 5.2f). This field is bound by the residuum solidus towards lower temperature, whereas the demise of biotite and hornblende delimits the field towards higher temperature. The introduction of garnet occurs towards higher pressure. Calculated Al-in-orthopyroxene values are consistently higher compared to those measured (∼0.03–0.04 *vs.* ∼0.01); these contours are therefore not overlain on the diagram. The reason for this mismatch is unclear, but it could be related to imperfect activity–composition formulations of complex phases, such as clinopyroxene and amphibole, having a knock-on effect on other phases such as orthopyroxene (Forshaw *et al.*, 2018).

Magnesian gneiss

The phase diagram for sample NMC44 is characterised by an elevated residuum solidus, spanning from ∼750 °C at lowest pressure and < 700 °C at highest pressure considered (Fig. 5.2g, h). At intermediate pressure the rock is modelled to be melt-bearing at a temperature in excess of ∼830 °C. Biotite is stable over the entire P–T range investigated. Quartz disappears towards high–T-low–P. Garnet replaces orthopyroxene towards high pressure. Two feldspars are expected to coexist in a narrow subsolidus field. Plagioclase is quickly exhausted at suprasolidus conditions, but minor amounts of K-feldspar (< 1 vol. %) persist up to a maximum of ∼880 °C at intermediate pressure. The calculated presence of feldspar is inconsistent with petrographic observations (see section 4). This is regarded as an artifact of the modelling since some feldspar-forming components, namely CaO and, in particular, Na_2O, are present in trace amounts in rock-forming cordierite and biotite, but not accounted for in the activity–composition formulations of White *et al.* (2014a). Whereas the employed bulk composition has been corrected for these components, modelling cannot perfectly reproduce the natural rock. Nonetheless, the calculations are deemed to satisfactorily replicate the inferred equilibrium assemblage – in particular because the predicted modes of main phases correspond to the observations within reason (see pie chart on Fig. 5.2h).

Inferred pseudomorphs after melt filled pores suggest the specimen experienced small degrees of partial melting (probably ≤10 vol. %), with melt unlikely to have been expelled.

Overall, the stability of the inferred peak assemblage of biotite–cordierite–orthopyroxene–K-feldspar–magnetite–quartz–melt is rather loosely constrained, spanning from the solidus at 830 °C to the demise of quartz at around 870 °C. The upper pressure limit is given by the introduction of garnet at ∼6 kbar, the demise of quartz suggests a minimum-pressure of ∼4 kbar, depending on temperature. The potential equilibration conditions may be further refined using measured Al–in–orthopyroxene (0.12–0.14) for pressure constrain and the residuum solidus and the 10 vol. % melt contour as lower- and upper thermal limit, respectively. Equilibrium conditions of ∼830–870 °C and 5–6 kbar are recorded by this sample (white area on Fig. 5.2h).

5.2.3 Protolith compositions – Hytkoras

Topologically the melt-reintegrated diagrams are similar to those for the residuum compositions (Fig. 5.2) and are presented in Figure 5.3. The diagrams have been modelled only for suprasolidus conditions, using the fluid content required to saturate the solidus at 5.5 kbar. At higher pressure the solidus is fluid-absent as the fluid content at this pressure does not suffice to saturate the assemblage above ∼6 kbar. Analogously, at lower temperature the assemblages require additional fluid for saturation, and have therefore not been calculated (Fig. 5.3). The diagrams have been contoured for melt production (vol. %, dashed lines); for each sample an isobaric modebox plot has been constructed to illustrate the phase modal rearrangements.

Aluminous metapelite

The protolith pseudosection for sample NMC89 shows the wet solidus at 670–700 °C for a pressure below ∼6 kbar (Fig. 5.3a). The first suprasolidus field is dominated by the upper-amphibolite facies assemblage garnet–biotite–sillimanite–muscovite, coexisting with plagioclase, ilmenite, quartz and minor amounts of melt. Contours for melt content are highly condensed in the narrow field at ∼700 °C that represents the introduction of K-feldspar and terminal breakdown of muscovite (Fig. 5.3a), corresponding to reaction 2.7 introduced in chapter 2. The modebox plot highlights the extensive phase reshuffling accompanying muscovite breakdown by reaction 2.7 (blue area on Fig. 5.3b). About 10 vol. % melt is modelled to be produced during this interval. A second such change occurs when ∼5 vol. % melt is produced by the consumption of biotite and sillimanite according to reaction 2.8 (see chapter 2) producing the inferred peak assemblage of garnet–biotite–cordierite–sillimanite–K-feldspar–plagioclase–ilmenite–magnetite–quartz–melt (Fig. 5.3a and red area on Fig. 5.3b; Waters, 1988). A total of ∼30 vol. % melt is modelled to be produced by the aluminous metapelite during its solidus-to-peak prograde evolution.

Magnesian metapelite

The protolith of sample NMC37 shows the wet solidus at ∼700 °C over the entire pressure range considered (Fig. 5.3c). Melt is first introduced to the amphibolite facies garnet–biotite–cordierite–sillimanite-bearing assemblage, which is notably muscovite-absent. Consequently, this sample does not undergo the muscovite breakdown reaction 2.7 and produces only negligible amounts of melt at lower granulite conditions below 750 °C (Fig. 5.3c, d). The rock is predicted to intersect reaction 2.8 between 750–800 °C, however, due to the metaluminous composition of this sample, sillimanite is quickly exhausted and only a small amount of melt is produced (red area on Fig. 5.3d). Between 800–850 °C, orthopyroxene is modelled to complete the inferred peak assemblage of garnet–biotite–cordierite–orthopyroxene–K-feldspar–plagioclase–ilmenite–quartz–melt ± magnetite. There, the reaction

$$\text{garnet} + \text{biotite} + \text{quartz} = \text{orthopyroxene} + \text{cordierite} + \text{K feldspar} + \text{melt} \tag{5.1}$$

(White *et al.*, 2001) advances at the expense of garnet and biotite, producing about 7 vol. % melt (purple area on Fig. 5.3d). A total of ∼20–25 vol. % melt is modelled to be produced during the prograde evolution.

Semi-metapelite

The protolith pseudosection of sample NMC67 is comparable to that of the aluminous metapelite (Fig. 5.3e). However, unlike the aluminous metapelite, K-feldspar is part of the amphibolite facies assemblages and sillimanite is absent. About ∼5 vol. % melt is produced by reaction 2.7 (blue area on Fig. 5.3f), whereas a further 3–4 vol. % is produced by reaction 2.8 (red area on Fig. 5.3f), with the intervening are dominated by continuous dehydration-melting of biotite. A total of 25–30 vol. % melt is calculated to be produced during the solidus-to-peak evolution of the semi-pelite.

Mafic granulite

The phase diagram for the melt-reintegrated protolith of sample NMC69 is characterised by a wet solidus intersected at lowest temperature at intermediate pressure (Fig. 5.3g). The solidus is displaced to higher temperature with decreasing and increasing pressure, respectively, from a minimum of ∼670 °C at 5.5 kbar (Fig. 5.3g). Melting commences in the epidote-amphibolite facies assemblage field of hornblende–epidote–biotite–augite–plagioclase–sphene–quartz. Despite having the wet solidus at comparably low temperatures, melt production is calculated to be negligible until orthopyroxene appears between 770 and 820 °C (cf. Stuck and Diener, 2017), marking the transition of melt-bearing amphibolite to granulite (Eskola, 1920; Palin *et al.*, 2016a). The introduction of orthopyroxene consumes large volumes of hornblende, biotite and quartz according to the multivariant reaction

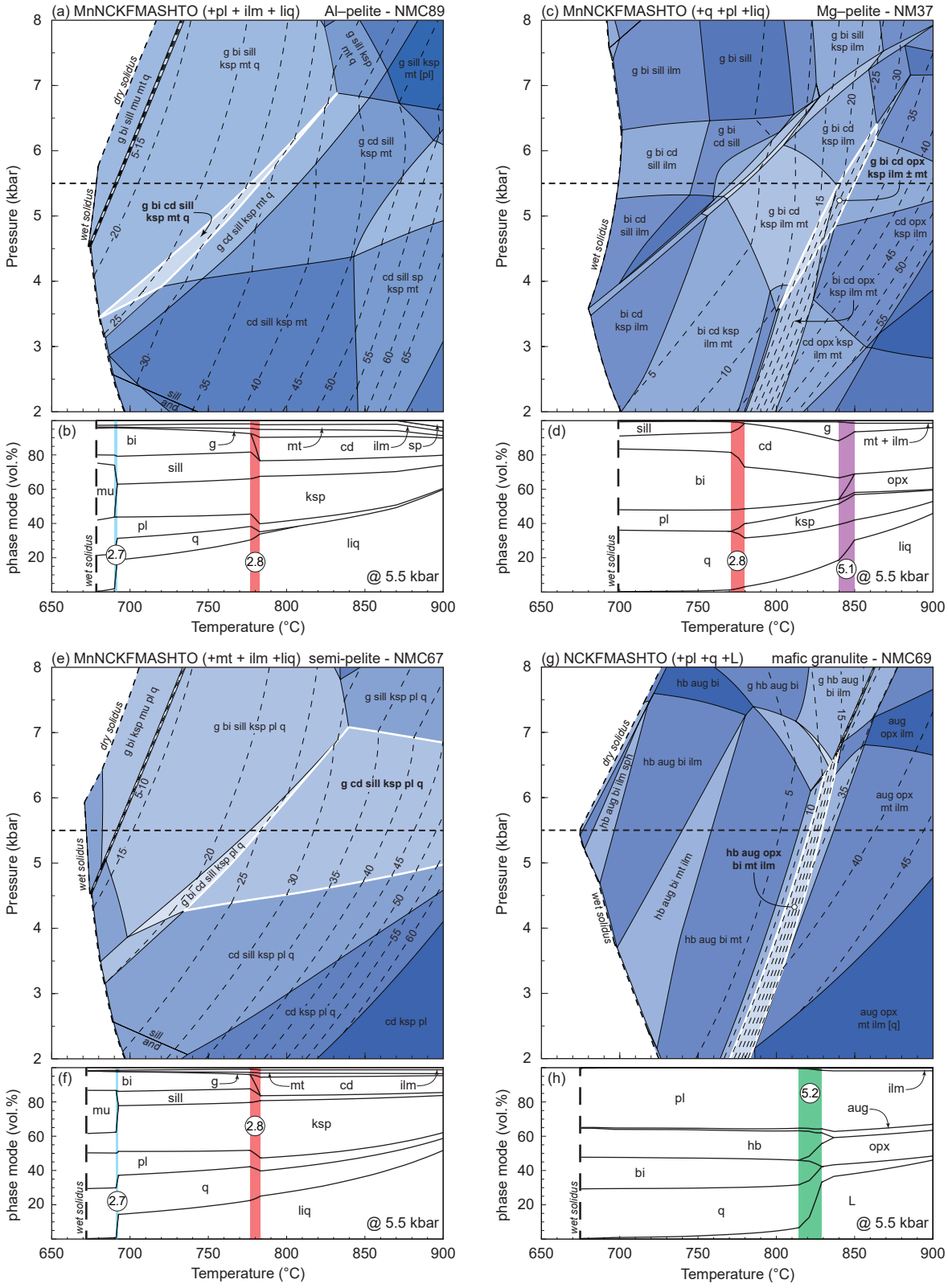

(a) MnNCKFMASHTO (+pl + ilm + liq)
Al–pelite - NMC89
(c) MnNCKFMASHTO (+q +pl +liq)
Mg–pelite - NM37
(e) MnNCKFMASHTO (+mt + ilm +liq) semi-pelite - NMC67
(g) NCKFMASHTO (+pl +q +L)
mafic granulite - NMC69
Pressure (kbar)
phase mode (vol.%)
Temperature (°C)
dry solidus
wet solidus
sill and
g bi sill ksp mt q
g bi sill mu mt q
g sill ksp mt q
g sill ksp mt [pl]
g cd sill ksp mt
g bi cd sill ksp mt q
g cd sill ksp mt q
cd sill sp ksp mt
cd sill ksp mt
g bi sill ksp pl q
g bi ksp mu pl q
g sill ksp pl q
g cd sill ksp pl q
g bi cd sill ksp pl q
cd sill ksp pl q
cd ksp pl q
cd ksp pl
g bi sill ilm
g bi sill
g bi sill ksp ilm
g bi cd sill ilm
g bi cd sill
g bi cd ksp ilm
g bi cd opx ksp ilm ± mt
bi cd sill ilm
g bi cd ksp ilm mt
cd opx ksp ilm
bi cd opx ksp ilm mt
bi cd ksp ilm
bi cd ksp ilm mt
cd opx ksp ilm mt
hb aug bi
g hb aug bi
g hb aug bi ilm
aug opx ilm
hb aug bi ilm
hb aug bi ilm spl
aug opx mt ilm
hb aug opx bi mt ilm
hb aug bi mt ilm
hb aug bi mt
aug opx mt ilm [q]
(b)
(d)
(f)
(h)
bi
g
mt
cd
ilm
sp
sill
mu
pl
q
ksp
liq
mt + ilm
opx
hb
aug
L
2.7
2.8
5.1
5.2
@ 5.5 kbar

Figure 5.3

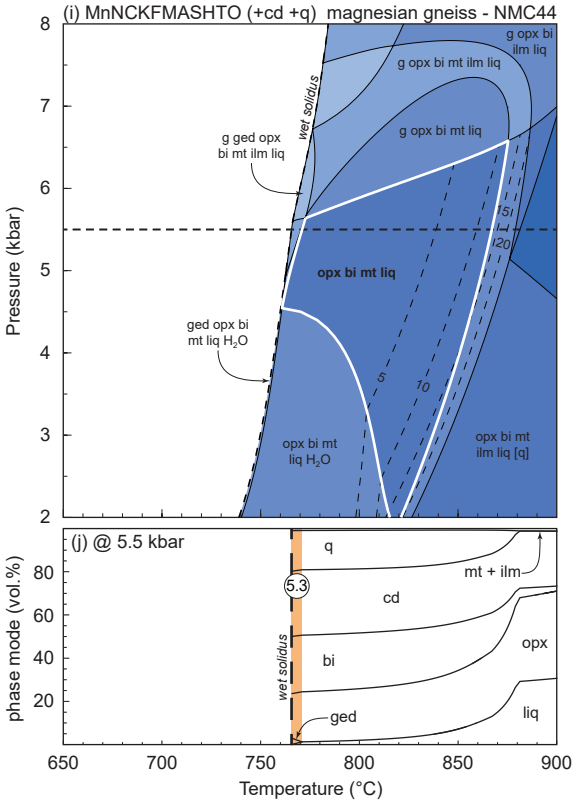


Figure 5.3: (continued) Calculated pressure–temperature pseudosection for melt-reintegrated bulk compositions and isobaric modebox plots drawn for 5.5 kbar (along thick dashed line). The coloured areas in the modeboxes highlight the loci of major melting reactions (see text). (a, b) Aluminous metapelite (sample NMC89). (c, d) Magnesian metapelite (sample NMC37). (e, f) Semi-pelite (sample NMC67). (g, h) Mafic granulite (sample NMC69). (i, j) Orthopyroxene-magnesian gneiss (sample NMC44).

$$\text{hornblende} + \text{biotite} + \text{quartz} = \text{augite} + \text{orthopyroxene} + \text{plagioclase} + \text{melt} \qquad (5.2)$$

that produces between 15–30 vol. % tonalitic melt in the narrow peak assemblage field of hornblende–augite–orthopyroxene–biotite–plagioclase–magnetite–ilmenite–quartz–melt (Fig. 5.3g and green area on Fig. 5.3h).

Magnesian gneiss

For the orthopyroxene-magnesian gneiss (sample NMC44), no melt-reintegration was applied as melt is assumed to not have been expelled in the first place. Only H_2O was added to the bulk composition in order to stabilise the wet solidus at 5.5 kbar. The resulting phase diagram (Fig. 5.3i) is topologically similar to the 'residuum' case (Fig. 5.2g, h), with an elevated wet solidus calculated at around 750–800 °C.

Melt first appears in the upper-amphibolite facies assemblage field of gedrite–orthopyroxene–biotite–cordierite–magnetite–ilmenite–quartz. There, the rock is predicted to be dominated by cordierite, biotite and quartz with minor gedrite and orthopyroxene (Fig. 5.3j). Feldspars are not predicted for this bulk composition, consistent with the feldspar-free thin section assemblage. Gedrite is expected to quickly break down at suprasolidus conditions according to the generalised reaction

$$\text{gedrite} + \text{biotite} + \text{quartz} = \text{orthopyroxene} + \text{cordierite} + \text{melt} \qquad (5.3)$$

that produces small amounts of melt and orthopyroxene (orange field on Fig. 5.3i and j). The exhaustion of gedrite stabilises the inferred peak assemblage of orthopyroxene–biotite–cordierite–magnetite–quartz–melt, occupying a stability range comparable to the 'residuum' case (Fig. 5.2g, h). Between 5–10 vol. % melt is expected to be generated up to this field. Following the demise of orthoamphibole, melting is gradual and continuous at the expense of biotite and quartz. The exhaustion of quartz at about 870 °C leads to a notable decrease in melt production, at which point the rock is modelled to have produced some 25–30 vol. % granitic melt.

5.2.4 Simplified magnesian gneiss compositions

The diagrams constructed in the reduced pelitic system are characterised by low-variance fields and the stability of several univariant reactions located at the conjunction of divariant fields (white fields on Fig. 5.4a–c). Biotite is ubiquitous except for sample NMC88 (Fig. 5.4b) where it is introduced at the upper thermal limit of the greenschist facies. Chlorite dominates the assemblages at greenschist facies conditions together with minor muscovite (Fig. 5.4a–c). Orthopyroxene-magnesian gneiss (sample NMC44, Fig. 5.4a) is modelled to be quartz bearing over the entire P–T range considered, whereas in the sapphirine–spinel- and spinel–cordierite

gneiss (sample NMC88, Fig. 5.4b and sample NMC90, Fig. 5.4c, respectively) quartz is present only at low grade conditions. Cordierite is introduced in all three cases at the greenschist- to amphibolite facies transition between 550–650 °C, depending on pressure.

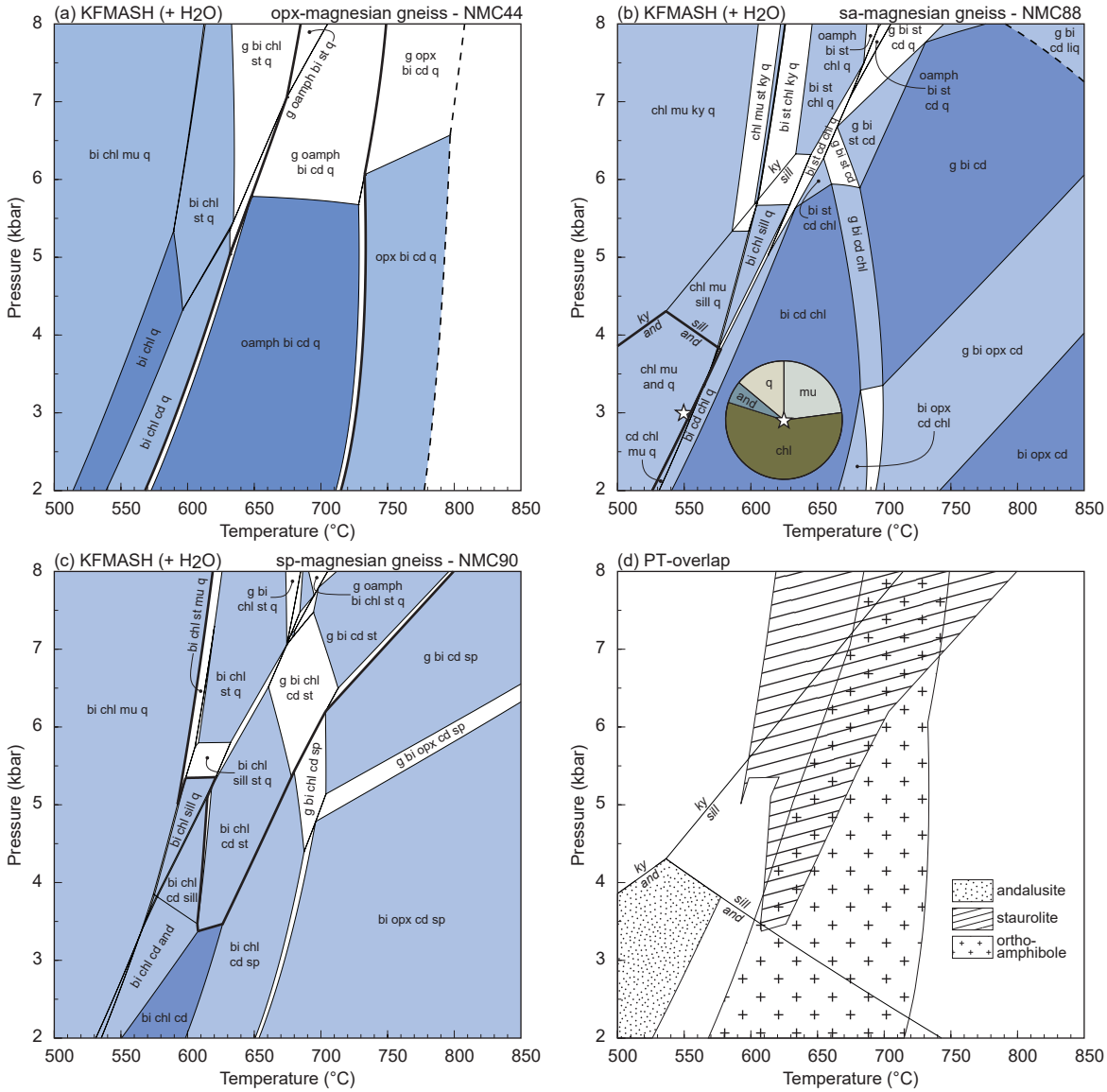


Figure 5.4: Calculated phase equilibria diagrams for selected magnesian gneisses in simplified model system (a–c). Pie chart in (b) displays phase modes calculated at 550 °C and 3 kbar (star). The stability range of inferred precursor phases (see text) is highlighted by bold lines and summarised in (d). Thick dashed line is the wet solidus.

Orthopyroxene-magnesian gneiss (sample NMC44) shows a near-isothermal wet solidus at ∼780 °C (Fig. 5.4a), at similar conditions as calculated for the full MnNCKFMASHTO-model system (cf. Fig. 5.3). Garnet is introduced above a pressure of about 6 kbar and ∼600 °C. Staurolite is stable in a narrow, wedge-shaped area between 600–700 °C and a pressure exceeding ∼5 kbar. Orthoamphibole is introduced at the expense of chlorite at the

boundary between the greenschist- and amphibolite facies and replaced by orthopyroxene at upper amphibolite facies conditions (Fig. 5.4a, d), in contrast to the full-system case where gedrite persists up to and beyond the wet solidus (Fig. 5.3).

The simplified diagram for the nodular sapphirine–spinel magnesian gneiss (sample NMC88) commences melting at the highest P–T conditions considered (Fig. 5.4b). Garnet is introduced between 650–700 °C, but is replaced by orthopyroxene towards lower pressure at high temperature. Staurolite displays a stability range comparable to sample NMC44 (Fig. 5.4a). Chlorite persists to upper amphibolite facies temperature. Aluminosilicate characterise the assemblages at greenschist facies conditions. Andalusite is expected to be present at the lowest conditions considered and disappears towards higher temperature between 550–600 °C (Fig. 5.4d). At these conditions the rock is dominated by chlorite (∼57 vol. %) and muscovite (∼23 vol. %) whereas andalusite is present with ∼6 vol. %. Quartz makes up about 14 vol. % of the rock matrix at the envisaged conditions (see pie chart on Fig. 5.3b). Muscovite is replaced by biotite and cordierite according to the univariant reaction

$$\text{chlorite} + \text{andalusite} + \text{muscovite} + \text{quartz} = \text{biotite} + \text{cordierite} + \text{H}_2\text{O} \qquad (5.4)$$

advancing at about 550 °C. Briefly after reaction 5.4 is completed, both andalusite and quartz are exhausted (Fig. 5.4a).

The diagram for nodular spinel–corundum Mg–Al gneiss sample NMC90 remains subsolidus throughout the entire P–T range investigated (Fig. 5.4c). Garnet is expected to be introduced at conditions exceeding ∼650 °C and 5 kbar; it is however replaced together with chlorite by orthopyroxene towards lower pressure. Spinel is modelled to join the assemblages at ∼600 °C at the lowest pressure considered and replaces staurolite with increasing temperature and pressure. Staurolite stability covers a wide, wedge-shape area roughly spanning amphibolite facies conditions starting at about 4 kbar (Fig. 5.4d). Figure 5.4d summarises the stability fields of precursors to pseudomorphs (orthoamphibole, andalusite and staurolite) in P–T space. Whereas fields of staurolite and orthoamphibole partly overlap within the stability range of sillimanite, andalusite is stable only at lower greenschist conditions.

Chapter 6

Zircon and Monazite geochronology and geochemistry

At least one sample of supracrustal rock per sampling locality was processed for geochronological and geochemical analysis.

6.1 Zircon and monazite morphology and petrography

Representative cathodoluminescence (CL) images of zircons from each sampling locality are presented on Figure 6.1. Backscattered-electron (BSE) images of representative monazites are portrayed on Figure 6.2. Textural description of zircon grains is based on CL imagery and abbreviated as follows: *C*–core, *R*–rim, *S*–sector zoned grain, *O*–oscillatory zoned grain. *h* and *l* indicated high and low CL response, respectively.

1. **Lepel se Kop:** Zircons from aluminous metapelite sample NMC47 are small (∼100 μm), spherical to ovoidal and of a clear pinkish colour. More than 80 grains were picked. CL imagery reveals a single population of zircon topology attributed to a single growth event. Observed CL-textures are consistent with neocrystallisation from anatectic melt during cooling from high-grade conditions, such as 'soccer-ball' or sector zoning patterns (Fig. 6.1a; e.g. Taylor *et al.*, 2016; Mitchell *et al.*, 2018, and references therein). Some grains display convoluted zoning patterns that have low CL response or appear largely unzoned. Grains showing clear oscillatory zoning characteristic of magmatic zircon are not observed.

   Monazites are of variable size (∼100–500 μm) and shape, ranging from elongated shards to sub-spherical grains. Monazites are clear with a strong yellow colour. About ∼40 grains were found. BSE imaging shows that most grains are unzoned to faintly zoned, with a convoluted zoning pattern (Fig. 6.2a; cf. Taylor *et al.*, 2016). Some grains display a thin rim of BSE-bright material. Monazites host rare inclusions of fine-grained sillimanite throughout the grain (Fig. 6.2a).

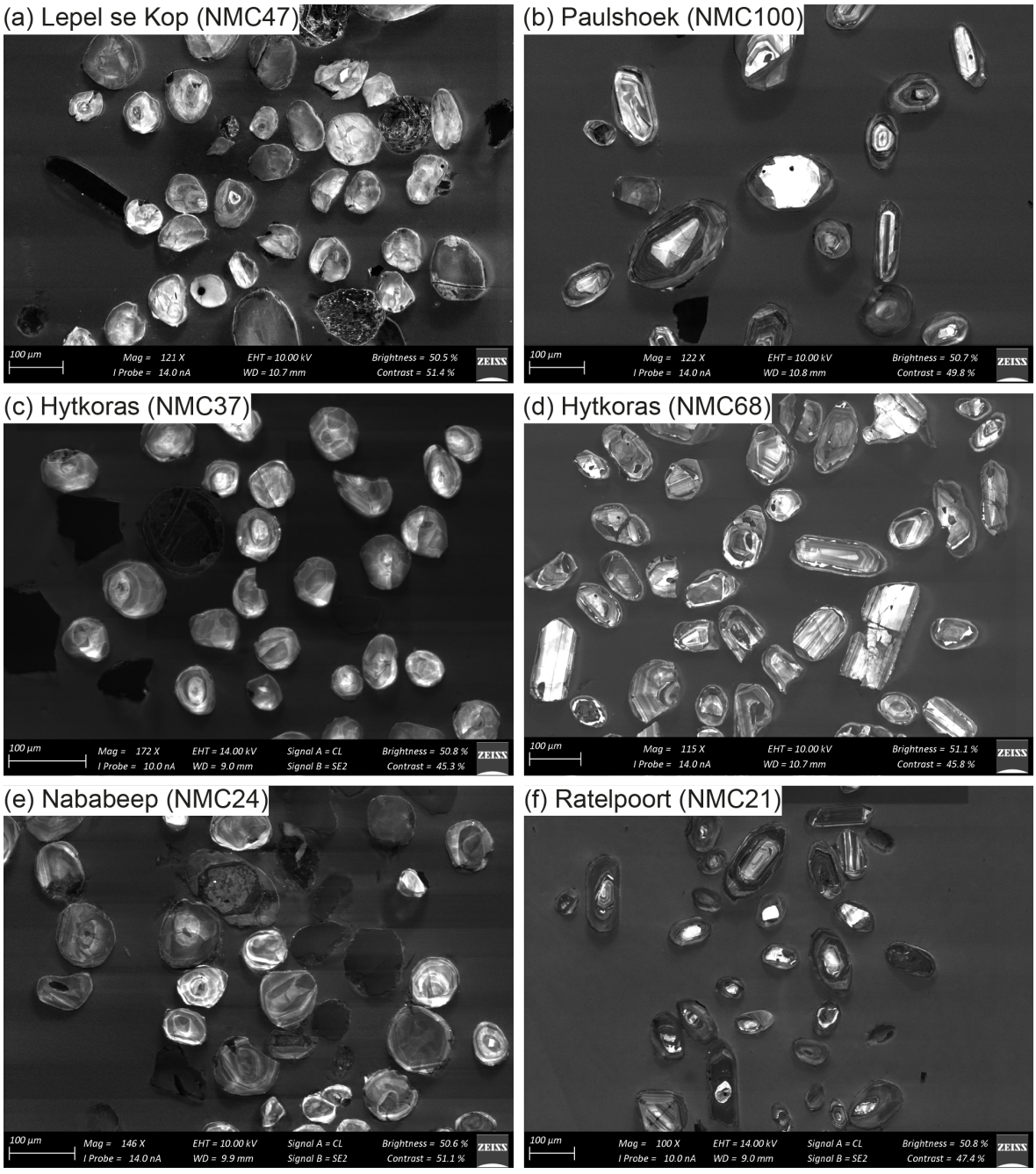

(a) Lepel se Kop (NMC47)
100 µm
Mag = 121 X
I Probe = 14.0 nA
EHT = 10.00 kV
WD = 10.7 mm
Brightness = 50.5 %
Contrast = 51.4 %
ZEISS
(b) Paulshoek (NMC100)
100 µm
Mag = 122 X
I Probe = 14.0 nA
EHT = 10.00 kV
WD = 10.8 mm
Brightness = 50.7 %
Contrast = 49.8 %
ZEISS
(c) Hytkoras (NMC37)
100 µm
Mag = 172 X
I Probe = 10.0 nA
EHT = 14.00 kV
WD = 9.0 mm
Signal A = CL
Signal B = SE2
Brightness = 50.8 %
Contrast = 45.3 %
ZEISS
(d) Hytkoras (NMC68)
100 µm
Mag = 115 X
I Probe = 14.0 nA
EHT = 10.00 kV
WD = 10.7 mm
Brightness = 51.1 %
Contrast = 45.8 %
ZEISS
(e) Nababeep (NMC24)
100 µm
Mag = 146 X
I Probe = 14.0 nA
EHT = 10.00 kV
WD = 9.9 mm
Signal A = CL
Signal B = SE2
Brightness = 50.6 %
Contrast = 51.1 %
ZEISS
(f) Ratelpoort (NMC21)
100 µm
Mag = 100 X
I Probe = 10.0 nA
EHT = 14.00 kV
WD = 9.0 mm
Signal A = CL
Signal B = SE2
Brightness = 50.8 %
Contrast = 47.4 %
ZEISS

Figure 6.1

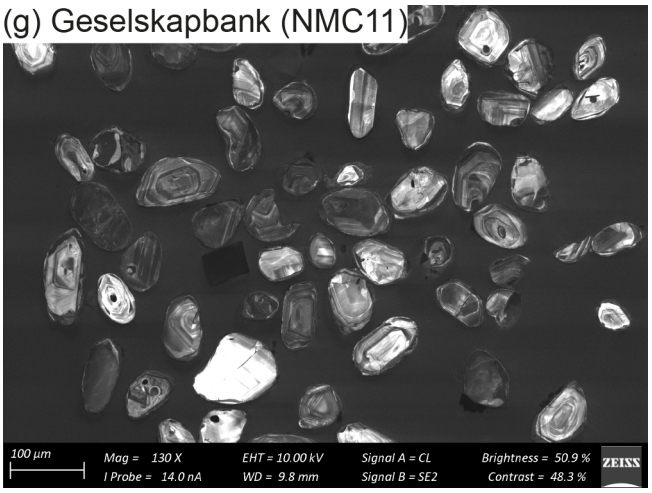


Figure 6.1: (continued) Cathodoluminesce images for zircons.

2. **Paulshoek:** Zircons from metapelite sample NMC100 (petrographically equivalent to NMC101 described in section 4) are grouped into two populations, one of stubby to elongated grains with rounded edges (∼100–150 μm in size) and a second – less abundant – population of small (<100 μm) rounded grains. Zircons are transparent and of a light-brown colour under in transmitted light. Over 160 grains were picked. Most cores of stubby to elongated grains are recognised as fragments of larger grains, as suggested by interrupted CL-zoning patterns, overgrown by a hypidioblastic rim showing weak CL-response (Fig. 6.1b). Cores commonly have a bright CL-response and show a more or less well developed oscillatory zoning pattern (Fig. 6.1b), attributed to magmatic crystallisation from a silicic melt. This population is interpreted to be of detrital origin. Some grains display a dark CL-response and a convoluted zoning pattern over the entire grain. Rounded grains displaying sector zoning and dark but homogeneous CL-response are devoid of CL-bright cores, suggesting they grew directly from anatectic melts during high-grade metamorphism (Fig. 6.1b; Taylor *et al.*, 2016).

   Monazites from this sample (∼50 grains) are of a clear yellow colour, mostly rounded and variable in size (<100 μm up to ∼500 μm). BSE images reveal that most grains display a patchy, roughly concentric or convoluted zoning pattern, with a small number of grains showing no zoning at all (Fig. 6.2b). A thin BSE-bright rim is observed on some grains.

3. **Hytkoras:** Zircons and monazites from magnesian metapelite (sample NMC37) and metagreywacke (NMC68) are separated for analysis. Zircons from sample NMC37 are small (<100 μm), rounded to ovoidal and transparent, with a faint pinkish colour. About 150 zircons were hand-picked. CL imagery suggests a single population of zircons displaying well-developed sector zoning indicative for crystallisation from anatectic melt following high-grade metamorphism (Fig. 6.1c; e.g. Taylor *et al.*, 2016). No monazite

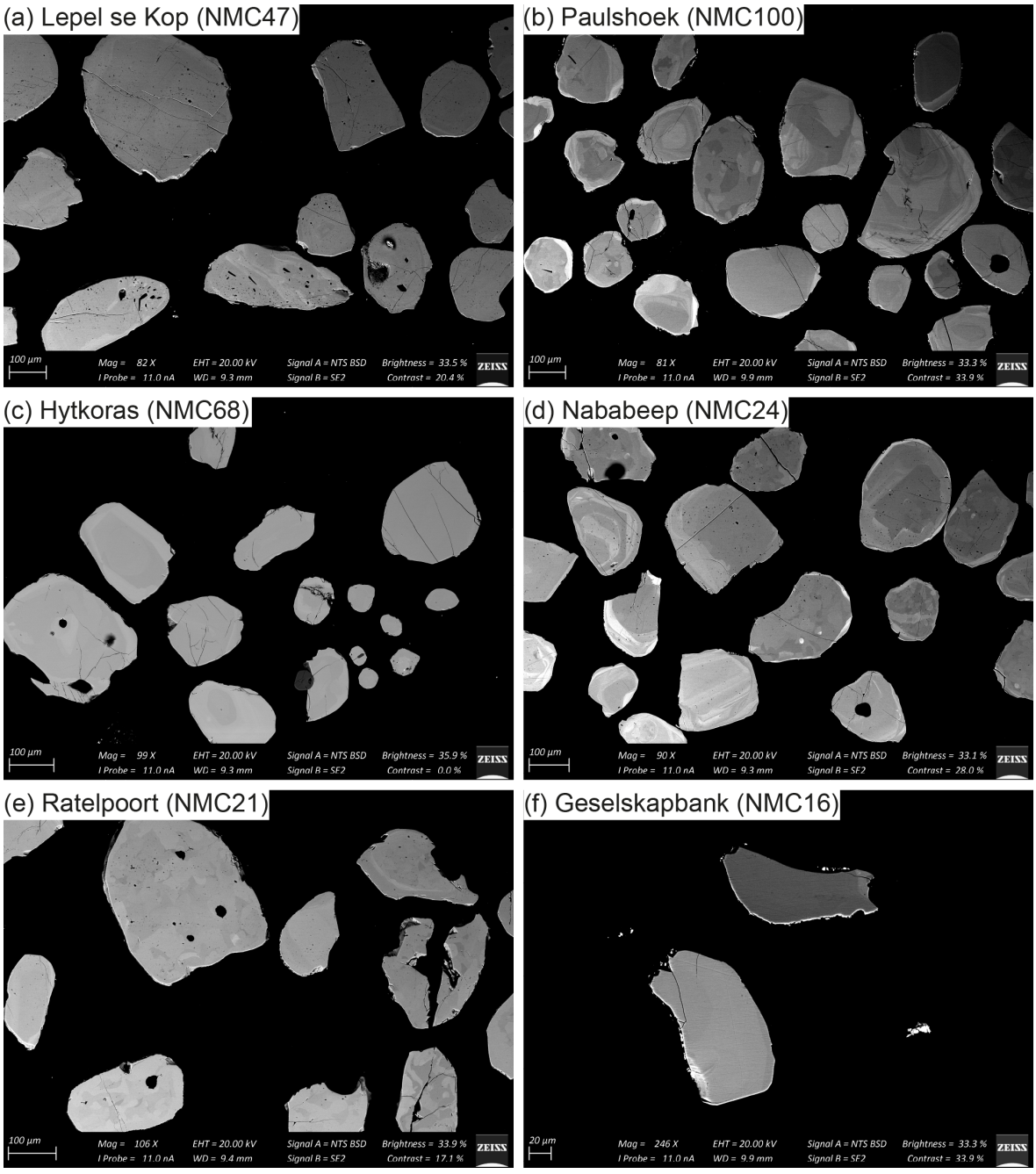


Figure 6.2: Backscattered-electron images for monazites.

was found in this specimen.

Zircon grains from metagreywacke NMC68 are stubby to elongated and of a clear, tan- to pinkish colour. More than 160 grains were separated. CL images reveal complex zoning patterns with variable CL response. Most grains display xenoblastic and broken cores showing oscillatory zoning that are commonly healed and overgrown by hypidioblastic rims having weak CL-response (Fig. 6.1d). Core-rim relations suggest a population of magmatic cores and one metamorphic rim growth event.

Fifteen monazites were separated. Grains display a roughly bimodal size-distribution, with large rounded grains (∼300 μm) and small drop-shaped grains (<50 μm). Grains are transparent and of yellow colour. BSE-images show a weak zoning pattern that is mostly concentric (Fig. 6.2c).

4. **Nababeep:** Aluminous metapelite sample NMC24 yielded small (∼100 μm), rounded to ovoidal grains of light pinkish colour (∼120 grains). In CL zircon grains display predominantly soccer-ball textures with variable CL-response (Fig. 6.1e). These grains are though to have directly crystallised from melts at granulite facies conditions. Rare elongated, hypidiomorphic grains show bright angular cores, overgrown by sector-zoned rims having dark CL-response. The cores are inferred to be of magmatic origin whereas the rims are attributed to a single anatectic event.

   Monazites from this sample (∼40 grains) are large and homogeneous in size (∼-200–300 μm) and rounded to angular in shape. In transmitted light grains have a bright yellow colour. BSE images show roughly concentric zoning that is in part convoluted (Fig. 6.2d).

5. **Ratelpoort:** Zircons recovered from aluminous metapelite sample NMC21 occur in two populations (∼180 grains). Hypidioblastic, large (∼200–300 μm) grains with high aspect ratio and rounded edges display oscillatory zoning and CL-bright cores surrounded by CL-dark rims (Fig. 6.1f). This population of grains is interpreted as detrital, originally magmatic zircon overgrown during a single high-grade metamorphic event. Rounded grains are smaller (<100 μm) and display weak concentric- to sector zoning (Fig. 6.1f); these grains are inferred to be have newly crystallised from anatectic melt during metamorphism.

   Monazites from sample NMC21 are large (∼300 μm) and of clear yellow colouring. Grains are rounded or occur as broken shards, characterised by a weak patchy to convoluted zoning pattern (Fig. 6.2e).

6. **Geselskapbank:** Amphibolite facies metapelite NMC11 yielded more than 150 small (<100 μm) stubby to rounded grains showing rounded edges. Zircons from this specimen are transparent and of faint-pink in colour. CL images reveal grains of variable CL-response and commonly displaying a well developed concentric oscillatory zoning pattern (Fig. 6.1g). Most cores are surrounded by an unzoned rim with mostly low,

and rarely high CL-response. The grains are interpreted as detrital magmatic zircons; the thin outer rim might have formed during minor fluid-assisted recrystallisation (e.g. Taylor *et al.*, 2016). Metamorphic 'soccer ball' zircons and monazite were not found in this specimen.

Migmatite sample NMC16 (equivalent to sample NMC15 described above) did not yield any zircon and only two shards of yellow monazite were recovered. The grains are small (∼100 μm) and elongated. BSE images show that monazite is not chemically zones, except for a thin BSE-bright rim (Fig. 6.2f).

6.2 U–Pb geochronology – results

The term 'discordance' refers to $^{207}Pb/^{206}Pb$ dates and is calculated as follows:

$$^{207}Pb/^{206}Pb \text{ discordance} = 100 \frac{^{207}Pb/^{206}Pb \text{ age} - ^{238}U/^{206}Pb \text{ age}}{^{207}Pb/^{206}Pb \text{ age}} \quad (6.1)$$

$^{238}U/^{206}Pb$ discordance for each analysis is calculated similarly and reported in appendix D together with full U–Pb isotopic and REE data for each sample including a brief description. Zircon analyses qualification follows recommendations of Spencer *et al.* (2016). These are:

- **D:** outside the discordance threshold. These analyses are interpreted to have experienced radiogenic Pb mobility
- **P:** concordant within the discordance threshold but interpreted to have experienced radiogenic-Pb loss (i.e. partial resetting)
- **M:** metamorphic grain (here inferred from CL texture)
- **S:** detrital grain (here referring to oscillatory zoned grains separated from metasedimentary samples)
- **Y:** youngest detrital analyses
- **I:** denotes age at igneous crystallisation
- **X:** inherited magmatic grain

Results of U–Pb geochronology are summarised in Table 6.1.

6.2.1 Lepel se Kop

Data of 29 out of 31 ablations on sector zoned zircons (classified as type M) from aluminous metapelite (sample NMC24) yield ages within the acceptable range of ±10% discordance and are graphically represented on Figure 6.3a–c. Error ellipses plot slightly negatively off Concordia, interpreted as the result of poor matrix match between ablation standards

and unknowns ('matrix effect'). Due to this caveat, only $^{207}Pb/^{206}Pb$ ages are regarded as geologically meaningful (N. Evans, pers. comm). Therefore, data for zircons from this sample are treated with caution. Data points plot roughly in two clusters, with the densest cluster yielding a poorly constrained weighted mean $^{207}Pb/^{206}Pb$ age of 1016.8 ± 6.9 Ma (MSWD=2.2, n=23; green ellipses and error bars on Fig. 6.3a). A second cluster plots over an age interval of *c.* 1120–1070 Ma. These analyses are interpreted to have incorporated common Pb and are excluded from age calculation. All data points are summarised on a probability density function (PDF) plot (Fig. 6.3b), showing a distinct peak at *c.* 1020 Ma. This date is interpreted to roughly reflect the age of granulite facies metamorphism for this sample. In terms of rare earth element (REE) trends both clusters lack a pronounced positive Ce-anomaly and are characterised by a distinct negative Eu-anomaly but show a wide scatter in heavy REE concentration (colour of lines in Fig. 6.3c corresponds to error ellipses in a).

U–Pb data for 57 out of 60 monazite ablations are plotted on Figure 6.3d. One analysis yield a discordant result that plots off Concordia and outside the main data cluster. This ablation is regarded as affected by Pb loss and not regarded further. All meaningful data in sum yield a weighted mean $^{238}U/^{206}Pb$ age of 1045.2 ± 3.7 Ma (MSWD=1.3, n=57; Fig. 6.3e). This age population is thought to record cooling from high garde conditions in this sample, yielding a minimum age for metamorphism. The observed age scatter is unrelated to core or rim ablation. Monazites display a similar compositional trend, with chondrite-normalised REE data of cores overlapping with rim. All analyses show a distinct negative Eu-anomaly (Fig. 6.3f) and describe a compositional trend that is opposite to that of coexisting zircons (Fig. 6.3c), with a strong enrichment and depletion in light and heavy REE, respectively.

6.2.2 Paulshoek

Seventy-eight out of a total of 107 zircon data are within ±10% discordance and regarded as geologically meaningful (Fig. 6.4a–c). Two concordant sector zoned grains (classified as type M) yield a Concordia age of 1043 ± 11 Ma (mean square standard deviation MSWD=0.77, probability p=0.46; Fig. 6.4a). This date is interpreted to reflect the age of granulite facies metamorphism for this sample. Highly concordant (within ±5% discordance) oscillatory zoned grains (all classified as group S) yield ages that range over a wide interval, bracketed by two data points concordant within individual uncertainty; the oldest detrital grain yields a $^{207}Pb/^{206}Pb$ age of 1861.1 ± 28 Ma, whereas the youngest detritus has a calculated $^{238}U/^{206}Pb$ age of 1100.5 ± 10 Ma (Fig. 6.4a). Several detrital age groups are recognised from a probability density function (PDF) plot for 51 oscillatory zoned grains (between ±1–5% discordant), with $^{207}Pb/^{206}Pb$ age peaks between *c.* 1800–1700 Ma and 1400–1300 Ma (Fig. 6.4c). Twenty-five analyses of oscillatory zoned S-type zircons are between ±5–10% discordant and are inferred to have experienced lead loss due to partial resetting during an earlier thermal event (classified as type P); they lie along a discordia line with an upper and lower intercept of 1819 ± 38 and 1090 ± 30 Ma (MSWD=1.5), respectively. Upper- and lower intercept roughly overlap with ages of the oldest detritus and sector zoned (M-type)

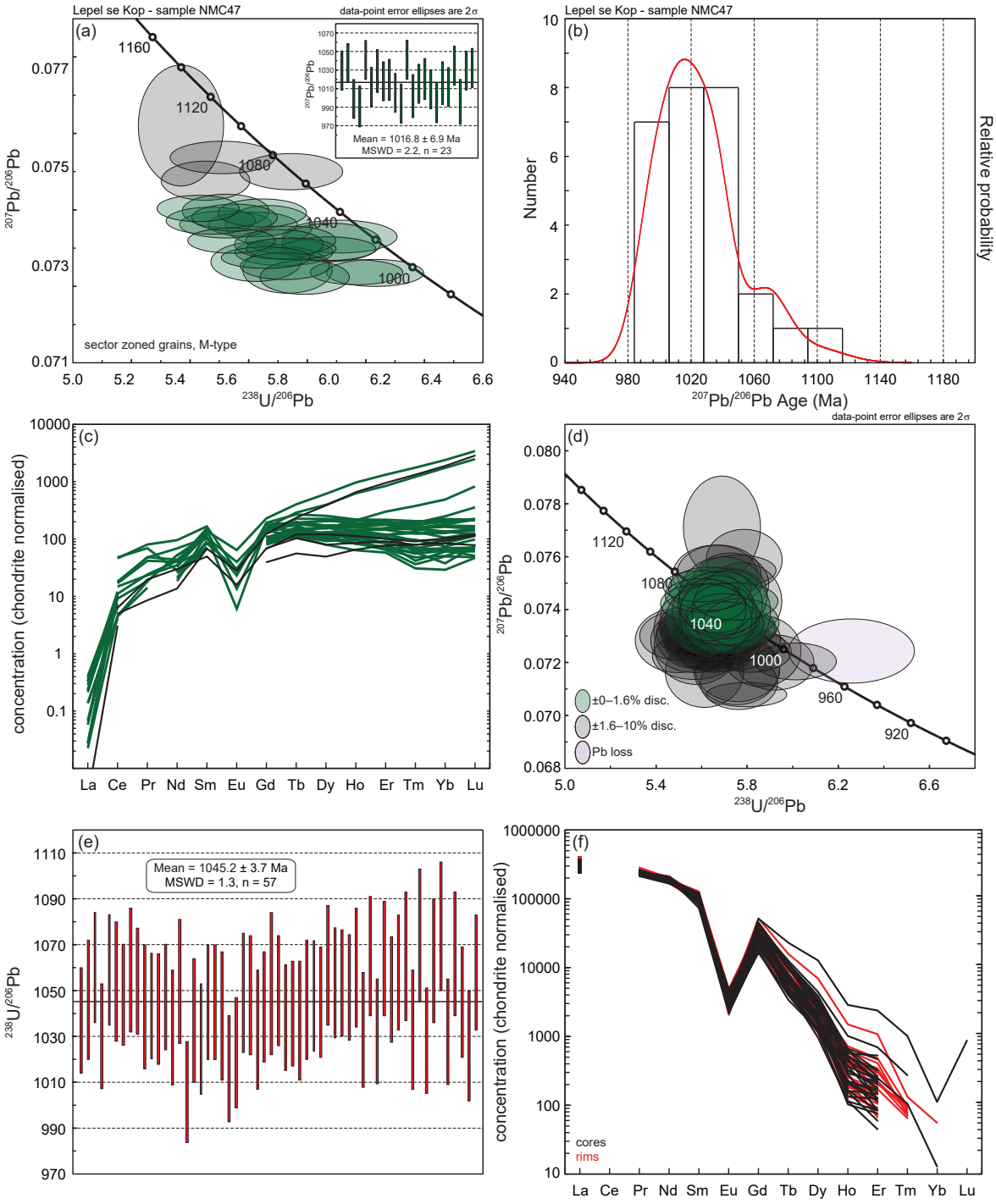


Figure 6.3: Results for zircon (a–c) and monazite (d–f) geochronological and geochemical analysis for locality Lepel se Kop (sample NMC47). Tera–Wasserburg plot of U–Pb isotope ratios for sector zoned zircons (a) and monazites (d). Insert in (a) displays weighted mean $^{207}Pb/^{206}Pb$ age for green error ellipses (see text). (b) Probability density function (PDF) plot for all considered zircon ablations. (e) $^{238}U/^{206}Pb$ weighted mean age calculation for monazite data. (c, f) Chondrite-normalised rare earth element plot for zircons and monazites, respectively.

zircons, respectively.

Chondrite-normalised REE reveal a complex array of compositional patterns, with all grains strongly impoverished in La, up to below the detection limit (Fig. 6.4d). A distinct negative Eu-anomaly is common to all analyses, but heavy-REE earth abundances vary by over an order of magnitude for oscillatory zoned zircons. However, heavy REE are enriched in all grains. This population is characterised by a pronounced positive Ce-anomaly. A single analysis of one of the concordant M-type grains (see insert on Fig. 6.4a) is strongly depleted in heavy REE.

U–Pb isotopic ratios for all 100 monazite data points are displayed on Figure 6.4e. All analyses are within ±10% discordance and seemingly of a single population, with 19 spots being ±0–1% discordant (green error ellipses Fig. 6.4e). Analyses with a discordance of ±1 to 5% are represented by grey error ellipses (Fig. 6.4e) yielding ages that spread along Concordia from *c.* 1070–1000 Ma. ±5–10% discordant analyses (purple ellipses on Fig. 6.4e) describe a similar age distribution. The total of monazite data yield a weighted mean $^{238}U/^{206}Pb$ age of 1035.6 ± 3.9 Ma (MSWD=2.6, n=100). This date overlaps within error with results from the soccer ball zircon and corroborates the age of high-grade metamorphism at around ∼1040–1030 Ma for Paulshoek. Normalised REE plots for monazite (Fig. 6.4f) display a distinct negative Eu-anomaly and strong enrichment in light REE compared to zircon REE patterns (Fig. 6.4d) and a general depletion in heavy REE, however describing a large variability and no clear distinction for core, mantle or rim ablations is observed.

6.2.3 Hytkoras

Zircons extracted from magnesian metapelite (sample NMC37) were ablated using IC machine settings (see subsection B.4.2). Age data are graphically summarised on Figure 6.5a, chondrite-normalised REE patterns are presented on Figure 6.5b. Twenty-eight out of a total of 30 ablations of a single population of sector zoned zircons (classified as type M) yield ages less within ±10 discordance. Error ellipses plot at similar $^{207}Pb/^{206}Pb$ ratios and yield a weighted mean $^{207}Pb/^{206}Pb$ age of 1031.6 ± 4.7 Ma (MSWD=1.2, n=28; insert on Fig. 6.5a). This age group is interpreted as timing of granulite facies metamorphism for this sample. Grains display a pronounced negative Eu-anomaly and are strongly depleted in La, with most values for Pr inferior to the limit of detection. A pronounced positive Ce-anomaly is not detected. Two broad clusters are outlined from variable enrichment in heavy REE on Figure 6.5b, with a group of depleted grains (black) and the other enriched (red). In this sample, no clear correlation between zircon morphology, crystallisation age and normalised REE pattern can be established.

Zircons from metagreywacke sample NMC68 from Hytkoras yield a total of 86 analyses, of which 67 are within ±10% discordance and discussed further (Fig. 6.5c–f). One analysed sector zoned soccer ball zircon (classified as type M) returned a metamorphic $^{238}U/^{206}Pb$ age of 1043.8 ± 22 Ma (Fig. 6.5c). Oscillatory zoned grains and oscillatory cores (n=66) are grouped in terms of their absolute discordance; 29 grains are within ±5% discordance and

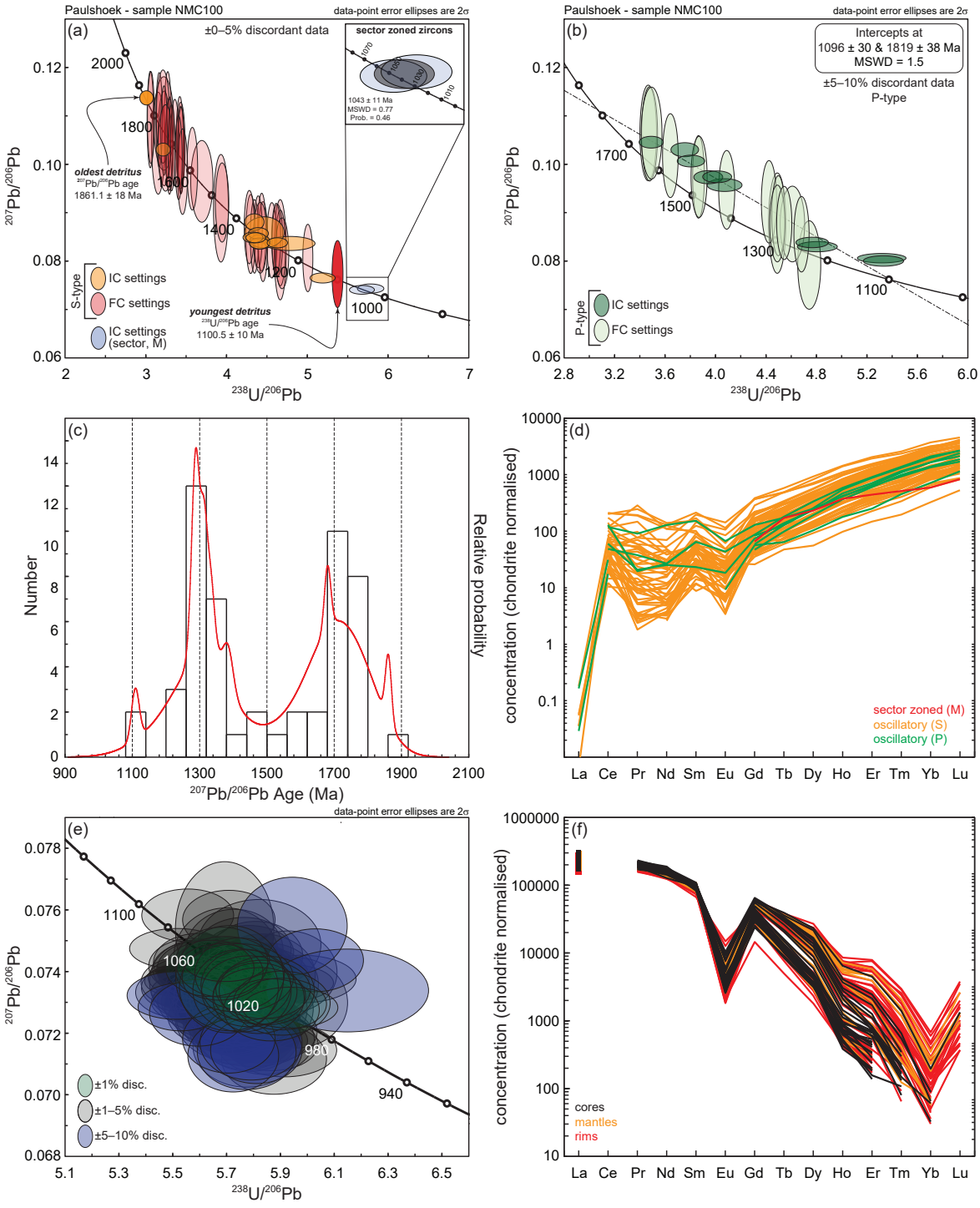


Figure 6.4: Results for zircon (a–d) and monazite (e, f) geochronological and geochemical analysis for locality Paulshoek (sample NMC100). Tera–Wasserburg plot of U–Pb isotope ratios for oscillatory- and sector zoned zircons (a, b) and monazites (e). Insert in (a) displays Concordia age for sector zoned grains. (b) Population of oscillatory zoned detrital grains ±5–10% discordant inferred to have been partly resetted (see text). (c) Probability density function (PDF) for $^{207}Pb/^{206}Pb$ ages of oscillatory zoned grains shown in (a). (d, f) Chondrite-normalised rare earth element plot for zircons and monazites, respectively.

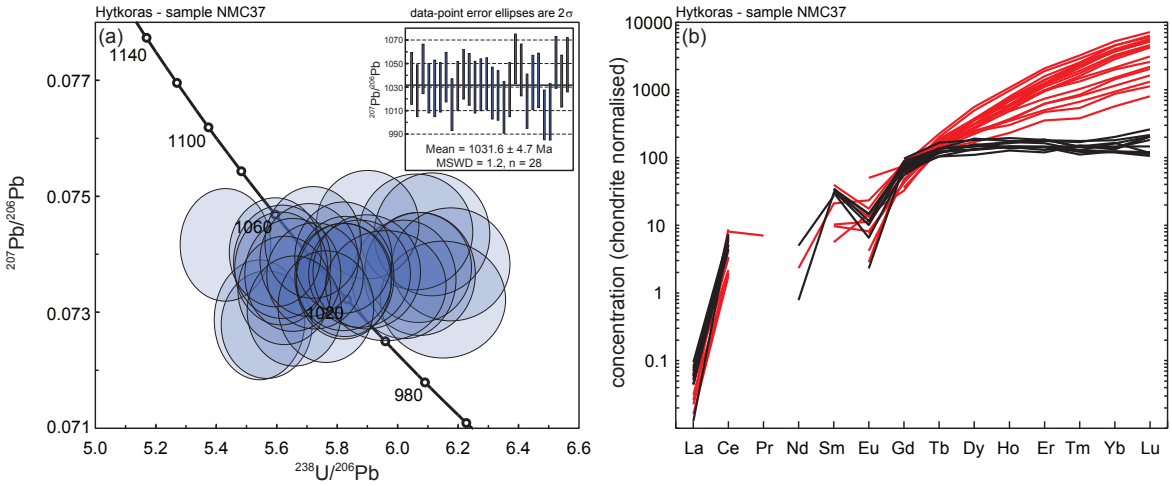


Figure 6.5: Results of geochronological and geochemical analysis for locality Hytkoras, sample NMC37 (a, b). (a) Tera-Wasserburg plot for U–Pb data and (b) chondrite-normalised REE plot of sector zoned zircons (M-type). Insert in (a) is weighted mean age calculation.

interpreted as detrital grains (type S; Fig. 6.5c). They plot over an age interval of between *c.* 1850–1500 Ma, bracketed by a concordant $^{238}U/^{206}Pb$ date of oldest detrital zircon of 1845 ± 50 Ma and age of youngest detritus of 1581 ± 64 Ma (Fig. 6.5c). $^{207}Pb/^{206}Pb$ dates of the same 29 analyses are plotted on a probability density plot, showing a pronounced peak at *c.* 1800–1750 Ma (Fig. 6.5e).

Thirty-six analyses of oscillatory zoned grains that are between ±5–10% discordant (classified as type P) define a discordia line with a respective upper and lower intercept of 1839 ± 33 and 1084 ± 79 Ma (MSWD=0.40; Fig. 6.5d). The youngest of these grains (spot no. 28) is a large prismatic zircon displaying healed cracks filled with CL-dark material and oscillatory zoning in unaltered portions (insert on Fig. 6.5d). It returns a $^{238}U/^{206}Pb$ age of 1106.5 ± 13 Ma even though it is texturally similar to the bulk of S- and P-type grains that plot at distinctly older ages (Fig. 6.1d and 6.5a). Upper- and lower intercept roughly overlap with ages of the oldest detritus and the single sector zoned (M-type) zircon, respectively.

Rare earth element plots normalised to chondrite reveal a limited variability for the analysed grains. A clear distinction cannot be established, however the single sector zoned, metamorphic zircon is the most depleted in heavy REE (red trend line on Fig. 6.5f). Analyses of oscillatory zoned grains roughly overlap for both detrital grains (S-type) and detrital grains that experienced Pb-loss (P-type) (orange and green line on Fig. 6.5f, respectively). However, both S- and P-type zircons display a pronounced positive Ce-anomaly. All analyses display a strong but variable negative Eu-anomaly and are depleted in Pr.

Monazite U–Pb isotopic analyses resulted in 39 out of 40 U–Pb analyses with an absolute discordance within ±10% (Fig. 6.5g). A weighted mean $^{238}U/^{206}Pb$ age of 1017.7 ± 5 Ma (MSWD=1.6, n=39) results from all concordant analyses, yielding age of metamorphism overlapping with the date from the soccer ball zircon within error. No significant age difference for

core and rim analyses is recognised. Figure 6.5h graphically represents chondrite-normalised REE analyses for monazite. All analyses plot in a small range, in particular data for light REE, in which monazite is strongly enriched compared to coexisting zircons (Fig. 6.5f). A pronounced negative Eu-anomaly is common to all analyses, as well as strong depletion in Yb (Fig. 6.5f). Analyses for cores and rims roughly overlap, thereby excluding a compositional trend in monazite composition.

6.2.4 Nababeep

Data from the single population of sector zoned zircons (classified as type M) recovered from aluminous metapelite sample NMC24 shows a small amount of reverse discordance. The data for this sample therefore is treated in the same manner as sample NMC47 from locality Lepel se Kop (see subsection 6.2.1). Two rough age clusters are identified from a total of 35 data points, with 3 analyses being disregarded due to high discordance. Twenty-three ages form a dense cluster (green ellipses on Fig. 6.6a), yielding a weighted mean $^{207}Pb/^{206}Pb$ age of 1006.9 ± 6.5 Ma (MSWD=1.8, n=23). The other, more discordant data (n=9) plot in an $^{238}U/^{206}Pb$ age age range between *c.* 1200–1020 Ma (black ellipses on Fig. 6.6a). These analyses are interpreted to have incorporated common Pb during analysis and are therefore not considered for further age calculation. REE plots for these analyses are presented on Figure 6.6b. The data displays a wide scatter for the heavy REE and a more or less pronounced negative Eu-anomaly. The grains are depleted in Ce as they lack an evident positive anomaly for this REE.

A total of 81 monazite ablations have been evaluated, with 76 of these returning ages that are within the acceptable rage of discordance. Three ablations have been excluded due to missed target. Forty-two data spots are within ± 3% discordance and yield a Concordia age of 1005.8 ± 3.2 Ma (MSWD=1.11, p=0.23, green ellipses on Fig. 6.6c). All acceptable data yield a weighted mean $^{238}U/^{206}Pb$ age of 1004.7 ± 3.4 Ma (MSWD=1.3, n=73) is calculated. Significant age differences between cores and rims are not observed. Together with dates from soccer ball zircons, monazite data yields an interpreted age of metamorphism of ∼1000 Ma for this locality. Chondrite-normalised REE plots reveal a distinct negative Eu-anomaly and a wide scatter for heavy REE concentrations. Analyses for cores and rims are similar and a compositional trend cannot be depicted (Fig. 6.6d).

6.2.5 Ratelpoort

Seventy-six data points were gathered from zircons extracted from aluminous metapelite (sample NMC21) collected at Ratelpoort. Of these, 25 ablations yield ages outside the discordance threshold with no trend indicating Pb loss due to metamorphic overprint (type P). Four ablations missed the target. All data regarded as geologically meaningful are graphically represented on Figure 6.7a. The data are treated in in the same manner as samples NMC47 and NMC24 due to some data plotting slightly reversely concordant (see subsection 6.2.1).

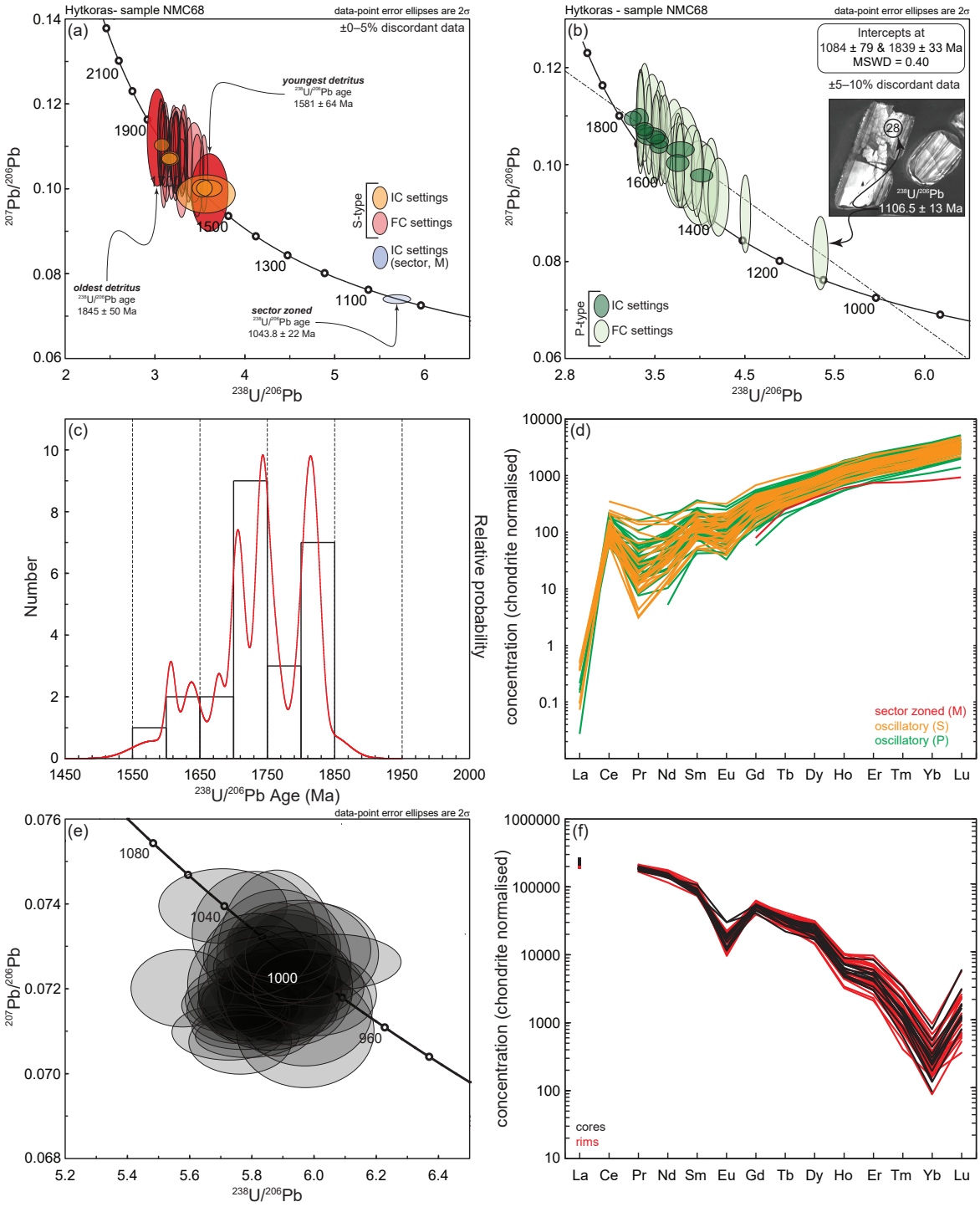


Figure 6.5: (continued). Results of geochronological and geochemical analysis for sample NMC68 from Hytkoras. (a, b, e) Tera–Wasserburg plot of U–Pb isotope ratios for oscillatory- and sector zoned zircons (a, b) and monazites (e) separated from sample NMC68. (b) Population of oscillatory zoned detrital grains inferred to have been partly resetted (±5–10% discordant, see text). Insert is CL image and spot location on youngest grain experiencing Pb-loss (P). (c) Probability density function (PDF) for $^{207}Pb/^{206}Pb$ ages of oscillatory zoned grains shown in (a). (d, f) Chondrite-normalised REE plot for zircons and monazites, respectively.

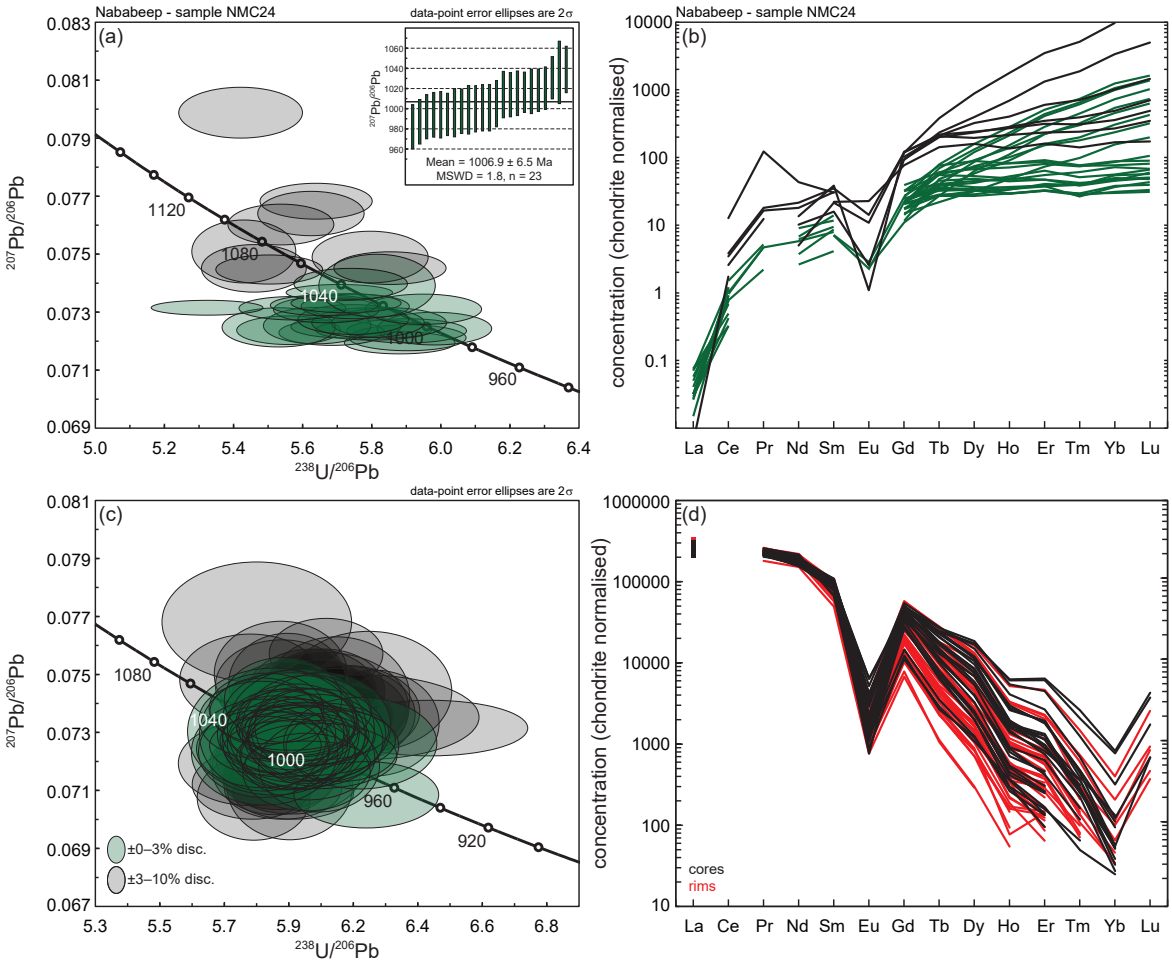


Figure 6.6: Results for zircon (a, b) and monazite (c, d) geochronological and geochemical analysis for locality Nababeep (sample NMC24). Tera–Wasserburg plot of U–Pb isotope ratios for sector zoned zircons (a) and monazites (c). Insert in (a) displays weighted mean $^{207}Pb/^{206}Pb$ age for green error ellipses (see text). (b, d) Chondrite-normalised rare earth element plot for zircons and monazites, respectively.

Six sector zoned zircons (grouped as type M) yield ages within the acceptable range of discordance (blue ellipses on Fig. 6.7a), yielding a poorly constrained weighted mean $^{207}Pb/^{206}Pb$ date of 1019 ± 22 Ma (MSWD=4.1; see insert on Fig. 6.7a). The bulk of analysed grains (n=42) display well developed oscillatory zoning, characteristic to magmatic zircon (classified as S-type zircons). These detrital grains plot over an age interval spanning between *c.* 2000–1200 Ma, with the oldest and youngest analysis of detrital S-type zircon yielding concordant $^{207}Pb/^{206}Pb$ ages of 2027.1 ± 18 Ma and 1171.4 ± 21 Ma, respectively (Fig. 6.7a). $^{207}Pb/^{206}Pb$ dates of these 42 analyses show two pronounced probability peaks between *c.* 1900–1700 Ma (Fig. 6.7b). Chondrite-normalised REE data are plotted on Figure 6.7c, displaying no clear difference for oscillatory zoned detrital grains or sector zoned metamorphic zircons. However, whereas detrital grains are characterised by variable Eu concentrations, all metamorphic grains display a pronounced negative Eu-anomaly.

A total of 45 spot analyses on monazites are evaluated, with two out of these yielding ages strongly discordant and therefore disregarded. The remaining 43 data points yield a weighted mean $^{238}U/^{206}Pb$ age of 1008.9 ± 4.2 Ma (MSWD=1.19), with no observable trend for rim and core ablations. Dates from soccer ball zircons and monazites overlap within error, suggesting timing of high-grade metamorphism at around 1020–1010 Ma at this locality. Chondrite-normalised REE data plots display a pronounced negative Eu-anomaly for all analyses and wide scatter for heavy REE concentrations (Fig. 6.7e).

6.2.6 Geselskapbank

A total of 67 zircons were ablated for the amphibolite facies metapelite sampled at Geselskapbank (sample NMC11). Of these, 63 yielded age data within the acceptable range of discordance and one analysis was disregarded due to inferred Pb loss. All analysed zircons display weak to pronounced oscillatory zoning and are classified as S-type grains; M-type sector zoned soccer ball zircons were not identified in this sample (see above). Analyses yield dates spreading over a broad interval, with the bulk of data falling between ∼2100–1600 Ma. The oldest detrital date is calculated from a highly concordant analysis yielding a $^{207}Pb/^{206}Pb$ date of 2108.6 ± 18 Ma (Fig. 6.8a). $^{207}Pb/^{206}Pb$ ages from all S-type zircon ablations are summarised in a probability density function plot (insert on Fig. 6.8a), displaying a major probability peaks at *c.* 2000 Ma and minor peaks between 1900–1700 Ma. Analyses of single oscillatory zoned zircons yield ages of *c.* 1.4, 1.2 and 1.1 Ga; with the youngest $^{238}U/^{206}Pb$ date of 981.3 ± 9.4 Ma (Fig. 6.8a). It is suggested that these grains represent a more ancient population of zircons that have been affected by recent modification and Pb loss (P-type; (Fig. 6.8a). The youngest detrital age is therefore ill-constrained, at around *c.* 1.6 Ga. Ablations within ±5–10% discordance are inferred to have been affected by radiogenic Pb loss and classified as P-type zircons. A simple linear regression through these data points yield a loosely constrained upper and lower intercept of 2011 ± 140 Ma and 1131 ± 82 Ma, respectively (Fig. 6.8a), consistent with ∼2.0–1.9 Ga zircons being partly resetted by a younger, ∼1.1 Ga thermal overprint. A single ablation on monazite yield data

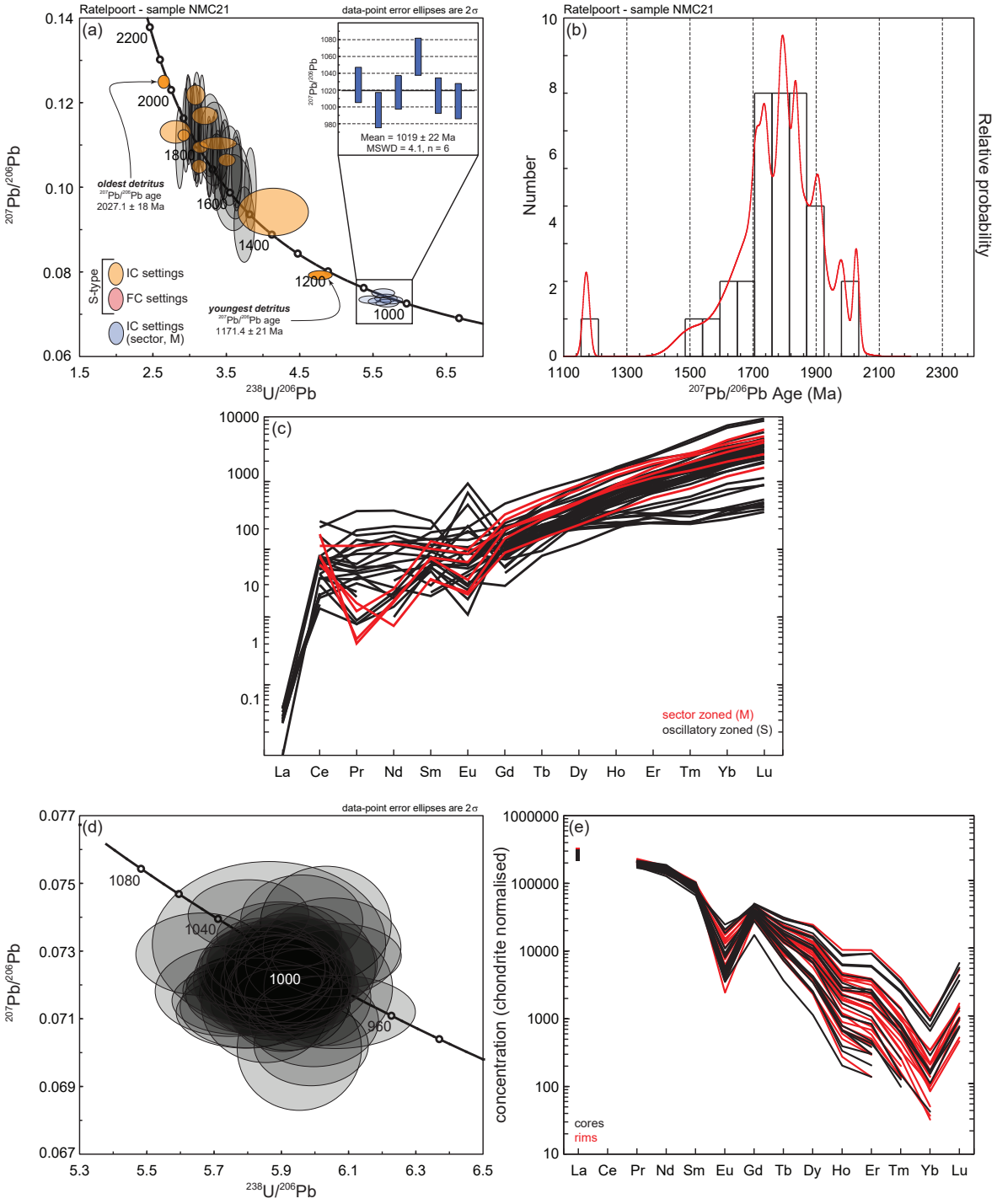


Figure 6.7: Results for zircon (a–c) and monazite (d, f) geochronological and geochemical analysis for locality Ratelpoort (sample NMC21). Tera–Wasserburg plot of U–Pb isotope ratios for oscillatory- and sector zoned zircons (a) and monazites (d). Insert in (a) displays weighted mean $^{207}Pb/^{206}Pb$ age for green error ellipses (see text). (b) Probability density function (PDF) for $^{207}Pb/^{206}Pb$ ages of oscillatory zoned grains shown in (a). (c, e) Chondrite-normalised rare earth element plot for zircons and monazites, respectively.

within the acceptable tolerance, and a $^{207}Pb/^{206}Pb$ date of 1143 ± 25 Ma. Within error, this date coincides with the lower intercept calculated from zircon ages; it is therefore tentatively interpreted as age of metamorphism that has affected and partly altered the older zircons.

In terms of chondrite-normalised REE patterns, zircons are characterised by a pronounced positive Ce-anomaly, a negative Eu-anomaly and no clear trend related to U–Pb age (Fig. 6.8b).

The investigated migmatite (sample NMC16) from Geselskapbank did not contain any zircons, and 7 ablations spots on monazite are reported (Fig. 6.8c). They yield a weighted mean $^{238}U/^{206}Pb$ age of 1018.7 ± 9.5 Ma for metamorphism in this sample (MSWD=0.75; insert on Fig. 6.8c). REE patterns normalised to chondrite describe a pronounced negative Eu-anomaly and a limited data scatter (Fig. 6.8d).

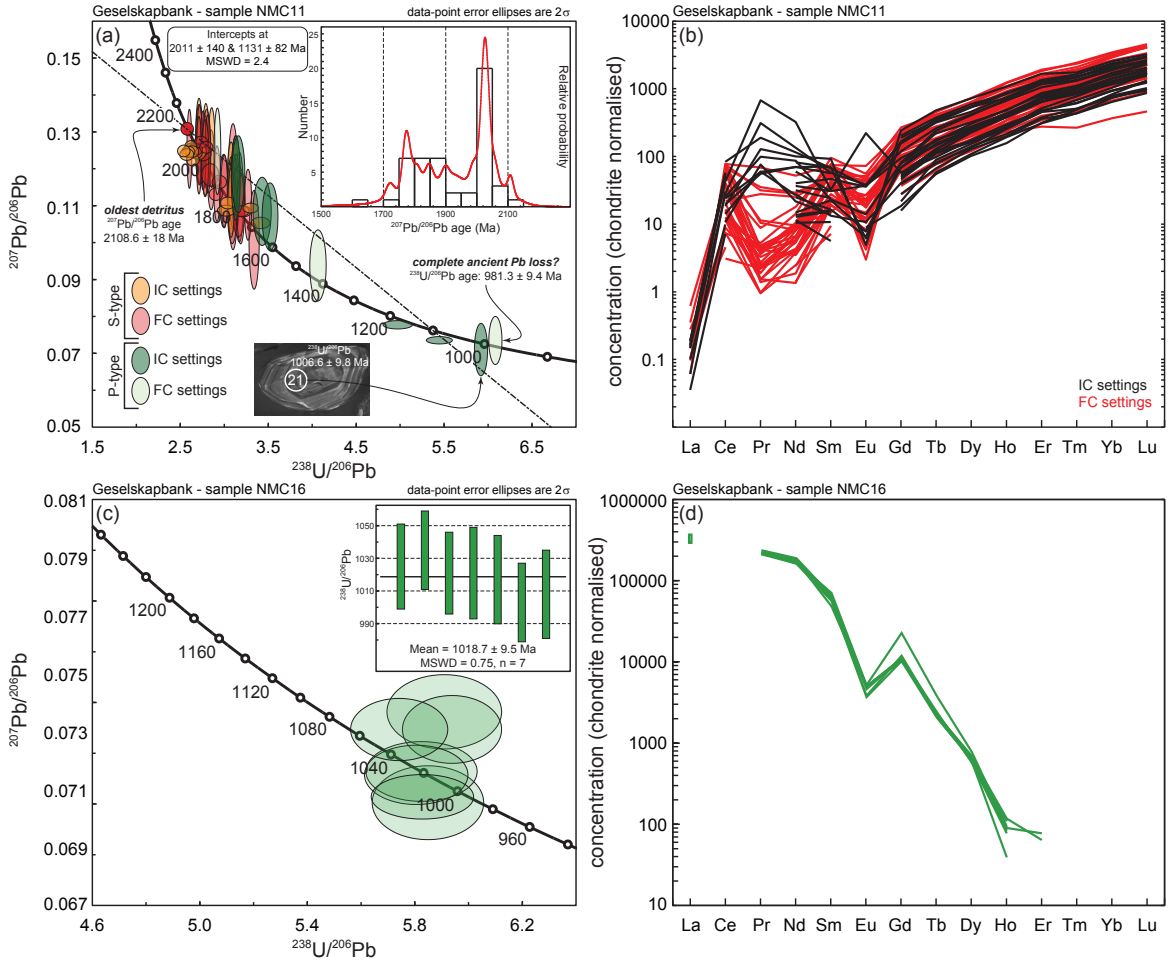


Figure 6.8: Results of geochronological and geochemical analysis for locality Geselskapbank, amphibolite facies gneiss NMC11 (a, b) and migmatite sample NMC16 (c,d). (a) Tera-Wasserburg plot for U–Pb data and (b) chondrite-normalised REE plot of oscillatory zoned zircons from sample NMC11 (see text). Insert in (a) is a probability function density (PDF) plot for S-type zircon $^{207}Pb/^{206}Pb$ ages. (c) Tera-Wasserburg plot for U–Pb data and (d) chondrite-normalised REE plot for monazites from sample NMC11. Insert in (c) displays weighted mean $^{238}U/^{206}Pb$ age for error ellipses.

Table 6.1: Results of U–Pb geochronology – summary

sample	locality	lithology	metamorphic age (Ma)	# ablations	type	detrital age spectrum (Ma)	# ablations	type
NMC24	Lepel se Kop	aluminous metapelite	∼1020	29	soccer ball zircon (type M)	none		
			1045.2 ± 3.7	57	monazite	none		
NMC100	Paulshoek	aluminous metapelite	1043 ± 11	2	soccer ball zircon (type M)	∼1860–1100, peaks at 1800–1700 Ma and 1400–1300	51	oscillatory zoned zircon cores (type S)
			1035.6 ± 3.9	100	monazite			
NMC37	Hytkoras	magnesian metapelite	1031.6 ± 4.7	28	soccer ball zircon (type M)	none		
NMC68		metagreywacke	1043.8 ± 22	1	soccer ball zircon (type M)	∼1850–1580, peak at ∼1800–1750	29	oscillatory zoned zircon cores (type S)
			1017.7 ± 5	39	monazite			
NMC24	Nababeep	aluminous metapelite	1006.9 ± 6.5	23	soccer ball zircon (type M)	none		
			1004.7 ± 3.4	73	monazite			
NMC21	Ratelpoort	aluminous metapelite	1019 ± 22	6	soccer ball zircon (type M)	∼2000–1200, peak at ∼1900–1700	42	oscillatory zoned zircon cores (type S)
			1008.9 ± 4.2	43	monazite			
NMC11	Geselskapbank	amphibolite	1157 ± 18	1	monazite	∼2100–1600, peaks at ∼2000 and 1900–1700	63	oscillatory zoned zircon cores (type S)
NMC16		migmatite	1018.7 ± 9.5	7	monazite	none		

Chapter 7

P–T–t distribution and metamorphic evolution of the Namaqua Sector

7.1 Regional P–T evolution

For the regionally sampled aluminous metapelites pseudosections tailored for residuum compositions are used to constrain the likely peak P–T conditions recorded by the rocks as well as, where possible, the peak-to-retrograde evolution. The diagrams are, however, unsuitable to deduce the prograde development because the rocks are inferred to have produced and lost variable amounts of silicic melt rendering the protolith composition unknown (see subsection 5.1.2). The potential early metamorphic pre-peak evolution is therefore semi-quantitatively constrained via petrographic relations, such as mineral inclusions and inferred paramorphs. Figure 7.0 displays a compilation of the inferred peak assemblage fields for aluminous metapelites from the various sample localities. Locality Hytkoras is discussed separately in detail (see below).

1. **Lepel se Kop** and **Nababeep**: Samples from these localities are petrographically and compositionally similar; their common peak assemblage of garnet–biotite–cordierite–sillimanite–plagioclase–K-feldspar–quartz–ilmenite–magnetite–melt records apparent P–T conditions comprised between 760–820 °C and 4.5–6.5 kbar (see section 5.2.1 and Figure 7.0a and c). Biotite and sillimanite are found as inclusions in garnet and in the rock matrix. It is therefore concluded that both minerals have persisted throughout the metamorphic evolution of the rocks. In the sample collected at Lepel se Kop (NMC47), randomly oriented fibrolite included in garnet as opposed to sillimanite needles oriented parallel to leucosomes found in the rock matrix are interpreted as indication for pretectonic garnet growth, with main deformation coinciding with high-grade metamorphism or at least postdating main garnet growth. For samples from both localities the inferred coexistence at equilibrium of biotite, sillimanite, garnet and cordierite (together with

oxides, quartz and feldspars) is interpreted as indication for the incomplete advance of reaction 2.8 that has been introduced in earlier chapters. Polymorphs of an aluminosilicate, other than sillimanite, or para/pseudomorphs thereafter are not identified. The early prograde evolution for these samples is therefore inferred to have not exceed pressures recorded at the thermal maximum. Cordierite is found exclusively as a peritectic product of reaction 2.8 and not as inclusions in garnet. Therefore, garnet stability is thought to have preceded that of cordierite, consistent with burial occurring during early metamorphism and followed by roughly isobaric heating. Similarly, textures indicative for substantial decompression, such as moats of cordierite growing at the expense of garnet, have not been found. In summary, a prograde clockwise P–T path dominated by heating accompanied by minor burial and followed by cooling and/or minor exhumation is anticipated for the localities Lepel se Kop and Nababeep, consistent with findings from the Aus Domain, north of the BSP (Diener *et al.*, 2013).

2. **Paulshoek**: These samples are unique compared to those from other localities because petrographic observations suggest the stable coexistence of hercynitic spinel and quartz at the thermal maximum (also see Waters, 1986b, 1991, 1989). The inferred peak assemblage of garnet–biotite–cordierite–spinel–plagioclase–K-feldspar–quartz–ilmenite–magnetite–melt ± sillimanite is however, not reproduced by the modelling presented here, as the stability of biotite and spinel is calculated as mutually exclusive (see subsection 5.2.1). This is in conflict with key petrographic observations (see subsection 4.1.2). This inconsistency is likely due to minor components present in the minerals but not accounted for by the a–x formulations. Of these, fluorine is known to significantly expand biotite stability towards higher temperature (e.g. Mouri *et al.*, 1996; Munoz and Luddington, 1977; Peterson *et al.*, 1991; Icenhower and London, 1997) whereas zinc stabilises spinel towards both lower temperature and higher pressure, as demonstrated by experiments (e.g. Shulters and Bohlen, 1989; Nichols *et al.*, 1992). It is therefore concluded that, if these components would have been accounted for, the modelled stability fields of biotite- and spinel-bearing assemblages would expand and overlap, thereby successfully reproducing the full inferred peak metamorphic assemblage of the investigated samples (cf. Tajčmanová and Konopásek, 2003).

   Alternatively, the mismatch may be due to not sampling the effective bulk composition, which may have been altered by retrograde coronae-formation and/or sequestration of crucial components in garnet porphyroblasts (e.g. Stüwe, 1997).

   Considering the mentioned caveats, phase modelling allows for a poor constraint on apparent peak conditions recorded by the samples from Paulshoek, namely ∼780–900 °C and 4.5–5.5 kbar (Fig. 7.0b). As for the prograde path, inclusions of biotite, sillimanite and cordierite in garnet imply that these phases were present as garnet grew to include them. Cordierite growth preceding that of garnet, as well as the dearth of kyanite is consistent with a path that involves heating but also substantial burial prior to attain-

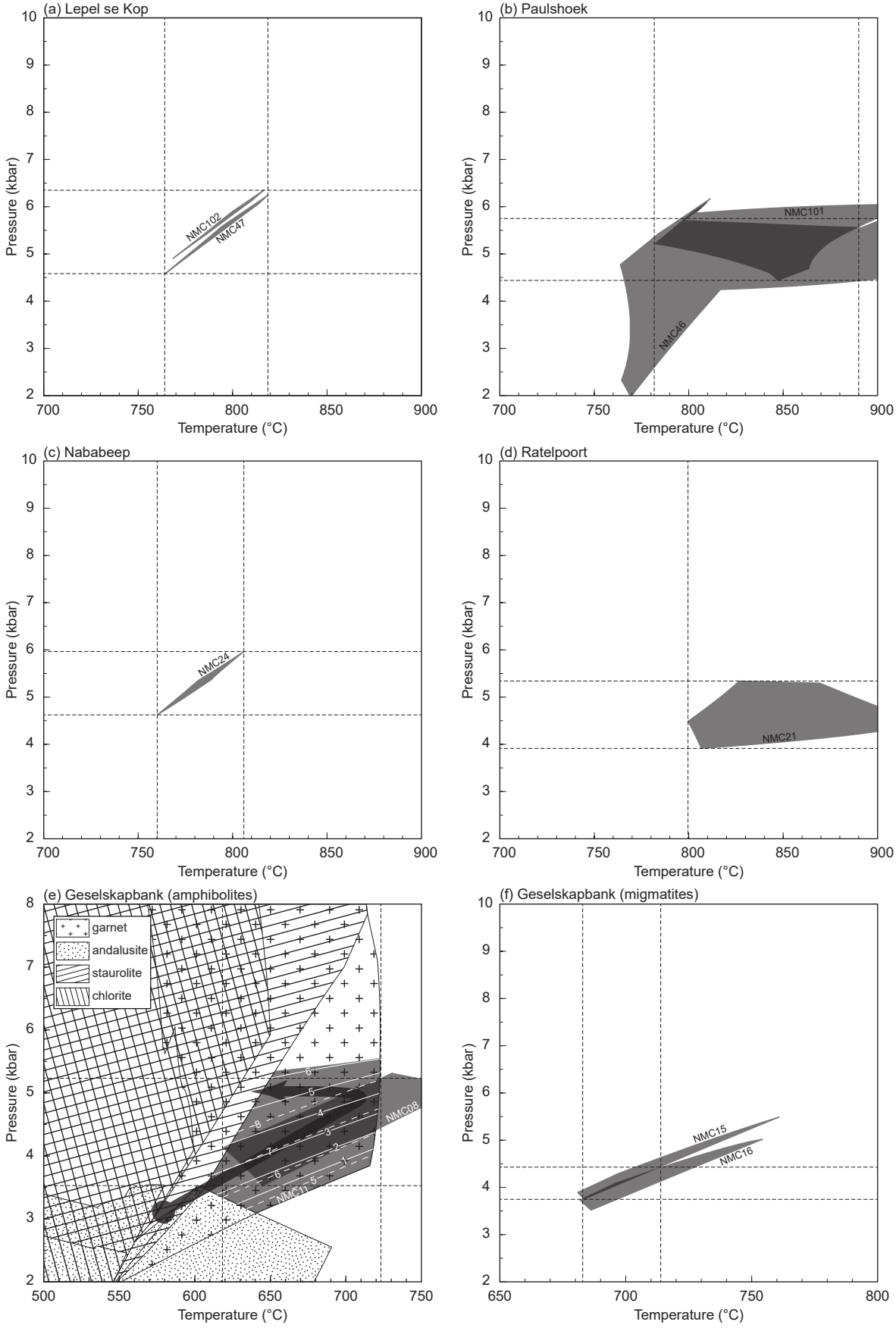

(a) Lepel se Kop
NMC102
NMC47
(b) Paulshoek
NMC101
NMC46
(c) Nababeep
NMC24
(d) Ratelpoort
NMC21
(e) Geselskapbank (amphibolites)
garnet
andalusite
staurolite
chlorite
NMC08
NMC11
(f) Geselskapbank (migmatites)
NMC15
NMC16
Pressure (kbar)
Temperature (°C)

Figure 7.0: Summary graph showing the stability fields of respective inferred peak assemblages of investigated samples. Shadings in (e) delineate the stability of key phases. Solid and dashed lines are modal contours for garnet and sillimanite (vol. %), respectively. Phase stabilities and modes calculated for sample NMC11. Arrow shows preferred P–T path for amphibolites from Geselskapbank.

ment of metamorphic peak conditions. Retrograde modification involves the formation of ubiquitous coronae of garnet, sillimanite or plagioclase separating peak metamorphic spinel from biotite, K-feldspar and in particular quartz.

The nature of coronae is however inferred to have been controlled by local gradients in chemical potential that might have been built up between domains of local bulk composition after melt loss rather than by significant changes in physical conditions (White and Powell, 2011; White *et al.*, 2002). The textures therefore cannot be used to deduce the retrograde evolution other than inferring minor cooling and the absence of significant decompression. The minor changes in P–T and/or local bulk composition due to melt extraction led to the formation of domains of local equilibrium that drove the formation of coronae in an attempt to equalise gradients of chemical potential (cf. Doukkari *et al.*, 2018). In conclusion, a path involving heating and burial to the metamorphic peak and followed by roughly isobaric cooling from a hot, transient geotherm is inferred for Paulshoek, consistent with an overall anticlockwise evolution as suggested in previous contributions (Waters, 1991, 1986a,b, 1989; Raith and Harley, 1998; Diener, 2014).

3. **Ratelpoort**: The investigated specimen of aluminous metapelite is characterised by the largely anhydrous inferred peak assemblage of garnet–cordierite–plagioclase–K-feldspar–quartz–ilmenite–magnetite–melt that occupies a large stability field yielding a tight constraint on pressure of 4–5.5 kbar, but ranges from ∼800 °C to in excess of 900 °C (Fig. 7.0d). Biotite and sillimanite are modally subordinate and confined to rare textures consisting of sillimanite inferred to replace early metamorphic andalusite. The textures are isolated from the matrix by moats of coarse-grained peritectic cordierite, suggesting that the reactants biotite and sillimanite have been removed from the reactive composition, marking the effective completion of melting reaction 2.8. Single-mineral inclusions of biotite, sillimanite and cordierite in garnet, and inferred paramorphs after andalusite are consistent with minor burial and heating from greenschist- to lower amphibolite (andalusite-)conditions to the thermal peak. Textures from which the nature of the retrograde path may be confidently deduced are absent; however, due to the similarity of the preferred prograde path to that of samples from Paulshoek and published paths, an anticlockwise path involving roughly isobaric cooling to a stable mid-crustal geotherm following the thermal maximum is inferred for Ratelpoort.

4. **Geselskapbank**: At this locality, granulite facies klippen of the LFROTZ are inferred to have been juxtaposed onto amphibolite facies rocks of the BSP along a wide thrust zone of the Groothoek Thrust (Fig. 3.1; cf. Macey *et al.*, 2017). The investigated amphibolite facies gneisses in the footwall are characterised by the inferred equilibrium assemblage of garnet–biotite–cordierite–sillimanite–plagioclase–ilmenite–magnetite–H_2O ± quartz, overlapping at conditions comprised between ∼620–720 °C and 3.5–5 kbar (Fig. 7.0e). A minimum pressure of ∼4 kbar is required to approximate the modal amount of garnet observed in thin section (∼5–10 vol. %). Because these rocks are unlikely to have melted during their metamorphic history, no modification of the bulk composition due to melt extraction has occurred and the calculated diagrams in Figure 5.1g and h may be used to investigate the potential pre-peak evolution. The presence of inferred paramorphs after andalusite confines early metamorphism to pressure <3.5 kbar whereas the absence of inclusions of staurolite in garnet is consistent with main garnet growth occurring at conditions exceeding the upper thermal stability of staurolite (Fig. 7.0e). Therefore, a prograde path leading from lower amphibolite/andalusite conditions to the metamorphic peak involving burial and heating, rather than near-isobaric heating, is suggested to satisfy petrographic observations (arrow on Fig. 7.0e). Randomly oriented fibrolite included in garnet versus isoriented sillimanite in the matrix is interpreted to suggest mainly pretectonic garnet growth followed by pervasive deformation prior to or at the thermal peak. Cordierite is partly consumed by texturally late beards of unoriented fibrolite. Isopleths monitoring the abundance of the aluminosilicate indicate that an increase of modal sillimanite is achieved via burial and/or cooling (Fig. 5.1g and 7.0e). In light of the predominant high-T–low-P evolution of the BSP where the thermal peak is commonly followed by roughly isobaric cooling, this scenario is also favoured for the amphibolites. Overall, an anticlockwise P–T path is suggested for the amphibolite facies portion of Geselskapbank (Fig. 7.0e), in agreement with thermobaric estimates and P–T path reported for the Aggeneys Terrane to the east of Geselskapbank (Diener, 2014).

   Garnet-absent oxidised migmatites with the inferred peak assemblage of biotite–cordierite–sillimanite–plagioclase–K-feldspar–quartz–ilmenite–magnetite–melt record peak conditions of 680–720 °C and ∼4 kbar. Textures indicating extensive decompression are absent, as are indications for the former stability of kyanite. Similar to other samples investigated here, a prograde path dominated by heating and minor concomitant burial is suggested for the migmatites. The observed replacement of coarse-grained peak metamorphic poikiloblastic sillimanite by fibrolite is attributed to reworking during final juxtaposition of the klippe onto the BSP rather than cooling from the thermal maximum. This is deduced from the fact that fibrolite is weakly isoriented, imprinting a secondary fabric on the otherwise apparently statically metamorphosed rocks.

   The assembly of the units to their final structural architecture is accompanied by low grade and possibly fluid-assisted reworking of both units. This common over-

print is inferred from stellar nodules of chlorite consuming cordierite in amphibolite facies gneisses, weakly isoriented fibrolite replacing peak metamorphic sillimanite in migmatites and extensive pinitisation of cordierite in both rock types. Chlorite stability calculated for the gneisses places a maximum temperature of ∼600 °C at 5 kbar for this event (Fig. 7.0e).

7.2 Hytkoras

The peak metamorphic conditions estimated from the investigated samples are summarised in Figure 7.1a. If it is assumed that all samples were buried to the same depth and only experienced lithostatic pressure (cf. Moulas *et al.*, 2013, and references therein), all indicate pressure conditions of 5–6 kbar (Fig. 7.1a), which is in very good agreement with previous estimates for this part of the BSP (Waters and Whales, 1984; Waters, 1986a,b; Raith and Harley, 1998; Clifford *et al.*, 2004). For an assumed peak pressure of 5.5 kbar, there is no unique point at which all temperature estimates overlap. Apparent peak temperatures of 775–790 °C are constrained for the aluminous metapelites, whereas the mafic granulite indicates 830 °C and the magnesian metapelite yields an estimate of 850 °C (Fig. 7.1a). The magnesian gneiss yields a residuum solidus T of 820 °C, but the peak assemblage field extends to 870 °C. Similarly, the semi-pelite has its residuum solidus at conditions that correspond to those constrained from the metapelites, but its peak range also overlaps with that of the mafic granulite, magnesian metapelite and magnesian gneiss and therefore does not further refine estimates from the other samples (Fig. 7.1a).

The range of temperatures constrained here are in good agreement with previous estimates from this area. According to Waters (1986b, 1989), Hytkoras falls into 'granulite-zone B' with estimated peak conditions spanning from 740 ± 30 °C to 770 ± 35 °C determined by conventional thermometry from garnet–cordierite pairs (Waters, 1989). Similarly, Waters and Whales (1984) suggests conditions around 750 °C for metapelites located within zone B and ascribes partial melting and assemblage formation to reaction 2.8, confirming our interpretation of the aluminous metapelites. Slightly higher temperatures of 750–800 °C are calculated for magnesian gneisses from and around Hytkoras (Waters, 1986a), roughly corresponding to our estimate for the same lithologies. Our inferred peak temperature for the magnesian metapelite is consistent with temperatures in excess of 800 °C (Waters, 1986b) and as high as 860 ± 25 °C (Waters, 1989) reported for central BSP zone C, estimated from metapelites hosting hercynite + quartz and rare osumilite.

Constraints on the early prograde metamorphic evolution are deduced from various nodular magnesian gneisses preserving information about pre-granulite conditions (see section 4.2.6 and 5.2.4). Accepting the interpretations of Waters (1986a), sample NMC88 developed cm-sized prisms of andalusite during early metamorphism of <550 °C and <4.5 kbar (Fig. 7.2). The inferred development of staurolite in sample NMC90 implies heating to ∼600–650 °C, and potentially concomitant burial. The shape of the respective stability field however does

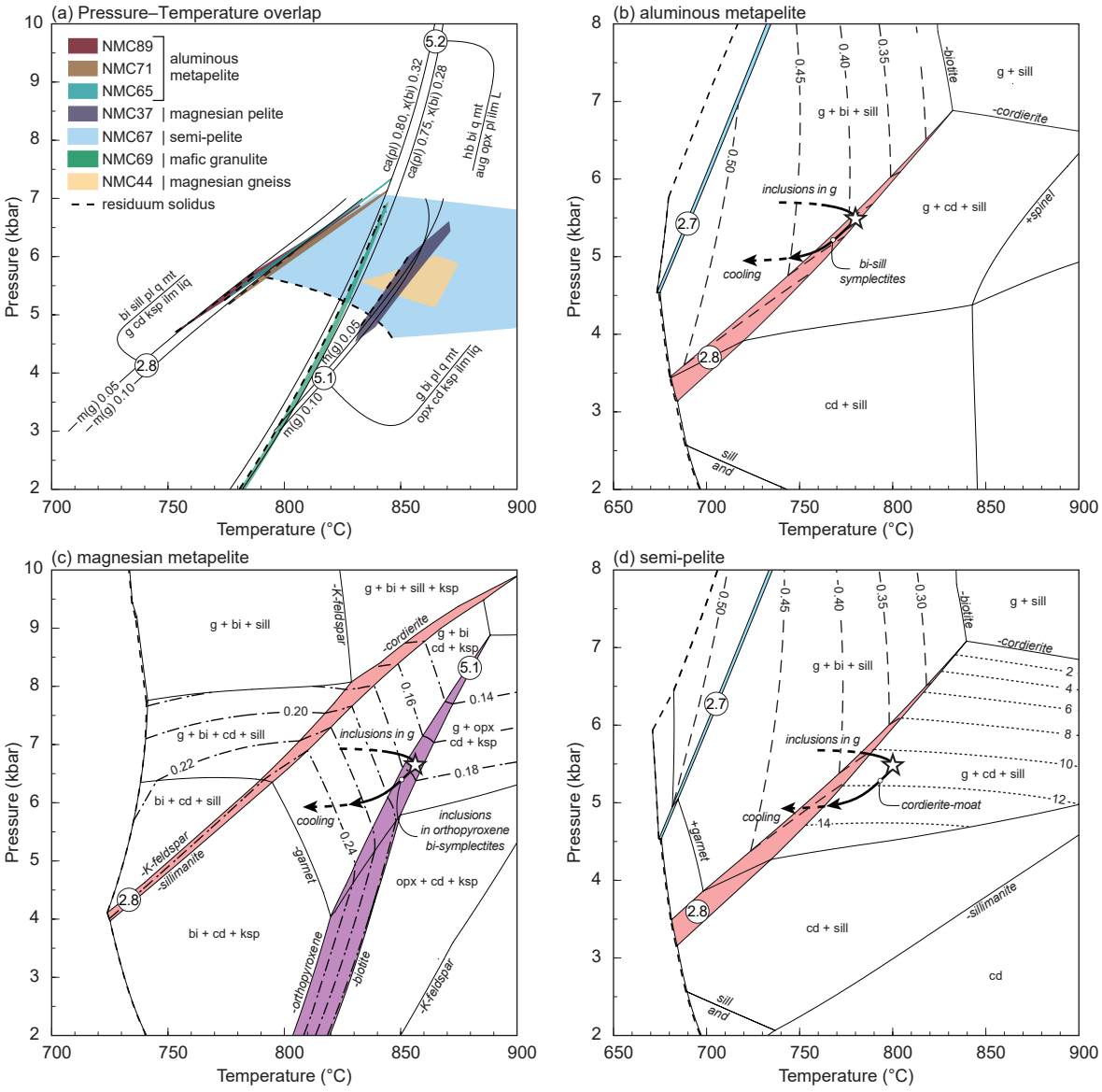


Figure 7.1: Summary of inferred peak assemblage fields and assemblage-forming melting reactions (a) and schematic P–T diagrams showing the interpreted evolution and texture formation (b–d). Coloured fields correspond to major melting reactions (see text). m(g), ca(pl) and x(bi) correspond to spessartine content in garnet, anorthite component in plagioclase and X_{Fe} in biotite, respectively (see text). (b) Schematic phase diagram for aluminous metapelite (sample NMC89). Dashed lines are compositional isopleths for X_{Fe} in biotite (c) Simplified phase diagram for magnesian metapelite (sample NMC37). Dot-dash lines are isopleths for X_{Fe} in cordierite. (d) Schematic diagram for the semi-pelite (sample NMC67), the dashed lines correspond to X_{Fe} in biotite. Dotted lines are modal isopleths for cordierite (vol. %). White star approximates apparent equilibration conditions.

not necessarily imply a significant increase in pressure (Fig. 7.2). The growth of orthoamphibole as forerunner of large porphyroblastic orthopyroxene in sample NMC44 indicates further heating, but does not allow for tighter constraints on metamorphic pressure (Fig. 7.2).

The shape of the near-peak metamorphic path can be constrained from petrographic relations, most notably the ubiquitous presence of sillimanite inclusions in peritectic cordierite in aluminous metapelites (Fig. 4.8b, c). This texture is characteristic of melting reaction 2.8, as has been similarly described for other parts of the NNMP (Diener *et al.*, 2013). The reaction can be intersected by a temperature increase and / or decompression (white star on Fig. 7.1b), suggesting a clockwise P–T trajectory at near-peak metamorphic conditions (cf. Diener *et al.*, 2013). This trajectory is supported by observations from other rock types. Magnesian metapelites contain inclusions of both cordierite and biotite in peritectic orthopyroxene (Fig. 4.9b, d). These are indicative of melting reaction 5.1, which is most readily intersected by a combination of heating and/or decompression (white star on Fig. 7.1c). Semi-pelites exhibit well-formed cordierite moats on garnet (Fig. 4.10b), indicating that cordierite abundance increased at the expense of garnet in these rocks. Isopleths monitoring the modal amount of cordierite overlain on the inferred peak assemblage field on Figure 7.1d indicate the growth of cordierite at the expense of garnet requires minor decompression shortly after the thermal maximum (white star on Fig. 7.1d). Approximately 4 vol. % of cordierite is calculated to grow in response to decompression of ∼1 kbar (Fig. 7.1d). Therefore, it is inferred that the rocks evolved along a tight, clockwise loop at near-peak metamorphic conditions. However, the amount of post-peak decompression was relatively minor, likely 1 kbar or less.

Retrograde symplectic textures found in the samples (Fig. 4.8c, d, 4.9c, d and 4.13a) are interpreted as indication for partial reversal of reaction 2.8 and 5.1, respectively, and limited by crystallisation of the last vestiges of melt (Ashworth, 1976; Ashworth and McLellan, 1985; Waters, 1988; Kriegsman and Hensen, 1998; White and Powell, 2011). This can be achieved by cooling and/or a pressure increase (Fig. 7.1b, c). Given the evidence for minor post-peak decompression, the symplectic textures are interpreted to have formed through early suprasolidus cooling. Cooling is also favoured over decompression in light of modelled mineral composition trends, symbolised by isopleths for X_{Fe} of major ferromagnesian phases (Fig. 7.1b–d). As shown in section 4, inclusions in peritectic porphyroblasts are persistently more magnesian compared to matrix varieties. This is consistent with inclusion entrapment occurring at near-peak conditions followed by retrograde modification of the matrix minerals during cooling (Fig. 7.1b–d).

In summary, the inferred presence of early andalusite, and the absence of inclusions of / pseudomorphs after kyanite suggests that low- to medium pressure conditions were not exceeded during metamorphism of the investigated samples, consistent with interpretations on Hytkoras and other parts of the Namaqua Sector (e.g. Waters, 1986a,b, 1989; Raith and Harley, 1998; Diener *et al.*, 2013). Prograde metamorphism from 500–550 °C and <4.5 kbar to peak conditions involved heating of 200–300 °C with minor concomitant burial of ∼2 kbar (≃7–8 km) suggesting a roughly isobaric prograde evolution (summarised on Fig. 7.2). The

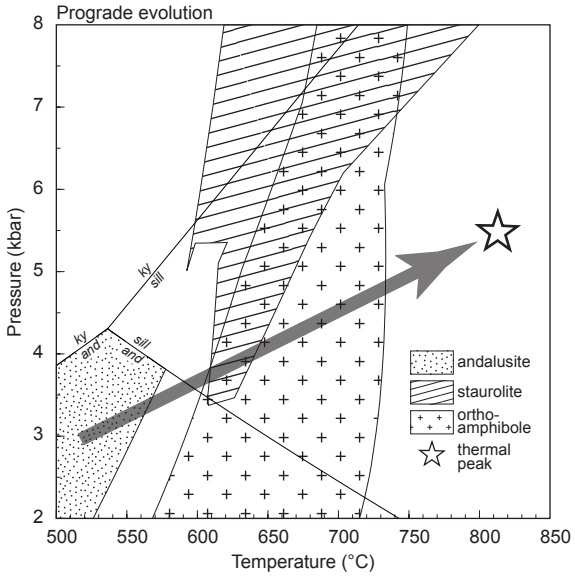


Figure 7.2: Summary of stability fields for precursors to pseudomorphs (see text). Grey arrow shows preferred prograde path.

clockwise near-peak P–T loop is inferred to have terminated in a significant period of near-isobaric cooling while the terrane remained at mid-crustal depth (Fig. 7.1). Therefore, a largely isobaric, low-pressure P–T path with a tight, clockwise near-peak loop is proposed for the rocks at Hytkoras. This evolution is similar to that proposed for the Aus Domain to the north of the BSP (Diener *et al.*, 2013), but in detail it differs from the anticlockwise path derived by Waters (1986a,b, 1989) for similar rocks from the BSP.

7.2.1 Pseudomorph-formation in magnesian gneisses

Symplectic textures specifically replace early, coarse-grained aluminous phases such as andalusite and staurolite, whereas orthoamphibole is replaced by orthopyroxene. In this subsection the spectacular cordierite–spinel–sapphirine textures (± corundum ± magnetite; Fig. 4.14 and 4.15) after andalusite found in sample NMC88 are investigated in detail.

According to Waters (1986a) the textures formed during near-isobaric heating from amphibolite to granulite facies conditions, with sapphirine being introduced at the expense of cordierite + spinel + corundum at or close to the metamorphic peak. The counter-intuitive formation of fine-grained high-temperature assemblages seemingly replacing coarse-grained low-grade precursors is explained via a melt- and fluid absent evolution of the refractory gneisses (Waters, 1986a). Absence of deformation might have further inhibited more complete equilibration, in spite of high-grade conditions.

All textures in the investigated sample display conspicuous, homogeneous monomineralic coronae of cordierite separating symplectic intergrowths from a seemingly well-equilibrated matrix (Fig. 4.14). Corona-formation and symplectic replacement is indicative of limited

diffusional exchange between the site of replacement and the rock matrix. The textures therefore represent distinct domains of local bulk composition that are at equilibrium only at the small scale (so-called 'local equilibrium' or 'mosaic equilibrium' in Khorzhinskii, 1959). As pioneered by Khorzhinskii (1959); Thompson (1959, 1970); Rumble (1982) and reviewed by White *et al.* (2008), the paradigm of local bulk equilibrium categorises elements in terms of their effective diffusivity. Identifying these elements is crucial for understanding the process(es) of texture formation (Baldwin *et al.*, 2015; Štípská *et al.*, 2010; White and Powell, 2011; White *et al.*, 2008). Three groups of elements are described: (a) effectively immobile elements whose concentration differ among compositional domains at texture scale; (b) highly mobile elements whose chemical potentials are assumed as constant over the entire texture and (c) conditionally mobile elements with variable chemical potentials over the scale of the texture. The phase rule dictates a direct relationship between immobile elements and phases participating in texture formation (Münster, 1970; White *et al.*, 2008; Khorzhinskii, 1959). As such, monomineralic coronae form with one immobile element, bimineralic symplectites with two immobile components, and so forth. Perfectly mobile elements are typically introduced from outside the site of texture formation, but are thought to have not influenced the textural development. Strongly-bonded elements such as Al and Si are considered as effectively immobile (e.g. Carlson, 2002), whereas H_2O is considered as perfectly mobile, if the texture hosts hydrous phases. The group of conditionally mobile elements controls textural development and is investigated in diagrams involving chemical potential relationships, where they are quantified as axes (Baldwin *et al.*, 2015; Schorn and Diener, 2017; Štípská *et al.*, 2010; White and Powell, 2011; White *et al.*, 2008).

Petrologic interpretation

In sample NMC88, the observed textural architecture is not unlike the examples described by Štípská *et al.* (2010) and Baldwin *et al.* (2015), where individual porphyroblasts of kyanite found in high-pressure granulites were rimmed by a layer of plagioclase ± garnet during exhumation. The kyanite-domains were thereby isolated from the rock matrix and formed local domains of bulk composition in limited diffusional communication with the surrounding rock matrix. This resulted in the formation of gradients in chemical potential between kyanite cores and the matrix, along which Al diffused away from the kyanite in the pursuit to equalise the gradient. However, the rate of diffusion of Al was outstripped by the growth rate of plagioclase-coronae that led to further isolation of the kyanite-domain from the matrix, resulting in the build-up of gradients in chemical potentials of additional elements, such as Fe, Mg and Si. Partial flattening of the chemical potential 'landscape' culminated in the formation of various symplectic intergrowths involving, among others, sapphirine and spinel (Štípská *et al.*, 2010; Baldwin *et al.*, 2015).

Whereas the formation of initial coronae of plagioclase on kyanite were driven by decompression in the published examples, the tectonic setting and grand metamorphic evolution of the magnesian gneisses and the BSP in general is completely different as it is dominated by

heating and cooling, rather than by (de)compression (e.g. Waters, 1986a,b; Raith and Harley, 1998; Robb *et al.*, 1999). However, the formation of a monomineralic layer of cordierite would exert a similar effect on andalusite as the plagioclase-moat did on kyanite, in particular because in both cases the slowest diffuser at this initial stage was Al. As soon as the growth of cordierite outstripped the diffusion of Al from andalusite towards matrix, additional gradients in chemical potential built up and led to diffusion attempting to restore a flat chemical potential 'landscape'. For sample NMC88, this process is simulated using the KFMASH model system; K_2O is required to account for muscovite and biotite – both important constituents at these conditions (Fig. 5.4a) that were most likely involved in corona-formation. The immobility of Al is inferred to have produced a layer of monomineralic cordierite, therefore, Al is considered to be immobile, with Si, K and H treated as passive variables. Fe and Mg are therefore the variables that have controlled texture formation.

No feldspars are identified in the textures or the rock matrix, suggesting that phlogopite-rich biotite was the only K_2O-bearing phase. Furthermore, coarse-grained biotite present within the textures randomly overgrows texture-forming minerals and is inferred to be texturally late and to have not participated in texture formation. Waters (1986a) interprets this type of biotite as the result of minor fluid ingression from leucosomes crystallising in nearby melt-bearing units shortly after the thermal peak. Hence, biotite (and feldspars) are not considered when modelling the development of cordierite–spinel symplectites and the final coronae of sapphirine on spinel in the andalusite-domains. The model system is therefore further reduced to FMAS (with H_2O in excess).

Bimineralic symplectites of spinel and cordierite within the textures (Fig. 4.14) imply the immobility of at least two components, inferred to be Fe and Mg. The sporadic occurrence of corundum and magnetite within the textures (Fig. 4.15) suggests that additional components were locally immobile, potentially Si and Fe^{3+}, respectively. For simplicity however, these features are not considered as the overall textural evolution may be explained using the simplified FMAS model system. The final overgrowth of monomineralic sapphirine separating spinel from cordierite is interpreted in terms of a single immobile component, taken to be Al.

The locus of texture-forming reactions is summarised on a partial petrogenetic grid presented on Figure 7.3. Chemical potential diagrams are shown on Figure 7.4 whereas the preferred textural evolution is summarised in simplified comics on Figure 7.5.

Phase relations and calculated chemical potential relationships

The growth of precursor coarse-grained andalusite is inferred to have occurred at greenschist facies conditions, here approximated with 550 °C and 3 kbar and simulated in the simplified KFMASH model system (Fig. 5.4a). There, the rock is inferred to have consisted of chlorite, muscovite, quartz and andalusite (pie chart on Fig. 5.4a and Fig. 7.5a).

As heating continued, chlorite, muscovite and quartz from the rock matrix reacted with andalusite porphyroblasts to produce cordierite, biotite and hydrous fluid according to reaction 5.4 intersected at ∼555 °C and 3 kbar. The reaction is however inferred to have not

completely consumed the entire grains of andalusite because (i) the formation of haloes of monomineralic cordierite suggests incomplete equilibration and hampered diffusion of at least one component between reaction sites and (ii) some andalusite is inferred to have not reacted with the matrix to then be consumed by spinel + cordierite at later stages of the evolution. It is suggested that in spite of fluid-present metamorphism, the sheer size of porphyroblasts inhibited complete consumption of the aluminosilicate as reaction 5.4 advanced. Furthermore, the formation of cordierite-coronae would obstruct efficient diffusional exchange of andalusite with the matrix if the growth rate of cordierite in the coronae outstrips the rate of diffusion of the slowest-diffusing component involved in corona-formation (cf. Štípská *et al.*, 2010; Baldwin *et al.*, 2015).

To simulate the formation of cordierite-coronae on andalusite, chemical potential relationships are constructed at constant pressure and at temperature just below and above the onset of reaction 5.4 (respective points I and II on Fig. 7.3).

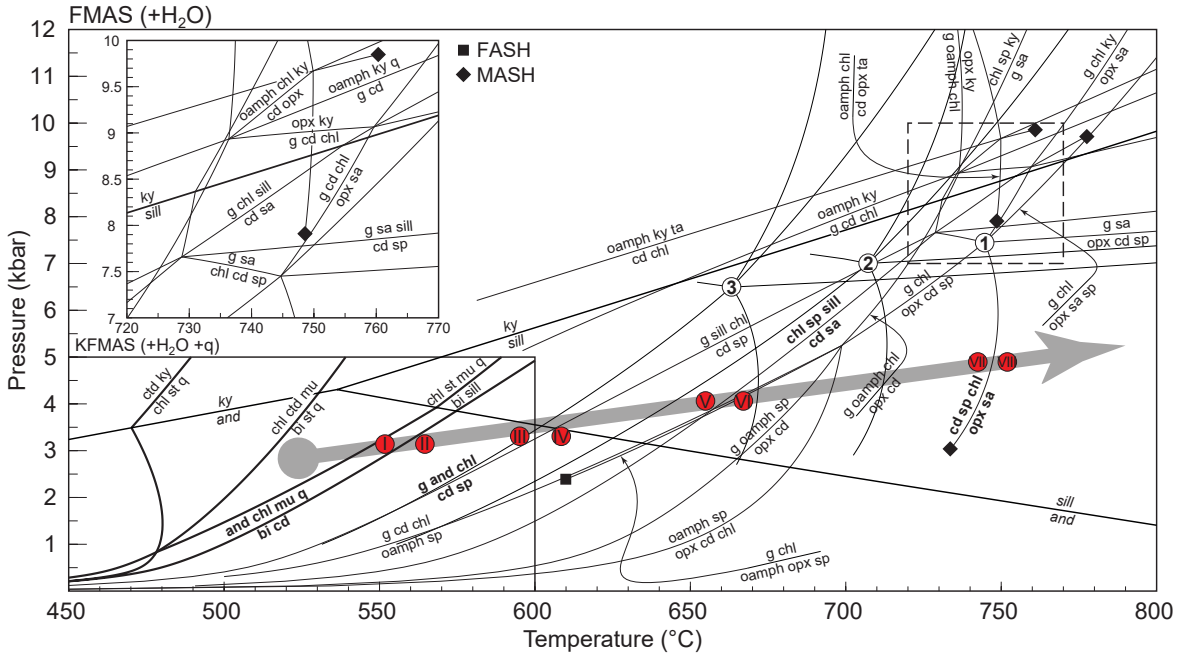


Figure 7.3: Simplified petrogenetic grid calculated in the (K)FMAS model system projected from H_2O. Equilibria are quartz-bearing in KFMAS and quartz-absent in FMAS. Roman numerals in red circles denote P–T conditions where chemical potential relationships are calculated. Arabic numerals 1, 2 and 3 in white circles correspond to the invariant point involving g–cd–chl–opx–sa–sp calculated at decreasing a_{H_2O} of 1.0, 0.8 and 0.6, respectively. Thin tie lines emanating from each point showcase the effect of variable a_{H_2O} on phase equilibria. Grey arrow symbolises the preferred prograde evolution.

On the left-hand side of reaction 5.4 (point I), andalusite, chlorite, muscovite and quartz coexist with either biotite or cordierite. This translates to the related chemical potential diagram presented in Figure 7.4a. There, the interface between a porphyroblast of andalusite and the rock matrix is symbolised by the red line denoting the coexistence of andalusite, chlorite and quartz (with H_2O in excess) at equilibrium. Note that in this case the assemblage

is biotite–muscovite-absent because the tie line is degenerate with respect to K_2O-bearing phases. As reaction 5.4 is crossed (point II), biotite and cordierite must coexist with three phases out of andalusite, chlorite, muscovite and quartz. The advance of reaction 5.4 was necessarily confined to the interface of large grains of andalusite and the rock matrix.

Because Fe and Mg are considered as relatively mobile components compared to Al, corona-formation probably advanced at the expense of andalusite with the reaction front advancing towards the core as portrayed in the texture sketch shown in Figure 7.4b. In μFeO–μMgO-space at set P–T conditions, the texture at this point is chlorite | cordierite | andalusite at conditions symbolised by the red dot (Fig. 7.4b). Reaction 5.4 terminated as soon as the corona of cordierite impeded diffusive exchange between matrix and andalusite, effectively removing andalusite from the reacting assemblage. By contrast, matrix cordierite and biotite (as predicted by pseudosection modelling, Fig. 5.4a) are inferred to have formed due to multivariant reactions independently of aluminosilicate. With the moat of cordierite shielding andalusite, the equilibrium assemblage in the rock matrix would consist of chlorite–biotite–cordierite ± quartz (depending on temperature; Fig. 5.4a) whereas the andalusite-cores form individual domains of local bulk composition in limited diffusional communication with the rock matrix (Fig. 7.5b). From this point onwards, predictions from pseudosection modelling (Fig. 5.4a) based on idealised diffusional exchange and equilibration are no longer applicable.

Further heating and concomitant burial along the inferred path (grey arrow on Fig. 7.3) led to the intersection of the univariant quartz-absent FMASH reaction

$$\text{garnet} + \text{chlorite} + \text{andalusite} = \text{cordierite} + \text{spinel} + H_2O \tag{7.1}$$

at ∼600 °C (Fig. 7.3). On the left-hand side of reaction 7.1 (point III), the stable coexistence of garnet, chlorite and andalusite (+ H_2O) with either cordierite or spinel is postulated. However, in μFeO–μMgO-space relative to the already-formed cordierite-moat on andalusite (red dot on Fig. 7.4c), cordierite is predicted to stably coexist with andalusite. At these fixed P–T–μFeO–μMgO conditions no further changes in assemblage are required because no equalisation of gradients in chemical potential is necessary at the interface of cordierite | andalusite – equilibration is achieved at this point. As soon as reaction 7.1 is crossed during isobaric heating (point IV), the right-hand side assemblage of cordierite and spinel (+ H_2O) with any two out of garnet, chlorite or andalusite must coexist. At the fixed P–T conditions of point IV, to produce the observed symplectites of spinel + cordierite (red dot on Fig.7.4d) at the expense of andalusite (black dot on Fig. 7.4d), diffusion of Fe + Mg along gradients of μFeO and μMgO, respectively, must occur in order to cross the tie line involving the three phases (thick grey arrow and dashed arrow on Fig. 7.4d).

At to upper-amphibolite facies conditions of ∼660 °C and 4 kbar the univariant reaction

$$\text{chlorite} + \text{spinel} + \text{sillimanite} = \text{cordierite} + \text{sapphirine} + H_2O \tag{7.2}$$

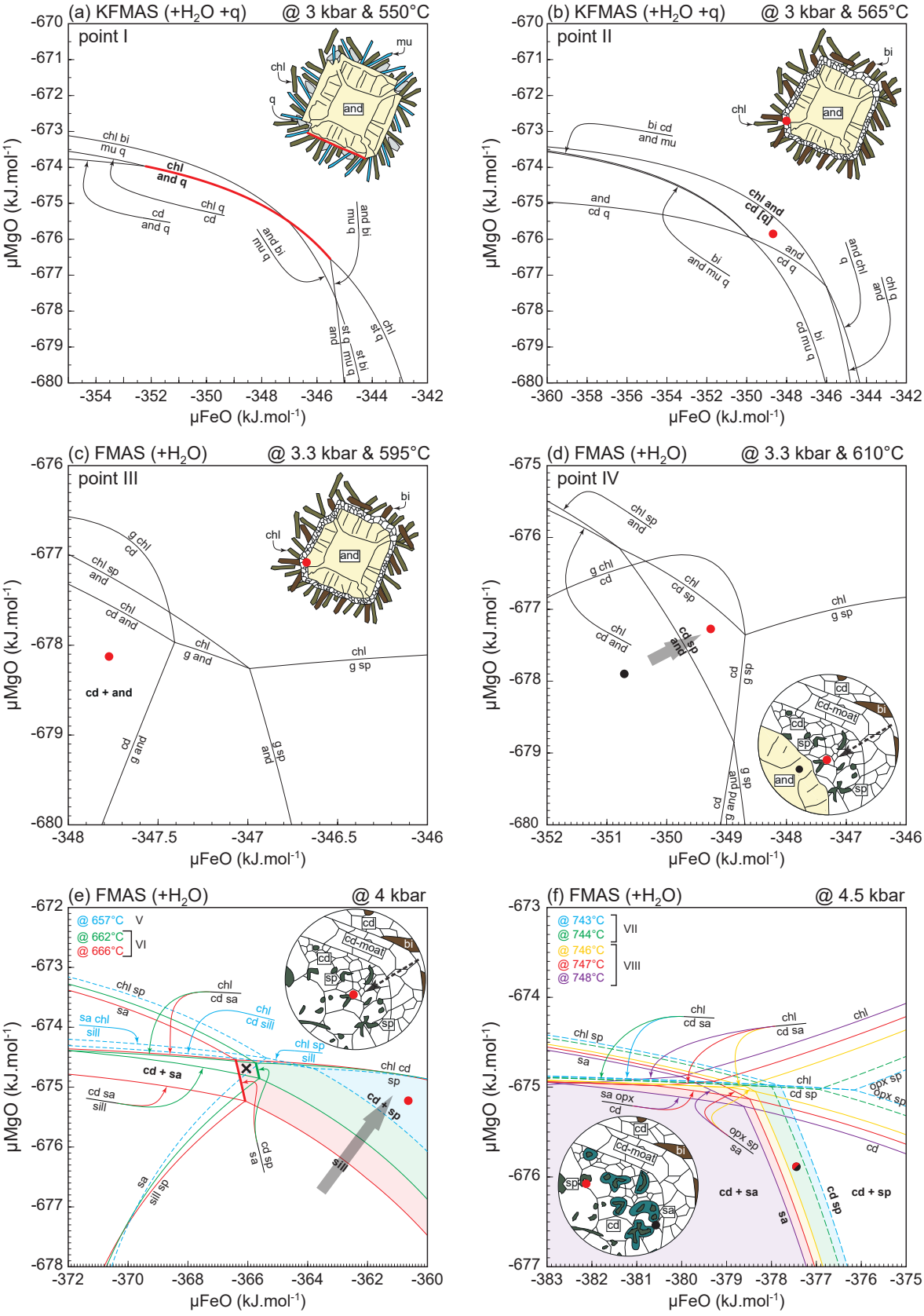


Figure 7.4: Calculated chemical potential relationships.

is intersected. On the low-temperature side of reaction 7.2 the predicted assemblages host clinochlore-rich chlorite, spinel and sillimanite (+ H_2O) with cordierite or sapphirine (point V). On the high-temperature side of the reaction (point VI), cordierite and sapphirine (+ H_2O) coexist with two out of chlorite, spinel and sillimanite. To better showcase the effect of heating on the phase relations, isobaric chemical potential relationships calculated at different temperature are overlain on Figure 7.4e. Of these, the dashed grid corresponds to the left-hand side of reaction 7.2 whereas the solid grids are calculated at increasing temperature on the right-hand side.

Phase relations reveal that the field occupied by cordierite + spinel opens towards lower μFeO–μMgO as temperature increases (shaded areas on Fig. 7.4e). This field is separated from the coexistence of cordierite + sapphirine by a tie line involving all three phases (bold coloured lines in Fig. 7.4e). Cordierite + sapphirine occupy a triangular field which opens as reaction 7.2 is crossed and sweeps towards lower μFeO–μMgO with increasing temperature (green and red diagram on Fig. 7.4e). Hence, at fixed μFeO–μMgO conditions the stable assemblage is controlled by temperature. For instance, at the bold cross cordierite + sapphirine are predicted at 662 °C but as temperature increases the field sweeps across the point of fixed μFeO–μMgO and the cross would switch from the left-hand side of the cd–sp–sa tie line to right-hand side where cordierite + spinel are stable (red area on Fig. 7.4e). Because the inferred peak conditions for Hytkoras are significantly higher compared to the ∼670 °C where the diagrams of Figure 7.4e were calculated, it seems unlikely that the observed coronae of sapphrine on spinel formed according to reaction 7.2. In fact, as temperature increased, the stability field of cordierite + sapphirine would continuously sweep towards lower μFeO–μMgO and hence away from the compositional space occupied by the sapphirine-absent symplectites that formed until this point. Therefore, the stable assemblage with increasing temperature would be cordierite + spinel (Fig. 7.5c).

In conclusion it appears more likely that as reaction 7.2 was crossed the stable assemblage remained unvaried, with continuous consumption of aluminosilicate to produce further symplectites of spinel + cordierite, as indicated by the red dot on Figure 7.4e. In light of the notable dimensions of the former andalusite-porphyroblasts significant diffusion of Fe + Mg into the texture site is expected to produce the observed symplectites (symbolised by dashed arrow on texture-sketch). Such an evolution is consistent with continuous breakdown of andalusite during prograde heating – essentially starting at the intersection of reaction 7.1 at ∼600 °C at the chosen pressure of 3.3 kbar to and beyond the onset of reaction 7.2.

At granulite facies condtions (∼745 °C and 4.5 kbar) the reaction

$$\text{chlorite} + \text{cordierite} + \text{spinel} = \text{orthopyroxene} + \text{sapphirine} + H_2O \tag{7.3}$$

produces the assemblage of chlorite, cordierite and spinel (+ H_2O) in equilibrium with either orthopyroxene or sapphirine at the low-temperature side (point VII). Once reaction 7.3 is crossed, orthopyroxene and sapphirine (+ H_2O) coexist with two out of chlorite, cordierite or spinel (point VIII; Fig. 7.3). Figure 7.4f shows isobaric chemical potential grids calculated

at fixed temperatures on the left-hand side, approaching reaction 7.3 (dashed grids) and on the right-hand side departing from the reaction (solid grids).

Topologically this situation is comparable to Figure 7.4e, with the stability fields of both cordierite + spinel and cordierite + sapphirine sweeping across μFeO–μMgO-space with changing temperature. Similar to the previous case, the predicted assemblage at any given μFeO–μMgO-pair is function of temperature. For example, at composition marked by the dot on Figure 7.4f, the stable paragenesis is cordierite + spinel at >746 °C (red dot on the texture-sketch), but cordierite + sapphirine at <744 °C (black dot on the texture-sketch). Therefore, as the the thermal maximum was reached and reaction 7.3 crossed, the stable texture assemblage is still cordierite + spinel, as predicted from previous calculations (Fig. 7.4e).

However, as roughly isobaric cooling commences from the metamorphic peak, the cd–sp–sa tie line would sweep through compositional space towards higher μFeO (Fig. 7.4e) and produce the observed monomineralic coronae of sapphirine that nucleate on spinel and partially consume the symplectites within the texture (Fig. 7.5d). The incomplete consumption of spinel by thin coronae is consistent with decreasing diffusional length-scales as cooling advances.

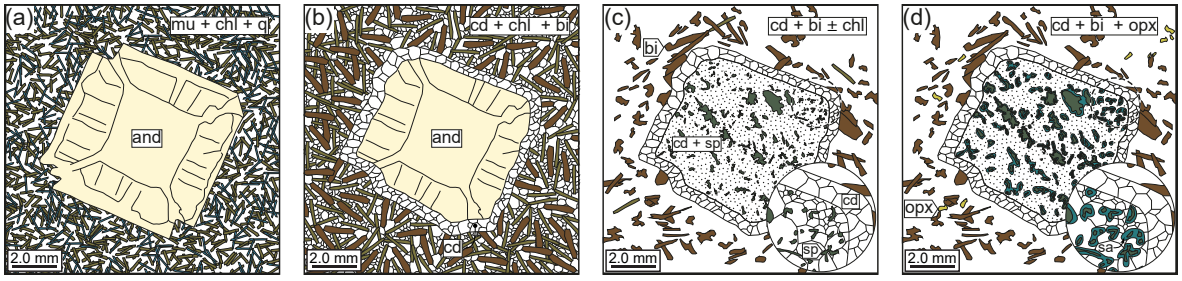


Figure 7.5: Cartoon summarising texture development.

Effect of a_{H_2O}

For granulite-formation at Hytkoras and other localities in the Namaqua Sector, following predictions by Powell (1983b), Waters (1988, 1986a) postulates the development of gradients in μH_2O between partially melted and unmelted lithologies during prograde metamorphism. In this scenario, fertile lithologies with the lowest solidus temperature lowered their effective a_{H_2O} as melting commenced, thereby imposing gradients of μH_2O onto neighbouring subsolidus but fluid-bearing units. Diffusion of H_2O along these gradients is inferred to have dehydrated adjacent rocks thereby preventing them from melting. Interlayered leucosome-present and -absent metapelites (near Bitterfontein, Waters and Whales, 1984) are inferred to have had contrasting a_{H_2O} that precluded melting in otherwise fertile rocks on a meter scale (Waters, 1988). Likewise, Waters (1988) interprets discrete (1–5 cm thick) symmetric anhydrous margins of pyroxene granulite on narrow (10 cm–3 m) layers of hornblende-granulite (cf. Fig. 3.10c) embedded in migmatitic metapelites as an indication for subsolidus dehydra-

tion of the mafic granulite during melting of the metapelite. On a similar note, Mg–Al-rich gneisses are typically fine-grained, granoblastic, leucosome-absent and host coarse grained pseudomorphs after early-metamorphic minerals. Waters (1986a) ascribes the preservation of prograde reaction textures and pseudomorph formation to a switch of fluid-present to fluid-absent conditions in the Mg-Al gneiss due to melting and volatile-scavenging by neighbouring rocks.

The calculations for this section are based on the premise of fluid saturation ($a_{H_2O} = 1$). This assumption is regarded as appropriate up to upper amphibolite facies conditions where neighbouring, more fertile rocks would commence melting (∼700 °C; e.g. Fig. 5.3a). At granulite facies conditions the effective a_{H_2O} of texture-bearing magnesian gneisses (e.g. sample NMC88) potentially was <1, even though it is speculated that these melt-absent rocks might have simply dehydrated during heating, thereby buffering a_{H_2O} at ∼1 – similar to a 'regular' sub-solidus evolution. Nonetheless, to explore the implications of a lowered a_{H_2O}, the phase relations inferred to have produced the sapphirine-coronae within the textures are recalculated using fixed $a_{H_2O} < 1$ (thin lines on Fig. 7.3). As a_{H_2O} decreases, the invariant point in which sapphirine-forming reaction 7.3 terminates is shifted towards lower P–T, but the topology of phase relations remains unvaried. Therefore, a decreased a_{H_2O} would simply shift the conditions of sapphirine-armouring of spinel in the textures towards lower temperature, but does not affect the overall interpretation presented here. It should be noted that if the postulate by Waters (1988) would be applied, i.e. a_{H_2O} of nearby melt-bearing lithologies (e.g. aluminous metapelites) is directly superimposed on refractory units, the minimum a_{H_2O} reached at the metamorphic peak would be ∼0.6 (see appendix E). Even in this extreme case texture formation would follow a grand evolution as described above.

Implications for metamorphic evolution

In summary, the documented textures are consistent with continuous heating and concomitant burial from greenschist conditions (∼550 °C and 3 kbar) to peak granulite conditions. Overall this fits well within the picture of a prograde path dominated by heating rather than compression, as previously suggested here and in the literature. However, contrary to the prediction by Waters (1986a), calculated chemical potential relationships imply that the final coronae of sapphirine on spinel grew during cooling, rather than during heating towards the thermal maximum, as has been suggested for similar coronae of sapphirine consuming spinel in gedritites from north-eastern Russia (Avchenko *et al.*, 2018). Furthermore, sapphirine formed at conditions <750 °C and does certainly not imply UHT conditions in this context. These observations tell a cautionary tale about applying conventional thermobarometry on sapphirine in symplectic textures to invoke extreme metamorphism (cf. Kanazawa *et al.*, 2009; Nishimiya *et al.*, 2010; Shazia *et al.*, 2012; Tsunogae and Santosh, 2003).

7.3 Timescales of sedimentation and metamorphism

U–Pb geochronology and geochemistry on zircon and monazite is used to estimate the temporal framework of deposition and metamorphism of the investigated samples (summarised in Table 6.1). Ages are interpreted in chronological order, beginning with the detrital age spectra and a discussion of potential sediment source regions. Then the timing and timescales of metamorphism are discussed.

7.3.1 Detrital age spectra and origin of detritus

S-type zircons separated from the investigated samples share common characteristics, such as oscillatory CL-zoning pattern typical to zircons crystallised from igneous felsics, such as granites (e.g. Corfu *et al.*, 2003). Morphologically, these zircons are mostly fragmented and rounded, and/or form cores that are overgrown by a second generation of zircon showing low CL-response and/or sector zoning. This is consistent with magmatic zircons being eroded from their hostrock, transported, deposited and finally overprinted by high-grade metamorphism (see below). A magmatic origin of these zircons is supported by their chondrite-normalised REE patterns, showing a positive heavy REE slope, a positive Ce-anomaly and a pronounced negative Eu-anomaly (Hinton and Upton, 1991; Paterson *et al.*, 1992; Hoskin, 1998; Cornell *et al.*, 1999; Hoskin and Black, 2000; Hoskin and Ireland, 2000; Rubatto, 2002).

Age populations of detrital zircons found in metasediments allow to speculate on the possible source from which the detritus derived. Furthermore, the youngest detrital age yields an approximate maximum age of deposition of the sediment. Detrital age spectra from S-type zircons and timing of metamorphism inferred from M-type soccer ball zircons are presented in Figure 7.6. For the investigated samples (from south to north), these are:

1. **Lepel se Kop**: Samples from this locality did not yield any detrital zircons.

2. **Paulshoek**: Dates of S-type zircons recovered from spinel-bearing aluminous metapelite (sample NMC100) reveal a large detrital age spectrum, spanning from about 1860–1100 Ma, with pronounced peaks at *c.* 1800–1700 Ma and 1400–1300 Ma (Fig. 6.4a, c and Table 6.1). Detritus yielding ∼1.9 Ga dates is interpreted to have originated from granitoids and/or volcanics of the Richtersveld Subprovince, such as the Vioolsdrif Domain (1911–1867 Ma; e.g. Macey *et al.*, 2017, and references therein). A portion of data plots around ∼1.7 Ga; these zircons might originate from a so-far undetected/unexposed source region (P. Macey, pers. comm). Detrital ages of *c.* 1300–1250 Ma are consistent with zircons being sourced from volcanosedimentary rocks of the Mesoproterozoic Areachap Domain (*c.* 1.30–1.24 Ga; Cornell and Pettersson, 2007a). However, Raith *et al.* (2003) argue that their 1250 Ma-aged detrital zircons found in a pelitic granulite from Bitterfontein (∼70 km south of Paulshoek) may correspond to ∼1.3 Ga xenocrysts from the Little Namaqualand Suite (Robb *et al.*, 1999). Raith *et al.* (2003) furthermore interpret ∼1.7 Ga old detritus in the same pelitic granulite to also be in-

herited from the Little Namaqualand Suite due to its inferred Sm–Nd crustal residence ages of ∼2.1–1.6 Ga (Clifford *et al.*, 1995; Yuhara *et al.*, 2001). Therefore, zircons with detrital ages of ∼1.7 and 1.5 Ga from Paulshoek fall within this age spectrum and may be interpreted as inherited grains from the Little Namaqualand Suite. Detrital ages of ∼1.2 Ga are attributed to zircons eroded from orthogneisses of the Little Namaqualand Suite (crystallisation ages of 1212–1191 Ma; Robb *et al.*, 1999; Clifford *et al.*, 2004; Macey *et al.*, 2011; Cornell and Pettersson, 2007b). The youngest detrital age from Paulshoek (1100.5 ± 10 Ma; Fig. 6.4a) was calculated from a zircon potentially derived from post-tectonic granitoids found in the Kakamas Terrane with intrusion ages between 1110 and 1078 Ma (the Keimoes Suite; Bailie *et al.*, 2017).

3. **Hytkoras**: Magnesian metapelite (sample NMC37) yielded strictly metamorphic soccer ball-type zircons. Detrital ages for S-type, oscillatory zoned zircons from metagreywacke (sample NMC68) span from *c.* 1850–1580 Ma with a roughly unimodal probability distribution with a maximum at about 1800–1750 Ma (Fig. 6.5c, e and Table 6.1. This age population is consistent with most of the detritus being sourced from the Richtersveld Subprovince, corroborated by characteristic CL-zoning patterns and REE signatures (Fig. 6.1d and 6.5f Rubatto, 2002, and references therein). Significantly younger detrital age groups, in particular dates indicating detritus deriving from the Little Namaqualand Suite, have not been identified from the U–Pb isotopic data. A population of texturally identical grains (stubby to elongated with oscillatory zoned fragments of magmatic zircons at the core, overgrown by rims with weak CL-response) are inferred to have suffered radiogenic Pb loss (type P). They systematically plot along a discordia line (Fig. 6.5d), defining an upper intercept that is consistent with magmatic crystallisation of the zircons at around 1800 Ma (i.e. Richtersveld Subprovince age) that have been affected by younger, high-grade metamorphism (see below).

4. **Nababeep**: Samples from this locality did not yield any detrital zircons.

5. **Ratelpoort**: Oscillatory zoned S-type zircons from the aluminous metapelite (sample NMC21) collected here plot between *c.* 2000–1200 Ma describing a broad peak between ∼1900 and 1700 Ma (Fig. 6.7a, b and Table 6.1). The oldest detrital zircon with a date of 2027.1 ± 18 Ma is inferred to have been eroded from the oldest terrane of the Namaqua Sector, namely the Sprocketing Domain of the Richtersveld Subprovince (∼2.1–2.0 Ga; Thomas *et al.*, 2016). The bulk of detrital grains is interpreted to derive from Richtersveld material; minor radiogenic Pb loss is though to explain the abundant ∼1.7 Ga dates calculated for these S-type zircons. Alternatively, the ∼1.7 Ga population might be inherited from the Little Namaqualand Suite, as previously suggested by Raith *et al.* (2003) for this age population. It can however not be excluded that these zircons derive from a so far unknown Paleoproterozoic crustal source (P. Macey, pers. comm). The youngest detrital age for Ratelpoort (1171.4 ± 21 Ma; Fig. 6.7a) falls within error of the inferred temporal range of crystallisation of the voluminous Little Namaqualand

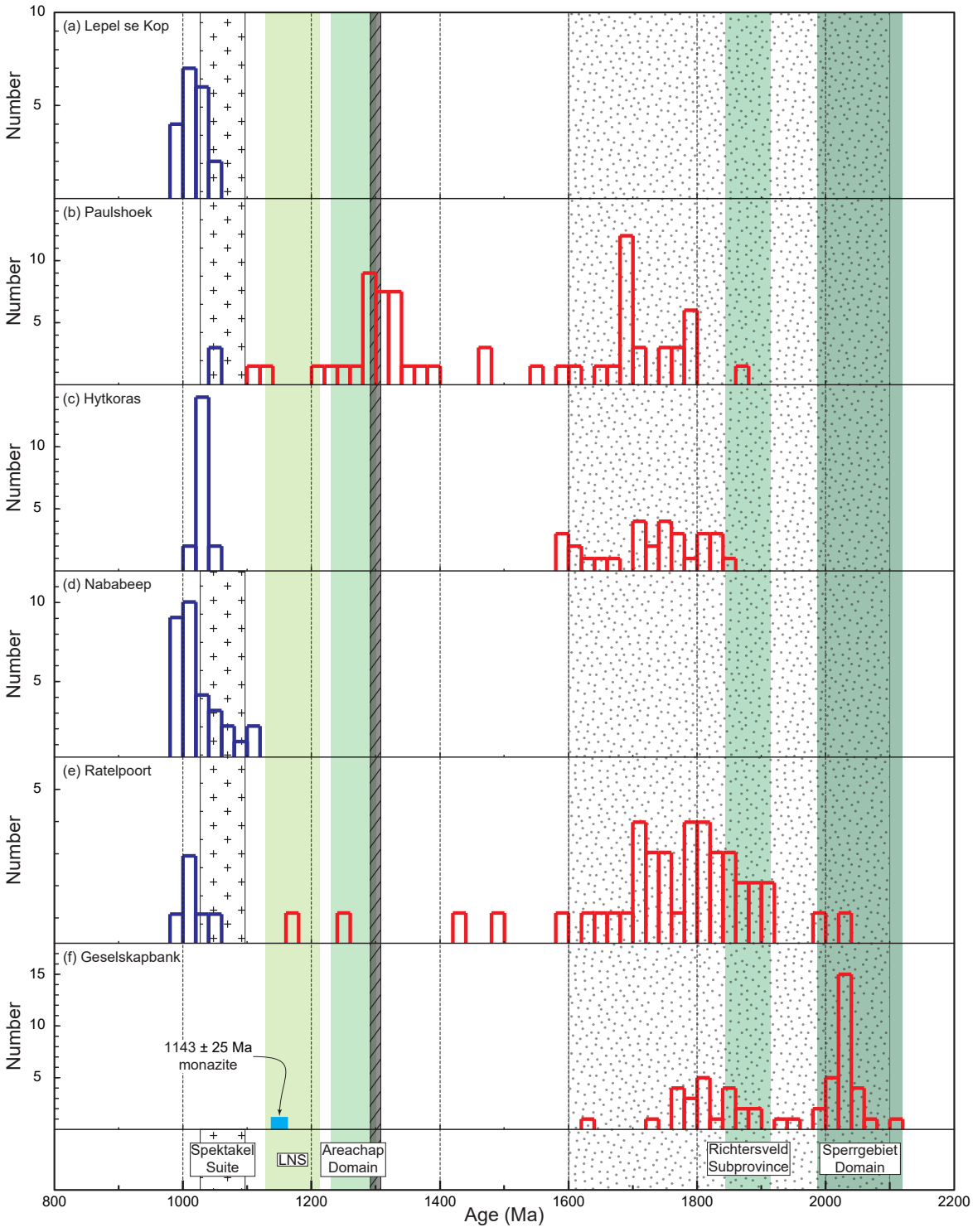


Figure 7.6: Age histogram of zircon ages ($^{207}Pb/^{206}Pb$ dates) for S-type (red boxes) and M-type zircons (blue boxes) summarising detrital and metamorphic ages for sample localities of the BSP. Age intervals corresponding to potential source regions are highlighted: Sperrgebiet Domain, Richtersveld Subprovince, Areachap Domain and Little Namaqualand Suite (LNS). Dotted shading brackets inferred LNS Sm–Nd crustal residence ages of ∼2.1–1.6 Ga (Clifford *et al.*, 1995; Yuhara *et al.*, 2001), hatched shading corresponds to ∼1.3 Ga xenocrysts from the LNS (Robb *et al.*, 1999). Crossed shading indicates intrusion ages of the Spektakel Suite (1097–1033 Ma; Macey *et al.*, 2018).

Suite (1212–1191 Ma; Robb *et al.*, 1999; Clifford *et al.*, 2004; Macey *et al.*, 2011; Cornell and Pettersson, 2007b).

6. **Geselskapbank**: S-type zircons of the amphibolite (sample NMC11) yield detrital ages falling preferentially between *c.* 2100–1600 Ma, with a dominant probability peak at *c.* 2.0 Ga and minor peaks spread over 1.9–1.7 Ga (Fig. 6.8a and Table 6.1). All analysed grains display CL-oscillatory zoning, a strong positive Ce-anomaly and steep heavy REE slopes, all inferred to point towards a magmatic origin of these detrital grains (Fig. 6.1g and 6.8b; Rubatto, 2002, and references therein). The Sperrgebiet Domain (Thomas *et al.*, 2016) is regarded as a feasible provenance for the zircons of the older, dominant age population of ∼2.0 Ga. The slightly younger zircon population with ages peaking around 1.8 Ga is inferred to derive from the Richtersverld Subprovince (e.g. Macey *et al.*, 2017) and/or gneisses of the Gladkop Suite (∼1.84–1.82 Ga; Van Aswegen, 1983), in line with detrital ages of amphibolites from the Bushmanland Group at Aggeneys (Bailie *et al.*, 2007). Of the inferred S-type detrital zircons, the youngest yields a date of ∼1.6 Ga, inferred to represent the maximum depositional age of the protolith. A number of texturally identical grains are interpreted to have been affected by ancient Pb loss during a younger thermal overprint (see below). The upper intercept of a linear regression through this data are consistent with detritus provenance from a ∼2.0–1.9 Ga source (Fig. 6.8a). The migmatite from this locality did not contain any zircons.

7.3.2 Timing of regional high-T–low-P metamorphism

Soccer ball-type zircons are thought to newly crystallise from anatectic melts following HT- to UHT granulite metamorphism (e.g. Taylor *et al.*, 2016) and are routinely used to constrain the timing of high-grade metamorphism (e.g. Mitchell *et al.*, 2018; Clark *et al.*, 2018; Korhonen *et al.*, 2013b). It is generally accepted that the U–Pb age recorded by these zircons corresponds to cooling through the elevated residuum solidus at the end of a thermal event (Kelsey, 2008; Taylor *et al.*, 2016; Corfu *et al.*, 2003); the ages of M-type soccer ball zircons presented here are therefore interpreted as minimum ages of high-grade metamorphism (cf. Roberts and Finger, 1997). Chondrite-normalised REE spectra reveal a largely missing positive Ce-anomaly, a limited negative Eu-anomaly and predominantly flat heavy REE slopes, consistent with concomitant zircon–garnet growth (Rubatto, 2002). In the case of the aluminous metapelites investigated here this likely coincides with the advance of reaction 2.8, in line with interpretations on similar rocks from the Reynolds Range (Australia; Rubatto *et al.*, 2001; Rubatto, 2002).

Monazite formed in granulite facies rocks commonly returns similar ages to zircon as a result of melt–mineral interaction at high-grade conditions (e.g. Hermann and Rubatto, 2003), however examples of granulite metamorphism where ages of metamorphic monazite dates postdate that of zircon have been described (e.g. Clark *et al.*, 2014). Contrasting Pb closure temperatures between the minerals have been invoked to explain monazite recording

younger ages compared to zircon, however thermobaric modelling of zircon and monazite growth in anatectic systems suggests that the discrepancy in recorded age is due to different temperature(s) at which zircon and monazite grow (Kelsey *et al.*, 2008).
Timing of regional metamorphism for the sampled localities is graphically summarised in Figures 7.6 and 7.7 and is as follows (from south to north):

1. **Lepel se Kop**: Soccer ball zircons record high-grade metamorphism at *c.* 1020 Ma (Fig. 6.3a, b and Table 6.1), however these results need to be interpreted with care due to matrix effects affecting the analyses (see subsection 6.2.1). Monazites return concordant ages peaking at around 1045 Ma (Fig. 6.3d, e), interpreted as timing of metamorphism. Due to the mentioned caveats, granulite metamorphism is inferred to have peaked between 1045–1020 Ma (Fig. 7.6a and 7.7a).

2. **Paulshoek**: Metamorphic zircons record a Concordia age of 1043 ± 11 Ma (Fig. 6.4a and Table 6.1) whereas monazites return a weighted mean age of 1035.6 ± 3.9 Ma (Fig. 6.4e and Table 6.1). These dates overlap within error; granulite metamorphism is therefore inferred to have affected Paulshoek at *c.* 1040–1035 Ma (Fig. 7.6b and 7.7b).

3. **Hytkoras**: All soccer ball zircons extracted from magnesian metapelite record high grade metamorphism at *c.* 1030 Ma; REE-plots reveal that zircons may be grouped in a cluster of heavy REE-depleted grains (black profiles on Fig. 6.5b) and one that is enriched in heavy REE (red profiles on Fig. 6.5b). Both the limited age scatter and the textural characteristics of the ablated zircons are consistent with neocrystallisation from anatectic melts at or around the timing of the thermal peak. The contrasting REE trends are therefore thought to be controlled by the dominating melting reaction(s) occurring at / or immediately prior to zircon growth. In this particular sample REE-depleted zircons may reflect the advance of reaction 2.8 that produces abundant peritectic garnet alongside other solids and melt. Because both garnet and zircon are enriched in heavy REE, concomitant nucleation of the two will affect each other's composition (Rubatto, 2002). Hence, assuming equilibrium between garnet–melt and zircon–melt, the zircons showing heavy REE depletion are inferred to record the timing of main garnet growth, which in this sample (and aluminous metapelites *sensu latu*) coincides with the advance of reaction 2.8. By contrast, the main assemblage-forming reaction 5.1 which affected the magnesian metapelite consumes garnet and biotite to produce melt and orthopyroxene. The resulting melt is therefore enriched in components previously sequestered by garnet, including heavy REE. Zircons crystallising from this melt would hence also be enriched in heavy REE, such as the dominant group symbolised by the red lines on Figure 6.5b. Seeing that there is no resolvable difference in the recorded U–Pb ages it is suggested that both reaction 2.8 and 5.1 occurred subsequently in a rather short timespan, of the order of ∼10 Ma. However, a certain component of REE budget inherited from subsolidus/detrital zircons might have affected the measured composition, even though this cannot be identified from carefully

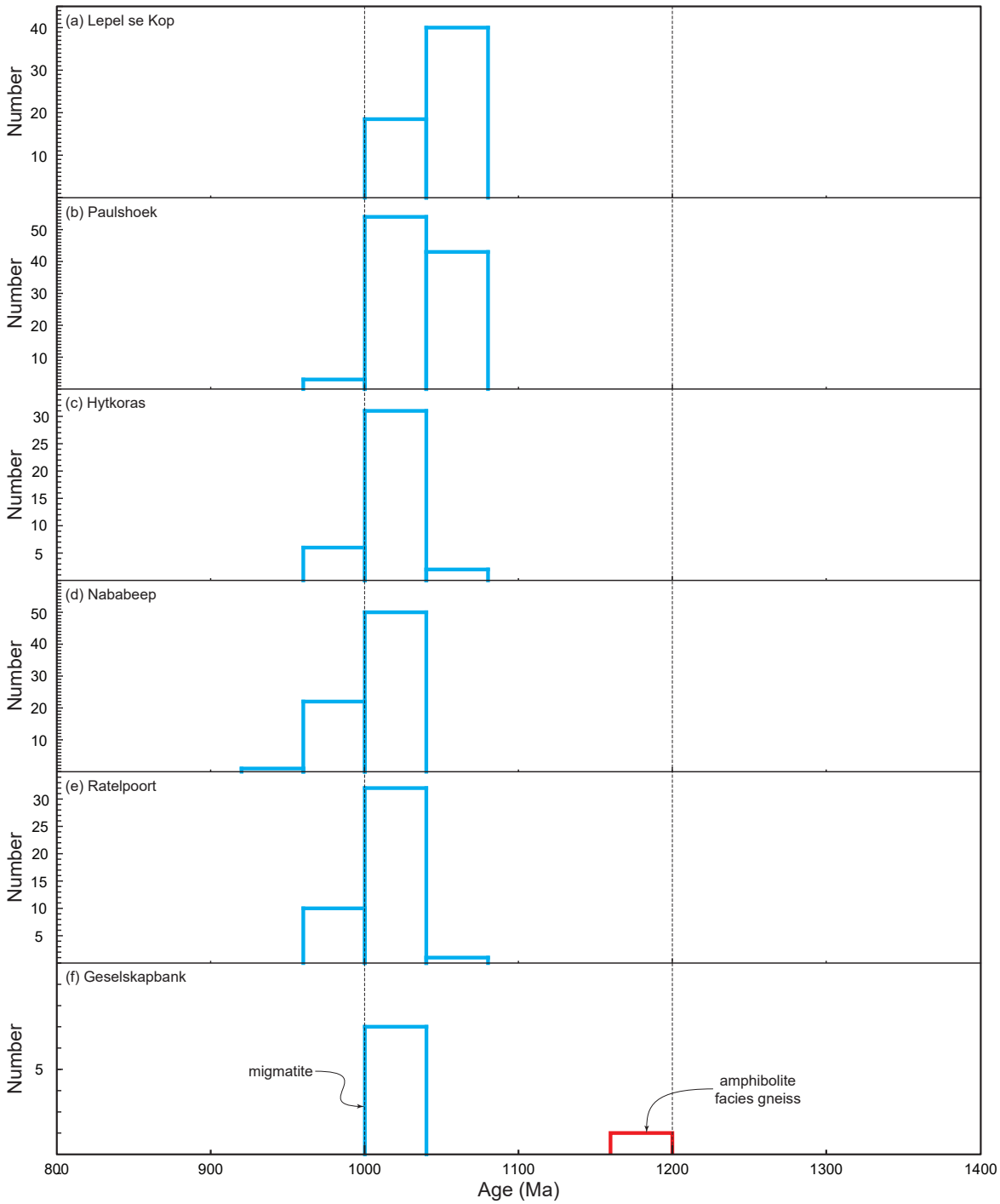


Figure 7.7: Age histogram of monazite ages ($^{238}U/^{206}Pb$ dates) summarising metamorphic ages for sample localities of the BSP.

studied CL-imagery.

A single metamorphic zircon from the metagreywacke collected at Hytkoras returned a poorly constrained date of 1043.8 ± 22 Ma (Fig. 6.5c). Monazites of the same sample yielded a weighted mean age of 1017.7 ± 5 Ma (Fig. 6.5g), which, within error, overlaps with the zircon-age. From both samples the timing of peak metamorphism at Hytkoras is constrained to have occurred between ∼1030–1020 Ma (Fig. 7.6c and 7.7c).

4. **Nababeep**: Ablations of metamorphic zircons from this sample are affected by matrix effects; the results are therefore interpreted with care. Zircons record high-grade metamorphism at *c.* 1000 Ma (Fig. 6.6a and 7.6d), consistent with highly concordant age data calculated from monazite ablation of the same sample (Fig. 6.6c and 7.7d).

5. **Ratelpoort**: Zircons record metamorphism at *c.* 1019 Ma (± 22 Ma; Fig. 6.7a and Table 6.1), however the data are inferred to have been affected by matrix effects. Monazites from the same aluminous metapelite return a well-constrained weighted mean age of 1008.9 ± 4.2 Ma (Fig. 6.7c and Table 6.1). Therefore, granulite metamorphism is inferred to have occurred at *c.* 1000 Ma at Ratelpoort (Fig. 7.6d and 7.7d).

6. **Geselskapbank**: Whereas the investigated amphibolite facies metapelite contained abundant detrital zircons, it is devoid of grains displaying clearly metamorphic textures. The timing of metamorphism is therefore rather loosely constrained. The upper limit for the timing of metamorphism for this sample is constrained by the youngest detrital age of ∼1.6 Ga (Fig. 6.8a). A series of grains are inferred to have been affected by radiogenic Pb loss; the lower intercept calculated for this population is consistent with partial reopening of the U–Pb isotopic system at around ∼1100 Ma, further corroborated by a single concordant monazite ablation yielding 1143 ± 25 Ma. Amphibolite facies metamorphism is therefore inferred to have occurred at *c.* 1140–1100 Ma at Geselskapbank (Fig. 7.6f and 7.7f).

   The sample of allochtonous migmatite was devoid of zircon, but an age of 1018.7 ± 9.5 Ma for migmatisation is calculated from monazite ablation. The timing of juxtaposition of the migmatitic portion onto the amphibolite facies part of Geselskapbank is a matter of speculation. The tectonic emplacement must however postdate the timing of peak metamorphism and partial melting in the migmatites, because reworking during juxtaposition is inferred to have not exceeded conditions of chlorite stability (see above).

Chapter 8

Concluding remarks

Until this point most part of this thesis was concerned with gathering petrographic and mineral chemical information that was distilled via thermodynamic modelling and augmented with U–Pb geochronology, to yield the most fundamental geodynamic parameters: pressure – temperature – timing of metamorphism.

In a first instance, these parameters are interpreted in a classical way, to better understand the piece of crust where they have been sampled from. Following this large-scale characterisation, rocks that coexist at a single locality are interrogated from a metamorphic heat budget-perspective – to show that even though the rocks had the same energy at their disposal, they might actually not have reached the same thermal conditions because of their strongly contrasting behaviour during partial melting. This point of view is then extrapolated to the rocks from Namaqualand as a whole, showing that the exact temperature that is estimated from thermobarometric constraints might not be that fundamental – but how the geographical distribution of recorded temperature might yield clues in identifying the heat source(s) that caused it.

8.1 Tectonometamorphic characteristics of the Namaqua Sector

The inferred pressure–temperature–time evolution for each sampling locality is portrayed and compared to published data on Figure 8.1; the geographical P–T–t distribution is graphically summarised on Figure 8.2. Overall apparent peak temperatures strongly vary between ∼650 °C at Aggeneys (Diener, 2014) to almost UHT conditions estimated for granulites at Paulshoek (also see Waters, 1989, 1986b, 1991) and Ratelpoort. This is in sharp contrast to the pressure recorded at the respective thermal peak, which tightly clusters at 5–6 kbar (equivalent to ∼19–22 km depth assuming an average crustal density of 2750 kg.m^{-3}). Moreover, results from zircon–monazite geochronology indicate a roughly contemporaneous attainment of peak conditions for the entire Bushmanland Subprovince (see Raith *et al.*, 2003).

Early prograde P–T paths are commonly constrained to have commenced within the

stability field of andalusite (Waters, 1990; Raith and Harley, 1998; Diener *et al.*, 2013, this study) and are dominated by heating with only minor concomitant compression followed by slow isobaric cooling. This is consistent with the fact that a thermal perturbation, rather than crustal over-thickening, caused the high-grade metamorphism (see Diener, 2014). The overall *P–T* evolution for the BSP follows anticlockwise paths, which is consistent with previous interpretations (Waters, 1986b, 1989; Raith and Harley, 1998; Robb *et al.*, 1999). However, in detail some localities (e.g. Hytkoras) preserve textures that are consistent with a clockwise prograde path with a hairpin-type loop at/close to the thermal maximum, similar to the documented evolution of the Aus Domain (Diener *et al.*, 2013). This is not seen to stand in conflict with previous interpretations, because this type of *P–T* path is still one dominated by heating and cooling, and it is argued that simply not all rocks preserve textures that allow for a detailed evaluation of the full tectonometamorphic evolution.

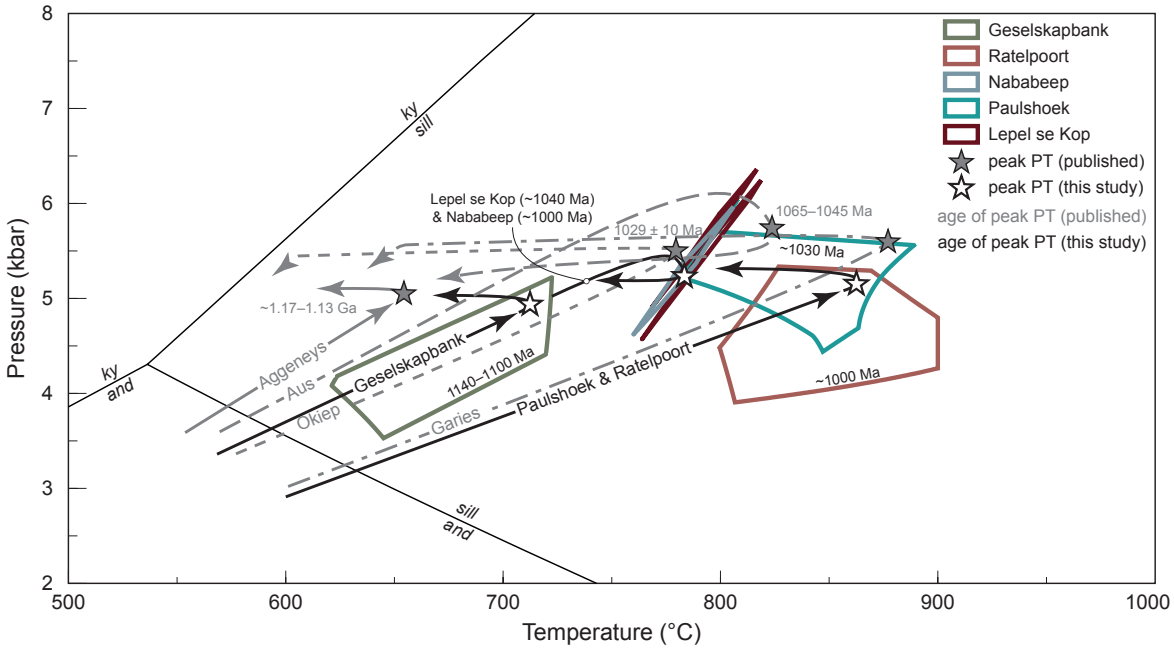


Figure 8.1: Summary of metamorphic peak conditions, timing of thermal peak and *P–T* paths for the Namaqua Sector. Paths are from Waters (1989) for the Garies terrane, Raith and Harley (1998) for the Okiep terrane, Diener (2014) for the Aggeneys terrane and Diener *et al.* (2013) for the Aus Domain.

Metamorphic peak conditions estimated here and published *P–T* paths confirm that all terranes of the western Namaqua Sector and the BSP in particular, have experienced high-grade metamorphism along average (Clifford *et al.*, 1975b) to elevated geotherms (Fig. 8.1; Waters, 1986a,b, 1988, 1989; Diener *et al.*, 2013; Diener, 2014; Bial *et al.*, 2015; Robb *et al.*, 1999; Raith *et al.*, 2003; Nowicki *et al.*, 1995). Of these, the Aggeneys terrane in the northeast apparently records the lowest conditions, even though of intermediate–upper amphibolite grade. Estimated peak conditions of ~650 °C and 5 kbar (Diener, 2014) are consistent with an average apparent geotherm of ~130 °C/kbar (or 35 °C/km for an average crustal density of

2750 kg.m^{-3}). The other terranes, including the upper amphibolite facies rocks at Geselskapbank, require significantly higher geotherms of between *c.* 140–160 °C/kbar (∼38–45 °C/km) to reach their respective recorded peak conditions. Of these, the localities Lepel se Kop and Nababeep record conditions that correspond to a similar geothermal gradient recorded by the amphibolite facies gneisses of Geselskapbank at slightly lower pressure (Fig. 8.1). Roughly the same geotherm is recorded by both the Okiep terrane (Fig. 8.1; Raith and Harley, 1998) and the Aus Domain (Fig. 8.1; Diener *et al.*, 2013). The highest metamorphic grade and geothermal gradients are recorded by units located in the central BSP (locality Paulshoek; upper granulite facies 'zone C' of Waters, 1986b, 1989) and the locality Ratelpoort, which, according to named studies, would fall at the northern boundary of lower granulite facies 'zone B' (Fig. 8.2). This suggests that the metamorphic isograds that have been cited in numerous studies since their publication might not be accurate.

Waters (1986b) takes the onset of reaction 2.8 as lower boundary for granulite facies conditions. However, as pointed out several times in this manuscript, it is important to determine whether or not the reactants biotite and/or sillimanite were part of the stable peak paragenesis and by implication whether or not the reaction went to completion. In the field it is however not always trivial to confidently do so. Whereas the *onset* and *advance* of reaction 2.8 may well be occurring at broadly constant and most importantly narrow P–T pairs for a wide range of pelitic compositions *s.l.*, biotite and/or sillimanite-absent assemblages are consistent with conditions well beyond 'lower granulite' facies conditions. Therefore, effectively biotite and/or sillimanite-absent pelitic granulites, such as those sampled at Ratelpoort, may as well record upper-, rather than lower granulite facies conditions. Moreover, Waters (1986b) approximates the conditions implied by the onset reaction 2.8 in metapelites with the transition of amphibolite- to two-pyroxene granulite in mafic lithologies. This is particularly problematic because at given pressure, the temperature at which orthopyroxene appears in mafic rock types is, in contrast to the onset of reaction 2.8 in pelitic rocks, strongly dependent on bulk composition and may vary significantly (see Palin *et al.*, 2016a; Stuck and Diener, 2017).

However, the apparent discrepancy between the thermal maxima recorded by rocks with strongly different bulk composition might be a consequence of thermal effects of melting reactions and is discussed later in this chapter.

8.1.1 Temporal relationship between sedimentation and metamorphism

As summarised in the previous chapter, all granulites record metamorphism between 1040–1000 Ma, peaking at *c.* 1030 Ma. U–Pb dating of metamorphic rims on igneous zircons of the Little Namaqualand Suite (Robb *et al.*, 1999; Clifford *et al.*, 2004; Raith *et al.*, 2003; Cornell and Pettersson, 2007b) and zircon overgrowths in pelitic amphibolites and granulites (Clifford *et al.*, 2004; Robb *et al.*, 1999; Raith *et al.*, 2003), suggest that "high-T, low-P metamorphism was broadly coeval in the northern amphibolite and lower- to upper-granulite zones of the Bushmanland Terrane" (Raith *et al.*, 2003).

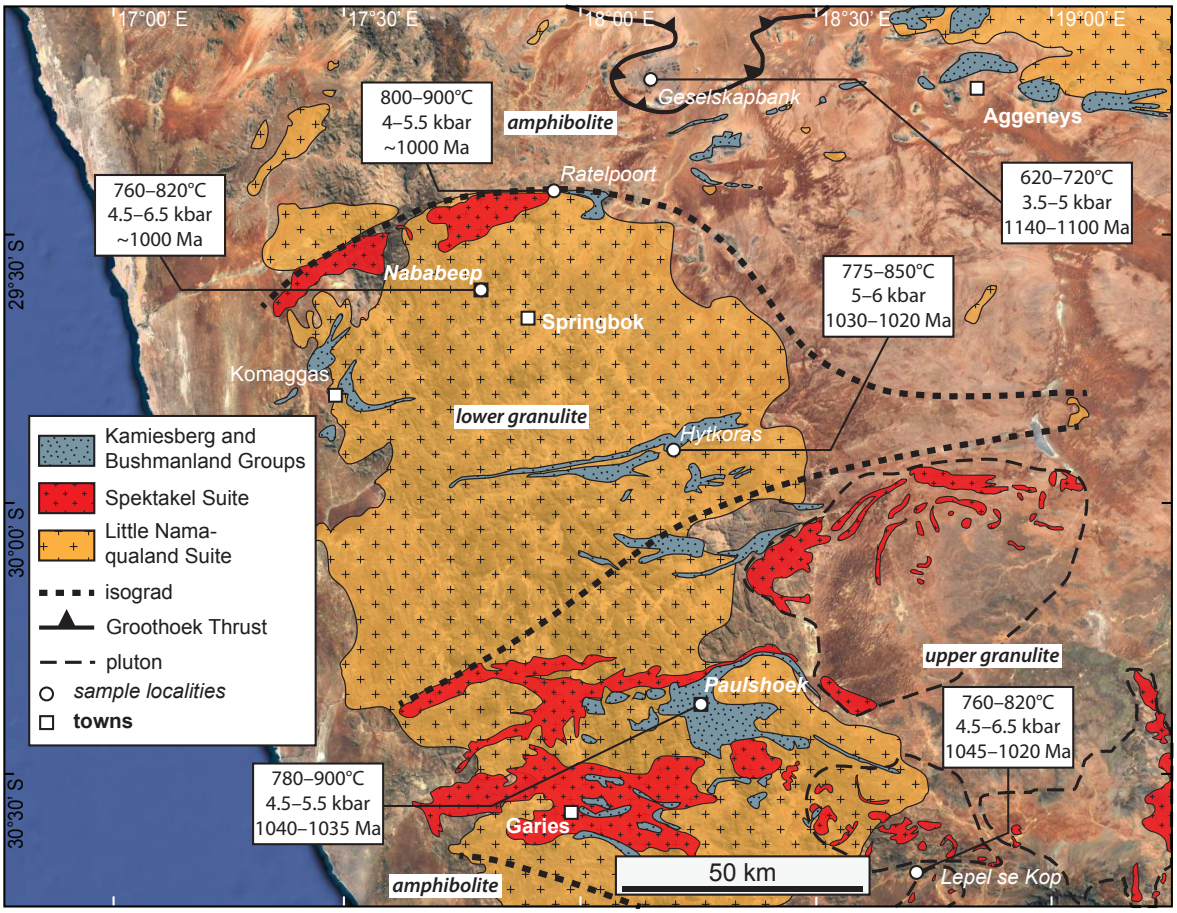


Figure 8.2: Map of the Bushmanland Subprovince summarising calculated peak *P–T* conditions and inferred timing of peak metamorphism. Allochtonous units (i.e. migmatites at Geselskapbank) are omitted. Overlain is the geographic distribution of supracrustals of the Kamiesberg and Bushmanland Groups, the Little Namaqualand Suite (crystallisation age of 1212–1191 Ma; Robb *et al.*, 1999) and Spektakel Suite (intrusion age of 1097–1033 Ma; Macey *et al.*, 2018). Thick dotted line represents metamorphic isograds after Waters (1986b, 1989). Background map from Google Earth®, lithological map simplified after Macey *et al.* (2018).

By contrast, detrital age spectra are highly variable between samples. For example, the aluminous metapelites collected at the localities of Paulshoek and Ratelpoort contain detritus inferred to be sourced from the voluminous Little Namaqualand Suite (Fig. 7.6 and 8.2). This implies that sedimentation postdates LNS emplacement (see Raith *et al.*, 2003). Part of the pre-LNS detritus found in these samples might represent a population of inherited xenocrysts from the LNS itself. By contrast, only pre-LNS detritus is detected in the samples from the other localities (Fig. 7.6). Notably, the dominant detrital age group becomes gradually older from south to north (Fig. 7.6). In the case of the amphibolite facies pelite collected at the northernmost locality of Geselskapbank, the dominant detrital age group is Paleoproterozoic, consistent with sediment deriving predominantly from the Sperrgebiet Domain to the north (Thomas *et al.*, 2016). Additionally, age groups consistent with the Richtersveld Subprovince as main source region have been identified in all detrital age spectra (Fig. 7.6). Detritus potentially deriving from the Areachap Domain (Cornell and Pettersson, 2007a) has also been identified, suggesting that no major tectonic displacement has occurred since erosion and deposition of the sediments, and the structural architecture of the western Namaqua Sector may be largely unchanged since these ancient times.

In summary, rocks from the BSP record similar high-grade metamorphism persisting over a vast areal extent (∼25.000 km^2) at comparable times. The localities Paulshoek and Ratelpoort record granulite conditions postdating the age of the youngest detritus (i.e. maximum age of deposition) by some 70 and 140 Ma. This time interval places a maximum duration for metamorphism at the two localities. This is in strong contrast to locality Hytkoras, where the youngest detrital age of *c.* 1580 Ma implies a hiatus between sedimentation and metamorphism of more than *c.* 550 Ma. Therefore, there seems to be no unique or straightforward temporal relationship between the timing of sedimentation and metamorphism and therefore no unequivocal link between the cause of the two processes.

8.1.2 Correlation of plutonism and metamorphism

Figure 8.3 highlights the strong temporal correlation of voluminous plutonism and high-grade metamorphism in the BSP. Overgrowths on magmatic/detrital zircons and sector zoned zircons record metamorphism at two distinct periods, with one older, minor age group at between *c.* 1200–1170 Ma and a younger, main age group at between 1070–990 Ma.

Early Namaquan ∼1.2 Ga amphibolite facies metamorphism

Metamorphic overgrowths on magmatic zircons of the Nababeep Gneiss (northern granulite zone) of the LNS record overprinting at *c.* 1165 Ma, interpreted as potential contact metamorphism caused by the intrusion of the Modderfontein Gneiss at ∼1200 Ma (Robb *et al.*, 1999). Raith *et al.* (2003) report metamorphic rims overgrowing detrital zircons recovered from a quartzo-feldspathic rock located within the southern amphibolite facies zone yielding an age of 1187 ± 15 Ma. Similarly, U–Pb geochronology on monazite presented here

constrains upper-amphibolite facies metamorphism at 1143 ± 25 Ma for Geselskapbank in the northern BSP (Fig. 7.6, 7.7 and 8.3). It is therefore concluded that the major ∼1.2 Ga tectono-magmatic event and voluminous LNS (*s.l.*) plutonism in the BSP (1212–1191 Ma; Robb *et al.*, 1999; Clifford *et al.*, 2004; Macey *et al.*, 2011; Cornell and Pettersson, 2007b) was accompanied by local contact metamorphism apparently not exceeding upper amphibolite facies conditions (Raith *et al.*, 2003; Bailie *et al.*, 2007, this study).

It is not yet resolved whether the amphibolite facies Aggeneys terrane (e.g. Diener, 2014) in the northern BSP recorded and preserved this type of early Namaquan contact metamorphism and/or the younger Namaquan event did not reach granulite facies conditions in this part of the Namaqua Sector. Whereas Diener (2014) does not recognise petrographic evidence for polymetamorphism in his samples, Bailie *et al.* (2007) present geochronological evidence for two distinct events recorded at Aggeneys. Overgrowths on detrital zircons record an event between ∼1.21 to ∼1.18 Ga (the so-called 'Kibaran' Orogeny) associated with extensive LNS magmatism, peak D_2 deformation and upper amphibolite facies M_2 metamorphism. Younger overgrowths dated at ∼1.04–1.01 Ga record the main Namaquan overprint (Bailie *et al.*, 2007). It appears therefore plausible that at both amphibolite terranes of Aggeneys and Geselskapbank, main metamorphism was related to voluminous ∼1.2 Ga LNS plutonism and the subsequent Namaquan metamorphism was of lower grade, not recorded due to fluid-absent conditions (Guiraud *et al.*, 2001; Tenczer *et al.*, 2006; Schorn, 2018) and/or restricted to localised fluid infiltration and minor metasomatism without obliterating older fabrics. Local growth of zircon and retrograde muscovite (Willner, 1995) may be related to this small-scale overprint that left the bulk of the terranes largely unaffected (Diener, 2014).

Both terranes are akin in terms of metamorphic evolution and detrital age spectra. These indicate mixed Paleoproterozoic source regions (∼2.12–1.97 and ∼1.88 Ga–1.64 Ga; Bailie *et al.*, 2007, this study), which are identified here as the Sperrgebiet Domain and the Richtersveld Subprovince. However, it is pointed out that an allochtonous origin of all samples from Geselskapbank, not only of the migmatites, can not be excluded. Further detailed mapping and geochronological sampling is under way to address this question (P. Macey, pers. comm).

In line with local contact metamorphism accompanying LNS magmatism, the inferred upper greenschist/lower amphibolite facies conditions ($< 550\,^{\circ}C$ and < 4.5 kbar) preserved by magnesian gneisses at Hytkoras – with a youngest detrital age of ∼1.6 Ga (see subsection 6.2.3) – are attributed to contact metamorphism related to voluminous LNS-plutonsim. The Mesklip Gneiss (1199 ± 12 Ma; e.g. Robb *et al.*, 1999) and Nababeep Gneiss (1212 ± 11 Ma; e.g. Robb *et al.*, 1999) of the LNS are dominant at this locality (see section 3.5) and constrain the timing of this metamorphism with their age of emplacement. As seen in most samples from Hytkoras and most parts of the BSP however, the Early Namaquan ∼1.2 Ga amphibolite facies event has been largely overprinted by the ∼1.03 Ma granulite metamorphism and the corresponding assemblages obliterated.

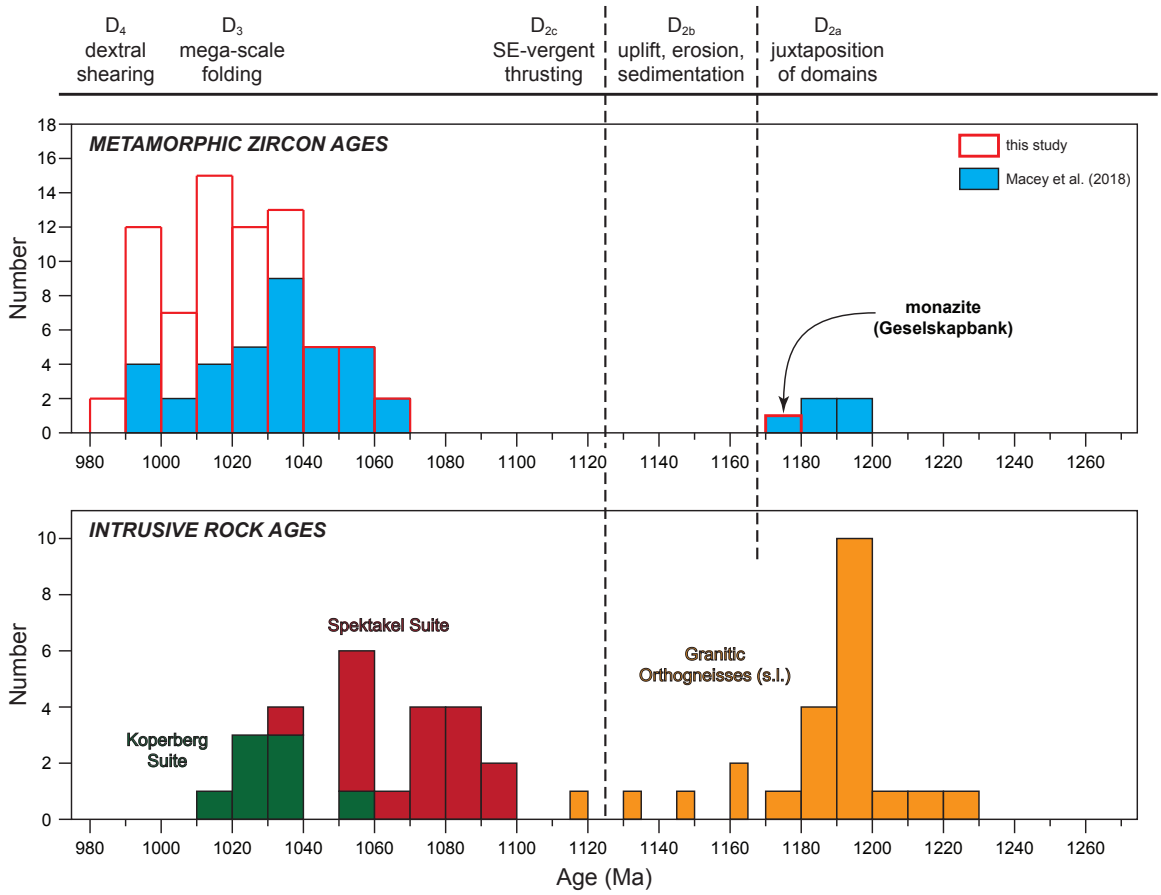


Figure 8.3: Summary of main tectonic, magmatic an metamorphic events in the BSP through time after Macey *et al.* (2018). Data from this study are $^{207}Pb/^{206}Pb$ zircon ages; quoted zircon ages are from Macey *et al.* (2018) and references therein.

Main Namaquan ∼1.03 Ga granulite facies metamorphism

Metamorphic zircons in granulites constrain the timing of high–T metamorphism of ∼780–850 °C and 5–6 kbar at c. 1030 Ma (Fig. 8.1). The highest conditions are estimated for the localities Paulshoek and Ratelpoort, both characterised by large outcrops of the Spektakel Suite (Fig. 8.2). Macey *et al.* (2018) interpreted the geographical distribution of the latter coinciding with the upper granulite facies conditions as well as the temporal correlation of plutonism and metamorphic zircon growth between ∼1065 and 990 Ma in terms of a causal link between the two events (Fig. 8.3). The authors suggest that the "prolonged period of intrusion of the Spektakel Suite raised the geothermal gradient through advective heat transfer into the crust resulting in low-P and high-T metamorphism", consistent with previous interpretations (Waters, 1986b, 1989; Robb *et al.*, 1999). The Spektakel Suite is however not regarded as the primary heat source, for which the authors refer to a combination of mafic underplating (Waters, 1986b, 1989, 1990) and radiogenic heating (Andreoli *et al.*, 2006) as discussed later in this chapter.

This scenario is adopted for the most localities investigated here, however it is rejected for the main study area of Hytkoras where the Spektakel Suite is notably absent (Fig. 7.6 and 8.2). It is possible that related plutons have not been identified yet, are not exposed or, of course, are entirely absent (see figure 2 in Macey *et al.*, 2018). In any case, samples from this locality record comparable granulite metamorphism at the same time as other parts of the BSP. The extensive hiatus between sedimentation and high-grade metamorphism observed at Hytkoras, combined with lower-grade metamorphism at ∼1.2 Ga versus granulite conditions at ∼1.03 Ga is interpreted in terms of a two-phase evolution as proposed by Macey *et al.* (2018). In this scenario, the intrusion of the LNS produces andalusite-grade contact metamorphism as recorded by nodular magnesian gneisses. The main event in this area is however the ubiquitous ∼1.03 Ga granulite facies event. The ∼150 Ma period separating the two events is a matter of speculation, but following the model of Macey *et al.* (2018) it is proposed that the metasediments and granitoids at Hytkoras have been subjected to "uplift, erosion, extension and deposition" during two distinct orogenic episodes at ∼1.2 and 1.1 Ga (Fig. 8.3). In this 'polymetamorphic' scenario the two events are distinct, and the granulite metamorphism is seemingly unrelated to the intrusion of the Spektakel Suite. However, it is not necessary or implied that the units have been completely exhumed to surface between the two events; cooling to a stable ambient geotherm is also a viable possibility.

8.2 Thermal buffering at the outcrop scale

8.2.1 Contrasting peak temperatures in coexisting rocks?

As described above, the various lithologies at Hytkoras record an apparent spread of ∼60–70 °C in peak temperature (Fig. 7.1a). Traditionally, this spread might be taken to reflect the inherent uncertainty associated with estimating the conditions of granulite facies meta-

morphism. In such an interpretation, all samples may be taken to have experienced the same conditions of, say, 815 ± 35 °C, and this would be a reasonable reflection of metamorphic conditions. Alternatively, a geological argument could be made for why estimates derived from one rock type may be preferred over those from the other rock types. For example, the aluminous metapelites may be argued to have retained more melt than the other rock types, which would have resulted in them undergoing more retrogression through melt crystallisation and only locking in their apparent peak metamorphic conditions further along the retrograde path. Another consideration is that elements that are known to expand the stability of key minerals had not been taken into account. The most pertinent candidate in this context is fluorine in biotite, which has been shown to increase the upper thermal stability of biotite by ∼100 °C (Munoz and Luddington, 1977; Peterson *et al.*, 1991; Icenhower and London, 1997). However, accounting for fluorine is likely to consistently displace all equilibria involving biotite, similar to the shift that occurs from the addition of Ti and Fe^{3+} (White *et al.*, 2014a). Therefore, this is unlikely to account for the relative temperature difference separating different biotite-bearing assemblages.

The disparity in temperature estimates appears robust when one considers that the relatively low-variance peak assemblages reflect specific melting reactions that were intersected by the various lithologies. This relationship is highlighted on Figure 7.1a, which shows the respective peak assemblage fields superimposed on the melting reactions responsible for their formation. Reactions 2.8 and 5.1 are well-known univariant reactions in KFMASH (White *et al.*, 2001, 2007, 2014a) that are separated by some 50 °C at 5.5 kbar (see figure 1a in White *et al.*, 2014a). With the addition of plagioclase, ilmenite and magnetite, these reactions become trivariant in the MnNCKFMASHTO model system, and can be made effectively univariant by fixing two compositional parameters. For reaction 2.8 the grossular content in garnet was fixed at 0.03, corresponding to the measured value from aluminous metapelites. For reaction 5.1 a grossular content of 0.04 was selected, corresponding to garnet in the magnesian metapelite. For both reactions a variable spessartine content of 0.05–0.10 is chosen to represent the observed variability in the composition of investigated samples. Similarly, reaction 5.2 becomes trivariant in NCKFMASHTO if magnetite and ilmenite are added. In order to further reduce the variance to that of a univariant reaction, the anorthite content in plagioclase and X_{Fe} for biotite are varied among measured values (see chapter 4). Figure 7.1a demonstrates that the inferred peak assemblage fields for each lithology fall closely on the corresponding major melting reaction. The P–T position of these reactions is strongly anchored, and does not change with variations in mineral mode or composition (e.g. Palin *et al.*, 2016). Such changes will only shift the assemblage field along the reaction. Therefore, the discrepancy in temperature is dictated by the underlying phase relations, and although it is small enough to argue that it is within the absolute uncertainty of the method, it is argued that it is real, and can be explained by considering the enthalpies involved.

8.2.2 Calculated pressure–enthalpy relations

It is not coincidental that the peak assemblages preserved in the various lithologies consist of the reactants and products of a major melting reaction, indicating that the reactions did not go to completion. Major melting reactions are known to be particularly endothermic (e.g. Vielzeuf *et al.*, 1990; Stüwe, 1995; Thompson and Connolly, 1995; Bea, 2012), and are also characterised by major phase rearrangements and large amounts of mineral consumption and growth. Heat is consumed by these processes, allowing melting reactions to be particularly effective buffers of temperature. To investigate this process, the enthalpy of reaction must be considered, as it quantifies the energy consumed by the reactants as well as the energy released by the crystallisation of peritectic products (cf. Schorn *et al.*, 2018).

Calculated pressure–enthalpy relations for the melt-integrated bulk compositions of the different lithologies are presented in Figure 8.4. The diagrams consider an enthalpy interval of 30 kJ.mol^{-1}, roughly overlapping with the temperature range of the diagrams in Figure 5.3. Whereas temperature is an intensive thermodynamic variable that is independent of the amount of material, enthalpy is extensive and therefore dependent on bulk composition (cf. Powell *et al.*, 2005). Hence the absolute enthalpy values for the diagrams in Figure 8.4 are not the same for the different samples, but relative changes can be quantitatively compared.

The strong endothermic nature of major melting reactions becomes particularly evident in the case of muscovite breakdown by reaction 2.7 on Figure 8.4a and c. The reaction assemblage occupies some 4 kJ.mol^{-1} in pressure–enthalpy space, whereas it occupies as little as 2–3 °C in pressure–temperature space (Fig. 5.3a, b and e, f). The diagrams are contoured for temperature, with isotherms showing sharp deflections shifted towards higher enthalpy values when they intersect individual melting reactions. The consequence of this is that temperature is effectively buffered at that of the reaction, and remains so until one of the reactants is exhausted (e.g. Schorn *et al.*, 2018).

The aluminous metapelite shows two intervals of focused melting and thermal buffering, corresponding to muscovite breakdown by reaction 2.7 and biotite–sillimanite melting by reaction 2.8 (Fig. 8.4a). About 4 kJ.mol^{-1} is consumed by reaction 2.7 to produce ∼10 vol. % melt at near-constant temperature of 690 °C (Fig. 5.3b and 8.4a). Following the demise of muscovite only little melt is produced over the next ∼80 °C (Fig. 5.3b) with isotherms showing equant slope and spacing (Fig. 8.4a). Once reaction 2.8 is intersected, the isotherms again display sharp deflections indicating a second, largely isothermal interval at about 780 °C (Fig. 8.4a). Reaction 2.8 requires more than 2 kJ.mol^{-1} to yield ∼5 vol. % melt in order to go to completion when all biotite is consumed. Beyond this reaction field, isotherms display wide spacing and constant slopes, suggesting a more linear relationship between enthalpy input and temperature increase. As argued above, the aluminous metapelites reached their thermal peak as reaction 2.8 advanced, but before it went to completion (indicated by the white star on Fig. 8.4a). The overall enthalpy budget necessary to heat the rock from 650 °C to the inferred peak temperatures of 780 °C is between 18 and 20 kJ.mol^{-1}. Reactions 2.7 and 2.8 together sequestered ∼5–6 kJ.mol^{-1} of this, amounting to between a quarter and a

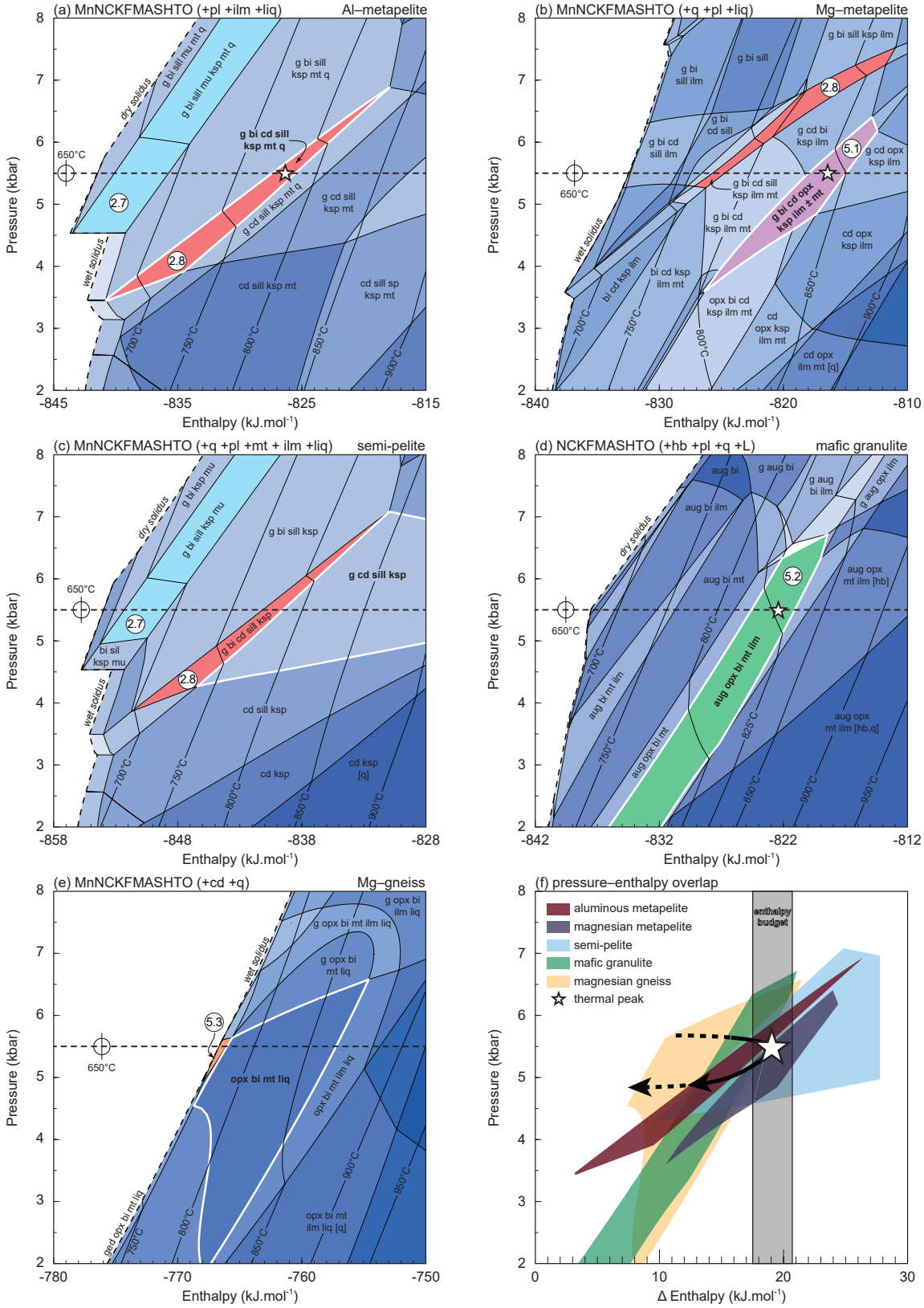

(a) MnNCKFMASHTO (+pl +ilm +liq)
Al–metapelite
(b) MnNCKFMASHTO (+q +pl +liq)
Mg–metapelite
(c) MnNCKFMASHTO (+q +pl +mt + ilm +liq)
semi-pelite
(d) NCKFMASHTO (+hb +pl +q +L)
mafic granulite
(e) MnNCKFMASHTO (+cd +q)
Mg–gneiss
(f) pressure–enthalpy overlap
Pressure (kbar)
Enthalpy (kJ.mol-1)
Δ Enthalpy (kJ.mol-1)
650°C
dry solidus
wet solidus
g bi sill
ksp mt q
g bi sill mu mt q
g bi sill mu ksp mt q
g bi cd sill
ksp mt q
g cd sill ksp mt q
g cd sill
ksp mt
cd sill ksp mt
cd sill sp
ksp mt
g bi sill ksp ilm
g bi sill
g bi
sill ilm
g bi
cd sill
g cd bi
ksp ilm
g cd opx
ksp ilm
g bi cd
sill ilm
g bi cd sill
ksp ilm mt
g bi cd opx
ksp ilm ± mt
g bi cd
ksp ilm mt
cd opx
ksp ilm
bi cd ksp
ilm mt
bi cd ksp ilm
opx bi cd
ksp ilm mt
cd
opx ksp
ilm mt
cd opx
ilm mt [q]
g bi ksp mu
g bi sill ksp mu
g bi sill ksp
g cd sill ksp
g bi cd sill ksp
bi sil
ksp mu
cd sill ksp
cd ksp
cd ksp
[q]
aug bi
g aug bi
g aug
bi ilm
g aug opx ilm
aug bi ilm
aug bi mt
aug opx
mt ilm [hb]
aug bi mt ilm
aug opx bi mt ilm
aug opx bi mt
aug opx
mt ilm [hb,q]
g opx bi
ilm liq
g opx bi mt ilm liq
g opx bi
mt liq
opx bi mt liq
opx bi mt ilm liq
ged opx bi mt liq
opx bi mt
ilm liq [q]
aluminous metapelite
magnesian metapelite
semi-pelite
mafic granulite
magnesian gneiss
thermal peak
enthalpy budget

Figure 8.4: Calculated pressure–enthalpy phase equilibrium diagrams contoured for temperature constructed for melt-integrated bulk compositions (a–e) and overlap of inferred peak assemblage fields (f). (a–e) Coloured areas and numbers correspond to major melting reactions (see text). White star indicates the inferred thermal maximum. Inferred peak assemblage field is highlighted with white border, assemblage in bold. Bold dashed lines indicates where the enthalpy profiles have been calculated. (a) aluminous metapelite (sample NMC89), reference point falls in the fluid-saturated assemblage of garnet–biotite–muscovite–sillimanite–plagioclase–ilmenite–magnetite–quartz–H_2O. (b) semi-pelite (sample NMC67), reference point corresponds to the assemblage biotite–muscovite–plagioclase–K-feldspar–ilmenite–magnetite–quartz–H_2O. (c) magnesian metapelite (sample NMC37), reference corresponds to the assemblage of garnet–biotite–staurolite–sillimanite–plagioclase–ilmenite–quartz–H_2O. (d) mafic granulite (sample NMC69), reference is the assemblage hornblende–biotite–plagioclase–epidote–sphene–quartz–H_2O. (e) magnesian gneiss (sample NMC44), reference falls into the assemblage garnet–gedrite–biotite–cordierite–ilmenite–magnetite–quartz–H_2O. (f) Overlay of peak assemblage fields, white star indicates thermal peak, black arrow depicts the preferred evolution (see text).

third of the total enthalpy budget available to the sample.

Similar to the aluminous metapelite, the magnesian metapelite shows two intervals of focused melting and thermal buffering, corresponding to reactions 2.8 and 5.1 (Fig. 8.4b). Reaction 2.8 occurs at ∼780 °C (Fig. 5.3d) and requires ∼2 kJ.mol^{-1} to go to completion once sillimanite is exhausted, producing < 5 vol. % melt in the process (Fig. 8.4b). Following this, temperature linearly increases with enthalpy and minor amounts of melt are produced until reaction 5.1 is intersected at ∼850 °C. About 3 kJ.mol^{-1} is necessary for reaction 5.1 to go to completion, consuming all biotite and producing ∼7 vol. % melt in the process (Fig. 8.4b). In analogy to the aluminous metapelite, the coexistence of reactant garnet and biotite with product orthopyroxene and cordierite indicates that metamorphism waned before this occurred (white star on Fig. 8.4b). An overall enthalpy budget of ∼19–22 kJ.mol^{-1} is required to drive the thermal evolution from the reference point at 650 °C to the inferred thermal peak at ∼850 °C. More than 4 kJ.mol^{-1} of this is consumed by the major melting reactions, amounting about a fifth of the entire enthalpy budget.

The semi-pelite shows a comparable evolution to the aluminous metapelite, with ∼3 kJ.mol^{-1} being consumed through muscovite melting by reaction 2.7 (Fig. 8.4c). After a period of linear heating and melting, reaction 2.8 is intersected at about 780 °C. However, because this sample contains about half of the biotite and sillimanite in the aluminous metapelite (Fig. 5.3b, f), it requires about 1 kJ.mol^{-1} to cross reaction 2.8 by exhausting biotite (Fig. 8.4c). Peak conditions are in the biotite-free field (marked with white border on Fig. 8.4c), but the exact conditions are unknown. However, 4–5 kJ.mol^{-1} of the overall heat budget is consumed to complete reactions 2.7 and 2.8.

The mafic granulite is predicted to undergo only one roughly isothermal melting episode corresponding to reaction 5.2 at around 830 °C (Fig. 8.4d). Completing reaction 5.2 requires a total of ∼4 kJ.mol^{-1} to consume all hornblende and biotite, producing 25–30 vol. %

melt in the process (Fig. 5.3h). The observed ratio of peritectic products (pyroxenes and plagioclase) to reactants (hornblende, biotite and quartz) in thin section (Fig. 4.10c) suggests that reaction 5.2 proceeded to about 80 % of completion, corresponding to a predicted melt production of 20–25 vol. % and an enthalpy consumption of about 3 kJ.mol^{-1} (white star on Fig. 8.4d). Overall, some 15–19 kJ.mol^{-1} are required to drive metamorphism from the reference temperature of 650 °C to the inferred thermal peak at ∼830 °C, with melting consuming a sixth of the heat budget.

The magnesian gneiss is not affected by significant buffering episodes (Fig. 8.4e). The terminal breakdown of minor orthoamphibole through reaction 5.3 consumes less than 1 kJ.mol^{-1} to yield negligible amounts of melt melt (Fig. 5.3j and 8.4e). Similar to the semi-pelite, the exact position of the thermal peak in the gedrite-absent field (highlighted with white border on Fig. 8.4e) is not known.

8.2.3 A common enthalpy budget to account for disparate temperatures

Figure 8.4f summarises the enthalpy budget required for the various lithologies to develop their observed peak assemblages from a common reference point at 650 °C and 5.5 kbar. There is a tight clustering of the peak assemblage fields around the same enthalpy value (white star on Fig. 8.4f), with all lithologies requiring the same enthalpy input of ∼18–20 kJ.mol^{-1} to stabilise the respective peak assemblages observed in each sample. This strongly suggests that all samples experienced the same metamorphic conditions in terms of heat budget, but because each lithology experienced a unique melting history and was thermally buffered to different extent, their identical heat budgets are recorded as different peak temperatures.

Figure 8.5 compares the buffering history and temperature paths of the different lithologies. Whereas all rock types are buffered to some degree over the 18 to 20 kJ.mol^{-1} enthalpy interval corresponding to peak conditions, only the aluminous metapelite and semi-pelite are also buffered during muscovite melting via reaction 2.7 at 690 °C (Fig 8.5). It is predominantly this melting episode that thermally retards these lithologies and leads them to eventually reach lower peak temperatures than muscovite-free protolith lithologies. This indicates that the disparity in recorded temperature may have developed relatively early during suprasolidus metamorphism, and was maintained during the prograde history from muscovite breakdown to peak conditions. The overall enthalpy budget can also be used to infer a likely peak temperature of 800–830 °C for the semi-pelite and 830–850 °C for the magnesian gneiss.

8.2.4 Could the same apparent disparity be achieved by melt retention?

The calculations above demonstrate that the seemingly disparate temperatures can be explained by lithologies with different melt fertilities receiving a common heat budget. It is worth considering whether it can equally be explained by variable retrogression due to melt retention, as suggested by Rao *et al.* (2012) for the example highlighted in the introduction.

Let's assume that all samples experienced a peak temperature that is well in excess of

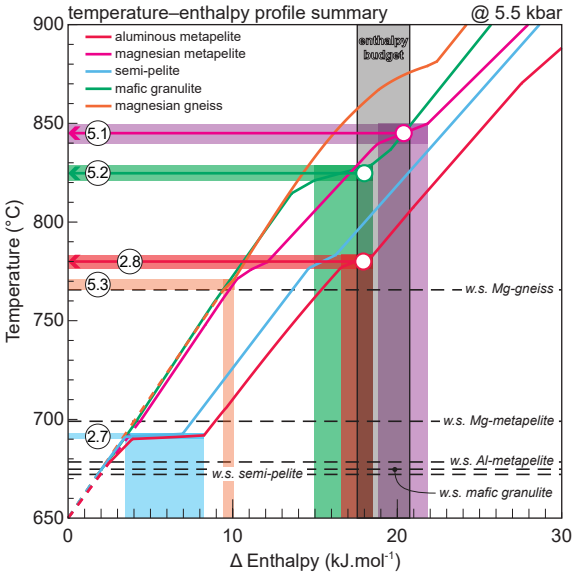


Figure 8.5: Temperature–enthalpy profiles calculated at 5.5 kbar. Dashed portion of profile indicates subsolidus evolution. Dashed isothermal lines indicate wet solidus (*w.s.*) for individual samples. Isothermal arrows indicate inferred peak temperature. Grey area highlights the envisaged heat budget common to all samples (see text).

the melting reactions described here (900 °C, for example). To attain these conditions, each sample would have to have completed their specific melting reactions by exhausting a reactant mineral. In the examples here, the limiting reactant is calculated to be biotite in all samples but the mafic gneiss, where hornblende is depleted (Fig. 5.3). Notably, all lithologies are modelled to be melt-bearing, but otherwise consist of entirely anhydrous mineral assemblages at the nominal peak conditions (Fig. 5.3).

Melt crystallisation during retrogression concurrently involves the growth of hydrous minerals (White and Powell, 2010). This implies that any melt that is retained in these samples after peak metamorphism will only be able to fully crystallise once a hydrous mineral (biotite or hornblende) is reintroduced during cooling or in extreme cases at the wet solidus. Once the hydrous mineral is present, melt will quickly crystallise and the residuum solidus will be intersected shortly afterwards to effectively arrest the sample's mineralogical evolution (White and Powell, 2002). The conditions where this arrest will occur are those of the melting reactions described for each sample, and will therefore result in the same disparate temperatures recorded by the sample suite. Importantly, such an evolution will occur regardless of the amount of melt that is retained. This implies that granulites that have developed completely anhydrous assemblages at peak conditions will always experience some degree of retrogression and not record their actual peak temperatures (e.g. Fitzsimons and Harley, 1994; White and Powell, 2010). Thus, rocks that experience distinctly different melt crystallisation equilibria would preserve solidus assemblages at different temperatures.

The melt retention model provides a possible explanation for many of the features de-

scribed here, particularly because the disparity in recorded temperature is only developed during retrogression, right at the point where each sample is about to arrest its mineralogical evolution, and where cooling and melt loss have shortened the length scales of diffusive and conductive equilibration. Unlike the thermal buffering model, it also does not require the disparate temperatures to be developed and maintained for a significant period of time. However, the model is not appropriate for the example described here because of the clear petrographic evidence against the melting reactions having gone to completion. Notably, prograde-peak biotite and hornblende are extensively preserved, and there is no evidence to suggest that the lithologies were ever devoid of these minerals, as is required by the melt retention model.

8.2.5 Length scale of thermal buffering

The expression of seemingly different peak temperatures in associated lithologies implies that they evolved in thermal isolation and that there was little to no conductive communication between them. The same is implied by each lithology having received a near-identical heat budget. Most samples are separated from one another by distances of tens to hundreds of metres, which seems rather short to allow for conductive isolation. Schorn *et al.* (2018) estimated the critical length scale for reaction 2.8 to be ∼4000–1500 m, which is an order of magnitude more than what is apparently preserved here. However, their calculation did not consider geometric factors or the role of advective cooling from the extraction of hot melt. For the particular example described here, a further factor that might have shortened the critical length scale at the thermal peak is the observation that all lithologies experienced focused melting reactions at that time. This means that all lithologies would have simultaneously been strong heat sinks, consuming any available heat through their own melting reaction, rather than communicating it on to adjacent lithologies. Unlike the case for muscovite melting, where most lithologies would likely have communicated some heat into the aluminous metapelites and semi-pelites undergoing the reaction, all rocks were intense consumers of heat at the thermal peak, and there were no lithologies willing or able to communicate any heat within the supracrustal succession. This competition is likely to have strongly compartmentalised the heat budget, leading to effective thermal isolation between discrete layers within the sequence.

It is freely acknowledged that this aspect of the model is poorly and unsatisfactorily constrained, and definitely does not imply that lithologies sampled from the same outcrop should be readily expected to have recorded temperatures that are meaningfully different. The general significance (or not) of thermal buffering can only be tested by carefully examining the thermal history of coexisting lithologies in other localities. However, for the example described here from Hytkoras, it appears that the temperature differences is real, as they are fundamentally related to the underlying phase relations. For that to have been the case, the rocks must have evolved in thermal isolation on an unusually small outcrop scale.

8.2.6 Implications for thermobarometry

The expression and preservation of apparently different peak temperatures as a function of rock composition has important consequences for thermobarometry in granulite terranes. This is particularly relevant because P–T conditions are typically constrained from volumetrically insignificant metapelites and readily extrapolated to large areas of other rock types. The calculations show that metapelites are likely to systematically preserve apparently lower temperatures compared to other rock types, thereby obscuring the effective peak temperature of a given portion of orogenic crust. This is largely related to the energy consumed through muscovite breakdown, and therefore potentially affects the entire granulite facies and all muscovite-free lithologies. It is therefore cautioned against the widely-held and general assumption that P–T conditions are well-constrained once they have been precisely determined from regionally-significant metapelites, and encourage workers to always test these results against those from other lithologies. This has not always been possible in the past, but the continued development of activity–composition relations for phases of petrological interest, coupled to new thermobarometric methods utilising trace elements, are providing more and more opportunities for validation.

A further implication relates to the validity and usefulness of temperature as a unique geodynamic parameter. Temperature is the product of material-specific properties combined with regionally-available heat flow, and the results show that it does not translate to an unbiased proxy for the energy input experienced in heterogeneous metamorphic crust. As an example, the definition of ultrahigh-temperature metamorphism to designate crust that has experienced very high heat flow becomes somewhat circular and self-defeating in this context. It would be more appropriate to directly describe the heat budget, as this is the underlying, geodynamically-relevant driving force. Enthalpy diagrams such as those presented here provide a useful tool for quantifying the orogenic heat budget, and investigating how it is utilised by petrogenetic processes in order to be translated to temperature.

8.3 Thermal buffering at the regional scale

8.3.1 Implications of apparent peak temperature on potential heat sources

It has been shown that large parts of the BSP experienced roughly coeval high-T–low-P metamorphism at similar pressure, but that a range of thermal maxima are recorded for individual sample localities (Fig. 8.1). However, are the apparently recorded temperatures significantly different? As has been discussed in this chapter, temperature might not be the best parameter to be quantified in order to understand a specific metamorphic environment. Because sampling for this thesis primarily targeted metapelites *s.l.*, the apparently recorded conditions may be directly compared to each other – based on the implicit assumption that similar bulk compositions have similar thermal properties. This is obviously not the case if temperatures recorded by strongly different rocks are compared to each other (see above).

For this reason, the locality of Hytkoras is not regarded to be as 'hot' as Ratelpoort or Paulshoek, even though the temperatures calculated for more refractory rocks at Hytkoras are comparable to those apparently recorded at the other two localities. Because only similar bulk compositions should be compared (say, aluminous metapelites), it results that metamorphism at Hytkoras appears comparable to that recorded at Lepel se Kop and Nababeep, where metapelites too preserve both the reactants and products of reaction 2.8.

From the pelitic granulites investigated here, the samples of Lepel se Kop and Nababeep – with reaction products garnet + cordierite and reactants biotite + sillimanite in apparent equilibrium – are consistent with the thermal peak being recorded as reaction 2.8 having advanced without going to completion. By contrast, samples at Ratelpoort are effectively devoid of biotite + sillimanite, both reactants of reaction 2.8. Assuming that the protoliths were comparable for samples from all three localities, it seems straightforward to assume that biotite–sillimanite-absent ([bi,sill]) rocks have indeed been subjected to a higher heat input and have therefore effectively recorded a higher temperature.

This is illustrated on Figure 8.6, calculated for the average amphibolite facies metapelite bulk composition, with a fully fluid-saturated subsolidus evolution (Ague, 1991, Table 2.2).

Assume isobaric heating starting at 600 °C (black arrow on Fig. 8.6a): the rock would experience a thermal evolution similar to what has been described in chapter 2 and for the aluminous metapelite from Hytkoras – with two intervals of thermal buffering as reactions 2.7 and 2.8 advance, separated by linear heating (black profile on Fig. 8.6b). Intuitively, to completely cross the reaction field of 2.8 and to produce the [bi,sill] assemblage inferred for Ratelpoort, a higher enthalpy input is necessary compared to what is required to form the assemblage inferred for Nababeep or Lepel se Kop (corresponding to reaction 2.8 itself; Fig. 8.6b). Based on the calculations shown in Figure 8.6b, an enthalpy difference of $\sim$3–4 kJ.mol^{-1} separating the stability field for the assemblages of the different localities is estimated (solid red field and dotted area on Fig. 8.6b). The exact value is obviously strongly dependent on the exact evolution and effective bulk composition, but it can be argued that samples from Ratelpoort must have had this slightly higher heat budget at their disposal. In light of the spatial relationship with intrusions of the Spektakel Suite and highest-grade metamorphism in the region (Macey *et al.*, 2018) – in particular at the localities Paulshoek and Ratelpoort (Fig. 8.1) – it is tentatively suggested that the difference in enthalpy that caused the effective crossing of reaction 2.8 for example at Ratelpoort was in fact caused by an additional heat-input due to the proximal emplacement of the Spektakel Suite. 'Colder' localities, such as Lepel se Kop, Hytkoras and Nababeep seem to have not been affected by this process and therefore had a slightly smaller metamorphic heat budget.

Nonetheless, the heat source responsible for more or less homogeneous granulite metamorphism on a regional scale must have been of significant dimensions. Moreover, the main heat source and geodynamic setting must be consistent with (i) heating from shallow low-grade conditions to granulite facies temperatures at a maximum depth of $\sim$20 km along a roughly isobaric heating path with minor concomitant burial, (ii) seemingly coeval peak

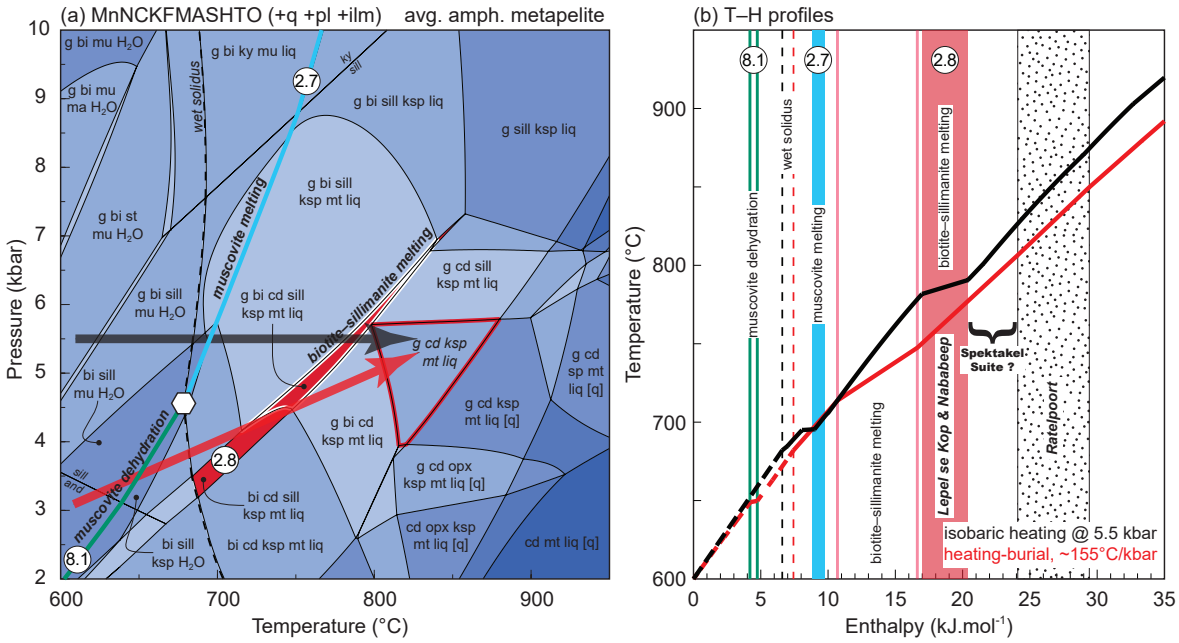


Figure 8.6: Conventional pressure–temperature phase equilibrium diagram (a) and temperature–enthalpy profiles (b) for average metapelite composition (Ague, 1991). Bold green and blue line in (a) highlight the respective sub- and suprasolidus muscovite-breakdown, intersected during heating below and above ∼4.5 kbar, respectively (white hexagon). Black arrow represents isobaric heating at 5.5 kbar, red arrow stands for heating involving concomitant burial. White border highlights assemblage field inferred for samples from Lepel se Kop and Nababeep, red border is the assemblage field inferred for Ratelpoort. *T*–*H* profiles in (b) are calculated along the same-coloured arrows. Dashed portion of profile corresponds to subsolidus evolution. Coloured fields highlight loci of endothermic breakdown reactions, filled boxes for isobaric path, empty boxes for heating + burial evolution. The assemblage field for samples from Lepel se Kop and Nababeep coincides with the stability of reaction 2.8. The [bi,sill] assemblage field for Ratelpoort is symbolised by the dotted field.

metamorphism recorded at a regional scale that (iii) post-dated the last penetrative deformation (D_2), was accompanied/preceded by voluminous felsic magmatism (iv) and was followed by (v) slow, largely isobaric cooling to an ambient geotherm with no significant attending exhumation (e.g. Waters, 1986b, 1989; Diener *et al.*, 2013; Raith and Harley, 1998, this study). Tectonic settings involving granulite-formation in a thickened crust related to terrane collision and amalgamation (as suggested for the Southern Granulite Terrane and Eastern Ghats Province, India; Clark *et al.*, 2015; Mitchell *et al.*, 2018, respectively), are therefore excluded as they would involve more pronounced exhumation rather than isobaric cooling. Granulite-formation as consequence of extension of a normally thick crust (in the sense of Sandiford and Powell, 1986) is also rejected in light of regional geological constraints (e.g. Waters, 1986b, 1989; Robb *et al.*, 1999).

The inferred magmatic and tectonometamorphic evolution of the Namaqua Sector is better consistent with long-lasting steady heat transfer into a thinned lithosphere located in a continental back-arc setting (Bial *et al.*, 2015). Heat transfer solely via conduction is however regarded as insufficient to produce the observed metamorphism (Waters, 1986b). The author therefore invokes advective heating via the emplacement of hot, dry felsic magma deriving from the lower crust above or close to the present-day level of erosion (cf. Clark *et al.*, 2014). Extensive crustal contamination of mantle-derived magmas would be a favourable mechanism to produce such melts (Waters, 1986b) – Macey *et al.* (2018) interpret the post-tectonic Spektakel Suite "as admixture of inherited Paleoproterozoic arc-type crust and a Mesoproterozoic A-type mantle component". Comparable felsic magmatism in close spatial and temporal relationship with high-grade metamorphism is also present in other parts of the Namaqua Sector, e.g. in the Kakamas Domain (the 1110–1085 Ma Keimos Suite; e.g. Bailie *et al.*, 2017) and in the Areachap Domain (the 1120–1105 Ma Komsberg Suite; e.g. Macey *et al.*, 2015).

Ultimately, the heat source for crustal-scale granulite metamorphism in the Namaqua Sector remains the asthenospheric mantle (e.g. Macey *et al.*, 2018; Diener *et al.*, 2013; Waters, 1986b). Macey *et al.* (2018) tentatively interpret volumetrically minor mafic magmatism intruding the Namaqua Sector (∼1.22, 1.15, 1.11 and 1.02 Ga; e.g. Robb *et al.*, 1999; Clifford *et al.*, 2004; Macey *et al.*, 2015) as representatives of the inferred underplating melts. Seismic velocities at a depth greater than ∼14 km consistent with a crust of dioritic or amphibolitic composition (Green and Durrheim, 1990), geochemical evidence for assimilation–fractional crystallisation of the ∼1.03 Ga Koperberg Suite (Robb *et al.*, 1999; Clifford *et al.*, 1995) and A-type mantle components recognised in the Spektakel Suite (Macey *et al.*, 2018) all point towards significant presence of mafic/mantle-related material in the unexposed crust of the BSP. Therefore, a combination of mafic underplating, potentially involving more or less extensive radiogenic heating (Andreoli *et al.*, 2006) and/or slow tectonic burial of hot, juvenile crust is considered as suitable driving force for roughly homogeneous granulite metamorphism at ∼1.03 Ga recorded in western Namaqualand (cf. Sandiford *et al.*, 2002; Clark *et al.*, 2011; Diener *et al.*, 2013; Diener, 2014). Locally-abundant intrusions of the coeval Spektakel Suite may have added additional energy to this 'base' heat budget, causing near, but not quite,

UHT conditions.

8.3.2 Relationship of P–T path and apparent peak temperature

So far all considerations are based on an isobaric evolution, and even though this appears to be consistent with some of the investigated localities, certain samples preserve evidence for an anticlockwise P–T path. Samples from Paulshoek and Ratelpoort are inferred to have experienced such an evolution. The following discussion is based on 'regular' aluminous metapelites such as those sampled at Ratelpoort; the spinel-bearing samples from Paulshoek are excluded because the inferred peak assemblage could not be reproduced by the modelling presented here. Nonetheless, the principles deduced here are regarded to be valid for these rocks as well.

A prograde anticlockwise path is approximated here with heating and concomitant burial from 600 °C and 3 kbar to the inferred peak conditions for Ratelpoort of 850 °C and 5.5 kbar (∼155 °C/kbar; red arrow on Fig. 8.6a). In this scenario, the breakdown of muscovite occurs at subsolidus conditions and corresponds to the major dehydration reaction

$$\text{muscovite} + \text{quartz} = \text{biotite} + \text{sillimanite} + \text{K feldspar} + \text{H}_2\text{O} \tag{8.1}$$

(e.g. Bearley and Rubie, 1990). Dehydration reactions, such as 8.1 are known to be highly endothermic (e.g. Stüwe and Powell, 1997; Lyubetskaya and Ague, 2009) and expected to exert a similar thermal effect as melting reactions. This property can be seen on the related heating profile portrayed on Figure 8.6b: the endothermic effect leads to a short roughly isothermal episode as dehydration advances, flagged by a kink in the heating profile. During this episode about 1 kJ.mol^{-1} is consumed – roughly the same amount of heat required to complete the suprasolidus breakdown of muscovite according to reaction 2.7. Due to the buffering effect the heating profile deviates from the isobaric case, however the two join up again as muscovite melts out (Fig. 8.6b) suggesting that the style of muscovite breakdown – dehydration or melting – has little effect on the buffering capacity of the reaction. Nonetheless, the subsolidus removal of muscovite has obvious implications on crystallographically-bound fluid-content of the rock at at the solidus and, by extension, on the overall melt fertility. The effect of variable fluid-content has been taken into account when constructing Figure 8.6b, the described evolution is therefore regarded as accurate.

The heating profiles for both experiments overlap as the respective solidus is exceeded, indicating that in both cases the rocks have virtually the same thermal properties, likely because melting here is continuous and not focussed by major melting reactions, regardless of the style of heating. Soon thereafter the sample evolving along the heating–burial path is affected by thermal buffering due to reaction 2.8. The effect is overall less pronounced compared to the isobaric case (Fig. 8.6b) but it occurs over a larger enthalpy interval because the P–T slope along which the rock is heated and buried approximates the slope of reaction 2.8 in P–T space. Modal abundances of reacting biotite and sillimanite are also function of

P–T, thereby affecting the heat required to drive reaction 2.8 that consumes them.

The isobaric example experiences roughly linear heating during this episode, however as soon as reaction 2.8 is intersected, the isobaric experiment is affected by extensive thermal buffering, as described in the previous examples. As buffering due to 2.8 is completed for the isobaric case, the two heating profile would almost join up again, suggesting that the style of prograde P–T has only limited effect on the overall thermal evolution of the rock. Once reaction 2.8 is completed, both examples would experience roughly linear heating. The slightly more pronounced buffering effect of 2.8 becomes significant only at very high heat-contents, i.e. temperatures at and around UHT conditions, where it would cause a temperature difference of ∼20–30 °C between the two cases.

8.3.3 Preconditioning and polymetamorphism

It has been previously suggested that rocks that have been affected by partial melting and melt loss would be 'preconditioned' and heat up more efficiently if affected by a second thermal event (e.g. Vielzeuf and Holloway, 1988; Vielzeuf *et al.*, 1990; Clark *et al.*, 2011; Caddick, 2013). This postulate appears plausible because when hydrous melt is removed, the source rock becomes more refractory (Brown, 2010; Kelsey and Hand, 2015) with the residuum solidus being shifted towards higher temperature. Hence, the potential for thermal buffering due to melting during a later event should decrease with the degree of melting and melt loss (Caddick, 2013).

This scenario is tested using the average amphibolite facies metapelite composition (Ague, 1991, Table 2.2). To simulate melt loss, melt is removed completely in a single step at different suprasolidus temperatures but at a constant pressure of 6 kbar. The resulting bulk composition is therefore increasingly dehydrated and refractory with increasing temperature of melt extraction because the higher the temperature, the more melt is produced and consequently removed. For each resulting bulk composition a temperature–enthalpy profile is calculated at 6 kbar, similar to the diagrams in chapter 2. The resulting isobaric T–H profiles are presented in Figure 8.7. The dashed profile corresponds to the 'first cycle' case, i.e. prograde metamorphism assuming a fluid saturated subsolidus evolution implying a wet solidus at ∼690 °C and is identical to the case presented in Figure 2.3e (chapter 2). The kinks in the 'first cycle' case correspond to reaction 2.7 and 2.8, at ∼700 and ∼800 °C respectively.

As expected, the residuum solidi are shifted towards higher temperature with the temperature at which melt has been extracted. Surprisingly however, the resulting heating profiles do not significantly differ from each other (Fig. 8.7). This seems to suggest, contrary to previous predictions, that this type of 'preconditioning' might not lead to significantly more efficient heating or a higher temperature attained during a second thermal event affecting the refractory rocks. In fact, if for simplicity a second, identical isobaric metamorphism is invoked, (say, adding another 20 kJ.mol^{-1} starting from 600 °C), the resulting temperatures only marginally differ from each other and do not significantly depart from the ∼800 °C that a 'first cycle' rock would record with this heat budget (black isobaric arrow on Fig. 8.7).

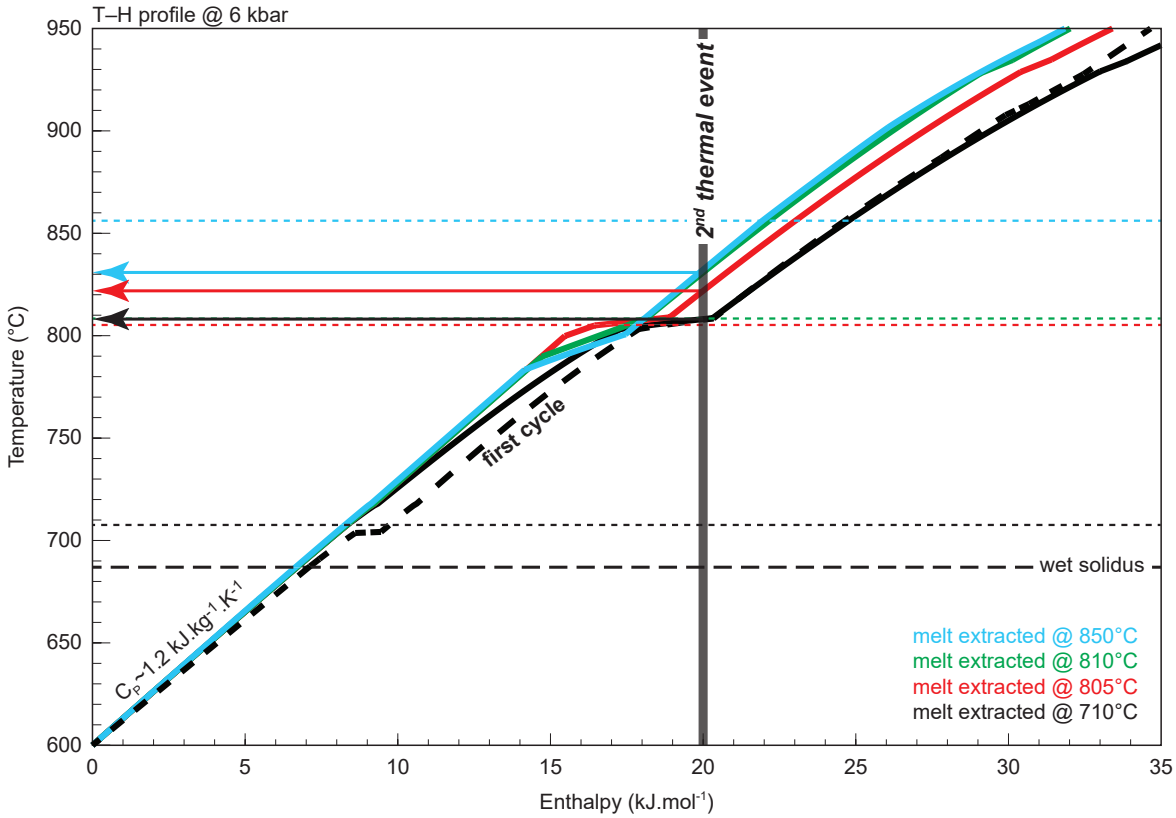


Figure 8.7: Isobaric temperature–enthalpy profiles calculated for average metapelite composition (Ague, 1991) at 6 kbar. The profiles are calculated for melt extracted bulk compositions, with melt completely removed at the indicated temperature. Bold dashed line is the wet solidus, coloured dotted lines are residuum solidii. Grey box symbolises a second thermal event adding 20 kJ.mol^{-1} to each composition at 600 °C.

Whereas the absolute amount of melt produced during the second event significantly decreases with the degree of 'preconditioning', the overall thermal properties of the assemblages remain largely unvaried. In particular at a temperature comprised between 600 and 800 °C the slope of all the heating profiles is virtually identical, translating to an average heat capacity of ∼1.2 kJ.kg^{-1}.K^{-1} – comparable to estimates for subsolidus metapelites of the Koralm Complex (Stüwe and Powell, 1997). This suggests that in this particular case the thermal behaviour is controlled by the overall properties, namely the average heat capacity, which seems to be generally unaffected by the degree of melt extraction. In this instance the effect of isolated episodes of pronounced thermal buffering seem to be subordinate. It is worth noting that the assemblage corresponding to reaction 2.8, even in the case where either biotite and/or melt are absent, is characterised by an extremely high heat capacity, as flagged by the pronounced kink in all heating profiles at around 800 °C. For example, in the case where melt was removed at 805 °C and 6 kbar (red profile on Fig. 8.7), melt extraction occurred within the assemblage field of reaction 2.8 as it was almost completed (see Fig. 8.6a for reference). Therefore, if the new residual bulk is affected by a second thermal event adding essentially the same amount of enthalpy that was required to produced the first melting and melt extraction, the resulting temperature is only slightly higher. However, because extensive melt extraction took place the rock would have skipped thermal buffering due to reaction 2.7 and buffering during reaction 2.8 would be minimal.

Due to the extensive property of enthalpy, the degree of thermal buffering may vary significantly with bulk composition. For example, the thermal evolution of pelitic schists that are particularly rich in white mica would be dominated by the breakdown thereof, as introduced earlier in this chapter. Rocks containing less modal white mica at subsolidus conditions would experience significantly less thermal buffering due to mica breakdown. The overall thermal evolution therefore varies from case to case, and consequently the effect of 'preconditioning' might be of importance for protoliths particularly rich in white mica. Once all white mica is decomposed to it's reaction products, heating during subsequent metamorphism and/or a second thermal event would be significantly more efficient.

'Preconditioned' rocks rich in K-feldspar and sillimanite might have had abundant mica in their protolith and would therefore require copious amounts of heat energy to cross the respective breakdown reaction during a first thermal event. If such gneisses were affected by a second event, thermal buffering due to muscovite dehydration/melting would not occur and the rocks might heat up more efficiently, in spite of a generally high heat capacity. Such 'preconditioned' terranes are therefore expected to host feldspar–aluminosilicate-rich gneisses rather than migmatites and may coexist with Mg–Al-rich units hosting characteristic UHT assemblages (Sandiford, 1985; Ouzegane *et al.*, 2003). Such occurrences are inferred to attest to 'preconditioning' as aid to the achievement if UHT conditions at the terrane scale (e.g. Vielzeuf and Holloway, 1988; Vielzeuf *et al.*, 1990; Clark *et al.*, 2011).

References

Agenbacht, A. L. D., 2007. *The geology of the Pofadder area. 1:250 000 map sheet explanation 2918*, Council for Geoscience.

Ague, J. J., 1991. Evidence for major mass-transfer and volume strain during regional metamorphism of pelites. *Geology*, **19**, 855–858.

Albat, H.-M., 1984. The Proterozoic granulite facies terrane around Kliprand, Namaqualand Metamorphic Complex. *Bulletin of the Precambrian Research Unit*, **33**. University of Cape Town, 382pp.

Aleinikoff, J. N., Schenck, W. S., Plank, M. O., Srogi, L. A., Fanning, C. M., Kamo, S. L. and Bosbyshell, H., 2006. Deciphering igneous and metamorphic events in high-grade rocks of the Wilmington complex, Delaware: Morphology, cathodoluminescence and backscattered electron zoning, and SHRIMP U–Pb geochronology of zircon and monazite. *Geological Society of America Bulletin*, **118**, 39–64.

Alessio, K. L., Hand, M., Morrissey, L. J., Kelsey, D. E. and Payne, J. L., 2017. Melt Reintegration Modelling: Testing against a Subsolidus Reference Assemblage. *Geosciences*, **7**, 75.

Andreoli, M. A. G., Hart, R. J., Ashwal, L. D. and Coetzee, H., 2006. Correlations between U, Th content and metamorphic grade in the western Namaqualand belt, South Africa, with implications for radioactive heating of the crust. *Journal of Petrology*, **47**, 1095–1118.

Ashworth, J. R., 1976. Petrogenesis of migmates in the Hubtly–Portsoy area, north-east Scotland. *Mineralogical Magazine*, **40**, 661–682.

Ashworth, J. R. and McLellan, E. L., 1985. *Migmatites*, Blackie, Glasgow.

Avchenko, O. V., Zhulanova, I. L., V., C. K. and Karabtsov, A. A., 2018. Spinel–Sapphirine Reaction Structures in the Garnet Metaultramafic Rocks of the Omolon Massif: Petrogenesis and Geological Interpretation (Northeast Asia). *Russian Journal of Pacific Geology*, **12**, 174–189.

Bailie, R., Armstrong, R. A. and Reid, D., 2007. The Bushmanland Group supracrustal succession, Aggeneys, Bushmanland, South Africa: Provenance, age of deposition and metamorphism. *South African Journal of Geology*, **110**, 59–86.

Bailie, R., Gutzmer, J. and Rajesh, H. M., 2010. Lithogeochemistry as a tracer of the tectonic setting, lateral integrity and mineralization of a highly metamorphosed Mesoproterozoic volcanic arc sequence on the eastern margin of the Namaqua Province, South Africa. *Lithos*, **119**, 345–362.

Bailie, R., Gutzmer, J., Rajesh, H. M. and Armstrong, R., 2011. Age of ferroan A-type post-tectonic granitoids of the southern part of the Keimoes Suite, Northern Cape Province, South Africa. *Journal of African Earth Sciences*, **60**, 153–174.

Bailie, R., Macey, P. H., Nethenzheni, S., Frei, D. and le Roux, P., 2017. The Keimoes Suite redefined: The geochronological and geochemical characteristics of the ferroan granites of the eastern Namaqua Sector, Mesoproterozoic Namaqua-Natal Metamorphic Province, southern Africa. *Journal of African Earth Sciences*, **134**, 737–765.

Bailie, R., Rajesh, H. M. and Gutzmer, J., 2012. Bimodal volcanism at the western margin of the Kaapvaal Craton in the aftermath of collisional events during the Namaqua-Natal Orogeny: The Koras Group, South Africa. *Precambrian Research*, **200–203**, 163–183.

Baldwin, J. A., Powell, R., White, R. W. and Štípská, P., 2015. Using calculated chemical potential relationships to account for replacement of kyanite by symplecite in high pressure granulites. *Journal of Metamorphic Geology*, **33**, 311–330.

Bartoli, O., 2017. Phase equilibria modelling of residual migmatites and granulites: An evaluation of the melt-reintegration approach. *Journal of Metamorphic Geology*, **35**, 919–942.

Bea, F., 2012. The sources of energy for crustal melting and the geochemistry of heat-producing elements. *Lithos*, **153**, 278–291.

Bearley, A. J. and Rubie, D. C., 1990. Effects of H_2O on the Disequilibrium Breakdown of Muscovite + Quartz. *Journal of Petrology*, **31**, 925–956.

Beaumont, C., Jamieson, R. A., Nguyen, M. H. and Lee, B., 2001. Himalayan tectonics explained by extrusion in a low-viscosity crustal chanesl coupled to focused denudation. *Nature*, **414**, 738–742.

Bial, J., Büttner, S. H. and Appel, P., 2016. Timing and conditions of regional metamorphism and crustal shearing in the granulite facies basement of south Namibia: Implications for the crustal evolution of the Namaqualand metamorphic basement in the Mesoproterozoic. *Journal of African Earth Sciences*, **123**, 145–176.

Bial, J., Büttner, S. H. and Frei, D., 2015b. Formation and emplacement of two contrasting late-Mesoproterozoic magma types in the central Namaqua Metamorphic Complex (South Africa, Namibia): Evidence from geochemistry and geochronology. *Lithos*, **224–225**, 272–294.

Bial, J., Büttner, S. H., Schenk, V. and Appel, P., 2015. The long-term high-temperature history of the central Namaqua Metamorphic Complex: Evidence for a Mesoproterozoic continental back-arc in southern Africa. *Precambrian Research*, **268**, 143–278.

Blignault, H. J., Van Aswegen, G., Van der Merwe, S. W. and Colliston, W. P., 1983. The Namaqualand geotraverse and environs: part of the Proterozoic Namaqua Mobile Belt. *Geological Society of South Africa, Special Publication*, **10**, 1–29.

Bohlen, S. R. and Essene, E. J., 1979. A critical evaluation of two-pyroxene thermometry in Adirondack granulites. *Lithos*, **12**, 335–345.

Boynton, W. V., 1984. Cosmochemistry of the rare earth elements: meteorite studies, *Developments in geochemistry*. Elsevier.

Brown, M., 2001. From microscope to mountain belt: 150 years of petrology and its contribution to understanding geodynamics, particularly the tectonics of orogens. *Journal of Geodynamics*, **32**, 115–164.

Brown, M., 2006. Duality of thermal regimes is the distinctive characteristic of plate tectonics since the Neoarchean. *Geology*, **34**, 961–964.

Brown, M., 2007. Metamorphic conditions in orogenic belts: a record of secular change. *International Geology Review*, **49**, 193–134.

Brown, M., 2010. The spatial and temporal patterning of the deep crust and implications for the process of melt extraction. *Philosophical Transactions of the Royal Society of London, Series A*, **368**, 11 – 51.

Brown, M. and Johnson, T., 2018. Secular change in metamorphism and the onset of global plate tectonics. *American Mineralogist*, **103**, 181–196.

Büttner, S. H., Sherlock, S., Fryer, L., Lodge, J., Diale, T., Kazondunge, R. and Macey, P., 2013. Controls of host rock mineralogy and H_2O content on the nature of pseudotachylyte melts: Evidence from pan-African faulting in the foreland of the Gariep belt, South Africa. *Tectonophysics*, **608**, 552–575.

Caddick, M. J., 2013. Petrologic preconditioning: A predisposition to polymetamorphism?, *Goldschmidt Conference Abstracts*.

Cagnard, F., Gapais, D. and Barbey, P., 2007. Collision tectonics involving juvenile crust: the sample of the southern Svecofennides. *Precambrian Research*, **154**, 125–141.

Carlson, W. D., 2002. Scales of disequilibrium and rates of equilibration during metamorphism. *American Mineralogist*, **87**, 185–204.

Chardon, D., Gapais, D. and Cagnard, F., 2009. Flow of ultra-hot orogens: A view from the Precambrian, clues for the Phanerozoic. *Tectonophysics*, **477**, 105–118.

Clark, C., Fitzsimons, I. C. W., Healy, D. and Harley, S. L., 2011. How does the continental crust get really hot? *Elements*, **7**, 235–240.

Clark, C., Healy, D., Johnson, T., Collins, A. S., J., T. R., Santosh, M. and Timms, N. E., 2015. Hot ororogen and supercontinent amalgamation: A Gondwanan example from southern India. *Gondwana Research*, **28**, 1310–1328.

Clark, C., Kirkland, C. L., Spaggiari, C. V., Oorschot, C., Wingate, M. T. D. and Taylor, R. J. M., 2014. Proterozoic granulite formation driven by mafic magmatism: An example from the Fraser Range Metamorphics, Western Australia. *Precambrian Research*, **240**, 1–21.

Clark, C., Taylor, R. J. M., Kylander-Clark, A. R. C. and Hacker, B. R., 2018. Prolonged (>100 Ma) ultrahigh temperature metamophism in the Napier Complex, East Antarctica: A petrochronological investigation of Earth's hottest crust. *Journal of metamorphic Geology*, **36**, 1117–1139.

Clark, M. K. and Royden, L. H., 2000. Topographic ooze: Building the eastern margin of Tibet by lower crustal flow. *Geology*, **28**, 703–706.

Clemens, J. D. and Vielzeuf, D., 1987. Constraints on melting and magma production in the crust. *Earth and Planetary Science Letters*, **86**, 287–306.

Clifford, H. T., Stumpfl, E. F. and McIver, J. R., 1975b. A sapphirine–cordierite–bronzite–phlogopite paragenesis from Namaqualand, South Africa. *Mineralogical Magazine*, **40**, 347–356.

Clifford, T. N., Barton, E. S. and Stern, R. A., 2004. U–Pb calendar for Namaqua (Grenville) crustal events in the granulite facies terrane of the O'okiep Copper District of South Africa. *Journal of Petrology*, **45**, 669–691.

Clifford, T. N., Barton, E. S., Retief, E. A., Rex, D. C. and Fanning, C. M., 1995. A Crustal Progenitor for the Intrusive Anorthosit–Charnockite Kindred of the Cupriferous Koperberg Suite, O'okiep District, Namaqualand, South Africa; New Isotope Data for the Country Rocks and the Intrusives. *Journal of Petrology*, **36**, 231–258.

Collins, W. J. and Vernon, R. H., 1991. Orogeny associated with anticlockwise P–T–t paths - evidence from low-P, high-T metamorphic terranes in the Arunta Inlier, Central Australia. *Geology*, **19**, 835–838.

Connolly, J. A. D., 1997. Devolatilization-generated fluid pressure and deformation-propagated fluid flow during prograde regional metamorphism. *Journal of Geophysical Research*, **102**, 18 149–18 173.

Connolly, J. A. D., 2010. The Mechanics of Fluid Expulsion. *Elements*, **6**, 165–172.

Corfu, F., Hanchar, J. M., Hoskin, P. W. O. and Kinny, P., 2003. Atlas of Zircon Textures. *Reviews in mineralogy and geochremistry*, **53**, 469–500.

Cornell, D. H. and Pettersson, Å., 2007a. Ion probe zircon dating of metasediments from the Areachap and Kakamas Terranes, Namaqua-Natal Province and tiie stratigraphie integrity of the Areachap Group. *South African Journal of Geology*, **110**, 575–584.

Cornell, D. H. and Pettersson, Å., 2007b. Ion probe dating of the Achab Gneiss, a young basement to the central Bushmanland ore district? *Journal of African Earth Sciences*, **47**, 112–116.

Cornell, D. H., Humphreys, H. C., Theart, H. F. J. and Scheepers, D. J., 1992. A collision-related pressure-temperature-time path for Prieska Copper Mine, Namaqua-Natal tec-tonic Province, South Africa. *Precambrian Research*, **59**, 43–71.

Cornell, D. H., Kröner, A., Humphreys, H. and Griffin, G., 1990. Age of origin of the poly-metamorphosed Copperton Formation, Namaqua–Natal Province, determined by single grain zircon Pb-Pb dating. *South African Journal of Geology*, **93**, 709–716.

Cornell, D. H., Pettersson, Å., Whitehouse, M. J. and Schersten, A., 2009. A new chronostratigraphic paradigm for the age and tectonic history of the Mesoproterozoic Bushmanland ore district, South Africa. *Economic Geology*, **104**, 385–404.

Cornell, D. H., Schersten, A., Hoskin, P. W. O. and Lindsay, J., 1999. Application of charge-radius concepts to trace elements in igneous and metamorphic zircon, *9th Annual V. M. Goldschmidt Conference. Lunar and Planetary Institute, Cambridge, MA*.

Cornell, D. H., Thomas, R. J., Gibson, R., Moen, H. F. G., Reid, D. L., Moore, J. M. and Gibson, R. L., 2006. *The Namaqua-Natal Province*, Geological Society of South Africa.

Cornell, D. H., Van Schijndel, V., Simoensen, S. L. and Frei, D., 2015. Geochronology of Mesoproterozoic hybrid intrusions in the Konkiep Terrane, Namibia, from passive to active continental margin in the Namaqua-Natal Wilson Cycle. *Precambrian Research*, **265**, 166–188.

Dachs, E., 1998. PET: petrological elementary tools for mathematica. *Computers and Geosciences*, **24**, 219–235.

De Beer, C. H., 2010. *The geology of the Garies area. 1:250 000 map sheet explanation 3017*, Council for Geoscience.

De Yoreo, J. J., Lux, D. R. and Guidotti, C. V., 1989. The role of crustal anataxis and magma migration in the thermal evolution of regions of thickened continental crust. *Geological Society of London Special Publications*, **43**, 187–202.

Depine, G. V., Andronicos, C. L. and Phipps-Morgan, J., 2008. Near-isothermal conditions in the middle and lower crust induced by melt migration. *Nature Letters*, **452**, 80–83.

Diener, J. F. A., 2014. Low-P–high-T metamorphism of the Aggeneys Terrane, Namaqua Metamorphic Complex, South Africa. *South African Journal of Geology*, **117**, 31–44.

Diener, J. F. A. and Fagereng, A., 2014. The influence of melting and melt drainage on crustal rheology during orogenesis. *J. Geophys. Res. Solid Earth*, **119**, 6193–6210.

Diener, J. F. A. and Powell, R., 2010. Influence of ferric iron on the stability of mineral assemblages. *Journal of Metamorphic Geology*, **28**, 599–613.

Diener, J. F. A., White, R. W. and Hudson, T. J. M., 2014b. Melt production, redistribution and accumulation in mid-crustal source rocks, with Implications for crustal-scale melt transfer. *Lithos*, **200**, 212–225.

Diener, J. F. A., White, R. W. and Powell, R., 2008a. Granulite facies metamorphism and subsolidus fluid-absent reworking, Strangways Range, Arunta Block, central Australia. *Journal of Metamorphic Geology*, **26**, 603–622.

Diener, J. F. A., White, R. W., Link, K., Dreyer, T. S. and Moodley, A., 2013. Clockwise, low-P metamorphism of the Aus granulite terrain, southern Namibia, during the Mesoproterozoic Namaqua Orogeny. *Precambrian Research*, **224**, 629–652.

Doukkari, S. A., Diener, J. F. A., Ouzegane, K. and Kienast, J. R., 2018. Mineral equilibrium modelling and calculated chemical potential relations of reaction textures in the ultrahigh-temperature In Ouzzal terrane (In Hihaou area, Western Hoggar, Algeria). *Journal of metamorphic Geology*, **00**, 1–24.

Droop, G. T. R., 1987. A general equation of estimating Fe^{3+} concentrations in ferromagnesian silicates and oxides from microprobe analyses using stoichiometric constraints. *Mineralogical Magazine*, **51**, 431–435.

Dumond, G., Mahan, K. H., Williams, M. L. and Karlstrom, K. E., 2007. Crustal segmentation, composite looping pressure–temperature paths, and magma enhanced metamorphic field gradients: Upper Granite Gorge, Grand Canyon, USA. *Geological Society of America Bulletin*, **119**, 202–220.

Eglington, B. M., 2006. Evolution of the Namaqua-Natal Belt, southern Africa – A geochronological and isotope geochemical review. *Journal of African Earth Sciences*, **46**, 93–111.

Eglington, B. M. and Armstrong, R. A., 2004. The Kaapvaal Craton and adjacent orogens, southern Africa: a geochronological database and overview of the geological development of the craton. *South African Journal of Geology*, **107**, 13–32.

England, P. C. and Thompson, A. B., 1984. Pressure–temperature–time paths of regional metamorphism.1. Heat transfer during the evolution of regions of thickened continental crust. *Journal of Petrology*, **24**, 894–928.

Eskola, P., 1920. The mineral facies of rocks. *Norsk Geologisk Tidsskrift*, **6**, 143–194.

Ferrero, S., Bartoli, O., Cesare, B., Salvioli-Mariani, E., Acosta-Vigil, A., Cavallo, A., Groppo, C. and Battiston, S., 2012. Microstructures of melt inclusions in anatectic metasedimentary rocks. *Journal of metamorphic Geology*, **30**, 303–322.

Fitzsimons, I. C. W. and Harley, S. L., 1994. The influence of retrograde cation-exchange on granulite P–T estimates and a convergence technique for the recovery of peak metamorphic conditions. *Journal of Petrology*, **35**, 543–576.

Forshaw, J. B., Waters, D. J., Pattison, D. R. M., Palin, R. M. and Gopon, P., 2018. A comparison of observed and thermodynamically predicted phase equilibria and mineral compositions in mafic granulites. *Journal of Metamorphic Geology*, .

Frost, B. R. and Chako, T., 1989. The Granulite Uncertainty Principle: Limitations on Thermobarometry in Granulites. *The Journal of Geology*, **97**, 435–450.

Fyfe, W. S., Price, N. J. and Thompson, A. B., 1978. *Fluids in the Earth's Crust*, Elsevier, Amsterdam.

Gapais, D., Cagnard, F., Gueydan, F., Barbey, P. and Ballèvre, M., 2009. Mountain building and exhumation processes through time: inferences from nature and models. *Terra Nova*, **21**, 188–194.

Gapais, D., Pelletier, A., Ménot, R. P. and Peucat, J. J., 2008. Palaeoproterozoic tectonics in the Terre Adélie Craton (East Antarctica). *Precambrian Research*, **162**, 531–539.

Gapais, D., Portel, A. and Machado, N., 2005. Kinematics of long-lasting Paleoproterozoic transpression within the Thompson Nickel Belt, Manitoba, Canada. *Tectonics*, **24**.

Geringer, G. J., Botha, B. J. V., Pretorius, J. J. and Ludick, D. J., 1986. Calc-alkaline volcanism along the eastern margin of the namaqua mobile belt, south Africa - A possible middle proterozoic volcanic arc. *Precambrian Research*, **33**, 139–170.

Geringer, G. J., Humphreys, H. C. and Scheepers, D. J., 1994. Lithostratigraphy, protolithology, and tectonic setting of the Areachap Group along the eastern margin of the Namaqua Mobile Belt, South Africa. *South African Journal of Geology*, **97**, 78–100.

Gibson, R. L., Robb, L. J., Kisters, A. F. M. and Cawthorn, R. G., 1996. Regional setting and geological evolution of the Okiep Copper District, Namaqualand, South Africa. *South African Journal of Geology*, **99**, 107–120.

Green, E. C. R., White, R. W., Diener, J. F. A., Powell, R., Holland, T. J. B. and Palin, R. M., 2016. Activity–composition relations for the calculation of partial melting equilibria in metabasic rocks. *Journal of Metamorphic Geology*, **34**, 845–869.

Green, R. W. E. and Durrheim, R. J., 1990. A seismic refraction investigation of the Namaqualand Metamorphic Complex, South Africa. *Journal of Geophysical Research*, **95**, 19927–19932.

Grütter, H. S., (1986). *The petrography and petrology of polymetamorphic cordierite–quartz gneisses near Geselskapbank, northeast of Springbok*, Master's thesis, University of Cape Town.

Guevara, V. E. and Caddick, M. J., 2016. Shooting at a moving target: phase equilibria modelling of high-temperature metamorphism. *Journal of metamorphic Geology*, **34**, 209–235.

Guiraud, M., Powell, R. and Rebay, G., 2001. H_2O in metamorphism and unexpected behaviour in the preservation of metamorphic assemblages. *Journal of Metamorphic Geology*, **19**, 445–454.

Handy, M. R., Mulch, A., Rosenau, M. and Rosenberg, C. L., 2001. The role of fault zone and melts as agents of weakening, hardening and differentiation of the continental crust: a synthesis. In: *Nature and tectonic significance of fault zone weakening*, (eds Holdsworth, R. E., Strachan, R. A., Magloughlin, J. F. and Knipe, R. J.), Vol. 186, pp. 305–332. Geological Society of London Special Publication.

Harley, S. L., 1989. The origins of granulites: a metamorphic perspective. *Geological Magazine*, **126**, 215–247.

Harley, S. L., 1998. On the occurrence and characterisation of ultrahigh-temperature (UHT) crustal metamorphism. In: *What Drives Metamorphic Reactions?*, (eds Treloar, P. J. and O'Brien, P. J.), Vol. 138, pp. 75–101. The Geological Society, London, Special Publication.

Harrison, T. M., 1981. Diffusion of ^{40}Ar in Hornblende. *Contributions in Mineralogy and Petrology*, **78**, 324–331.

Hartnady, C. J. H., Joubert, P. and Stowe, C., 1985. Proterozoic crustal evolution in southwestern Africa. *Episodes*, **8**, 236–244.

Hartnady, M. I. H., 2018. *Crustal Evolution of the Albany-Fraser Orogen, Southwest Australia.* PhD thesis, West Australian School of Mines, Curtin University, Australia.

Hayden, L. A., Watson, E. B. and Wark, D. A., 2008. A thermobarometer for sphene (titanite). *Contributions to Mineraloogy and Petrology*, **155**, 529–540.

Hermann, J. and Rubatto, D., 2003. Relating zircon and monazite domains to garnet growth zones: age and duration of granulite facies metamorphism in the Val Malenco lower crust. *Journal of metamorphic Geology*, **21**, 833–852.

Hinton, R. W. and Upton, B. G. J., 1991. The chemistry of zircon: Variations within and between large crystals from syenite and alkali basalt xenoliths. *Geochemica et Cosmochimica Acta*, **55**, 3287–3302.

Hodges, K. V., Le Fort, P. and A., P., 1988. Possible thermal buffering by crustal anatexis in collisional orogens: Thermobarometric evidence from the Nepalese Himalaya. *Geology*, **16**(6), 707–710.

Holland, T. J. B. and Powell, R., 2003. Activity–composition relations for phases in petrological calculations: an asymmetric multicomponent formulation. *Contributions to Mineralogy and Petrology*, **145**, 492–501.

Holland, T. J. B. and Powell, R., 2011. An improved and extended internally consistent thermodynamic dataset for phases of petrological interest, involving a new equation of state for solids. *Journal of Metamorphic Geology*, **29**, 333–383.

Holness, M. B. and Sawyer, E. W., 2008. On the Pseudomorphing of Melt-filled Pores During the Crystallization of Migmatites. *Journal of Petrology*, **7**, 1343–1363.

Hoskin, P. W. O., 1998. Minor and trace element analysis of natural zircon ($ZrSiO_4$) by SIMS and laser ablation ICPMS: A consideration and comparison of two broadly competitive techniques. *Journal of Trace and Microprobe Techniques*, **16**, 301–326.

Hoskin, P. W. O. and Black, L. P., 2000. Metamorphic zircon formation by solid-state recrystallization of protolith igneous zircon. *Journal of metamorphic Geology*, **18**, 423–439.

Hoskin, P. W. O. and Ireland, T. R., 2000. Rare earth element chemistry of zircon and its use as a provenance indicator. *Geology*, **28**, 627–630.

Hugo, P. J., Anhaeusser, C. R. and Maske, S., 1986. Some deposits of feldspar, mica and beryl in the North-western Cape Province. *Mineral Deposits of Southern Africa, Geol. Soc. S. Afr., Johannesburg*, **2**, 1651–1662.

Icenhower, J. P. and London, K., 1997. Partitioning of fluorine and chlorine between biotite and granitic melt: Experiemental calibration at 200 MPa H_2O. *Contributions to Mineralogy and Petrology*, **127**, 17–29.

Jackson, M. P. A., 1976. High-grade metamorphism and migmatisation of the Namaqua metamorphic complex around Aus in the southern Namib desert, South West Africa. *Bulletin of the Precambrian Research Unit*, **18**. University of Cape Town, 299pp.

Jackson, S. E., Pearson, N. J., Griffin, W. L. and Belousova, E. A., 2004. The application of laser ablation-inductively coupled plasma mass spectrometry to in situ U-Pb zircon geochronology. *Chemical Geology*, **211**, 47–69.

Jacobs, J., Pisarevsky, S., Thomas, R. J. and Becker, T., 2008. The Kalahari Craton during the assembly and dispersal of Rodinia. *Precambrian Research*, **160**, 142–158.

Jacobs, J., Thomas, R. J. and Weber, K., 1993. Accretion and indentation tectonics at the southern edge of the Kaapvaal craton during the Kibaran (Grenville) orogeny. *Geology*, **21**, 203–206.

Joubert, P., 1971. The regional tectonism of the gneisses of part of Namaqualand. *Bull. Precambrian Res. Unit, Univ. Cape Town*, **10**, 220.

Joubert, P., 1986a. Namaqualand—a model of Proterozoic accretion? *Transactions of the Geological Society of South Africa*, **89**, 79–96.

Joubert, P., 1986b. The Namaqualand Metamorphic Complex – a summary. In: *Mineral Deposits of Southern Africa*, (eds Anhauesser, C. R. and Maske, S.), pp. 1395–1420. Geological Society of South Africa.

Kanazawa, T., Tsunogae, T., Sato, K. and Santosh, M., 2009. The stability and origin of sodicgedrite in ultrahigh-temperature Mg-Al granulites: a case study from the Gondwana suture in southern India. *Contributions in Mineralogy and Petrology*, **157**, 95–110.

Kelsey, D. E., 2008. On ultrahigh-temperature crustal metamorphism. *Gondwana Research*, **13**, 1–29.

Kelsey, D. E. and Hand, M., 2015. On ultrahigh-temperature crustal metamorphism: Phase equilibria, trace element thermometry, bulk composition, heat sources, timescales and tectonic settings. *Geoscience Frontiers*, **6**, 311–356.

Kelsey, D. E., Clark, C. and Hand, M., 2008. Thermobarometric modelling of zircon and monazite growth in melt-bearing systems: examples using model metapelitic and metapsammitic granulites. *Journal of metamorphic Geology*, **26**, 199–212.

Kent, L. E., 1980. *Stratigraphy of South Africa (Part 1)*, R. and E. Publishers.

Khorzhinskii, D. S., 1959. *Physicochemical Basis of the Analysis of the Paragenesis of Minerals*, Consultants Bureau, New York, NY.

Kisters, A. F. M., Charlesworth, E. G., Gibson, R. L. and Anhaeusser, C. L., 1996. Steep structure formation in the okiep copper district, south africa: bulk inhomogeneous shortening of a high-grade metamorphic granite-gneiss sequence. *Journal of Structural Geology*, **18**(6), 735–751.

Korhonen, F. J., Brown, M., Clark, C. and Bhattacharya, S., 2013a. Osumilite–melt interactions in ultrahigh temperature granulites: phase equilibria modelling and implications for the P–T–t evolution of the Eastern Ghats Province, India. *Journal of Metamorphic Geology*, **31**, 881–907.

Korhonen, F. J., Clark, C., Brown, M., Bhattacharya, S. and Taylor, R. J. M., 2013b. How long-lived is ultrahigh temperature (UHT) metamorphism? Constraints from zircon and monazite geochronology in the Eastern Ghats orogenic belt, India. *Precambrian Research*, **234**, 322–350.

Korhonen, F. J., Saito, S., Brown, M. and Siddoway, C. S., 2010. Modeling multiple melt loss events in the evolution of an active continental margin. *Lithos*, **116**, 230–248.

Kriegsman, L. M. and Hensen, B. J., 1998. Back reaction between restite and melt: Implications for geothermobarometry and pressure-temperature paths. *Geology*, **26**, 1111–1114.

Lambert, C. W., (2013). *Granitic melt transport and emplacement along transcurrent shear zones: Case study of the Pofadder Shear Zone in South Africa and Namibia*, Master's thesis, University of Stellenbosch, 128pp.

Leake, B. E., Woolley, A. R., Arps, C. E. S., Birch, W. D., Gilbert, M. C., Grice, J. D., Hawthorne, F. C., Kato, A., Kisch, . H. J., Krivovichev, V. G., Linthout, K., Laird, J., Mandarino, J., Maresch, W. V., Nickel, E. H., Rock, N. M. S., Schumacher, J. C., Smith, D. C., Stephenson, N. C. N., Ungaretti, L., Whittacker, E. J. W. and Youzhi, G., 1997. Nomenclature of amphiboles; Report of the Subcommittee on Amphiboles of the International Mineralogical Association Commission on New Minerals and Mineral Names. *European Journal of Mineralogy*, **9**, 623–651.

Li, X. H., Long, W. G., Li, Q. L., Zheng, Y. F., Yang, Y. H., Chamberlian, K. R., Wan, D. F., Guo, C. H., Wang, X. C. and Tao, H., 2010. Penglai zircon megacryst: A potential new working reference material for microbeam determination of Hf isotopes and U–Pb age. *Geostandards and Geoanalytical research*, **34**, 117–134.

Li, Z. X., Bogdanova, S. V., Collins, A. S., Davidson, A., De Waele, B., Ernst, R. E., Fitzsimons, I. C. W., Fuck, R. A., Gladkochub, D. P., Jacobs, J., Karlstrom, K. E., Lu, S., Natapov, L. M., Pease, V., Pisarevsky, S. A., Thrane, K. and Vernikovsky, V., 2008. Assembly, configuration, and break-up history of Rodinia: a synthesis. *Precambrian Research*, **160**, 179–210.

Ludwig, K. R., 2008. Icebergsoplot 4.15: A Geochronological Toolkit for Microsoft Excel™. *Berkley Geochronology Center, Berkley, California*, .

Lyubetskaya, T. and Ague, J. J., 2009. Effect of metamorphic reactions on thermal evolution in collisional orogens. *Journal of metamorphic Geology*, **27**, 579–600.

Macey, P. H., Bailie, R. H., Miller, J. A., Thomas, R. J., de Beer, C., Frei, D. and Le Reux, P. J., 2018. Implications of the distribution, age and origins of the granites of the Mesoproterozoic Spektakel Suite for the timing of the Namaqua Orogeny in the Bushmanland Subprovince of the Namaqua-Natal Metamorphic Province, South Africa. *Precambrian Research*, .

Macey, P. H., Minnaar, H., Miller, J. A., Lambert, C. W., Kisters, A. F. M., Diener, J. F. A., Thomas, R. J., Groenewald, C. A., Indongo, J., Angombe, M., Smith, H., Shifatoka, G., Le Roux, P. and Frei, D., (2015). The Precambrian geology of the Warmbad region, southern Namibia. An interim explanation to 1:50 000 Geological Map Sheets of the 1:250 000 2818 Warmbad sheet, *Technical report*, Geological Survey of Namibia and Council for Geoscience of South Africa.

Macey, P. H., Siegfried, H. P., Minnaar, H., Almond, J. and Botha, P. M. W., 2011. *The geology of the Loeriesfontein area. 1:250 000 map sheet explanation 3018*, Council for Geoscience.

Macey, P. H., Thomas, R. J., Minnaar, H., Gresse, P. G., Lambert, C. W., Groenewald, C. A., Miller, J. A., Indongo, J., Angombe, M., G., S., Frei, D., Diener, J. F. A., Kisters, A. F. M., Dhansay, T., Smith, H., Doggart, S., Le Roux, P., Hartnady, M. I. and Tinguely, C., 2017. Origin and evolution of the ∼1.9 Ga Richtersveld Magmatic Arc, SW Africa. *Precambrian Research*, **292**, 417–451.

McClung, C. R., 2006. *Basin analysis of the Bushmanland Basin, Namaqua metamorphic complex, Northern Cape province, South Africa.* PhD thesis, University of Johannesburg.

McStay, J. H., 1991. *Granulite-facies metamorphism, fluid buffering and partial melting in the Buffels River area of the Namaqualand metamorphic complex, South Africa.* PhD thesis, University of Cape Town.

Melcher, F., Graupner, T., Henjes-Kunst, F., Oberthür, T., Sitnikova, M., Gäbler, E., Gerdes, A., Brätz, H., Davis, D. and Dewaele, S., 2008. Analytical fingerprint of columbite-tantalite (coltan) mineralization in pegmatites: focus on Africa, *Proceedings, ninth international congress for applied mineralogy (ICAM).*

Miller, R. M., 2008. *The Geology of Namibia*, Vol. 2, Geological Survey of Namibia, Windhoek.

Miller, R. M., 2012. Review of Mesoproterozoic magmatism, sedimentation and terrane amalgamation in southwestern Africa. *South African Journal of Geology*, **115**, 417–448.

Mitchell, R. J., Johnson, T. E., Clark, C., Gupta, S., Brown, M., Harley, S. L. and Taylor, R. J. M., 2018. Neoproterozoic evolution and Cambrian reworking of ultrahigh temperature granulites in the Eastern Ghats Province, India. *Journal of metamorphic Geology*, **00**, 1–30.

Moen, H. F. G. and Toogood, D. J., 2007. *The geology of the Onseepkans area. Explanation: Sheet 2818*, Council for Geoscience.

Moore, J. M. and Waters, D. J., 1990. Geochemistry and origin of cordierite–orthoamphibole/orthopyroxene–phlogopite rocks from Namaqualand, South Africa. *Chemical Geology*, **85**, 77–100.

Moulas, E., Podladchikov, Y. Y., Aranovich, L. Y. and D., K., 2013. The Problem of Depth in Geology: When Pressure Does Not Translate into Depth. *Petrology*, **21**, 527–538.

Mouri, H., Andreoli, M. A. G., Kienast, J. R., Guiraud, M. and de Waal, S. A., 2003. First occurrence of the rare "corundum + quartz" assemblage in the high-grade zone from the Namaqualand Metamorphic Complex, South Africa: evidence for higher-PT metamorphism? *Mineralogical Magazine*, **67**, 1015–1021.

Mouri, H., Guiraud, M. and Hensen, B. J., 1996. Petrology of phlogopite–sapphirine-bearing Al–Mg granulites from Ihouhaouene, In Ouzzal, Hoggar, Algeria: an example of phlogopite stability at high temperature. *Journal of metamorphic Geology*, **14**, 725–738.

Mouri, H., Guiraud, M. and Osanai, Y., 2004. Review of "corundum + quartz" assemblage in nature: Possible indicator of ultra-high temperature conditions? *Journal of Mineralogical and Petrological Sciences*, **99**, 159–163.

Munoz, J. L. and Luddington, S., 1977. Fluorine-hydroxyl exchange in synthetic muscovite and its application to muscovite-biotite assemblages. *American Mineralogist*, **62**, 304–308.

Münster, A., 1970. *Classical thermodynamics*, John Wiley and Sons.

Nakano, N., Osanai, Y., Baba, S., Adachi, T., Hokada, T. and Toyoshima, T., 2011. Inferred ultrahigh-temperature metamorphism of amphibolitized olivine granulite from the Sør Rondane Mountains, East Antarctica. *Polar Science*, **5**, 345–359.

Nichols, G. T., Berry, R. F. and Green, D. H., 1992. Internally consistent gahnitic spinel-cordierite-garnet equilibria in the FMASHZn system: geothermobarometry and applications. *Contributions in Mineralogy and Petrology*, **111**, 362–377.

Nicolaysen, L. O. and Burger, A. J., 1965. Note on an extensive zone of 1000 million-year old Metamorphic and Igneous rocks in southern Africa. *Sciences de la Terre*, **10**, 497–518.

Nironen, M., 1997. The Svecofennian Orogen: a tectonic model. *Precambrian Research*, **86**, 21–44.

Nishimiya, Y., Tsunogae, T. and Santosh, M., 2010. Sapphirine + quartz corona around magnesian (XMg ∼0.58) staurolite from the Palghat-Cauvery Suture Zone, southern India: Evidence for high-pressure and ultrahigh-temperature metamorphism within the Gondwana suture. *Lithos*, **114**, 490–502.

Nowicki, T. E., Frimmel, H. E. and Waters, D. J., 1995. The occurrence of osumilite in pelitic granulites of the Namaqualand Metamorphic Complex, South Africa. *South African Journal of Geology*, **98**, 191–201.

Ouzegane, K., Kienast, J. R., Bendaoud, A. and Drareni, A., 2003. A review of Archaean and Paleoproterozoic evolution of the In Ouzzal granulitic terrane (Western Hoggar, Algeria). *Journal of African Earth Sciences*, **37**, 207–227.

Palin, R. M., Weller, O. M., Waters, D. J. and Dyck, B., 2016. Quantifying geological uncertainty in metamorphic phase equilibria modelling; a Monte Carlo assessment and implications for tectonic interpretations. *Geoscience Frontiers*, **7**, 591–607.

Palin, R. M., White, R. W., Green, E. C. R., Powell, R., Diener, J. F. A. and Holland, T. J. B., 2016a. High-grade metamorphism and partial melting of basic and intermediate rocks. *Journal of Metamorphic Geology*, **34**, 871–892.

Paterson, B. A., Stephens, W. E., Rogers, G., Williams, I. S., Hinton, R. W. and Herd, D. A., (1992). *The nature of zircon inheritance in two granite plutons*, The Geological Society of America, chapter The nature of zircon inheritance in two granite plutons.

Paton, C., Hellstrom, J., Paul, B., Woodhead, J. and Hergt, J., 2011. Iolite: Freeware for the visualisation and processing of mass spec- trometric data. *Journal of Analytical Atomic Spectrometry*, **26**, 2508–2518.

Peterson, J. W., Chako, T. and Kuehner, S. M., 1991. The effects of fluorine on the vapor-absent melting of phlogopite + quartz: implications for deep-crustal processes. *American Mineralogist*, **76**, 470–476.

Pettersson, Å., 2008. *Mesoproterozoic crustal evolution in Southern Africa.* PhD thesis, University of Gothenburg.

Pettersson, Å., Cornell, D. H., Moen, H. F. G., Reddy, S. and Evans, D., 2007. Ion-probe dating of 1.2 Ga collision and crustal architecture in the Namaqua-Natal Province of southern Africa. *Precambrian Research*, **158**, 79–92.

Pettersson, Å., Cornell, D. H., Yuhara, M. and Hirahara, Y., 2009. Sm–Nd data for granitoids across the Namaqua sector of the Namaqua–Natal Province, South Africa. *Geological Society of London Special Publications*, **323**, 219–230.

Powell, R., 1983b. Fluids and melting under upper amphibolite facies conditions. *J. geol. Soc. London*, **140**, 629–633.

Powell, R. and Holland, T. J. B., 1988. An internally consistent thermodynamic dataset with uncertainties and correlations: 3. Application, methods, worked examples and a computer program. *Journal of Metamorphic Geology*, **6**, 173–204.

Powell, R. and Holland, T. J. B., 1994. Optimal geothermometry and geobarometry. *American Mineralogist*, **79**, 120–133.

Powell, R. and Holland, T. J. B., 2008. On thermobarometry. *Journal of Metamorphic Geology*, **26**, 155–179.

Powell, R., Guiraud, M. and White, R. W., 2005. Truth and beauty in metamorphic phase equilibria: Conjugate variables and phase diagrams. *Canadian Mineralogist*, **43**, 21–33.

Raith, J. G. and Harley, S. L., 1998. Low-P/high-T metamorphism in the Okiep Copper District, western Namaqualand, South Africa. *Journal of Metamorphic Geology*, **16**, 281–305.

Raith, J. G., Cornell, D. H., Frimmel, H. E. and De Beer, C. H., 2003. New insights into the geology of the Namaqua tectonic province, South Africa, from ion probe dating of detrital and metamorphic zircon. *Journal of Geology*, **111**, 347–366.

Rao, C. V. D., Santosh, M. and Chmielowski, R. M., 2012. Sapphirine granulites from Panasapattu, Eastern Ghats belt, India: Ultrahigh-temperature metamorphism in a Proterozoic convergent plate margin. *Geoscience Frontiers*, **3**, 9–31.

Reid, D. L., Welke, H. J., Erlank, A. J. and Moyes, A. B., 1987. Composition, age and tectonic setting of amphibolites in the central Bushmanland Group, western Namaqua Province, southern Africa. *Precambrian Research*, **36**, 99–126.

Reuber, G., Kaus, B. J. P., Schmalholz, S. M. and White, R. W., 2016. Nonlithostatic pressure during subduction and collision and the formation of (ultra) high-pressure rocks. *Geology*, **44**, 343–346.

Rice, J. M. and Ferry, J. M., 1982. Buffering, infiltration and the control of intensive variables during metamorphism., *Characterization of metamorphism through mineral equilibria*. Reviews in mineralogy, Vol. 10. Mineral. Soc. of America, 263–326.

Ridley, J., 1986. Modelling of the relations between reaction enthalpy and the buffering of reaction progress in metamorphism. *Mineralogical Magazine*, **50**, 375–384.

Robb, L. J., Armstrong, R. A. and Waters, D. J., 1999. Nature and duration of mid-crustal granulite facies metamorphism and crustal growth: evidence from single zircon U–Pb geochronology in Namaqualand, South Africa. *Journal of Petrology*, **40**, 1747–1770.

Roberts, M. P. and Finger, F., 1997. Do U–Pb ages from granulites reflect peak metamorphic conditions? *Geology*, **25**, 319–322.

Rosenberg, C. L. and Handy, M. R., 2005. Experimental deformation of partially melted granite revisited: implications for the continental crust. *Journal of Metamorphic Geology*, **23**, 19–28.

Rubatto, D., 2002. Zircon trace element geochemistry: partitioning with garnet and the link between U–Pb ages and metamorphism. *Chemical Geology*, **184**, 123–138.

Rubatto, D., Williams, I. S. and Buick, I. S., 2001. Zircon and monazite response to prograde metamorphism in the Reynolds Range, central Australia. *Contributions in Mineralogy and Petrology*, **140**, 458–468.

Rumble, D., 1982. The role of perfectly mobile components in metamorphism. *Annual Review of Earth and Planetary Sciences*, **109**, 221–233.

Sandiford, M., 1985. The metamorphic evolution of granulites at Fyfe Hills; implications for Archean crustal thickness in Enderby Land, Antarctica. *Journal of metamorphic Geology*, **3**, 155–178.

Sandiford, M. and Powell, R., 1986. Deep crustal metamorphism during continental extension: modern and ancient examples. *Earth and Planetary Science Letters*, **79**, 151–158.

Sandiford, M., McLaren, S. and Neumann, N., 2002. Long-term thermal consequences of the redistribution of heat-producing elements associated with large-scale granitic complexes. *Journal of Metamorphic Geology*, **20**, 87–98.

Santosh, M., Tsunogae, T. and Koshimoto, S., 2004. First Report of Sapphirine-bearing Rocks from the Palghat-Cauvery Shear Zone System, Southern India. *Gondwana Research*, **7**, 620–626.

Santosh, M., Tsunogae, T., Li, J. H. and Liu, S. J., 2007. Discovery of sapphirine-bearing Mg–Al granulites in the North China Craton: Implications for Paleoproterozoic ultrahigh temperature metamorphism. *Gondwana Research*, **11**, 263–285.

Schorn, S., 2018. Dehydration of metapelites during high-P metamorphism: The coupling between fluid sources and fluid sinks. *Journal of metamorphic Geology*, **36**, 369–391.

Schorn, S. and Diener, J. F. A., 2017. Details of the gabbro-to-eclogite transition determined from microtextures and calculated chemical potential relationships. *Journal of Metamorphic Geology*, **35**, 55–75.

Schorn, S., Diener, J. F. A., Powell, R. and Stüwe, K., 2018. Thermal buffering in the orogenic crust. *Geology*, **46**, 643–646.

Shazia, J. R., Santosh, M. and Sajeev, K., 2012. Peraluminous sapphirine–cordierite pods in Mg-rich orthopyroxene granulite from southern India: Implications for lower crustal processes. *Journal of Asian Earth Sciences*, **58**, 88–97.

Shulters, J. C. and Bohlen, S. R., 1989. The stability of hercynite and hercynite-gahnite spinels in corundum-or quartz-bearing assemblages. *Journal of Petrology*, **30**, 1017–1031.

Sizova, E., Gerya, T. and Brown, M., 2014. Contrasting styles of Phanerozoic and Precambrian continental collision. *Gondwana Research*, **25**, 522–545.

Sláma, J., Košler, J., Condon, D. J., Crowley, J. L., Gerdes, A., Hanchar, J. M., Horstwood, M. S. A., Morris, G. A., Nasdala, L., Norberg, N., Schaltegger, U., Schoene, B., Turbett, M. N. and Whitehouse, M. J., 2008. Plešovice zircon–a new natural reference material for U–Pb and Hf isotopic microanalysis. *Chemical Geology*, **249**, 1–35.

Spencer, C. J., Kirkland, C. L. and Taylor, R. J. M., 2016. Strategies towards statistically robust interpretations of *in situ* U–Pb zircon geochronology. *Geoscience Frontiers*, **7**, 581–589.

Stern, R. A., Bodorkos, S., Kamo, S. L., Hickman, A. H. and Corfu, F., 2009. Measurement of SIMS instrumental mass fractionation of Pb isotopes during zircon dating. *Geostandards and Geoanalytical Research*, **33**, 145–168.

Štípská, P., Powell, R., White, R. W. and Baldwin, J. A., 2010. Using chemical potential relationships to account for coronas around kyanite: an example from the Bohemian Massif. *Journal of Metamorphic Geology*, **28**, 97–116.

Stowe, C. W., 1986. Synthesis and interpretation of structures along the north-eastern boundary of the Namaqua tectonic province, South Africa. *South African Journal of Geology*, **89**, 185–198.

Stuck, T. J. and Diener, J. F. A., 2017. Mineral equilibria constraints on open-system melting in metamafic compositions. *Journal of metamorphic Geology*, **36**, 255–281.

Stüwe, K., 1995. Thermal buffering effects at the solidus - implications for the equilibration of partially melted metamorphic rocks. *Tectonophysics*, **248**, 39–51.

Stüwe, K., 1997. Effective bulk composition changes due to cooling: a model predicting complexities in retrograde reaction textures. *Contributions in Mineralogy and Petrology*, **129**, 43–52.

Stüwe, K., 2007. *Geodynamics of the lithosphere: an introduction*, Springer Science and Business Media.

Stüwe, K. and Powell, R., 1997. Reaction Enthalpies of Subsolidus Equilibria in Pelitic Rocks. Magnitude and Influence on Cretaceous Metamorphism of the Koralm Complex, Eastern Alps. *Naturwissenschaftlicher Verein für Steiermark*, **127**, 45–60.

Stüwe, K., Sandiford, M. and Powell, R., 1993. Episodic metamorphism and deformation in low-pressure, high-temperature terranes. *Geology*, **21**, 829–832.

Tajčmanová, L. and Konopásek, J., 2003. The role of zinc in stabilization of spinel-bearing mineral assemblages–examples from the Bohemian Massif and NW Namibia. *Geolines*, **16**, 102–103.

Tajčmanová, L., Vrijmoed, J. and Moulas, E., 2015. Grain-scale pressure variations in metamorphic rocks: implications for the interpretation of petrographic observations. *Lithos*, **216**, 338–351.

Taylor, R. J. M., Kirkland, C. L. and Clark, C., 2016. Accessories after the facts: Constraining the timing, duration and conditions of high-temperature metamorphic processes. *Lithos*, **264**, 239–257.

Tenczer, V., Powell, R. and Stüwe, K., 2006. Evolution of H_2O content in a polymetamorphic terrane: the Plattengneiss Shear Zone (Koralpe, Austria). *Journal of Metamorphic Geology*, **24**, 281–295.

Thomas, R. J., Agenbacht, A. L. D., Cornell, D. H. and Moore, J. M., 1994. The Kibaran of southern Africa: tectonic evolution and metallogeny. *Ore Geology Reviews*, **9**, 103–160.

Thomas, R. J., Cornell, D. H., Moore, J. M. and Jacobs, J., 1994b. Crustal evolution of the Namaqua–Natal Metamorphic Province, South Africa. *South African Journal of Geology*, **97**, 8–14.

Thomas, R. J., Macey, P. H., Spencer, C., Dhansay, T., Diener, J. F. A., Lambert, C. W., Frei, D. and Nguno, A., 2016. The Sperrgebiet Domain, Aurus Mountains, SW Namibia: A ∼2020–850 Ma window within the Pan-African Gariep Orogen. *Precambrian Research*, **286**, 35–58.

Thompson, A. B. and Connolly, J. A. D., 1995. Melting of the continental crust: petrological constraints on anatexis in zones and other tectonic settings. *Journal of Geophysical Research*, **100**, 15565–15579.

Thompson, J. B., 1959. Local equilibrium in metasomatic processes. In: *Researches in Geochemistry*, (ed. Abelson, P. H.), pp. 427–457. Wiley, New York.

Thompson, J. B., 1970. Geochemical reaction and open systems. *Geochimica et Cosmochimica Acta*, **34**, 529–551.

Tomascak, P. B., Krogstad, E. J. and Walker, R. J., 1996. U–Pb monazite geochronology of granitic rocks from Maine: Implications for Late Paleozoic tectonics in the Northern Appalachians. *The Journal of Geology*, **104**, 185–195.

Tsunogae, T. and Santosh, M., 2003. Sapphirine and Corundum-bearing Granulites from Karur, Madurai Block, Southern India. *Gondwana Research*, **6**, 925–930.

Van Aswegen, G., (1983). *The Namaqualand Metamorphic Complex*, Geological Society of South Africa, chapter The Gladkop Suite–the grey and pink gneisses of Steinkopf, pp. 31–44.

van Niekerk, H. S., 2006. *The origin of the Kheis Terrane and its relationship with the Archean Kaapvaal Craton and the Grenvillian Namaqua province in southern Africa.* PhD thesis, University of Johannesburg.

Vielzeuf, D. and Holloway, J. R., 1988. Experimental determination of the fluid-absent melting relations in the pelitic system - consequences for crustal differentiation. *Contributions to Mineralogy and Petrology*, **98**, 257–276.

Vielzeuf, D., Clemens, J. D., Pin, C. and Moinet, E., 1990. Granites, granulites and crustal differentiation, *Granulites and Crustal Evolution.* NATO Scientific Publication, Kluwer Academic Publishers, Dordrecht.

Vrijmoed, J. C. and Podladchikov, Y. Y., 2015. Thermodynamic equilibrium at heterogeneous pressure. *Contributions to Mineralogy and Petrology*, **170**, 9–27.

Walther, J. V. and Orville, P. M., 1982. Volatile production and transport in regional metamorphism. *Contributions in Mineralogy and Petrology*, **79**, 252–257.

Waters, D. J., 1986a. Metamorphic history of sapphirine-bearing and related magnesian gneisses from Namaqualand, South Africa. *Journal of Petrology*, **27**, 541–565.

Waters, D. J., 1986b. Metamorphic zonation and thermal history of pelitic gneisses from western Namaqualand, South Africa. *South African Journal of Geology*, **89**, 97–102.

Waters, D. J., 1988. Partial melting and the formation of granulite facies mineral assemblages in Namaqualand, South Africa. *Journal of Metamorphic Geology*, **6**, 387–404.

Waters, D. J., 1989. Metamorphic evidence for the heating and cooling path of Namaqualand granulites. In: *Evolution of metamorphic belts*, (eds Daly, J. S., Cliff, R. A. and Yardley, B. W. D.), Vol. 4, pp. 357–363. Geological Society of London Special Publications.

Waters, D. J., 1990. Thermal history and tectonic setting of the Namaqualand granulites, southern Africa: clues to Proterozoic crustal development. In: *Granulites and Crustal Evolution*, (eds Vielzeuf, D. and Vidal, P.), Dordrecht, pp. 243–256. Kluver.

Waters, D. J., 1991. Hercynite–quartz granulites: Phase relations and implications for crustal processes. *European Journal of Mineralogy*, **3**, 367–386.

Waters, D. J. and Whales, C. J., 1984. Dehydration melting and the granulite transition in metapelites from southern Namaqualand, South Africa. *Contributions to Mineralogy and Petrology*, **88**, 269–275.

Watson, E. B., Wark, D. A. and Thomas, J. B., 2006. Crystallization thermometers for zircon and rutile. *Contributions to Mineralogy and Petrology*, **151**, 413–433.

Whalen, J. B., L., C. K. and Chappell, B. W., 1987. A-type granites: geochemical characteristics, discrimination and petrogenesis. *Contributions in Mineralogy and Petrology*, **95**, 407–419.

White, R. W. and Powell, R., 2002. Melt loss and the preservation of granulite facies mineral assemblages. *Journal of Metamorphic Geology*, **20**, 621–632.

White, R. W. and Powell, R., 2010. Retrograde melt–residue interaction and the formation of near-anhydrous leucosomes in migmatites. *Journal of Metamorphic Geology*, **28**, 579–597.

White, R. W. and Powell, R., 2011. On the interpretation of retrograde reaction textures in granulite facies rocks. *Journal of Metamorphic Geology*, **29**, 131–149.

White, R. W., Powell, R. and Baldwin, J. A., 2008. Calculated phase equilibria involving chemical potentials to investigate the textural evolution of metamorphic rocks. *Journal of Metamorphic Geology*, **26**, 181–198.

White, R. W., Powell, R. and Clarke, G. L., 2002. The interpretation of reaction textures in Fe-rich metapelitic granulites of the Musgrave Block, central Australia: constraints from mineral equilibria calculations in the system K_2O–FeO–MgO–Al_2O_3–SiO_2–H_2O–TiO_2–Fe_2O_3. *Journal of Metamorphic Geology*, **20**, 41–55.

White, R. W., Powell, R. and Halpin, J. A., 2004. Spatially-focussed melt formation in aluminous metapelites from Broken Hill, Australia. *Journal of Metamorphic Geology*, **22**, 825–845.

White, R. W., Powell, R. and Holland, T. J. B., 2001. Calculation of partial melting equilibria in the system Na_2O–CaO–K_2O–FeO–MgO–Al_2O_3–SiO_2–H_2O (NCKFMASH). *Journal of Metamorphic Geology*, **19**, 139–153.

White, R. W., Powell, R. and Holland, T. J. B., 2007. Progress relating to calculation of partial melting equilibria for metapelites. *Journal of Metamorphic Geology*, **25**, 511–527.

White, R. W., Powell, R. and Johnson, T. E., 2014b. The effect of Mn on mineral stability in metapelites revisited: new a–x relations for manganese-bearing minerals. *Journal of Metamorphic Geology*, **32**, 809–828.

White, R. W., Powell, R., Holland, T. J. B. and Worley, B. A., 2000. The effect of TiO_2 and Fe_2O_3 on metapelitic assemblages at greenschist and amphibolite facies conditions: mineral equilibria calculations in the system K_2O–FeO–MgO–Al_2O_3–SiO_2–H_2O–TiO_2–Fe_2O_3. *Journal of Metamorphic Geology*, **18**, 497–511.

White, R. W., Powell, R., Holland, T. J. B., Johnson, T. E. and Green, E. C. R., 2014a. New mineral activity–composition relations for thermodynamic calculations in metapelitic systems. *Journal of Metamorphic Geology*, **32**, 261–286.

Wiedenbeck, M., Allé, P., Corfu, F., Griffin, W. L., Meier, M., Oberli, F., von Quadt, A., Roddick, J. C. and Spiegel, W., 1995. Three natural zircon standards for U–Th–Pb, Lu–Hf, trace element and REE analyses. *Geostandards Newsletter*, **19**, 1–23.

Willner, A. P., 1995. Pressure–temperature evolution of a low-pressure amphibolite facies terrane in central Bushmanland (Namaqua mobile belt, South Africa). *Communications of the Geological Survey of Namibia*, **10**, 5–19.

Yakymchuk, C. and Brown, M., 2014. Consequences of open system melting in tectonics. *Journal of the Geological Society*, **171**, 21–40.

Yamato, P. and Brun, J.-P., 2017. Metamorphic record of catastrophic pressure drops in subduction zones. *Nature Geoscience*, **10**, 46.

Yuhara, M., Kagami, H. and Tsuchiya, N., 2001. Rb–Sr and Sm–Nd systematics of granitic and metamorphic rocks in the Namaqualand Metamorphic Complex, South Africa: Implications for evolution of marginal part of Kaapvaal craton. *Mem. Natl. Inst. Polar Res.*, **55**, 127–144.

Zack, T., Moraes, R. and Kronz, A., 2004. Temperature dependence of Zr in rutile: empirical calibration of a rutile thermometer. *Contributions to Mineralogy and Petrology*, **148**, 471–488.

Zen, E. A., 1988. Thermal modelling of stepwise anataxis in a thrust-thickened sialic crust. *Transactions of the Royal Society of Edinburgh. Earth Sciences*, **79**, 223–235.

Appendix A

Enthalpy calculations in THERMOCALC

The following is based on a personal communication by R. Powell.
When calculating volume, we start with molar G of a system

$$G = \sum p_k G_k = \sum p_k \sum p_{k\ell}\, \mu_{k\ell} \tag{A.1}$$

in which p_k is the proportion of phase k in the system, and $p_{k\ell}$ the proportion of end-member ℓ in phase k. The chemical potential, $\mu_{k\ell}$, is also a function of $p_{k\ell}$.
The molar volume is

$$V = \left(\frac{\partial G}{\partial P}\right)_{\text{equil}}$$

the rate of change of the G of the equilibrium system with P (at constant temperature, θ and composition X, of the system). This is calculated using a central difference

$$V \approx \frac{G|_{P+\delta} - G|_{P-\delta}}{2\delta}$$

evaluating the *equilibrium* G at $P \pm \delta$.
THERMOCALC calculates V using

$$\sum p_k \sum p_{k\ell} \left(\frac{\partial \mu_{k\ell}}{\partial P}\right)_{p_i, p_{ij}} \approx \sum p_k \sum p_{k\ell} \frac{\mu_{k\ell}|_{P+\delta} - \mu_{k\ell}|_{P-\delta}}{2\delta} \tag{A.2}$$

ignoring the fact that the proportions of phases and end-members are changing as P changes. This is convenient because the equilibrium does not need to be calculated at $P \pm \delta$. The $\mu_{k\ell}$ in A.2 are calculated at the indicated $P \pm \delta$, but with the $p_{k\ell}$ calculated at P.
The reason this works is a little subtle: we rewrite (A.1) for an arbitrary amount of system as

$$nG = \sum \sum n_{k\ell} \mu_{k\ell}$$

in which $n_{k\ell} = n\, p_k\, p_{k\ell}$. Now, by the chain rule

$$nV = n\left(\frac{\partial G}{\partial P}\right)_{\text{equil}} = n\left(\frac{\partial G}{\partial P}\right)_{n_{ij}} + n\sum\sum\left(\frac{\partial G}{\partial n_{k\ell}}\right)\left(\frac{\partial n_{k\ell}}{\partial P}\right) \tag{A.3}$$

The key is that, at equilibrium

$$\left(\frac{\partial G}{\partial n_{k\ell}}\right) = 0$$

zeroing the double sum in A.3. Therefore, as evaluated by THERMOCALC

$$V = \left(\frac{\partial G}{\partial P}\right)_{\theta, n_{ij}} \qquad \text{and, e.g.,} \qquad H = \left(\frac{\partial \frac{G}{T}}{\partial \frac{1}{T}}\right)_{P, n_{ij}}$$

Appendix B

Methods

B.1 Mineral chemistry determination

Mineral compositions were determined using a JEOL JXA-8100 electron microprobe located at the University of Cape Town, South Africa. Analyses were carried out using a 15 kV acceleration voltage, 20 nA probe current and 2–3 μm spot size. Counting times were 5 s for both backgrounds and 10 s for peaks on all elements. A range of synthetic and natural mineral standards were employed for element calibration. Mineral formulae were calculated using the software PET 7 (Dachs, 1998). Representative analyses are reported in appendix .

B.2 Bulk rock composition determination

Whole rock powders were prepared from the freshest available samples and alteration crusts were carefully removed. The samples were split using a hydraulic splitter and crushed into fragments smaller than 10 mm using a jaw crusher. About 50–200 g of sample material was ground to powder using a SeibTechnik carbon steel swing mill. Whole-rock major elements were determined on fusion discs, for which 2 g of sample powder were dried at $\sim$110 °C overnight and weighted to determine the adsorbed volatile content. The sample was then roasted at $\sim$850 °C for four hours to remove all structural volatiles (e.g. H_2O and CO_2). The weight loss was used to determine wt. % loss on ignition (L.O.I.). Flux fusion discs were prepared using 0.7 g of roasted sample powder and 6 g of Claisse flux beads containing 57% Li tetraborate- 43% Li metaborate with a small amount of LiBr as a releasing agent. The mixture was then melted and homogenized in a Pt crucible over a gas flame in a Claisse M4 automated fluxer and poured into a Pt mold to form a fusion disc. All samples were analysed for whole-rock major elements using a Panalytical Axios XRF wavelength-dispersive spectrometer housed at the Department of Geosciences, University of Cape Town. Machine calibration was based on a series of well-characterised natural rock powder standard reference materials issued by organisations such as MINTEK, the United States Geological Survey and the Geological Survey of Japan, prepared identically as the samples for analysis. In all cases,

calibration curves of known concentration versus measured analysis peak intensities corrected for background were used to obtain elemental concentrations in unknowns. Absorption and enhancement effects were corrected through iterative correction routines employing mass attenuation coefficients. The statistically calculated lower limits of detection are in the range of parts per million, however the propagated uncertainty due to sample preparation are conventionally quantified as 1 % relative (1σ). The chosen relatively large sample sizes are thought as appropriate for investigating the prograde-to-peak metamorphic history, as the rocks were fluid- or melt-bearing during this time and consequently consisted of relatively large equilibration volumes (cf. Guevara and Caddick, 2016).

B.3 Phase diagram modelling

Phase diagrams are constructed using THERMOCALC v3.45e (Powell and Holland, 1988) and an updated version of the dataset ds6 (file tc-ds63.txt, created 05/01/2015; Holland and Powell, 2011). *P–T* projection and chemical potential diagrams in section 7.2.1 are calculated using dataset file tc-ds62.txt (created 06/02/2012) because of improved consistency between phase relations and petrographic observations. The activity–composition relationships for biotite, chlorite, chloritoid, cordierite, garnet, orthopyroxene, staurolite are those of White *et al.* (2014b), ilmenite–hematite is from White *et al.* (2000) with updates for geikielite solid solution of White *et al.* (2014b), spinel–magnetite is from White *et al.* (2002), C1 plagioclase and K-feldspar are from Holland and Powell (2003) and muscovite–paragonite solid solution is from White *et al.* (2014a), but with a reduced G^{mod} value (see notation in Green *et al.*, 2016) for the margarite end-member of 5 kJ.mol^{-1} from 6.5 kJ.mol^{-1} (Palin *et al.*, 2016a). Granitic melt is from White *et al.* (2014a), tonalitic melt and augitic clinopyroxene are from Green *et al.* (2016). Orthoamphibole is from Diener and Powell (2010), updated for use with the Holland and Powell (2011) dataset in the same way as the clinoamphibole and omphacite models were in Green *et al.* (2016). The aluminosilicates, sphene, rutile, quartz and aqueous fluid (H_2O) are taken as pure end-member phases.

B.4 Zircon and Monazite geochronology and geochemistry

B.4.1 Sample preparation

Representative samples were selected for in-situ zircon- and monazite geochronological and geochemical analysis to constrain the timing of high-grade metamorphism and, where possible, the age of deposition of precursor sediments. Sample preparation was carried out at Central Analytical Facilities, University of Stellenbosch (South Africa). Heavy minerals were separated from 1–2 kg samples using standard methods. Samples were jaw-crushed to gravel–coarse sand size and further comminuted to sand size using a disc mill. After careful sieving heavy minerals were manually concentrated using water–gravity separation on a Super Panner. Zircons and monazites were separated from other heavy minerals using a

Frantz magnetic separator and heavy liquids (Tetrabromoethane). A representative number of zircon and monazite grains ranging between 50–150 μm was hand-picked and mounted in epoxy resin. After polishing, cathodoluminescent (CL) images were collected for zircon using a Carl Zeiss MERLIN high resolution field emission scanning electron microscope (FE SEM) equipped with a CL detector. Working conditions were 10 kV acceleration voltage and 9.6–10.9 mm working distance. Backscattered-electron (BSE) images of monazite were taken using the same instrument and acceleration voltage of 20 kV and a working distance of 9.8 mm.

B.4.2 Laser ablation split stream inductively coupled plasma mass spectrometry (LASS ICP-MS)

Elemental and isotopic composition data were collected using the Laser Ablation Split Stream ICP-MS housed at the GeoHistory Facility in the John de Laeter Centre at Curtin University (Perth, Australia). The LASS set-up is shown schematically in Figure B.1. Samples were ablated using a Resonetics RESOlution M-50A-LR system utilising a Compex 102-193 nm excimer UV laser equipped with a Laurin Technic S155 cell. For zircons, laser spot diameter was 33 and 22 μm for cores and rims, respectively. The laser operated at a repetition rate of 4 Hz and a respective laser energy of $\sim$2.4 J.cm^{-2} and $\sim$2.3 J.cm^{-2} for zircon cores and rims. The sample cell was flushed with ultrahigh purity He (350 ml.min^{-1}) and N_2 (3.8 ml.min^{-1}). Data acquisition consisted of two laser pulses at the beginning of analyses to remove any surface contamination, followed by 30 s of baseline acquisition and 20 s of sample data acquisition and another 15 s of background counting. $\sim$3 s with no laser firing allowed for dispersal of all sample material before the next measurement. Unknowns were bracketed by a suite of standard zircons, with the standard block analysed every 25 unknowns (28 standard blocks).

For monazite ablation beam diameter was 7 μm in diameter, repetition rate was 4 Hz and laser energy was 0.7 J.cm^{-2} measured at the sample surface. The sample cell was flushed with ultrahigh purity He (320 ml.min^{-1}) and N_2 (1.2 ml.min^{-1}). Each analysis consisted of 40 s of background acquisition followed by 20 s of sample data acquisition and another 15 s of background counting.

High purity Ar was utilized as the plasma/carrier gas. The ablation mixture was then split into two paths. One path carried the ablated mixture to a Nu Plasma II multi-collector ICP-MS for U–Th–Pb isotopic measurement. The second path carried the mixture to an Agilent 7700x Series quadrupole ICP-MS for measurement of trace element concentrations (selected REE's and Ti). Full instrument setup is listed in the Table D.1 and D.2.

For zircon U–Pb analysis, rims were analysed using the following multi-collector setup (detector in brackets: H or L – Faraday Cup; IC – Ion Counter) over an 0.8 s integration time: ^{238}U (H10), ^{232}Th (H8), ^{208}Pb (IC0), ^{207}Pb (IC1), ^{206}Pb (IC2), ^{204}Pb (IC3), and ^{202}Hg (IC4). Instrument settings for rim ablations are referred to as IC in this manuscript. The primary reference material used for rims was 91500 (1062.4 $\pm$ 0.4 Ma; Wiedenbeck *et al.*,

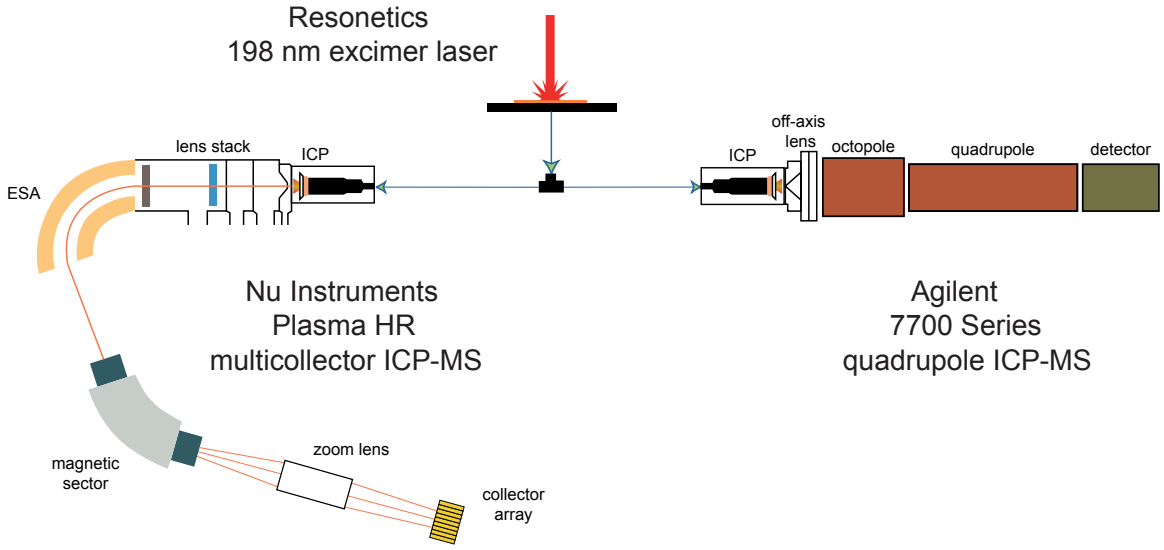


Figure B.1: Schematic diagram showing the LASS instrument setup in the John de Laeter Centre at Curtin University. From Hartnady (2018).

1995) with Plešovice (PLES) (337.13 ± 0.37 Ma; Sláma *et al.*, 2008) and GJ-1 (608.5 ± 0.4; Jackson *et al.*, 2004) used as secondary age standards. $^{206}Pb/^{238}U$ ages calculated for all zircon age standards, treated as unknowns, were found to be within 2% of the accepted value. Zircon cores were measured using the following setup over a 0.8 s integration time: ^{238}U (H10), ^{208}Pb (L2), ^{207}Pb (L3), ^{206}Pb (L4), ^{204}Pb (IC0), ^{202}Hg (IC2) and ^{200}Hg (IC3). Instrument settings for core analysis are referred to as FC here. The primary reference material used for cores was GJ-1 with Plešovice and OGC (3465 ± 0.6 Ma; Stern *et al.*, 2009) used as secondary age standards. $^{206}Pb/^{238}U$ ages calculated for all zircon age standards, treated as unknowns, were found to be within 3% of the accepted value. The results for standards are summarised in Table B.1.

Table B.1: Summary for U–Pb data for zircon standards.

settings	# analyses	standard	Concordia Age	MSWD	$^{206}Pb/^{238}U$ Age (Ma)	MSWD	$^{207}Pb/^{206}Pb$ Age (Ma)	MSWD
FC	22	91500	1062.9 ± 3.1	1.5	1062.5 ± 4.8	2.60	1030 ± 58	0.64
FC	12	OGC	3502.4 ± 8.1	1.8	3505 ± 16	3.50	3460 ± 31	0.0074
FC	23	PLES	336.1 ± 0.76	1.2	336.04 ± 0.96	1.90	369 ± 40	0.45
IC	18	GJ1	600.3 ± 2.8	1.3	600.5 ± 3.0	1.04	598.8 ± 7.7	1.60
IC	20	OGC	n/a	n/a	3492 ± 28	4.0	3462 ± 3.5	0.48
IC	21	PLES	336.6 ± 1.6	1.5	336.9 ± 2.0	1.50	329.5 ± 7.2	1.50

On the quadrupole, the following elements ablated from zircon were monitored for 0.01–0.02 s each (^{27}Al, ^{29}Si, ^{31}P, ^{44}Ca, ^{49}Ti, ^{57}Fe, ^{89}Y, ^{90}Zr, ^{91}Zr, ^{93}Nb, ^{139}La, ^{140}Ce, ^{141}Pr, ^{146}Nd, ^{147}Sm, ^{151}Eu, ^{157}Gd, ^{159}Tb, ^{163}Dy, ^{165}Ho, ^{166}Er ^{169}Tm, ^{175}Lu, ^{178}Hf, ^{181}Ta, ^{204}Pb, ^{232}Th, ^{238}U). In-house zircon standard PL-1 (fully characterized megacryst of Penglai zircon; Li *et al.*, 2010) was used as the primary standard to calculate elemental concentrations (^{91}Zr as the internal standard element, 43.14% Zr assumed in unknowns). During the time-resolved analysis, contamination resulting from inclusions and compositional zoning were monitored

and only the relevant part of the signal was integrated. The trace element results for NIST 612 (secondary standard) using NIST 610 as the reference material and assuming 33.6% Si, indicate that the accuracy was better than 3% for most elements with the exception of P (5%) and Fe (10%). The analytical precision was less than 7% for most elements.

For monazite U–Pb analysis, the following elements were monitored on the MC-ICPMS (detector in brackets: H – Faraday Cup; IC – Ion Counter) over an 0.8 s integration time: ^{238}U (H10), ^{232}Th (H8), ^{208}Pb (IC0), ^{207}Pb (IC1), ^{206}Pb (IC2), ^{204}Pb (IC3), and ^{202}Hg (IC4). Unknowns were bracketed by a suite of monazite reference materials, with the standard block analysed every 20 unknowns. For monazite analysis, reduction of isotopic data was carried out using natural monazite 44069 (424.9±1.0 Ma; Aleinikoff *et al.*, 2006) as primary standard with Trebilcock (272±4.0 Ma; Tomascak *et al.*, 1996) treated as a secondary age standard. Trebilcock yielded a weighted mean (n=18) ^{206}Pb/^{238}U age of 271.1 ± 1.5 (MSWD=0.44) within uncertainty of the accepted value.

For trace element determination on the quadrupole multi-collector, elements were monitored for 0.01-0.02 s each (^{28}Si, ^{31}P, ^{44}Ca, ^{88}Sr, ^{89}Y, ^{139}La, ^{140}Ce, ^{141}Pr, ^{146}Nd, ^{147}Sm, ^{151}Eu, ^{157}Gd, ^{159}Tb, ^{163}Dy, ^{165}Ho, ^{166}Er ^{169}Tm, ^{175}Lu, ^{178}Hf, ^{232}Th, ^{238}U). A series of well-characterised monazite megacrysts with known Ce content were utilized to plot an external calibration curve, from which the Ce content of each unknown was determined. To determine final trace element content, in-house megacryst VK-1 was utilized as the primary standard with ^{140}Ce as internal reference. The Trace Elements IS DRS in Iolite was used to reduce the data.

For zircon and monazite U–Pb geochronology, the time-resolved mass spectra were reduced using the U–Pb Geochron4 data reduction scheme in Iolite v.3.5 software (Paton *et al.*, 2011) and in-house Microsoft Excel macros. Common lead corrections were omitted due to low ^{204}Pb counts. For trace element quantification the spectra were reduced using the Trace Elements data reduction scheme in Iolite v.3.5 (Paton *et al.*, 2011). U–Pb isotopic data and trace element analyses are presented in appendix . Geochronological and geochemical data were handled using ISOPLOT v.4.15 (Ludwig, 2008). REE data were normalised with respect to chondrite (Boynton, 1984).

Appendix C

Mineral chemical data

Table C.1: EMPA data (wt. %). Sample NMC47. Lepel se Kop

phase	garnet	garnet	biotite	cordierite	K-feldspar	plagioclase
position	core	rim	matrix	matrix	matrix	matrix
label	NMC47b_grt_core_6	NMC47b_grt_rim_3	NMC47b_bi_10	NMC47b_cd_4	NMC47b_feld_8	NMC47b_feld_1
SiO_2	38.83	38.10	37.11	49.64	65.33	58.69
TiO_2	0.02	0.06	5.24	0.00	0.04	0.04
Al_2O_3	22.22	21.93	16.91	32.83	18.55	26.06
Cr_2O_3	0.06	0.02	0.03	0.00	0.00	0.00
FeO	30.56	32.41	16.87	6.70	0.00	0.05
MnO	0.60	0.67	0.00	0.08	0.03	0.04
MgO	6.92	5.81	11.75	9.10	0.00	0.00
ZnO	0.00	0.00	0.00	0.00	0.00	0.00
CaO	1.31	1.26	0.00	0.00	0.03	8.02
Na_2O	0.00	0.00	0.07	0.14	1.22	6.73
K_2O	0.00	0.00	9.61	0.00	14.70	0.21
Cl	0.00	0.00	0.10	0.00	0.00	0.00
F	0.00	0.00	0.33	0.00	0.00	0.00
Total	100.53	100.26	98.02	98.50	99.91	99.84
Oxygen	12	12	11	8	8	8
Si	3.01	2.99	2.72	5.06	3.00	2.63
Ti	0.00	0.00	0.29	0.00	0.00	0.00
Al	2.03	2.03	1.46	3.94	1.00	1.37
Cr	0.00	0.00	0.00	0.00	0.00	0.00
Fe^{2+}	1.98	2.13	1.04	0.57	0.00	0.00
Fe^{3+*}	0.00	0.00	0.00	0.00	0.00	0.00
Mn	0.04	0.05	0.00	0.01	0.00	0.00
Mg	0.80	0.68	1.29	1.38	0.00	0.00
Zn	0.00	0.00	0.00	0.00	0.00	0.00
Ca	0.11	0.11	0.00	0.00	0.00	0.38
Na	0.00	0.00	0.01	0.03	0.11	0.58
K	0.00	0.00	0.90	0.00	0.86	0.01
Cl	0.00	0.00	0.01	0.00	0.00	0.00
F	0.00	0.00	0.08	0.00	0.00	0.00
Total	7.97	7.99	7.80	10.99	4.98	4.98
$X_{Fe}^{\dagger}$	0.71	0.76	0.45	0.29		
X_{alm}	0.68	0.72				
X_{prp}	0.27	0.23				
X_{grs}	0.04	0.04				
X_{sps}	0.01	0.02				
X_{ab}					0.11	0.60
X_{an}					0.00	0.39
X_{or}					0.89	0.01

*Fe^{3+} recalculated after Droop (1987). $^{\dagger}X_{Fe} = Fe^{2+}/(Fe^{2+} + Mg)$.

Table C.2: EMPA data (wt. %). Sample NMC102. Lepel se Kop

phase	garnet	garnet	biotite	cordierite	K-feldspar	plagioclase
position	core	rim	matrix	matrix	matrix	matrix
label	NMC102_g_large_core_4	NMC102_g_large_rim_12	NMC102_bi_1	NMC102_cd_2	NMC102_ksp_4	NMC102_pl_6
SiO_2	38.86	38.70	37.08	48.54	63.72	60.86
TiO_2	0.00	0.02	2.55	0.04	0.00	0.00
Al_2O_3	22.91	22.83	17.94	33.43	19.20	24.95
Cr_2O_3	0.05	0.03	0.00	0.00	0.00	0.00
FeO	28.98	29.98	11.62	6.18	0.01	0.07
MnO	0.59	0.65	0.02	0.05	0.00	0.00
MgO	8.13	7.45	16.08	8.94	0.00	0.00
ZnO	0.00	0.00	0.00	0.00	0.00	0.00
CaO	0.89	0.92	0.00	0.00	0.22	5.46
Na_2O	0.00	0.00	0.08	0.10	1.47	7.79
K_2O	0.00	0.00	9.63	0.00	15.19	0.16
Cl	0.00	0.00	0.10	0.00	0.00	0.00
F	0.00	0.00	1.58	0.00	0.00	0.00
Total	100.40	100.56	96.66	97.28	99.81	99.28
Oxygen	12	12	11	8	8	9
Si	2.99	2.99	2.73	5.00	2.95	2.71
Ti	0.00	0.00	0.14	0.00	0.00	0.00
Al	2.08	2.08	1.55	4.06	1.05	1.31
Cr	0.00	0.00	0.00	0.00	0.00	0.00
Fe^{2+}	1.86	1.93	0.71	0.53	0.00	0.00
Fe^{3+*}	0.00	0.00	0.00	0.00	0.00	0.00
Mn	0.04	0.04	0.00	0.00	0.00	0.00
Mg	0.93	0.86	1.76	1.37	0.00	0.00
Zn	0.00	0.00	0.00	0.00	0.00	0.00
Ca	0.07	0.08	0.00	0.00	0.01	0.26
Na	0.00	0.00	0.01	0.02	0.13	0.67
K	0.00	0.00	0.90	0.00	0.90	0.01
Cl	0.00	0.00	0.01	0.00	0.00	0.00
F	0.00	0.00	0.37	0.00	0.00	0.00
Total	7.97	7.97	8.19	10.98	5.04	4.98
$X_{Fe}{}^{\dagger}$	0.67	0.69	0.29	0.28		
X_{alm}	0.64	0.66				
X_{prp}	0.32	0.29				
X_{grs}	0.03	0.03				
X_{sps}	0.01	0.01				
X_{ab}					0.13	0.71
X_{an}					0.01	0.28
X_{or}					0.86	0.01

*Fe^{3+} recalculated after Droop (1987). $^{\dagger}X_{Fe} = Fe^{2+}/(Fe^{2+} + Mg)$.

Table C.3: EMPA data (wt. %). Sample NMC46. Paulshoek

phase	garnet	garnet	biotite	biotite	cordierite	cordierite	K-feldspar	plagioclase
position	core	rim	inclusion	matrix	inclusion	matrix	matrix	matrix
label	NMC46c_grt_core_1	NMC46c_grt_rim_7	NMC46c_bio_inlc_22	NMC46c_bio_15	NMC46c_cd_incl_7	NMC46c_cd_4	NMC46b_ksp_3	NMC46b_plg_9
SiO_2	39.08	38.48	37.83	37.06	49.11	48.87	64.90	59.71
TiO_2	0.08	0.02	4.48	4.55	0.00	0.01	0.03	0.03
Al_2O_3	23.10	23.05	16.48	15.70	33.51	33.50	19.56	26.50
Cr_2O_3	0.00	0.03	0.03	0.00	0.03	0.00	0.00	0.00
FeO	28.95	29.75	10.33	13.99	5.60	5.70	0.04	0.08
MnO	1.79	1.78	0.02	0.05	0.11	0.17	0.05	0.09
MgO	7.51	7.20	18.16	15.44	9.88	9.61	0.00	0.00
ZnO	0.00	0.00	0.00	0.00	0.00	0.00	0.00	0.00
CaO	0.87	0.96	0.00	0.00	0.00	0.02	0.18	6.61
Na_2O	0.00	0.00	0.18	0.09	0.06	0.13	1.83	7.67
K_2O	0.00	0.00	10.15	9.85	0.00	0.00	13.31	0.27
Cl	0.00	0.00	0.12	0.12	0.00	0.00	0.00	0.00
F	0.00	0.00	2.41	1.61	0.00	0.00	0.00	0.00
Total	101.39	101.28	100.18	98.46	98.30	98.01	99.90	100.95
Oxygen	12	12	11	11	8	8	8	8
Si	2.99	2.96	2.70	2.72	4.99	4.99	2.97	2.64
Ti	0.01	0.00	0.24	0.25	0.00	0.00	0.00	0.00
Al	2.08	2.09	1.39	1.36	4.02	4.03	1.05	1.38
Cr	0.00	0.00	0.00	0.00	0.00	0.00	0.00	0.00
Fe^{2+}	1.85	1.92	0.62	0.86	0.48	0.49	0.00	0.00
Fe^{3+*}	0.00	0.00	0.00	0.00	0.00	0.00	0.00	0.00
Mn	0.12	0.12	0.00	0.00	0.01	0.02	0.00	0.00
Mg	0.86	0.83	1.93	1.69	1.50	1.46	0.00	0.00
Zn	0.00	0.00	0.00	0.00	0.00	0.00	0.00	0.00
Ca	0.07	0.08	0.00	0.00	0.00	0.00	0.01	0.31
Na	0.00	0.00	0.03	0.01	0.01	0.03	0.16	0.66
K	0.00	0.00	0.93	0.92	0.00	0.00	0.78	0.02
Cl	0.00	0.00	0.02	0.02	0.00	0.00	0.00	0.00
F	0.00	0.00	0.55	0.37	0.00	0.00	0.00	0.00
Total	7.97	7.99	8.40	8.21	11.00	11.01	4.97	5.01
$X_{Fe}{}^{\dagger}$	0.68	0.70	0.24	0.34	0.24	0.25		
X_{alm}	0.64	0.65						
X_{prp}	0.30	0.28						
X_{grs}	0.02	0.03						
X_{sps}	0.04	0.04						
X_{ab}							0.17	0.67
X_{an}							0.01	0.32
X_{or}							0.82	0.02

*Fe^{3+} recalculated after Droop (1987). $^{\dagger}X_{Fe} = Fe^{2+}/(Fe^{2+} + Mg)$.

Table C.4: EMPA data (wt. %). Sample NMC101. Paulshoek

phase	garnet	garnet	garnet	biotite	biotite	cordierite	spinel	K-feldspar	plagioclase
position	core	rim	rim on spinel	inclusion	matrix	matrix	matrix	matrix	matrix
label	NMC101_g_core_11	NMC101_g_rim_6	NMC101_g_rim_text_16	NMC101_bio_incl_1	NMC101_bio_6	NMC101_cd_8	NMC101A_sp_def_4	NMC101_fsp_1	NMC101_fsp_4
SiO_2	38.55	38.93	38.53	38.15	37.09	49.01	0.00	66.06	60.02
TiO_2	0.02	0.04	0.02	4.18	4.75	0.00	0.00	0.03	0.04
Al_2O_3	22.46	22.49	22.41	16.14	15.14	33.66	57.71	20.27	26.12
Cr_2O_3	0.00	0.02	0.00	0.00	0.00	0.00	0.18	0.00	0.00
FeO	28.50	28.11	29.46	10.20	15.33	6.01	34.14	0.02	0.04
MnO	1.27	1.26	1.23	0.01	0.08	0.09	0.07	0.00	0.01
MgO	7.94	8.23	7.37	18.29	15.22	9.14	7.74	0.00	0.00
ZnO	0.00	0.00	0.00	0.00	0.00	0.00	0.21	0.00	0.00
CaO	0.91	0.91	0.94	0.00	0.00	0.00	0.00	0.68	6.52
Na_2O	0.00	0.00	0.00	0.31	0.17	0.00	0.00	2.68	7.13
K_2O	0.00	0.00	0.00	9.16	8.96	0.00	0.00	7.81	0.19
Cl	0.00	0.00	0.00	0.12	0.07	0.00	0.00	0.00	0.00
F	0.00	0.00	0.00	1.88	1.68	0.00	0.00	0.00	0.00
Total	99.65	99.99	99.95	98.43	98.49	97.93	100.07	97.54	100.06
Oxygen	12	12	12	11	11	8	4	8	8
Si	3.01	3.01	3.01	2.74	2.73	5.00	0.00	3.00	2.66
Ti	0.00	0.00	0.00	0.23	0.26	0.00	0.00	0.00	0.00
Al	2.04	2.04	2.04	1.37	1.31	4.05	1.88	1.08	1.37
Cr	0.00	0.00	0.00	0.00	0.00	0.00	0.00	0.00	0.00
Fe^{2+}	1.84	1.81	1.90	0.61	0.94	0.51	0.68	0.00	0.00
Fe^{3+*}	0.00	0.00	0.00	0.00	0.00	0.00	0.12	0.00	0.00
Mn	0.08	0.08	0.08	0.00	0.01	0.01	0.00	0.00	0.00
Mg	0.91	0.95	0.85	1.96	1.67	1.39	0.32	0.00	0.00
Zn	0.00	0.00	0.00	0.00	0.00	0.00	0.00	0.00	0.00
Ca	0.08	0.08	0.08	0.04	0.00	0.00	0.00	0.03	0.31
Na	0.00	0.00	0.00	0.84	0.02	0.05	0.00	0.24	0.61
K	0.00	0.00	0.00	0.02	0.84	0.00	0.00	0.45	0.01
Cl	0.00	0.00	0.00	0.43	0.01	0.00	0.00	0.00	0.00
F	0.00	0.00	0.00	0.00	0.39	0.00	0.00	0.00	0.00
Total	7.97	7.97	7.97	8.23	8.19	11.00	3.02	4.84	5.00
$X_{Fe}^{\dagger}$	0.67	0.66	0.69	0.24	0.36	0.27	0.68		
X_{alm}	0.63	0.62	0.65						
X_{prp}	0.31	0.32	0.29						
X_{grs}	0.03	0.03	0.03						
X_{sps}	0.03	0.03	0.03						
X_{ab}								0.33	0.66
X_{an}								0.05	0.33
X_{or}								0.63	0.01
X_{Zn}**							0.00		

*Fe^{3+} recalculated after Droop (1987). $^{\dagger}X_{Fe} = Fe^{2+}/(Fe^{2+} + Mg)$. **$X_{Zn} = Zn/(Zn + Fe^{2+} + Fe^{3+} + Mg + Mn + Cr)$.

Table C.5: EMPA data (wt. %). Sample NMC89. Hytkoras

phase	garnet	garnet	biotite	biotite	biotite	cordierite	K-feldspar	plagioclase
position	core	rim	inclusion	matrix	symplectite	matrix	matrix	matrix
label	NMC89A_g_large_core_10	NMC89A_g_large_rim_2	NMC89B_bi_incl_large_g_5	NMC89A_bi_6	NMC89A_bio_sympl_8	NMC89A_cd_2	NMC89A_ksp_5	NMC89A_pl_2
SiO_2	38.88	38.82	38.62	37.32	37.46	48.56	64.84	61.34
TiO_2	0.03	0.02	4.51	4.81	4.68	0.00	0.00	0.00
Al_2O_3	22.69	22.34	16.39	15.64	15.15	33.57	19.23	24.91
Cr_2O_3	0.04	b.d	0.06	0.02	0.00	0.00	0.00	0.00
FeO	28.30	30.04	10.57	15.59	14.37	6.40	0.00	0.09
MnO	0.73	0.81	0.00	0.00	0.07	0.06	0.00	0.00
MgO	8.68	7.12	18.01	14.33	14.66	9.31	0.00	0.00
ZnO	0.00	0.00	0.00	0.00	0.00	0.00	0.00	0.00
CaO	0.84	0.83	0.00	0.00	0.00	0.00	0.12	5.31
Na_2O	0.00	0.00	0.35	0.13	0.14	0.12	2.18	8.06
K_2O	0.00	0.00	9.53	9.72	9.42	0.00	13.16	0.26
Cl	0.00	0.00	0.05	0.05	0.02	0.00	0.00	0.00
F	0.00	0.00	2.21	1.22	1.40	0.00	0.00	nd.
Total	100.19	99.98	98.03	97.56	96.77	98.02	99.52	99.96
Oxygen	12	12	11	11	11	8	8	8
Si	2.99	3.02	2.74	2.73	2.77	4.97	2.98	2.72
Ti	0.00	0.00	0.24	0.27	0.26	0.00	0.00	0.00
Al	2.06	2.05	1.37	1.35	1.32	4.05	1.04	1.30
Cr	0.00	0.00	0.00	0.00	0.00	0.00	0.00	0.00
Fe^{2+}	1.82	1.95	0.63	0.95	0.89	0.55	0.00	0.00
Fe^{3+*}	0.00	0.00	0.00	0.00	0.00	0.00	0.00	0.00
Mn	0.05	0.05	0.00	0.00	0.00	0.01	0.00	0.00
Mg	1.00	0.83	1.90	1.56	1.62	1.42	0.00	0.00
Zn	0.00	0.00	0.00	0.00	0.00	0.00	0.00	0.00
Ca	0.07	0.07	0.00	0.00	0.00	0.00	0.01	0.25
Na	0.00	0.00	0.05	0.02	0.02	0.02	0.19	0.69
K	0.00	0.00	0.86	0.91	0.89	0.00	0.77	0.02
Cl	0.00	0.00	0.01	0.01	0.00	0.00	0.00	0.00
F	0.00	0.00	0.50	0.28	0.33	0.00	0.00	0.00
Total	7.98	7.96	7.79	7.79	7.77	11.02	4.99	4.98
$X_{Fe}^{\dagger}$	0.65	0.70	0.25	0.38	0.35	0.28		
X_{alm}	0.62	0.67						
X_{prp}	0.34	0.29						
X_{grs}	0.02	0.02						
X_{sps}	0.02	0.02						
X_{ab}							0.20	0.72
X_{an}							0.01	0.26
X_{or}							0.79	0.02

*Fe^{3+} recalculated after Droop (1987). $^{\dagger}X_{Fe} = Fe^{2+}/(Fe^{2+} + Mg)$.

Table C.6: EMPA data (wt. %). Sample NMC71. Hytkoras

phase	garnet	garnet	biotite	biotite	cordierite	K-feldspar	plagioclase
position	core	rim	inclusion in g	matrix	matrix	matrix	matrix
label	NMC71_g_core_3	NMC71_g_rim_6	NMC71_bi_incl_3	NMC71_bi_5	NMC71_cd_4	NMC71_fsp_7	NMC71_fsp_4
SiO_2	39.06	38.57	36.49	35.71	48.96	64.37	59.42
TiO_2	0.01	0.03	5.29	3.86	0.01	0.03	0.02
Al_2O_3	22.42	22.32	18.28	18.76	33.18	19.30	26.16
Cr_2O_3	0.01	0.04	0.08	0.05	0.00	0.00	0.00
FeO	27.94	29.49	14.65	18.29	6.72	0.00	0.04
MnO	1.59	1.69	0.00	0.01	0.12	0.00	0.00
MgO	7.81	6.16	12.89	10.99	8.91	0.00	0.00
ZnO	0.00	0.00	0.00	0.00	0.00	0.00	0.00
CaO	1.22	1.23	0.00	0.00	0.00	0.02	7.08
Na_2O	0.00	0.00	0.20	0.15	0.12	0.93	7.00
K_2O	0.00	0.00	9.61	9.79	0.00	14.63	0.30
Cl	0.00	0.00	0.11	0.06	0.00	0.00	0.00
F	0.00	0.00	0.27	0.17	0.00	0.00	0.00
Total	100.05	99.52	97.50	97.60	98.01	99.29	100.02
Oxygen	12	12	11	11	8	8	8
Si	3.01	3.04	2.66	2.65	5.02	2.97	2.65
Ti	0.00	0.00	0.29	0.22	0.00	0.00	0.00
Al	2.04	2.05	1.57	1.64	4.01	1.05	1.37
Cr	0.00	0.00	0.01	0.00	0.00	0.00	0.00
Fe^{2+}	1.81	1.92	0.89	1.13	0.58	0.00	0.00
Fe^{3+*}	0.00	0.00	0.00	0.00	0.00	0.00	0.00
Mn	0.10	0.11	0.00	0.00	0.01	0.00	0.00
Mg	0.90	0.72	1.40	1.21	1.36	0.00	0.00
Zn	0.00	0.00	0.00	0.00	0.00	0.00	0.00
Ca	0.10	0.10	0.00	0.00	0.00	0.00	0.34
Na	0.00	0.00	0.03	0.02	0.02	0.08	0.60
K	0.00	0.00	0.89	0.93	0.00	0.86	0.02
Cl	0.00	0.00	0.01	0.01	0.00	0.00	0.00
F	0.00	0.00	0.06	0.04	0.00	0.00	0.00
Total	7.96	7.94	7.81	7.85	11.00	4.96	4.98
$X_{Fe}{}^{\dagger}$	0.67	0.73	0.39	0.48	0.30		
X_{alm}	0.62	0.67					
X_{prp}	0.31	0.25					
X_{grs}	0.03	0.04					
X_{sps}	0.03	0.04					
X_{ab}						0.09	0.63
X_{an}						0.00	0.35
X_{or}						0.91	0.02

*Fe^{3+} recalculated after Droop (1987). $^{\dagger}X_{Fe} = Fe^{2+}/(Fe^{2+} + Mg)$.

Table C.7: EMPA data (wt. %). Sample NMC65. Hytkoras

phase	garnet	garnet	biotite	biotite	cordierite	spinel	K-feldspar	plagioclase
position	core	rim	inclusion in g	matrix	matrix	armored by sill	matrix	matrix
label	NMC65_g_core_4	NMC65_g_rim_2	NMC65_bi_incl_4	NMC65_bi_6	NMC65_cd_2	NMC65_sp_3	NMC65_ksp_6	NMC65_pl_4
SiO_2	38.95	39.00	37.38	36.93	48.87	0.00	63.88	61.89
TiO_2	0.05	0.04	4.90	3.58	0.00	0.02	0.00	0.00
Al_2O_3	22.67	22.54	18.59	19.46	33.26	58.15	20.68	24.80
Cr_2O_3	0.00	0.02	0.02	0.00	0.00	0.05	0.00	0.00
FeO	26.02	25.87	11.85	14.04	4.71	30.48	0.00	0.00
MnO	2.86	3.05	0.02	0.09	0.20	0.51	0.00	0.00
MgO	8.73	8.47	15.79	13.18	10.17	7.58	0.00	0.00
ZnO	0.00	0.00	0.00	0.00	0.00	2.92	0.00	0.00
CaO	0.94	0.94	0.00	0.00	0.00	0.00	1.26	5.51
Na_2O	0.00	0.00	0.30	0.08	0.10	0.00	1.72	7.98
K_2O	0.00	0.00	8.59	9.24	0.00	0.00	12.45	0.48
Cl	0.00	0.00	0.07	0.11	0.00	0.00	0.00	0.00
F	0.00	0.00	0.28	0.19	0.00	0.00	0.00	0.00
Total	100.22	99.93	97.44	96.60	97.31	99.71	99.99	100.66
Oxygen	12	12	11	11	8	4	8	8
Si	2.99	3.00	2.67	2.69	5.00	0.00	2.91	2.73
Ti	0.00	0.00	0.26	0.20	0.00	0.00	0.00	0.00
Al	2.05	2.05	1.56	1.67	4.01	1.90	1.11	1.29
Cr	0.00	0.00	0.00	0.00	0.00	0.00	0.00	0.00
Fe^{2+}	1.67	1.67	0.71	0.86	0.40	0.62	0.00	0.00
Fe^{3+*}	0.00	0.00	0.00	0.00	0.00	0.09	0.00	0.00
Mn	0.19	0.20	0.00	0.01	0.02	0.01	0.00	0.00
Mg	1.00	0.97	1.68	1.43	1.55	0.31	0.00	0.00
Zn	0.00	0.00	0.00	0.00	0.00	0.06	0.00	0.00
Ca	0.08	0.08	0.00	0.00	0.00	0.00	0.06	0.26
Na	0.00	0.00	0.04	0.01	0.02	0.00	0.15	0.68
K	0.00	0.00	0.78	0.86	0.00	0.00	0.73	0.03
Cl	0.00	0.00	0.01	0.01	0.00	0.00	0.00	0.00
F	0.00	0.00	0.06	0.04	0.00	0.00	0.00	0.00
Total	7.98	7.97	7.70	7.73	11.00	2.99	4.96	4.99
$X_{Fe}{}^{\dagger}$	0.63	0.63	0.30	0.38	0.21	0.67		
X_{alm}	0.57	0.57						
X_{prp}	0.34	0.33						
X_{grs}	0.03	0.03						
X_{sps}	0.06	0.07						
X_{ab}							0.16	0.70
X_{an}							0.06	0.27
X_{or}							0.78	0.03
X_{Zn}						0.06		

*Fe^{3+} recalculated after Droop (1987). $^{\dagger}X_{Fe} = Fe^{2+}/(Fe^{2+} + Mg)$. **$X_{Zn} = Zn/(Zn + Fe^{2+} + Fe^{3+} + Mg + Mn + Cr)$.

Table C.8: EMPA data (wt. %). Sample NMC37. Hytkoras

phase	garnet	garnet	biotite	biotite	biotite	biotite	orthopyroxene	cordierite	cordierite	cordierite	K-feldspar	plagioclase	plagioclase
position	core	symplectite	inclusion in g	inclusion in opx	matrix	symplectite	matrix	inclusion in g	inclusion in opx	matrix	matrix	inclusion in opx	matrix
label	NMC37c_g_core_6	NMC37c_g_sym_2	NMC37c_bi_in_g_5	NMC37c_bi_in_opx_3	NMC37c_bi_11	NMC37c_bi_sym_4	NMC37c_opx_7	NMC37c_cd_in_g_5	NMC37c_cd_in_opx_3	NMC37c_cd_9	NMC37c_ksp_3	NMC37c_pl_in_opx_4	NMC37c_pl_4
SiO_2	39.14	38.74	36.74	36.37	36.46	36.48	48.18	48.51	48.71	48.87	64.90	60.39	61.20
TiO_2	0.04	0.01	4.54	5.51	5.32	5.35	0.12	0.00	0.00	0.01	0.00	0.00	0.00
Al_2O_3	23.16	22.49	18.25	17.21	17.25	17.11	7.62	32.89	33.82	33.50	19.56	24.52	24.51
Cr_2O_3	0.00	0.02	0.02	0.00	0.01	0.01	0.02	0.00	0.00	0.00	0.00	0.00	0.00
FeO	26.24	29.93	11.36	15.13	15.72	15.55	23.94	3.60	4.51	5.70	0.00	0.00	0.00
MnO	1.22	0.99	0.07	0.03	0.09	0.09	0.42	0.07	0.12	0.17	0.00	0.00	0.00
MgO	9.69	6.99	16.28	13.23	12.98	13.04	19.29	10.95	10.33	9.61	0.00	0.00	0.00
ZnO	0.00	0.00	0.00	0.00	0.00	0.00	0.00	0.00	0.00	0.00	0.00	0.00	0.00
CaO	0.92	0.96	0.00	0.00	0.00	0.00	0.06	0.00	0.01	0.02	0.18	5.65	5.38
Na_2O	0.00	0.00	0.22	0.32	0.17	0.19	0.00	0.10	0.11	0.13	1.83	8.08	8.77
K_2O	0.00	0.00	9.85	9.34	10.07	9.93	0.00	0.00	0.00	0.00	13.31	0.21	0.16
Cl	0.00	0.00	0.10	0.08	0.09	0.08	0.00	0.00	0.00	0.00	0.00	0.00	0.00
F	0.00	0.00	0.00	0.28	0.00	0.00	0.00	0.00	0.00	0.00	0.00	0.00	0.00
Total	100.40	100.13	97.32	97.51	98.07	97.75	99.65	96.11	97.61	98.01	99.78	98.85	100.02
Oxygen	12	12	11	11	11	11	6	8	8	8	8	8	8
Si	2.98	3.01	2.64	2.67	2.66	2.67	1.81	5.00	4.97	4.99	2.97	2.71	2.72
Ti	0.00	0.00	0.25	0.30	0.29	0.29	0.00	0.00	0.00	0.00	0.00	0.00	0.00
Al	2.08	2.06	1.55	1.49	1.49	1.48	0.34	4.00	4.06	4.03	1.05	1.30	1.28
Cr	0.00	0.00	0.00	0.00	0.00	0.00	0.00	0.00	0.00	0.00	0.00	0.00	0.00
Fe^{2+}	1.67	1.94	0.68	0.93	0.96	0.95	0.72	0.31	0.38	0.49	0.00	0.00	0.00
Fe^{3+*}	0.00	0.00	0.00	0.00	0.00	0.00	0.04	0.00	0.00	0.00	0.00	0.00	0.00
Mn	0.08	0.07	0.00	0.00	0.01	0.01	0.01	0.01	0.01	0.02	0.00	0.00	0.00
Mg	1.10	0.81	1.75	1.45	1.41	1.42	1.08	1.68	1.57	1.46	0.00	0.00	0.00
Zn	0.00	0.00	0.00	0.00	0.00	0.00	0.00	0.00	0.00	0.00	0.00	0.00	0.00
Ca	0.08	0.08	0.00	0.00	0.00	0.00	0.00	0.00	0.00	0.00	0.01	0.27	0.26
Na	0.00	0.00	0.03	0.05	0.02	0.03	0.00	0.02	0.02	0.03	0.16	0.70	0.76
K	0.00	0.00	0.90	0.87	0.94	0.93	0.00	0.00	0.00	0.00	0.78	0.01	0.01
Cl	0.00	0.00	0.01	0.01	0.01	0.01	0.00	0.00	0.00	0.00	0.00	0.00	0.00
F	0.00	0.00	0.00	0.07	0.00	0.00	0.00	0.00	0.00	0.00	0.00	0.00	0.00
Total	7.99	7.97	7.81	7.84	7.79	7.79	4.00	11.02	11.01	11.02	4.97	4.99	5.03
$X_{Fe}{}^{\dagger}$	0.60	0.71	0.28	0.39	0.41	0.40	0.40	0.16	0.19	0.25			
X_{alm}	0.57	0.67											
X_{prp}	0.38	0.28											
X_{grs}	0.03	0.03											
X_{sps}	0.03	0.02											
X_{ab}											0.17	0.71	0.74
X_{an}											0.01	0.28	0.25
X_{or}											0.82	0.01	0.01
$y_{opx}{}^{\#}$							0.15						

*Fe^{3+} recalculated after Droop (1987). $^{\dagger}X_{Fe} = Fe^{2+}/(Fe^{2+} + Mg)$. **$X_{Zn} = Zn/(Zn + Fe^{2+} + Fe^{3+} + Mg + Mn + Cr)$. $^{\#}y_{opx} = (Al^{tot} - Fe^{3+})/2$.

Table C.9: EMPA data (wt. %). Sample NMC67. Hytkoras

phase	garnet	garnet	biotite	biotite	cordierite	spinel	K-feldspar	plagioclase
position	core	rim	inclusion in g	inclusion in ksp	matrix	armored by sill	matrix	matrix
label	NMC67b_g_core_4	NMC67b_g_rim_6	NMC67b_bi_in_g_3	NMC67b_bi_in_fsp_5	NMC67b_cd_7	NMC67b_sp_3	NMC67b_ksp_6	NMC67b_pl_3
SiO_2	39.17	38.86	37.22	37.03	48.73	0.00	66.10	62.33
TiO_2	0.03	0.02	4.15	3.30	b.d	4.49	0.00	0.00
Al_2O_3	22.54	22.66	18.61	19.36	33.59	60.54	19.79	25.39
Cr_2O_3	b.d	0.03	0.04	0.02	b.d	0.17	0.00	0.00
FeO	26.08	26.17	11.76	13.17	4.60	24.55	0.00	0.00
MnO	3.19	3.35	0.00	0.10	0.20	0.25	0.00	0.00
MgO	8.60	8.36	16.46	14.57	10.05	6.09	0.00	0.00
ZnO	0.00	0.00	0.00	0.00	0.00	1.22	0.00	0.00
CaO	1.08	0.95	0.00	0.00	b.d	0.00	0.13	5.50
Na_2O	0.00	0.00	0.47	0.14	0.08	0.00	1.90	6.76
K_2O	0.00	0.00	8.78	9.20	0.00	0.00	12.31	0.19
Cl	0.00	0.00	0.08	0.18	0.00	0.00	0.00	0.00
F	0.00	0.00	0.16	0.29	0.00	0.00	0.00	0.00
Total	100.68	100.38	97.50	96.87	97.25	97.31	100.23	100.17
Oxygen	12	12	11	11	8	4	8	8
Si	2.99	2.99	2.66	2.68	4.99	0.00	2.99	2.74
Ti	0.00	0.00	0.22	0.18	0.00	0.09	0.00	0.00
Al	2.04	2.05	1.57	1.65	4.05	1.97	1.05	1.31
Cr	0.00	0.00	0.00	0.00	0.00	0.00	0.00	0.00
Fe^{2+}	1.67	1.68	0.70	0.80	0.39	0.57	0.00	0.00
Fe^{3+*}	0.00	0.00	0.00	0.00	0.00	0.00	0.00	0.01
Mn	0.21	0.22	0.00	0.01	0.02	0.01	0.00	0.00
Mg	0.98	0.96	1.75	1.57	1.53	0.25	0.00	0.00
Zn	0.00	0.00	0.00	0.00	0.00	0.03	0.00	0.00
Ca	0.09	0.08	0.00	0.00	0.00	0.00	0.01	0.26
Na	0.00	0.00	0.07	0.02	0.02	0.00	0.17	0.58
K	0.00	0.00	0.80	0.85	0.00	0.00	0.71	0.01
Cl	0.00	0.00	0.01	0.02	0.00	0.00	0.00	0.00
F	0.00	0.00	0.04	0.07	0.00	0.00	0.00	0.00
Total	7.99	7.98	7.77	7.75	11.00	2.92	4.93	4.90
$X_{Fe}{}^{\dagger}$	0.63	0.64	0.29	0.34	0.20	0.70		
X_{alm}	0.57	0.57						
X_{prp}	0.33	0.33						
X_{grs}	0.03	0.03						
X_{sps}	0.07	0.07						
X_{ab}							0.19	0.68
X_{an}							0.01	0.31
X_{or}							0.80	0.01
X_{Zn}						0.03		

*Fe^{3+} recalculated after Droop (1987). $^{\dagger}X_{Fe} = Fe^{2+}/(Fe^{2+} + Mg)$. **$X_{Zn} = Zn/(Zn + Fe^{2+} + Fe^{3+} + Mg + Mn + Cr)$.

Table C.10: EMPA data (wt. %). Sample NMC67. Hytkoras

phase	hornblende	augite	orthopyroxene	biotite	plagioclase
position	matrix	matrix	matrix	matrix	matrix
label	NMC69_hb_6	NMC69_cpx_4	NMC69_opx_6	NMC69_bi_3	NMC69_pl_8
SiO_2	43.61	52.11	52.71	37.47	49.21
TiO_2	1.54	0.20	0.05	4.65	0.00
Al_2O_3	11.07	2.53	1.40	15.26	32.75
Cr_2O_3	0.06	0.06	0.01	0.03	0.00
FeO	14.03	9.02	20.94	13.46	0.00
MnO	0.21	0.27	0.65	0.05	0.00
MgO	12.83	13.77	23.72	16.20	0.00
ZnO	0.00	0.00	0.00	0.00	0.00
CaO	12.04	21.76	0.43	0.00	15.25
Na_2O	0.97	0.42	0.00	0.07	2.66
K_2O	1.45	0.00	0.00	9.64	0.13
Cl	0.15	0.00	0.00	0.14	0.00
F	0.24	0.00	0.00	0.48	0.00
Total	97.80	100.13	99.90	96.82	99.99
Oxygen	23	6	6	11	8
Si	6.43	1.94	1.95	2.74	2.24
Ti	0.17	0.01	0.00	0.26	0.00
Al	1.92	0.11	0.06	1.31	1.76
Cr	0.01	0.00	0.00	0.00	0.00
Fe^{2+}	1.40	0.24	0.61	0.82	0.00
Fe^{3+*}	0.33	0.04	0.04	0.00	0.00
Mn	0.03	0.01	0.02	0.00	0.00
Mg	2.82	0.76	1.31	1.76	0.00
Zn	0.00	0.00	0.00	0.00	0.00
Ca	1.90	0.87	0.02	0.00	0.75
Na	0.28	0.03	0.00	0.01	0.24
K	0.27	0.00	0.00	0.90	0.01
Cl	0.04	0.00	0.00	0.02	0.00
F	0.11	0.00	0.00	0.11	0.00
Total	15.55	4.00	4.00	7.81	5.01
$X_{Fe}{}^{\dagger}$	0.33	0.24	0.32	0.32	
X_{ab}					0.24
X_{an}					0.75
X_{or}					0.01
$y_{opx}{}^{\#}$			0.01		
$X_{jd}{}^{\dagger\dagger}$		0.03			

*Fe^{3+} recalculated after Droop (1987). $^{\dagger}X_{Fe} = Fe^{2+}/(Fe^{2+} + Mg)$. $^{\#}y_{opx} = (Al^{tot} - Fe^{3+})/2$. $^{\dagger\dagger}X_{jd} = Na/(Na + Ca)$.

Table C.11: EMPA data (wt. %). Sample NMC68. Hytkoras

phase	garnet	biotite	K-feldspar	plagioclase
position	matrix	matrix	matrix	matrix
label	NMC68A_g_6	NMC68A_bio_4	NMC68A_fsp_12	NMC68A_fsp_1
SiO_2	38.42	36.01	63.51	59.69
TiO_2	0.02	5.61	0.03	0.01
Al_2O_3	22.68	17.15	19.71	26.03
Cr_2O_3	0.05	0.00	0.00	0.00
FeO	26.94	17.40	0.02	0.06
MnO	3.45	0.14	0.03	0.00
MgO	7.41	11.83	0.00	0.02
ZnO	0.00	0.00	0.00	0.00
CaO	1.45	0.00	0.11	7.12
Na_2O	0.00	0.17	0.70	6.73
K_2O	0.00	9.40	14.87	0.39
Cl	0.00	0.05	0.00	0.00
F	0.00	0.36	0.00	0.00
Total	100.44	98.11	98.96	100.06
Oxygen	12	11	8	8
Si	2.96	2.65	2.95	2.65
Ti	0.00	0.31	0.00	0.00
Al	2.08	1.49	1.08	1.36
Cr	0.00	0.00	0.00	0.00
Fe^{2+}	1.75	1.07	0.00	0.00
Fe^{3+*}	0.00	0.00	0.00	0.00
Mn	0.23	0.01	0.00	0.00
Mg	0.86	1.30	0.00	0.00
Zn	0.00	0.00	0.00	0.00
Ca	0.12	0.00	0.01	0.34
Na	0.00	0.02	0.06	0.58
K	0.00	0.88	0.88	0.02
Cl	0.00	0.01	0.00	0.00
F	0.00	0.08	0.00	0.00
Total	8.00	7.84	4.98	4.96
$X_{Fe}{}^{\dagger}$	0.67	0.45		
X_{alm}	0.59			
X_{prp}	0.29			
X_{grs}	0.04			
X_{sps}	0.08			
X_{ab}			0.07	0.62
X_{an}			0.01	0.36
X_{or}			0.93	0.02

*Fe^{3+} recalculated after Droop (1987). $^{\dagger}X_{Fe} = Fe^{2+}/(Fe^{2+} + Mg)$.

Table C.12: EMPA data (wt. %). Sample NMC44. Hytkoras

phase	orthopyroxene	orthopyroxene	biotite	biotite	biotite	cordierite	cordierite
position	core	rim	inclusion in opx	matrix	symplectite	inclusion in opx	matrix
label	NMC44b_opx_core_7	NMC44b_opx_rim_4	NMC44b_bi_opx_7	NMC44b_bi_12	NMC44b_bi_sym_3	NMC44b_cd_opx_5	NMC44b_cd_2
SiO_2	49.89	49.64	37.29	37.58	37.17	49.72	48.76
TiO_2	0.04	0.11	3.41	3.40	3.19	0.01	0.01
Al_2O_3	6.41	6.87	17.53	17.25	17.10	33.91	33.87
Cr_2O_3	0.00	0.00	0.12	0.12	0.09	0.00	0.00
FeO	22.16	21.93	12.50	12.91	13.30	4.48	4.87
MnO	0.44	0.49	0.12	0.10	0.11	0.10	0.13
MgO	20.92	20.86	16.43	16.88	16.91	10.62	10.15
ZnO	0.00	0.00	0.00	0.00	0.00	0.00	0.00
CaO	0.11	0.12	0.00	0.00	0.00	0.01	0.01
Na_2O	0.00	0.00	0.24	0.33	0.26	0.11	0.13
K_2O	0.00	0.00	9.12	9.21	8.43	0.00	0.00
Cl	0.00	0.00	0.18	0.15	0.17	0.00	0.00
F	0.00	0.00	0.15	0.27	0.11	0.00	0.00
Total	99.97	100.02	96.76	97.77	96.56	98.97	97.94
Oxygen	6	6	11	11	11	8	8
Si	1.85	1.84	2.70	2.70	2.70	5.00	4.96
Ti	0.00	0.00	0.19	0.18	0.17	0.00	0.00
Al	0.28	0.30	1.50	1.46	1.46	4.02	4.06
Cr	0.00	0.00	0.01	0.01	0.01	0.00	0.00
Fe^{2+}	0.68	0.67	0.76	0.78	0.81	0.38	0.42
Fe^{3+*}	0.01	0.00	0.00	0.00	0.00	0.00	0.00
Mn	0.01	0.02	0.01	0.01	0.01	0.01	0.01
Mg	1.16	1.15	1.77	1.81	1.83	1.59	1.54
Zn	0.00	0.00	0.00	0.00	0.00	0.00	0.00
Ca	0.00	0.01	0.00	0.00	0.00	0.00	0.00
Na	0.00	0.00	0.03	0.05	0.04	0.02	0.03
K	0.00	0.00	0.84	0.84	0.78	0.00	0.00
Cl	0.00	0.00	0.02	0.02	0.02	0.00	0.00
F	0.00	0.00	0.03	0.06	0.03	0.00	0.00
Total	3.99	3.99	7.86	7.92	7.86	11.02	11.02
$X_{Fe}{}^{\dagger}$	0.37	0.37	0.30	0.30	0.31	0.19	0.21
$y_{opx}{}^{\#}$	0.14	0.15					

*Fe^{3+} recalculated after Droop (1987). $^{\dagger}X_{Fe} = Fe^{2+}/(Fe^{2+} + Mg)$. $^{\#}y_{opx} = (Al^{tot} - Fe^{3+})/2$.

Table C.13: EMPA data (wt. %). Sample NMC27. Hytkoras

phase	hornblende	augite	orthopyroxene	biotite	plagioclase
position	matrix	matrix	matrix	matrix	matrix
label	NMC27_amph_7	NMC27_cpx_3	NMC27_opx_3	NMC27_bio_3	NMC27_plg_13
SiO_2	44.05	53.20	53.41	38.22	47.34
TiO_2	2.35	0.37	0.06	4.59	0.03
Al_2O_3	10.71	2.22	1.42	15.17	33.59
Cr_2O_3	0.49	0.26	0.10	0.51	0.00
FeO	12.26	8.09	21.10	12.71	0.20
MnO	0.16	0.28	0.64	0.12	0.03
MgO	13.97	13.87	22.94	16.75	0.00
ZnO	0.00	0.00	0.00	0.00	0.00
CaO	11.56	21.78	0.48	0.01	16.88
Na_2O	1.10	0.39	0.00	0.09	1.64
K_2O	1.54	0.00	0.00	9.88	0.04
Cl	0.00	0.00	0.00	0.32	0.00
F	0.00	0.00	0.00	0.36	0.00
Total	98.20	100.46	100.14	98.73	99.77
Oxygen	23	6	6	11	8
Si	6.45	1.96	1.97	2.75	2.18
Ti	0.26	0.01	0.00	0.25	0.00
Al	1.85	0.10	0.06	1.29	1.82
Cr	0.06	0.01	0.00	0.03	0.00
Fe^{2+}	1.43	0.25	0.65	0.77	0.00
Fe^{3+*}	0.08	0.00	0.00	0.00	0.01
Mn	0.02	0.01	0.02	0.01	0.00
Mg	3.05	0.76	1.26	1.80	0.00
Zn	0.00	0.00	0.00	0.00	0.00
Ca	1.81	0.86	0.02	0.00	0.83
Na	0.31	0.03	0.00	0.01	0.15
K	0.29	0.00	0.00	0.91	0.00
Cl	0.00	0.00	0.00	0.04	0.00
F	0.00	0.00	0.00	0.08	0.00
Total	15.60	3.99	3.99	7.93	4.99
$X_{Fe}{}^{\dagger}$	0.32	0.25	0.34	0.30	
X_{ab}					0.15
X_{an}					0.85
X_{or}					0.00
$y_{opx}{}^{\#}$			0.03		
$X_{jd}{}^{\dagger\dagger}$		0.03			

*Fe^{3+} recalculated after Droop (1987). $^{\dagger}X_{Fe} = Fe^{2+}/(Fe^{2+} + Mg)$. $^{\#}y_{opx} = (Al^{tot} - Fe^{3+})/2$. $^{\dagger\dagger}X_{jd} = Na/(Na + Ca)$.

Table C.14: EMPA data (wt. %). Sample NMC88. Hytkoras

phase	orthopyroxene	biotite	biotite	cordierite	cordierite	cordierite	spinel	sapphirine
position	matrix	matrix	texture	matrix	moat	texture	texture	texture
label	NMC88A_opx_7	NMC88_bio_matrix_6	NMC88_bio_texture_4	NMC88A_cd_matrix_9	NMC88A_cd_moat_4	NMC88A_cd_texture_15	NMC88A_sp_texture_1	NMC88A_sa_texture_2
SiO_2	50.41	38.75	37.41	49.33	49.25	49.46	0.02	12.92
TiO_2	0.06	3.21	3.81	0.08	0.04	0.00	0.04	0.00
Al_2O_3	5.25	17.09	18.10	34.11	34.01	34.08	62.71	61.77
Cr_2O_3	0.03	0.03	0.00	0.00	0.00	0.00	0.01	0.00
FeO	20.38	11.61	11.56	3.59	3.26	3.37	25.73	10.42
MnO	0.63	0.02	0.09	0.05	0.11	0.08	0.31	0.18
MgO	23.15	17.53	17.06	10.82	10.84	10.93	11.08	14.70
ZnO	0.00	0.00	0.00	0.00	0.00	0.00	0.36	0.00
CaO	0.06	0.03	0.00	0.01	0.03	0.02	0.00	0.00
Na_2O	0.00	0.28	0.22	0.13	0.13	0.08	0.00	0.00
K_2O	0.00	8.74	9.11	0.00	0.00	0.00	0.00	0.00
Cl	0.00	0.06	0.07	0.00	0.00	0.00	0.00	0.00
F	0.00	0.79	0.51	0.00	0.00	0.00	0.00	0.00
Total	99.97	98.12	97.94	98.11	97.67	98.03	100.25	99.98
Oxygen	6	11	11	8	8	8	4	20
Si	1.85	2.76	2.68	4.98	4.99	4.99	0.00	1.55
Ti	0.00	0.17	0.21	0.01	0.00	0.00	0.00	0.00
Al	0.23	1.44	1.53	4.06	4.06	4.05	1.98	8.75
Cr	0.00	0.00	0.00	0.00	0.00	0.00	0.00	0.00
Fe^{2+}	0.56	0.69	0.69	0.30	0.28	0.28	0.55	0.90
Fe^{3+*}	0.06	0.00	0.00	0.00	0.00	0.00	0.02	0.15
Mn	0.02	0.00	0.01	0.00	0.01	0.01	0.01	0.02
Mg	1.27	1.86	1.82	1.63	1.64	1.64	0.44	2.63
Zn	0.00	0.00	0.00	0.00	0.00	0.00	0.01	0.00
Ca	0.00	0.00	0.00	0.00	0.00	0.00	0.00	0.00
Na	0.00	0.04	0.03	0.03	0.03	0.02	0.00	0.00
K	0.00	0.80	0.83	0.00	0.00	0.00	0.00	0.00
Cl	0.00	0.01	0.01	0.00	0.00	0.00	0.00	0.00
F	0.00	0.18	0.12	0.00	0.00	0.00	0.00	0.00
Total	4.01	7.95	7.91	11.01	11.00	10.99	3.02	14.00
$X_{Fe}{}^{\dagger}$	0.31	0.27	0.28	0.16	0.14	0.15	0.56	0.25
$y_{opx}{}^{\#}$	0.08							
$X_{Zn}{}^{**}$							0.01	

*Fe^{3+} recalculated after Droop (1987). $^{\dagger}X_{Fe} = Fe^{2+}/(Fe^{2+} + Mg)$. $^{\#}y_{opx} = (Al^{tot} - Fe^{3+})/2$. $^{**}X_{Zn} = Zn/(Zn + Fe^{2+} + Fe^{3+} + Mg + Mn + Cr)$.

Table C.15: EMPA data (wt. %). Sample NMC91. Hytkoras

phase	gedrite	orthopyroxene	biotite	cordierite	cordierite	spinel	sapphirine
position	matrix	matrix	matrix	matrix	rim on spinel	matrix	matrix
label	NMC91A_ged_5	NMC91A_opx_7	NMC91A_bio_11	NMC91A_cd_3	NMC91A_cd_rim_spinel_7	NMC91A_sp_10	NMC91A_sa_2
SiO_2	42.55	50.84	38.74	49.13	48.89	0.00	13.26
TiO_2	0.60	0.11	2.72	0.00	0.00	0.00	0.07
Al_2O_3	19.60	6.75	17.91	33.78	33.73	60.69	61.46
Cr_2O_3	0.09	0.09	0.03	0.00	0.00	1.11	0.35
FeO	12.13	15.25	7.16	2.02	2.21	23.13	8.53
MnO	0.16	0.19	0.01	0.03	0.00	0.06	0.00
MgO	19.76	26.70	21.24	11.80	11.66	14.94	16.35
ZnO	0.00	0.00	0.00	0.00	0.00	0.09	0.00
CaO	0.41	0.04	0.01	0.02	0.01	0.00	0.00
Na_2O	2.34	0.00	0.60	0.10	0.08	0.00	0.00
K_2O	0.03	0.00	8.13	0.00	0.00	0.00	0.00
Cl	0.03	0.00	0.04	0.00	0.00	0.00	0.00
F	0.40	0.00	0.78	0.00	0.00	0.00	0.00
Total	98.07	99.97	97.38	96.89	96.58	100.02	100.03
Oxygen	23	6	11	8	8	4	20
Si	6.00	1.82	2.72	4.99	4.98	0.00	1.58
Ti	0.06	0.00	0.14	0.00	0.00	0.00	0.01
Al	3.26	0.29	1.48	4.04	4.05	1.88	8.63
Cr	0.01	0.00	0.00	0.00	0.00	0.02	0.03
Fe^{2+}	1.43	0.39	0.42	0.17	0.19	0.41	0.68
Fe^{3+*}	0.00	0.07	0.00	0.00	0.00	0.10	0.17
Mn	0.02	0.01	0.00	0.00	0.00	0.00	0.00
Mg	4.15	1.43	2.22	1.79	1.77	0.59	2.90
Zn	0.00	0.00	0.00	0.00	0.00	0.00	0.00
Ca	0.06	0.00	0.00	0.00	0.00	0.00	0.00
Na	0.64	0.00	0.08	0.02	0.02	0.00	0.00
K	0.01	0.00	0.73	0.00	0.00	0.00	0.00
Cl	0.01	0.00	0.01	0.00	0.00	0.00	0.00
F	0.18	0.00	0.17	0.00	0.00	0.00	0.00
Total	15.82	4.00	7.98	11.01	11.00	3.01	14.01
$X_{Fe}{}^{\dagger}$	0.26	0.22	0.16	0.09	0.10	0.41	0.19
$y_{opx}{}^{\#}$						0.01	
$X_{Zn}{}^{**}$							

*Fe^{3+} recalculated after Droop (1987). $^{\dagger}X_{Fe} = Fe^{2+}/(Fe^{2+} + Mg)$. $^{\#}y_{opx} = (Al^{tot} - Fe^{3+})/2$. $^{**}X_{Zn} = Zn/(Zn + Fe^{2+} + Fe^{3+} + Mg + Mn + Cr)$.

Table C.16: EMPA data (wt. %). Sample NMC24. Nababeep

phase	garnet	garnet	biotite	biotite	K-feldspar	plagioclase
position	core	rim	matrix	inclusion	matrix	matrix
label	NMC24c_grt_core_5	NMC24c_grt_rim_1	NMC24c_bi_3	NMC24c_bi_incl_13	NMC24c_feld_13	NMC24c_feld_1
SiO_2	38.30	38.47	37.92	38.85	65.73	59.03
TiO_2	0.02	0.04	4.77	5.58	0.00	0.01
Al_2O_3	22.55	22.52	16.23	17.54	18.80	26.12
Cr_2O_3	0.04	0.00	0.04	0.06	0.00	0.01
FeO	30.94	30.74	14.08	11.22	0.05	0.01
MnO	0.99	1.08	0.08	0.02	0.00	0.00
MgO	6.76	6.97	14.51	15.12	0.00	0.02
ZnO	0.00	0.00	0.00	0.00	0.00	0.00
CaO	1.10	1.10	0.00	0.01	0.06	7.64
Na_2O	0.00	0.00	0.13	0.32	2.24	6.90
K_2O	0.00	0.00	9.52	8.97	13.51	0.11
Cl	0.00	0.00	0.07	0.11	0.00	0.00
F	0.00	0.00	1.25	1.38	0.00	0.00
Total	100.70	100.92	98.60	99.18	100.39	99.85
Oxygen	12	12	11	11	8	8
Si	2.98	2.98	2.76	2.75	2.99	2.64
Ti	0.00	0.00	0.26	0.30	0.00	0.00
Al	2.06	2.06	1.39	1.47	1.01	1.37
Cr	0.00	0.00	0.00	0.00	0.00	0.00
Fe^{2+}	2.01	1.99	0.86	0.67	0.00	0.00
Fe^{3+*}	0.00	0.00	0.00	0.00	0.00	0.00
Mn	0.07	0.07	0.01	0.00	0.00	0.00
Mg	0.78	0.80	1.57	1.60	0.00	0.00
Zn	0.00	0.00	0.00	0.00	0.00	0.00
Ca	0.09	0.09	0.00	0.00	0.00	0.37
Na	0.00	0.00	0.02	0.04	0.20	0.60
K	0.00	0.00	0.88	0.81	0.79	0.01
Cl	0.00	0.00	0.01	0.01	0.00	0.00
F	0.00	0.00	0.29	0.31	0.00	0.00
Total	7.99	7.99	8.04	7.96	4.99	4.98
$X_{Fe}{}^{\dagger}$	0.72	0.71	0.35	0.29		
X_{alm}	0.68	0.67				
X_{prp}	0.27	0.27				
X_{grs}	0.03	0.03				
X_{sps}	0.02	0.02				
X_{ab}					0.20	0.62
X_{an}					0.00	0.38
X_{or}					0.80	0.01

*Fe^{3+} recalculated after Droop (1987). $^{\dagger}X_{Fe} = Fe^{2+}/(Fe^{2+} + Mg)$.

Table C.17: EMPA data (wt. %). Sample NMC21. Ratelpoort

phase	garnet	garnet	biotite	cordierite	cordierite	K-feldspar	plagioclase
position	core	rim	matrix	matrix	inclusion	matrix	matrix
label	NMC21a_g_core_11	NMC21a_g_rim_1	NMC21Aa_bi_8	NMC21Aa_cd_5	NMC21B_cd_incl_3	NMC21Aa_ksp_6	NMC21Aa_plg_9
SiO_2	38.59	37.97	35.48	48.52	48.34	65.35	60.59
TiO_2	0.05	0.03	3.45	0.00	0.00	0.01	0.01
Al_2O_3	22.30	22.38	18.82	33.46	33.52	19.16	25.14
Cr_2O_3	0.07	0.03	0.12	0.00	0.00	0.00	0.02
FeO	29.71	30.20	16.39	6.87	5.27	0.00	0.08
MnO	1.39	1.44	0.02	0.10	0.06	0.01	0.05
MgO	7.00	6.90	13.11	9.03	10.17	0.00	0.00
ZnO	0.00	0.00	0.00	0.00	0.00	0.00	0.00
CaO	1.02	1.01	0.02	0.00	0.01	0.12	5.94
Na_2O	0.00	0.00	0.17	0.10	0.15	2.45	7.92
K_2O	0.00	0.00	9.09	0.00	0.00	12.96	0.24
Cl	0.00	0.00	0.23	0.00	0.00	0.00	0.00
F	0.00	0.00	0.00	0.00	0.00	0.00	0.00
Total	100.13	99.96	96.90	98.08	97.52	100.06	99.98
Oxygen	12	12	11	8	8	8	8
Si	3.00	2.97	2.62	4.97	4.95	2.98	2.69
Ti	0.00	0.00	0.19	0.00	0.00	0.00	0.00
Al	2.04	2.06	1.64	4.04	4.05	1.03	1.32
Cr	0.00	0.00	0.01	0.00	0.00	0.00	0.00
Fe^{2+}	1.93	1.98	1.01	0.59	0.45	0.00	0.00
Fe^{3+*}	0.00	0.00	0.00	0.00	0.00	0.00	0.00
Mn	0.09	0.10	0.00	0.01	0.01	0.00	0.00
Mg	0.81	0.81	1.45	1.38	1.55	0.00	0.00
Zn	0.00	0.00	0.00	0.00	0.00	0.00	0.00
Ca	0.09	0.09	0.00	0.00	0.00	0.01	0.28
Na	0.00	0.00	0.02	0.02	0.03	0.22	0.68
K	0.00	0.00	0.86	0.00	0.00	0.75	0.01
Cl	0.00	0.00	0.03	0.00	0.00	0.00	0.00
F	0.00	0.00	0.00	0.00	0.00	0.00	0.00
Total	7.97	8.00	7.83	11.02	11.04	4.99	5.00
$X_{Fe}{}^{\dagger}$	0.70	0.71	0.41	0.30	0.23		
X_{alm}	0.66	0.67					
X_{prp}	0.28	0.27					
X_{grs}	0.03	0.03					
X_{sps}	0.03	0.03				0.03	0.29
X_{ab}						0.00	0.00
X_{an}						0.97	0.71
X_{or}							

*Fe^{3+} recalculated after Droop (1987). $^{\dagger}X_{Fe} = Fe^{2+}/(Fe^{2+} + Mg)$.

Table C.18: EMPA data (wt. %). Sample NMC05. Geselskapbank

phase	garnet	garnet	biotite	cordierite	plagioclase
position	core	rim	matrix	matrix	matrix
label	NMC05_grt_1	NMC05_grt_7	NMC05_bi_11	NMC05_cd_1	NMC05_plag_3
SiO_2	38.45	37.94	36.18	49.17	51.67
TiO_2	0.00	0.02	2.76	0.00	0.00
Al_2O_3	22.45	21.86	20.98	33.28	31.54
Cr_2O_3	0.05	0.00	0.01	0.01	0.00
FeO	34.23	33.92	18.54	7.24	0.05
MnO	0.27	0.21	0.02	0.04	0.01
MgO	4.79	5.00	10.44	8.26	0.00
ZnO	0.00	0.00	0.00	0.00	0.00
CaO	0.62	0.72	0.00	0.01	13.25
Na_2O	0.00	0.00	0.20	0.21	3.86
K_2O	0.00	0.00	8.72	0.00	0.02
Cl	0.00	0.00	0.06	0.00	0.00
F	0.00	0.00	0.00	0.00	0.00
Total	100.86	99.67	97.91	98.22	100.40
Oxygen	12	12	11	8	8
Si	3.01	3.01	2.65	5.03	2.33
Ti	0.00	0.00	0.15	0.00	0.00
Al	2.07	2.04	1.81	4.02	1.68
Cr	0.00	0.00	0.00	0.00	0.00
Fe^{2+}	2.24	2.25	1.13	0.62	0.00
Fe^{3+*}	0.00	0.00	0.00	0.00	0.00
Mn	0.02	0.01	0.00	0.00	0.00
Mg	0.56	0.59	1.14	1.26	0.00
Zn	0.00	0.00	0.00	0.00	0.00
Ca	0.05	0.06	0.00	0.00	0.64
Na	0.00	0.00	0.03	0.04	0.34
K	0.00	0.00	0.81	0.00	0.00
Cl	0.00	0.00	0.01	0.00	0.00
F	0.00	0.00	0.00	0.00	0.00
Total	7.95	7.97	7.73	10.98	5.00
$X_{Fe}{}^{\dagger}$	0.80	0.79	0.50	0.33	
X_{alm}	0.78	0.77			
X_{prp}	0.19	0.20			
X_{grs}	0.02	0.02			
X_{sps}	0.01	0.00			
X_{ab}					0.35
X_{an}					0.65
X_{or}					0.00

*Fe^{3+} recalculated after Droop (1987). $^{\dagger}X_{Fe} = Fe^{2+}/(Fe^{2+} + Mg)$.

Table C.19: EMPA data (wt. %). Sample NMC11. Geselskapbank

phase	garnet	garnet	biotite	cordierite	plagioclase
position	core	rim	matrix	matrix	matrix
label	NMC11a_gt_core_17	NMC11a_gt_rim_11	NMC11a_bi_10	NMC11a_cd_2	NMC11_plag_8
SiO_2	37.72	37.82	35.11	47.64	50.37
TiO_2	0.03	0.00	1.48	0.00	0.01
Al_2O_3	22.37	22.38	20.98	33.25	32.57
Cr_2O_3	0.00	0.03	0.18	0.00	0.02
FeO	34.92	34.77	20.20	8.30	0.03
MnO	0.71	0.67	0.05	0.09	0.03
MgO	3.82	3.63	9.49	7.71	0.00
ZnO	0.00	0.00	0.00	0.00	0.00
CaO	1.61	1.72	0.00	0.01	13.19
Na_2O	0.00	0.00	0.18	0.33	3.69
K_2O	0.00	0.00	8.84	0.00	0.02
Cl	0.00	0.00	0.69	0.00	0.00
F	0.00	0.00	0.00	0.00	0.00
Total	101.18	101.02	97.20	97.32	99.93
Oxygen	12	12	11	8	8
Si	2.97	2.98	2.63	4.96	2.29
Ti	0.00	0.00	0.08	0.00	0.00
Al	2.08	2.08	1.86	4.08	1.74
Cr	0.00	0.00	0.01	0.00	0.00
Fe^{2+}	2.30	2.29	1.27	0.72	0.00
Fe^{3+*}	0.00	0.00	0.00	0.00	0.00
Mn	0.05	0.05	0.00	0.01	0.00
Mg	0.45	0.43	1.06	1.20	0.00
Zn	0.00	0.00	0.00	0.00	0.00
Ca	0.14	0.15	0.00	0.00	0.64
Na	0.00	0.00	0.03	0.07	0.33
K	0.00	0.00	0.85	0.00	0.00
Cl	0.00	0.00	0.09	0.00	0.00
F	0.00	0.00	0.00	0.00	0.00
Total	7.99	7.98	7.88	11.04	5.00
$X_{Fe}{}^{\dagger}$	0.84	0.84	0.54	0.38	
X_{alm}	0.78	0.79			
X_{prp}	0.15	0.15			
X_{grs}	0.05	0.05			
X_{sps}	0.02	0.02			
X_{ab}					0.34
X_{an}					0.66
X_{or}					0.00

*Fe^{3+} recalculated after Droop (1987). $^{\dagger}X_{Fe} = Fe^{2+}/(Fe^{2+} + Mg)$.

Table C.20: EMPA data (wt. %). Sample NMC15. Geselskapbank

phase	biotite	cordierite	K-feldspar	plagioclase
position	matrix	matrix	matrix	matrix
label	NMC15_bi_1	NMC15_cd_4	NMC15_ksp_1	NMC15_feld_14
SiO_2	37.37	48.82	63.19	60.49
TiO_2	2.13	0.00	0.00	0.00
Al_2O_3	21.09	33.96	19.34	25.20
Cr_2O_3	0.00	0.00	0.02	0.00
FeO	12.16	3.53	0.09	0.06
MnO	0.32	0.94	0.03	0.10
MgO	14.93	10.62	0.00	0.00
ZnO	0.00	0.00	0.00	0.00
CaO	0.00	0.00	0.00	5.85
Na_2O	0.17	0.09	0.74	8.16
K_2O	9.05	0.00	16.03	0.13
Cl	0.03	0.00	0.00	0.00
F	0.00	0.00	0.00	0.00
Total	97.25	97.97	99.46	99.99
Oxygen	11	8	8	8
Si	2.67	4.96	2.94	2.69
Ti	0.12	0.00	0.00	0.00
Al	1.78	4.06	1.06	1.32
Cr	0.00	0.00	0.00	0.00
Fe^{2+}	0.73	0.30	0.00	0.00
Fe^{3+*}	0.00	0.00	0.00	0.00
Mn	0.02	0.08	0.00	0.00
Mg	1.59	1.61	0.00	0.00
Zn	0.00	0.00	0.00	0.00
Ca	0.00	0.00	0.00	0.28
Na	0.02	0.02	0.07	0.70
K	0.83	0.00	0.95	0.01
Cl	0.00	0.00	0.00	0.00
F	0.00	0.00	0.00	0.00
Total	7.75	11.02	5.03	5.00
$X_{Fe}{}^{\dagger}$	0.31	0.16		
X_{ab}			0.07	0.71
X_{an}			0.00	0.28
X_{or}			0.93	0.01

*Fe^{3+} recalculated after Droop (1987). $^{\dagger}X_{Fe} = Fe^{2+}/(Fe^{2+} + Mg)$.

Table C.21: EMPA data (wt. %). Sample NMC16. Geselskapbank

phase	biotite	cordierite	K-feldspar	plagioclase
position	matrix	matrix	matrix	matrix
label	NMC16b_bi_8	NMC16b_cd_4	NMC16b_fsp_8	NMC16b_fsp_15
SiO_2	37.19	49.51	64.68	59.71
TiO_2	2.27	0.00	0.02	0.02
Al_2O_3	21.10	33.73	19.42	25.82
Cr_2O_3	0.01	0.00	0.00	0.01
FeO	12.48	3.11	0.05	0.09
MnO	0.43	0.97	0.06	0.04
MgO	14.91	10.90	0.00	0.00
ZnO	0.00	0.00	0.00	0.00
CaO	0.00	0.00	0.00	6.56
Na_2O	0.17	0.23	1.36	8.30
K_2O	9.81	0.00	14.49	0.09
Cl	0.04	0.00	0.00	0.00
F	0.00	0.00	0.00	0.00
Total	98.41	98.45	100.09	100.63
Oxygen	11	8	8	8
Si	2.65	4.99	2.97	2.65
Ti	0.12	0.00	0.00	0.00
Al	1.77	4.01	1.05	1.35
Cr	0.00	0.00	0.00	0.00
Fe^{2+}	0.74	0.26	0.00	0.00
Fe^{3+*}	0.00	0.00	0.00	0.00
Mn	0.03	0.08	0.00	0.00
Mg	1.58	1.64	0.00	0.00
Zn	0.00	0.00	0.00	0.00
Ca	0.00	0.00	0.00	0.31
Na	0.02	0.05	0.12	0.71
K	0.89	0.00	0.85	0.01
Cl	0.01	0.00	0.00	0.00
F	0.00	0.00	0.00	0.00
Total	7.81	11.03	4.99	5.04
$X_{Fe}{}^{\dagger}$	0.32	0.14		
X_{ab}			0.12	0.69
X_{an}			0.00	0.30
X_{or}			0.88	0.00

*Fe^{3+} recalculated after Droop (1987). $^{\dagger}X_{Fe} = Fe^{2+}/(Fe^{2+} + Mg)$.

Appendix D

U–Pb isotopic and geochemical data

Table D.1: Instrument parameters for LA-MC-ICPMS – zircon ablation

Nu Plasma II MC ICPMS	Nu Instruments Ltd., Wrexham, UK
RF forward power	1300 W
RF reflected power	4 W
Coolant	13 l.min^{-1}
Carrier gas (Ar)	1.0 l.min^{-1}
Make up gas (He+N2) flow	350 ml.min^{-1} (He); 1.2 ml.min^{-1} (N_2)
Monitored masses (rims)	^{238}U (H10), ^{232}Th (H8), ^{208}Pb (IC0), ^{207}Pb (IC1), ^{206}Pb (IC2), ^{204}Pb (IC3), ^{202}Hg (IC4)
Monitored masses (cores)	^{238}U (H10), ^{208}Pb (L2), ^{207}Pb (L3), ^{206}Pb (L4), ^{204}Pb (IC0), ^{202}Hg (IC2), ^{200}Hg (IC3)
Dwell Time	115 ms
Integration	0.8 s
RESOlution 193 nm Excimer Laser	ASI Ltd., Canberra, Australia
Laser	Compex 102 excimer
Cell	Lauren Technic S155
Fluence	1.8 J.cm^{-2}
Repetition rate	4 Hz
Excavation rate	$\sim\mu$m/pulse
Delay between analyses	55 s
Ablation duration	30 s

Table D.2: Instrument parameters for LA-MC-ICPMS – monazite ablation

Nu Plasma II MC ICPM	Nu Instruments Ltd., Wrexham, UK
RF forward power	1300 W
RF reflected power	4 W
Coolant	13 l.min^{-1}
Carrier gas (Ar)	1.0 l.min^{-1}
Make up gas (He + N_2) flow	320 mL/min (He); 1.2 mL/min (N2)
Monitored masses	^{238}U (H10), ^{232}Th (H8), ^{208}Pb (IC0), ^{207}Pb (IC1), ^{206}Pb (IC2), ^{204}Pb (IC3), ^{202}Hg (IC4)
Dwell Time	115 ms
Integration	0.8 s
RESOlution 193 nm Excimer Laser	ASI Ltd., Canberra, Australia
Laser	Compex 102 excimer
Cell	Lauren Technic S155
Fluence	1.8 J.cm^{-2}
Repetition rate	4 Hz
Excavation rate	$\sim\mu$m/pulse
Delay between analyses	55 s
Ablation duration	30 s

Table D.3: LASS ICP-MS U–Pb isotopic data for zircon standards – FC machine settings for core analyses.

standard	spot	$^{238}U/^{206}Pb$	2σ	$^{207}Pb/^{206}Pb$	2σ	$^{206}Pb/^{238}U$ Age (Ma)	2σ	$^{207}Pb/^{206}Pb$ Age (Ma)	2σ
PLES	PLES - 1	18.59773	0.1867728	0.0538	0.0055	337.6	3.3	350	220
PLES	PLES - 2	18.77934	0.1869118	0.0547	0.0046	334.5	3.3	380	190
PLES	PLES - 3	18.76525	0.1831099	0.053	0.0052	334.7	3.2	330	230
PLES	PLES - 4	18.74414	0.1897252	0.0535	0.0051	335.1	3.3	410	220
PLES	PLES - 5	18.60465	0.1869118	0.0536	0.0052	337.5	3.3	350	230
PLES	PLES - 7	18.76173	0.1830412	0.0564	0.0049	334.8	3.2	440	200
PLES	PLES - 8	18.7864	0.183523	0.0524	0.0049	334.3	3.2	330	210
PLES	PLES - 9	18.65672	0.1740365	0.05335	0.0039	336.56	3.1	339	160
PLES	PLES - 10	18.74063	0.1756056	0.0537	0.0039	335.12	3.1	362	170
PLES	PLES - 12	18.44338	0.1700791	0.0529	0.0039	340.36	3.1	338	170
PLES	PLES - 13	18.59427	0.176331	0.0539	0.0049	337.7	3.1	330	190
PLES	PLES - 14	18.88931	0.178403	0.0546	0.0042	332.56	3.1	397	180
PLES	PLES - 15	18.76525	0.1831099	0.0528	0.0042	334.7	3.2	322	190
PLES	PLES - 16	18.58045	0.176069	0.0525	0.0043	337.91	3.1	330	200
PLES	PLES - 17	18.59082	0.2108273	0.055	0.0058	337.8	3.7	370	230
PLES	PLES - 18	18.8537	0.1848402	0.0541	0.0048	333.2	3.2	350	200
PLES	PLES - 19	18.80406	0.1874041	0.0527	0.0045	334	3.2	320	190
PLES	PLES - 20	18.59427	0.1832459	0.0581	0.0048	337.7	3.2	513	190
PLES	PLES - 21	18.87861	0.185329	0.0517	0.0046	332.7	3.2	250	200
PLES	PLES - 22	18.6846	0.1815395	0.0577	0.0048	336.1	3.2	500	180
PLES	PLES - 23	18.47746	0.187779	0.0559	0.0053	339.8	3.4	410	210
PLES	PLES - 24	18.51509	0.1954009	0.0566	0.005	339.1	3.5	450	190
PLES	PLES - 25	18.66716	0.2021086	0.051	0.0052	336.4	3.6	270	210
OGC	OGC - 12	1.35428	0.01485599	0.2967	0.021	3565	30	3452.3	110
OGC	OGC - 14	1.395479	0.01382626	0.2968	0.021	3483	27	3452.9	110
OGC	OGC - 15	1.386578	0.01403497	0.2989	0.021	3501	27	3463.6	110
OGC	OGC - 16	1.367241	0.01308543	0.2984	0.021	3538.7	26	3461.1	110
OGC	OGC - 18	1.376273	0.01269065	0.29783	0.021	3520.9	25	3458.3	110
OGC	OGC - 19	1.387732	0.01328803	0.2983	0.021	3498.3	26	3460.5	110
OGC	OGC - 20	1.401542	0.01335737	0.2988	0.021	3471.5	26	3463.5	110
OGC	OGC - 21	1.392564	0.01299287	0.2982	0.021	3488.8	25	3460.2	110
OGC	OGC - 22	1.394895	0.01381469	0.2992	0.021	3484	27	3465	110
OGC	OGC - 23	1.381025	0.01354133	0.2974	0.021	3511	26	3456.1	110
OGC	OGC - 24	1.385617	0.01343955	0.29901	0.021	3503	26	3464.3	110
OGC	OGC - 25	1.380834	0.01315625	0.2995	0.021	3511.7	26	3467	110
91500	91500 - 1	5.552471	0.06474286	0.0746	0.0081	1067.2	12	1050	200
91500	91500 - 2	5.633803	0.06665344	0.0753	0.0086	1053.5	12	1000	230
91500	91500 - 3	5.681818	0.07747934	0.0713	0.01	1045.1	13	830	330
91500	91500 - 4	5.633803	0.07617536	0.0763	0.0097	1053.3	13	1060	270
91500	91500 - 5	5.614823	0.07566297	0.0761	0.0088	1056.3	13	1020	250
91500	91500 - 6	5.592841	0.06881572	0.0731	0.0094	1060.1	12	1000	260
91500	91500 - 8	5.621135	0.06951376	0.0772	0.0095	1055.2	12	1090	250
91500	91500 - 10	5.633803	0.09204523	0.078	0.012	1053	16	1080	310
91500	91500 - 11	5.640158	0.09543414	0.079	0.014	1052	17	1010	400
91500	91500 - 13	5.652911	0.07349743	0.0722	0.011	1050	12	1010	280
91500	91500 - 14	5.583473	0.07170289	0.0766	0.0094	1062.2	12	1010	280
91500	91500 - 15	5.558644	0.083426	0.072	0.0098	1067	15	920	300
91500	91500 - 16	5.583473	0.08417296	0.077	0.012	1062	15	1000	330
91500	91500 - 17	5.467469	0.08370099	0.0792	0.01	1083	15	1060	280
91500	91500 - 18	5.521811	0.07927504	0.0722	0.011	1073	14	890	350
91500	91500 - 19	5.586592	0.07490403	0.0696	0.01	1061.5	13	880	310
91500	91500 - 20	5.595971	0.08141871	0.0836	0.0085	1060	14	1280	210
91500	91500 - 21	5.56483	0.07741834	0.0756	0.0094	1065	13	980	290
91500	91500 - 22	5.50055	0.06656331	0.0746	0.0097	1076.8	12	940	280
91500	91500 - 23	5.461496	0.08053545	0.077	0.012	1084	15	980	360
91500	91500 - 24	5.482456	0.06913185	0.074	0.013	1080.1	12	830	410
91500	91500 - 25	5.605381	0.08169277	0.083	0.01	1058	14	1210	260

Table D.4: LASS ICP-MS U–Pb isotopic data for zircon standards – IC machine settings for rim analyses.

standard	spot	$^{238}U/^{206}Pb$	2σ	$^{207}Pb/^{206}Pb$	2σ	$^{206}Pb/^{238}U$ Age (Ma)	2σ	$^{207}Pb/^{206}Pb$ Age (Ma)	2σ
GJ1	GJ1 - 1	10.23646	0.2305274	0.06023	0.00063	601	13	612	23
GJ1	GJ1 - 2	10.2976	0.2332893	0.06027	0.00062	597	13	613	22
GJ1	GJ1 - 3	10.21033	0.229352	0.05993	0.00062	602	13	601	23
GJ1	GJ1 - 5	10.34554	0.2247635	0.05947	0.00064	595	12	584	24
GJ1	GJ1 - 6	10.32525	0.2345435	0.05968	0.00062	596	13	592	23
GJ1	GJ1 - 11	10.37883	0.2369841	0.05978	0.00068	593	13	596	25
GJ1	GJ1 - 12	10.21242	0.2294457	0.05977	0.00065	602	13	595	24
GJ1	GJ1 - 13	10.13582	0.2362901	0.06022	0.00069	607	13	611	25
GJ1	GJ1 - 14	10.39501	0.2377237	0.06038	0.00066	592	13	617	24
GJ1	GJ1 - 18	10.27855	0.2324268	0.06023	0.00074	599	13	612	27
GJ1	GJ1 - 19	10.09897	0.2345751	0.05938	0.00065	609	13	581	24
GJ1	GJ1 - 21	10.09285	0.2241046	0.06041	0.00066	609	13	618	24
GJ1	GJ1 - 22	10.03412	0.231572	0.05934	0.00071	612	13	580	26
GJ1	GJ1 - 23	10.31566	0.2341082	0.05944	0.00077	596	13	583	28
GJ1	GJ1 - 24	10.42427	0.2281972	0.05896	0.00075	591	12	566	28
GJ1	GJ1 - 25	10.26799	0.2319498	0.05934	0.00067	599	13	580	25
GJ1	GJ1 - 26	10.08268	0.2236529	0.06013	0.00069	610	13	608	25
GJ1	GJ1 - 27	10.21033	0.229352	0.0603	0.00068	602	13	614	25
OGC	OGC - 1	1.349346	0.03095247	0.29813	0.0029	3575	62	3461	15
OGC	OGC - 3	1.381215	0.0305241	0.29732	0.0029	3511	59	3456	15
OGC	OGC - 4	1.35888	0.03139145	0.29763	0.0029	3555	62	3458	15
OGC	OGC - 6	1.403509	0.03151739	0.29797	0.0029	3468	59	3460	15
OGC	OGC - 7	1.383317	0.03253063	0.29821	0.0029	3507	62	3461	15
OGC	OGC - 8	1.414027	0.03199156	0.29769	0.0029	3448	59	3458	15
OGC	OGC - 10	1.402131	0.03145555	0.29959	0.003	3471	59	3468	16
OGC	OGC - 11	1.428571	0.03265306	0.2984	0.003	3421	60	3462	16
OGC	OGC - 12	1.359065	0.03139998	0.29784	0.003	3555	62	3459	16
OGC	OGC - 13	1.372307	0.03013162	0.2984	0.003	3529	59	3462	16
OGC	OGC - 14	1.474057	0.03259264	0.2971	0.0031	3338	57	3455	16
OGC	OGC - 15	1.42106	0.03231059	0.30119	0.003	3435	59	3476	16
OGC	OGC - 16	1.385042	0.03069344	0.3008	0.003	3504	59	3474	16
OGC	OGC - 17	1.40056	0.0313851	0.29892	0.003	3474	59	3465	16
OGC	OGC - 18	1.344809	0.03074469	0.2982	0.0033	3584	62	3461	17
OGC	OGC - 19	1.387347	0.03079572	0.2978	0.003	3499	59	3459	16
OGC	OGC - 20	1.362398	0.02969805	0.2976	0.0031	3548	58	3458	16
OGC	OGC - 22	1.41623	0.03209132	0.299	0.0032	3444	59	3465	17
OGC	OGC - 26	1.37893	0.03042316	0.29795	0.003	3516	59	3460	16
OGC	OGC - 28	1.39334	0.03300373	0.2991	0.0034	3487	63	3466	18
PLES	PLES - 1	18.46381	0.4090948	0.05299	0.00057	340	7	328	25
PLES	PLES - 2	18.74414	0.4216115	0.05331	0.00059	335	7	342	25
PLES	PLES - 3	18.54943	0.4128978	0.05319	0.00058	338	7	337	25
PLES	PLES - 4	18.61851	0.4159786	0.05306	0.00057	337	7	331	25
PLES	PLES - 5	18.51852	0.4115226	0.05295	0.00055	339	7	327	24
PLES	PLES - 6	18.63933	0.4169095	0.0528	0.00057	337	7	320	25
PLES	PLES - 7	18.80406	0.4243113	0.05323	0.00057	334	7	339	24
PLES	PLES - 8	18.96813	0.4317481	0.05336	0.00057	331	7	344	24
PLES	PLES - 9	18.74414	0.4216115	0.05295	0.00054	335	7	327	23
PLES	PLES - 11	18.64976	0.4173761	0.05262	0.00061	337	7	312	27
PLES	PLES - 12	18.05054	0.4235687	0.05278	0.0006	348	8	319	26
PLES	PLES - 13	18.56321	0.4135112	0.05307	0.00058	338	7	332	25
PLES	PLES - 14	18.97893	0.4322399	0.05338	0.00064	331	7	345	27
PLES	PLES - 18	18.80406	0.4243113	0.05345	0.00065	334	7	348	28
PLES	PLES - 19	18.58736	0.414588	0.05275	0.00062	338	7	318	27
PLES	PLES - 20	18.40943	0.4066883	0.0529	0.00063	341	7	325	27
PLES	PLES - 23	18.9179	0.4294642	0.0522	0.00062	332	7	294	27
PLES	PLES - 24	19.0295	0.434546	0.05245	0.00058	330	7	305	25
PLES	PLES - 25	18.56321	0.4135112	0.05277	0.00066	338	7	319	29
PLES	PLES - 26	18.18182	0.3966942	0.0531	0.0006	345	7	333	26
PLES	PLES - 27	18.47746	0.4096997	0.05389	0.00059	340	7	366	25

Table D.5: LASS ICP-MS U–Pb isotopic data for monazite standard.

standard	spot	^{238}U/ ^{206}Pb	2σ	^{207}Pb/^{206}Pb	2σ	^{206}Pb/^{238}U Age (Ma)	2σ	^{207}Pb/^{206}Pb Age (Ma)	2σ
TREBI	Trebilcock - 1	23.41372	0.5482023	0.0517	0.001	269.6	6.3	267	47
TREBI	Trebilcock - 2	23.45216	0.6600044	0.05004	0.00076	269.2	7.5	194	35
TREBI	Trebilcock - 3	23.34267	0.5993683	0.05015	0.0006	270.4	6.9	200	28
TREBI	Trebilcock - 4	23.42469	0.6035877	0.05047	0.00082	269.5	7	214	38
TREBI	Trebilcock - 5	23.16423	0.5902399	0.05097	0.00064	272.5	6.5	237	29
TREBI	Trebilcock - 6	22.99379	0.5815859	0.0506	0.00087	274.4	6.7	220	40
TREBI	Trebilcock - 7	23.34812	0.5996482	0.0505	0.00075	270.3	6.5	216	34
TREBI	Trebilcock - 8	23.39729	0.6021763	0.04991	0.00063	269.8	6.9	189	30
TREBI	Trebilcock - 9	23.11604	0.5877866	0.04976	0.00083	273	6.8	181	39
TREBI	Trebilcock - 10	23.16423	0.5902399	0.05119	0.00062	272.5	6.5	247	28
TREBI	Trebilcock - 11	23.61833	0.5578254	0.0513	0.001	267.3	6.3	249	46
TREBI	Trebilcock - 12	23.55158	0.5546768	0.05093	0.00075	268.1	6.4	245	37
TREBI	Trebilcock - 13	23.14815	0.5894204	0.05064	0.00071	272.6	6.9	222	33
TREBI	Trebilcock - 14	22.93578	0.578655	0.05127	0.00071	275.1	6.5	251	32
TREBI	Trebilcock - 15	23.18034	0.5910611	0.05054	0.00072	272.2	6.8	218	33
TREBI	Trebilcock - 16	23.38634	0.546921	0.0504	0.0013	269.9	6.3	208	58
TREBI	Trebilcock - 17	23.35903	0.5347313	0.0508	0.001	270.2	6	229	46
TREBI	Trebilcock - 18	23.08936	0.5864302	0.05229	0.00088	273.3	6.6	295	38

Table D.6: LASS ICP-MS U–Pb isotopic data for zircon – IC machine settings for rim analyses. Sample NMC47.

sample ID	spot	instrument settings	CL	group	comment	^{238}U/ ^{206}Pb	2σ	^{207}Pb/^{206}Pb	2σ	^{206}Pb/^{238}U Age (Ma)	2σ	^{207}Pb/^{206}Pb Age (Ma)	2σ	7/6 discordance (%)	6/8 discordance (%)
NMC47	NMC47 - 1	IC	Sh	M	small rounded sector zoned grain, bright CL	5.543237	0.1444192	0.07499	0.00082	1069	26	1067	22	-0.19	0.19
NMC47	NMC47 - 2	IC	Sl	M	small rounded sector zoned grain, faint CL	5.411255	0.1259112	0.0736	0.00076	1093.1	23	1029.6	21	-6.17	5.81
NMC47	NMC47 - 3	IC	Sh	M	small rounded sector zoned grain, bright CL	5.443658	0.1244603	0.0739	0.00078	1087.2	23	1037.6	21	-4.78	4.56
NMC47	NMC47 - 4	IC	Sh	M	small rounded sector zoned grain, bright CL	5.521811	0.1250106	0.0725	0.00076	1073.2	22	998.9	21	-7.44	6.92
NMC47	NMC47 - 5	IC	Sh	D	small rounded sector zoned grain, bright CL	5.813953	0.2230936	0.0917	0.0016	1023	36	1459	34	29.88	-42.62
NMC47	NMC47 - 6	IC	Sh	M	small rounded sector zoned grain, bright CL	5.589715	0.1249797	0.07221	0.00079	1061.1	22	991	22	-7.07	6.61
NMC47	NMC47 - 7	IC	Sl	M	small rounded sector zoned grain, faint CL	5.224115	0.1146238	0.07402	0.00077	1129.1	23	1041	21	-8.46	7.80
NMC47	NMC47 - 8	IC	Sh	M	small rounded sector zoned grain, bright CL	5.67215	0.1319105	0.07296	0.00075	1046.8	22	1011.9	21	-3.45	3.33
NMC47	NMC47 - 9	IC	Sl	M	large ovoidal sector zoned grain, faint CL	5.46717	0.1225488	0.07357	0.00083	1082.9	22	1029	23	-5.24	4.98
NMC47	NMC47 - 10	IC	Sh	M	small rounded sector zoned grain, bright CL	5.542316	0.1259408	0.07318	0.00077	1069.3	22	1017.9	21	-5.05	4.81
NMC47	NMC47 - 11	IC	Cl	M?	rounded grain with CL dark core, no visible zoning	5.339028	0.1225725	0.07317	0.00076	1106.6	23	1019.5	22	-8.54	7.87
NMC47	NMC47 - 12	IC	Sh	M	small rounded sector zoned grain, bright CL	5.455537	0.1250041	0.07273	0.00074	1084.7	23	1005.5	21	-7.88	7.30
NMC47	NMC47 - 13	IC	Sh	M	small rounded sector zoned grain, bright CL	5.165289	0.120061	0.0762	0.0015	1141	24	1098	38	-3.92	3.77
NMC47	NMC47 - 14	IC	Sh	D	small rounded sector zoned grain, bright CL	5.446623	0.1275625	0.0927	0.0052	1086.8	23	1460	110	25.56	-34.34
NMC47	NMC47 - 15	IC	Sh	M	small rounded sector zoned grain, bright CL	5.830904	0.1359978	0.07232	0.00076	1020.6	22	994.1	21	-2.67	2.60
NMC47	NMC47 - 16	IC	Sh	M	small rounded sector zoned grain, bright CL	5.319149	0.1216614	0.07395	0.0008	1110.4	23	1041.2	21	-6.65	6.23
NMC47	NMC47 - 17	IC	Cl	M?	rounded grain with CL dark core, no visible zoning	5.422993	0.1264581	0.07262	0.00082	1090.7	23	1002	23	-8.85	8.13
NMC47	NMC47 - 18	IC	Sh	M	small rounded sector zoned grain, bright CL	5.501761	0.1241044	0.07308	0.00077	1076.6	22	1015.3	21	-6.04	5.69
NMC47	NMC47 - 19	IC	Sh	M	small rounded sector zoned grain, bright CL	5.711022	0.1598173	0.07328	0.00079	1040	27	1020.5	22	-1.91	1.88
NMC47	NMC47 - 20	IC	Sh	M	small rounded sector zoned grain, bright CL	5.307856	0.1465013	0.07536	0.00081	1113	28	1077.1	22	-3.33	3.23
NMC47	NMC47 - 21	IC	Sh	M	small rounded sector zoned grain, bright CL	5.518764	0.1370554	0.07287	0.00076	1073	25	1009.4	21	-6.30	5.93
NMC47	NMC47 - 22	IC	Sh	M	small rounded sector zoned grain, bright CL	5.767013	0.1297079	0.07234	0.00075	1031	22	994.5	21	-3.67	3.54
NMC47	NMC47 - 23	IC	Sl	M	small rounded sector zoned grain, low CL	5.681818	0.1388171	0.07313	0.00082	1045	24	1016	23	-2.85	2.78
NMC47	NMC47 - 24	IC	Sh	M	small ovoidal/elongated sector zoned grain, bright CL	5.249344	0.1240002	0.07475	0.00084	1124.1	24	1063	21	-5.75	5.44
NMC47	NMC47 - 25	IC	Sh	M	small rounded sector zoned grain, bright CL	5.543237	0.1259827	0.07296	0.00074	1069.4	22	1011.7	21	-5.70	5.40
NMC47	NMC47 - 26	IC	Cl	M?	large round grain, CL-dark, no clear zoning	5.34931	0.1201835	0.07378	0.00077	1104.8	23	1034.6	21	-6.79	6.35
NMC47	NMC47 - 27	IC	Sh	D	small rounded sector zoned grain, bright CL	5.219207	0.1225805	0.07321	0.00088	1129.8	24	1018	24	-10.98	9.90
NMC47	NMC47 - 28	IC	CL	M?	rounded grain with CL dark core, no visible zoning	5.530973	0.1254258	0.0724	0.00086	1071.5	22	996	24	-7.58	7.05
NMC47	NMC47 - 29	IC	Sl	M	small rounded sector zoned grain, faint CL	5.319149	0.1301494	0.0736	0.00077	1111	25	1029.5	21	-7.92	7.34
NMC47	NMC47 - 30	IC	Sl	M	small rounded sector zoned grain, faint CL	5.265929	0.1247851	0.0737	0.00077	1120.9	24	1032.2	21	-8.59	7.91
NMC47	NMC47 - 31	IC	Sl	D	small rounded sector zoned grain, faint CL	5.352173	0.1203122	0.07285	0.00081	1104.3	23	1009	23	-9.44	8.63

Table D.7: LASS ICP-MS chondrite-normalised REE data for zircon (ppm) – IC machine settings for rim analyses. Sample NMC47.

sample ID	spot	instrument settings	CL	group	La	Ce	Pr	Nd	Sm	Eu	Gd	Tb	Dy	Ho	Er	Tm	Yb	Lu
NMC47	NMC47 - 1	IC	Sh	M	b.d	5.0248	8.5246	13.6667	67.6923	27.7551	122.3938	236.2869	385.0932	657.3816	947.6190	1320.9877	1875.5981	2844.7205
NMC47	NMC47 -2	IC	Sl	M	0.0581	2.8960	b.d	b.d	49.2308	b.d	61.0039	99.5781	77.0186	79.5265	75.2381	73.1481	65.5502	72.6708
NMC47	NMC47 - 3	IC	Sh	M	0.0603	3.8614	b.d	b.d	31.7949	b.d	43.6293	59.0717	54.6584	49.8607	39.5238	28.3951	30.1435	31.3665
NMC47	NMC47 - 4	IC	Sh	M	0.0503	3.2797	b.d	7.8333	29.7436	b.d	40.5405	62.8692	46.2733	37.3259	32.3810	23.4568	26.7943	21.1180
NMC47	NMC47 - 5	IC	Sh	D	b.d	143.5644	598.3607	570.0000	338.4615	170.0680	202.3166	259.4937	257.7640	288.3008	262.3810	296.2963	258.3732	319.8758
NMC47	NMC47 - 6	IC	Sh	M	b.d	4.0718	b.d	9.3333	31.7949	b.d	69.1120	53.3755	42.2360	45.6825	29.0476	19.7531	21.0526	32.6087
NMC47	NMC47 - 7	IC	Sl	M	b.d	2.8465	6.3934	22.0000	48.2051	8.4354	99.2278	146.4135	136.9565	115.5989	114.7619	107.7160	107.6555	115.2174
NMC47	NMC47 - 8	IC	Sh	M	b.d	6.0644	19.9180	17.6667	52.3077	1.7687	77.9923	87.7637	54.0373	38.1616	30.4762	31.1728	27.2727	28.8820
NMC47	NMC47 - 9	IC	Sl	M	0.0077	3.0817	b.d	b.d	42.5641	b.d	49.4208	64.7679	60.8696	49.1643	49.0476	44.7531	33.0144	45.3416
NMC47	NMC47 - 10	IC	Sh	M	b.d	3.2178	b.d	12.5000	68.7179	4.4898	75.2896	100.2110	109.6273	99.0251	95.7143	76.5432	81.8182	75.4658
NMC47	NMC47 - 11	IC	Cl	M?	b.d	4.3069	b.d	21.3333	57.4359	b.d	94.5946	98.1013	107.7640	115.7382	94.7619	102.7778	118.6603	114.5963
NMC47	NMC47 - 12	IC	Sh	M	b.d	18.8119	36.0656	43.8333	84.1026	10.3401	73.3591	93.0380	82.9193	50.4178	50.4762	25.9259	29.6651	27.0186
NMC47	NMC47 - 13	IC	Sh	M	b.d	6.3119	19.6721	30.0000	49.7436	15.7823	69.4981	103.1646	79.1925	85.3760	90.9524	79.6296	84.2105	77.9503
NMC47	NMC47 - 14	IC	Sh	D	b.d	235.1485	565.5738	508.3333	266.6667	190.4762	173.7452	183.5443	214.2857	247.9109	233.3333	256.1728	258.3732	257.7640
NMC47	NMC47 - 15	IC	Sh	M	b.d	5.8168	16.8033	16.0000	61.5385	b.d	49.4208	79.9578	57.4534	63.2312	56.6667	65.4321	49.7608	60.8696
NMC47	NMC47 - 16	IC	Sh	M	0.0387	2.2401	b.d	7.3333	42.0513	b.d	39.3822	51.4768	35.4037	27.5766	24.7619	11.7284	11.0048	19.2547
NMC47	NMC47 - 17	IC	Cl	M?	0.0358	3.1064	b.d	14.5000	30.2564	b.d	35.9073	53.5865	49.0683	36.9081	31.2857	25.0000	14.8325	33.8509
NMC47	NMC47 - 18	IC	Sh	M	0.0213	1.1015	b.d	b.d	45.6410	b.d	74.1313	100.6329	87.8882	88.3008	92.3810	71.2963	87.5598	84.4720
NMC47	NMC47 - 19	IC	Sh	M	0.0403	3.3911	b.d	6.5000	58.9744	b.d	72.9730	71.0970	77.0186	84.1226	91.9048	74.3827	66.5072	68.6335
NMC47	NMC47 - 20	IC	Sh	M	b.d	19.5545	30.3279	10.5000	37.9487	11.4286	79.9228	160.3376	229.8137	394.1504	557.1429	854.9383	1306.2201	1965.8385
NMC47	NMC47 - 21	IC	Sh	M	0.0681	1.8317	b.d	b.d	19.4872	b.d	39.7683	76.3713	77.0186	111.4206	167.1429	219.1358	296.6507	543.4783
NMC47	NMC47 - 22	IC	Sh	M	0.0032	3.9728	b.d	b.d	24.6154	b.d	45.9459	63.9241	59.0062	71.3092	71.4286	59.2593	61.7225	74.2236
NMC47	NMC47 - 23	IC	Sl	M	b.d	4.2946	b.d	b.d	48.7179	b.d	49.0347	76.5823	59.0062	57.2423	52.8571	30.2469	38.2775	54.0373
NMC47	NMC47 - 24	IC	Sh	M	0.0026	1.2500	b.d	b.d	24.1026	b.d	40.1544	58.6498	63.9752	66.0167	75.7143	98.7654	135.4067	204.9689
NMC47	NMC47 - 25	IC	Sh	M	0.0213	1.2376	4.7541	b.d	34.8718	b.d	35.5212	70.8861	58.6957	64.6240	56.6667	61.7284	65.0718	59.0062
NMC47	NMC47 - 26	IC	Cl	M?	b.d	3.2302	b.d	13.1667	58.4615	b.d	40.1544	55.0633	63.0435	43.4540	38.0952	16.6667	25.8373	26.0870
NMC47	NMC47 - 27	IC	Sh	D	b.d	1.4109	b.d	b.d	33.8462	b.d	67.5676	119.8312	120.1863	112.8134	100.4762	90.1235	103.3493	119.5652
NMC47	NMC47 - 28	IC	CL	M?	0.0094	3.5396	8.8525	16.5000	74.8718	b.d	84.5560	100.8439	80.4348	68.2451	57.6190	43.2099	44.9761	54.3478
NMC47	NMC47 - 29	IC	Sl	M	b.d	1.2624	6.3934	b.d	37.9487	b.d	61.7761	95.3586	84.4720	93.8719	106.1905	87.6543	114.3541	112.1118
NMC47	NMC47 - 30	IC	Sl	M	0.0745	3.1931	b.d	15.6667	77.4359	b.d	50.9653	58.0169	47.2050	38.1616	28.0952	14.1975	20.5742	19.8758
NMC47	NMC47 - 31	IC	Sl	D	0.0032	3.0198	b.d	b.d	65.1282	b.d	39.3822	56.1181	49.0683	65.4596	77.6190	78.3951	92.8230	114.2857

Table D.8: LASS ICP-MS chondrite-normalised REE data for zircon (ppm) – IC machine settings for rim analyses. Sample NMC47.

sample ID	spot	instrument settings	CL	group	La	Ce	Pr	Nd	Sm	Eu	Gd	Tb	Dy	Ho	Er	Tm	Yb	Lu
NMC47	NMC47 - 1	IC	Sh	M	b.d	5.02	8.52	13.67	67.69	27.76	122.39	236.29	385.09	657.38	947.62	1320.99	1875.60	2844.72
NMC47	NMC47 - 2	IC	Sl	M	0.06	2.90	b.d	b.d	49.23	b.d	61.00	99.58	77.02	79.53	75.24	73.15	65.55	72.67
NMC47	NMC47 - 3	IC	Sh	M	0.06	3.86	b.d	b.d	31.79	b.d	43.63	59.07	54.66	49.86	39.52	28.40	30.14	31.37
NMC47	NMC47 - 4	IC	Sh	M	0.05	3.28	b.d	7.83	29.74	b.d	40.54	62.87	46.27	37.33	32.38	23.46	26.79	21.12
NMC47	NMC47 - 5	IC	Sh	D	b.d	143.56	598.36	570.00	338.46	170.07	202.32	259.49	257.76	288.30	262.38	296.30	258.37	319.88
NMC47	NMC47 - 6	IC	Sh	M	b.d	4.07	b.d	9.33	31.79	b.d	69.11	53.38	42.24	45.68	29.05	19.75	21.05	32.61
NMC47	NMC47 - 7	IC	Sl	M	b.d	2.85	6.39	22.00	48.21	8.44	99.23	146.41	136.96	115.60	114.76	107.72	107.66	115.22
NMC47	NMC47 - 8	IC	Sh	M	b.d	6.06	19.92	17.67	52.31	1.77	77.99	87.76	54.04	38.16	30.48	31.17	27.27	28.88
NMC47	NMC47 - 9	IC	Sl	M	0.01	3.08	b.d	b.d	42.56	b.d	49.42	64.77	60.87	49.16	49.05	44.75	33.01	45.34
NMC47	NMC47 - 10	IC	Sh	M	b.d	3.22	b.d	12.50	68.72	4.49	75.29	100.21	109.63	99.03	95.71	76.54	81.82	75.47
NMC47	NMC47 - 11	IC	Cl	M?	b.d	4.31	b.d	21.33	57.44	b.d	94.59	98.10	107.76	115.74	94.76	102.78	118.66	114.6
NMC47	NMC47 - 12	IC	Sh	M	b.d	18.81	36.07	43.83	84.10	10.34	73.36	93.04	82.92	50.42	50.48	25.93	29.67	27.02
NMC47	NMC47 - 13	IC	Sh	M	b.d	6.31	19.67	30.00	49.74	15.78	69.50	103.16	79.19	85.38	90.95	79.63	84.21	77.95
NMC47	NMC47 - 14	IC	Sh	D	b.d	235.15	565.57	508.33	266.67	190.48	173.75	183.54	214.29	247.91	233.33	256.17	258.37	257.76
NMC47	NMC47 - 15	IC	Sh	M	b.d	5.82	16.80	16.00	61.54	b.d	49.42	79.96	57.45	63.23	56.67	65.43	49.76	60.87
NMC47	NMC47 - 16	IC	Sh	M	0.04	2.24	b.d	7.33	42.05	b.d	39.38	51.48	35.40	27.58	24.76	11.73	11.00	19.25
NMC47	NMC47 - 17	IC	Cl	M?	0.04	3.11	b.d	14.50	30.26	b.d	35.91	53.59	49.07	36.91	31.29	25.00	14.83	33.85
NMC47	NMC47 - 18	IC	Sh	M	0.02	1.10	b.d	b.d	45.64	b.d	74.13	100.63	87.89	88.30	92.38	71.30	87.56	84.47
NMC47	NMC47 - 19	IC	Sh	M	0.04	3.39	b.d	6.50	58.97	b.d	72.97	71.10	77.02	84.12	91.90	74.38	66.51	68.63
NMC47	NMC47 - 20	IC	Sh	M	b.d	19.55	30.33	10.50	37.95	11.43	79.92	160.34	229.81	394.15	557.14	854.94	1306.22	1965.84
NMC47	NMC47 - 21	IC	Sh	M	0.07	1.83	b.d	b.d	19.49	b.d	39.77	76.37	77.02	111.42	167.14	219.14	296.65	543.48
NMC47	NMC47 - 22	IC	Sh	M	0.00	3.97	b.d	b.d	24.62	b.d	45.95	63.92	59.01	71.31	71.43	59.26	61.72	74.22
NMC47	NMC47 - 23	IC	Sl	M	b.d	4.29	b.d	b.d	48.72	b.d	49.03	76.58	59.01	57.24	52.86	30.25	38.28	54.04
NMC47	NMC47 - 24	IC	Sh	M	0.00	1.25	b.d	b.d	24.10	b.d	40.15	58.65	63.98	66.02	75.71	98.77	135.41	204.97
NMC47	NMC47 - 25	IC	Sh	M	0.02	1.24	4.75	b.d	34.87	b.d	35.52	70.89	58.70	64.62	56.67	61.73	65.07	59.01
NMC47	NMC47 - 26	IC	Cl	M?	b.d	3.23	b.d	13.17	58.46	b.d	40.15	55.06	63.04	43.45	38.10	16.67	25.84	26.09
NMC47	NMC47 - 27	IC	Sh	D	b.d	1.41	b.d	b.d	33.85	b.d	67.57	119.83	120.19	112.81	100.48	90.12	103.35	119.57
NMC47	NMC47 - 28	IC	CL	M?	0.01	3.54	8.85	16.50	74.87	b.d	84.56	100.84	80.43	68.25	57.62	43.21	44.98	54.35
NMC47	NMC47 - 29	IC	Sl	M	b.d	1.26	6.39	b.d	37.95	b.d	61.78	95.36	84.47	93.87	106.19	87.65	114.35	112.11
NMC47	NMC47 - 30	IC	Sl	M	0.07	3.19	b.d	15.67	77.44	b.d	50.97	58.02	47.21	38.16	28.10	14.20	20.57	19.88
NMC47	NMC47 - 31	IC	Sl	D	0.00	3.02	b.d	b.d	65.13	b.d	39.38	56.12	49.07	65.46	77.62	78.40	92.82	114.29

Table D.9: LASS ICP-MS chondrite-normalised REE data for monazite (ppm). Sample NMC47.

sample ID	spot	location	La	Ce	Pr	Nd	Sm	Eu	Gd	Tb	Dy	Ho	Er	Tm	Yb	Lu
NMC47	NMC47 - 1	core	336129.03	n/a	252459.02	190000.00	118461.54	2802.72	39806.95	10337.55	3198.76	523.68	233.33	b.d	b.d	b.d
NMC47	NMC47 - 3	core	337741.94	n/a	222131.15	173333.33	109230.77	3374.15	34980.70	9578.06	2568.32	317.55	200.00	b.d	b.d	b.d
NMC47	NMC47 - 6	core	352580.65	n/a	263934.43	180166.67	118974.36	3782.31	43822.39	11455.70	3881.99	644.85	319.05	b.d	b.d	b.d
NMC47	NMC47 - 7	core	348064.52	n/a	250000.00	208333.33	102051.28	4149.66	27451.74	7278.48	2763.98	662.95	466.67	b.d	b.d	b.d
NMC47	NMC47 - 9	core	318064.52	n/a	231147.54	187000.00	113333.33	3605.44	40115.83	11518.99	3478.26	623.96	261.90	b.d	b.d	b.d
NMC47	NMC47 - 16	core	338387.10	n/a	235245.90	187666.67	100000.00	3088.44	29613.90	7257.38	1543.48	161.56	147.62	b.d	b.d	b.d
NMC47	NMC47 - 19	core	343225.81	n/a	229508.20	196666.67	104102.56	2448.98	31737.45	6898.73	2037.27	369.08	123.81	b.d	b.d	b.d
NMC47	NMC47 - 22	core	310967.74	n/a	222131.15	182500.00	99487.18	3687.07	39189.19	10042.19	2888.20	500.00	319.05	b.d	b.d	b.d
NMC47	NMC47 - 23	core	297096.77	n/a	224590.16	196666.67	92307.69	3809.52	25907.34	5949.37	1773.29	325.91	180.95	b.d	b.d	b.d
NMC47	NMC47 - 27	core	330967.74	n/a	244262.30	191666.67	101538.46	2897.96	33783.78	8016.88	2049.69	190.81	b.d	b.d	b.d	b.d
NMC47	NMC47 - 28	core	384193.55	n/a	250819.67	182833.33	114358.97	3006.80	44054.05	11624.47	3198.76	366.30	233.33	b.d	b.d	b.d
NMC47	NMC47 - 30	core	344193.55	n/a	255737.70	190000.00	120512.82	3646.26	43088.80	11497.89	3167.70	530.64	214.29	b.d	b.d	b.d
NMC47	NMC47 - 31	core	333870.97	n/a	240163.93	196666.67	102051.28	3482.99	34131.27	7341.77	1885.09	291.09	219.05	b.d	b.d	b.d
NMC47	NMC47 - 33	core	304838.71	n/a	248360.66	196666.67	94871.79	2993.20	20154.44	4915.61	1295.03	199.16	b.d	b.d	b.d	b.d
NMC47	NMC47 - 34	core	354838.71	n/a	252459.02	178166.67	107179.49	2789.12	33745.17	7025.32	1993.79	275.77	85.71	b.d	b.d	b.d
NMC47	NMC47 - 35	core	309354.84	n/a	216393.44	191500.00	75384.62	2598.64	17104.25	3396.62	1248.45	103.06	76.19	b.d	b.d	b.d
NMC47	NMC47 - 36	core	309677.42	n/a	243442.62	203333.33	73333.33	2176.87	17528.96	3945.15	1167.70	114.21	84.29	b.d	b.d	b.d
NMC47	NMC47 - 37	core	337741.94	n/a	223770.49	183500.00	98461.54	4721.09	30193.05	6645.57	1658.39	133.70	123.81	b.d	b.d	b.d
NMC47	NMC47 - 38	core	303870.97	n/a	232786.89	198333.33	83076.92	2530.61	16293.44	4135.02	1198.76	224.23	157.14	b.d	b.d	b.d
NMC47	NMC47 - 39	core	344193.55	n/a	232786.89	183000.00	92307.69	3346.94	30386.10	6455.70	1518.63	155.99	59.52	b.d	b.d	b.d
NMC47	NMC47 - 40	core	341290.32	n/a	225409.84	177333.33	98461.54	2721.09	26023.17	4641.35	959.63	114.21	44.76	b.d	b.d	b.d
NMC47	NMC47 - 41	core	323548.39	n/a	235245.90	195500.00	82564.10	2625.85	22664.09	4303.80	1285.71	169.92	b.d	b.d	b.d	b.d
NMC47	NMC47 - 44	core	325161.29	n/a	212295.08	165000.00	101538.46	2380.95	51351.35	22995.78	12701.86	2869.08	2371.43	1012.35	111.48	869.57
NMC47	NMC47 - 46	core	371290.32	n/a	263114.75	188333.33	118461.54	3102.04	45057.92	11624.47	3090.06	474.93	123.81	b.d	b.d	b.d
NMC47	NMC47 - 48	core	310000.00	n/a	235245.90	193333.33	94358.97	3088.44	27490.35	7257.38	2484.47	431.75	247.62	104.94	12.92	b.d
NMC47	NMC47 - 52	core	314516.13	n/a	224590.16	196666.67	90256.41	4448.98	23320.46	5084.39	1540.37	207.52	114.29	b.d	b.d	b.d
NMC47	NMC47 - 53	core	367741.94	n/a	229508.20	191666.67	101538.46	2517.01	30926.64	7489.45	1872.67	214.48	128.57	b.d	b.d	b.d
NMC47	NMC47 - 54	core	281935.48	n/a	247540.98	192666.67	87692.31	3387.76	20000.00	5696.20	2267.08	565.46	528.57	b.d	33.97	b.d
NMC47	NMC47 - 55	core	335483.87	n/a	242622.95	192166.67	98974.36	3700.68	31544.40	6054.85	1456.52	164.35	84.29	b.d	b.d	b.d
NMC47	NMC47 - 58	core	375161.29	n/a	232786.89	172500.00	109230.77	3727.89	40193.05	12616.03	4440.99	1016.71	695.24	271.60	b.d	b.d
NMC47	NMC47 - 59	core	341290.32	n/a	230327.87	177333.33	94358.97	3755.10	30810.81	6793.25	2000.00	213.09	b.d	b.d	b.d	b.d
NMC47	NMC47 - 60	core	273548.39	n/a	236885.25	203500.00	90256.41	2571.43	19189.19	5168.78	1583.85	221.45	171.43	b.d	b.d	b.d
NMC47	NMC47 - 2	rim	330645.16	n/a	243442.62	189000.00	121025.64	4680.27	39382.24	9767.93	3509.32	472.14	219.05	b.d	b.d	b.d
NMC47	NMC47 - 4	rim	360967.74	n/a	251639.34	190000.00	127179.49	3768.71	51428.57	15738.40	6925.47	1490.25	1080.95	132.72	55.50	b.d
NMC47	NMC47 - 5	rim	330322.58	n/a	259016.39	208333.33	86666.67	2911.56	22123.55	6223.63	2350.93	481.89	295.24	b.d	b.d	b.d
NMC47	NMC47 - 8	rim	364838.71	n/a	236885.25	193500.00	101025.64	4217.69	36486.49	8101.27	2841.61	526.46	147.62	b.d	b.d	b.d
NMC47	NMC47 - 10	rim	387096.77	n/a	253278.69	208833.33	108717.95	2489.80	32471.04	7341.77	1916.15	179.67	171.43	b.d	b.d	b.d
NMC47	NMC47 - 11	rim	360967.74	n/a	240983.61	179000.00	103076.92	2734.69	34054.05	7700.42	2360.25	391.36	223.81	83.33	b.d	b.d
NMC47	NMC47 - 12	rim	315161.29	n/a	245081.97	200000.00	104102.56	3374.15	30270.27	7447.26	2639.75	497.21	342.86	77.16	b.d	b.d
NMC47	NMC47 - 13	rim	332903.23	n/a	229508.20	168333.33	109743.59	3510.20	38185.33	8164.56	2170.81	225.63	142.86	b.d	b.d	b.d
NMC47	NMC47 - 14	rim	313870.97	n/a	240983.61	181166.67	86666.67	3374.15	22162.16	4936.71	1217.39	183.84	123.81	b.d	b.d	b.d
NMC47	NMC47 - 15	rim	339354.84	n/a	243442.62	181666.67	87692.31	3523.81	31081.08	6962.03	1596.27	229.81	66.67	b.d	b.d	b.d
NMC47	NMC47 - 17	rim	364516.13	n/a	281967.21	200000.00	115897.44	2748.30	42200.77	11392.41	3540.37	533.43	266.67	b.d	b.d	b.d
NMC47	NMC47 - 18	rim	325161.29	n/a	259016.39	206166.67	92820.51	3510.20	22393.82	4345.99	1114.91	121.17	b.d	b.d	b.d	b.d
NMC47	NMC47 - 20	rim	301290.32	n/a	233606.56	186666.67	111282.05	4312.93	36795.37	9219.41	3416.15	612.81	409.52	70.99	b.d	b.d
NMC47	NMC47 - 21	rim	350000.00	n/a	264754.10	187166.67	116410.26	4843.54	38108.11	10105.49	3105.59	623.96	200.00	101.85	b.d	b.d
NMC47	NMC47 - 24	rim	320000.00	n/a	244262.30	205000.00	96410.26	2585.03	23899.61	6054.85	2291.93	399.72	304.76	89.51	b.d	b.d
NMC47	NMC47 - 25	rim	324838.71	n/a	215573.77	182166.67	91794.87	3061.22	30038.61	5421.94	1447.21	136.49	91.90	b.d	b.d	b.d
NMC47	NMC47 - 26	rim	310967.74	n/a	250819.67	208333.33	93846.15	3877.55	21119.69	4303.80	1559.01	197.77	114.29	b.d	b.d	b.d
NMC47	NMC47 - 29	rim	302258.06	n/a	259016.39	198500.00	94358.97	2829.93	18880.31	4556.96	1515.53	203.34	b.d	b.d	b.d	b.d
NMC47	NMC47 - 32	rim	309677.42	n/a	255737.70	186666.67	100512.82	3510.20	23783.78	5443.04	2015.53	387.19	247.62	b.d	22.97	b.d
NMC47	NMC47 - 42	rim	343548.39	n/a	241803.28	184833.33	100512.82	4748.30	39420.85	9578.06	2888.20	502.79	323.81	b.d	b.d	b.d
NMC47	NMC47 - 43	rim	300967.74	n/a	228688.52	211666.67	94871.79	3510.20	26640.93	7911.39	2950.31	717.27	480.95	95.68	b.d	b.d
NMC47	NMC47 - 45	rim	330000.00	n/a	213934.43	181166.67	98461.54	2054.42	34401.54	8248.95	1953.42	254.87	171.43	b.d	b.d	b.d
NMC47	NMC47 - 47	rim	301290.32	n/a	236885.25	172500.00	89230.77	2938.78	27490.35	7805.91	1965.84	448.47	166.67	b.d	b.d	b.d
NMC47	NMC47 - 49	rim	326129.03	n/a	230327.87	172500.00	85641.03	3129.25	25637.07	5886.08	2173.91	431.75	171.43	64.81	b.d	b.d
NMC47	NMC47 - 50	rim	313870.97	n/a	230327.87	195000.00	96923.08	3224.49	30270.27	7426.16	2670.81	488.86	214.29	70.99	b.d	b.d
NMC47	NMC47 - 51	rim	299677.42	n/a	247540.98	200000.00	88205.13	2857.14	20193.05	4725.74	1450.31	165.74	104.76	b.d	b.d	b.d
NMC47	NMC47 - 56	rim	300645.16	n/a	227049.18	183333.33	102564.10	3795.92	30540.54	6814.35	1795.03	281.34	109.52	b.d	b.d	b.d
NMC47	NMC47 - 57	rim	345161.29	n/a	224590.16	168333.33	86666.67	3659.86	29652.51	7805.91	2034.16	225.63	72.86	b.d	b.d	b.d

Table D.10: LASS ICP-MS U–Pb isotopic data for zircon – IC machine settings for rim analyses. Sample NMC37.

sample ID	spot	instrument settings	CL	group	comment	$^{238}U/^{206}Pb$	2σ	$^{207}Pb/^{206}Pb$	2σ	$^{206}Pb/^{238}U$ Age (Ma)	2σ	$^{207}Pb/^{206}Pb$ Age (Ma)	2σ	7/6 discordance (%)	6/8 discordance (%)	U (ppm)	Pb (ppm)
NMC37	NMC37 - 1	IC	S	M	rounded soccer ball	5.819028	0.1286721	0.07352	0.00082	1022.3	21	1027	22	0.46	-0.46	n/a	n/a
NMC37	NMC37 - 2	IC	S	M	rounded soccer ball	5.959476	0.1633706	0.07344	0.00078	1000	25	1025	22	2.44	-2.50	n/a	n/a
NMC37	NMC37 - 3	IC	S	M	rounded soccer ball	5.824112	0.1322891	0.0736	0.00085	1021.4	21	1029	24	0.74	-0.74	n/a	n/a
NMC37	NMC37 - 4	IC	S	M	rounded soccer ball	5.760037	0.1293943	0.07308	0.00079	1032	21	1015.1	22	-1.66	1.64	n/a	n/a
NMC37	NMC37 - 5	IC	S	M	rounded soccer ball	5.81869	0.1320429	0.07359	0.00076	1022.3	21	1029.1	21	0.66	-0.67	n/a	n/a
NMC37	NMC37 - 6	IC	S	M	rounded soccer ball	5.899705	0.1392261	0.0745	0.00077	1009.2	22	1054.1	21	4.26	-4.45	n/a	n/a
NMC37	NMC37 - 7	IC	S	M	rounded soccer ball	6.150062	0.1702047	0.0732	0.00083	971	25	1018	23	4.62	-4.84	n/a	n/a
NMC37	NMC37 - 8	IC	S	M	rounded soccer ball	6.176652	0.1602343	0.07381	0.0008	967	23	1035.1	22	6.58	-7.04	n/a	n/a
NMC37	NMC37 - 9	IC	S	D	rounded soccer ball	6.565988	0.1508927	0.07385	0.0008	913.7	20	1036.3	22	11.83	-13.42	n/a	n/a
NMC37	NMC37 - 10	IC	S	M	rounded soccer ball	5.896226	0.146015	0.07368	0.00081	1010	23	1032	22	2.13	-2.18	n/a	n/a
NMC37	NMC37 - 11	IC	S	M	rounded soccer ball	5.871991	0.1379211	0.07365	0.00076	1013.5	22	1030.9	21	1.69	-1.72	n/a	n/a
NMC37	NMC37 - 12	IC	S	D	rounded soccer ball	6.067961	0.1804187	0.07585	0.00084	983	27	1090	22	9.82	-10.89	n/a	n/a
NMC37	NMC37 - 13	IC	S	M	rounded soccer ball	6.02047	0.1413596	0.07355	0.00084	990.5	22	1028	23	3.65	-3.79	n/a	n/a
NMC37	NMC37 - 14	IC	S	M	rounded soccer ball	6.060606	0.15427	0.07437	0.00082	985	23	1051	22	6.28	-6.70	n/a	n/a
NMC37	NMC37 - 15	IC	S	M	rounded soccer ball	6.071645	0.151146	0.07365	0.00087	983	23	1034	23	4.93	-5.19	n/a	n/a
NMC37	NMC37 - 16	IC	S	M	rounded soccer ball	5.818351	0.1320275	0.07393	0.00079	1022.4	21	1038.5	21	1.55	-1.57	n/a	n/a
NMC37	NMC37 - 17	IC	S	M	rounded soccer ball	5.425936	0.1236513	0.07415	0.0008	1090.2	23	1044.6	22	-4.37	4.18	n/a	n/a
NMC37	NMC37 - 18	IC	S	M	rounded soccer ball	5.717553	0.1307616	0.07419	0.00079	1039	22	1045.5	21	0.62	-0.63	n/a	n/a
NMC37	NMC37 - 19	IC	S	M	rounded soccer ball	6.067961	0.1435986	0.07376	0.00078	983.4	22	1035.8	23	5.06	-5.33	n/a	n/a
NMC37	NMC37 - 20	IC	S	M	rounded soccer ball	6.112469	0.1569216	0.07433	0.00087	977	23	1049	23	6.86	-7.37	n/a	n/a
NMC37	NMC37 - 21	IC	S	M	rounded soccer ball	5.724098	0.1310612	0.07361	0.00075	1037.8	22	1029.9	21	-0.77	0.76	n/a	n/a
NMC37	NMC37 - 22	IC	S	M	rounded soccer ball	5.704507	0.1334197	0.07389	0.0008	1041.4	22	1037.4	22	-0.39	0.38	n/a	n/a
NMC37	NMC37 - 23	IC	S	M	rounded soccer ball	5.611672	0.1259635	0.07374	0.0008	1057.2	22	1033	22	-2.34	2.29	n/a	n/a
NMC37	NMC37 - 24	IC	S	M	rounded soccer ball	5.655789	0.1279518	0.073	0.00078	1049.5	22	1012.9	22	-3.61	3.49	n/a	n/a
NMC37	NMC37 - 25	IC	S	M	rounded soccer ball	5.539552	0.1227466	0.07285	0.00085	1069.8	22	1009	24	-6.03	5.68	n/a	n/a
NMC37	NMC37 - 26	IC	S	M	rounded soccer ball	5.562973	0.1237867	0.07277	0.00076	1065.6	22	1006.4	21	-5.88	5.56	n/a	n/a
NMC37	NMC37 - 27	IC	S	M	rounded soccer ball	5.592216	0.1250915	0.07402	0.00077	1060.5	22	1040.9	21	-1.88	1.85	n/a	n/a
NMC37	NMC37 - 28	IC	S	M	rounded soccer ball	5.614823	0.1324102	0.07386	0.0008	1056.4	23	1036.6	22	-1.91	1.87	n/a	n/a
NMC37	NMC37 - 29	IC	S	M	rounded soccer ball	5.649718	0.1308692	0.07363	0.0008	1050.5	22	1030	22	-1.99	1.95	n/a	n/a
NMC37	NMC37 - 30	IC	S	M	rounded soccer ball	5.622084	0.1264313	0.07336	0.00077	1055.3	22	1022.9	21	-3.17	3.07	n/a	n/a

Table D.11: LASS ICP-MS chondrite-normalised REE data for zircon – IC machine settings for rim analyses. Sample NMC37.

sample ID	spot	instrument settings	CL	group	La	Ce	Pr	Nd	Sm	Eu	Gd	Tb	Dy	Ho	Er	Tm	Yb	Lu
NMC37	NMC37 - 1	IC	S	M	0.10	6.73	b.d	b.d	b.d	2.31	74.52	123.63	129.19	143.45	145.24	147.84	132.06	204.97
NMC37	NMC37 - 2	IC	S	M	0.08	5.20	b.d	b.d	b.d	11.16	54.83	118.14	156.52	143.45	129.05	146.91	139.71	181.68
NMC37	NMC37 - 3	IC	S	M	0.05	6.41	b.d	5.00	27.18	b.d	70.66	115.82	153.11	168.52	180.95	176.23	179.90	214.29
NMC37	NMC37 - 4	IC	S	M	0.04	7.43	b.d	b.d	34.36	14.83	79.54	134.60	151.55	137.05	143.33	129.63	122.97	113.04
NMC37	NMC37 - 5	IC	S	M	b.d	1.75	b.d	b.d	b.d	4.22	47.88	160.34	349.38	704.74	1261.90	2287.04	3669.86	5295.03
NMC37	NMC37 - 6	IC	S	M	0.02	1.92	b.d	b.d	5.64	14.69	32.43	151.90	315.22	683.84	1195.24	2123.46	3784.69	5279.50
NMC37	NMC37 - 7	IC	S	M	0.06	5.14	b.d	b.d	34.87	11.56	88.42	135.44	190.06	175.49	176.19	169.75	201.91	260.87
NMC37	NMC37 - 8	IC	S	M	0.08	6.30	b.d	b.d	39.49	17.55	88.03	172.36	249.07	346.80	503.33	669.75	937.80	1316.77
NMC37	NMC37 - 10	IC	S	M	0.06	3.35	b.d	b.d	b.d	7.48	43.63	140.72	357.45	611.42	1193.81	1907.41	3253.59	4608.70
NMC37	NMC37 - 11	IC	S	M	b.d	7.67	b.d	b.d	29.23	b.d	64.09	157.38	235.09	370.47	619.05	808.64	1153.11	1639.75
NMC37	NMC37 - 12	IC	S	M	b.d	3.82	b.d	b.d	b.d	50.34	74.90	162.45	306.83	523.68	952.86	1496.91	2143.54	3130.43
NMC37	NMC37 - 13	IC	S	M	b.d	1.99	b.d	b.d	9.74	8.16	42.47	175.11	369.57	735.38	1390.48	2441.36	4004.78	5677.02
NMC37	NMC37 - 14	IC	S	M	b.d	8.04	7.05	b.d	22.56	b.d	94.98	151.90	281.06	484.68	742.86	1033.95	1521.53	2204.97
NMC37	NMC37 - 15	IC	S	M	0.06	7.08	b.d	b.d	32.31	10.07	74.90	137.76	144.41	168.52	163.33	128.09	162.20	204.97
NMC37	NMC37 - 16	IC	S	M	0.06	2.18	b.d	b.d	b.d	b.d	57.53	149.58	374.53	750.70	1409.52	2283.95	3684.21	5186.34
NMC37	NMC37 - 17	IC	S	M	b.d	1.06	b.d	b.d	b.d	b.d	35.52	127.85	265.53	491.64	980.95	1611.11	2846.89	4236.02
NMC37	NMC37 - 18	IC	S	M	0.02	1.77	b.d	b.d	b.d	b.d	35.91	133.12	271.74	587.74	1114.29	1756.17	3047.85	4475.16
NMC37	NMC37 - 19	IC	S	M	b.d	5.45	b.d	b.d	25.13	b.d	81.08	135.02	149.69	162.67	184.76	141.67	145.93	145.96
NMC37	NMC37 - 20	IC	S	M	0.07	6.81	b.d	b.d	33.33	14.56	66.41	103.80	110.25	127.72	119.05	150.93	139.71	203.11
NMC37	NMC37 - 21	IC	S	M	0.04	3.43	b.d	2.33	21.03	23.40	80.31	225.74	561.18	1076.60	2080.95	3246.91	5220.10	7155.28
NMC37	NMC37 - 22	IC	S	M	0.06	3.26	b.d	b.d	10.26	11.29	58.69	202.53	499.38	976.32	1895.24	2904.32	4535.89	6055.90
NMC37	NMC37 - 23	IC	S	M	0.03	2.01	b.d	b.d	b.d	b.d	45.17	189.87	373.91	798.05	1595.24	2549.38	4511.96	6332.30
NMC37	NMC37 - 24	IC	S	M	0.01	6.00	b.d	0.78	30.26	6.53	65.64	120.68	132.92	143.45	142.38	110.49	123.45	119.88
NMC37	NMC37 - 25	IC	S	M	0.07	5.12	b.d	b.d	29.74	b.d	60.23	104.43	133.54	147.63	144.76	120.99	119.62	105.59
NMC37	NMC37 - 26	IC	S	M	b.d	6.34	b.d	b.d	13.85	b.d	58.30	166.67	310.25	572.42	995.24	1339.51	2004.78	2593.17
NMC37	NMC37 - 27	IC	S	M	0.05	4.23	b.d	b.d	29.74	13.33	79.54	155.70	241.93	302.23	470.95	540.43	875.60	1130.43
NMC37	NMC37 - 28	IC	S	M	0.05	4.38	b.d	b.d	34.36	b.d	64.48	136.50	223.29	356.55	626.19	848.77	1440.19	2034.16
NMC37	NMC37 - 29	IC	S	M	0.05	4.47	b.d	b.d	29.23	b.d	96.14	166.67	181.37	193.59	182.38	146.30	164.11	117.39
NMC37	NMC37 - 30	IC	S	M	0.03	8.66	b.d	b.d	b.d	2.86	75.29	133.12	169.25	232.59	354.29	380.56	569.38	807.45

Table D.12: LASS ICP-MS U–Pb isotopic data for zircon – IC machine settings for rim analyses, FC machine settings for core analyses. Sample NMC100.

sample ID	spot	instrument settings	CL	group	comment	$^{238}U/^{206}Pb$	2σ	$^{207}Pb/^{206}Pb$	2σ	$^{206}Pb/^{238}U$ Age (Ma)	2σ	$^{207}Pb/^{206}Pb$ Age (Ma)	2σ	7/6 discordance (%)	6/8 discordance (%)	U (ppm)	Pb (ppm)
NMC100c	1	FC	Oh	S	oscillatory fragment as core in ovoidal grain, faint sector zoned rim	3.06560	0.03383	0.10980	0.00780	1819.9	17	1798	120	-1.22	1.20	209.8	2163
NMC100	1	IC		D	oscillatory zoned fragment, discordant and disregarded	4.84966	0.11289	0.08770	0.00130	1208.6	25	1375	29	12.10	-13.77	n/a	n/a
NMC100	2	IC	Oi	P	oscillatory zoned grain, ovoidal grain	3.48189	0.07759	0.10452	0.00100	1627.7	32	1705	19	4.53	-4.75	n/a	n/a
NMC100c	3	FC	Cb	S	bright core, convoluted/oscillatory, hypidioblastic grain	3.21750	0.06625	0.11000	0.00790	1744	31	1797	130	2.95	-3.04	168.1	591
NMC100	3	IC		D	oscillatory zoned fragment, discordant and disregarded	4.82859	0.20051	0.09060	0.00230	1212	46	1433	50	15.42	-18.23	n/a	n/a
NMC100	4	IC		D	oscillatory zoned fragment, discordant and disregarded	5.09944	0.13782	0.08790	0.00270	1154	29	1373	60	15.95	-18.98	n/a	n/a
NMC100c	4	FC		D	thin rim on oscillatory zoned fragment, discordant and disregarded (mixed ages?)	7.63359	1.22371	0.09930	0.00800	780	120	1598	150	51.19	-104.87	900	2305
NMC100c	5	FC	Oi	S	hypidioblastic detrital grain, oscillatory zoned, concordant	3.22893	0.06151	0.10550	0.00800	1739	29	1742	160	0.17	-0.17	77	610
NMC100	5	IC		D	thin rim on oscillatory zoned fragment, discordant and disregarded (mixed ages?)	5.76369	0.13620	0.09550	0.00190	1031.5	22	1535	38	32.80	-48.81	n/a	n/a
NMC100c	6	FC		D	oscillatory zoned fragment, discordant and disregarded	4.73934	0.16621	0.08990	0.00660	1233	39	1418	140	13.05	-15.00	728	1.01E+04
NMC100	7	IC	Ri	S	CL-low convoluted rim	3.21647	0.07242	0.10313	0.00110	1744.9	34	1680.3	19	-3.84	3.70	n/a	n/a
NMC100c	7	FC		D	oscillatory zoned fragment, discordant and disregarded	4.60193	0.05506	0.08740	0.00620	1267.5	14	1367	140	7.28	-7.85	399	937
NMC100	8	IC	Oi	P	oscillatory grain surrounded by faint rim (core spot 11)	4.06504	0.11237	0.09558	0.00110	1418	35	1538	22	7.80	-8.46	n/a	n/a
NMC100c	8	FC	Cl	S	hypidioblastic grain, convoluted/oscillatory zoning, concordant	3.40716	0.03715	0.10145	0.00710	1658.8	16	1650	130	-0.53	0.53	465	1630
NMC100	9	IC	Oi	P	oscillatory zoned grain, ovoidal grain	4.76281	0.10662	0.08365	0.00090	1228.6	25	1283.4	21	4.27	-4.46	n/a	n/a
NMC100c	9	FC	Oi	S	hypidioblastic detrital grain, oscillatory zoned, rim on spot 5	5.00501	0.05261	0.08066	0.00570	1174.3	11	1211	140	3.03	-3.13	488.3	986
NMC100	10	IC	Oi	S	oscillatory rim	4.62727	0.10278	0.08389	0.00084	1261.3	25	1289.2	19	2.16	-2.21	n/a	n/a
NMC100c	10	FC		D	oscillatory zoned fragment, discordant and disregarded	3.48189	0.05334	0.13800	0.01600	1627	22	2150	190	24.33	-32.15	293	5.80E+03
NMC100c	11	FC	Oi	P	faint oscillatory fragment as core in ovoidal grain, faint sector zoned rim	3.63372	0.05150	0.10171	0.00710	1567	20	1654	130	5.26	-5.55	419	2505
NMC100	11	IC	Oi	S	hypidioblastic oscillatory zoned grain	4.34216	0.09804	0.08820	0.00140	1336.2	27	1385	30	3.52	-3.65	n/a	n/a
NMC100c	12	FC	Oh	S	oscillatory fragment as core in ovoidal grain, faint sector zoned rim	4.68604	0.06807	0.08170	0.00600	1247	17	1234	150	-1.05	1.04	254.9	1170
NMC100	12	IC		D	oscillatory zoned fragment, discordant and disregarded	4.04204	0.15194	0.10410	0.00260	1424	48	1695	45	15.99	-19.03	n/a	n/a
NMC100	13	IC	Oi	P	elongated faint oscillatory grain	4.00641	0.09470	0.09731	0.00099	1436	30	1572.3	19	8.67	-9.49	n/a	n/a
NMC100c	13	FC		D	thin rim on oscillatory zoned fragment, discordant and disregarded (mixed ages?)	10.20501	0.58350	0.10430	0.00760	592	31	1699	140	65.16	-186.99	940	2090
NMC100	14	IC		D	thin rim on oscillatory zoned fragment, discordant and disregarded (mixed ages?)	5.99161	0.21181	0.07946	0.00090	1002	37	1183	22	15.30	-18.06	n/a	n/a
NMC100c	14	FC		D	thin rim on oscillatory zoned fragment, discordant and disregarded (mixed ages?)	6.32911	0.60087	0.08120	0.00640	941	81	1214	150	22.49	-29.01	438	1204
NMC100c	15	FC	Ch	S	elongated grain with bright core	3.24675	0.07695	0.10350	0.00730	1730	36	1686	130	-2.61	2.54	368	1222
NMC100	15	IC		D	oscillatory zoned fragment, discordant and disregarded	5.98444	0.15758	0.07664	0.00100	996	24	1115	29	10.67	-11.95	n/a	n/a
NMC100c	16	FC	Ch	S	bright oscillatory fragment as core in ovoidal grain, faint sector zoned rim	4.62749	0.05139	0.08440	0.00610	1261.2	13	1298	140	2.84	-2.92	327	1360
NMC100	16	IC	Oi	S	oscillatory zoned grain, ovoidal grain	4.78469	0.25183	0.08373	0.00120	1222	61	1285	28	4.90	-5.16	n/a	n/a
NMC100c	17	FC	Oi	S	oscillatory fragment as core in ovoidal grain, faint sector zoned rim	3.69686	0.11070	0.09660	0.00690	1542	41	1556	130	0.90	-0.91	231	888
NMC100	17	IC		D	thin rim on oscillatory zoned fragment, discordant and disregarded (mixed ages?)	5.48847	0.21990	0.08260	0.00160	1078	40	1257	38	14.24	-16.60	n/a	n/a
NMC100c	18	FC	Ch	P	bright core, convoluted/oscillatory, hypidioblastic grain	3.85654	0.03867	0.09730	0.00700	1486.2	13	1569	130	5.28	-5.57	182.9	999
NMC100	18	IC	Sh	S	large rounded grain, sector zoned (LNS aged?)	4.40723	0.10295	0.08374	0.00091	1318.4	28	1285.5	21	-2.56	2.50	n/a	n/a
NMC100	19	IC	Ch	S	bright core in hypidioblastic grain, concordant	3.01205	0.06714	0.11386	0.00120	1848	36	1861.1	18	0.70	-0.71	n/a	n/a
NMC100c	19	FC		D	oscillatory zoned fragment, discordant and disregarded	4.48431	0.05228	0.09560	0.00810	1297.5	14	1520	160	14.64	-17.15	264	1026
NMC100c	20	FC	Oi	S	oscillatory fragment as core in ovoidal grain, faint sector zoned rim	4.43597	0.04132	0.08610	0.00660	1310.5	11	1331	150	1.54	-1.56	183.8	979
NMC100	20	IC		D	oscillatory zoned fragment, discordant and disregarded	5.39665	0.18639	0.08120	0.00150	1095	35	1224	37	10.54	-11.78	n/a	n/a
NMC100	21	IC	Ri	P	faint convoluted rim on cracked and healed hypidioblastic core (spot 66)	5.32765	0.13057	0.07984	0.00088	1109	25	1192	22	6.96	-7.48	n/a	n/a
NMC100c	21	FC	Ch	S	CL-bright core with faint sector zoned rim	3.43277	0.03299	0.10310	0.00740	1648.1	14	1691	130	2.54	-2.60	139.3	763
NMC100	22	IC	Ch	P	bright sector/convoluted zoning on core	3.74953	0.08998	0.10292	0.00120	1528	38	1676	21	8.83	-9.69	n/a	n/a
NMC100c	22	FC	Oi	S	CL-low oscillatory zoned elongated grain	3.22477	0.10087	0.10860	0.00790	1740	49	1772	130	1.81	-1.84	187	2.30E+03
NMC100	23	IC	Si	M	rounded, sector zoned, concordant meta age	5.67376	0.12555	0.07414	0.00073	1046.4	22	1044.4	20	-0.19	0.19	n/a	n/a
NMC100c	23	FC		D	oscillatory zoned fragment, discordant and disregarded	4.29923	0.05175	0.10450	0.00790	1348.1	15	1711	130	21.21	-26.92	156.9	549
NMC100c	24	FC	Oi	P	faint core, oscillatory, hypidioblastic grain	4.53927	0.04945	0.08770	0.00620	1283.6	13	1373	140	6.51	-6.96	446	3663
NMC100	24	IC	Ch	S	CL-bright, convoluted zoning pattern	4.46628	0.19948	0.08600	0.00260	1302	54	1331	60	2.18	-2.23	n/a	n/a
NMC100c	25	FC		D	oscillatory zoned fragment, discordant and disregarded	3.89712	0.09264	0.12130	0.00880	1472	31	1971	130	25.32	-33.90	386	1960
NMC100	25	IC		D	oscillatory zoned fragment, discordant and disregarded	5.34759	0.17158	0.10800	0.00330	1105	33	1760	60	37.22	-59.28	n/a	n/a
NMC100c	26	FC	Cl	P	faint core, convoluted/oscillatory, hypidioblastic grain	3.86250	0.05222	0.09730	0.00690	1484	18	1570	130	5.48	-5.80	298	1069
NMC100c	27	FC	Oh	S	oscillatory fragment as core in prismatic grain, faint convoluted zoned rim	3.05717	0.03178	0.10940	0.00820	1824.1	17	1793	130	-1.73	1.70	98.3	571
NMC100	27	IC	Oi	S	oscillatory rim on bright core, hypidioblastic elongated grain	5.18941	0.12657	0.07658	0.00087	1139	27	1109	23	-2.71	2.63	n/a	n/a
NMC100	28	IC	Oi	P	rim on hypidioblastic detrital grain that has a bright core (spot 43), oscillatory zoned	4.80307	0.12919	0.08281	0.00085	1219	30	1263.8	20	3.54	-3.68	n/a	n/a
NMC100c	28	FC	Ch	P	bright convoluted fragment as core in ovoidal grain, faint sector zoned rim	4.08330	0.05169	0.09460	0.00670	1412	16	1518	130	6.98	-7.51	328	977
NMC100c	29	FC	Ch	P	bright core, convoluted/oscillatory, hypidioblastic grain	3.45901	0.05384	0.10640	0.00810	1637	23	1731	140	5.43	-5.74	88	236
NMC100	29	IC	Ch	S	bright oscillatory zoned grain	4.36110	0.09890	0.08489	0.00086	1330.6	27	1312.1	20	-1.41	1.39	n/a	n/a
NMC100	30	IC	Ri	P	faint unzoned rim on hypidioblastic bright core (spot 41)	3.79939	0.08950	0.10055	0.00100	1506	32	1633.3	19	7.79	-8.45	n/a	n/a
NMC100c	30	FC		D	oscillatory zoned fragment, discordant and disregarded	3.34113	0.08484	0.09420	0.00740	1687	38	1503	150	-12.24	10.91	130.2	382
NMC100c	31	FC	Oi	S	CL-low oscillatory zoned grain	3.36022	0.04404	0.10467	0.00730	1679	19	1707	130	1.64	-1.67	410	1805
NMC100	31	IC		D	thin rim on oscillatory zoned fragment, discordant and disregarded (mixed ages?)	5.45703	0.12209	0.07224	0.00072	1084.7	22	991.7	20	-9.38	8.57	n/a	n/a
NMC100c	32	FC	Oh	S	oscillatory fragment as core in ovoidal grain, faint sector zoned rim	4.66418	0.06091	0.08240	0.00850	1252	15	1240	220	-0.97	0.96	84	389
NMC100	32	IC		D	thin rim on oscillatory zoned fragment, discordant and disregarded (mixed ages?)	6.15385	0.24615	0.08200	0.00180	970	36	1242	43	21.90	-28.04	n/a	n/a
NMC100	33	IC	Oi	P	CL-low oscillatory rim on bright core	5.31632	0.15827	0.08039	0.00081	1111	30	1205.7	20	7.85	-8.52	n/a	n/a
NMC100c	33	FC	Ch	S	bright core in oscillatory rim, hypidioblastic grain, outermost sector zoned rim	3.27225	0.03641	0.10830	0.00900	1719.1	17	1772	160	2.99	-3.08	61.1	441
NMC100c	34	FC	Oh	S	oscillatory fragment as core in ovoidal grain, faint sector zoned rim	4.66418	0.05221	0.08280	0.00640	1252.4	13	1274	170	1.70	-1.72	179	652
NMC100c	35	IC	Ch	P	bright convoluted fragment as core in ovoidal grain, faint oscillatory zoned rim	3.93546	0.09448	0.09723	0.00110	1460	31	1570	22	7.01	-7.53	n/a	n/a
NMC100c	35	FC		D	oscillatory zoned fragment, discordant and disregarded	4.64900	0.05836	0.09810	0.00720	1255.9	14	1584	140	20.71	-26.12	400	1052
NMC100	36	IC	Si	M	faint sector zoned rim on oscillatory zoned fragment	5.78035	0.13365	0.07437	0.00076	1028.8	22	1050.6	21	2.08	-2.12	n/a	n/a
NMC100c	36	FC	Oi	S	oscillatory fragment as core in ovoidal grain, faint oscillatory rim	3.57910	0.05380	0.09921	0.00700	1588	21	1608	130	1.24	-1.26	499	1326
NMC100c	37	FC	Oi	S	oscillatory fragment as core in ovoidal grain, faint sector zoned rim	4.27899	0.05127	0.08710	0.00620	1353.7	15	1361	140	0.54	-0.54	436	3420
NMC100	37	IC	Ch	S	bright core in small rounded grain	4.41112	0.10507	0.08405	0.00120	1317	29	1292	28	-1.93	1.90	n/a	n/a
NMC100c	38	FC	Cl	S	CL-low core in oscillatory zoned elongated grain	4.61340	0.04470	0.08460	0.00610	1264.7	11	1303	140	2.94	-3.03	392	2868
NMC100	38	IC	Ch	S	bright core in hypidioblastic grain, concordant	4.39367	0.10231	0.08586	0.00096	1322.1	28	1334	21	0.89	-0.90	n/a	n/a
NMC100c	39	FC	Ch	P	bright core in faint convoluted rim	4.41891	0.04882	0.09210	0.00700	1315	13	1460	150	9.93	-11.03	147.3	610
NMC100	39	IC		D	oscillatory zoned fragment, discordant and disregarded	4.15110	0.09477	0.10470	0.00410	1391.3	29	1699	71	18.11	-22.12	n/a	n/a
NMC100c	40	FC	Oi	S	oscillatory fragment as core in ovoidal grain, faint sector zoned rim	3.32005	0.03638	0.10354	0.00730	1697.5	16	1687	130	-0.62	0.62	242	2107
NMC100	40	IC	Oi	S	oscillatory rim, but older than core (spot 23), could be an older fragment?	4.32526	0.09915	0.08500	0.00094	1340.8	28	1314	22	-2.04	2.00	n/a	n/a
NMC100c	41	FC	Ch	S	bright core in hypidioblastic grain, faint rim, concordant	3.29707	0.03587	0.10400	0.00820	1707.6	17	1686	150	-1.28	1.26	81.1	481
NMC100c	42	FC	Ch	S	elongated grain with bright core	3.15457	0.06866	0.10450	0.00860	1775	34	1691	150	-4.97	4.73	82	336
NMC100c	43	FC	Ch	S	oscillatory fragment as core in ovoidal grain, faint oscillatory zoned rim	3.42466	0.03753	0.10480	0.00760	1651.3	16	1707	130	3.26	-3.37	123	1063
NMC100c	44	FC	Ch	P	bright core in hypidioblastic oscillatory grain (rim spot 27)	4.49398	0.04241	0.08920	0.00680	1295.2	11	1401	150	7.55	-8.17	183	848
NMC100c	45	FC	Oh	P	bright oscillatory fragment as core in ovoidal grain, faint sector zoned rim	4.67727	0.05032	0.08540	0.00640	1249	12	1328	140	5.95	-6.33	206.5	729
NMC100c	46	FC	Oi	P	elongated grain with oscillatory core	4.48632	0.04830	0.08760	0.00650	1297.4	12	1369	140	5.23	-5.52	284.3	1403
NMC100c	47	FC		D	oscillatory zoned fragment, discordant and disregarded	4.47087	0.04398	0.09550	0.00690	1301.2	12	1543	140	15.67	-18.58	509	3776
NMC100c	48	FC	Oi	S	oscillatory fragment as core in hypidioblastic grain, faint sector zoned rim	3.43171	0.04475	0.10403	0.00730	1649	19	1699	140	2.94	-3.03	454	2604
NMC100c	49	FC	Oi	S	rim on hypidioblastic detrital grain that has a bright core, oscillatory zoned, concordant	4.41696	0.06828	0.08491	0.00600	1316	18	1312	140	-0.30	0.30	340	1510
NMC100c	50	FC	Oh	S	bright oscillatory zoned core overgrown by faint sector zoned rim	4.29923	0.04806	0.08570	0.00670	1348.2	13	1320	150	-2.14	2.09	127.6	1051
NMC100c	51	FC	Oi	S	oscillatory fragment as core in ovoidal grain, faint sector zoned rim	3.43820	0.03192	0.10300	0.00730	1645.8	13	1678	130	1.92	-1.96	201.4	3420
NMC100c	52	FC	Ch	S	bright core in hypidioblastic grain, concordant	3.29381	0.04123	0.10420	0.00780	1709	19	1694	140	-0.89	0.88	99	336
NMC100c	53	FC	Oh	S	bright core in hypidioblastic grain, concordant	3.94477	0.06691	0.09220	0.00670	1456	22	1467	140	0.75	-0.76	317	681
NMC100c	54	FC	Ch	S	bright oscillatory fragment as core in ovoidal grain, faint sector zoned rim	3.45782	0.05141	0.09860	0.00720	1637	21	1593	140	-2.76	2.69	188	787
NMC100c	55	FC	Oi	S	oscillatory fragment as core in ovoidal grain, faint sector zoned rim	4.39232	0.04244	0.08618	0.00610	1322.3	12	1345	140	1.69	-1.72	300	931
NMC100c	56	FC	Ch	S	bright core in hypidioblastic grain, concordant	3.93236	0.07577	0.09100	0.00910	1460	25	1470	180	0.68	-0.68	72.9	356
NMC100c	57	FC		D	oscillatory zoned fragment, discordant and disregarded	4.20168	0.21185	0.13570	0.01300	1373	62	2150	160	36.14	-56.59	264	1120
NMC100c	58	FC	Ch	S	bright core in hypidioblastic grain, concordant	4.45236	0.04758	0.08410	0.00680	1306.3	13	1301	170	-0.41	0.41	94.4	400
NMC100c	59	FC		D	oscillatory zoned fragment, discordant and disregarded	5.00000	0.10250	0.08800	0.00620	1175	22	1380	140	14.86	-17.45	416.2	1720
NMC100c	60	FC	Oh	Y	hypidioblastic oscillatory zoned core, faint sector zoned rim, youngest detritus	5.37172	0.05483	0.07740	0.00570	1100.5	10	1137	150	3.21	-3.32	255	887
NMC100c	61	FC	Cl	P	faint core in bright elongated prismatic grain	4.48230	0.05625	0.08770	0.00850	1298	15	1390	170	6.62	-7.09	83.4	773
NMC100c	62	FC		D	oscillatory zoned fragment, discordant and disregarded	5.93082	0.04172	0.10500	0.00710	1460.9	14	1720	130	15.06	-17.74	150	558
NMC100c	63	FC	Oi	P	oscillatory zoned grain, elongated ovoidal grain	4.73934	0.07412	0.07900	0.00750	1234	18	1160	190	-6.38	6.00	113.2	715
NMC100c	64	FC	Oh	S	oscillatory fragment as core in ovoidal grain, faint sector zoned rim	4.55996	0.05198	0.08440	0.00640	1278.2	13	1295	140	1.30	-1.31	202	4200
NMC100c	65	FC	Oh	S	oscillatory fragment as core in ovoidal grain, faint sector zoned rim	3.16857	0.03213	0.10930	0.00800	1768	16	1783	130	0.84	-0.85	141.2	1267
NMC100c	66	FC	Oh	S	oscillatory fragment as core in ovoidal grain, faint sector zoned rim	3.22893	0.03336	0.10710	0.00760	1720.1	16	1749	130	0.57	-0.57	205.9	1844
NMC100c	67	FC	Oh	S	oscillatory fragment as core in ovoidal grain, faint sector zoned rim	4.34613	0.04156	0.08520	0.00620	1335	11	1324	130	-0.83	0.82	254.4	1380
NMC100c	68	FC	Ch	P	bright core in oscillatory grain	4.60617	0.08062	0.08750	0.00640	1266	20	1376	130	7.99	-8.69	313	1968
NMC100c	69	FC		D	oscillatory zoned fragment, discordant and disregarded	4.26803	0.13298	0.11520	0.01100	1356	38	1860	170	27.10	-37.17	308	1050
NMC100c	70	FC	Oh	P	bright oscillatory fragment as core in ovoidal grain, faint sector zoned rim	3.46981	0.05177	0.10620	0.00800	1632	22	1754	130	6.96	-7.48	144	987
NMC100c	71	FC	Oh	P	bright oscillatory fragment as core in ovoidal grain, faint sector zoned rim	3.48432	0.06799	0.10640	0.00780	1626	28	1735	140	6.28	-6.70	192	1190

Table D.13: LASS ICP-MS chondrite-normalised REE data for zircon (ppm) – IC machine settings for rim analyses, FC machine settings for core analyses. Sample NMC100.

sample ID	spot	instrument settings	CL	group	La	Ce	Pr	Nd	Sm	Eu	Gd	Tb	Dy	Ho	Er	Tm	Yb	Lu
NMC100	2	IC	Ol	P	b.d	48.64	37.70	26.67	64.62	b.d	83.01	127.85	240.06	422.01	627.62	932.10	1349.28	1704.97
NMC100	8	IC	Ol	P	0.16	31.06	b.d	b.d	14.36	b.d	47.10	98.10	192.24	366.30	601.90	993.83	1397.13	1885.09
NMC100	9	IC	Ol	P	b.d	57.18	b.d	8.00	b.d	9.25	56.37	63.92	103.73	178.83	250.00	450.62	714.83	1149.07
NMC100	13	IC	Ol	P	b.d	118.81	90.16	128.33	152.82	66.67	128.57	173.00	249.69	409.47	658.57	1092.59	1660.29	2409.94
NMC100	21	IC	Rl	P	b.d	59.90	20.74	25.17	23.08	18.23	74.13	138.61	235.40	467.97	709.05	1157.41	1641.15	2139.75
NMC100	22	IC	Ch	P	b.d	129.95	19.59	26.67	64.62	43.54	86.87	180.17	334.78	584.96	906.19	1376.54	2105.26	2664.60
NMC100	28	IC	Ol	P	0.03	17.57	b.d	b.d	13.33	b.d	59.07	128.90	256.83	548.75	875.24	1324.07	1980.86	2677.02
NMC100	30	IC	Rl	P	25.81	b.d	b.d	b.d	b.d	b.d	3.63	434.60	29.50	703.34	69.52	4716.05	185.65	320496.89
NMC100	33	IC	Ol	P	142.26	2.75	210.66	26.33	15.59	752.38	69.11	4052.74	216.15	3979.11	281.43	15216.05	471.29	267080.75
NMC100	35	IC	Ch	P	209.68	15.35	852.46	42.67	20.00	474.83	31.27	1930.38	105.90	2314.76	190.95	12808.64	423.92	391614.91
NMC100	7	IC	Rl	S	209.68	15.35	852.46	42.67	20.00	474.83	31.27	1930.38	105.90	2314.76	190.95	12808.64	423.92	391614.91
NMC100	10	IC	Ol	S	65.48	0.94	52.46	6.33	2.10	200.00	23.17	1345.99	82.61	1541.78	118.10	6731.48	225.84	270807.45
NMC100	11	IC	Ol	S	3.32	b.d	b.d	3.67	b.d	253.06	33.59	2413.50	112.73	1980.50	114.76	6811.73	205.26	334161.49
NMC100	16	IC	Ol	S	166.45	3.00	147.54	22.00	14.67	469.39	36.29	2242.62	122.36	2250.70	172.86	9475.31	302.39	294099.38
NMC100	18	IC	Sh	S	b.d	1.53	b.d	b.d	b.d	3.54	47.10	149.79	251.55	335.65	439.05	608.02	980.86	1347.83
NMC100	19	IC	Ch	S	b.d	52.60	77.05	125.00	91.28	48.30	67.95	108.65	188.51	380.22	619.05	1104.94	1779.90	2624.22
NMC100	24	IC	Ch	S	b.d	32.92	6.15	7.00	b.d	14.29	54.05	86.71	145.03	254.87	393.81	604.94	990.43	1462.73
NMC100	27	IC	Ol	S	b.d	25.37	26.23	43.00	39.49	28.30	42.86	128.27	294.10	511.14	963.81	1790.12	2923.44	4158.39
NMC100	29	IC	Ch	S	0.18	75.74	b.d	b.d	7.69	b.d	67.95	159.92	294.41	529.25	796.19	1138.89	1689.00	2357.14
NMC100	36	IC	Sl	M	b.d	4.96	b.d	b.d	19.49	b.d	65.64	171.73	232.30	373.26	442.86	512.35	592.34	829.19
NMC100	37	IC	Ch	S	b.d	71.04	20.08	23.00	8.72	15.24	44.02	94.73	191.93	392.76	695.24	1141.98	1937.80	3037.27
NMC100	38	IC	Ch	S	b.d	51.61	33.85	47.00	21.03	27.48	25.87	47.26	55.28	97.91	147.14	195.68	323.92	531.06
NMC100	40	IC	Ol	S	b.d	24.13	b.d	b.d	10.26	b.d	37.84	65.40	124.53	215.88	312.86	466.05	698.56	866.46
NMC100c	1	FC	Oh	S	b.d	52.60	17.21	12.00	29.23	19.32	105.41	168.35	298.45	519.50	850.48	1212.96	1808.61	2459.63
NMC100c	3	FC	Ch	S	0.04	12.23	b.d	1.42	13.33	b.d	71.04	167.09	342.55	633.70	1039.05	1441.36	2210.53	2829.19
NMC100c	5	FC	Ol	S	b.d	22.40	8.11	6.17	23.59	16.60	64.09	100.00	185.40	317.55	496.19	688.27	1133.97	1596.27
NMC100c	8	FC	Cl	S	b.d	24.01	9.84	7.83	40.51	6.39	150.19	265.82	478.26	837.05	1309.52	1793.21	2650.72	3245.34
NMC100c	9	FC	Ol	S	b.d	18.69	8.85	9.67	52.82	25.99	192.28	326.58	557.45	972.14	1442.86	1944.44	2875.60	3562.11
NMC100c	11	FC	Ol	S	b.d	59.28	11.48	5.33	11.95	5.85	40.15	74.05	115.22	195.26	334.76	501.23	881.34	1285.71
NMC100c	12	FC	Oh	S	b.d	52.60	10.90	16.33	59.49	27.62	167.18	301.69	503.11	834.26	1271.43	1700.62	2583.73	3291.93
NMC100c	15	FC	Ch	S	b.d	50.74	70.49	38.83	55.90	20.82	97.68	149.58	259.94	494.43	780.95	1145.06	1689.00	2282.61
NMC100c	16	FC	Ch	S	b.d	68.07	51.64	31.33	62.56	24.08	166.41	264.35	435.71	732.59	1105.24	1441.36	2124.40	2732.92
NMC100c	17	FC	Ol	S	b.d	39.48	48.36	30.33	30.77	25.31	53.28	96.62	175.47	324.51	518.57	793.21	1272.73	1785.71
NMC100c	18	FC	Ch	S	b.d	75.50	97.54	38.33	59.49	3.81	149.03	263.71	404.35	646.24	943.81	1287.04	1889.95	2453.42
NMC100c	20	FC	Ol	S	b.d	117.57	286.89	108.33	101.03	21.63	152.51	189.24	267.70	416.43	600.00	823.46	1295.22	1689.44
NMC100c	21	FC	Ch	S	b.d	103.59	23.44	17.00	42.56	29.80	130.12	241.98	415.53	727.02	1141.90	1564.81	2449.76	3152.17
NMC100c	22	FC	Ol	S	b.d	754.95	2622.95	1133.33	871.79	29.93	328.19	295.36	341.61	493.04	786.19	1074.07	1630.14	2142.86
NMC100c	24	FC	Ol	S	b.d	207.43	192.62	130.17	212.82	114.15	370.27	483.12	717.70	1107.24	1551.90	2101.85	3057.42	3785.71
NMC100c	26	FC	Cl	S	b.d	37.75	43.44	23.83	45.64	11.84	147.88	231.86	397.52	633.70	990.48	1277.78	1842.11	2198.76
NMC100c	27	FC	Oh	S	b.d	20.79	b.d	1.30	7.38	5.99	55.98	131.86	235.71	430.36	700.00	1074.07	1559.81	2006.21
NMC100c	28	FC	Ch	S	b.d	14.48	14.59	6.00	19.49	6.94	94.59	173.00	328.88	577.99	923.81	1293.21	2052.63	2621.12
NMC100c	29	FC	Ch	S	b.d	7.18	b.d	b.d	4.15	b.d	37.45	77.43	145.65	264.90	427.62	608.02	922.49	1183.23
NMC100c	31	FC	Ol	S	b.d	54.83	31.97	21.00	43.08	16.60	131.27	226.16	419.57	778.55	1256.19	1811.73	2913.88	3925.47
NMC100c	32	FC	Oh	S	b.d	21.41	3.20	3.43	20.00	9.39	51.35	85.23	151.24	260.03	396.19	583.33	923.44	1329.19
NMC100c	33	FC	Ch	S	0.06	21.56	2.38	3.75	30.77	15.10	108.88	217.09	391.61	658.77	994.29	1398.15	2086.12	2614.91
NMC100c	34	FC	Oh	S	b.d	24.13	11.07	11.67	22.05	13.88	59.46	84.81	132.30	230.08	367.14	506.17	850.72	1114.91
NMC100c	36	FC	Ol	S	b.d	41.46	43.44	26.33	42.56	17.82	111.20	185.44	351.55	604.46	965.24	1367.28	2081.34	2649.07
NMC100c	37	FC	Ol	S	b.d	200.50	245.90	140.00	153.33	48.71	166.80	201.69	303.11	527.86	857.14	1259.26	2057.42	2819.88
NMC100c	38	FC	Cl	S	b.d	173.27	76.23	69.50	195.38	142.86	369.50	489.45	683.23	1037.60	1509.52	2030.86	3100.48	4024.84
NMC100c	39	FC	Ch	S	b.d	12.24	3.52	5.15	41.54	21.77	153.67	259.49	448.76	708.91	1049.52	1277.78	1856.94	2298.14
NMC100c	40	FC	Ol	S	b.d	36.88	12.46	15.50	80.51	34.15	206.56	340.51	569.25	995.82	1418.57	1861.11	2693.78	3307.45
NMC100c	41	FC	Ch	S	b.d	20.50	3.36	3.20	11.49	6.67	44.02	72.15	136.34	223.68	355.71	485.19	811.00	1049.69
NMC100c	42	FC	Ch	S	b.d	19.06	3.52	2.83	14.10	10.34	35.14	59.28	92.86	144.85	225.24	338.89	594.26	826.09
NMC100c	43	FC	Ch	S	b.d	141.58	17.79	19.00	89.74	34.83	287.26	490.72	824.84	1405.29	1938.10	2361.11	3186.60	3704.97
NMC100c	44	FC	Ch	S	b.d	162.25	537.70	405.00	548.72	43.13	471.43	314.35	271.74	339.83	512.86	731.48	1205.74	1708.07
NMC100c	45	FC	Oh	S	b.d	22.03	2.95	5.67	27.18	15.78	96.53	141.35	239.13	380.22	547.62	740.74	1086.12	1301.24
NMC100c	46	FC	Ol	S	b.d	112.50	59.02	52.83	124.10	84.35	221.24	309.70	435.09	694.99	966.19	1228.40	1832.54	2313.66
NMC100c	48	FC	Ol	S	b.d	57.80	54.10	29.67	47.69	17.82	115.06	182.07	282.92	533.70	874.29	1200.62	1886.12	2462.73
NMC100c	49	FC	Ol	S	b.d	86.14	2.79	3.63	28.72	18.91	88.80	159.70	258.07	442.90	668.57	929.01	1468.90	1860.25
NMC100c	50	FC	Oh	S	b.d	81.31	8.03	11.00	56.92	42.86	147.49	253.16	402.80	650.42	990.48	1342.59	2038.28	2549.69
NMC100c	51	FC	Ol	S	b.d	125.00	18.36	30.50	144.10	106.12	383.40	582.28	925.47	1438.72	2057.14	2564.81	3732.06	4559.01
NMC100c	52	FC	Ch	S	b.d	10.42	9.34	5.17	21.03	3.40	83.01	164.14	267.08	445.68	657.62	889.20	1222.01	1549.69
NMC100c	53	FC	Oh	S	b.d	25.73	1.72	2.55	4.67	6.26	32.43	53.16	103.42	200.70	376.67	601.85	1119.62	1708.07
NMC100c	54	FC	Ch	S	b.d	23.14	3.11	3.28	32.31	13.06	104.25	193.04	344.10	601.67	928.10	1287.04	1937.80	2468.94
NMC100c	55	FC	Ol	S	b.d	88.86	59.02	25.50	50.77	33.20	62.16	90.72	143.79	254.87	442.38	679.01	1176.56	1813.66
NMC100c	56	FC	Ch	S	b.d	14.02	b.d	2.60	21.54	5.99	74.52	116.24	209.01	331.48	489.52	651.23	990.43	1192.55
NMC100c	58	FC	Ch	S	b.d	29.95	17.21	7.17	15.90	7.62	55.21	92.41	123.60	186.63	293.81	404.32	645.45	863.35
NMC100c	61	FC	Cl	S	b.d	37.00	5.41	5.47	25.13	16.73	66.41	99.79	178.26	307.80	528.57	783.95	1382.78	2099.38
NMC100c	63	FC	Ol	S	0.04	69.93	5.25	7.17	43.08	16.73	170.27	298.52	483.54	813.37	1201.43	1518.52	2239.23	2826.09
NMC100c	64	FC	Oh	S	0.01	48.89	2.54	4.33	26.15	17.41	87.26	131.86	177.95	314.76	464.29	675.00	1063.64	1431.68
NMC100c	65	FC	Oh	S	b.d	116.34	147.54	48.33	18.46	6.67	59.85	73.42	123.91	229.25	383.81	567.90	947.37	1500.00
NMC100c	66	FC	Oh	S	b.d	35.89	5.08	4.83	29.23	21.50	116.60	215.40	378.57	681.06	1065.24	1395.06	2224.88	2891.30
NMC100c	67	FC	Oh	S	b.d	75.50	49.18	21.67	32.82	9.93	66.02	111.18	205.59	388.86	661.43	967.59	1655.50	2341.61
NMC100c	68	FC	Ch	S	b.d	39.11	8.77	9.83	47.18	22.31	116.60	199.16	322.36	550.14	863.81	1191.36	1756.94	2232.92
NMC100c	70	FC	Oh	S	b.d	209.16	188.52	110.00	169.74	61.22	219.31	295.36	431.68	658.77	995.24	1354.94	2028.71	2624.22
NMC100c	71	FC	Oh	S	b.d	42.57	25.98	27.67	67.69	42.04	160.62	255.06	420.81	668.52	1028.57	1231.48	1942.58	2434.78
NMC100c	60	FC	Oh	Y	b.d	31.19	1.80	3.73	22.05	5.58	108.88	220.89	422.67	742.34	1223.81	1657.41	2511.96	3248.45

Table D.14: LASS ICP-MS U–Pb isotopic data for monazite. Sample NMC100.

sample ID	spot	location	$^{238}U/^{206}Pb$	2σ	$^{207}Pb/^{206}Pb$	2σ	$^{206}Pb/^{238}U$ Age (Ma)	2σ	$^{207}Pb/^{206}Pb$ Age (Ma)	2σ	7/6 discordance (%)	6/8 discordance (%)	U (ppm)	Th (ppm)	Pb (ppm)
NMC100	NMC100 - 1	rim	5.75705	0.14583	0.07223	0.0006	1033	24	991	17-Jan	-4.24	04-Jan	3460	75000	4880
NMC100	NMC100 - 2	rim	5.74713	0.13542	0.07395	0.00095	1034.1	22	1038	26	0.38	-0.38	2660	134000	8400
NMC100	NMC100 - 3	rim	5.70776	0.14009	0.0757	0.00079	1041	24	1086	21	4.14	-4.32	4130	67000	4590
NMC100	NMC100 - 4	rim	5.68182	0.13882	0.07432	0.00093	1045	24	1049	25	0.38	-0.38	4240	41400	2790
NMC100	NMC100 - 5	mantle	5.63698	0.13346	0.07412	0.00075	1052.5	23	1043	20	-0.91	0.9	4330	45900	3050
NMC100	NMC100 - 6	core	5.61798	0.14203	0.07305	0.0008	1056	24	1019	20	-3.63	3.5	4360	42000	2860
NMC100	NMC100 - 7	rim	5.61482	0.14187	0.07408	0.00079	1056	25	1042	21	-1.34	1.33	4720	44600	3020
NMC100	NMC100 - 8	rim	6.02773	0.14533	0.07439	0.00083	989.4	22	1050	23	5.77	-6.12	3970	76000	4950
NMC100	NMC100 - 9	rim	5.81734	0.13875	0.07315	0.00094	1022.4	22	1023	24	0.06	-0.06	3740	85000	5430
NMC100	NMC100 - 10	mantle	5.82072	0.13891	0.07323	0.00075	1021.9	22	1019	21	-0.28	0.28	3700	57600	3660
NMC100	NMC100 - 11	core	5.90319	0.13591	0.07297	0.00069	1008.8	22	1012	19	0.32	-0.32	3110	95000	5940
NMC100	NMC100 - 12	rim	5.64972	0.13406	0.074	0.00082	1050.7	23	1040	22	-1.03	1.02	4150	45000	3040
NMC100	NMC100 - 13	rim	5.90319	0.15681	0.07365	0.00051	1009	25	1031	14	2.13	-2.18	2410	91000	5960
NMC100	NMC100 - 14	core	5.70125	0.15927	0.0733	0.0015	1042	27	1018	42	-2.36	2.3	1730	106000	6670
NMC100	NMC100 - 15	rim	5.76369	0.15613	0.0726	0.0011	1035	24	1009	33	-2.58	2.51	1770	88000	5760
NMC100	NMC100 - 16	rim	5.67215	0.13191	0.074	0.00074	1046.9	22	1040	20	-0.66	0.66	4420	50600	3350
NMC100	NMC100 - 17	mantle	5.92768	0.14758	0.074	0.0011	1005	23	1039	29	3.27	-3.38	2620	120000	7600
NMC100	NMC100 - 18	mantle	5.65291	0.13741	0.0732	0.001	1050	24	1019	28	-3.04	2.95	4230	56600	3800
NMC100	NMC100 - 19	mantle	5.78035	0.13699	0.07465	0.00071	1028.5	23	1058	19	2.79	-2.87	3130	82000	5340
NMC100	NMC100 - 20	core	5.94177	0.16593	0.0755	0.0013	1002	26	1079	35	7.14	-7.68	2650	119000	7590
NMC100	NMC100 - 21	rim	5.54324	0.13213	0.07366	0.00069	1069	23	1031	19	-3.69	3.55	4370	65300	4280
NMC100	NMC100 - 22	rim	5.77034	0.13652	0.07358	0.00094	1030.4	22	1028	26	-0.23	0.23	4360	41600	2720
NMC100	NMC100 - 23	mantle	5.69476	0.13296	0.07442	0.0006	1042.7	23	1052	16	0.88	-0.89	4850	49400	3340
NMC100	NMC100 - 24	core	5.76701	0.14634	0.07271	0.0009	1031	24	1004	25	-2.69	2.62	3070	133000	8460
NMC100	NMC100 - 25	rim	5.83431	0.14296	0.07344	0.00078	1019.6	23	1025	21	0.53	-0.53	3150	64400	4190
NMC100	NMC100 - 26	rim	5.8072	0.14164	0.07454	0.00091	1024.3	23	1054	25	2.82	-2.9	2980	77900	5150
NMC100	NMC100 - 27	core	5.71102	0.14025	0.0722	0.00069	1040	24	997	22	-4.31	4.13	3260	82000	5240
NMC100	NMC100 - 28	rim	5.70776	0.14009	0.07182	0.0009	1041	24	979	26	-6.33	5.96	2640	112000	7250
NMC100	NMC100 - 29	rim	5.76369	0.14285	0.07474	0.00085	1031	24	1060	23	2.74	-2.81	2660	139000	8930
NMC100	NMC100 - 30	rim	5.72738	0.14761	0.0747	0.0011	1038	25	1058	31	1.89	-1.93	2410	107000	7010
NMC100	NMC100 - 31	core	5.78369	0.15387	0.072	0.001	1028	25	984	28	-4.47	4.28	2160	155000	9960
NMC100	NMC100 - 32	rim	5.58659	0.14045	0.0737	0.0011	1061	25	1031	29	-2.91	2.83	4120	47600	3210
NMC100	NMC100 - 33	rim	5.73066	0.13793	0.0731	0.0007	1036.8	23	1015	19	-2.15	2.1	3860	50600	3490
NMC100	NMC100 - 34	core	5.59597	0.14405	0.07336	0.00054	1060	25	1023	15	-3.62	3.49	4380	46800	3190
NMC100	NMC100 - 35	rim	5.77367	0.14668	0.07404	0.00067	1030	24	1046	16	1.53	-1.55	3420	58000	3980
NMC100	NMC100 - 37	rim	5.59597	0.13779	0.07311	0.00054	1060	24	1020	16	-3.92	3.77	3930	64100	4440
NMC100	NMC100 - 38	core	5.73066	0.13793	0.07216	0.00095	1036.9	23	989	27	-4.84	4.62	2250	132000	8310
NMC100	NMC100 - 39	mantle	5.91366	0.15737	0.07146	0.00071	1007	25	969	20	-3.92	3.77	3260	118000	7390
NMC100	NMC100 - 40	mantle	5.90319	0.14636	0.07299	0.00085	1009	23	1019	26	0.98	-0.99	2370	115000	7510
NMC100	NMC100 - 41	rim	5.60538	0.15082	0.07303	0.0006	1058	26	1018	15	-3.93	3.78	3520	79000	5190
NMC100	NMC100 - 42	rim	5.68828	0.14237	0.07245	0.00073	1044	24	997	20	-4.71	4.5	2370	63200	4260
NMC100	NMC100 - 43	core	5.67537	0.15783	0.07253	0.00078	1046	27	999	22	-4.7	4.49	2780	62700	4200
NMC100	NMC100 - 44	rim	5.76369	0.1362	0.0731	0.001	1031.4	23	1015	28	-1.62	1.59	3360	57600	3850
NMC100	NMC100 - 45	rim	5.72738	0.13449	0.0732	0.0011	1037.4	22	1016	30	-2.11	2.06	2700	73200	4820
NMC100	NMC100 - 46	rim	5.73395	0.15124	0.0729	0.0013	1036	25	1019	40	-1.67	1.64	2710	69000	4500
NMC100	NMC100 - 47	core	6.14628	0.24555	0.0734	0.0011	971	36	1023	30	5.08	-5.36	3440	58500	3930
NMC100	NMC100 - 48	rim	5.81058	0.13843	0.07147	0.00089	1023.9	23	969	26	-5.67	5.36	2580	70000	4510
NMC100	NMC100 - 49	core	5.8548	0.15083	0.0736	0.0011	1016	24	1028	30	1.17	-1.18	2330	88000	5780
NMC100	NMC100 - 50	rim	5.8651	0.14104	0.07165	0.0007	1014.7	23	974	20	-4.18	4.01	2620	112000	7200
NMC100	NMC100 - 51	rim	5.84795	0.14363	0.0734	0.00091	1017.4	23	1023	25	0.55	-0.55	3550	99000	6390
NMC100	NMC100 - 52	core	5.57414	0.13361	0.0742	0.00073	1063.4	24	1046	20	-1.66	1.64	3250	44800	3030
NMC100	NMC100 - 53	rim	5.83771	0.13632	0.07381	0.00082	1019.3	22	1040	21	1.99	-2.03	4130	48400	3230
NMC100	NMC100 - 54	core	5.53097	0.13766	0.07334	0.00068	1071	25	1022	19	-4.79	4.58	4170	41100	2870
NMC100	NMC100 - 55	rim	5.97729	0.16435	0.07378	0.00063	997	25	1034	17	3.58	-3.71	2490	158000	10400
NMC100	NMC100 - 56	core	5.65291	0.1438	0.07356	0.0008	1050	24	1028	22	-2.14	2.1	6710	43800	2910
NMC100	NMC100 - 57	rim	5.83431	0.16339	0.07207	0.00083	1020	27	986	23	-3.45	3.33	2580	153000	10000
NMC100	NMC100 - 58	rim	5.70451	0.13667	0.07334	0.00089	1041	23	1022	25	-1.86	1.83	3340	64000	4430
NMC100	NMC100 - 59	core	5.58972	0.13435	0.0741	0.00074	1060.7	23	1043	20	-1.7	1.67	3780	48000	3390
NMC100	NMC100 - 60	rim	5.7971	0.16467	0.07177	0.00069	1026	27	978	19	-4.91	4.68	2700	86300	5530
NMC100	NMC100 - 61	rim	5.52792	0.12834	0.07286	0.00063	1071.6	23	1009	17	-6.2	5.84	3890	73000	5060
NMC100	NMC100 - 62	rim	5.54631	0.13227	0.0735	0.00065	1068.4	23	1027	18	-4.03	3.87	4820	46300	3320
NMC100	NMC100 - 63	core	5.51572	0.14299	0.07477	0.00053	1074	26	1061	14	-1.23	1.21	8800	46000	3180
NMC100	NMC100 - 64	core	5.69152	0.14901	0.0754	0.0018	1043	26	1075	47	2.98	-3.07	1400	92000	6190
NMC100	NMC100 - 65	core	5.78369	0.14384	0.07338	0.00094	1028	23	1023	26	-0.49	0.49	3530	51000	3500
NMC100	NMC100 - 66	rim	5.75705	0.15909	0.07264	0.00084	1032	26	1002	23	-2.99	2.91	1800	132000	8700
NMC100	NMC100 - 68	core	5.8309	0.1598	0.0739	0.0011	1020	26	1035	31	1.45	-1.47	1560	54400	3690
NMC100	NMC100 - 69	rim	5.93472	0.14441	0.07284	0.00054	1003.7	23	1008	15	0.43	-0.43	2510	149000	9500
NMC100	NMC100 - 70	rim	5.87544	0.1588	0.07117	0.00094	1013	26	967	25	-4.76	4.54	2950	140000	9200
NMC100	NMC100 - 71	rim	5.71102	0.16308	0.0738	0.0014	1040	27	1034	39	-0.58	0.58	2270	131000	8800
NMC100	NMC100 - 72	mantle	5.75705	0.14915	0.0734	0.0011	1033	25	1023	30	-0.98	0.97	1800	122000	8000
NMC100	NMC100 - 73	rim	5.8651	0.14448	0.07277	0.00082	1015	23	1006	23	-0.89	0.89	2320	130000	8600
NMC100	NMC100 - 74	rim	5.82072	0.16263	0.0728	0.0011	1022	26	1006	30	-1.59	1.57	2960	104000	6930
NMC100	NMC100 - 75	core	5.82072	0.18634	0.0749	0.0012	1022	30	1064	32	3.95	-4.11	1820	119000	7700
NMC100	NMC100 - 76	rim	5.65291	0.14699	0.07359	0.00058	1050	25	1029	16	-2.04	2	4470	55200	3890
NMC100	NMC100 - 77	rim	5.77367	0.15001	0.0714	0.001	1029	25	966	29	-6.52	6.12	2970	136000	9100
NMC100	NMC100 - 78	rim	5.77034	0.16315	0.0723	0.0012	1030	27	992	35	-3.83	3.69	2160	114200	7650
NMC100	NMC100 - 79	rim	5.95593	0.15608	0.073	0.0012	1001	24	1012	32	1.09	-1.1	2530	76900	4970
NMC100	NMC100 - 80	core	5.79039	0.15423	0.0717	0.00099	1027	26	976	28	-5.23	4.97	1700	46100	3090
NMC100	NMC100 - 81	core	5.78369	0.14718	0.07184	0.00051	1028	24	980	15	-4.9	4.67	3620	89200	5810
NMC100	NMC100 - 82	rim	5.77367	0.16334	0.0716	0.0011	1030	27	981	28	-4.99	4.76	2260	89000	6110
NMC100	NMC100 - 83	core	5.69152	0.15549	0.07307	0.00095	1043	26	1014	27	-2.86	2.78	2710	75000	5110
NMC100	NMC100 - 84	mantle	5.66251	0.14108	0.0727	0.00085	1048	24	1004	24	-4.38	4.2	2430	67400	4750
NMC100	NMC100 - 85	rim	5.59284	0.14702	0.07268	0.00088	1060	26	1003	25	-5.68	5.38	5430	42200	2920
NMC100	NMC100 - 86	mantle	5.84112	0.15012	0.07181	0.00093	1019	24	979	26	-4.09	3.93	3540	74000	5010
NMC100	NMC100 - 87	mantle	5.65291	0.15978	0.07304	0.00071	1050	27	1019	21	-3.04	2.95	5600	51600	3510
NMC100	NMC100 - 88	rim	5.72738	0.14105	0.0724	0.00091	1037	24	995	26	-4.22	4.05	3070	72000	4860
NMC100	NMC100 - 89	mantle	5.51268	0.14891	0.07324	0.00063	1075	27	1019	17	-5.5	5.21	5990	55100	3850
NMC100	NMC100 - 90	mantle	5.59284	0.1345	0.07431	0.00077	1060.2	24	1048	21	-1.16	1.15	4610	58400	4120
NMC100	NMC100 - 92	rim	5.70776	0.14986	0.0735	0.0012	1041	25	1034	29	-0.68	0.67	3210	110000	7360
NMC100	NMC100 - 93	rim	5.76369	0.14617	0.0723	0.00048	1031	24	993	14	-3.83	3.69	2940	70400	4750
NMC100	NMC100 - 94	core	5.7241	0.13761	0.07128	0.00097	1037.7	23	964	28	-7.65	7.1	1880	74000	4920
NMC100	NMC100 - 95	core	5.82751	0.13924	0.0728	0.001	1020.7	22	1007	29	-1.36	1.34	3080	91000	6080
NMC100	NMC100 - 96	core	5.69801	0.15909	0.0745	0.0013	1042	27	1054	35	1.14	-1.15	1660	124000	8400
NMC100	NMC100 - 97	core	5.56174	0.1361	0.0737	0.00047	1065.7	24	1032	13	-3.27	3.16	4500	37800	2660
NMC100	NMC100 - 98	rim	5.70125	0.15927	0.0726	0.0012	1042	27	1001	35	-4.1	3.93	1940	63600	4340
NMC100	NMC100 - 99	core	5.57725	0.13686	0.07382	0.00056	1062.9	24	1035	15	-2.7	2.62	5400	42800	3020
NMC100	NMC100 - 100	rim	5.74053	0.16806	0.07382	0.00091	1035	28	1035	25	0	0	2990	131000	8780
NMC100	NMC100 - 101	rim	5.65291	0.15019	0.07294	0.00091	1050	26	1011	25	-3.86	3.71	3380	63900	4260
NMC100	NMC100 - 102	core	5.55556	0.13889	0.07585	0.0007	1067	24	1090	18	2.11	-2.16	8290	43500	3120
NMC100	NMC100 - 103	rim	5.78369	0.14049	0.07408	0.00075	1027.8	23	1042	20	1.36	-1.38	4080	56000	3970

Table D.15: LASS ICP-MS chondrite-normalised REE data for monazite (ppm). Sample NMC100.

sample ID	spot	location	La	Ce	Pr	Nd	Sm	Eu	Gd	Tb	Dy	Ho	Er	Tm	Yb	Lu
NMC100	NMC100 - 1	rim	241935.48	n/a	202459.02	161833.33	100512.82	3360.54	39691.12	12763.71	4316.77	513.93	138.10	b.d	b.d	b.d
NMC100	NMC100 - 2	rim	219354.84	n/a	218852.46	170000.00	103589.74	3047.62	35637.07	10232.07	3664.60	428.97	200.00	b.d	b.d	b.d
NMC100	NMC100 - 4	rim	255806.45	n/a	190983.61	151500.00	89743.59	4897.96	47876.45	21940.93	7732.92	1309.19	561.90	b.d	b.d	b.d
NMC100	NMC100 - 5	mantle	220645.16	n/a	185245.90	138833.33	80512.82	5510.20	36795.37	14662.45	6459.63	1072.42	609.52	123.46	66.99	b.d
NMC100	NMC100 - 6	core	199677.42	n/a	194262.30	153166.67	100512.82	3891.16	55984.56	29261.60	17981.37	4874.65	3904.76	941.36	177.03	900.62
NMC100	NMC100 - 7	rim	176129.03	n/a	178688.52	145333.33	73333.33	2952.38	26640.93	7616.03	2332.30	410.86	176.19	b.d	b.d	b.d
NMC100	NMC100 - 8	rim	253548.39	n/a	178688.52	154166.67	91794.87	2571.43	47374.52	20928.27	10465.84	2994.43	1671.43	416.67	58.37	b.d
NMC100	NMC100 - 9	rim	255483.87	n/a	192622.95	141333.33	91282.05	7891.16	57528.96	32489.45	18012.42	3983.29	2419.05	444.44	44.02	b.d
NMC100	NMC100 - 10	mantle	195483.87	n/a	175409.84	158666.67	90769.23	2843.54	33552.12	10147.68	3322.98	384.40	185.71	b.d	b.d	b.d
NMC100	NMC100 - 11	core	253548.39	n/a	213934.43	168666.67	89230.77	4054.42	33050.19	11919.83	4378.88	696.38	533.33	b.d	b.d	b.d
NMC100	NMC100 - 12	rim	249032.26	n/a	222131.15	166600.00	89230.77	3224.49	32586.87	10590.72	4192.55	674.09	333.33	b.d	b.d	b.d
NMC100	NMC100 - 13	rim	267096.77	n/a	205737.70	153000.00	99487.18	5945.58	49189.19	20527.43	7608.70	1253.48	585.71	80.25	b.d	b.d
NMC100	NMC100 - 14	core	228064.52	n/a	222950.82	165000.00	105641.03	4204.08	31196.91	11645.57	4316.77	738.16	409.52	b.d	b.d	b.d
NMC100	NMC100 - 15	rim	283548.39	n/a	195081.97	154333.33	96410.26	8163.27	59459.46	32700.42	16645.96	3676.88	2128.57	546.30	89.00	b.d
NMC100	NMC100 - 16	rim	241290.32	n/a	231967.21	179333.33	108717.95	3591.84	44826.25	14957.81	5031.06	1128.13	657.14	b.d	26.32	b.d
NMC100	NMC100 - 17	mantle	224516.13	n/a	200000.00	155166.67	94358.97	2748.30	35173.75	10485.23	3478.26	483.29	185.71	b.d	b.d	b.d
NMC100	NMC100 - 18	mantle	246129.03	n/a	209016.39	182000.00	95384.62	3755.10	36756.76	11751.05	3540.37	529.25	157.14	108.02	b.d	b.d
NMC100	NMC100 - 19	mantle	265483.87	n/a	188524.59	147833.33	104102.56	9170.07	58301.16	33755.27	16180.12	3036.21	1700.00	345.68	b.d	b.d
NMC100	NMC100 - 20	core	290967.74	n/a	204918.03	158666.67	90256.41	5863.95	48262.55	21940.93	8850.93	1434.54	766.67	163.58	b.d	b.d
NMC100	NMC100 - 21	rim	249677.42	n/a	219672.13	162166.67	101538.46	3931.97	43436.29	15970.46	5962.73	877.44	285.71	b.d	b.d	b.d
NMC100	NMC100 - 22	rim	225483.87	n/a	212295.08	171666.67	102564.10	3564.63	37760.62	10949.37	4409.94	749.30	476.19	b.d	b.d	b.d
NMC100	NMC100 - 23	mantle	266451.61	n/a	198360.66	170500.00	104102.56	5306.12	55328.19	26202.53	10776.40	1796.66	819.05	225.31	b.d	b.d
NMC100	NMC100 - 24	core	225483.87	n/a	192622.95	141666.67	90769.23	3401.36	26254.83	8438.82	3354.04	649.03	361.90	b.d	b.d	b.d
NMC100	NMC100 - 25	rim	241935.48	n/a	186885.25	127666.67	95384.62	9795.92	59459.46	39240.51	23229.81	6462.40	4476.19	1401.23	196.17	1335.40
NMC100	NMC100 - 26	rim	292258.06	n/a	186885.25	156666.67	97435.90	9360.54	59459.46	32489.45	15155.28	2785.52	1261.90	194.44	b.d	b.d
NMC100	NMC100 - 27	core	208064.52	n/a	183606.56	171666.67	82564.10	3918.37	25405.41	8459.92	3167.70	616.99	342.86	b.d	b.d	b.d
NMC100	NMC100 - 28	rim	241290.32	n/a	203278.69	163000.00	95384.62	2979.59	30810.81	10654.01	4503.11	662.95	495.24	b.d	18.66	b.d
NMC100	NMC100 - 29	rim	250322.58	n/a	218852.46	154666.67	96410.26	4625.85	28494.21	11476.79	5000.00	887.19	438.10	b.d	b.d	b.d
NMC100	NMC100 - 30	rim	241612.90	n/a	224590.16	188333.33	86666.67	3170.07	30270.27	10232.07	3509.32	821.73	447.62	b.d	b.d	b.d
NMC100	NMC100 - 31	core	200000.00	n/a	186065.57	152833.33	86153.85	2775.51	23861.00	9050.63	3229.81	647.63	238.10	b.d	b.d	b.d
NMC100	NMC100 - 32	rim	189032.26	n/a	170491.80	149500.00	90769.23	2612.24	35791.51	11139.24	4720.50	961.00	609.52	212.96	32.54	b.d
NMC100	NMC100 - 33	rim	216129.03	n/a	207377.05	158166.67	106153.85	3945.58	41930.50	13523.21	4813.66	1114.21	714.29	148.15	60.77	b.d
NMC100	NMC100 - 34	core	183548.39	n/a	177049.18	141500.00	90256.41	2557.82	32702.70	10253.16	3757.76	905.29	695.24	132.72	b.d	b.d
NMC100	NMC100 - 36	rim	269032.26	n/a	184426.23	134333.33	97948.72	8571.43	61003.86	36075.95	18695.65	3802.23	1909.52	320.99	59.33	b.d
NMC100	NMC100 - 37	rim	240000.00	n/a	185245.90	150666.67	98974.36	5727.89	52664.09	21814.35	9844.72	2089.14	1133.33	253.09	69.86	b.d
NMC100	NMC100 - 38	core	230322.58	n/a	189344.26	130333.33	97435.90	7755.10	59073.36	35021.10	17888.20	3662.95	1666.67	416.67	56.94	b.d
NMC100	NMC100 - 39	mantle	264193.55	n/a	185245.90	145166.67	98461.54	6598.64	51737.45	26160.34	11521.74	2047.35	876.19	225.31	b.d	b.d
NMC100	NMC100 - 40	mantle	197419.35	n/a	170491.80	148000.00	86153.85	2884.35	29729.73	8987.34	2981.37	512.53	190.48	b.d	b.d	b.d
NMC100	NMC100 - 41	rim	183870.97	n/a	177868.85	159333.33	93846.15	3673.47	29652.51	8987.34	3229.81	550.14	352.38	b.d	b.d	b.d
NMC100	NMC100 - 42	rim	191612.90	n/a	193442.62	152000.00	87179.49	2680.27	28532.82	8713.08	3012.42	513.93	300.00	b.d	b.d	b.d
NMC100	NMC100 - 43	core	232580.65	n/a	181147.54	143000.00	91282.05	3224.49	52934.36	25337.55	12546.58	2743.73	1980.95	549.38	100.00	590.06
NMC100	NMC100 - 44	rim	207741.94	n/a	186885.25	152166.67	95897.44	3782.31	48301.16	24620.25	12298.14	3077.99	1585.71	555.56	153.11	465.84
NMC100	NMC100 - 45	rim	252580.65	n/a	195901.64	157666.67	94871.79	5619.05	50579.15	23502.11	11987.58	2660.17	1580.95	385.80	50.24	372.67
NMC100	NMC100 - 46	rim	222580.65	n/a	183606.56	143000.00	89743.59	5768.71	50579.15	28691.98	16801.24	4220.06	2666.67	836.42	114.83	366.46
NMC100	NMC100 - 47	core	199677.42	n/a	176229.51	138000.00	98974.36	4095.24	59459.46	28016.88	15869.57	4275.77	3261.90	910.49	116.27	1024.84
NMC100	NMC100 - 48	rim	200645.16	n/a	172131.15	141166.67	91282.05	2884.35	51737.45	25738.40	14440.99	4164.35	3380.95	1188.27	173.68	838.51
NMC100	NMC100 - 49	core	219032.26	n/a	184426.23	142000.00	98974.36	3469.39	49420.85	24156.12	11987.58	3077.99	2176.19	743.83	138.76	434.78
NMC100	NMC100 - 50	rim	193870.97	n/a	180327.87	141833.33	98461.54	3319.73	57915.06	30168.78	19472.05	5139.28	3914.29	1175.93	181.82	1304.35
NMC100	NMC100 - 51	rim	206451.61	n/a	185245.90	137666.67	108717.95	3578.23	58687.26	32067.51	19565.22	5640.67	4561.90	1546.30	229.67	962.73
NMC100	NMC100 - 52	core	249354.84	n/a	168852.46	128833.33	74358.97	9646.26	46640.93	31856.54	23602.48	7214.48	7571.43	2870.37	598.09	2577.64
NMC100	NMC100 - 53	rim	234516.13	n/a	204918.03	154000.00	85641.03	2625.85	32007.72	10295.36	3913.04	832.87	357.14	b.d	b.d	b.d
NMC100	NMC100 - 54	core	225161.29	n/a	165573.77	132333.33	76923.08	4707.48	47490.35	32067.51	23385.09	8551.53	7904.76	2962.96	674.64	3788.82
NMC100	NMC100 - 55	rim	195806.45	n/a	186065.57	138333.33	93846.15	3170.07	56756.76	36497.89	22857.14	7214.48	5809.52	2067.90	349.28	2639.75
NMC100	NMC100 - 56	core	225806.45	n/a	184426.23	144166.67	93333.33	3006.80	58301.16	30168.78	19192.55	5264.62	4714.29	1388.89	234.45	1180.12
NMC100	NMC100 - 57	rim	213870.97	n/a	182786.89	140666.67	86153.85	4312.93	58301.16	32911.39	20217.39	5933.15	4495.24	1481.48	277.51	1304.35
NMC100	NMC100 - 58	rim	208064.52	n/a	179508.20	130333.33	92820.51	3333.33	55984.56	33122.36	20869.57	6657.38	5333.33	1774.69	291.87	1770.19
NMC100	NMC100 - 59	core	200322.58	n/a	192622.95	160000.00	100512.82	3061.22	34324.32	11983.12	4006.21	785.52	295.24	b.d	b.d	b.d
NMC100	NMC100 - 60	rim	247096.77	n/a	179508.20	131666.67	99487.18	7346.94	49227.80	28902.95	15062.11	3342.62	2609.52	895.06	112.92	652.17
NMC100	NMC100 - 61	rim	258064.52	n/a	160655.74	123333.33	77948.72	9972.79	47876.45	32911.39	22329.19	7033.43	5714.29	1975.31	392.34	1552.80
NMC100	NMC100 - 62	rim	282903.23	n/a	166393.44	130333.33	78461.54	12653.06	52509.65	33966.24	22919.25	6587.74	5333.33	1972.22	258.37	776.40
NMC100	NMC100 - 63	core	204838.71	n/a	190163.93	151500.00	93333.33	3401.36	31544.40	11181.43	4689.44	803.62	476.19	b.d	b.d	b.d
NMC100	NMC100 - 64	core	187419.35	n/a	197540.98	162333.33	89743.59	2312.93	31891.89	10316.46	4130.43	806.41	433.33	b.d	b.d	b.d
NMC100	NMC100 - 65	core	220967.74	n/a	224590.16	171000.00	94358.97	3401.36	34208.49	11012.66	4534.16	874.65	314.29	b.d	b.d	b.d
NMC100	NMC100 - 66	rim	262580.65	n/a	171311.48	138833.33	93333.33	9795.92	61389.96	37974.68	27018.63	7604.46	6095.24	1975.31	373.21	1614.91
NMC100	NMC100 - 68	core	259032.26	n/a	185245.90	136666.67	87179.49	7727.89	49266.41	27215.19	15776.40	4247.91	2714.29	762.35	167.46	465.84
NMC100	NMC100 - 69	rim	235806.45	n/a	177049.18	130833.33	74871.79	8571.43	52123.55	32911.39	23571.43	6908.08	6238.10	2376.54	449.76	1987.58
NMC100	NMC100 - 70	rim	211612.90	n/a	181967.21	149833.33	100512.82	4095.24	36602.32	12637.13	4316.77	823.12	376.19	175.93	b.d	b.d
NMC100	NMC100 - 71	rim	270000.00	n/a	179508.20	141833.33	82051.28	9659.86	52123.55	32067.51	16770.19	3133.70	1842.86	311.73	48.80	b.d
NMC100	NMC100 - 72	mantle	170322.58	n/a	166393.44	135166.67	93333.33	3360.54	32046.33	9662.45	3385.09	491.64	280.95	92.59	b.d	b.d
NMC100	NMC100 - 73	rim	234516.13	n/a	186065.57	148333.33	93846.15	4149.66	54440.15	22025.32	9285.71	1699.16	890.48	287.04	35.89	b.d
NMC100	NMC100 - 74	rim	244193.55	n/a	183606.56	127833.33	88205.13	7891.16	53281.85	29535.87	15124.22	2827.30	1495.24	345.68	b.d	341.61
NMC100	NMC100 - 75	core	214193.55	n/a	172131.15	149166.67	81538.46	1850.34	46332.05	22827.00	12142.86	2896.94	1814.29	604.94	74.16	b.d
NMC100	NMC100 - 76	rim	203548.39	n/a	181147.54	144500.00	86666.67	3850.34	53667.95	27426.16	14409.94	3690.81	2485.71	657.41	157.89	931.68
NMC100	NMC100 - 77	rim	251935.48	n/a	187704.92	132500.00	86153.85	4897.96	54054.05	28902.95	16242.24	3927.58	2252.38	706.79	86.60	869.57
NMC100	NMC100 - 78	rim	271290.32	n/a	168852.46	128333.33	66666.67	14829.93	40694.98	25443.04	17515.53	5710.31	5361.90	2561.73	483.25	3509.32
NMC100	NMC100 - 79	rim	222258.06	n/a	182786.89	161833.33	96410.26	3605.44	36756.76	13270.04	5186.34	970.75	552.38	64.81	b.d	b.d
NMC100	NMC100 - 80	core	226451.61	n/a	192622.95	162500.00	85641.03	2217.69	30077.22	8776.37	2822.98	589.14	371.43	b.d	19.14	b.d
NMC100	NMC100 - 81	core	248064.52	n/a	184426.23	139166.67	77435.90	2625.85	47876.45	22299.58	10683.23	2437.33	1580.95	354.94	46.41	b.d
NMC100	NMC100 - 82	rim	217096.77	n/a	196721.31	148666.67	90769.23	2054.42	32818.53	9915.61	2981.37	459.61	252.38	b.d	b.d	b.d
NMC100	NMC100 - 83	core	225483.87	n/a	181967.21	161000.00	84615.38	1823.13	28610.04	8459.92	3381.99	633.70	328.57	b.d	b.d	b.d
NMC100	NMC100 - 84	mantle	199677.42	n/a	181147.54	133833.33	86153.85	3061.22	36795.37	12552.74	4347.83	740.95	195.24	b.d	b.d	b.d
NMC100	NMC100 - 85	rim	240645.16	n/a	181147.54	137333.33	88717.95	2285.71	49691.12	24915.61	12422.36	3871.87	2480.95	496.91	93.30	b.d
NMC100	NMC100 - 86	mantle	190322.58	n/a	192622.95	158333.33	99487.18	2707.48	31389.96	9831.22	3198.76	607.24	185.71	b.d	b.d	b.d
NMC100	NMC100 - 87	mantle	239032.26	n/a	159836.07	138833.33	83076.92	6204.08	53667.95	28691.98	14192.55	2869.08	1623.81	256.17	59.81	b.d
NMC100	NMC100 - 88	rim	178387.10	n/a	161475.41	147166.67	83076.92	2802.72	26525.10	8502.11	2770.19	442.90	261.90	b.d	b.d	b.d
NMC100	NMC100 - 89	mantle	232580.65	n/a	194262.30	145500.00	75384.62	2108.84	14555.98	4978.90	1801.24	461.00	195.24	b.d	b.d	b.d
NMC100	NMC100 - 90	mantle	188387.10	n/a	192622.95	143166.67	78974.36	1972.79	30231.66	8839.66	3354.04	601.67	257.14	b.d	b.d	b.d
NMC100	NMC100 - 92	rim	201290.32	n/a	181967.21	152666.67	90256.41	3442.18	29768.34	9767.93	2950.31	434.54	171.43	b.d	b.d	316.77
NMC100	NMC100 - 93	rim	172258.06	n/a	177049.18	147500.00	91282.05	2897.96	51351.35	23417.72	12422.36	3314.76	2380.95	660.49	141.15	1211.18
NMC100	NMC100 - 94	core	210000.00	n/a	173770.49	133666.67	87179.49	3319.73	39266.41	15147.68	6149.07	1016.71	547.62	b.d	b.d	b.d
NMC100	NMC100 - 95	core	262258.06	n/a	207377.05	158500.00	91794.87	7727.89	52123.55	24050.63	14068.32	3245.13	1990.48	444.44	53.59	b.d
NMC100	NMC100 - 96	core	196451.61	n/a	184426.23	155666.67	105641.03	3102.04	46718.15	20400.84	9006.21	2158.77	1104.76	382.72	71.29	b.d
NMC100	NMC100 - 97	core	172258.06	n/a	163934.43	140833.33	79487.18	2748.30	26602.32	8649.79	3198.76	561.28	233.33	b.d	b.d	b.d
NMC100	NMC100 - 98	rim	198709.68	n/a	156557.38	129333.33	73846.15	5346.94	44401.54	20864.98	8881.99	1754.87	1080.95	191.36	30.14	b.d
NMC100	NMC100 - 99	core	174193.55	n/a	168032.79	124666.67	84102.56	3319.73	29922.78	9535.87	3478.26	583.57	309.52	b.d	b.d	b.d
NMC100	NMC100 - 100	rim	282580.65	n/a	185245.90	152000.00	96410.26	10340.14	64864.86	35801.69	21677.02	4108.64	2438.10	654.32	65.55	b.d
NMC100	NMC100 - 101	rim	293548.39	n/a	204918.03	156166.67	107179.49	5850.34	61003.86	29746.84	12391.30	2116.99	728.57	219.14	b.d	b.d
NMC100	NMC100 - 102	core	262903.23	n/a	188524.59	162666.67	103076.92	7959.18	61389.96	30801.69	13757.76	2423.40	828.57	169.75	b.d	b.d
NMC100	NMC100 - 103	rim	289354.84	n/a	204918.03	156333.33	104615.38	7619.05	62934.36	29324.89	13664.60	2381.62	1100.00	299.38	b.d	b.d

Table D.16: LASS ICP-MS U–Pb isotopic data for zircon – IC machine settings for rim analyses, FC machine settings for core analyses. Sample NMC68.

sample ID	spot	instrument settings	CL	group	comment	$^{238}U/^{206}Pb$	2σ	$^{207}Pb/^{206}Pb$	2σ	$^{206}Pb/^{238}U$ Age (Ma)	2σ	$^{207}Pb/^{206}Pb$ Age (Ma)	2σ	7/6 discordance (%)	6/8 discordance (%)	U (ppm)	Pb (ppm)
NMC68	1	IC	Oh	S	bright oscillatory grain, elongated, no clear overgrowth	3.594536	0.1149942	0.1	0.0016	1582	45	1621	29	2.41	-2.465234	n/a	n/a
NMC68c	1	FC	Oh	S	bright oscillatory grain, elongated, no clear overgrowth (same as rim spot 1)	3.198976	0.03786376	0.1099	0.0079	1754	18	1796	130	2.34	-2.394527	185	2510
NMC68	2	IC	Oh	P	bright oscillatory fragment as core in ovoidal grain, faint rim	3.746722	0.101073	0.1002	0.0014	1525	37	1626	27	6.21	-6.622951	n/a	n/a
NMC68c	2	FC	Oi	P	faint oscillatory fragment as core in ovoidal grain, faint rim	3.32668	0.03430708	0.1093	0.008	1694.3	15	1784	130	5.03	-5.294222	125.1	1310
NMC68c	3	FC	Oh	P	bright oscillatory fragment as core in ovoidal grain, faint rim	4.50045	0.04658432	0.0897	0.0066	1293.3	12	1415	140	8.60	-9.410036	196.4	719
NMC68c	3	FC	Oh	S	bright oscillatory fragment as core in ovoidal grain, faint rim	3.532321	0.03618414	0.1036	0.0074	1606.8	14	1688	130	4.81	-5.053523	308	3419
NMC68	3	IC	Oi	S	faint oscillatory fragment as core in ovoidal grain, faint rim	3.156566	0.08469321	0.10704	0.0014	1774	42	1748	24	-1.49	1.465614	n/a	n/a
NMC68	4	IC	MR	D	thin rim on oscillatory zoned core, discordant	5.892752	0.1354256	0.07911	0.00096	1010.6	21	1174	24	13.92	-16.168613	no value	no value
NMC68	5	IC	Oi	P	elongated hypidioblastic grain with oscillatory zoning	3.533569	0.08240832	0.1036	0.0011	1606	33	1688.6	20	4.89	-5.143213	n/a	n/a
NMC68c	5	FC	Oh	S	bright oscillatory fragment as core in rounded grain, faint rim	3.012048	0.09072434	0.112	0.0094	1845	50	1816	160	-1.60	1.571816	65	750
NMC68	6	IC	MR	D	thin rim on oscillatory zoned core, discordant	28.08989	1.262467	0.0592	0.0021	225.4	10	565	80	60.11	-150.665484	no value	no value
NMC68c	6	FC	Oh	S	bright oscillatory fragment as core in rounded grain, faint rim	3.284072	0.05716119	0.1024	0.0076	1713	26	1673	130	-2.39	2.335085	123.4	1893
NMC68c	7	FC	C	D	oscillatory zoned fragment, discordant and disregarded	3.93391	0.04797452	0.1002	0.0071	1460	16	1625	130	10.15	-11.301370	265.6	2020
NMC68	7	IC	MR	D	thin rim on oscillatory zoned core, discordant	4.273504	0.09861933	0.1009	0.0017	1355.5	28	1640	31	17.35	-20.988565	no value	no value
NMC68	8	IC	Oh	P	bright oscillatory fragment as core in ovoidal grain, faint rim	3.372681	0.07962485	0.10724	0.0011	1674	35	1752.1	19	4.46	-4.665472	n/a	n/a
NMC68c	8	FC	Oh	S	bright oscillatory fragment as core in rounded grain, faint rim	3.218539	0.04350777	0.1076	0.0086	1744	21	1777	150	1.86	-1.892202	76.7	1150
NMC68	9	IC	MR	D	thin rim on oscillatory zoned core, discordant	5.567929	0.1705101	0.08744	0.00096	1064	30	1369	21	22.28	-28.665414	no value	no value
NMC68c	9	FC	Oh	S	bright oscillatory fragment as core in elongated grain, faint rim	3.216468	0.03931354	0.1082	0.0078	1745	18	1766	130	1.19	-1.203438	166	2210
NMC68	10	IC	Oh	P	bright oscillatory fragment as core in ovoidal grain, faint rim	4.009623	0.1028933	0.09763	0.0011	1435	33	1578.4	21	9.09	-9.993003	n/a	n/a
NMC68c	10	FC	Oh	Y	bright oscillatory fragment as core in rounded grain, faint rim	3.597122	0.1682108	0.099	0.0075	1581	64	1599	140	1.13	-1.138520	173	905
NMC68c	11	FC	Cl	D	elongated hypidioblastic grain with low Cl response (metamict?)	5.291005	0.2603511	0.0809	0.0069	1115	50	1219	170	8.53	-9.327354	433	400
NMC68	11	IC	Oh	S	bright oscillatory fragment as core in ovoidal grain, faint rim	3.558719	0.2659541	0.0986	0.0037	1590	100	1588	71	-0.13	0.125786	n/a	n/a
NMC68	12	IC	Oi	P	faint oscillatory fragment as core in ovoidal grain, faint rim	3.773585	0.1238875	0.10299	0.0013	1515	44	1677	24	9.66	-10.693069	n/a	n/a
NMC68c	12	FC	Oi	P	faint oscillatory fragment as core in elongated grain, faint rim	3.748126	0.04916957	0.1014	0.0075	1524	18	1645	140	7.36	-7.939633	178	1330
NMC68c	13	FC	C	D	oscillatory zoned fragment, discordant and disregarded	4.361099	0.05705755	0.0987	0.0072	1331	16	1595	140	16.55	-19.834711	293	1748
NMC68	13	IC	Oi	S	oscillatory part of core overgrown by faint sector zoned rim	3.064664	0.06856283	0.11019	0.0012	1820.6	36	1801.6	19	-1.05	1.043612	n/a	n/a
NMC68	14	IC	Oh	P	bright oscillatory fragment as core in ovoidal grain, faint rim (mixed age?)	4.009623	0.1028933	0.09763	0.0011	1435	33	1578.4	21	9.09	-9.993003	n/a	n/a
NMC68c	14	FC	Oh	S	bright oscillatory fragment as core in rounded cracked and healed grain, faint rim	3.054368	0.03171915	0.1109	0.0084	1826	17	1808	140	-1.00	0.985761	120	1064
NMC68	15	IC	Oi	S	hypidioblastic oscillatory zoned grain	3.516174	0.09025342	0.1	0.0017	1613	37	1623	32	0.62	-0.619963	n/a	n/a
NMC68c	15	FC	Oh	S	bright oscillatory fragment as core in ovoidal grain, faint rim	3.422313	0.09018417	0.1061	0.0077	1652	39	1729	130	4.45	-4.661017	193.5	1656
NMC68c	16	FC	C	D	oscillatory zoned fragment, discordant and disregarded	4.734848	0.05156322	0.0927	0.0066	1235.3	12	1487	130	16.93	-20.375617	418	2130
NMC68	16	IC	Oh	D	bright oscillatory fragment as core in ovoidal grain, faint rim, mixed age!	5.567929	0.1333079	0.07746	0.0008	1065	24	1132.1	21	5.93	-6.300469	n/a	n/a
NMC68	17	IC	MR	D	thin rim on oscillatory zoned core, discordant	4.830918	0.2800532	0.0912	0.0013	1210	62	1448	28	16.44	-19.669421	no value	no value
NMC68c	17	FC	Oh	P	bright oscillatory fragment as core in elongated grain, faint rim, healed cracks	3.912363	0.09796214	0.0992	0.0072	1467	33	1604	140	8.54	-9.338787	246	2159
NMC68c	18	FC	Oh	P	bright oscillatory fragment as core in elongated grain, faint rim	3.323363	0.03755213	0.1088	0.0088	1696	17	1802	140	5.88	-6.250000	94.7	1472
NMC68	18	IC	Oi	P	faint oscillatory fragment as core in ovoidal grain, faint rim	3.311258	0.08442612	0.1093	0.0018	1701	38	1786	30	4.76	-4.997061	n/a	n/a
NMC68c	19	FC	Oh	P	bright oscillatory fragment as core in elongated hypidioblastic grain, faint rim	3.556188	0.05564447	0.1075	0.0079	1597	22	1753	130	8.90	-9.768316	130.1	1860
NMC68	19	IC	Oh	P	bright oscillatory fragment as core in ovoidal grain, faint rim	3.244646	0.07685243	0.10945	0.0012	1732	36	1791.7	21	3.33	-3.446882	n/a	n/a
NMC68	20	IC	MR	D	thin rim on oscillatory zoned core, discordant	3.878976	0.1263902	0.10559	0.0012	1478	43	1724	21	14.27	-16.644114	no value	no value
NMC68c	20	FC	Oh	P	bright oscillatory fragment as core in elongated grain, faint rim	4.065041	0.1007998	0.0952	0.0072	1417	31	1535	130	7.69	-8.327452	154.2	1235
NMC68	21	IC	Si	M	faint sector zoned rim overgrowing oscillatory zoned fragment	5.688929	0.1262193	0.07379	0.00087	1043.8	22	1035	24	-0.85	0.843073	n/a	n/a
NMC68c	21	FC	Oi	P	faint oscillatory fragment as core in ovoidal grain, faint rim	3.773585	0.03844785	0.0997	0.0071	1515.2	14	1615	130	6.18	-6.586589	246.6	1909
NMC68	22	IC	MR	D	thin rim on oscillatory zoned core, discordant	4.158004	0.09508949	0.10147	0.0011	1389.3	29	1650.3	19	15.82	-18.786439	no value	no value
NMC68c	22	FC	Oi	P	faint oscillatory fragment as core in fragmented grain, faint rim	3.703704	0.09465021	0.1041	0.0076	1540	35	1694	140	9.09	-10.000000	180	1351
NMC68	23	IC	Oh	P	bright oscillatory fragment as core in ovoidal grain, faint rim	3.546099	0.07922137	0.10471	0.0012	1601.4	32	1711	20	6.41	-6.844011	n/a	n/a
NMC68c	23	FC	Oh	S	bright oscillatory fragment as core in rounded grain, faint rim	3.460208	0.05268136	0.103	0.008	1636	22	1669	150	1.98	-2.017115	102	1363
NMC68c	24	FC	Oh	P	bright oscillatory fragment as core in elongated grain, faint rim	3.759398	0.1370908	0.0998	0.0072	1519	50	1617	140	6.06	-6.451613	304	2405
NMC68	24	IC	Oi	P	faint oscillatory fragment as core in ovoidal grain, faint rim	3.445899	0.1306164	0.1057	0.0015	1642	54	1725	27	4.81	-5.054811	n/a	n/a
NMC68	25	IC	Cl	D	faint, convoluted zonig at core of rounded grain (Pb loss?), missed grain	6.02047	0.1449842	0.07511	0.00089	990.5	22	1070	24	7.43	-8.026249	n/a	n/a
NMC68c	25	FC	Oi	P	faint oscillatory fragment as core in ovoidal grain, faint rim	3.07787	0.03410382	0.1055	0.0077	1814	18	1719	130	-5.53	5.237045	112.3	1477
NMC68	26	IC	MR	D	thin rim on oscillatory zoned core, discordant	5.763689	0.1959986	0.0855	0.0024	1031	32	1332	56	22.60	-29.194956	no value	no value
NMC68c	26	FC	Oh	P	bright oscillatory fragment as core in elongated grain, faint rim	3.802281	0.1590308	0.1013	0.0085	1503	58	1632	160	7.90	-8.582834	123	850
NMC68	27	IC	MR	D	thin rim on oscillatory zoned core, discordant	3.910833	0.0871793	0.10344	0.0012	1467.7	29	1686	21	12.95	-14.873612	no value	no value
NMC68c	27	FC	Oi	P	faint oscillatory fragment as core in ovoidal grain, faint rim	3.957262	0.05011174	0.0981	0.0073	1452	16	1606	140	9.59	-10.606061	199.4	1340
NMC68c	28	FC	Oh	P	bright oscillatory part of angular cracked and healed grain	5.339028	0.06841254	0.0816	0.0062	1106.5	13	1229	150	9.97	-11.070944	199	404
NMC68	28	IC	Oi	S	oscillatory zoned core of round grain	3.149606	0.07142414	0.107	0.0011	1777.7	35	1748	19	-1.70	1.670698	n/a	n/a
NMC68c	29	FC	Oi	P	faint oscillatory fragment as core in elongated grain, faint rim	3.762227	0.03680132	0.1011	0.0072	1519.6	13	1642	140	7.45	-8.054751	242.2	2023
NMC68	29	IC	Oi	P	faint oscillatory fragment as core in ovoidal grain, faint rim	3.373819	0.07626379	0.10665	0.0012	1673.4	33	1742	21	3.94	-4.099438	n/a	n/a
NMC68c	30	FC	Oh	S	bright oscillatory fragment as core in ovoidal grain, faint rim	3.096934	0.0402822	0.1103	0.0082	1804	20	1800	130	-0.22	0.221729	136	1810
NMC68c	31	FC	Oi	P	faint oscillatory fragment as core in elongated grain, faint rim	3.599712	0.05831067	0.1051	0.0075	1580	23	1715	130	7.87	-8.544304	287	3370
NMC68c	32	FC	Oi	P	faint oscillatory fragment as core in ovoidal grain, faint rim	3.332223	0.03442149	0.1097	0.0081	1691.6	15	1790	140	5.50	-5.816978	160.4	1707
NMC68c	33	FC	Oh	S	bright oscillatory fragment as core in rounded grain, faint rim	3.229974	0.0312982	0.1088	0.0077	1738.9	15	1779	130	2.25	-2.306056	250	2616
NMC68c	34	FC	C	D	oscillatory zoned fragment, discordant and disregarded	3.998401	0.09752197	0.1096	0.0094	1438	32	1800	140	20.11	-25.173853	85.3	890
NMC68c	35	FC	Oh	S	bright oscillatory fragment as core in elongated grain, faint rim	3.075031	0.03593209	0.1103	0.0079	1815	18	1802	130	-0.72	0.716253	151.1	1690
NMC68c	36	FC	Oi	P	faint oscillatory fragment as core in ovoidal grain, faint rim	3.517411	0.0408282	0.1059	0.0076	1613	17	1733	140	6.92	-7.439554	236.2	2440
NMC68c	37	FC	Oi	S	faint oscillatory fragment as core in elongated grain, faint rim	3.219575	0.03938952	0.1083	0.0077	1743	19	1769	130	1.47	-1.491681	257.7	2340
NMC68c	38	FC	Oi	P	faint oscillatory fragment as core in elongated grain, faint rim	4.199916	0.09701612	0.09316	0.0066	1376	29	1489	130	7.59	-8.212209	313	807
NMC68c	39	FC	C	D	oscillatory zoned fragment, discordant and disregarded	4.230118	0.0554711	0.0948	0.0068	1368	16	1527	130	10.41	-11.622807	244	1180
NMC68c	40	FC	Oi	P	faint oscillatory fragment as core in ovoidal grain, faint rim	3.422548	0.03162735	0.1072	0.0076	1652.4	14	1755	140	5.85	-6.209150	252	2197
NMC68c	41	FC	Oh	S	bright oscillatory fragment as core in ovoidal grain, faint rim	3.362475	0.03617996	0.1067	0.0082	1678.5	16	1736	140	3.31	-3.425678	129	1743
NMC68c	42	FC	Oi	P	faint oscillatory fragment as core in anhedral grain, faint rim	3.984064	0.1746904	0.0961	0.0071	1444	55	1555	130	7.14	-7.686981	329	1487
NMC68c	43	FC	Oh	S	bright oscillatory fragment as core in rounded grain, faint rim	3.060912	0.03372906	0.1109	0.0081	1822	18	1810	130	-0.66	0.658617	121	1610
NMC68c	44	FC	Oh	S	bright oscillatory fragment as core in ovoidal grain, faint rim	3.087373	0.03336154	0.1076	0.01	1808.9	17	1810	160	0.06	-0.060810	64.8	755
NMC68c	45	FC	Oh	S	bright oscillatory fragment as core in ovoidal grain, faint rim	3.114295	0.04267486	0.107	0.0083	1795	21	1739	140	-3.22	3.119777	77.7	1280
NMC68c	46	FC	Oi	P	faint oscillatory fragment as core in ovoidal grain, faint rim	3.373819	0.05918981	0.1107	0.0083	1673	26	1805	140	7.31	-7.890018	129.5	1490
NMC68c	47	FC	Oh	S	bright oscillatory fragment as core in elongated grain, faint rim	3.228931	0.07819498	0.1096	0.0078	1739	37	1790	130	2.85	-2.932720	197	3290
NMC68c	48	FC	Oh	S	bright oscillatory fragment as core in rounded grain, faint rim	3.292723	0.03686289	0.1073	0.0076	1710	17	1753	130	2.45	-2.514620	384	4383
NMC68c	49	FC	Oi	P	faint oscillatory fragment as core in ovoidal grain, faint rim	3.500175	0.04042904	0.1052	0.0075	1620	17	1716	130	5.59	-5.925926	354	3510
NMC68c	50	FC	Oi	S	faint oscillatory fragment as core in ovoidal grain, faint rim	3.298153	0.03698457	0.1086	0.0082	1707.2	17	1769	140	3.49	-3.619963	107	1590
NMC68c	51	FC	C	D	oscillatory zoned fragment, discordant and disregarded	4.050223	0.05577464	0.1016	0.0073	1422	18	1650	130	13.82	-16.033755	232	2110
NMC68c	52	FC	Oh	S	bright oscillatory fragment as core in ovoidal grain, faint rim	3.312355	0.03401226	0.1097	0.0082	1700.7	15	1789	140	4.94	-5.191980	153.9	1386
NMC68c	53	FC	Oh	P	bright oscillatory fragment as core in elongated grain, faint rim	3.563792	0.04191202	0.1048	0.0076	1594	17	1707	130	6.62	-7.089084	183	1314
NMC68c	54	FC	C	D	oscillatory zoned fragment, discordant and disregarded	4.889976	0.08369151	0.0864	0.0064	1199	19	1352	150	11.32	-12.760634	244	895
NMC68c	55	FC	Oi	D	faint oscillatory fragment as core in angular grain, faint rim	4.118616	0.0695483	0.0963	0.0074	1401	21	1546	140	9.38	-10.349750	121.2	1085
NMC68c	56	FC	Oh	P	bright oscillatory fragment as core in elongated cracked and healed grain, faint rim	3.456619	0.1015599	0.1073	0.0092	1637	43	1757	140	6.83	-7.330483	74.5	616
NMC68c	57	FC	Oh	S	bright oscillatory fragment as core in elongated grain, faint rim	3.171583	0.03721806	0.1072	0.008	1767	18	1746	140	-1.20	1.188455	127	1970

Table D.17: LASS ICP-MS chondrite-normalised REE data for zircon (ppm) – IC machine settings for rim analyses, FC machine settings for core analyses. Sample NMC68.

sample ID	spot	instrument settings	CL	group	La	Ce	Pr	Nd	Sm	Eu	Gd	Tb	Dy	Ho	Er	Tm	Yb	Lu
NMC68	NMC68 - 21	IC	Sl	M	0.00	3.58	0.00	0.00	0.00	0.00	35.52	137.34	238.82	378.83	483.33	496.91	545.93	627.33
NMC68	NMC68 - 2	IC	Oh	P	0.00	60.15	0.00	15.00	58.97	36.73	125.87	266.03	433.54	768.80	1163.81	1598.77	2162.68	3195.65
NMC68	NMC68 - 5	IC	Ol	P	0.00	71.53	20.49	45.17	122.56	70.75	267.95	468.35	731.99	1387.19	1861.90	2484.57	3229.67	4472.05
NMC68	NMC68 - 8	IC	Oh	P	0.02	112.75	16.56	44.67	122.05	94.42	280.70	497.89	782.61	1373.26	1980.95	2558.64	3325.36	4658.39
NMC68	NMC68 - 10	IC	Oh	P	0.00	46.29	11.31	31.83	84.10	61.22	164.86	335.44	525.78	885.79	1338.10	1768.52	2258.37	3217.39
NMC68	NMC68 - 12	IC	Ol	P	0.00	59.90	9.75	18.50	31.28	25.85	98.07	196.20	298.14	522.28	795.24	1160.49	1679.43	2543.48
NMC68	NMC68 - 14	IC	Oh	P	0.00	64.11	20.82	34.17	58.46	62.59	105.41	213.08	360.87	547.35	866.67	1154.32	1492.82	2198.76
NMC68	NMC68 - 16	IC	Oh	P	0.00	12.62	0.00	0.00	19.49	0.00	48.65	148.95	278.57	516.71	740.95	1033.95	1387.56	1937.89
NMC68	NMC68 - 18	IC	Ol	P	0.00	98.76	81.15	115.00	141.03	66.67	234.36	379.75	596.27	987.47	1409.05	1891.98	2473.68	3652.17
NMC68	NMC68 - 19	IC	Oh	P	0.00	94.93	50.00	90.00	211.28	156.46	343.63	521.10	807.45	1267.41	1690.48	2160.49	2765.55	3944.10
NMC68	NMC68 - 23	IC	Oh	P	0.04	35.52	0.00	15.83	34.87	12.79	88.42	179.32	322.98	603.06	957.14	1287.04	1741.63	2655.28
NMC68	NMC68 - 24	IC	Ol	P	0.03	24.26	0.00	0.00	17.95	0.00	56.37	147.05	247.52	470.75	722.38	972.22	1392.34	2096.27
NMC68	NMC68 - 25	IC	Cl	P	0.00	5.33	0.00	0.00	0.00	0.00	24.71	90.51	200.62	339.83	494.76	626.54	779.90	1012.42
NMC68	NMC68 - 29	IC	Ol	P	0.00	61.14	0.00	15.17	62.05	31.43	120.85	225.74	392.24	681.06	1028.57	1388.89	1784.69	2559.01
NMC68c	NMC68c - 2	FC	Ol	P	0.00	44.06	5.57	11.83	54.87	30.88	136.29	232.07	354.04	597.49	919.05	1185.19	1665.07	2347.83
NMC68c	NMC68c - 11	FC	Cl	P	0.00	23.02	5.82	7.50	22.05	16.19	72.20	158.02	320.50	519.50	752.38	922.84	1148.33	1574.53
NMC68c	NMC68c - 12	FC	Ol	P	0.00	76.98	9.02	14.17	71.79	53.88	172.97	322.78	498.76	824.51	1227.14	1524.69	2090.91	2773.29
NMC68c	NMC68c - 17	FC	Oh	P	0.00	90.97	22.05	35.67	116.41	88.98	282.24	414.77	649.07	1093.31	1580.00	2024.69	2684.21	3726.71
NMC68c	NMC68c - 18	FC	Oh	P	0.00	43.56	5.74	15.83	69.23	70.88	195.37	274.47	418.63	664.35	967.14	1228.40	1622.01	2251.55
NMC68c	NMC68c - 19	FC	Oh	P	0.00	56.81	13.85	24.17	97.95	93.88	239.38	358.65	521.74	806.41	1168.10	1425.93	1918.66	2757.76
NMC68c	NMC68c - 20	FC	Oh	P	0.00	51.11	24.26	40.33	147.69	134.69	307.72	440.93	618.01	969.36	1352.38	1626.54	2129.19	3006.21
NMC68c	NMC68c - 21	FC	Ol	P	0.00	66.34	5.82	11.67	44.62	20.82	132.05	233.33	348.45	637.88	986.67	1333.33	1822.97	2618.01
NMC68c	NMC68c - 22	FC	Ol	P	0.00	42.33	8.03	14.17	42.05	36.33	153.67	236.29	364.91	643.45	970.00	1243.83	1712.92	2496.89
NMC68c	NMC68c - 24	FC	Oh	P	0.00	89.11	33.61	31.67	84.62	57.14	174.90	312.24	478.26	839.83	1257.14	1694.44	2272.73	3319.88
NMC68c	NMC68c - 25	FC	Ol	P	0.00	59.28	8.11	15.67	78.97	75.37	187.26	314.35	496.89	810.59	1166.67	1469.14	1990.43	2742.24
NMC68c	NMC68c - 26	FC	Oh	P	0.00	38.49	10.25	19.17	51.79	40.27	138.22	206.33	318.32	532.03	795.24	996.91	1430.62	2012.42
NMC68c	NMC68c - 27	FC	Ol	P	0.00	58.17	15.00	21.50	69.23	47.07	156.76	240.72	378.57	689.42	1056.19	1422.84	1897.13	2795.03
NMC68c	NMC68c - 28	FC	Oh	P	0.00	33.79	25.33	36.83	105.13	75.10	154.83	206.75	279.50	431.75	607.14	808.64	1081.34	1627.33
NMC68c	NMC68c - 29	FC	Ol	P	0.00	48.64	4.51	10.83	42.56	28.03	137.84	281.01	419.57	761.84	1194.29	1570.99	2181.82	3090.06
NMC68c	NMC68c - 31	FC	Ol	P	0.00	97.28	25.33	48.33	136.92	74.15	327.41	455.49	713.66	1178.27	1704.76	2203.70	2889.95	3947.21
NMC68c	NMC68c - 32	FC	Ol	P	0.00	52.35	4.67	8.33	42.05	41.50	148.65	259.70	413.98	729.81	1152.38	1515.43	1952.15	2739.13
NMC68c	NMC68c - 36	FC	Ol	P	0.00	65.72	7.87	18.83	74.36	51.70	182.24	311.39	506.21	877.44	1347.62	1703.70	2320.57	3217.39
NMC68c	NMC68c - 38	FC	Ol	P	0.00	56.68	27.13	37.17	80.51	40.95	131.27	176.79	265.84	462.81	750.95	1095.68	1584.21	2462.73
NMC68c	NMC68c - 40	FC	Ol	P	0.00	69.93	4.75	8.33	48.72	29.12	147.49	240.51	422.36	740.95	1218.10	1645.06	2220.10	3257.76
NMC68c	NMC68c - 42	FC	Ol	P	0.00	60.15	7.21	7.33	33.33	25.31	89.96	155.06	275.78	508.36	870.95	1200.62	1746.41	2708.07
NMC68c	NMC68c - 46	FC	Ol	P	0.00	65.47	4.92	14.33	68.21	75.78	214.67	329.11	537.27	863.51	1285.71	1660.49	2095.69	2934.78
NMC68c	NMC68c - 49	FC	Ol	P	0.00	75.50	11.15	17.00	76.92	31.70	186.49	300.00	506.83	919.22	1430.95	1984.57	2602.87	3729.81
NMC68c	NMC68c - 53	FC	Oh	P	0.00	55.94	0.00	1.48	20.00	17.28	77.22	136.92	245.03	452.65	737.62	981.48	1425.84	2062.11
NMC68c	NMC68c - 55	FC	Ol	P	0.00	36.39	2.46	6.83	47.18	27.62	149.81	254.43	386.34	662.95	981.90	1277.78	1674.64	2251.55
NMC68c	NMC68c - 56	FC	Oh	P	0.00	31.56	2.30	3.27	16.92	17.69	57.14	112.66	179.50	332.87	541.43	740.74	1052.63	1512.42
NMC68	NMC68 - 1	IC	Oh	S	-0.10	42.82	0.00	26.33	53.33	35.37	106.56	210.97	357.14	643.45	880.95	1086.42	1459.33	2124.22
NMC68	NMC68 - 3	IC	Ol	S	0.00	64.36	3.61	27.50	48.21	34.83	162.55	329.11	552.80	984.68	1404.76	1898.15	2703.35	3850.93
NMC68	NMC68 - 11	IC	Oh	S	0.01	45.67	0.00	0.00	20.51	22.18	61.78	151.90	251.24	505.57	780.95	1191.36	1736.84	2645.96
NMC68	NMC68 - 13	IC	Ol	S	0.00	64.36	11.56	29.17	48.21	72.11	190.73	345.99	534.16	928.97	1371.43	1793.21	2459.33	3493.79
NMC68	NMC68 - 15	IC	Ol	S	0.09	52.10	0.00	8.50	36.92	16.87	77.22	171.94	262.42	495.82	729.05	1037.04	1425.84	1947.21
NMC68	NMC68 - 28	IC	Ol	S	0.07	58.42	6.48	20.50	38.97	19.32	130.89	248.95	401.24	715.88	1152.38	1577.16	2114.83	3096.27
NMC68c	NMC68c - 1	FC	Oh	S	0.00	115.10	66.39	66.67	122.56	56.73	231.66	390.30	592.55	1005.57	1475.24	1907.41	2497.61	3540.37
NMC68c	NMC68c - 3	FC	Oh	S	0.00	26.14	3.93	6.83	36.92	27.89	112.74	187.34	299.07	498.61	793.81	1098.77	1591.39	2198.76
NMC68c	NMC68c - 5	FC	Oh	S	0.06	25.74	0.78	4.20	22.46	33.06	99.61	163.71	260.87	459.61	680.95	867.28	1224.88	1711.18
NMC68c	NMC68c - 6	FC	Oh	S	0.00	64.36	12.87	23.83	100.51	113.88	279.92	402.95	603.73	966.57	1390.95	1759.26	2339.71	3124.22
NMC68c	NMC68c - 8	FC	Oh	S	0.00	45.05	7.30	17.00	62.05	70.34	187.26	268.35	445.03	740.95	1076.19	1376.54	1794.26	2487.58
NMC68c	NMC68c - 9	FC	Oh	S	0.01	66.21	4.02	15.83	82.56	79.59	235.14	394.51	607.76	991.64	1434.29	1830.25	2344.50	3304.35
NMC68c	NMC68c - 10	FC	Oh	S	0.00	30.45	2.87	10.83	34.36	23.67	109.65	174.68	277.64	498.61	784.76	1058.64	1413.88	2130.43
NMC68c	NMC68c - 14	FC	Oh	S	0.01	42.33	0.00	3.70	21.03	15.10	88.03	161.39	271.12	467.97	759.52	1030.86	1468.90	2158.39
NMC68c	NMC68c - 15	FC	Oh	S	0.00	52.48	4.84	11.33	61.54	65.31	205.02	341.77	506.52	889.97	1336.19	1746.91	2244.02	3124.22
NMC68c	NMC68c - 23	FC	Oh	S	0.00	40.35	3.77	13.17	73.33	109.52	252.90	386.08	596.27	935.93	1312.86	1672.84	2090.91	2897.52
NMC68c	NMC68c - 30	FC	Oh	S	0.06	75.99	2.79	7.33	44.10	63.54	179.92	319.20	492.24	810.59	1228.57	1561.73	1933.01	2714.29
NMC68c	NMC68c - 33	FC	Oh	S	0.00	107.92	2.53	7.33	46.15	58.23	206.95	357.59	619.57	1128.13	1745.71	2333.33	2995.22	4285.71
NMC68c	NMC68c - 34	FC	Oh	S	0.00	51.24	26.80	34.83	87.69	63.95	175.29	251.05	354.04	547.35	766.67	950.62	1282.30	1726.71
NMC68c	NMC68c - 37	FC	Ol	S	0.00	59.16	9.84	14.00	58.46	36.87	154.83	266.46	442.86	784.12	1250.00	1703.70	2354.07	3400.62
NMC68c	NMC68c - 41	FC	Oh	S	0.07	36.88	3.80	12.00	71.79	61.77	223.94	396.62	590.37	940.11	1379.52	1756.17	2162.68	2888.20
NMC68c	NMC68c - 43	FC	Oh	S	0.00	198.02	131.15	75.00	45.13	44.76	132.82	221.52	357.14	625.35	976.19	1231.48	1645.93	2350.93
NMC68c	NMC68c - 44	FC	Oh	S	0.09	46.91	1.15	5.50	32.31	39.32	100.39	179.75	278.26	504.18	789.05	990.74	1411.48	2006.21
NMC68c	NMC68c - 45	FC	Oh	S	0.00	32.92	5.57	10.33	79.49	91.16	212.74	316.46	478.26	749.30	1142.86	1419.75	1822.97	2487.58
NMC68c	NMC68c - 47	FC	Oh	S	0.00	129.95	75.41	80.00	189.74	176.87	426.64	639.24	870.50	1337.05	1871.43	2314.81	2889.95	3906.83
NMC68c	NMC68c - 48	FC	Oh	S	0.00	112.62	45.90	30.00	65.13	35.24	178.76	308.86	501.24	870.47	1305.71	1787.04	2349.28	3229.81
NMC68c	NMC68c - 50	FC	Ol	S	0.00	59.78	4.02	13.33	68.72	69.52	193.82	316.46	503.11	818.94	1185.71	1524.69	1937.80	2723.60
NMC68c	NMC68c - 52	FC	Oh	S	0.00	60.40	0.81	4.53	36.92	30.61	114.29	215.82	353.11	630.92	1037.62	1398.15	1971.29	2816.77
NMC68c	NMC68c - 57	FC	Oh	S	0.00	74.88	18.52	27.50	111.79	97.96	267.95	382.28	574.84	959.61	1357.14	1685.19	2172.25	2953.42

Table D.18: LASS ICP-MS U–Pb isotopic data for monazite. Sample NMC68.

sample ID	spot	location	$^{238}U/^{206}Pb$	2σ	$^{207}Pb/^{206}Pb$	2σ	$^{206}Pb/^{238}U$ Age (Ma)	2σ	$^{207}Pb/^{206}Pb$ Age (Ma)	2σ	7/6 discordance (%)	6/8 discordance (%)	U (ppm)	Th (ppm)	Pb (ppm)
NMC68	NMC68 - 1	rim	5.924171	0.1579311	0.07244	0.00064	1005	25	997	18	-0.80	0.80	11300	50500	3150
NMC68	NMC68 - 2	rim	5.793743	0.1376266	0.07176	0.00065	1026.6	22	978	18	-4.97	4.73	10100	45800	2890
NMC68	NMC68 - 3	rim	5.724098	0.1507204	0.07097	0.00054	1038	25	955	16	-8.69	8.00	7130	49700	3120
NMC68	NMC68 - 4	rim	5.841121	0.1364748	0.07249	0.0006	1018.8	22	998	17	-2.08	2.04	7380	48200	2950
NMC68	NMC68 - 5	rim	5.845902	0.1332808	0.07245	0.00031	1018	21	997.6	8.6	-2.04	2.00	9700	43800	2700
NMC68	NMC68 - 6	rim	5.882353	0.1487889	0.07193	0.00036	1012	23	987	12	-2.53	2.47	7170	48500	3010
NMC68	NMC68 - 7	core	5.803831	0.1347378	0.07148	0.00067	1024.5	22	970	19	-5.62	5.32	4880	49600	3130
NMC68	NMC68 - 8	rim	5.910165	0.1432132	0.07298	0.00072	1007.9	22	1012	20	0.41	-0.41	9600	42300	2650
NMC68	NMC68 - 9	rim	5.892752	0.145843	0.073	0.00062	1010	23	1013	17	0.30	-0.30	9800	44800	2730
NMC68	NMC68 - 10	rim	5.878895	0.1589825	0.0726	0.0018	1013	26	1012	56	-0.10	0.10	1120	93000	5710
NMC68	NMC68 - 11	rim	5.810575	0.1384274	0.07275	0.00083	1023.9	23	1006	23	-1.78	1.75	1440	101000	6000
NMC68	NMC68 - 12	rim	5.991612	0.1759071	0.0728	0.001	995	27	1005	29	1.00	-1.01	1350	99700	5910
NMC68	NMC68 - 13	rim	5.970149	0.1817777	0.071	0.0011	998	28	956	32	-4.39	4.21	1320	111000	6480
NMC68	NMC68 - 14	core	5.78369	0.1371494	0.07086	0.00041	1028.3	22	952	12	-8.01	7.42	6700	52000	3030
NMC68	NMC68 - 15	core	5.885815	0.1420356	0.0718	0.00086	1011.3	22	978	24	-3.40	3.29	5720	50600	3170
NMC68	NMC68 - 16	rim	5.970149	0.1782134	0.0715	0.0011	998	28	981	37	-1.73	1.70	1260	120000	7120
NMC68	NMC68 - 17	rim	5.740528	0.1384054	0.07159	0.00054	1034.9	23	973	15	-6.36	5.98	13600	50500	3120
NMC68	NMC68 - 18	core	5.787037	0.1339592	0.07159	0.00062	1027.5	22	973	18	-5.60	5.30	11500	47500	2900
NMC68	NMC68 - 19	rim	5.813953	0.1453488	0.07171	0.00055	1023	24	977	16	-4.71	4.50	8180	47100	2890
NMC68	NMC68 - 20	rim	5.807201	0.1652456	0.0733	0.0012	1024	27	1020	34	-0.39	0.39	1540	94000	5790
NMC68	NMC68 - 21	core	5.75374	0.1357326	0.07145	0.00062	1032.7	22	969	18	-6.57	6.17	10100	51500	3160
NMC68	NMC68 - 22	core	5.854801	0.1885328	0.072	0.0012	1016	30	985	34	-3.15	3.05	1620	90000	5360
NMC68	NMC68 - 23	rim	5.885815	0.1905355	0.0725	0.0015	1011	30	1008	44	-0.30	0.30	1110	109000	6480
NMC68	NMC68 - 24	rim	5.767013	0.1330337	0.07105	0.00041	1030.6	22	958	12	-7.58	7.04	10700	49700	3020
NMC68	NMC68 - 25	core	5.952381	0.1877834	0.07291	0.00096	1001	29	1010	27	0.89	-0.90	1090	103000	6160
NMC68	NMC68 - 26	rim	5.574136	0.1367124	0.072	0.00075	1064	24	984	21	-8.13	7.52	5980	42200	2470
NMC68	NMC68 - 27	core	5.760369	0.1360456	0.07073	0.00062	1031.7	23	948	18	-8.83	8.11	7600	43700	2690
NMC68	NMC68 - 28	rim	5.743825	0.1319661	0.07174	0.00062	1034.5	22	977	18	-5.89	5.56	8800	45100	2820
NMC68	NMC68 - 29	rim	5.885815	0.1524284	0.07141	0.00052	1012	24	968	15	-4.55	4.35	3330	51600	3170
NMC68	NMC68 - 30	rim	5.882353	0.1418685	0.0728	0.001	1011.9	22	1005	28	-0.69	0.68	3840	43300	2680
NMC68	NMC68 - 31	rim	5.78369	0.15722	0.0721	0.0011	1028	26	986	30	-4.26	4.09	1750	70600	4360
NMC68	NMC68 - 32	core	5.402485	0.1926332	0.07139	0.00099	1095	36	967	28	-13.24	11.69	3580	43900	2640
NMC68	NMC68 - 33	core	6.064281	0.1765224	0.07262	0.00054	984	26	1002	15	1.80	-1.83	8700	37700	2350
NMC68	NMC68 - 34	core	5.865103	0.1444776	0.07184	0.00077	1014.6	23	980	22	-3.53	3.41	2950	69500	4280
NMC68	NMC68 - 35	core	5.704507	0.1692153	0.07395	0.00072	1041	28	1039	20	-0.19	0.19	2930	92000	5830
NMC68	NMC68 - 36	rim	6.002401	0.1621297	0.07184	0.00079	993	25	980	23	-1.33	1.31	2180	61700	3750
NMC68	NMC68 - 37	core	5.934718	0.1514498	0.07185	0.00047	1004	24	981	13	-2.34	2.29	5600	53700	3320
NMC68	NMC68 - 38	rim	5.980861	0.1466599	0.07202	0.00073	996.7	23	993	25	-0.37	0.37	2420	57100	3470
NMC68	NMC68 - 39	rim	5.938242	0.1516297	0.072	0.0011	1003	24	984	31	-1.93	1.89	2300	63600	3680
NMC68	NMC68 - 40	rim	5.892752	0.1597328	0.07203	0.00077	1011	25	985	22	-2.64	2.57	3890	52200	3200

Table D.19: LASS ICP-MS chondrite-normalised REE data for monazite (ppm). Sample NMC68.

sample ID	spot	location	La	Ce	Pr	Nd	Sm	Eu	Gd	Tb	Dy	Ho	Er	Tm	Yb	Lu
NMC68	NMC68 - 1	rim	322548.39	n/a	186885.25	146333.33	93846.15	19183.67	57451.74	41561.18	30900.62	10139.28	8571.43	2777.78	564.59	2577.64
NMC68	NMC68 - 2	rim	281290.32	n/a	167213.11	148666.67	76923.08	20136.05	49806.95	34177.22	27981.37	9150.42	6904.76	2814.81	674.64	2236.02
NMC68	NMC68 - 3	rim	289677.42	n/a	202459.02	152500.00	94358.97	15510.20	55212.36	34177.22	24782.61	8022.28	5952.38	1820.99	315.79	2298.14
NMC68	NMC68 - 4	rim	298387.10	n/a	200819.67	152833.33	86666.67	18639.46	57528.96	36075.95	26118.01	8662.95	6619.05	2222.22	320.57	2267.08
NMC68	NMC68 - 5	rim	311290.32	n/a	197540.98	153333.33	101025.64	19863.95	62162.16	38396.62	30993.79	10334.26	8714.29	2654.32	468.90	3012.42
NMC68	NMC68 - 6	rim	297096.77	n/a	177868.85	146666.67	89743.59	15782.31	54054.05	33544.30	25000.00	7869.08	6047.62	1728.40	377.99	1770.19
NMC68	NMC68 - 7	core	280000.00	n/a	181967.21	144500.00	83076.92	13061.22	52123.55	30590.72	22080.75	6155.99	5047.62	1450.62	253.59	1273.29
NMC68	NMC68 - 8	rim	283548.39	n/a	184426.23	133500.00	91282.05	18095.24	50965.25	36708.86	25590.06	8454.04	7142.86	2654.32	555.02	2298.14
NMC68	NMC68 - 9	rim	283548.39	n/a	171311.48	143000.00	83076.92	17278.91	57142.86	37763.71	29068.32	10027.86	7190.48	2746.91	559.81	2391.30
NMC68	NMC68 - 10	rim	243870.97	n/a	170491.80	141000.00	84615.38	11292.52	53552.12	26434.60	16677.02	4387.19	2595.24	712.96	158.37	590.06
NMC68	NMC68 - 11	rim	290322.58	n/a	196721.31	163666.67	102564.10	11972.79	60231.66	34388.19	21801.24	5515.32	3728.57	1126.54	239.23	652.17
NMC68	NMC68 - 12	rim	265806.45	n/a	209016.39	174666.67	111282.05	11156.46	61776.06	32489.45	18416.15	4916.43	3542.86	891.98	220.10	714.29
NMC68	NMC68 - 13	rim	259354.84	n/a	189344.26	158166.67	96410.26	10476.19	54054.05	30168.78	18385.09	5250.70	3071.43	783.95	171.77	683.23
NMC68	NMC68 - 14	core	288709.68	n/a	172131.15	138500.00	75384.62	17687.07	54826.25	32489.45	24409.94	7465.18	5238.10	1358.02	239.23	1180.12
NMC68	NMC68 - 15	core	280322.58	n/a	183606.56	144500.00	89743.59	17959.18	55598.46	34810.13	26242.24	7242.34	5238.10	1481.48	267.94	1894.41
NMC68	NMC68 - 16	rim	238064.52	n/a	168852.46	144000.00	90256.41	11020.41	53667.95	29113.92	18633.54	4860.72	3028.57	827.16	162.68	b.d
NMC68	NMC68 - 17	rim	304838.71	n/a	190983.61	147833.33	86153.85	22176.87	54826.25	38396.62	27577.64	8356.55	5809.52	1620.37	354.07	621.12
NMC68	NMC68 - 18	core	310000.00	n/a	190163.93	144666.67	89230.77	19863.95	54826.25	36075.95	24813.66	7270.20	5190.48	1320.99	306.22	1614.91
NMC68	NMC68 - 19	rim	293870.97	n/a	190983.61	150166.67	88717.95	17687.07	59073.36	37974.68	26024.84	7437.33	4795.24	1317.90	267.94	1366.46
NMC68	NMC68 - 20	rim	288064.52	n/a	180327.87	146833.33	91794.87	11564.63	56370.66	28270.04	18540.37	4763.23	2966.67	901.23	177.03	b.d
NMC68	NMC68 - 21	core	294193.55	n/a	189344.26	143166.67	85128.21	19183.67	51544.40	34177.22	22857.14	6448.47	4485.71	1070.99	143.54	b.d
NMC68	NMC68 - 22	core	264193.55	n/a	188524.59	152666.67	87692.31	12925.17	51351.35	27004.22	18167.70	4721.45	3023.81	864.20	133.97	807.45
NMC68	NMC68 - 23	rim	246774.19	n/a	185245.90	158333.33	98974.36	9523.81	51737.45	24535.87	14596.27	3384.40	2280.95	404.32	157.89	b.d
NMC68	NMC68 - 24	rim	273548.39	n/a	180327.87	139833.33	81025.64	21088.44	52857.14	33122.36	25621.12	7325.91	5761.90	2194.44	373.21	1863.35
NMC68	NMC68 - 25	core	243225.81	n/a	191803.28	147000.00	94358.97	11564.63	55173.75	30168.78	17422.36	5097.49	3390.48	1185.19	267.94	1118.01
NMC68	NMC68 - 26	rim	260645.16	n/a	165573.77	114333.33	72820.51	14557.82	39073.36	24472.57	16552.80	4401.11	3390.48	1043.21	224.88	931.68
NMC68	NMC68 - 27	core	290645.16	n/a	186885.25	140000.00	83589.74	15374.15	46795.37	26793.25	20434.78	4930.36	3033.33	629.63	97.13	b.d
NMC68	NMC68 - 28	rim	310322.58	n/a	204098.36	151833.33	88205.13	17551.02	44749.03	24662.45	17422.36	4415.04	3142.86	762.35	177.99	360.25
NMC68	NMC68 - 29	rim	285806.45	n/a	190163.93	170000.00	89743.59	19455.78	57528.96	36075.95	28850.93	9986.07	9666.67	3456.79	956.94	5652.17
NMC68	NMC68 - 31	rim	267419.35	n/a	204918.03	162666.67	95384.62	10068.03	51351.35	26160.34	14192.55	3217.27	2104.76	549.38	88.04	527.95
NMC68	NMC68 - 32	core	354838.71	n/a	201639.34	159333.33	76923.08	30340.14	41158.30	22025.32	16708.07	5278.55	5476.19	2191.36	545.45	3136.65
NMC68	NMC68 - 33	core	288387.10	n/a	188524.59	144000.00	89743.59	19727.89	51814.67	33270.04	28105.59	8969.36	8476.19	3395.06	803.83	5962.73
NMC68	NMC68 - 34	core	268064.52	n/a	179508.20	148000.00	84102.56	11700.68	44787.64	27004.22	20931.68	7423.40	6047.62	2101.85	440.19	1770.19
NMC68	NMC68 - 35	core	267741.94	n/a	190163.93	135666.67	107179.49	30204.08	54633.20	32447.26	21273.29	5752.09	4104.76	1567.90	349.28	1832.30
NMC68	NMC68 - 36	rim	293225.81	n/a	210655.74	142000.00	88205.13	16190.48	47567.57	27426.16	16801.24	4888.58	3642.86	898.15	186.60	776.40
NMC68	NMC68 - 37	core	312903.23	n/a	181147.54	149833.33	85128.21	17006.80	51351.35	30801.69	21024.84	5738.16	4333.33	1141.98	196.17	1211.18
NMC68	NMC68 - 38	rim	309354.84	n/a	188524.59	152000.00	89743.59	16734.69	47142.86	29746.84	19316.77	5905.29	3900.00	1462.96	277.51	652.17
NMC68	NMC68 - 39	rim	293870.97	n/a	203278.69	157833.33	95897.44	17142.86	52509.65	28059.07	18416.15	4972.14	3523.81	1185.19	196.17	1180.12
NMC68	NMC68 - 40	rim	308709.68	n/a	188524.59	161666.67	82564.10	17823.13	48648.65	30168.78	19130.43	5264.62	4100.00	1163.58	277.51	1055.90

Table D.20: LASS ICP-MS U–Pb isotopic data for zircon – IC machine settings for rim analyses. Sample NMC24.

sample ID	spot	instrument settings	CL	group	comment	$^{238}U/^{206}Pb$	2σ	$^{207}Pb/^{206}Pb$	2σ	$^{206}Pb/^{238}U$ Age (Ma)	2σ	$^{207}Pb/^{206}Pb$ Age (Ma)	2σ	7/6 discordance (%)	6/8 discordance (%)
NMC24	NMC24 - 1	IC	Sl	M	rounded faint sector zoned soccer ball type	5.425936	0.1236513	0.07507	0.0011	1090.5	23	1068	31	-2.11	2.06
NMC24	NMC24 - 2	IC	Sl	M	rounded faint sector zoned soccer ball type	5.787037	0.1339592	0.07259	0.00081	1027.7	22	1001	23	-2.67	2.60
NMC24	NMC24 - 3	IC	Sh	M	ovoidal bright sector zoned grain	5.737235	0.134955	0.07394	0.00084	1035.5	23	1039	23	0.34	-0.34
NMC24	NMC24 - 4	IC	Sl	M	rounded faint sector zoned soccer ball type	5.319149	0.1329787	0.07312	0.00074	1110	26	1016.3	20	-9.22	8.44
NMC24	NMC24 - 5	IC	Sl	M	rounded faint sector zoned soccer ball type	5.621135	0.1263887	0.07638	0.00097	1055.6	22	1104	25	4.38	-4.59
NMC24	NMC24 - 6	IC	Sl	M	elongated faint sector zoned soccer ball type, has small bright core	5.704181	0.126897	0.07364	0.00075	1041.3	22	1030.6	21	-1.04	1.03
NMC24	NMC24 - 7	IC	Sh	M	rounded bright sector zoned soccer ball type	5.803831	0.1381062	0.07234	0.00075	1024.9	22	994.4	21	-3.07	2.98
NMC24	NMC24 - 8	IC	Sl	M	rounded faint sector zoned soccer ball type	5.636979	0.1334572	0.07681	0.0009	1052.6	23	1115	23	5.60	-5.93
NMC24	NMC24 - 9	IC	Sh	M	rounded bright sector zoned soccer ball type	5.567929	0.1271075	0.07309	0.00078	1064.9	22	1015.3	22	-4.89	4.66
NMC24	NMC24 - 10	IC	Sh	M	rounded bright sector zoned soccer ball type	5.847953	0.1367942	0.07259	0.00082	1017.8	22	1001	23	-1.68	1.65
NMC24	NMC24 - 12	IC	Sh	M	rounded bright sector zoned soccer ball type	5.899705	0.1427067	0.07232	0.00078	1009.3	23	993.9	22	-1.55	1.53
NMC24	NMC24 - 13	IC	Sl	M	rounded faint sector zoned soccer ball type	5.682464	0.1259325	0.07225	0.00078	1045	22	992	22	-5.34	5.07
NMC24	NMC24 - 14	IC	Sl	M	rounded faint sector zoned soccer ball type	5.813953	0.1385884	0.07388	0.0011	1023.3	23	1036	31	1.23	-1.24
NMC24	NMC24 - 15	IC	Sh	M	rounded bright sector zoned soccer ball type	5.534034	0.1255647	0.076	0.00093	1070.9	22	1094	25	2.11	-2.16
NMC24	NMC24 - 16	IC	Sh	D	rounded bright sector zoned soccer ball type	5.91576	0.1329856	0.0794	0.0021	1006.8	21	1177	52	14.46	-16.91
NMC24	NMC24 - 17	IC	Sl	M	rounded faint sector zoned soccer ball type	5.879932	0.1313797	0.0719	0.00076	1012.5	21	982.1	22	-3.10	3.00
NMC24	NMC24 - 18	IC	Sl	M	rounded faint sector zoned soccer ball type	5.903188	0.1393905	0.07208	0.00078	1009	22	987	22	-2.23	2.18
NMC24	NMC24 - 19	IC	Sl	M	rounded faint sector zoned soccer ball type	5.55679	0.1235117	0.07234	0.0008	1066.7	22	994	23	-7.31	6.82
NMC24	NMC24 - 20	IC	Sl	D	rounded faint sector zoned soccer ball type	8.116883	0.434833	0.086	0.0076	749	38	1300	140	42.38	-73.56
NMC24	NMC24 - 21	IC	Sl	D	rounded faint sector zoned soccer ball type	5.500248	0.1240362	0.0889	0.0039	1076.9	22	1390	81	22.53	-29.07
NMC24	NMC24 - 22	IC	Sh	M	rounded bright sector zoned soccer ball type	5.793743	0.1376266	0.07487	0.001	1028.2	21	1063	27	3.27	-3.38
NMC24	NMC24 - 23	IC	Sh	M	rounded bright sector zoned soccer ball type	5.750101	0.1289483	0.07316	0.00079	1033.6	22	1017.3	22	-1.60	1.58
NMC24	NMC24 - 24	IC	Sh	M	rounded bright sector zoned soccer ball type	5.527916	0.1344546	0.07243	0.00089	1072	24	1000	23	-7.20	6.72
NMC24	NMC24 - 25	IC	Sl	M	rounded faint sector zoned soccer ball type	5.50055	0.1270754	0.07444	0.00083	1076.7	23	1052	22	-2.35	2.29
NMC24	NMC24 - 26	IC	Sh	M	rounded bright sector zoned soccer ball type	5.980861	0.1359287	0.07239	0.00084	996.4	21	996	24	-0.04	0.04
NMC24	NMC24 - 27	IC	Sl	M	rounded faint sector zoned soccer ball type	5.65931	0.1281111	0.0732	0.00076	1048.7	22	1018.5	21	-2.97	2.88
NMC24	NMC24 - 28	IC	Sl	M	rounded faint sector zoned soccer ball type	5.94884	0.1380159	0.07306	0.00082	1001.7	22	1014	23	1.21	-1.23
NMC24	NMC24 - 29	IC	Sl	M	rounded faint sector zoned soccer ball type	5.417118	0.1467258	0.07988	0.0011	1092	27	1193	26	8.47	-9.25
NMC24	NMC24 - 30	IC	Sh	M	rounded bright sector zoned soccer ball type	5.455537	0.1250041	0.07448	0.00099	1084.8	23	1053	27	-3.02	2.93
NMC24	NMC24 - 31	IC	Sl	M	rounded faint sector zoned soccer ball type	5.724098	0.1310612	0.07245	0.00077	1037.8	22	997.6	22	-4.03	3.87
NMC24	NMC24 - 32	IC	Sl	M	rounded faint sector zoned soccer ball type	5.666686	0.1252342	0.07305	0.0008	1047.7	22	1014	22	-3.32	3.22
NMC24	NMC24 - 33	IC	Sl	M	rounded faint sector zoned soccer ball type	5.743825	0.1319661	0.07271	0.00082	1034.8	22	1005	23	-2.97	2.88
NMC24	NMC24 - 34	IC	Sl	M	rounded faint sector zoned soccer ball type	5.640158	0.1272455	0.0725	0.00087	1052.1	22	999	24	-5.32	5.05
NMC24	NMC24 - 35	IC	Sl	M	rounded faint sector zoned rim on CL-dark rounded core	5.724098	0.1310612	0.07327	0.00076	1037.9	22	1020.5	21	-1.71	1.68
NMC24	NMC24 - 36	IC	Sl	M	rounded faint sector zoned soccer ball type	5.851375	0.1335305	0.07449	0.00085	1017	22	1054	23	3.51	-3.64

Table D.21: LASS ICP-MS chondrite-normalised REE data for zircon (ppm) – IC machine settings for rim analyses. Sample NMC24.

sample ID	spot	instrument settings	CL	group	La	Ce	Pr	Nd	Sm	Eu	Gd	Tb	Dy	Ho	Er	Tm	Yb	Lu
NMC24	NMC24 - 1	IC	Sl	M	0.01	1.73	b.d	5.00	21.54	10.88	116.60	381.86	884.78	1775.77	3490.48	5129.63	9698.56	13819.88
NMC24	NMC24 - 2	IC	Sl	M	0.10	0.57	b.d	b.d	9.74	b.d	74.13	236.29	576.40	1107.24	2419.05	3820.99	6736.84	9819.88
NMC24	NMC24 - 3	IC	Sh	M	b.d	1.44	b.d	b.d	6.15	b.d	61.00	130.38	245.65	410.86	793.81	1030.86	1708.13	2512.42
NMC24	NMC24 - 4	IC	Sl	M	b.d	3.47	14.75	b.d	21.54	7.35	96.91	350.21	791.61	1548.75	3076.19	4746.91	8760.77	11956.52
NMC24	NMC24 - 5	IC	Sl	M	b.d	2.04	b.d	13.50	38.46	1.09	121.62	204.64	194.10	215.88	234.76	240.74	268.42	346.27
NMC24	NMC24 - 6	IC	Sl	M	0.04	0.79	b.d	b.d	16.41	b.d	47.49	160.34	392.24	750.70	1571.43	2654.32	4708.13	6947.21
NMC24	NMC24 - 7	IC	Sh	M	b.d	1.72	b.d	b.d	10.26	b.d	50.58	78.48	122.05	196.38	323.81	456.79	779.90	1031.06
NMC24	NMC24 - 8	IC	Sl	M	b.d	2.57	12.30	b.d	22.05	22.59	76.83	141.77	158.39	135.10	160.00	140.43	167.46	172.67
NMC24	NMC24 - 9	IC	Sh	M	0.02	1.96	b.d	b.d	14.36	b.d	76.45	106.96	108.07	129.53	161.43	155.25	229.19	242.24
NMC24	NMC24 - 10	IC	Sh	M	0.03	1.96	b.d	18.00	29.74	b.d	59.85	101.90	122.67	131.89	146.67	156.17	204.31	196.89
NMC24	NMC24 - 12	IC	Sh	M	0.04	1.57	b.d	b.d	16.92	b.d	61.00	150.84	168.63	218.66	273.81	212.65	236.84	285.71
NMC24	NMC24 - 13	IC	Sl	M	b.d	0.85	b.d	b.d	16.41	b.d	100.39	236.29	314.29	371.87	415.24	339.51	399.04	409.94
NMC24	NMC24 - 14	IC	Sl	M	b.d	2.05	13.11	b.d	b.d	5.99	35.14	101.05	270.81	522.28	1166.67	1805.56	3315.79	4739.13
NMC24	NMC24 - 15	IC	Sh	M	b.d	3.84	17.95	21.50	34.87	14.15	118.15	217.51	240.99	271.59	315.24	308.64	356.46	490.68
NMC24	NMC24 - 16	IC	Sh	D	0.02	2.14	b.d	b.d	39.49	b.d	96.14	137.76	145.96	147.21	160.00	155.25	144.98	182.30
NMC24	NMC24 - 17	IC	Sl	M	b.d	1.51	b.d	b.d	b.d	b.d	73.75	303.80	639.75	1240.95	2590.48	4141.98	7320.57	10341.61
NMC24	NMC24 - 18	IC	Sl	M	0.04	0.58	b.d	b.d	13.33	b.d	79.92	184.39	199.07	181.06	191.90	152.47	185.17	204.97
NMC24	NMC24 - 19	IC	Sl	M	0.08	1.39	b.d	b.d	21.03	5.58	79.92	253.16	417.08	678.27	1185.71	1669.75	2722.49	3944.10
NMC24	NMC24 - 20	IC	Sl	D	b.d	110.15	573.77	300.00	90.26	352.38	116.22	253.16	348.76	459.61	771.43	1043.21	1689.00	2422.36
NMC24	NMC24 - 21	IC	Sl	D	0.07	4.80	b.d	b.d	31.28	b.d	46.33	61.39	78.26	105.85	144.29	125.93	169.86	179.50
NMC24	NMC24 - 22	IC	Sh	M	b.d	7549.51	55737.70	30666.67	2358.97	43.54	617.76	350.21	313.66	374.65	447.62	645.06	933.01	1428.57
NMC24	NMC24 - 23	IC	Sh	M	0.05	1.76	b.d	b.d	12.82	b.d	72.97	100.42	100.62	111.28	123.81	110.80	149.76	156.52
NMC24	NMC24 - 24	IC	Sh	M	0.07	1.61	5.41	b.d	18.97	b.d	78.76	161.18	181.68	192.20	231.90	259.26	316.27	296.58
NMC24	NMC24 - 25	IC	Sl	M	b.d	3.45	16.39	18.00	30.77	b.d	92.28	234.18	394.41	693.59	1323.81	1882.72	3349.28	5000.00
NMC24	NMC24 - 26	IC	Sh	M	0.00	1.55	b.d	10.00	26.67	b.d	80.31	139.45	132.61	111.00	126.19	109.88	113.88	118.01
NMC24	NMC24 - 27	IC	Sl	M	0.11	0.95	b.d	b.d	16.41	b.d	122.78	337.55	404.35	366.30	385.24	333.33	341.63	363.35
NMC24	NMC24 - 28	IC	Sl	M	0.10	2.66	b.d	28.17	37.95	b.d	88.42	123.63	128.57	143.45	152.38	161.73	194.26	209.01
NMC24	NMC24 - 29	IC	Sl	M	b.d	97.77	614.75	333.33	49.23	15.65	71.43	200.42	282.30	473.54	861.90	1148.15	1851.67	2608.70
NMC24	NMC24 - 30	IC	Sh	M	b.d	12.75	122.95	43.33	30.26	b.d	101.54	210.97	323.91	403.90	598.57	703.70	1009.57	1450.31
NMC24	NMC24 - 31	IC	Sl	M	0.03	2.69	b.d	b.d	21.03	b.d	154.83	257.38	294.10	313.37	359.52	327.16	385.17	493.79
NMC24	NMC24 - 32	IC	Sl	M	0.04	2.49	b.d	b.d	36.92	b.d	123.55	232.07	220.19	201.95	192.86	169.44	186.12	254.66
NMC24	NMC24 - 33	IC	Sl	M	b.d	2.29	b.d	20.00	46.67	b.d	122.39	161.81	141.61	140.67	148.10	98.46	143.54	173.91
NMC24	NMC24 - 34	IC	Sl	M	b.d	1.19	b.d	6.67	11.28	b.d	37.45	196.20	329.50	472.14	755.24	910.49	1258.37	1804.35
NMC24	NMC24 - 35	IC	Sl	M	b.d	2.19	13.11	16.67	24.10	b.d	91.89	132.28	126.09	110.03	123.33	104.01	119.14	128.26
NMC24	NMC24 - 36	IC	Sl	M	b.d	3.03	b.d	10.17	15.90	2.59	93.82	200.42	234.16	284.12	346.67	391.98	488.04	701.86

Table D.22: LASS ICP-MS U–Pb isotopic data for monazite. Sample NMC24.

sample ID	spot	location	$^{238}U/^{206}Pb$	2σ	$^{207}Pb/^{206}Pb$	2σ	$^{206}Pb/^{238}U$ Age (Ma)	2σ	$^{207}Pb/^{206}Pb$ Age (Ma)	2σ	7/6 discordance (%)	6/8 discordance (%)	U (ppm)	Th (ppm)	Pb (ppm)
NMC24	NMC24 - 1	rim	5.892752	0.1423706	0.07427	0.00094	1010.4	23	1047	26	3.50	-3.62	1950	171000	9960
NMC24	NMC24 - 2	rim	5.892752	0.1493155	0.0747	0.0014	1010	24	1056	39	4.36	-4.55	1730	170000	10200
NMC24	NMC24 - 3	core	5.878895	0.148614	0.0741	0.0012	1013	24	1041	33	2.69	-2.76	1740	147000	8900
NMC24	NMC24 - 4	core	5.899705	0.16011	0.0711	0.0015	1009	25	958	42	-5.32	5.05	1640	136000	8080
NMC24	NMC24 - 5	core	5.91716	0.150555	0.0733	0.0011	1006	24	1021	29	1.47	-1.49	2090	163000	9900
NMC24	NMC24 - 6	rim	5.899705	0.1705519	0.0734	0.0014	1009	27	1023	38	1.37	-1.39	1370	160000	9500
NMC24	NMC24 - 7	rim	5.973716	0.1570152	0.07286	0.00084	997	24	1008	24	1.09	-1.10	1740	161000	9600
NMC24	NMC24 - 8	rim	5.980861	0.1860076	0.07301	0.00081	996	29	1013	23	1.68	-1.71	2350	131000	8000
NMC24	NMC24 - 9	missed spot	5.344735	0.1942501	0.0737	0.0016	1105	37	1029	45	-7.39	6.88	910	103000	6180
NMC24	NMC24 - 10	rim	6.035003	0.1529693	0.07353	0.00096	988	23	1027	26	3.80	-3.95	2970	78000	4970
NMC24	NMC24 - 11	rim	6.045949	0.1864229	0.0742	0.0017	986	28	1044	46	5.56	-5.88	920	112000	6820
NMC24	NMC24 - 12	rim	5.955926	0.2234803	0.0727	0.001	1001	35	1004	28	0.30	-0.30	1390	125000	7300
NMC24	NMC24 - 13	rim	6.045949	0.1791122	0.0736	0.0013	987	27	1038	31	4.91	-5.17	920	105000	6400
NMC24	NMC24 - 14	rim	5.98444	0.1754863	0.0729	0.0013	996	27	1019	32	2.26	-2.31	1510	91000	6090
NMC24	NMC24 - 15	rim	6.119951	0.1947598	0.0726	0.0013	975	29	1000	36	2.50	-2.56	1750	102000	6590
NMC24	NMC24 - 16	rim	5.910165	0.1536922	0.07088	0.00075	1008	24	952	22	-5.88	5.56	2280	90000	5730
NMC24	NMC24 - 17	rim	5.847953	0.2188708	0.073	0.0018	1017	35	1008	49	-0.89	0.88	1940	109000	7000
NMC24	NMC24 - 18	D	6.176652	0.2098307	0.0763	0.0017	967	30	1099	44	12.01	-13.65	1750	112000	6820
NMC24	NMC24 - 19	core	5.871991	0.1689533	0.075	0.0015	1014	27	1065	39	4.79	-5.03	1040	99700	6290
NMC24	NMC24 - 20	core	5.817336	0.1658228	0.0723	0.0013	1022	27	992	38	-3.02	2.94	1160	103000	6150
NMC24	NMC24 - 21	core	5.777008	0.1802186	0.0748	0.0013	1029	30	1061	34	3.02	-3.11	1190	109000	6820
NMC24	NMC24 - 22	missed spot	6.455778	0.1833791	0.07094	0.00084	928	25	954	24	2.73	-2.80	10800	361000	19400
NMC24	NMC24 - 23	rim	5.858231	0.151003	0.0729	0.0011	1016	24	1010	30	-0.59	0.59	1610	86000	5470
NMC24	NMC24 - 24	missed spot	5.995204	0.1473641	0.0739	0.0013	994.4	23	1045	38	4.84	-5.09	1600	92000	5770
NMC24	NMC24 - 25	core	5.970149	0.1639563	0.0744	0.0012	998	25	1049	32	4.86	-5.11	1480	86000	5430
NMC24	NMC24 - 26	rim	5.910165	0.1432132	0.07309	0.00068	1007.6	22	1015	19	0.73	-0.73	3370	105000	6540
NMC24	NMC24 - 27	core	5.927682	0.1510909	0.073	0.00093	1005	23	1012	26	0.69	-0.70	3490	88000	5290
NMC24	NMC24 - 28	rim	5.810575	0.1586851	0.0734	0.0011	1024	26	1024	31	0.00	0.00	2240	127000	7800
NMC24	NMC24 - 29	rim	5.903188	0.205601	0.0737	0.0011	1008	33	1030	31	2.14	-2.18	1000	208000	12200
NMC24	NMC24 - 30	rim	5.817336	0.1624387	0.0729	0.0016	1023	26	1008	46	-1.49	1.47	990	197000	12500
NMC24	NMC24 - 31	core	6.146281	0.2115499	0.0744	0.0017	979	35	1048	46	6.58	-7.05	950	113000	6980
NMC24	NMC24 - 32	core	6.071645	0.1916974	0.0737	0.0013	983	29	1030	36	4.56	-4.78	950	110000	6690
NMC24	NMC24 - 33	rim	5.787037	0.1440061	0.0707	0.0012	1028	23	946	34	-8.67	7.98	2780	154000	9100
NMC24	NMC24 - 34	D	5.000	0.35	0.182	0.045	1175	77	2420	400	51.45	-105.96	1470	73000	4780
NMC24	NMC24 - 35	core	5.941771	0.144749	0.07397	0.00067	1002.7	23	1039	18	3.49	-3.62	3750	87200	5130
NMC24	NMC24 - 36	rim	5.955926	0.1560814	0.07284	0.00082	1001	25	1008	23	0.69	-0.70	1720	71000	4370
NMC24	NMC24 - 37	rim	5.777008	0.183556	0.0719	0.0012	1029	30	981	34	-4.89	4.66	900	75800	4740
NMC24	NMC24 - 38	rim	5.878895	0.1520702	0.0724	0.0008	1012	24	996	22	-1.61	1.58	3810	80000	4780
NMC24	NMC24 - 39	rim	5.931198	0.1407164	0.07307	0.00077	1004.5	22	1014	21	0.94	-0.95	4430	78000	4880
NMC24	NMC24 - 40	core	6.006006	0.2164326	0.0738	0.0016	993	33	1032	43	3.78	-3.93	870	125000	7400
NMC24	NMC24 - 41	D	6.184292	0.1835782	0.075	0.0014	966	27	1067	39	9.47	-10.46	820	132000	7900
NMC24	NMC24 - 42	rim	5.955926	0.1596288	0.07194	0.0006	1001	25	983	17	-1.83	1.80	2280	118000	6860
NMC24	NMC24 - 43	core	5.824112	0.1424652	0.07251	0.00083	1021	23	999	23	-2.20	2.15	3960	78500	4640
NMC24	NMC24 - 44	D	4.854369	0.3299086	0.223	0.042	1206	75	2860	320	57.83	-137.15	2710	82000	5180
NMC24	NMC24 - 45	rim	5.952381	0.1629819	0.0716	0.0011	1001	25	973	31	-2.88	2.80	1860	162000	9700
NMC24	NMC24 - 46	core	5.878895	0.1555263	0.073	0.0012	1012	25	1011	34	-0.10	0.10	2430	79000	4750
NMC24	NMC24 - 47	rim	5.98444	0.2041371	0.07216	0.00093	996	32	989	26	-0.71	0.70	1050	106000	6030
NMC24	NMC24 - 48	core	6.053269	0.1942029	0.0736	0.0014	986	29	1029	39	4.18	-4.36	970	90000	5270
NMC24	NMC24 - 49	D	5.896226	0.1738274	0.0805	0.0026	1010	28	1204	63	16.11	-19.21	1520	83000	5000
NMC24	NMC24 - 50	core	5.78369	0.1538749	0.07118	0.00099	1028	25	961	29	-6.97	6.52	2020	113000	6610
NMC24	NMC24 - 51	rim	5.851375	0.1472259	0.07196	0.00087	1017	23	983	24	-3.46	3.34	1730	129000	7500
NMC24	NMC24 - 52	core	5.955926	0.1525341	0.07273	0.00074	1001	24	1005	21	0.40	-0.40	3120	74000	4270
NMC24	NMC24 - 53	rim	5.991612	0.1543675	0.0718	0.0013	995	24	979	35	-1.63	1.61	2780	112000	6500
NMC24	NMC24 - 54	rim	5.875441	0.1691519	0.0746	0.0013	1013	27	1054	36	3.89	-4.05	1260	80000	4900
NMC24	NMC24 - 55	core	6.013229	0.1446357	0.0757	0.001	991.7	22	1086	27	8.68	-9.51	1940	77000	4520
NMC24	NMC24 - 56	core	5.827506	0.1460272	0.0738	0.001	1021	23	1033	28	1.16	-1.18	2530	78000	4550
NMC24	NMC24 - 57	rim	6.006006	0.1551101	0.0744	0.0012	993	24	1049	34	5.34	-5.64	2460	108000	6290
NMC24	NMC24 - 58	rim	6.138735	0.184652	0.07081	0.00094	973	27	950	27	-2.42	2.36	6100	300000	16300
NMC24	NMC24 - 59	core	6.161429	0.1670381	0.0733	0.0015	970	24	1018	42	4.72	-4.95	950	82000	4770
NMC24	NMC24 - 60	rim	5.896226	0.1564447	0.0726	0.0013	1010	25	1001	36	-0.90	0.89	1180	110000	6510
NMC24	NMC24 - 61	rim	5.980861	0.1716994	0.0727	0.0013	996	26	1003	36	0.70	-0.70	1670	97000	5810
NMC24	NMC24 - 62	rim	6.123699	0.2999975	0.0735	0.0012	975	45	1026	33	4.97	-5.23	1350	101000	5580
NMC24	NMC24 - 63	core	6.337136	0.2489876	0.07312	0.00079	944	35	1016	22	7.09	-7.63	2760	73600	4410
NMC24	NMC24 - 64	rim	5.934718	0.1866707	0.0731	0.0017	1004	29	1014	47	0.99	-1.00	1100	116000	6630
NMC24	NMC24 - 65	core	5.924171	0.1509119	0.07335	0.00096	1005	24	1022	27	1.66	-1.69	3140	74100	4290
NMC24	NMC24 - 66	rim	5.854801	0.1611099	0.0717	0.0013	1016	26	985	40	-3.15	3.05	1140	93000	5350
NMC24	NMC24 - 67	core	5.952381	0.1488095	0.0729	0.0013	1001	23	1009	35	0.79	-0.80	3430	53100	3330
NMC24	NMC24 - 68	rim	5.878895	0.148614	0.07103	0.00087	1012	24	956	25	-5.86	5.53	4120	184000	10700
NMC24	NMC24 - 69	rim	5.945303	0.1590598	0.0731	0.0015	1002	25	1015	42	1.28	-1.30	1160	96000	5630
NMC24	NMC24 - 70	core	5.834306	0.1497721	0.07192	0.00089	1020	24	982	25	-3.87	3.73	2550	79300	4440
NMC24	NMC24 - 71	core	6.002401	0.1720383	0.0732	0.0015	993	26	1017	41	2.36	-2.42	1390	79000	4700
NMC24	NMC24 - 72	rim	5.885815	0.159357	0.0727	0.0014	1011	25	1002	38	-0.90	0.89	1330	84000	5240
NMC24	NMC24 - 73	rim	5.865103	0.1410377	0.07129	0.00081	1015	23	964	23	-5.29	5.02	2010	160000	8900
NMC24	NMC24 - 74	core	5.892752	0.145843	0.0728	0.00072	1010	23	1007	20	-0.30	0.30	3170	65000	3890
NMC24	NMC24 - 75	rim	6.064281	0.1434245	0.0725	0.001	984	21	997	28	1.30	-1.32	7440	174000	9180
NMC24	NMC24 - 76	core	5.924171	0.1474023	0.0722	0.001	1005	23	989	29	-1.62	1.59	3300	66000	3950
NMC24	NMC24 - 77	core	5.820722	0.1863444	0.0723	0.0015	1022	30	1003	44	-1.89	1.86	780	73000	4380
NMC24	NMC24 - 78	rim	5.797101	0.241966	0.0768	0.0017	1026	40	1125	48	8.80	-9.65	515	98000	5760
NMC24	NMC24 - 79	rim	5.906675	0.174444	0.0715	0.0011	1008	28	971	30	-3.81	3.67	1640	131000	7680
NMC24	NMC24 - 80	core	5.817336	0.169207	0.0724	0.0011	1027	30	1002	28	-2.50	2.43	1270	141000	8200
NMC24	NMC24 - 81	rim	5.955926	0.1702707	0.0721	0.0012	1000	26	985	34	-1.52	1.50	2550	105000	5820

Table D.23: LASS ICP-MS chondrite-normalised REE data for monazite (ppm). Sample NMC24.

sample ID	spot	location	La	Ce	Pr	Nd	Sm	Eu	Gd	Tb	Dy	Ho	Er	Tm	Yb	Lu
NMC24	NMC24 - 1	rim	312903.23	n/a	246721.31	193666.67	95384.62	1564.63	30501.93	7341.77	2639.75	409.47	257.14	77.16	b.d	b.d
NMC24	NMC24 - 2	rim	291290.32	n/a	233606.56	213333.33	103076.92	1510.20	33088.80	9409.28	2763.98	541.78	257.14	b.d	b.d	b.d
NMC24	NMC24 - 3	core	263870.97	n/a	225409.84	199166.67	98461.54	1142.86	36254.83	11434.60	3913.04	874.65	419.05	117.28	b.d	b.d
NMC24	NMC24 - 4	core	272258.06	n/a	224590.16	190000.00	91794.87	761.90	36718.15	10717.30	4006.21	795.26	428.57	b.d	b.d	b.d
NMC24	NMC24 - 5	core	293870.97	n/a	242622.95	200000.00	98461.54	1632.65	31853.28	7953.59	2512.42	412.26	247.62	b.d	b.d	b.d
NMC24	NMC24 - 6	rim	265806.45	n/a	222131.15	196666.67	85641.03	1537.42	29652.51	7299.58	2515.53	476.32	219.05	b.d	26.79	b.d
NMC24	NMC24 - 7	rim	258387.10	n/a	213114.75	203333.33	81025.64	1564.63	28223.94	7679.32	2431.68	420.61	290.48	b.d	b.d	b.d
NMC24	NMC24 - 8	rim	309677.42	n/a	226229.51	195833.33	62564.10	1619.05	13474.90	3227.85	1037.27	186.63	64.29	b.d	b.d	b.d
NMC24	NMC24 - 10	rim	374193.55	n/a	254098.36	208833.33	83076.92	2163.27	19806.95	4831.22	1381.99	278.55	138.10	b.d	b.d	b.d
NMC24	NMC24 - 11	rim	321387.10	n/a	242622.95	193333.33	78461.54	816.33	21853.28	4873.42	1695.65	338.44	85.71	b.d	b.d	b.d
NMC24	NMC24 - 12	rim	286774.19	n/a	227049.18	181000.00	87692.31	1755.10	22200.77	5886.08	1987.58	355.15	290.48	b.d	b.d	b.d
NMC24	NMC24 - 13	rim	303548.39	n/a	260655.74	206000.00	70769.23	1455.78	14362.93	3586.50	1493.79	286.91	133.33	b.d	b.d	b.d
NMC24	NMC24 - 14	rim	339032.26	n/a	256557.38	218333.33	85641.03	1020.41	18803.09	4894.51	1633.54	339.83	161.90	b.d	b.d	b.d
NMC24	NMC24 - 15	rim	286774.19	n/a	230327.87	205000.00	73333.33	1319.73	17760.62	4367.09	1652.17	388.58	285.71	b.d	22.97	b.d
NMC24	NMC24 - 16	rim	316451.61	n/a	241803.28	186166.67	78974.36	1210.88	14285.71	3565.40	1139.75	282.73	161.90	b.d	b.d	b.d
NMC24	NMC24 - 17	rim	306129.03	n/a	238524.59	188333.33	69743.59	925.17	13166.02	3607.59	1372.67	288.30	95.24	b.d	b.d	b.d
NMC24	NMC24 - 19	core	312258.06	n/a	235245.90	193333.33	94358.97	1428.57	37335.91	9873.42	3260.87	537.60	304.76	b.d	21.05	b.d
NMC24	NMC24 - 20	core	307741.94	n/a	217213.11	175000.00	84102.56	1074.83	26872.59	6687.76	2003.11	295.26	95.24	b.d	b.d	b.d
NMC24	NMC24 - 21	core	308709.68	n/a	228688.52	190000.00	94871.79	1401.36	27297.30	6308.02	1987.58	369.08	166.67	49.38	24.88	b.d
NMC24	NMC24 - 23	rim	358064.52	n/a	228688.52	171666.67	84615.38	1333.33	42857.14	16476.79	8478.26	1754.87	1157.14	209.88	b.d	b.d
NMC24	NMC24 - 25	core	363548.39	n/a	247540.98	184166.67	88717.95	1931.97	37992.28	14135.02	6801.24	1462.40	747.62	222.22	27.27	b.d
NMC24	NMC24 - 26	rim	324516.13	n/a	236065.57	187333.33	90256.41	1646.26	35212.36	12616.03	5310.56	1065.46	676.19	145.06	b.d	b.d
NMC24	NMC24 - 27	core	364193.55	n/a	222131.15	153666.67	94358.97	4122.45	43590.73	23670.89	11832.30	2701.95	1914.29	388.89	132.54	b.d
NMC24	NMC24 - 28	rim	294193.55	n/a	219672.13	182333.33	104615.38	2244.90	40849.42	13459.92	5124.22	1169.92	761.90	b.d	26.32	b.d
NMC24	NMC24 - 29	rim	234516.13	n/a	211475.41	176333.33	56923.08	993.20	10231.66	2362.87	711.18	169.92	147.62	b.d	b.d	b.d
NMC24	NMC24 - 30	rim	267096.77	n/a	237704.92	207833.33	65641.03	870.75	11119.69	2257.38	822.98	158.77	133.33	b.d	b.d	b.d
NMC24	NMC24 - 31	core	309677.42	n/a	252459.02	201666.67	67692.31	1251.70	11042.47	2890.30	1071.43	357.94	138.10	b.d	b.d	b.d
NMC24	NMC24 - 32	core	335161.29	n/a	256557.38	215000.00	66153.85	897.96	12239.38	2658.23	1204.97	296.66	157.14	64.81	b.d	b.d
NMC24	NMC24 - 33	rim	272580.65	n/a	219672.13	173833.33	64615.38	1333.33	12432.43	4261.60	1838.51	562.67	371.43	70.99	b.d	b.d
NMC24	NMC24 - 35	core	321741.94	n/a	213114.75	154833.33	79487.18	4108.84	43320.46	24050.63	16832.30	6225.63	6380.95	2592.59	818.18	4285.71
NMC24	NMC24 - 36	rim	357419.35	n/a	216393.44	160000.00	94871.79	2013.61	47104.25	26793.25	16118.01	5153.20	4628.57	1472.22	397.13	2546.58
NMC24	NMC24 - 37	rim	324516.13	n/a	207377.05	160500.00	86153.85	1632.65	41583.01	17995.78	10714.29	3300.84	2285.71	731.48	205.74	931.68
NMC24	NMC24 - 38	rim	357741.94	n/a	242622.95	176833.33	107692.31	3782.31	57451.74	26582.28	12453.42	3175.49	2042.86	302.47	100.00	465.84
NMC24	NMC24 - 39	rim	322903.23	n/a	209836.07	175000.00	91282.05	4027.21	56756.76	27848.10	13198.76	3286.91	2223.81	604.94	112.92	838.51
NMC24	NMC24 - 40	core	300322.58	n/a	227868.85	203333.33	75384.62	1360.54	14517.37	3481.01	1245.34	261.84	133.33	b.d	b.d	b.d
NMC24	NMC24 - 42	rim	273870.97	n/a	220491.80	173666.67	66153.85	1020.41	12084.94	2573.84	850.93	146.24	b.d	b.d	b.d	b.d
NMC24	NMC24 - 43	core	370967.74	n/a	206557.38	159500.00	90256.41	6435.37	39189.19	13607.59	5341.61	912.26	628.57	160.49	b.d	b.d
NMC24	NMC24 - 45	rim	256774.19	n/a	222950.82	184500.00	83076.92	1319.73	28648.65	8417.72	2732.92	596.10	285.71	98.77	b.d	b.d
NMC24	NMC24 - 46	core	339354.84	n/a	218852.46	169166.67	95897.44	2176.87	49806.95	24219.41	11490.68	2980.50	1785.71	472.22	110.05	b.d
NMC24	NMC24 - 47	rim	309032.26	n/a	242622.95	203333.33	75384.62	1251.70	12857.14	2320.68	711.18	93.31	b.d	b.d	b.d	b.d
NMC24	NMC24 - 48	core	319354.84	n/a	240983.61	195333.33	105128.21	2231.29	35984.56	10991.56	3975.16	706.13	457.14	b.d	b.d	b.d
NMC24	NMC24 - 50	core	288064.52	n/a	222950.82	186500.00	101538.46	1387.76	44401.54	15021.10	5838.51	1392.76	809.52	358.02	52.15	b.d
NMC24	NMC24 - 51	rim	347096.77	n/a	236065.57	186833.33	68205.13	1292.52	14555.98	2721.52	881.99	76.60	142.86	b.d	b.d	b.d
NMC24	NMC24 - 52	core	320645.16	n/a	213934.43	166250.00	96410.26	6299.32	45173.75	24683.54	17360.25	6058.50	6095.24	2067.90	765.55	3726.71
NMC24	NMC24 - 53	rim	307741.94	n/a	228688.52	176333.33	70256.41	1346.94	19305.02	6160.34	3167.70	867.69	704.76	135.80	b.d	b.d
NMC24	NMC24 - 54	rim	357419.35	n/a	239344.26	168833.33	90256.41	2448.98	41428.57	16350.21	6708.07	1518.11	980.95	293.21	65.07	369.57
NMC24	NMC24 - 55	core	370967.74	n/a	231967.21	177833.33	86153.85	3034.01	40424.71	16624.47	7670.81	1573.82	1157.14	358.02	55.50	683.23
NMC24	NMC24 - 56	core	343548.39	n/a	213934.43	160000.00	89743.59	2272.11	47606.18	20464.14	10434.78	1949.86	971.43	277.78	32.54	b.d
NMC24	NMC24 - 57	rim	318709.68	n/a	213934.43	186333.33	93846.15	2054.42	30077.22	12299.58	5248.45	1002.79	557.14	108.02	34.45	b.d
NMC24	NMC24 - 58	rim	174193.55	n/a	179508.20	151500.00	49076.92	761.90	6718.15	1118.14	298.14	54.32	b.d	b.d	b.d	b.d
NMC24	NMC24 - 59	core	304516.13	n/a	214754.10	170666.67	89230.77	1931.97	33011.58	12869.20	6863.35	1754.87	1328.57	250.00	53.11	b.d
NMC24	NMC24 - 60	rim	291935.48	n/a	220491.80	182333.33	98461.54	1238.10	39382.24	13691.98	4472.05	869.08	471.43	b.d	b.d	b.d
NMC24	NMC24 - 61	rim	306129.03	n/a	234426.23	168166.67	98974.36	1034.01	38262.55	14198.31	5000.00	969.36	709.52	132.72	b.d	b.d
NMC24	NMC24 - 62	rim	300967.74	n/a	218852.46	183333.33	95384.62	1741.50	33243.24	10084.39	4658.39	1044.57	623.81	135.80	33.49	b.d
NMC24	NMC24 - 63	core	339032.26	n/a	201639.34	178166.67	98974.36	3414.97	49420.85	22573.84	11677.02	2604.46	1919.05	438.27	55.98	b.d
NMC24	NMC24 - 64	rim	300967.74	n/a	240983.61	183333.33	78974.36	925.17	21467.18	4388.19	1381.99	221.45	114.29	b.d	b.d	b.d
NMC24	NMC24 - 65	core	371612.90	n/a	217213.11	181166.67	102051.28	5170.07	54208.49	27426.16	14844.72	4080.78	2657.14	688.27	122.49	683.23
NMC24	NMC24 - 66	rim	301935.48	n/a	256557.38	201500.00	74871.79	1523.81	17027.03	3966.24	1459.63	214.48	123.81	b.d	b.d	b.d
NMC24	NMC24 - 67	core	346774.19	n/a	238524.59	185666.67	108205.13	4095.24	49034.75	17890.30	8447.21	1657.38	1257.14	287.04	51.20	b.d
NMC24	NMC24 - 68	rim	252580.65	n/a	214754.10	170166.67	64615.38	993.20	7799.23	1054.85	288.82	b.d	b.d	b.d	b.d	b.d
NMC24	NMC24 - 69	rim	294516.13	n/a	232786.89	183333.33	93846.15	1115.65	36139.00	11687.76	4472.05	988.86	585.71	166.67	45.93	b.d
NMC24	NMC24 - 70	core	336129.03	n/a	209836.07	160000.00	89230.77	2857.14	50579.15	23417.72	11242.24	2799.44	1866.67	469.14	93.78	b.d
NMC24	NMC24 - 71	core	314193.55	n/a	234426.23	183333.33	91794.87	1741.50	26139.00	7151.90	2484.47	505.57	257.14	b.d	b.d	b.d
NMC24	NMC24 - 72	rim	314516.13	n/a	240983.61	198333.33	83076.92	925.17	19729.73	5210.97	2226.71	493.04	309.52	b.d	b.d	b.d
NMC24	NMC24 - 73	rim	259677.42	n/a	216393.44	183333.33	82564.10	1142.86	24903.47	7784.81	2701.86	557.10	400.00	b.d	b.d	b.d
NMC24	NMC24 - 74	core	376451.61	n/a	240163.93	169666.67	101025.64	3863.95	49922.78	20928.27	9534.16	1922.01	1123.81	283.95	38.28	b.d
NMC24	NMC24 - 75	missed	296129.03	n/a	231967.21	182666.67	75897.44	1346.94	18069.50	3649.79	1307.45	188.02	119.05	b.d	b.d	b.d
NMC24	NMC24 - 76	core	338709.68	n/a	222950.82	159333.33	87692.31	3782.31	49034.75	26793.25	18478.26	5417.83	4476.19	1240.74	315.79	1739.13
NMC24	NMC24 - 77	core	346129.03	n/a	211475.41	172166.67	88205.13	2163.27	43243.24	17700.42	8260.87	1601.67	957.14	250.00	b.d	b.d
NMC24	NMC24 - 78	rim	292580.65	n/a	206557.38	170833.33	81538.46	1401.36	25559.85	8059.07	3198.76	527.86	400.00	80.25	b.d	b.d
NMC24	NMC24 - 79	rim	263870.97	n/a	219672.13	170333.33	89743.59	1156.46	28918.92	7721.52	2795.03	447.08	333.33	b.d	b.d	b.d
NMC24	NMC24 - 80	core	256129.03	n/a	212295.08	182500.00	89230.77	1428.57	28185.33	7257.38	2329.19	448.47	261.90	b.d	b.d	b.d
NMC24	NMC24 - 81	rim	264838.71	n/a	242622.95	198833.33	98974.36	1333.33	41312.74	14367.09	5590.06	1323.12	852.38	305.56	56.94	b.d

Table D.24: LASS ICP-MS U–Pb isotopic data for zircon – IC machine settings for rim analyses, FC machine settings for core analyses. Sample NMC21.

sample ID	spot	instrument settings	CL	group	comment	$^{238}U/^{206}Pb$	2σ	$^{207}Pb/^{206}Pb$	2σ	$^{206}Pb/^{238}U$ Age (Ma)	2σ	$^{207}Pb/^{206}Pb$ Age (Ma)	2σ	7/6 discordance (%)	6/8 discordance (%)	U (ppm)	Pb (ppm)
NMC21Bc	NMC21Bc - 1	FC	Ob	S	bright core in oscillatory zoned elongated grain	3.818251	0.0670636	0.0994	0.008	1499	24	1630	150	8.04	-8.74	107.4	616
NMC21Bc	NMC21Bc - 2	FC	Ob	S	bright core in oscillatory zoned elongated grain	3.061849	0.03937467	0.113	0.0095	1822	20	1831	160	0.49	-0.49	57.8	281
NMC21Bc	NMC21Bc - 3	FC	Ob	S	bright core in oscillatory zoned elongated grain	3.083565	0.05514855	0.115	0.01	1810	28	1857	160	2.53	-2.60	55.9	353
NMC21Bc	NMC21Bc - 4	FC	Ob	S	bright core in oscillatory zoned elongated grain	3.056235	0.06631805	0.1141	0.0084	1824	34	1862	130	2.04	-2.08	147	398
NMC21Bc	NMC21Bc - 5	FC	Ol	D	oscillatory zoned grain	3.802281	0.2160602	0.103	0.008	1503	80	1682	150	10.64	-11.91	166	1750
NMC21Bc	NMC21Bc - 6	FC	Ob	S	bright core in oscillatory zoned elongated grain	3.259975	0.03382029	0.1072	0.0078	1729.1	16	1755	130	1.48	-1.50	154.8	1227
NMC21Bc	NMC21Bc - 7	FC	Ol	S	faint core in oscillatory zoned elongated grain	3.026634	0.0302297	0.11389	0.008	1840.3	16	1861	130	1.11	-1.12	268	2550
NMC21Bc	NMC21Bc - 8	FC	Ob	S	bright core in oscillatory zoned elongated grain	3.631082	0.06064988	0.1042	0.0075	1568	23	1706	120	8.09	-8.80	190	4150
NMC21Bc	NMC21Bc - 9	FC	Cb	D	very bright core in prismatic grain, oscillatory zoned	4.071661	0.06299802	0.0991	0.0081	1416	20	1612	160	12.16	-13.84	141.4	839
NMC21Bc	NMC21Bc - 10	FC	Cl	S	convoluted zoning in elongated grain, apparently magmatic	3.443526	0.04150255	0.1062	0.0075	1643	17	1733	130	5.19	-5.48	301	682
NMC21Bc	NMC21Bc - 11	FC	Ol	D	faint oscillatory zoning	3.607504	0.06897464	0.1067	0.0076	1577	27	1741	130	9.42	-10.40	276.9	1780
NMC21Bc	NMC21Bc - 12	FC	Ch	S	bright core in oscillatory zoned elongated grain	3.348962	0.0437 4063	0.1089	0.0077	1684	19	1779	130	5.34	-5.64	225.2	380
NMC21Bc	NMC21Bc - 13	FC	Cl	S	faint core in small grain	3.084516	0.03139698	0.11027	0.0077	1810.3	16	1803	130	-0.40	0.40	267	1960
NMC21Bc	NMC21Bc - 14	FC	Ch	S	bright core in oscillatory zoned elongated grain	3.322259	0.1765985	0.1102	0.0081	1693	81	1806	130	6.26	-6.67	160	1820
NMC21Bc	NMC21Bc - 15	FC	Ob	S	strongly oscillatory zoned grain, clearly magmatic	3.088326	0.03528971	0.10933	0.0077	1808	18	1787	130	-1.18	1.16	321	1840
NMC21Bc	NMC21Bc - 16	FC	Ch	S	bright convoluted zoning in core, faint rim	3.157562	0.03290166	0.1162	0.0085	1773.7	16	1909	130	7.09	-7.63	112.8	887
NMC21Bc	NMC21Bc - 17	FC	Ch	S	bright core in oscillatory zoned elongated grain	3.533569	0.1373472	0.105	0.0077	1606	55	1710	140	6.08	-6.48	223	1352
NMC21Bc	NMC21Bc - 18	FC	Ol	D	oscillatory zoned grain	6.207325	0.1425643	0.08419	0.0059	963	20	1295	140	25.64	-34.48	706	298
NMC21Bc	NMC21Bc - 19	FC	Ol	D	oscillatory zoned grain	3.926188	0.1418175	0.0998	0.0072	1462	47	1616	130	9.53	-10.53	359	429
NMC21Bc	NMC21Bc - 20	FC	Ch	S	bright core in oscillatory zoned elongated grain	3.260515	0.03401907	0.1067	0.0075	1724.3	16	1742	130	1.02	-1.03	256.2	1990
NMC21Bc	NMC21Bc - 21	FC	Ch	S	bright core in oscillatory zoned elongated grain	3.465093	0.05763	0.1065	0.0077	1634	24	1736	140	5.88	-6.24	180	1350
NMC21Bc	NMC21Bc - 22	FC	Ch	D	bright core, ablated mix of rim and core	4.371776	0.04204733	0.0971	0.007	1327.9	11	1567	140	15.26	-18.01	274	1196
NMC21Bc	NMC21Bc - 23	FC	Ch	S	convoluted zoning in elongated grain, apparently magmatic	3.629764	0.05401827	0.10305	0.0072	1568	21	1679	130	6.61	-7.08	430	989
NMC21Bc	NMC21Bc - 24	FC	Ch	S	oscillatory fragment in ovoidal grain	3.354579	0.1114067	0.1035	0.0074	1681	49	1686	130	0.30	-0.30	226.2	1361
NMC21Bc	NMC21Bc - 25	FC	Ob	D	bright oscillatory zoning, missed spot	3.73413	0.1394373	0.1053	0.0077	1528	52	1714	140	10.85	-12.17	205	7.66E+03
NMC21Bc	NMC21Bc - 26	FC	Ob	S	strongly oscillatory zoned grain, clearly magmatic (core next to rim spot 29)	2.965599	0.03517911	0.1164	0.0084	1873	19	1898	130	1.32	-1.33	118.4	837
NMC21Bc	NMC21Bc - 27	FC	Ob	S	strongly oscillatory zoned fragment (core next to rim spot 30)	3.267974	0.1388355	0.1122	0.008	1721	62	1834	130	6.16	-6.57	347	2051
NMC21Bc	NMC21Bc - 28	FC	Ob	S	strongly oscillatory zoned fragment (core next to rim spot 31)	3.372681	0.0534624	0.1043	0.0074	1674	23	1700	130	1.53	-1.55	333.3	648
NMC21Bc	NMC21Bc - 29	FC	Ch	S	bright core in small grain	3.736921	0.115906	0.091	0.0073	1527	43	1433	160	-6.56	6.16	119.8	228
NMC21Bc	NMC21Bc - 30	FC	Ob	S	oscillatory zoned hypidiomorphic grain, magmatic origin	2.970885	0.03795249	0.1157	0.0086	1870	21	1885	130	0.80	-0.80	109.3	1034
NMC21Bc	NMC21Bc - 31	FC	Ob	D	bright oscillatory zoning, missed spot	4.046945	0.1195576	0.1306	0.0096	1423	38	2102	130	32.30	-47.72	277	1165
NMC21Bc	NMC21Bc - 32	FC	Ob	S	strongly oscillatory zoned grain, clearly magmatic	2.93772	0.0345208	0.1135	0.0082	1889	19	1854	130	-1.89	1.85	201.3	1665
NMC21Bc	NMC21Bc - 33	FC	Cl	S	CL-dark grain	3.610108	0.1563946	0.1013	0.0073	1572	59	1645	130	4.44	-4.64	378	419
NMC21Bc	NMC21Bc - 34	FC	Ch	S	oscillatory fragment in ovoidal grain	3.137747	0.03150546	0.11005	0.0077	1793.2	15	1799	130	0.88	-0.89	462.2	4165
NMC21Bc	NMC21Bc - 35	FC	Ob	D	bright oscillatory zoning, missed spot/rim-core overlap	4.045307	0.09491417	0.0993	0.007	1424	30	1610	130	11.55	-13.06	360	2726
NMC21Bc	NMC21Bc - 36	FC	Ch	S	convoluted zoning in elongated grain, apparently magmatic	3.31565	0.03737802	0.10757	0.0075	1699.3	17	1757	130	3.28	-3.40	312	1039
NMC21Bc	NMC21Bc - 37	FC	Ob	S	oscillatory core	3.584229	0.2055472	0.0986	0.0074	1584	81	1592	140	0.50	-0.51	364	574
NMC21Bc	NMC21Bc - 38	FC	Ob	S	oscillatory core	2.849815	0.0438558	0.1092	0.0079	1938	26	1783	130	-8.69	8.00	142.2	693
NMC21B	NMC21B - 1	IC	Si	D	faint sector zoned rim on elongated hypidiomorphic grain with oscillatory zoned fragment at core, mxed ablation	5.98444	0.1611609	0.07562	0.00085	1000	27	1087	21	8.00	-8.70	n/a	n/a
NMC21B	NMC21B - 2	IC	Ol	D	oscillatory mantle, part of magmatic grain, mixed age?	5.717553	0.2517162	0.1033	0.0018	1038	42	1682	32	38.29	-62.04	n/a	n/a
NMC21B	NMC21B - 3	IC	Si	D	faint sector zoned rim on elongated hypidiomorphic grain with oscillatory zoned fragment at core	4.163197	0.1577231	0.0961	0.0021	1387	47	1547	41	10.34	-11.54	n/a	n/a
NMC21B	NMC21B - 4	IC	Ob	S	oscillatory mantle, part of magmatic grain	3.117207	0.08259432	0.1048	0.0013	1793	42	1710	23	-4.85	4.63	n/a	n/a
NMC21B	NMC21B - 5	IC	Ch	D	spot on bright idiobastic core, rim is convoluted and CL-dark	5.36504	0.1519746	0.0972	0.0016	1113	29	1569	31	29.06	-40.97	n/a	n/a
NMC21B	NMC21B - 6	IC	Ol	S	oscillatory part of hypidoblastic, elongated grain	3.378378	0.2054419	0.11028	0.0012	1666	91	1803.1	20	7.60	-8.23	n/a	n/a
NMC21B	NMC21B - 7	IC	Si	M	sector zoned, faint rim on rounded grain	5.636979	0.1302797	0.07472	0.00081	1052.5	22	1059.8	22	0.69	-0.69	n/a	n/a
NMC21B	NMC21B - 8	IC	Ri	M	rim, odd zoning, intermediate between sector and oscillatory	5.675369	0.1256183	0.07348	0.00076	1046.2	22	1026.3	21	-1.94	1.90	n/a	n/a
NMC21B	NMC21B - 9	IC	Ol	D	oscillatory rim, part of magmatic grain, mixed age?	6.22665	0.2016101	0.07624	0.0012	960	29	1099	31	12.65	-14.48	n/a	n/a
NMC21B	NMC21B - 10	IC	Si	M	sector zoned, faint rim on rounded grain	5.586592	0.127961	0.07278	0.00074	1061.6	22	1007	21	-5.42	5.14	n/a	n/a
NMC21B	NMC21B - 11	IC	Ri	D	dark rim on bright core, mixed age?	5.813953	0.4394267	0.111	0.0099	1024	69	1780	130	42.47	-73.83	n/a	n/a
NMC21B	NMC21B - 12	IC	Ob	S	CL-bright mantle, part of magmatic grain	3.067485	0.1035041	0.1218	0.0019	1818	55	1981	28	8.23	-8.97	n/a	n/a
NMC21B	NMC21B - 13	IC	Ol	S	CL-dark mantle, part of magmatic grain	3.194888	0.1429023	0.1169	0.0017	1755	68	1907	26	7.97	-8.66	n/a	n/a
NMC21B	NMC21B - 14	IC	Ob	S	oscillatory mantle on magmatic grain	3.132832	0.08440588	0.10938	0.0011	1786	42	1788.2	18	0.12	-0.12	n/a	n/a
NMC21B	NMC21B - 15	IC	Ri	D	dark rim on bright core, mixed age?	5.068424	0.1310135	0.089	0.0013	1161	28	1402	29	17.19	-20.76	n/a	n/a
NMC21B	NMC21B - 16	IC	Ri	M	CL-dark rim on bright core	5.45286	0.1219081	0.07316	0.00073	1085.4	22	1017.4	20	-6.68	6.26	n/a	n/a
NMC21B	NMC21B - 17	IC	Ri	D	dark rim on dark core, mixed age?	4.810005	0.1642666	0.0877	0.0014	1217	38	1374	31	11.43	-12.90	n/a	n/a
NMC21B	NMC21B - 18	IC	Ri	D	dark rim on bright core, seems to have ablated part of resin	6.21118	0.1581729	0.07336	0.00077	962	23	1022.9	21	5.95	-6.33	n/a	n/a
NMC21B	NMC21B - 19	IC	Ri	D	dark rim on dark core, mixed age?	5.790388	0.1408201	0.0862	0.0039	1027	23	1330	80	22.78	-29.50	n/a	n/a
NMC21B	NMC21B - 20	IC	Ri	S	dark rim on bright core	4.132231	0.3927327	0.094	0.0046	1390	120	1492	93	6.84	-7.34	n/a	n/a
NMC21B	NMC21B - 21	IC	Ri	D	dark rim on bright core, seems to have ablated part of resin	5.810575	0.1356511	0.07652	0.00084	1023.5	22	1108	22	7.63	-8.26	n/a	n/a
NMC21B	NMC21B - 22	IC	Ri	D	dark rim on dark core, mixed age?	4.746084	0.1171317	0.08692	0.0012	1233	28	1357	26	9.14	-10.06	n/a	n/a
NMC21B	NMC21B - 23	IC	Ri	D	dark rim on dark core, mixed age?	4.741584	0.1911022	0.09839	0.0012	1233	45	1593	23	22.60	-29.20	n/a	n/a
NMC21B	NMC21B - 24	IC	Ol	S	oscillatory zoned fragment as core in rounded grain	2.905288	0.0666815	0.11222	0.0011	1907	38	1834.8	18	-3.94	3.79	n/a	n/a
NMC21B	NMC21B - 25	IC	Ri	D	dark rim on dark core, mixed age?	5.104645	0.1276813	0.08308	0.0011	1153	27	1270	26	9.21	-10.15	n/a	n/a
NMC21B	NMC21B - 26	IC	Ri	D	dark rim on dark core, mixed age?	3.749531	0.08716571	0.10461	0.0011	1524	32	1706.6	19	10.70	-11.98	n/a	n/a
NMC21B	NMC21B - 27	IC	Si	M	textbook sector zoned grain	5.746136	0.1287705	0.07302	0.00075	1034.2	22	1013.5	21	-2.04	2.00	n/a	n/a
NMC21B	NMC21B - 28	IC	Ri	D	dark rim on dark core, mixed age?	13.1926	0.6613711	0.0807	0.0023	471	22	1208	54	61.01	-156.48	n/a	n/a
NMC21B	NMC21B - 29	IC	Ol	S	tip of idiolbastic oscillatory zoned core	3.497726	0.09297909	0.10634	0.0012	1621	38	1736	21	6.62	-7.09	n/a	n/a
NMC21B	NMC21B - 30	IC	Ol	S	dark rim on bright core, mixed age?	5.688282	0.2135533	0.0824	0.0013	1044	36	1254	32	16.75	-20.11	n/a	n/a
NMC21B	NMC21B - 31	IC	Ri	D	dark rim on bright core, seems to have ablated part of resin	6.195787	0.1612287	0.07468	0.00095	965	23	1059	25	8.88	-9.74	n/a	n/a
NMC21B	NMC21B - 32	IC	Ri	D	dark rim on bright core, seems to have ablated part of resin	6.30517	0.2425065	0.07369	0.00079	949	34	1031.9	22	8.03	-8.74	n/a	n/a
NMC21B	NMC21B - 33	IC	Cl	Y	dark rim on needle-shaped grain with small bright core	4.77327	0.1298694	0.07901	0.00083	1226	30	1171.4	21	-4.66	4.45	n/a	n/a
NMC21B	NMC21B - 34	IC	Ob	S	oscillatory zoned fragment as core in rounded grain	2.633658	0.06173178	0.12494	0.0013	2075	42	2027.1	18	-2.36	2.31	n/a	n/a
NMC21B	NMC21B - 35	IC	Ob	D	oscillatory zoned fragment as core in rounded grain	3.824092	0.09797864	0.10137	0.0012	1498	34	1648	21	9.10	-10.01	n/a	n/a
NMC21B	NMC21B - 36	IC	Ob	S	oscillatory zoned fragment as core in rounded grain	2.64131	0.08371823	0.1105	0.0018	2069	55	1806	30	-14.56	12.71	n/a	n/a
NMC21B	NMC21B - 37	IC	Ch	S	bright core in oscillatory zoned elongated grain	2.793296	0.1716551	0.113	0.0022	1967	100	1846	34	-6.55	6.15	n/a	n/a
NMC21B	NMC21B - 38	IC	Ri	M	CL-dark overgrowth on sector zoned fragment	5.688929	0.1262193	0.07241	0.00073	1043.9	21	996.4	21	-4.77	4.55	n/a	n/a

Table D.25: LASS ICP-MS chondrite-normalised REE data for zircon (ppm) – IC machine settings for rim analyses, FC machine settings for core analyses. Sample NMC21.

sample ID	spot	instrument settings	CL	group	La	Ce	Pr	Nd	Sm	Eu	Gd	Tb	Dy	Ho	Er	Tm	Yb	Lu
NMC21Bc	NMC21Bc - 1	FC	Oh	S	b.d	17.90	1.69	7.00	37.44	22.45	112.36	251.48	412.73	736.77	1208.10	1617.28	2478.47	3406.83
NMC21Bc	NMC21Bc - 2	FC	Oh	S	b.d	11.04	b.d	0.95	7.95	8.57	39.77	79.54	136.02	248.61	401.90	574.07	895.22	1273.29
NMC21Bc	NMC21Bc - 3	FC	Oh	S	b.d	24.13	b.d	b.d	8.26	8.16	27.03	59.07	109.01	188.44	320.95	472.22	781.82	1164.60
NMC21Bc	NMC21Bc - 4	FC	Oh	S	b.d	12.87	1.15	5.00	29.74	8.84	114.67	217.30	450.31	873.26	1557.14	2333.33	3722.49	5155.28
NMC21Bc	NMC21Bc - 5	FC	Ol	D	b.d	990.10	1098.36	1150.00	1025.64	51.70	474.90	238.40	218.94	330.08	490.00	680.25	1049.76	1409.94
NMC21B	NMC21Bc - 6	FC	Oh	S	b.d	46.13	b.d	b.d	11.49	5.31	55.60	111.39	201.86	395.54	647.62	898.15	1336.84	1807.45
NMC21B	NMC21Bc - 7	FC	Ol	S	b.d	58.17	31.15	41.67	58.46	28.03	113.90	184.39	294.72	530.64	905.24	1308.64	2191.39	3304.35
NMC21B	NMC21Bc - 8	FC	Oh	S	b.d	1670.79	1590.16	1633.33	748.72	55.37	467.18	377.64	522.67	800.84	1246.67	1552.47	2306.22	3164.60
NMC21Bc	NMC21Bc - 9	FC	Ch	D	b.d	25.87	2.30	4.00	27.18	19.46	89.96	158.65	261.18	454.04	751.90	1012.35	1531.10	2173.91
NMC21B	NMC21Bc - 10	FC	Cl	S	b.d	12.25	1.07	1.87	16.92	6.80	96.14	266.88	543.17	1059.89	1971.43	2972.22	4689.00	6428.57
NMC21Bc	NMC21Bc - 11	FC	Ol	D	b.d	163.37	44.43	67.00	101.54	152.38	124.32	179.96	274.22	448.47	725.24	1006.17	1622.01	2180.12
NMC21B	NMC21Bc - 12	FC	Ch	S	b.d	6.75	1.20	4.17	17.95	2.72	50.97	121.94	212.42	402.51	648.10	972.53	1570.81	2239.13
NMC21B	NMC21Bc - 13	FC	Cl	S	b.d	32.55	9.18	16.83	56.41	44.22	260.23	502.11	894.41	1571.03	2419.05	3114.20	4421.05	5841.61
NMC21B	NMC21Bc - 14	FC	Ch	S	b.d	878.71	1065.57	1266.67	1179.49	65.31	706.56	518.99	537.27	725.63	980.95	1194.44	1760.77	2341.61
NMC21B	NMC21Bc - 15	FC	Oh	S	b.d	19.80	1.09	5.67	27.18	13.74	92.28	171.52	282.92	540.39	890.48	1287.04	2062.20	3080.75
NMC21B	NMC21Bc - 16	FC	Ch	S	b.d	17.51	1.33	8.17	47.18	25.03	177.61	375.53	633.54	1140.67	1757.14	2299.38	3459.33	4453.42
NMC21B	NMC21Bc - 17	FC	Ch	S	b.d	28.71	1.54	4.17	17.95	25.99	87.26	158.65	294.41	559.89	961.90	1317.90	2033.49	3015.53
NMC21Bc	NMC21Bc - 18	FC	Ol	D	b.d	17.57	6.07	6.83	18.46	25.17	54.44	113.71	221.12	420.61	767.62	1367.28	2559.81	3807.45
NMC21Bc	NMC21Bc - 19	FC	Ol	D	b.d	16.46	3.69	4.83	10.46	22.59	25.87	59.92	123.29	267.41	508.10	830.25	1526.32	2431.68
NMC21B	NMC21Bc - 20	FC	Ch	S	b.d	37.38	17.21	6.67	29.74	10.75	94.98	157.17	238.20	412.26	671.90	947.53	1400.00	1922.36
NMC21B	NMC21Bc - 21	FC	Ch	S	b.d	30.57	b.d	4.00	27.18	14.69	110.04	175.32	298.45	509.75	784.29	1021.60	1545.45	2027.95
NMC21Bc	NMC21Bc - 22	FC	Ch	D	b.d	68.69	6.23	10.50	29.74	30.20	122.01	231.65	399.38	745.13	1260.48	1802.47	2851.67	4226.71
NMC21B	NMC21Bc - 23	FC	Ch	S	b.d	35.77	11.72	16.50	30.26	47.76	69.88	139.24	257.45	493.04	886.19	1358.02	2301.44	3409.94
NMC21B	NMC21Bc - 24	FC	Ch	S	b.d	29.08	b.d	2.12	12.82	b.d	61.39	122.36	227.64	395.54	660.48	916.05	1399.04	1996.89
NMC21Bc	NMC21Bc - 25	FC	Oh	D	b.d	58.29	4.26	9.50	47.69	15.78	106.95	151.48	243.79	431.75	685.71	956.79	1468.90	2021.74
NMC21B	NMC21Bc - 26	FC	Oh	S	b.d	19.55	b.d	2.47	12.87	10.61	73.75	160.97	289.13	511.14	830.95	1182.10	1711.00	2400.62
NMC21B	NMC21Bc - 27	FC	Oh	S	b.d	40.22	5.08	8.67	16.92	17.69	35.52	69.62	122.98	236.91	425.71	716.05	1215.31	1922.36
NMC21B	NMC21Bc - 28	FC	Oh	S	0.06	15.16	0.75	1.98	11.28	7.48	60.23	133.33	250.31	455.43	757.62	1148.15	1933.01	2900.62
NMC21B	NMC21Bc - 29	FC	Ch	S	b.d	24.01	5.00	1.97	13.33	7.07	39.00	70.46	121.12	216.02	365.71	536.42	882.30	1257.76
NMC21B	NMC21Bc - 30	FC	Oh	S	b.d	35.15	1.16	5.50	30.77	12.79	102.32	169.62	310.56	543.18	833.81	1108.02	1602.87	2177.02
NMC21Bc	NMC21Bc - 31	FC	Oh	D	b.d	51.61	51.72	57.17	45.64	37.55	103.47	185.23	312.11	598.89	986.19	1555.56	2385.17	3521.74
NMC21B	NMC21Bc - 32	FC	Oh	S	b.d	32.43	3.61	8.83	62.05	44.08	184.94	353.16	615.53	1079.39	1672.86	2253.09	3334.93	4509.32
NMC21B	NMC21Bc - 33	FC	Cl	S	b.d	8.29	b.d	b.d	12.82	7.76	69.88	154.01	298.14	623.96	1233.33	2117.28	3861.24	5962.73
NMC21B	NMC21Bc - 34	FC	Oh	S	b.d	83.29	0.96	5.17	31.79	26.53	147.49	292.41	507.14	912.26	1468.10	2015.43	2851.67	3885.09
NMC21Bc	NMC21Bc - 35	FC	Oh	D	b.d	76.49	20.98	38.33	89.23	109.39	288.03	487.34	763.98	1236.77	1738.10	2225.31	3009.57	3922.36
NMC21B	NMC21Bc - 36	FC	Ch	S	b.d	10.43	2.13	4.33	18.46	3.13	96.91	236.92	422.36	839.83	1374.76	1962.96	2889.95	3972.05
NMC21B	NMC21Bc - 37	FC	Oh	S	b.d	16.46	2.46	7.67	40.51	23.13	131.27	227.43	359.32	636.49	947.62	1274.69	2057.42	2888.20
NMC21B	NMC21Bc - 38	FC	Oh	S	b.d	22.22	b.d	2.83	22.05	5.85	57.14	110.34	185.09	314.48	492.38	759.26	1079.90	1512.42
NMC21Bc	NMC21B - 1	IC	Sl	D	b.d	13.49	16.80	21.83	b.d	40.82	51.35	120.25	205.28	353.76	652.38	858.02	1368.42	1826.09
NMC21Bc	NMC21B - 2	IC	Ol	D	b.d	6.19	11.15	6.83	23.08	451.70	54.44	109.92	208.07	388.58	762.38	1225.31	2196.17	3167.70
NMC21Bc	NMC21B - 3	IC	Sl	D	b.d	14.36	7.95	b.d	23.59	43.54	49.81	87.34	195.34	378.83	739.05	1166.67	1918.66	2586.96
NMC21B	NMC21B - 4	IC	Oh	S	b.d	29.33	36.89	38.50	33.33	10.75	36.29	69.41	132.92	295.26	576.19	811.73	1459.33	1925.47
NMC21Bc	NMC21B - 5	IC	Ch	D	b.d	20.30	17.95	b.d	b.d	38.10	29.73	42.19	138.51	222.84	466.67	777.78	1444.98	1987.58
NMC21B	NMC21B - 6	IC	Ol	S	b.d	46.66	b.d	12.50	27.69	9.93	64.09	163.92	264.29	526.46	962.86	1222.22	1904.31	2537.27
NMC21Bc	NMC21B - 7	IC	Sl	M	b.d	5.64	b.d	b.d	24.10	23.27	67.57	120.68	140.68	162.95	180.00	170.37	245.93	341.93
NMC21Bc	NMC21B - 8	IC	Rl	M	0.05	7.05	b.d	b.d	16.92	b.d	56.37	82.28	121.74	135.79	130.00	126.23	153.59	206.21
NMC21Bc	NMC21B - 9	IC	Ol	D	b.d	29.70	20.49	b.d	43.08	36.73	82.24	110.76	134.47	128.13	160.95	128.40	217.70	257.76
NMC21Bc	NMC21B - 10	IC	Sl	M	0.07	4.13	b.d	b.d	12.31	b.d	31.66	78.27	113.35	174.09	241.90	333.33	511.96	608.70
NMC21Bc	NMC21B - 11	IC	Rl	D	b.d	6.96	14.34	9.33	6.67	15.37	33.20	92.83	217.70	473.54	987.62	1564.81	2684.21	4155.28
NMC21B	NMC21B - 12	IC	Oh	S	b.d	12.75	b.d	b.d	b.d	11.97	10.04	34.39	57.14	104.60	180.48	277.78	420.57	627.33
NMC21B	NMC21B - 13	IC	Ol	S	b.d	33.04	24.59	61.67	53.85	48.98	83.01	151.90	263.35	500.00	904.76	1194.44	1904.31	2664.60
NMC21B	NMC21B - 14	IC	Oh	S	b.d	141.09	78.69	91.67	65.64	88.44	114.67	168.78	332.30	640.67	1052.38	1527.78	2550.24	3385.09
NMC21Bc	NMC21B - 15	IC	Rl	D	b.d	19.55	66.39	54.67	41.03	93.88	33.59	106.33	242.55	525.07	1028.57	1790.12	3665.07	5332.30
NMC21Bc	NMC21B - 16	IC	Rl	M	b.d	4.73	b.d	b.d	26.15	b.d	64.86	104.85	107.45	121.87	133.33	137.04	184.21	229.81
NMC21Bc	NMC21B - 17	IC	Rl	D	b.d	9.16	b.d	18.67	b.d	b.d	37.07	107.59	219.57	451.25	914.29	1506.17	2693.78	3701.86
NMC21Bc	NMC21B - 18	IC	Rl	D	0.04	7.49	b.d	b.d	23.08	b.d	59.85	82.28	102.17	113.93	132.86	135.80	192.34	285.71
NMC21Bc	NMC21B - 19	IC	Rl	D	b.d	20.42	18.52	26.17	32.82	24.35	81.85	118.14	139.44	165.32	190.95	213.27	221.53	305.90
NMC21B	NMC21B - 20	IC	Rl	S	b.d	10.52	b.d	7.67	17.95	b.d	80.70	179.32	291.93	520.89	761.90	1030.86	1468.90	1822.98
NMC21Bc	NMC21B - 21	IC	Rl	D	b.d	5.83	b.d	5.83	21.03	8.57	46.72	103.38	122.36	197.77	283.33	383.02	650.72	816.77
NMC21Bc	NMC21B - 22	IC	Rl	D	b.d	4.58	b.d	b.d	b.d	b.d	16.99	52.74	151.55	299.44	533.33	879.63	1693.78	2437.89
NMC21Bc	NMC21B - 23	IC	Rl	D	b.d	24.75	52.46	78.33	47.18	276.19	40.54	77.00	172.67	374.65	699.05	1253.09	2631.58	3875.78
NMC21B	NMC21B - 24	IC	Ol	S	0.07	35.64	b.d	b.d	b.d	b.d	53.28	145.15	257.45	472.14	823.81	1098.77	1851.67	2347.83
NMC21Bc	NMC21B - 25	IC	Rl	D	0.07	6.32	b.d	b.d	6.15	b.d	22.78	74.68	155.59	341.23	596.19	944.44	1655.50	2301.24
NMC21Bc	NMC21B - 26	IC	Rl	D	b.d	29.95	21.56	22.83	10.26	44.90	40.93	104.64	240.68	472.14	857.14	1496.91	2693.78	3767.08
NMC21Bc	NMC21B - 27	IC	Sl	M	b.d	7.30	b.d	b.d	38.97	b.d	105.41	159.28	187.58	211.70	190.00	193.83	239.71	250.93
NMC21Bc	NMC21B - 28	IC	Rl	D	b.d	33.54	97.54	115.00	103.59	657.14	94.98	282.70	608.70	1277.16	2119.05	3895.06	7033.49	9285.71
NMC21B	NMC21B - 29	IC	Ol	S	b.d	27.60	16.07	6.00	24.10	20.41	43.63	81.22	172.36	366.30	671.43	1089.51	2028.71	3021.74
NMC21B	NMC21B - 30	IC	Ol	S	b.d	13.49	13.20	18.50	21.54	115.65	21.24	81.01	217.08	428.97	796.67	1388.89	2578.95	3763.98
NMC21Bc	NMC21B - 31	IC	Rl	D	b.d	4.00	2.13	6.50	b.d	b.d	29.34	107.59	186.96	355.15	548.57	864.20	1488.04	1972.05
NMC21Bc	NMC21B - 32	IC	Rl	D	b.d	5940.59	13606.56	10833.33	2871.79	100.68	567.57	278.48	291.93	396.94	422.38	648.15	995.22	1447.21
NMC21B	NMC21B - 33	IC	Cl	S	b.d	16.21	42.62	60.00	68.21	65.31	96.14	223.63	559.01	1147.63	2019.05	3521.60	6382.78	8478.26
NMC21B	NMC21B - 34	IC	Oh	S	0.01	14.36	b.d	b.d	24.62	b.d	55.21	147.68	269.25	547.35	799.52	1163.58	1779.90	2413.04
NMC21Bc	NMC21B - 35	IC	Oh	D	b.d	110.15	213.11	216.67	143.59	23.13	100.39	173.00	267.70	583.57	861.90	1302.47	2320.57	3049.69
NMC21B	NMC21B - 36	IC	Oh	S	0.04	26.49	6.39	b.d	7.69	17.82	45.17	100.84	163.98	274.37	441.90	638.89	1081.34	1605.59
NMC21B	NMC21B - 37	IC	Ch	S	0.04	6.83	b.d	b.d	14.87	b.d	46.33	122.36	174.84	362.12	513.81	811.73	1325.36	1804.35
NMC21Bc	NMC21B - 38	IC	Rl	M	0.04	0.24	b.d	b.d	b.d	b.d	47.10	119.41	192.55	325.91	473.81	740.74	1277.51	1965.84

Table D.26: LASS ICP-MS U–Pb isotopic data for monazite. Sample NMC21.

sample ID	spot	location	$^{238}U/^{206}Pb$	2σ	$^{207}Pb/^{206}Pb$	2σ	$^{206}Pb/^{238}U$ Age (Ma)	2σ	$^{207}Pb/^{206}Pb$ Age (Ma)	2σ	7/6 discordance (%)	6/8 discordance (%)	U (ppm)	Th (ppm)	Pb (ppm)
NMC21B	NMC21B - 1	rim	5.941771	0.144749	0.0723	0.0014	1002.7	23	992	39	-1.08	1.1	1450	9.30E+04	5880
NMC21B	NMC21B - 2	rim	5.851375	0.1574975	0.0714	0.0014	1017	25	966	40	-5.28	5.0	1740	6.72E+04	4310
NMC21B	NMC21B - 3	core	5.743825	0.1814534	0.0718	0.0011	1035	30	978	32	-5.83	5.5	2680	5.73E+04	3680
NMC21B	NMC21B - 4	rim	5.934718	0.158494	0.07196	0.0009	1004	25	983	26	-2.14	2.1	2230	5.66E+04	3580
NMC21B	NMC21B - 5	core	5.767013	0.1596405	0.07152	0.00082	1031	26	971	23	-6.18	5.8	2730	5.29E+04	3370
NMC21B	NMC21B - 6	core	5.847953	0.1607332	0.0723	0.0012	1018	26	991	32	-2.72	2.7	1500	5.98E+04	3790
NMC21B	NMC21B - 7	core	6.038647	0.1568006	0.0719	0.0014	988	24	979	41	-0.92	0.9	2030	8.60E+04	5370
NMC21B	NMC21B - 8	core	5.924171	0.1438928	0.0719	0.0012	1005.7	22	980	36	-2.62	2.6	1670	5.65E+04	3470
NMC21B	NMC21B - 9	core	5.65931	0.1601389	0.0729	0.001	1049	27	1009	28	-3.96	3.8	1120	4.80E+04	3010
NMC21B	NMC21B - 10	core	5.844535	0.1502978	0.0725	0.0012	1018	24	999	34	-1.90	1.9	2170	1.48E+05	9.60E+03
NMC21B	NMC21B - 11	rim	5.896226	0.1703509	0.07141	0.00087	1010	27	967	25	-4.45	4.3	2870	5.12E+04	3190
NMC21B	NMC21B - 12	core	6.060606	0.194674	0.07118	0.00089	984	29	961	26	-2.39	2.3	1250	7.09E+04	4360
NMC21B	NMC21B - 13	rim	5.861665	0.2851806	0.0732	0.002	1015	46	1015	56	0.00	0.0	870	6.80E+04	4220
NMC21B	NMC21B - 14	rim	5.817336	0.1658228	0.07204	0.00061	1022	27	986	17	-3.65	3.5	1650	6.80E+04	4330
NMC21B	NMC21B - 15	rim	6.064281	0.1581347	0.07284	0.00079	984	24	1008	22	2.38	-2.4	2400	3.40E+04	2140
NMC21B	NMC21B - 16	rim	5.892752	0.1527879	0.07343	0.00083	1010	24	1024	23	1.37	-1.4	1990	8.90E+04	5550
NMC21B	NMC21B - 17	rim	5.977286	0.1536302	0.0716	0.0012	997	24	980	36	-1.73	1.7	1380	9.80E+04	6180
NMC21B	NMC21B - 18	core	5.844535	0.170793	0.0721	0.0012	1018	28	996	30	-2.21	2.2	1310	7.06E+04	4320
NMC21B	NMC21B - 19	rim	5.920663	0.1577441	0.0724	0.0014	1006	25	996	39	-1.00	1.0	1600	1.09E+05	6550
NMC21B	NMC21B - 20	rim	5.824112	0.1797775	0.07182	0.00088	1021	29	979	25	-4.29	4.1	1500	6.30E+04	4060
NMC21B	NMC21B - 21	rim	6.049607	0.1683496	0.0731	0.0012	986	26	1014	35	2.76	-2.8	1770	5.64E+04	3520
NMC21B	NMC21B - 22	rim	5.988024	0.1613539	0.0726	0.0011	996	25	1000	32	0.40	-0.4	1640	6.90E+04	4390
NMC21B	NMC21B - 23	core	5.970149	0.1710849	0.0725	0.0015	998	27	1008	46	0.99	-1.0	1630	6.64E+04	4170
NMC21B	NMC21B - 24	rim	5.885815	0.159357	0.072	0.0012	1011	25	984	33	-2.74	2.7	1560	6.34E+04	3930
NMC21B	NMC21B - 25	core	5.841121	0.1535342	0.0717	0.001	1019	25	976	29	-4.41	4.2	1930	8.80E+04	5390
NMC21B	NMC21B - 26	rim	5.903188	0.1428753	0.0716	0.0013	1008.9	22	973	36	-3.69	3.6	1570	7.00E+04	4410
NMC21B	NMC21B - 27	rim	5.903188	0.1428753	0.0728	0.0013	1008.7	23	1006	37	-0.27	0.3	1960	5.22E+04	3300
NMC21B	NMC21B - 28	rim	5.91716	0.150555	0.0715	0.0012	1007	24	968	35	-4.03	3.9	1930	4.71E+04	2940
NMC21B	NMC21B - 29	rim	5.988024	0.1398401	0.07019	0.00098	995.7	22	932	29	-6.83	6.4	4310	5.05E+04	3100
NMC21B	NMC21B - 30	core	5.868545	0.1584232	0.07263	0.00089	1014	26	1002	25	-1.20	1.2	2220	5.96E+04	3710
NMC21B	NMC21B - 31	rim	5.959476	0.1491645	0.0739	0.0011	1000	23	1037	29	3.57	-3.7	1850	7.50E+04	4720
NMC21B	NMC21B - 32	rim	5.797101	0.1646713	0.07133	0.00099	1026	27	965	28	-6.32	5.9	1790	4.90E+04	3190
NMC21B	NMC21B - 33	core	5.793743	0.171194	0.07117	0.00087	1026	28	961	25	-6.76	6.3	1650	6.29E+04	3920
NMC21B	NMC21B - 34	core	5.931198	0.1407164	0.07167	0.00073	1004.6	22	975	21	-3.04	2.9	7430	4.43E+04	2830
NMC21B	NMC21B - 35	core	5.837712	0.1567628	0.0724	0.0011	1019	25	996	31	-2.31	2.3	1410	6.54E+04	4060
NMC21B	NMC21B - 36	core	6.031363	0.1600603	0.0738	0.0014	989	25	1032	39	4.17	-4.3	1630	7.30E+04	4520
NMC21B	NMC21B - 37	core	5.865103	0.1616773	0.07233	0.00091	1015	26	994	26	-2.11	2.1	2440	2.08E+04	1380
NMC21B	NMC21B - 38	rim	5.913661	0.1608684	0.072	0.0012	1007	25	983	35	-2.44	2.4	1510	3.14E+04	2000
NMC21B	NMC21B - 39	rim	5.885815	0.1697498	0.0727	0.001	1012	27	1004	29	-0.80	0.8	1470	5.37E+04	3390
NMC21B	NMC21B - 40	core	5.800464	0.1480397	0.07406	0.00086	1025	24	1041	23	1.54	-1.6	3650	4.90E+04	3130
NMC21B	NMC21B - 41	rim	5.810575	0.1620614	0.07173	0.00097	1024	26	977	27	-4.81	4.6	2040	5.71E+04	3660
NMC21B	NMC21B - 42	rim (D)	5.521811	0.1615991	0.116	0.01	1073	29	1860	150	42.31	-73.3	1370	7.50E+04	4460
NMC21B	NMC21B - 43	core (D)	5.333333	0.2417778	0.132	0.017	1107	46	2060	220	46.26	-86.1	1620	5.22E+04	3520
NMC21B	NMC21B - 44	rim	5.952381	0.1523526	0.0701	0.0015	1001	24	929	42	-7.75	7.2	1680	6.58E+04	4060
NMC21B	NMC21B - 45	rim	5.995204	0.1581469	0.0709	0.0011	994	24	960	31	-3.54	3.4	1770	7.40E+04	4590

Table D.27: LASS ICP-MS chondrite-normalised REE data for monazite (ppm). Sample NMC21.

sample ID	spot	location	La	Ce	Pr	Nd	Sm	Eu	Gd	Tb	Dy	Ho	Er	Tm	Yb	Lu
NMC21B	NMC21B - 1	rim	267741.94	n/a	214754.10	175500.00	92307.69	2435.37	29073.36	7173.00	2310.56	274.37	138.10	b.d	b.d	b.d
NMC21B	NMC21B - 2	rim	263225.81	n/a	208196.72	168333.33	86153.85	4761.90	41698.84	17890.30	11863.35	3676.88	3690.48	947.53	344.50	1521.74
NMC21B	NMC21B - 3	core	296129.03	n/a	206557.38	164500.00	77948.72	9251.70	44787.64	22784.81	16118.01	6114.21	5857.14	2438.27	660.29	3664.60
NMC21B	NMC21B - 4	rim	314838.71	n/a	193442.62	152500.00	86153.85	13877.55	44787.64	21772.15	13850.93	4373.26	3861.90	1027.78	172.25	1459.63
NMC21B	NMC21B - 5	core	310000.00	n/a	196721.31	152666.67	88205.13	18367.35	47451.74	22341.77	15279.50	4470.75	3819.05	1364.20	287.08	1428.57
NMC21B	NMC21B - 6	core	305483.87	n/a	212295.08	164833.33	87179.49	4517.01	31042.47	9915.61	3416.15	681.06	300.00	b.d	b.d	b.d
NMC21B	NMC21B - 7	core	280967.74	n/a	209836.07	171666.67	98461.54	4421.77	37220.08	10358.65	4130.43	661.56	380.95	b.d	b.d	b.d
NMC21B	NMC21B - 8	core	331290.32	n/a	186065.57	163000.00	89743.59	8027.21	40463.32	17721.52	10559.01	2618.38	2452.38	824.07	153.11	1024.84
NMC21B	NMC21B - 9	core	309677.42	n/a	200000.00	168333.33	82564.10	8435.37	50193.05	31434.60	22608.70	8816.16	9095.24	3364.20	928.23	6645.96
NMC21B	NMC21B - 10	core	245161.29	n/a	186885.25	146333.33	71282.05	3496.60	17297.30	3670.89	1136.65	203.34	138.10	b.d	b.d	b.d
NMC21B	NMC21B - 11	rim	345806.45	n/a	209836.07	167333.33	94871.79	20000.00	42779.92	22151.90	13726.71	3662.95	2595.24	725.31	140.67	b.d
NMC21B	NMC21B - 12	core	300000.00	n/a	216393.44	186666.67	94358.97	3564.63	31969.11	7995.78	2546.58	334.26	204.76	b.d	b.d	b.d
NMC21B	NMC21B - 13	rim	281290.32	n/a	221311.48	180000.00	91794.87	5278.91	40424.71	16012.66	7701.86	2256.27	1690.48	546.30	99.52	962.73
NMC21B	NMC21B - 14	rim	312903.23	n/a	229508.20	180000.00	104102.56	5891.16	33976.83	10379.75	4099.38	686.63	409.52	b.d	b.d	b.d
NMC21B	NMC21B - 15	rim	364838.71	n/a	216393.44	173666.67	99487.18	17278.91	46718.15	22742.62	12950.31	3955.43	3166.67	1024.69	220.10	1055.90
NMC21B	NMC21B - 16	rim	312580.65	n/a	217213.11	175000.00	96410.26	4707.48	35057.92	9789.03	3975.16	681.06	447.62	b.d	32.54	b.d
NMC21B	NMC21B - 17	rim	242903.23	n/a	205737.70	162333.33	81025.64	4489.80	30000.00	9704.64	3478.26	600.28	304.76	b.d	b.d	b.d
NMC21B	NMC21B - 18	core	315161.29	n/a	202459.02	165166.67	86666.67	4870.75	27799.23	7236.29	2437.89	394.15	300.00	b.d	b.d	b.d
NMC21B	NMC21B - 19	rim	228709.68	n/a	190163.93	165166.67	84615.38	4040.82	31930.50	10126.58	4068.32	779.94	509.52	138.89	b.d	b.d
NMC21B	NMC21B - 20	rim	299354.84	n/a	202459.02	167666.67	85641.03	3619.05	34980.70	13227.85	6987.58	1880.22	1371.43	450.62	91.39	b.d
NMC21B	NMC21B - 21	rim	290322.58	n/a	200819.67	148833.33	89230.77	7510.20	39305.02	17236.29	8540.37	2632.31	2080.95	614.20	138.76	b.d
NMC21B	NMC21B - 22	rim	298387.10	n/a	203278.69	155166.67	87692.31	3877.55	29806.95	8945.15	4099.38	899.72	685.71	200.62	b.d	b.d
NMC21B	NMC21B - 23	core	295161.29	n/a	210655.74	160333.33	94871.79	4789.12	41505.79	18481.01	10993.79	2910.86	2680.95	737.65	170.33	1024.84
NMC21B	NMC21B - 24	rim	286129.03	n/a	181967.21	154000.00	81538.46	4707.48	41737.45	18059.07	9968.94	2701.95	2261.90	750.00	210.53	962.73
NMC21B	NMC21B - 25	core	262258.06	n/a	193442.62	149000.00	87692.31	4081.63	35598.46	10147.68	3944.10	681.06	433.33	126.54	b.d	b.d
NMC21B	NMC21B - 26	rim	318387.10	n/a	197540.98	154333.33	81538.46	4367.35	30154.44	10000.00	3788.82	1211.70	766.67	160.49	36.84	b.d
NMC21B	NMC21B - 27	rim	310645.16	n/a	200000.00	158000.00	92820.51	5306.12	47104.25	24198.31	16490.68	4749.30	3900.00	1441.36	220.10	1677.02
NMC21B	NMC21B - 28	rim	317096.77	n/a	190163.93	151666.67	82051.28	15102.04	38841.70	17215.19	9316.77	2075.21	1385.71	351.85	50.72	b.d
NMC21B	NMC21B - 29	rim	305806.45	n/a	209836.07	148166.67	97948.72	5156.46	39884.17	15780.59	5714.29	1169.92	580.95	132.72	b.d	b.d
NMC21B	NMC21B - 30	core	322451.61	n/a	204918.03	163666.67	92307.69	10884.35	37760.62	13565.40	6645.96	1685.24	1066.67	253.09	b.d	b.d
NMC21B	NMC21B - 31	rim	297419.35	n/a	206557.38	158333.33	83076.92	4394.56	36525.10	14303.80	7546.58	1935.93	1333.33	333.33	105.74	b.d
NMC21B	NMC21B - 32	rim	320000.00	n/a	184426.23	157000.00	83589.74	12925.17	35521.24	14008.44	6583.85	1448.47	942.86	259.26	32.54	b.d
NMC21B	NMC21B - 33	core	317419.35	n/a	203278.69	150500.00	85641.03	4789.12	38841.70	14915.61	7701.86	2214.48	1700.00	632.72	162.20	776.40
NMC21B	NMC21B - 34	core	310000.00	n/a	207377.05	165666.67	102564.10	5646.26	46061.78	16835.44	6832.30	1100.28	828.57	145.06	b.d	b.d
NMC21B	NMC21B - 35	core	281612.90	n/a	206557.38	179500.00	95384.62	5687.07	35752.90	11666.67	4102.48	793.87	471.43	98.77	b.d	b.d
NMC21B	NMC21B - 36	core	284838.71	n/a	213114.75	162666.67	82051.28	4285.71	32586.87	10632.91	4254.66	1086.35	838.10	148.15	42.58	b.d
NMC21B	NMC21B - 37	core	310967.74	n/a	180327.87	136000.00	81025.64	20680.27	49150.58	29324.89	23167.70	8440.11	9190.48	3549.38	952.15	5683.23
NMC21B	NMC21B - 38	rim	292258.06	n/a	195081.97	136500.00	84615.38	5374.15	49420.85	29936.71	24378.88	10362.12	10333.33	3981.48	1086.12	5310.56
NMC21B	NMC21B - 39	rim	304193.55	n/a	204098.36	144166.67	84615.38	6217.69	37876.45	16561.18	8664.60	2325.91	1576.19	719.14	84.69	465.84
NMC21B	NMC21B - 40	core	318709.68	n/a	168852.46	143500.00	75897.44	24489.80	40540.54	25949.37	18167.70	6350.97	6047.62	2592.59	765.55	4440.99
NMC21B	NMC21B - 41	rim	314516.13	n/a	204918.03	150500.00	87179.49	11156.46	40694.98	18839.66	10714.29	2980.50	1995.24	629.63	100.00	527.95
NMC21B	NMC21B - 42	rim (D)	273870.97	n/a	182786.89	155166.67	84102.56	6068.03	31737.45	11582.28	5186.34	988.86	809.52	280.86	43.54	b.d
NMC21B	NMC21B - 43	core (D)	240967.74	n/a	175409.84	126833.33	66153.85	5428.57	39613.90	20000.00	12049.69	3398.33	2366.67	608.02	111.48	745.34
NMC21B	NMC21B - 44	rim	290645.16	n/a	186065.57	146166.67	75384.62	5537.42	44633.20	23628.69	12857.14	4275.77	3523.81	1114.20	339.71	1304.35
NMC21B	NMC21B - 45	rim	281290.32	n/a	208196.72	166400.00	83589.74	5482.99	29382.24	8333.33	2422.36	502.79	295.24	b.d	b.d	b.d

Table D.28: LASS ICP-MS U–Pb isotopic data for zircon – IC machine settings for rim analyses, FC machine settings for core analyses. Sample NMC11.

sample ID	spot	instrument settings	CL	group	comment	$^{238}U/^{206}Pb$	2σ	$^{207}Pb/^{206}Pb$	2σ	$^{206}Pb/^{238}U$ Age (Ma)	2σ	$^{207}Pb/^{206}Pb$ Age (Ma)	2σ	7/6 discordance (%)	6/8 discordance (%)	U (ppm)	Pb (ppm)
NMC11c	NMC11c - 1	FC	OI	S	weak osc. Zoned fragment	2.710762	0.08817875	0.12502	0.0014	2024	58	2028	20	0.20	-0.20	n/a	n/a
NMC11c	NMC11c - 2	FC	CI	S	odd convoluted zoning in hypidioblastic grain	2.771619	0.02995929	0.1228	0.0086	1985.8	18	1996	120	0.51	-0.51	318.5	232
NMC11c	NMC11c - 3	FC	SI	S	weak sector/convoluted zoning	2.824859	0.07979827	0.1182	0.0025	1953	49	1927	38	-1.35	1.33	n/a	n/a
NMC11c	NMC11c - 4	FC	Oh	S	bright oscillatory zoned fragment	2.566735	0.05731672	0.13085	0.0014	2120.7	40	2108.6	18	-0.57	0.57	n/a	n/a
NMC11c	NMC11c - 5	FC	Ch	P	large bright core in anhedral grain, next to rim spot 1	4.05515	0.07564351	0.0936	0.0079	1421	24	1501	170	5.33	-5.63	138	969
NMC11c	NMC11c - 6	FC	Oh	S	bright oscillatory zoned fragment	2.781641	0.06344773	0.12575	0.0013	1980	39	2038.5	18	2.87	-2.95	n/a	n/a
NMC11c	NMC11c - 7	FC	Oh	S	oscillatory zoned fragment	3.079766	0.04363081	0.1091	0.0078	1813	23	1787	120	-1.45	1.43	193.2	1778
NMC11c	NMC11c - 8	FC	Oh	S	clear oscillatory zoned grain	2.78474	0.03257005	0.1254	0.0088	1978	20	2033	120	2.71	-2.78	308	2040
NMC11c	NMC11c - 9	FC	SI	S	weak sector/convoluted zoning	2.721829	0.062971	0.12718	0.0013	2017	40	2058.5	18	2.02	-2.06	n/a	n/a
NMC11c	NMC11c - 10	FC	Oh	S	large fragment, strong osc. Zoning	3.32668	0.04758724	0.1006	0.011	1694	21	1630	210	-3.93	3.78	52	828
NMC11c	NMC11c - 11	FC	Oh	S	textbook osc. Zoned grain	2.988643	0.03126196	0.1138	0.0081	1860.6	17	1858	130	-0.14	0.14	207.8	2754
NMC11c	NMC11c - 12	FC	Oh	P	bright oscillatory zoned fragment with dark overgrowth	6.081985	0.06288392	0.0731	0.0053	981.3	9.4	1021	130	3.89	-4.05	568	1056
NMC11c	NMC11c - 13	FC	Oh	S	CL-bright core	3.08642	0.04667734	0.115	0.014	1809	24	1810	230	0.06	-0.06	42.9	493
NMC11c	NMC11c - 14	FC	Ch	S	bright fragment	2.911208	0.03135799	0.1247	0.0096	1903.4	18	2029	150	6.19	-6.60	78.2	638
NMC11c	NMC11c - 15	FC	Oh	S	bright oscillatory zoned fragment with dark overgrowth	3.163556	0.03602911	0.1122	0.01	1770	18	1810	170	2.21	-2.26	70.7	424
NMC11c	NMC11c - 16	FC	OI	S	oscillatory zoned hypidiolastic grain	2.706513	0.03208819	0.12653	0.0089	2031	21	2049	120	0.88	-0.89	301	1560
NMC11c	NMC11c - 17	FC	OI	S	CL-dark osc. Zoning, next to rim spot 12	2.980626	0.040867	0.1139	0.0081	1865	22	1864	120	-0.05	0.05	342	2240
NMC11c	NMC11c - 18	FC	Oh	S	small osc. Grain	3.175611	0.03227042	0.1088	0.0077	1764.7	16	1776	130	0.64	-0.64	278	2750
NMC11c	NMC11c - 19	FC	OI	S	oscillatory zoned fragment	2.749519	0.0309954	0.1249	0.0088	2000	19	2026	130	1.28	-1.30	223	1312
NMC11c	NMC11c - 20	FC	Oh	S	clear oscillatory zoned grain	2.837684	0.03543079	0.1197	0.0089	1946	21	1947	130	0.05	-0.05	129.4	624
NMC11c	NMC11c - 21	FC	RI	S	CL-dark convoluted rim on oscillatory fragment	2.60078	0.06628777	0.12486	0.0013	2097	45	2025.9	18	-3.51	3.39	n/a	n/a
NMC11c	NMC11c - 22	FC	Oh	S	textbook osc. Zoned grain	3.08928	0.04008334	0.1137	0.0082	1808	21	1856	130	2.59	-2.65	210.6	2004
NMC11c	NMC11c - 23	FC	OI	S	weak osc. Zoned fragment	3.203075	0.07489573	0.10829	0.0012	1751	36	1769.9	20	1.07	-1.08	n/a	n/a
NMC11c	NMC11c - 24	FC	OI	D	weak osc. Zoning pattern	3.30033	0.2069514	0.1158	0.0083	1700	97	1889	130	10.01	-11.12	624	3480
NMC11c	NMC11c - 25	FC	Oh	S	elongated grain with oscillatory core and CL-dark rim	2.665245	0.06038002	0.1246	0.0016	2054	40	2021	22	-1.63	1.61	n/a	n/a
NMC11c	NMC11c - 26	FC	Oh	S	clear oscillatory zoned grain	2.800101	0.02587386	0.1239	0.0087	1968.6	16	2012	120	2.16	-2.20	421	2356
NMC11c	NMC11c - 27	FC	OI	S	oscillatory zoned grain, low CL-response	2.892682	0.06443057	0.11297	0.0014	1914	37	1847	22	-3.63	3.50	n/a	n/a
NMC11c	NMC11c - 28	FC	CI	S	CL-dark core	2.594034	0.02422444	0.12533	0.0088	2102	17	2032.5	120	-3.42	3.31	898	5760
NMC11c	NMC11c - 29	FC	SI	S	weak sector/convoluted zoning	2.658867	0.06362618	0.12521	0.0013	2058	42	2030.8	19	-1.34	1.32	n/a	n/a
NMC11c	NMC11c - 30	FC	Oh	S	oscillatory zoned grain, high CL-response	3.181674	0.07288594	0.10841	0.0012	1762	35	1771.9	20	0.56	-0.56	n/a	n/a
NMC11c	NMC11c - 31	FC	OI	S	osc. Zoned fragment	2.9036	0.03372358	0.1159	0.0084	1908	19	1891	130	-0.90	0.89	147.7	1626
NMC11c	NMC11c - 32	FC	OI	S	osc. Zoned fragment	2.706636	0.02710022	0.1264	0.0089	2026.9	17	2048	120	1.03	-1.04	312	1537
NMC11c	NMC11c - 33	FC	OI	S	weak oscillatory/convoluted zoning	2.733734	0.08229633	0.124	0.0016	2009	52	2013	23	0.20	-0.20	n/a	n/a
NMC11c	NMC11c - 34	FC	CI	S	odd convoluted zoning	2.699055	0.02768262	0.12361	0.0086	2031.9	18	2008	120	-1.19	1.18	650	2335
NMC11c	NMC11c - 35	FC	Oh	S	clear oscillatory zoned grain	3.123048	0.034137	0.1136	0.0085	1790.9	17	1852	130	3.30	-3.41	173.5	1400
NMC11c	NMC11c - 36	FC	Oh	S	clear oscillatory zoned grain	3.150599	0.06154288	0.1109	0.0079	1776	30	1813	130	2.04	-2.08	244	2220
NMC11c	NMC11c - 37	FC	Oh	S	bright oscillatory zoned fragment	2.929974	0.06867796	0.1163	0.0015	1893	38	1899	23	0.32	-0.32	n/a	n/a
NMC11c	NMC11c - 38	FC	OI	S	angular oscillatory grain	3.259452	0.0339969	0.1101	0.0079	1724.7	16	1798	130	4.08	-4.25	186	1070
NMC11	NMC11 - 1	IC	CI	D	odd convoluted zoning, fluid alteration?	2.44858	0.06595097	0.12311	0.0013	2207	53	2060.9	19	-10.30	9.34	n/a	n/a
NMC11	NMC11 - 2	IC	Oh	S	textbook osc. Zoned grain	3.417635	0.08526567	0.10835	0.0076	1654	37	1770	130	6.55	-7.01	530	3870
NMC11	NMC11 - 3	IC	OI	S	weak oscillatory/convoluted zoning	2.523341	0.05666852	0.12481	0.0013	2152.1	41	2025.2	18	-6.27	5.90	n/a	n/a
NMC11	NMC11 - 4	IC	CI	S	CL-dark, unzoned grain	2.604167	0.05832248	0.12579	0.0014	2095	40	2039	20	-2.75	2.67	n/a	n/a
NMC11	NMC11 - 5	IC	Oh	S	textbook osc. Zoned fragment	2.558199	0.06544382	0.12379	0.0013	2127	49	2010.6	19	-5.79	5.47	n/a	n/a
NMC11	NMC11 - 6	IC	OI	S	weak osc. Zoning pattern	2.767783	0.03370674	0.1235	0.0089	1988	21	2005	130	0.85	-0.86	232.5	1285
NMC11	NMC11 - 7	IC	RI	P	convoluted CL-dark rim on large anhedral CL-bright core	5.440992	0.121378	0.07311	0.00081	1087.6	22	1016	22	-7.05	6.58	n/a	n/a
NMC11	NMC11 - 8	IC	OI	S	weak osc. Zoned grain	2.699055	0.02986809	0.1276	0.0094	2032	19	2061	130	1.41	-1.43	144.3	647
NMC11	NMC11 - 9	IC	Oh	S	clear oscillatory zoned grain	3.287311	0.07348361	0.10918	0.0011	1712.2	34	1784.9	19	4.07	-4.25	n/a	n/a
NMC11	NMC11 - 10	IC	CI	S	CL-dark, unzoned grain	2.62743	0.0600595	0.12233	0.0014	2079	41	1989	21	-4.52	4.33	n/a	n/a
NMC11	NMC11 - 11	IC	Oh	S	ovoidal oscillatory zoned grain	3.008424	0.07964539	0.10848	0.0012	1850	42	1773	20	-4.34	4.16	n/a	n/a
NMC11	NMC11 - 12	IC	OI	S	oscillatory zoned hypidiolastic grain	3.064664	0.03099415	0.11064	0.0077	1820.5	16	1809.1	130	-0.63	0.63	792	6870
NMC11	NMC11 - 13	IC	Oh	P	elongated, hypidiomorphic grain with bright osc. zoning	4.96771	0.1381976	0.07743	0.00095	1182	30	1131	24	-4.51	4.31	n/a	n/a
NMC11	NMC11 - 14	IC	CI	S	CL-dark, weak convoluted zoned grain	2.57334	0.06992313	0.1245	0.0013	2116	43	2020.9	18	-4.71	4.49	n/a	n/a
NMC11	NMC11 - 15	IC	CI	D	odd convoluted zoning, fluid alteration? Mixed ablation	9.23361	0.2216749	0.06323	0.00072	662.6	15	715	24	7.33	-7.91	n/a	n/a
NMC11	NMC11 - 16	IC	Oh	S	CL-bright oscillatory zoned core next to rim spot 2	3.116236	0.04078588	0.1174	0.0094	1794	20	1933	140	7.19	-7.75	204	2000
NMC11	NMC11 - 17	IC	Oh	S	rounded fragment of oscillatory zoned grain	3.400204	0.09017882	0.10515	0.0013	1662	39	1720	25	3.37	-3.49	n/a	n/a
NMC11	NMC11 - 18	IC	OI	S	weak osc. Zoned grain	3.072197	0.03775357	0.1126	0.0086	1816	19	1833	140	0.93	-0.94	115	1260
NMC11	NMC11 - 19	IC	Ch	S	bright core	3.068426	0.039544	0.1154	0.0097	1818	20	1869	160	2.73	-2.81	51.4	806
NMC11	NMC11 - 20	IC	Ch	D	odd convoluted zoning	5.62968	0.05704793	0.0789	0.0061	1054	10	1179	130	10.60	-11.86	263.6	323
NMC11	NMC11 - 21	IC	Oh	P	clear oscillatory zoned grain	5.91681	0.06301555	0.0707	0.0058	1006.6	9.8	928	180	-8.47	7.81	261.3	355
NMC11	NMC11 - 22	IC	SI	S	odd sector/convoluted zoning pattern	2.707626	0.06452441	0.1247	0.0018	2026	41	2023	25	-0.15	0.15	n/a	n/a
NMC11	NMC11 - 23	IC	CI	S	CL-dark core, weak oscillatory overgrowth	3.512469	0.07402464	0.10689	0.0075	1615	30	1746	130	7.50	-8.11	820	3400
NMC11	NMC11 - 24	IC	OI	S	clear oscillatory zoned grain	2.841716	0.03068634	0.1257	0.0089	1943.5	18	2037	130	4.59	-4.81	232	496
NMC11	NMC11 - 25	IC	Oh	S	CL-bright oscillatory zoned grain	3.029385	0.07066424	0.11055	0.0013	1839	37	1807	22	-1.77	1.74	n/a	n/a
NMC11	NMC11 - 26	IC	OI	S	CL-dark, weak oscillatory zoning	2.621232	0.05977646	0.12457	0.0013	2083	41	2021.8	18	-3.03	2.94	n/a	n/a
NMC11	NMC11 - 27	IC	CI	S	odd convoluted zoning	3.148615	0.06047402	0.1184	0.0086	1778	30	1928	130	7.78	-8.44	222	636
NMC11	NMC11 - 28	IC	OI	S	weak osc. Zoning pattern	2.777778	0.0316358	0.1267	0.009	1982	19	2051	130	3.36	-3.48	213.8	826
NMC11	NMC11 - 29	IC	OI	S	weak osc. Zoned fragment	2.610966	0.06067258	0.12517	0.0014	2090	41	2030.2	19	-2.95	2.86	n/a	n/a

Table D.29: LASS ICP-MS chondrite-normalised REE data for zircon (ppm) – IC machine settings for rim analyses, FC machine settings for core analyses. Sample NMC11.

sample ID	spot	instrument settings	CL	group	La	Ce	Pr	Nd	Sm	Eu	Gd	Tb	Dy	Ho	Er	Tm	Yb	Lu
NMC11	NMC11 - 2	IC	Oh	P	0.17	53.59	b.d	27.50	13.33	10.75	40.54	80.80	134.16	253.48	452.38	679.01	1028.71	1664.60
NMC11	NMC11 - 3	IC	Ol	S	b.d	25.37	99.18	86.67	23.08	13.88	80.31	144.30	249.69	380.22	643.81	833.33	1157.89	1559.01
NMC11	NMC11 - 4	IC	Cl	S	b.d	82.92	188.52	115.00	67.18	36.73	119.69	261.60	422.98	671.31	1047.62	1305.56	1870.81	2664.60
NMC11	NMC11 - 5	IC	Oh	S	b.d	19.68	55.74	70.00	56.41	b.d	188.42	339.66	546.58	884.40	1295.24	1518.52	2066.99	2618.01
NMC11	NMC11 - 6	IC	Ol	S	0.16	57.55	b.d	13.67	15.90	b.d	53.67	129.32	235.09	380.22	705.71	876.54	1401.91	1869.57
NMC11	NMC11 - 7	IC	Rl	P	b.d	34.90	b.d	31.67	24.10	b.d	80.70	240.51	407.14	690.81	1180.00	1472.22	2277.51	2975.16
NMC11	NMC11 - 8	IC	Ol	S	b.d	21.66	b.d	11.50	5.64	b.d	45.56	110.34	161.18	281.34	476.67	611.11	928.71	1223.60
NMC11	NMC11 - 9	IC	Oh	S	b.d	9.80	b.d	b.d	b.d	b.d	15.83	58.02	108.70	192.20	307.62	435.19	641.15	866.46
NMC11	NMC11 - 10	IC	Cl	S	0.19	42.95	b.d	40.00	46.67	35.78	155.21	317.30	459.01	746.52	1266.67	1456.79	2186.60	2928.57
NMC11	NMC11 - 11	IC	Oh	S	b.d	23.89	59.02	70.00	70.77	b.d	203.47	373.42	593.17	839.83	1290.48	1527.78	2019.14	2577.64
NMC11	NMC11 - 12	IC	Ol	S	b.d	44.80	b.d	b.d	10.77	b.d	48.65	115.19	225.78	384.40	770.48	1027.78	1607.66	2304.35
NMC11	NMC11 - 13	IC	Oh	S	b.d	10.64	76.23	21.67	13.85	b.d	27.80	66.46	128.88	197.77	361.90	435.19	727.75	1003.11
NMC11	NMC11 - 14	IC	Cl	S	b.d	36.88	b.d	81.67	68.72	6.12	166.02	354.43	538.20	732.59	1173.81	1342.59	1956.94	2431.68
NMC11	NMC11 - 16	IC	Oh	P	0.18	55.45	b.d	14.83	22.56	7.76	67.95	156.33	247.52	381.62	640.00	901.23	1282.30	1608.70
NMC11	NMC11 - 17	IC	Oh	S	0.15	55.82	b.d	36.67	30.77	36.87	94.59	168.57	304.04	490.25	814.76	1098.77	1717.70	2360.25
NMC11	NMC11 - 18	IC	Ol	S	0.04	7.18	b.d	b.d	8.21	b.d	39.00	78.06	140.68	215.88	377.14	509.26	754.07	944.10
NMC11	NMC11 - 19	IC	Ch	S	b.d	21.66	b.d	b.d	b.d	b.d	56.76	126.16	262.42	408.08	726.67	969.14	1421.05	1931.68
NMC11	NMC11 - 21	IC	Oh	P	0.15	27.85	b.d	12.83	15.38	b.d	77.99	221.52	318.94	481.89	868.10	1111.11	1550.24	2059.01
NMC11	NMC11 - 22	IC	Sl	S	b.d	14.23	59.84	26.67	b.d	b.d	21.62	89.24	153.11	268.80	517.62	771.60	1220.10	1748.45
NMC11	NMC11 - 23	IC	Cl	P	0.10	9.90	b.d	10.50	10.77	b.d	50.58	120.46	169.57	259.05	452.38	508.64	791.39	1024.84
NMC11	NMC11 - 24	IC	Ol	S	b.d	14.48	b.d	60.00	30.77	b.d	68.34	175.11	274.84	431.75	732.38	895.06	1282.30	1754.66
NMC11	NMC11 - 25	IC	Oh	S	0.06	29.70	b.d	b.d	b.d	8.98	18.53	55.06	102.17	157.38	315.24	487.65	825.84	1319.88
NMC11	NMC11 - 26	IC	Ol	S	b.d	28.47	311.48	135.00	57.44	38.10	164.86	320.68	532.61	845.40	1342.86	1632.72	2358.85	2996.89
NMC11	NMC11 - 27	IC	Cl	P	b.d	18.44	128.69	100.00	91.79	4.90	241.70	481.01	720.19	1079.39	1666.67	1746.91	2535.89	3226.71
NMC11	NMC11 - 28	IC	Ol	S	b.d	13.86	b.d	24.83	16.41	6.53	80.70	177.43	254.66	401.11	647.62	854.94	1196.17	1704.97
NMC11	NMC11 - 29	IC	Ol	S	b.d	42.57	672.13	323.33	32.31	220.41	57.53	98.10	175.78	298.05	480.95	623.46	933.01	1301.24
NMC11c	NMC11c - 1	FC	Ol	S	b.d	73.64	4.51	8.17	35.38	26.67	104.63	163.08	272.05	508.36	830.95	1222.22	1961.72	2854.04
NMC11c	NMC11c - 2	FC	Cl	S	b.d	75.99	31.56	28.33	48.72	17.55	101.54	173.00	260.87	434.54	757.14	929.01	1459.33	2232.92
NMC11c	NMC11c - 3	FC	Sl	S	b.d	67.20	35.25	29.00	51.28	44.90	65.25	102.74	173.60	308.50	557.62	845.68	1397.13	2046.58
NMC11c	NMC11c - 4	FC	Oh	S	b.d	20.05	1.88	8.00	61.03	18.23	158.30	265.19	437.89	706.13	1119.05	1413.58	2066.99	2763.98
NMC11c	NMC11c - 5	FC	Ch	P	b.d	35.77	8.77	18.00	75.90	2.99	235.14	403.80	637.89	1062.67	1536.67	1944.44	2626.79	3344.72
NMC11c	NMC11c - 6	FC	Oh	S	b.d	15.76	3.77	10.17	59.49	50.34	189.19	267.93	394.41	625.35	900.00	1074.07	1540.67	1944.10
NMC11c	NMC11c - 7	FC	Oh	S	0.11	7.46	0.95	2.48	7.18	b.d	42.86	86.08	137.58	240.11	397.62	485.19	753.11	984.47
NMC11c	NMC11c - 8	FC	Oh	S	b.d	1.37	b.d	b.d	11.08	b.d	57.92	120.46	176.40	231.20	276.67	265.43	366.51	462.73
NMC11c	NMC11c - 9	FC	Sl	S	b.d	15.35	1.48	b.d	17.44	b.d	61.39	111.60	179.81	345.40	511.90	697.53	943.54	1257.76
NMC11c	NMC11c - 10	FC	Oh	S	b.d	38.00	4.02	10.50	72.82	46.67	219.31	398.73	636.34	1086.35	1647.62	2104.94	3133.97	4074.53
NMC11c	NMC11c - 11	FC	Oh	S	b.d	77.23	68.85	52.00	73.85	38.23	200.77	385.44	627.33	1217.27	1828.57	2435.19	3454.55	4562.11
NMC11c	NMC11c - 12	FC	Oh	S	b.d	16.58	2.20	4.17	21.54	14.69	82.24	148.95	233.85	399.72	665.71	891.98	1311.00	1819.88
NMC11c	NMC11c - 13	FC	Oh	S	b.d	22.03	27.87	25.33	49.23	51.70	123.17	238.82	360.25	603.06	933.33	1209.88	1708.13	2260.87
NMC11c	NMC11c - 14	FC	Ch	P	0.35	39.36	2.70	8.75	54.36	41.90	150.58	236.29	357.45	591.92	879.52	1080.25	1617.22	2024.84
NMC11c	NMC11c - 15	FC	Oh	S	b.d	12.71	4.34	6.67	38.46	4.90	98.46	166.46	259.32	428.97	645.71	811.73	1125.36	1500.00
NMC11c	NMC11c - 16	FC	Ol	S	b.d	3.09	2.21	5.33	45.13	4.22	134.36	259.28	419.25	733.98	1095.24	1441.36	1995.22	2546.58
NMC11c	NMC11c - 17	FC	Ol	S	b.d	59.41	11.39	9.50	14.87	46.26	60.62	118.57	207.76	405.29	672.86	993.83	1689.00	2381.99
NMC11c	NMC11c - 18	FC	Oh	S	0.19	8.85	2.21	6.50	68.21	10.48	239.77	453.59	729.81	1242.34	1914.29	2336.42	3320.57	4270.19
NMC11c	NMC11c - 19	FC	Ol	S	b.d	11.57	0.97	3.78	22.05	19.46	71.81	135.44	222.98	392.76	602.38	790.12	1215.31	1708.07
NMC11c	NMC11c - 20	FC	Oh	S	b.d	7.38	b.d	b.d	7.44	b.d	27.41	62.66	138.82	345.40	719.05	1172.84	1980.86	3232.92
NMC11c	NMC11c - 21	FC	Rl	S	b.d	63.24	1.39	1.87	22.56	10.61	81.47	153.16	289.75	572.42	933.81	1345.68	2172.25	3108.70
NMC11c	NMC11c - 22	FC	Oh	S	b.d	68.69	1.53	4.10	41.54	36.87	139.38	253.16	413.04	781.34	1309.52	1851.85	2885.17	4149.07
NMC11c	NMC11c - 23	FC	Ol	S	b.d	15.10	4.02	5.67	36.41	10.48	123.17	217.30	331.99	565.46	842.86	1040.12	1421.05	1767.08
NMC11c	NMC11c - 25	FC	Oh	S	b.d	12.12	3.28	5.67	24.62	11.97	79.54	128.06	198.76	339.83	522.38	694.44	1047.85	1434.78
NMC11c	NMC11c - 26	FC	Oh	S	b.d	12.55	1.49	5.83	27.69	12.24	86.49	173.63	256.21	448.47	685.24	888.89	1255.98	1664.60
NMC11c	NMC11c - 27	FC	Ol	S	0.06	80.20	b.d	3.87	41.54	19.32	133.98	262.87	455.28	856.55	1388.57	1901.23	3033.49	4052.80
NMC11c	NMC11c - 28	FC	Cl	S	b.d	9.91	b.d	1.42	9.44	b.d	36.68	76.37	120.19	212.26	343.33	454.01	668.42	900.62
NMC11c	NMC11c - 29	FC	Sl	S	b.d	16.21	1.53	1.35	19.23	b.d	71.81	132.49	205.90	383.70	586.19	750.00	1116.75	1428.57
NMC11c	NMC11c - 30	FC	Oh	S	0.28	4.58	b.d	2.38	19.49	7.76	90.73	181.01	348.45	586.35	972.86	1308.64	1947.37	2633.54
NMC11c	NMC11c - 31	FC	Ol	S	b.d	29.83	2.46	4.33	21.54	26.67	79.54	122.36	236.02	422.01	714.29	1000.00	1598.09	2279.50
NMC11c	NMC11c - 32	FC	Ol	S	0.10	55.94	3.61	9.33	74.36	72.24	228.96	373.42	556.83	920.61	1352.38	1657.41	2354.07	2940.99
NMC11c	NMC11c - 33	FC	Ol	S	b.d	72.15	10.49	8.17	22.56	23.54	69.11	136.29	233.23	444.29	761.90	1129.63	1956.94	2906.83
NMC11c	NMC11c - 34	FC	Cl	S	0.62	36.76	2.47	6.53	38.46	21.77	116.99	187.13	285.71	506.96	815.24	1132.72	1765.55	2378.88
NMC11c	NMC11c - 35	FC	Oh	S	b.d	40.22	3.85	9.33	55.90	23.13	139.77	249.58	382.92	664.35	1006.19	1339.51	1976.08	2636.65
NMC11c	NMC11c - 36	FC	Oh	S	b.d	11.55	5.25	14.17	95.38	55.65	267.57	418.78	609.01	1018.11	1419.05	1817.90	2564.59	3276.40
NMC11c	NMC11c - 37	FC	Oh	S	b.d	7.30	4.84	8.67	77.44	19.32	176.45	278.48	375.78	594.71	823.81	969.14	1392.34	1720.50
NMC11c	NMC11c - 38	FC	Ol	S	b.d	76.61	4.18	3.50	18.97	8.30	62.55	147.26	263.98	526.46	855.24	1212.96	1842.11	2381.99

Table D.30: LASS ICP-MS U–Pb isotopic data for monazite. Sample NMC11.

sample ID	spot	location	$^{238}U/^{206}Pb$	2σ	$^{207}Pb/^{206}Pb$	2σ	$^{206}Pb/^{238}U$ Age (Ma)	2σ	$^{207}Pb/^{206}Pb$ Age (Ma)	2σ	7/6 discordance (%)	6/8 discordance (%)	U (ppm)	Pb (ppm)
NMC11	NM11 - 3		5.027652	0.1238587	0.0779	0.001	1170	26	1143	25	1690	3400		

Table D.31: LASS ICP-MS U–Pb isotopic data for monazite. Sample NMC16.

sample ID	spot	location	$^{238}U/^{206}Pb$	2σ	$^{207}Pb/^{206}Pb$	2σ	$^{206}Pb/^{238}U$ Age (Ma)	2σ	$^{207}Pb/^{206}Pb$ Age (Ma)	2σ	7/6 discordance (%)	6/8 discordance (%)	U (ppm)	Th (ppm)	Pb (ppm)
NMC16	NMC16 - 1	rim	5.847953	0.1709928	0.072	0.0012	1017	27	982	33	-3.56	3.44	1520	55300	3470
NMC16	NMC16 - 2	rim	5.740528	0.1482915	0.0749	0.001	1035	24	1063	27	2.63	-2.71	1900	60200	3910
NMC16	NMC16 - 3	rim	5.803831	0.1583169	0.07311	0.00095	1025	26	1015	27	-0.99	0.98	1540	49700	3140
NMC16	NMC16 - 4	rim	5.938242	0.1516297	0.0749	0.0011	1003	24	1063	30	5.64	-5.98	1530	50200	3190
NMC16	NMC16 - 5	rim	5.910165	0.1746503	0.0756	0.0012	1008	27	1083	31	6.93	-7.44	1490	52100	3330
NMC16	NMC16 - 6	rim	5.827506	0.1562152	0.07223	0.00072	1021	25	991	20	-3.03	2.94	1420	43000	2720
NMC16	NMC16 - 7	rim	5.824112	0.1696014	0.07324	0.00097	1021	28	991	27	-3.03	2.94	1400	47700	3080

Table D.32: LASS ICP-MS chondrite-normalised REE data for monazite (ppm). Sample NMC16.

sample ID	spot	location	La	Ce	Pr	Nd	Sm	Eu	Gd	Tb	Dy	Ho	Er	Tm	Yb	Lu
NMC16	NMC16 - 1	rim	347741.94	n/a	213934.43	178333.33	48717.95	4884.35	10154.44	2088.61	608.70	82.17	b.d	b.d	b.d	b.d
NMC16	NMC16 - 2	rim	339032.26	n/a	224590.16	173000.00	71794.87	5210.88	22779.92	3755.27	773.29	93.31	b.d	b.d	b.d	b.d
NMC16	NMC16 - 3	rim	351612.90	n/a	224590.16	171000.00	58974.36	4979.59	11003.86	2046.41	605.59	107.24	b.d	b.d	b.d	b.d
NMC16	NMC16 - 4	rim	340645.16	n/a	227868.85	180000.00	60512.82	3850.34	12046.33	2236.29	658.39	115.60	61.90	b.d	b.d	b.d
NMC16	NMC16 - 5	rim	341935.48	n/a	241803.28	190333.33	66153.85	4666.67	11196.91	2257.38	698.76	89.14	76.19	b.d	b.d	b.d
NMC16	NMC16 - 6	rim	338709.68	n/a	218852.46	160666.67	63589.74	4897.96	10965.25	2426.16	568.32	76.60	b.d	b.d	b.d	b.d
NMC16	NMC16 - 7	rim	312580.65	n/a	214754.10	162500.00	57435.90	3714.29	10308.88	2362.87	586.96	39.00	b.d	b.d	b.d	b.d

Appendix E

Evolution of a_{H_2O} during granulite metamorphism

Figure E.1 shows an isobaric T–X section for a representative samples of migmatitic aluminous metapelite (NMC89) from Hytkoras. The diagram was constructed at 5.5 kbar, tailored for the roughly isobaric evolution reaching thermal maximum at this pressure (see section 7.2). The employed bulk composition is listed in Table E.1. As described above, the aluminous metapelite is inferred to have experienced extensive melt production and -extraction. To adequately reproduce these circumstances, the compositional axis on Figure E.1a spans from the melt-integrated composition (white isochemical line) with additional H_2O (10 mol. %) to guarantee subsolidus fluid saturation at the left compositional extreme ($X = 0$) to the residual composition (black isochemical line) producing the inferred peak assemblage. The right compositional extreme is the anhydrous residuum composition ($X = 1$). Therefore, as the bulk rock composition changes from the left to the right compositional extreme, only H_2O is removed from the bulk between X = 0 to X = 0.3 (i.e. wet solidus composition, white isochemical line) and between X = 0.87 (i.e. residuum composition, black isochemical line) to X = 1. In the intermitted compositional space (X = 0.3 to X = 0.87) components of granitic melt are removed, including H_2O, to reverse melt integration and to produce the residuum composition from the melt-integrated wet solidus composition.

Within the paradigm of conjugate variables (Powell *et al.*, 2005), a_{H_2O} is the active or passive variable of the absolute amount of H_2O, $M(H_2O)$, during sub- and suprasolidus metamorphism, respectively. The generally-accepted assumption for prograde subsolidus evolution involves progressive fluid loss from hydrous assemblages via dehydration reactions, that is subsequently expelled (e.g. Connolly, 1997, 2010; Walther and Orville, 1982; Guiraud *et al.*, 2001; Schorn, 2018). In this case the rocks evolve along the fluid saturation line (broken part of path on Fig. E.1), implying a fixed $a_{H_2O} = 1$. As fluid is progressively lost, $M(H_2O)$ decreases, involving a_{H_2O} (at a fixed value of unity) as effectively the controlling variable (Powell *et al.*, 2005). During suprasolidus metamorphism the system is typically H_2O undersaturated; making $M(H_2O)$ the controlling factor with $a_{H_2O} < 1$ as passive variable

(Powell *et al.*, 2005).

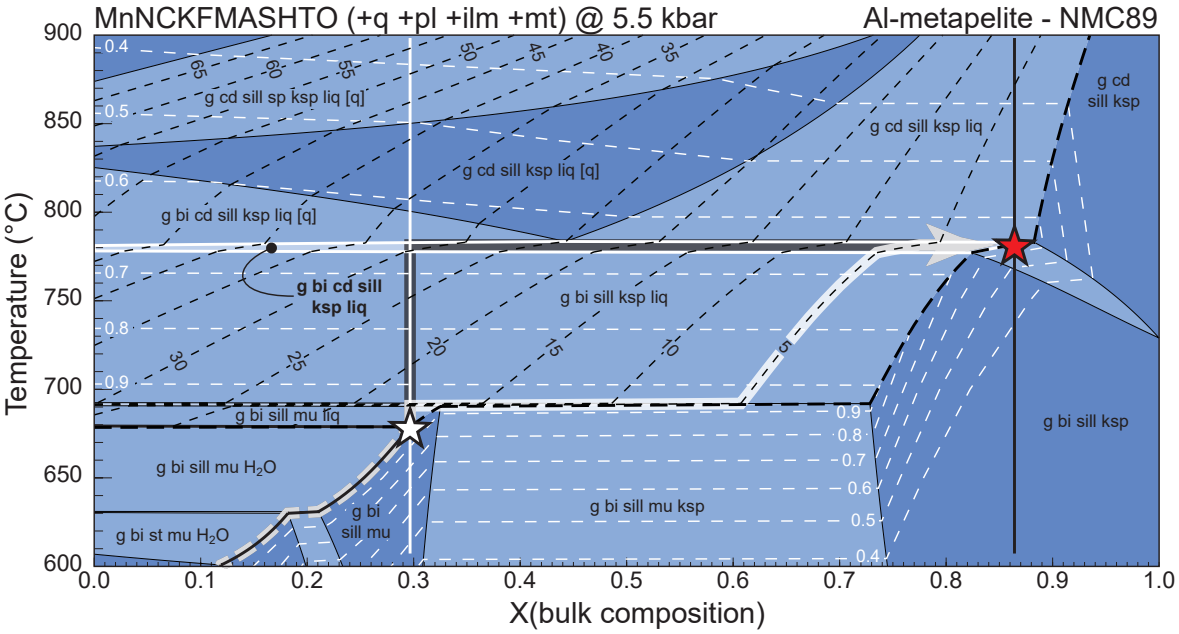


Figure E.1: T–X phase diagrams for aluminous metapelite (sample NMC89), calculated at 5.5 kbar. The solidus is highlighted with a bold dashed line, fluid-saturated assemblages are delimited from undersaturated ones with a bold line (the fluid saturation line). Inferred peak assemblages are labelled in bold, the respective fields are highlighted with a bold white border. The red star indicates approximate peak conditions in terms of temperature and bulk composition; the white star highlights the intersection of the fluid saturation line and the solidus (i.e. the wet solidus). The diagram is contoured for melt modes (∼vol. %; thin dashed lines) and a_{H_2O} (white dashed lines).

For isobaric heating of the aluminous metapelite at 5.5 kbar, starting at 600 °C and fully H_2O-saturated conditions (Fig. E.1a), the rock is expected to be fully fluid saturated and to dehydrate continuously during heating (broken path) until fluid-present melting commences at ∼680 °C (white star). Two generic suprasolidus paths are drawn on the diagram. The grey path involves a closed-system evolution at initially fixed composition at the wet solidus (white isochemical line) with continuous but episodic melt production until the peak assemblage field is reached. Under these conditions ∼30 vol. % melt is potentially generated. In order to produce the highly residual thin section assemblage of garnet–biotite–cordierite–sillimanite–plagioclase–K-feldspar–quartz–ilmenite–magnetite, all melt is removed at once at the inferred peak temperature of ∼780 °C. Thereby the residual composition of the pelitic granulite is produced (black isochemical line), as symbolised by the grey arrow terminating at the inferred P–T–X conditions (red star). The white path describes a simplified open-system case, with melt being continuously removed once a threshold of 5 vol. % is reached (cf. Yakymchuk and Brown, 2014). Therefore the path tracks the respective contour line for melt volume. The peak conditions are attained following a discontinuous heating path, with the final 5 vol. % melt removed at once to produce the peak assemblage at the residuum solidus (red star).

Interestingly, a_{H_2O} appears to be independent of $M(H_2O)$ during the entire solidus-to-peak evolution, as demonstrated by the isothermal lines of constant a_{H_2O} (white dashed lines). Moreover, during heating a_{H_2O} varies exclusively with temperature and is path-independent, regardless of closed- or open system behaviour. Hence, without regard of the exact heating path, a_{H_2O} progressively decreases from unity at the wet solidus (white star) to $a_{H_2O} \approx 0.65$ at peak conditions (red star). It appears that this observation applies to assemblages involving two hydrous phases (e.g. biotite–melt, biotite–muscovite) and K-feldspar, being effective buffers of a_{H_2O} for variable $M(H_2O)$.

Table E.1: Bulk composition used in thermodynamic calculations (mol. %).

sample	locality	lithology	comment	H_2O	SiO_2	Al_2O_3	CaO	MgO	FeO	K_2O	Na_2O	TiO_2	MnO	O	XFe^{3+}	Figure
NMC89	Hytkoras	aluminous metapelite	residuum	1.60	57.07	16.58	0.76	3.82	10.36	3.75	2.21	1.28	0.25	2.33	0.45	E.1
NMC89	Hytkoras	aluminous metapelite	X = 0	10.00	57.50	13.41	0.60	2.73	7.41	3.34	2.26	0.91	0.18	1.66	0.45	E.1
NMC89	Hytkoras	aluminous metapelite	X = 1	0.00	58.00	16.85	0.77	3.88	10.53	3.81	2.24	1.30	0.25	2.37	0.45	E.1

Appendix F

Acknowledgements

Thanks to...

Johann Diener for his patience and guidance throughout countless discussions – be it in the office, on conferences or at braais in the field. Paul Macey for sharing his extensive knowledge on Namaqualand and showing me remote corners of Bushmanland. Roger Powell for making THERMOCALC tell us what we need. Kurt Stüwe for being my idol. Dave Waters for sharing his insights on Hytkoras. Richard Spiess for support. Rene and Dave for making a disproportionate amount of thin sections. Christel and Nic for support at the probe. Moritz for helping me out with zircon sample preparation and for letting me crash at his place in Stellies. Mareli Grobbelar for helping with zircon preparation and polishing. Brad McDonald and Noreen Evans for lasering at Curtin and helping understand the data. Chris Clark for help and discussions on geochron. Mike and Kate for having me in Perth and explaining even the most basic principles of geochronology. Bogdana for her never ending patience and for always being there for me. Martin for entertaining the entire office – and for not having accidentally killed himself (yet). Lorena for enduring both Martin and me. Chris Harris for his wise support in the office and on hikes with Ben (dog). Ben (human) and Toni for sharing adventures with me. Susi and Paul Whitehead for providing a home away from home. Matt for his inspiring awesomeness. Luke, Brady and Quinten for sharing a genuinely good time. Giacomo, Dominik and Philip for our endless discussions on petrology and for being my friends. Shane for sharing my passion for Namaqualand. Christelle for managing our flat – so that we would never run out of toilet paper. My parents, Tine and Roland, and my brother Jakob for making studying as easy as possible.

Without you and many other great people nothing during these awesome three years of Ph.D. would have worked out.



Figure F.1: Some impressions from Namaqualand. Photographs courtesy of Martin Giger.